VIBRATION OF PIEZOELECTRIC CRYSTAL PLATES

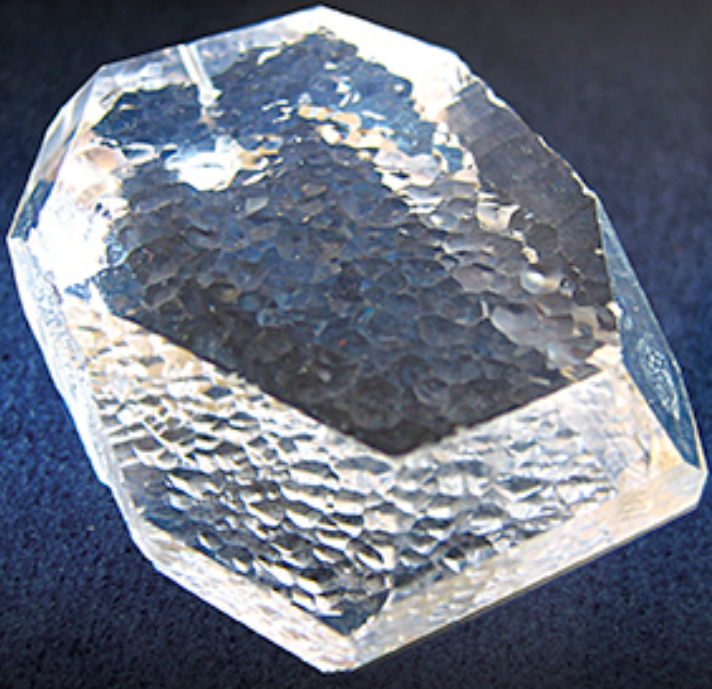

YANG Jiashi

World Scientific

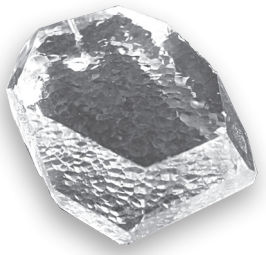

VIBRATION OF PIEZOELECTRIC CRYSTAL PLATES

This page intentionally left blank

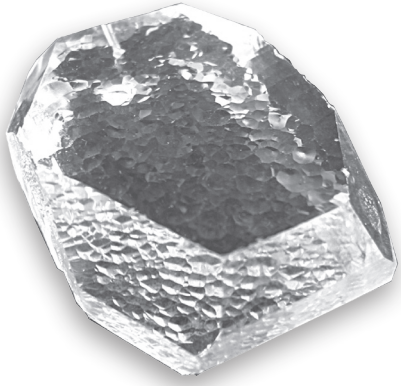

VIBRATION OF PIEZOELECTRIC CRYSTAL PLATES

YANG Jiashi
University of Nebraska-Lincoln, USA

World Scientific
NEW JERSEY • LONDON • SINGAPORE • BEIJING • SHANGHAI • HONG KONG • TAIPEI • CHENNAI

Published by

World Scientific Publishing Co. Pte. Ltd.

5 Toh Tuck Link, Singapore 596224

USA office: 27 Warren Street, Suite 401-402, Hackensack, NJ 07601

UK office: 57 Shelton Street, Covent Garden, London WC2H 9HE

Library of Congress Cataloging-in-Publication Data

Yang, Jiashi, 1956–

Vibration of piezoelectric crystal plates / Yang Jiashi.

pages cm

Includes bibliographical references and index.

ISBN 978-9814449847

1. Piezoelectric devices. 2. Piezoelectricity. 3. Plates (Engineering)--Vibration.
4. Quartz crystals--Electric properties. I. Title.

TK7872.P54Y364 2013

537'.244--dc23

2013000658

British Library Cataloguing-in-Publication Data

A catalogue record for this book is available from the British Library.

Copyright © 2013 by World Scientific Publishing Co. Pte. Ltd.

All rights reserved. This book, or parts thereof, may not be reproduced in any form or by any means, electronic or mechanical, including photocopying, recording or any information storage and retrieval system now known or to be invented, without written permission from the Publisher.

For photocopying of material in this volume, please pay a copying fee through the Copyright Clearance Center, Inc., 222 Rosewood Drive, Danvers, MA 01923, USA. In this case permission to photocopy is not required from the publisher.

In-house Editor: Amanda Yun

Printed in Singapore

Preface

Piezoelectric crystals exhibit electromechanical coupling. They experience mechanical deformations when placed in an electric field, and become electrically polarized under mechanical loads. These materials have been used for a long time to make various electromechanical devices. Examples include transducers for converting electrical energy into mechanical energy and vice versa, resonators and filters for frequency control and selection for applications in telecommunication and precise timing, and acoustic wave sensors.

For piezoelectric devices, dynamic problems are frequently encountered. This is because a lot of piezoelectric devices are resonant devices operating with a particular frequency and the corresponding mode. These devices are called acoustic wave devices. Both surface acoustic waves (SAWs) and bulk acoustic waves (BAWs) are used. In the analysis of resonant piezoelectric devices, usually vibration characteristics like frequency and wave speed are of primary interest rather than stress and strain for strength and failure consideration. How the basic vibration characteristics vary under the influence of other effects like temperature change, stress, additional surface mass or contact with a fluid is the foundation of many acoustic wave sensors.

Many acoustic wave devices are based on BAWs of a crystal plate. A rather unique feature of these devices is that they often operate with the so-called high-frequency modes. For plates, high-frequency modes, e.g., thickness-shear (TSh) and thickness-stretch (TSt), are modes whose frequencies are determined by the plate thickness — the smallest dimension. This is in contrast to the so-called low-frequency modes of extension and flexure in traditional structural engineering whose frequencies depend strongly on the length and/or width of the plate in addition to its thickness. Another characteristic of the high-frequency plate modes is that for long waves their frequencies do not go to zero but have finite cutoff frequencies. This has implications in certain useful behaviors of high-frequency modes such as energy trapping which is of fundamental importance in device mounting.

Quartz is one of the most widely used materials for resonant piezoelectric devices. It is a material with weak piezoelectric coupling. For frequency analysis of a quartz plate, the small piezoelectric coupling can often be neglected and an elastic analysis is sufficient. Such an analysis is relatively simple and can usually exhibit the basic frequency behavior of a device. Generalization from an elastic solution to include piezoelectric coupling is not always possible analytically. An electrically forced vibration analysis including piezoelectric coupling is necessary when the electrical admittance (or impedance) of a device is wanted. Piezoelectric coupling also causes a stiffening effect that affects the resonant frequencies of a crystal plate. This needs to be considered in certain situations. Free vibration frequency analysis and electrically forced vibration analysis for admittance together provide a complete simulation of a crystal device as a circuit element.

Due to the anisotropy of piezoelectric crystals and their electromechanical coupling, analyzing piezoelectric devices using the three-dimensional (3-D) theories of elasticity or piezoelectricity usually presents considerable mathematical challenges. Only a few relatively simple problems can find exact solutions from the 3-D equations. In general, various approximations need to be made.

This book focuses on vibrations of crystal plates for applications in acoustic wave devices. The 3-D theories of anisotropic elasticity and piezoelectricity are used. Most of the results are for plates of monoclinic crystals which include the most widely used AT-cut quartz plates as a special case.

A brief summary of the basic theory of piezoelectricity relevant to crystal vibration is given in Chapter 1. Chapters 2 and 3 are on pure thickness modes in plates from elasticity and piezoelectricity, respectively. Spatially, these modes only vary along the plate thickness (without in-plane variations). Chapters 4 and 5 discuss shear-horizontal (SH) or antiplane motions in unbounded and finite plates, respectively. Chapter 6 discusses straight-crested waves propagating along the digonal axis of a plate of monoclinic crystals. Vibrations of finite plates are treated in Chapter 7 approximately using a single equation for the main shear displacement. Chapter 8 is very specialized. It is based on a scalar equation which is in fact two-dimensional — depending on the two in-plane coordinates of a crystal plate.

Some basic equations are repeated in different sections so that many sections can be read independently. A list of notations is provided in

Appendix 1. Material constants of some common piezoelectric crystals are given in Appendix 2. Literature on the vibration of crystal plates is abundant. The references listed in the book are not exhaustive, and mostly comprise of papers from which some results are directly used in this book.

The author is grateful to Professor Ji Wang of Ningbo University for providing Fig. 6.2; Mr. Peng Li, a graduate student at Xi'an Jiaotong University, for plotting the figures in Section 8.6; and Mr. Nan Liu and Mr. Hujing He, graduate students at University of Nebraska–Lincoln, for reading the first draft of the book and identifying some errors.

This book is the fifth of the author's monologues on piezoelectric theories, structures, devices, and their applications since "*An introduction to the Theory of Piezoelectricity*" (Springer, 2005). His previous publications include "*The Mechanics of Piezoelectric Structures*" and "*Analysis of Piezoelectric Devices*" (World Scientific, 2006), and "*Antiplane Motions of Piezoceramics and Acoustic Wave Devices*" (World Scientific, 2010).

Jiashi Yang
Lincoln, Nebraska
December, 2012

This page intentionally left blank

Contents

Preface **v**

Chapter 1: Theory of Piezoelectricity **1**
1.1 Basic Equations 1
1.2 Free Vibration Eigenvalue Problem 6
1.3 Inertial Effect of a Mass Layer: Perturbation Integral 13
1.4 Effect of Mass Layer Stiffness: Perturbation Integral 18
1.5 Frequency Perturbation Due to Contact with a Fluid 24
1.6 Quartz and Langasite 27
1.7 Lithium Niobate and Lithium Tantalate 31
1.8 Polarized Ceramics and Crystals in Class 6mm 33

Chapter 2: Thickness Modes in Plates: Elastic Analysis **37**
2.1 Equations of Anisotropic Elasticity 37
2.2 Thickness Modes in a Quartz Plate 40
2.3 Inertial Effect of a Mass Layer: Sauerbrey Equation 44
2.4 Inertial Effect of a Mass Layer: Perturbation 45
2.5 Inertial Effect of a Mass Layer: Differential Equation 45
2.6 Plate with Asymmetric Mass Layers 47
2.7 Plate in Contact with a Fluid: Differential Equation 51
2.8 Plate in Contact with a Fluid: Perturbation 54
2.9 Plate with Particles 55
2.10 Plate with an Array of Rods in Extension 63
2.11 Plate with an Array of Beams in Bending 72
2.12 Plate with Beams: Effect of Couple Stress 80
2.13 Plate with an Inhomogeneous Layer of Finite Thickness 96

Chapter 3: Thickness Modes in Plates: Piezoelectric Analysis **105**
3.1 Unelectroded Plate 105
3.2 Thickness Field Excitation 108
3.3 Lateral Field Excitation 113
3.4 Plate with Separated Electrodes 114

3.5 Effect of Electrode Inertia 120
3.6 Imperfectly Bonded Electrodes 123
3.7 Effect of Electrode Shear Stiffness 131
3.8 Plate in Contact with a Fluid under a Separated Electrode 138
3.9 Plate in Contact with a Fluid: Lateral Field Excitation 147
3.10 Plate with Surface Load Described by Acoustic Impedance 156
3.11 Transient Thickness-shear Vibration 159

Chapter 4: Shear-horizontal Waves in Unbounded Plates 173
4.1 Governing Equations 173
4.2 Face-shear Wave 174
4.3 Thickness-twist Wave 175
4.4 Symmetric Mass Layers 179
4.5 Partial Mass Layers and Bechmann's Number 183
4.6 Asymmetric Mass Layers 185
4.7 Imperfectly Bonded Mass Layer 190
4.8 Mass Layer Stiffness 196
4.9 Thick Mass Layer 200
4.10 Plate on a Substrate 208
4.11 Plate in Contact with a Fluid 215
4.12 Effect of Piezoelectric Coupling 224

Chapter 5: Shear-horizontal Vibrations of Finite Plates 233
5.1 Plate with Tilted Edges 233
5.2 Unelectroded Plate 237
5.3 Fully Electroded Plate 239
5.4 Partially Electroded Plate 243
5.5 Plate with a Partial Mass Layer 250
5.6 Plate with Misaligned Electrodes 254
5.7 Plate with a Mass Layer Array 258
5.8 Mesa Resonator 265
5.9 Filter 272
5.10 Contoured Resonator 282
5.11 Plate with a Nonuniform Mass Layer 298
5.12 Plate with an Imperfectly Bonded Mass Layer 303
5.13 Frequency Spectra 314

Chapter 6: Waves Propagating along Digonal Axis **319**
6.1 Governing Equations 319
6.2 Wave Solution 320
6.3 Dispersion Curves 322
6.4 Long Wavelength Limit 323
6.5 Other Results 325
6.6 Approximate Equations for u_1 and u_2 325
6.7 Straight-crested Waves of u_1 and u_2 326

Chapter 7: Vibration of Rectangular Plates **329**
7.1 Approximate Equation for u_1 329
7.2 Unelectroded Plate 330
7.3 Fully Electroded Plate 332
7.4 Partially Electroded Plate 334
7.5 Contoured Plate 341

Chapter 8: Scalar Equation for Thickness Modes **347**
8.1 Scalar Equation for AT-cut Quartz Plates 347
8.2 Rectangular Plate 350
8.3 Elliptical Plate 352
8.4 Circular Plate 354
8.5 Unbounded Plate with Parabolic Contour 363
8.6 Unbounded Plate with Hyperbolic Contour 368
8.7 Elliptical Plate with Parabolic Contour 376
8.8 Scalar Equation for SC-cut Quartz Plates 387
8.9 Optimal Electrode Shape and Size 392

Appendix 1 Notation **395**

Appendix 2 Material Constants **397**

References **407**

Index **417**

This page intentionally left blank

Chapter 1

Theory of Piezoelectricity

This chapter presents a brief summary of the basic theory of linear piezoelectricity based mainly on the *IEEE Standard on Piezoelectricity* [1] and the classical book on piezoelectricity [2] by H.F. Tiersten (who also wrote the theoretical part of [1]). The same basic equations and other aspects of the theory can also be found in Chap. 2 of *An Introduction to the Theory of Piezoelectricity* [3]. Most of the results in this chapter are general theoretical results — only Section 1.4 has an example. Solutions to specific problems are systematically given in later chapters. This chapter uses the Cartesian tensor notation, the summation convention for repeated tensor indices, and the convention that a comma followed by an index denotes partial differentiation with respect to the coordinate associated with the index. A superimposed dot represents a time derivative.

1.1. Basic Equations

The equations of linear piezoelectricity can be obtained by linearizing the nonlinear electroelastic equations [4] under the assumption of infinitesimal deformation and fields. The resulting equations of motion and the charge equation of electrostatics are

$$\begin{aligned} T_{ji,j} + f_i &= \rho \ddot{u}_i, \\ D_{i,i} &= q, \end{aligned} \tag{1.1}$$

where $\mathbf{T}$ is the stress tensor, ρ is the mass density, $\mathbf{f}$ is the body force per unit volume, $\mathbf{u}$ is the displacement vector, $\mathbf{D}$ is the electric displacement vector, and q is the body free charge density. In this book, $\mathbf{f}$ and q are usually zero. Constitutive relations are given by an electric enthalpy function H defined by

$$H(\mathbf{S},\mathbf{E}) = \frac{1}{2} c_{ijkl}^{E} S_{ij} S_{kl} - e_{ijk} E_i S_{jk} - \frac{1}{2} \varepsilon_{ij}^{S} E_i E_j \tag{1.2}$$

through

$$\begin{aligned} T_{ij} &= \frac{\partial H}{\partial S_{ij}} = c^E_{ijkl} S_{kl} - e_{kij} E_k, \\ D_i &= -\frac{\partial H}{\partial E_i} = e_{ikl} S_{kl} + \varepsilon^S_{ik} E_k, \end{aligned} \tag{1.3}$$

where the strain tensor, **S**, and the electric field vector, **E**, are related to the displacement, **u**, and the electric potential, ϕ, by

$$S_{ij} = (u_{i,j} + u_{j,i})/2, \quad E_i = -\phi_{,i} \ . \tag{1.4}$$

c^E_{ijkl}, e_{ijk}, and ε^S_{ij} are the elastic, piezoelectric, and dielectric constants. The superscript, *E*, in c^E_{ijkl} indicates that the independent electric constitutive variable is the electric field, **E**. The superscript, *S*, in ε^S_{ij} indicates that the mechanical constitutive variable is the strain tensor, **S**. The material constants have the following symmetries:

$$\begin{aligned} &c^E_{ijkl} = c^E_{jikl} = c^E_{klij}, \\ &e_{kij} = e_{kji}, \quad \varepsilon^S_{ij} = \varepsilon^S_{ji}. \end{aligned} \tag{1.5}$$

We also assume that the elastic and dielectric tensors are positive definite in the following sense:

$$\begin{aligned} &c^E_{ijkl} S_{ij} S_{kl} \ge 0 \quad \text{for any} \quad S_{ij} = S_{ji}, \\ &\quad \text{and} \quad c^E_{ijkl} S_{ij} S_{kl} = 0 \quad \Rightarrow \quad S_{ij} = 0, \\ &\varepsilon^S_{ij} E_i E_j \ge 0 \quad \text{for any} \quad E_i, \\ &\quad \text{and} \quad \varepsilon^S_{ij} E_i E_j = 0 \quad \Rightarrow \quad E_i = 0. \end{aligned} \tag{1.6}$$

Similar to Eq. (1.3), linear constitutive relations can also be written as

$$\begin{aligned} T_{ij} &= c^D_{ijkl} S_{kl} - h_{kij} D_k, \\ E_i &= -h_{ikl} S_{kl} + \beta^S_{ik} D_k. \end{aligned} \tag{1.7}$$

$$\begin{aligned} S_{ij} &= s^E_{ijkl} T_{kl} + d_{kij} E_k, \\ D_i &= d_{ikl} T_{kl} + \varepsilon^T_{ik} E_k, \end{aligned} \tag{1.8}$$

$$\begin{aligned} S_{ij} &= s_{ijkl}^{D} T_{kl} + g_{kij} D_k, \\ E_i &= -g_{ikl} T_{kl} + \beta_{ik}^{T} D_k. \end{aligned} \tag{1.9}$$

With successive substitutions from Eqs. (1.3) and (1.4), Eq. (1.1) can be written as four equations for **u** and ϕ

$$\begin{aligned} c_{ijkl} u_{k,lj} + e_{kij} \phi_{,kj} + f_i &= \rho \ddot{u}_i, \\ e_{ikl} u_{k,li} - \varepsilon_{ij} \phi_{,ij} &= q, \end{aligned} \tag{1.10}$$

where we have neglected the superscripts of the material constants.

Let the region occupied by a piezoelectric body be V and its boundary surface be S, as shown in Fig. 1.1. Let the unit outward normal of S be **n**.

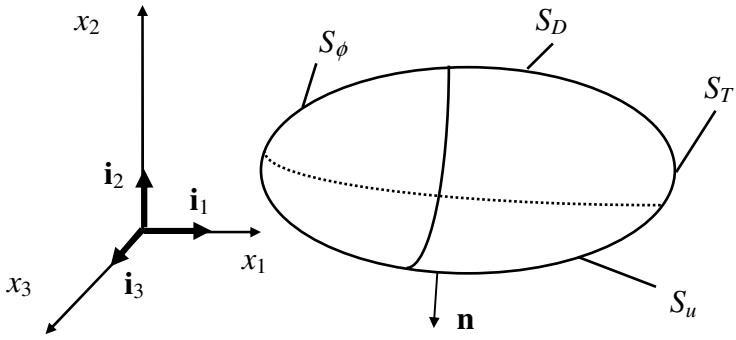

Fig. 1.1. A piezoelectric body and partitions of its surface.

For boundary conditions, we consider the following partitions of S:

$$\begin{aligned} S_u \cup S_T &= S_\phi \cup S_D = S, \\ S_u \cap S_T &= S_\phi \cap S_D = 0, \end{aligned} \tag{1.11}$$

where S_u is the part of S on which the mechanical displacement is prescribed, and S_T is the part of S where the traction vector is prescribed. S_ϕ represents the part of S which is electroded where the electric potential is no more than a function of time, and S_D is the unelectroded

part. For mechanical boundary conditions, we have prescribed displacement $\bar{u}_i$

$$u_i = \bar{u}_i \quad \text{on} \quad S_u, \tag{1.12}$$

and prescribed traction $\bar{t}_j$

$$T_{ij} n_i = \bar{t}_j \quad \text{on} \quad S_T. \tag{1.13}$$

Electrically, on the unelectroded part of *S*, the charge condition can be written as

$$D_j n_j = -\bar{\sigma} \quad \text{on} \quad S_D, \tag{1.14}$$

where $\bar{\sigma}$ is surface free charge density. On the electroded portion of *S*,

$$\phi = \bar{\phi} \quad \text{on} \quad S_\phi, \tag{1.15}$$

where $\bar{\phi}$ does not vary spatially. At this stage, we assume very thin electrodes. The mechanical effects like the inertia and stiffness of the electrodes are neglected. On an electrode, S_ϕ, the total free electric charge, Q_e (a scalar), can be represented by

$$Q_e = \int_{S_\phi} - n_i D_i dS. \tag{1.16}$$

The electric current flowing out of the electrode is given by

$$I = -\dot{Q}_e. \tag{1.17}$$

Sometimes there are two (or more) electrodes on a body, and the electrodes are connected to an electric circuit. In such a case, circuit equation(s) may need to be considered.

We now introduce a compact matrix notation. This notation consists of replacing pairs of indices, *ij* or *kl*, by single indices, *p* or *q*, where *i*, *j*, *k* and *l* take the values of 1, 2, and 3; and *p* and *q* take the values of 1, 2, 3, 4, 5 and 6 according to

ij or *kl*:	11	22	33	23 or 32	31 or 13	12 or 21
p or *q*:	1	2	3	4	5	6

(1.18)

Thus

$$c_{ijkl} \to c_{pq}, \quad e_{ikl} \to e_{ip}, \quad T_{ij} \to T_p . \tag{1.19}$$

For the strain tensor, we introduce S_p such that

$$\begin{aligned} &S_1 = S_{11}, \quad S_2 = S_{22}, \quad S_3 = S_{33}, \\ &S_4 = 2S_{23}, \quad S_5 = 2S_{31}, \quad S_6 = 2S_{12}. \end{aligned} \tag{1.20}$$

The constitutive relations in Eq. (1.3) can then be written as

$$\begin{aligned} T_p &= c_{pq}^E S_q - e_{kp} E_k, \\ D_i &= e_{iq} S_q + \varepsilon_{ik}^S E_k . \end{aligned} \tag{1.21}$$

In matrix form, Eq. (1.21) becomes

$$\begin{Bmatrix} T_1 \\ T_2 \\ T_3 \\ T_4 \\ T_5 \\ T_6 \end{Bmatrix} = \begin{pmatrix} c_{11}^E & c_{12}^E & c_{13}^E & c_{14}^E & c_{15}^E & c_{16}^E \\ c_{21}^E & c_{22}^E & c_{23}^E & c_{24}^E & c_{25}^E & c_{26}^E \\ c_{31}^E & c_{32}^E & c_{33}^E & c_{34}^E & c_{35}^E & c_{36}^E \\ c_{41}^E & c_{42}^E & c_{43}^E & c_{44}^E & c_{45}^E & c_{46}^E \\ c_{51}^E & c_{52}^E & c_{53}^E & c_{54}^E & c_{55}^E & c_{56}^E \\ c_{61}^E & c_{62}^E & c_{63}^E & c_{64}^E & c_{65}^E & c_{66}^E \end{pmatrix} \begin{Bmatrix} S_1 \\ S_2 \\ S_3 \\ S_4 \\ S_5 \\ S_6 \end{Bmatrix} - \begin{pmatrix} e_{11} & e_{21} & e_{31} \\ e_{12} & e_{22} & e_{32} \\ e_{13} & e_{23} & e_{33} \\ e_{14} & e_{24} & e_{34} \\ e_{15} & e_{25} & e_{35} \\ e_{16} & e_{26} & e_{36} \end{pmatrix} \begin{Bmatrix} E_1 \\ E_2 \\ E_3 \end{Bmatrix}, \tag{1.22}$$

$$\begin{Bmatrix} D_1 \\ D_2 \\ D_3 \end{Bmatrix} = \begin{bmatrix} e_{11} & e_{12} & e_{13} & e_{14} & e_{15} & e_{16} \\ e_{21} & e_{22} & e_{23} & e_{24} & e_{25} & e_{26} \\ e_{31} & e_{32} & e_{33} & e_{34} & e_{35} & e_{36} \end{bmatrix} \begin{Bmatrix} S_1 \\ S_2 \\ S_3 \\ S_4 \\ S_5 \\ S_6 \end{Bmatrix} + \begin{pmatrix} \varepsilon_{11}^S & \varepsilon_{12}^S & \varepsilon_{13}^S \\ \varepsilon_{21}^S & \varepsilon_{22}^S & \varepsilon_{23}^S \\ \varepsilon_{31}^S & \varepsilon_{32}^S & \varepsilon_{33}^S \end{pmatrix} \begin{Bmatrix} E_1 \\ E_2 \\ E_3 \end{Bmatrix}. \tag{1.23}$$

For harmonic motions, simple dissipative effects in the material can be represented by complex material constants [5–7].

1.2. Free Vibration Eigenvalue Problem

In this section we prove a few general properties of the eigenvalue problem for the free vibration of a piezoelectric body [8]. The free vibration of a piezoelectric body with frequency ω is governed by the following differential equations:

$$\begin{aligned} &-c_{jikl}u_{k,lj} - e_{kji}\phi_{,kj} = \rho\omega^2 u_i, \\ &-e_{ikl}u_{k,li} + \varepsilon_{ik}\phi_{,ki} = 0. \end{aligned} \tag{1.24}$$

We want to determine those values of ω corresponding to which nontrivial u_i and/or ϕ exist.

1.2.1. Abstract formulation

We introduce the following notation:

$$\begin{aligned} &\lambda = \omega^2, \quad \mathbf{U} = \{u_i, \phi\}, \quad \mathbf{V} = \{v_i, \psi\}, \\ &\mathbf{AU} = \{-c_{jikl}u_{k,lj} - e_{kji}\phi_{,kj}, -e_{ikl}u_{k,li} + \varepsilon_{ik}\phi_{,ki}\}, \\ &\mathbf{BU} = \{\rho u_i, 0\}, \end{aligned} \tag{1.25}$$

where **U** and **V** are four-vectors. **A** and **B** are operators. Then the eigenvalue problem for the free vibration of a piezoelectric body can be written as

$$\begin{aligned}
&\mathbf{AU} = \lambda \mathbf{BU} \quad \text{in} \quad V, \\
&u_i = 0 \quad \text{on} \quad S_u, \\
&T_{ji}(\mathbf{U}) n_j = (c_{jikl} u_{k,l} + e_{kji} \phi_{,k}) n_j = 0 \quad \text{on} \quad S_T, \\
&\phi = 0 \quad \text{on} \quad S_\phi, \\
&D_i(\mathbf{U}) n_i = (e_{ikl} u_{k,l} - \varepsilon_{ik} \phi_{,k}) n_i = 0 \quad \text{on} \quad S_D,
\end{aligned} \tag{1.26}$$

which is a homogeneous system. We are interested in nontrivial solutions of **U**. **A** and **B** are real but λ and **U** may be complex. We note that for a nontrivial **U**, its first three components u_i have to be nontrivial, because $u_i = 0$ implies, through Eq. (1.26), that $\phi = 0$. For convenience we denote the collection of all four-vectors that are smooth enough and satisfy the boundary conditions in Eq. $(1.26)_{2\text{-}5}$ by

$$H = \{\mathbf{U} \mid \mathbf{U} \text{ satisfies all boundary conditions in Eqs. } (1.26)_{2\text{-}5}\}. \tag{1.27}$$

A scalar product over H is defined by

$$< \mathbf{U}; \mathbf{V} >= \int_V (u_i v_i + \phi \psi) dV \,, \tag{1.28}$$

which has the following properties:

$$\begin{aligned}
&< \mathbf{U}; \mathbf{V} >=< \mathbf{V}; \mathbf{U} >, \\
&< \mathbf{U}; \alpha \mathbf{V} + \beta \mathbf{W} >= \alpha < \mathbf{U}; \mathbf{V} > + \beta < \mathbf{U}; \mathbf{W} >,
\end{aligned} \tag{1.29}$$

where α and β are scalars.

1.2.2. Self-adjointness

For any $\mathbf{U}$, $\mathbf{V} \in H$, we have

$$
\begin{aligned}
&< \mathbf{AU}; \mathbf{V} >=< \{-c_{jikl}u_{k,lj} - e_{kji}\phi_{,kj}, -e_{ikl}u_{k,li} + \varepsilon_{ik}\phi_{,ki}\}; \{v_i, \psi\} > \\
&= \int_V [(-c_{jikl}u_{k,lj} - e_{kji}\phi_{,kj})v_i + (-e_{ikl}u_{k,li} + \varepsilon_{ik}\phi_{,ki})\psi]dV \\
&= \int_S [-T_{ji}(\mathbf{U})n_j v_i - D_i(\mathbf{U})n_i\psi]dS \\
&\quad + \int_V [(c_{jikl}u_{k,l}v_{i,j} + e_{kji}\phi_{,k}v_{i,j} + e_{ikl}u_{k,l}\psi_{,i} - \varepsilon_{ik}\phi_{,k}\psi_{,i})dV \\
&= -\int_S [T_{ji}(\mathbf{U})n_j v_i + D_i(\mathbf{U})n_i\psi]dS \\
&\quad + \int_S [T_{kl}(\mathbf{V})n_l u_k + D_k(\mathbf{V})n_k\phi]dS \\
&\quad + \int_V [(-c_{klij}v_{i,jl} - e_{ikl}\psi_{,il})u_k + (-e_{kji}v_{i,jk} + \varepsilon_{ik}\psi_{,ki})\phi]dV \\
&= -\int_S [T_{ji}(\mathbf{U})n_j v_i + D_i(\mathbf{U})n_i\psi]dS \\
&\quad + \int_S [T_{kl}(\mathbf{V})n_l u_k + D_k(\mathbf{V})n_k\phi]dS \\
&\quad + < \mathbf{U}; \mathbf{AV} >=< \mathbf{U}; \mathbf{AV} >,
\end{aligned}
\tag{1.30}
$$

and

$$
< \mathbf{BU}; \mathbf{V} >=< \mathbf{U}; \mathbf{BV} > . \tag{1.31}
$$

Hence both $\mathbf{A}$ and $\mathbf{B}$ are self-adjoint on H. Equation (1.30) is called the reciprocal theorem in elasticity and Green's identity in mathematics.

1.2.3. Reality

Let λ be an eigenvalue and $\mathbf{U}$ the corresponding eigenvector. Hence

$$
\mathbf{AU} = \lambda\mathbf{BU} . \tag{1.32}
$$

Take complex conjugate

$$
\mathbf{AU}^* = \lambda^*\mathbf{BU}^* , \tag{1.33}
$$

where an asterisk means complex conjugate, and we have made use of the fact that **A** and **B** are real. Multiply Eq. (1.32) by $\mathbf{U}^*$ and Eq. (1.33) by $\mathbf{U}$ through the scalar product, and subtract the resulting equations:

$$0 = (\lambda - \lambda^*) < \mathbf{BU}; \mathbf{U}^* > . \tag{1.34}$$

Since $< \mathbf{BU}; \mathbf{U}^* >$ is strictly positive, we have

$$\lambda - \lambda^* = 0 , \tag{1.35}$$

or λ is real. Then let the real and imaginary parts of **U** be $\mathbf{U}^R$ and $\mathbf{U}^I$. Equation (1.32) can be written as

$$\mathbf{A}(\mathbf{U}^R + i\mathbf{U}^I) = \lambda \mathbf{B}(\mathbf{U}^R + i\mathbf{U}^I) , \tag{1.36}$$

which implies that

$$\mathbf{AU}^R = \lambda \mathbf{BU}^R , \quad \mathbf{AU}^I = \lambda \mathbf{BU}^I . \tag{1.37}$$

Equation (1.37) shows that $\mathbf{U}^R$ and $\mathbf{U}^I$ are also eigenvectors of λ. In the rest of this section, we will assume that the eigenvectors have been chosen as real functions.

1.2.4. Orthogonality

Let $\mathbf{U}^{(m)}$ and $\mathbf{U}^{(n)}$ be two eigenvectors corresponding to two distinct eigenvalues $\lambda^{(m)}$ and $\lambda^{(n)}$, respectively. Then

$$\begin{aligned} \mathbf{AU}^{(m)} &= \lambda^{(m)} \mathbf{BU}^{(m)} , \\ \mathbf{AU}^{(n)} &= \lambda^{(n)} \mathbf{BU}^{(n)} . \end{aligned} \tag{1.38}$$

Multiply Eq. $(1.38)_1$ by $\mathbf{U}^{(n)}$ and Eq. $(1.38)_2$ by $\mathbf{U}^{(m)}$ through the scalar product, and subtract the resulting equations:

$$0 = (\lambda^{(m)} - \lambda^{(n)}) < \mathbf{BU}^{(m)}; \mathbf{U}^{(n)} > , \tag{1.39}$$

which implies that

$$< \mathbf{BU}^{(m)}; \mathbf{U}^{(n)} >= 0 . \tag{1.40}$$

The multiplication of Eq. $(1.38)_1$ by $\mathbf{U}^{(n)}$ then leads to

$$< \mathbf{A}\mathbf{U}^{(m)}; \mathbf{U}^{(n)} >= 0 . \tag{1.41}$$

Equations (1.41) and (1.40) are called the orthogonality conditions. In unabbreviated form they become

$$\begin{aligned} &< \mathbf{A}\mathbf{U}^{(m)}; \mathbf{U}^{(n)} > \\ &\quad = \int_V (c_{ijkl} u^{(m)}_{k,l} u^{(n)}_{i,j} + e_{kji} \phi^{(m)}_{,k} u^{(n)}_{i,j} \\ &\qquad + e_{ikl} u^{(m)}_{k,l} \phi^{(n)}_{,i} - \varepsilon_{ik} \phi^{(m)}_{,k} \phi^{(n)}_{,i}) dV = 0, \\ &< \mathbf{B}\mathbf{U}^{(m)}; \mathbf{U}^{(n)} > = \int_V \rho_0 u^{(m)}_i u^{(n)}_i dV = 0. \end{aligned} \tag{1.42}$$

1.2.5. Positivity

A subset of H consisting of $\mathbf{U}$ that also satisfies the charge equation is denoted by

$$H^* = \{\mathbf{U} \in H \mid \mathbf{U} \text{ real}, \ -e_{ikl} u_{k,li} + \varepsilon_{ik} \phi_{,ki} = 0 \ \text{ in } V\}. \tag{1.43}$$

For any $\mathbf{U} \in H^*$, we have

$$\begin{aligned} &< \mathbf{A}\mathbf{U}; \mathbf{U} >=< \{-c_{jikl} u_{k,lj} - e_{kji} \phi_{,kj}, -e_{ikl} u_{k,li} + \varepsilon_{ik} \phi_{,ki}\}; \{u_i, \phi\} > \\ &= \int_V [(-c_{jikl} u_{k,lj} - e_{kji} \phi_{,kj}) u_i + (-e_{ikl} u_{k,li} + \varepsilon_{ik} \phi_{,ki}) \phi] dV \\ &= \int_S [-T_{ji}(\mathbf{U}) n_j u_i - D_i(\mathbf{U}) n_i \phi] dS \\ &\quad + \int_V [(c_{jikl} u_{k,l} u_{i,j} + e_{kji} \phi_{,k} u_{i,j} + e_{ikl} u_{k,l} \phi_{,i} - \varepsilon_{ik} \phi_{,k} \phi_{,i}) dV \\ &= \int_V [c_{jikl} u_{k,l} u_{i,j} + \varepsilon_{ik} \phi_{,k} \phi_{,i} + 2(e_{ikl} u_{k,l} \phi_{,i} - \varepsilon_{ik} \phi_{,k} \phi_{,i})] dV \\ &= \int_V [c_{jikl} u_{k,l} u_{i,j} + \varepsilon_{ik} \phi_{,k} \phi_{,i} - 2(e_{ikl} u_{k,li} - \varepsilon_{ik} \phi_{,ki}) \phi] dV \\ &\quad + \int_S 2(e_{ikl} u_{k,l} - \varepsilon_{ik} \phi_{,k}) n_i \phi dS \\ &= \int_V (c_{jikl} u_{k,l} u_{i,j} + \varepsilon_{ik} \phi_{,k} \phi_{,i}) dV \geq 0, \end{aligned} \tag{1.44}$$

and

$$< \mathbf{BU}; \mathbf{U} > \quad \geq 0 . \tag{1.45}$$

Multiply Eq. (1.32) by $\mathbf{U}$

$$< \mathbf{AU}; \mathbf{U} >= \lambda < \mathbf{BU}; \mathbf{U} >, \tag{1.46}$$

which shows that λ is nonnegative.

1.2.6. Variational formulation

Consider the following functional (Rayleigh quotient) of $\mathbf{U} \in H$

$$\begin{aligned} &\Pi(\mathbf{U}) = \frac{\Lambda(\mathbf{U})}{\Gamma(\mathbf{U})}, \\ &\Lambda(\mathbf{U}) =< \mathbf{AU}; \mathbf{U} >, \quad \Gamma(\mathbf{U}) =< \mathbf{BU}; \mathbf{U} > . \end{aligned} \tag{1.47}$$

The first variation of Π is

$$\delta\Pi = \frac{\Gamma\delta\Lambda - \Lambda\delta\Gamma}{\Gamma^2} = \frac{\delta\Lambda - \Pi\delta\Gamma}{\Gamma} . \tag{1.48}$$

Therefore $\delta\Pi = 0$ implies that

$$\delta\Lambda - \Pi\delta\Gamma = 0 . \tag{1.49}$$

From the expressions of Λ and Γ in Eq. (1.47) we have

$$\begin{aligned} \delta\Lambda - \Pi\delta\Gamma =& < \mathbf{AU}; \delta\mathbf{U} > + < \delta\mathbf{AU}; \mathbf{U} > \\ & - \Pi < \mathbf{BU}; \delta\mathbf{U} > - \Pi < \delta\mathbf{BU}; \mathbf{U} > \\ =& < \mathbf{AU}; \delta\mathbf{U} > + < \mathbf{A}\delta\mathbf{U}; \mathbf{U} > \\ & - \Pi < \mathbf{BU}; \delta\mathbf{U} > - \Pi < \mathbf{B}\delta\mathbf{U}; \mathbf{U} > \\ =& < \mathbf{AU}; \delta\mathbf{U} > + < \delta\mathbf{U}; \mathbf{AU} > \\ & - \Pi < \mathbf{BU}; \delta\mathbf{U} > - \Pi < \delta\mathbf{U}; \mathbf{BU} > \\ =& 2 < \mathbf{AU} - \Pi\mathbf{BU}; \delta\mathbf{U} >, \end{aligned} \tag{1.50}$$

where the small variation $\delta\mathbf{U} \in H$. Equation (1.50) implies that

$$\mathbf{AU} - \Pi\mathbf{BU} = 0 . \tag{1.51}$$

Hence the $\mathbf{U}$ that makes $\delta\Pi = 0$ is an eigenvector corresponding to the eigenvalue Π.

1.2.7. Perturbation based on variational formulation

Next we consider the case when **A** and **B** are slightly perturbed but are still self-adjoint, which causes small perturbations in λ and **U**:

$$(\mathbf{A}+\Delta\mathbf{A})(\mathbf{U}+\Delta\mathbf{U})=(\lambda+\Delta\lambda)(\mathbf{B}+\Delta\mathbf{B})(\mathbf{U}+\Delta\mathbf{U})\,. \tag{1.52}$$

We are interested in an expression of $\Delta\lambda$ linear in $\Delta\mathbf{A}$ and $\Delta\mathbf{B}$. From Eq. (1.47),

$$\begin{aligned}
\lambda+\Delta\lambda &= \frac{<(\mathbf{A}+\Delta\mathbf{A})(\mathbf{U}+\Delta\mathbf{U});\mathbf{U}+\Delta\mathbf{U}>}{<(\mathbf{B}+\Delta\mathbf{B})(\mathbf{U}+\Delta\mathbf{U});\mathbf{U}+\Delta\mathbf{U}>}\\
&\cong \frac{<\mathbf{AU}+(\Delta\mathbf{A})\mathbf{U}+\mathbf{A}(\Delta\mathbf{U});\mathbf{U}+\Delta\mathbf{U}>}{<\mathbf{BU}+(\Delta\mathbf{B})\mathbf{U}+\mathbf{B}(\Delta\mathbf{U});\mathbf{U}+\Delta\mathbf{U}>}\\
&\cong \frac{<\mathbf{AU};\mathbf{U}>+<\mathbf{AU};\Delta\mathbf{U}>+<(\Delta\mathbf{A})\mathbf{U}+\mathbf{A}(\Delta\mathbf{U});\mathbf{U}>}{<\mathbf{BU};\mathbf{U}>+<\mathbf{BU};\Delta\mathbf{U}>+<(\Delta\mathbf{B})\mathbf{U}+\mathbf{B}(\Delta\mathbf{U});\mathbf{U}>}\\
&= \frac{<\mathbf{AU};\mathbf{U}>+2<\mathbf{AU};\Delta\mathbf{U}>+<(\Delta\mathbf{A})\mathbf{U};\mathbf{U}>}{<\mathbf{BU};\mathbf{U}>+2<\mathbf{BU};\Delta\mathbf{U}>+<(\Delta\mathbf{B})\mathbf{U};\mathbf{U}>}\\
&\cong \frac{<\mathbf{AU};\mathbf{U}>}{<\mathbf{BU};\mathbf{U}>}\left(1+\frac{2<\mathbf{AU};\Delta\mathbf{U}>+<(\Delta\mathbf{A})\mathbf{U};\mathbf{U}>}{<\mathbf{AU};\mathbf{U}>}\right)\\
&\quad\times\left(1-\frac{2<\mathbf{BU};\Delta\mathbf{U}>+<(\Delta\mathbf{B})\mathbf{U};\mathbf{U}>}{<\mathbf{BU};\mathbf{U}>}\right)\\
&\cong \frac{<\mathbf{AU};\mathbf{U}>}{<\mathbf{BU};\mathbf{U}>}\left(1+\frac{2<\mathbf{AU};\Delta\mathbf{U}>+<(\Delta\mathbf{A})\mathbf{U};\mathbf{U}>}{<\mathbf{AU};\mathbf{U}>}\right.\\
&\quad\left.-\frac{2<\mathbf{BU};\Delta\mathbf{U}>+<(\Delta\mathbf{B})\mathbf{U};\mathbf{U}>}{<\mathbf{BU};\mathbf{U}>}\right)\\
&= \frac{<\mathbf{AU};\mathbf{U}>}{<\mathbf{BU};\mathbf{U}>}+\frac{2<\mathbf{AU};\Delta\mathbf{U}>+<(\Delta\mathbf{A})\mathbf{U};\mathbf{U}>}{<\mathbf{BU};\mathbf{U}>}\\
&\quad-\frac{<\mathbf{AU};\mathbf{U}>}{<\mathbf{BU};\mathbf{U}>}\frac{2<\mathbf{BU};\Delta\mathbf{U}>+<(\Delta\mathbf{B})\mathbf{U};\mathbf{U}>}{<\mathbf{BU};\mathbf{U}>}\\
&= \lambda+\frac{2<\mathbf{AU}-\lambda\mathbf{BU};\Delta\mathbf{U}>+<(\Delta\mathbf{A})\mathbf{U};\mathbf{U}>-\lambda<(\Delta\mathbf{B})\mathbf{U};\mathbf{U}>}{<\mathbf{BU};\mathbf{U}>}\\
&= \lambda+\frac{<(\Delta\mathbf{A})\mathbf{U};\mathbf{U}>-\lambda<(\Delta\mathbf{B})\mathbf{U};\mathbf{U}>}{<\mathbf{BU};\mathbf{U}>}.
\end{aligned} \tag{1.53}$$

Hence,

$$\Delta\lambda = \frac{<(\Delta\mathbf{A})\mathbf{U};\mathbf{U}> - \lambda <(\Delta\mathbf{B})\mathbf{U};\mathbf{U}>}{<\mathbf{BU};\mathbf{U}>}. \tag{1.54}$$

1.2.8. Perturbation based on differential equations

Equation (1.54) can also be obtained from the following perturbation procedure directly from Eq. (1.52). Expand both sides of Eq. (1.52). The zero-order terms represent the unperturbed eigenvalue problem. The first-order terms are

$$\mathbf{A}(\Delta\mathbf{U}) + (\Delta\mathbf{A})\mathbf{U} = \Delta\lambda\mathbf{BU} + \lambda(\Delta\mathbf{B})\mathbf{U} + \lambda\mathbf{B}(\Delta\mathbf{U}). \tag{1.55}$$

Multiply both sides by **U**:

$$\begin{aligned} &<\mathbf{A}(\Delta\mathbf{U});\mathbf{U}> + <(\Delta\mathbf{A})\mathbf{U};\mathbf{U}> \\ &\quad = \Delta\lambda <\mathbf{BU};\mathbf{U}> + \lambda <(\Delta\mathbf{B})\mathbf{U};\mathbf{U}> + \lambda <\mathbf{B}(\Delta\mathbf{U});\mathbf{U}>, \end{aligned} \tag{1.56}$$

or

$$\begin{aligned} &<\Delta\mathbf{U};\mathbf{AU}> + <(\Delta\mathbf{A})\mathbf{U};\mathbf{U}> \\ &\quad = \Delta\lambda <\mathbf{BU};\mathbf{U}> + \lambda <(\Delta\mathbf{B})\mathbf{U};\mathbf{U}> + \lambda <\Delta\mathbf{U};\mathbf{BU}>. \end{aligned} \tag{1.57}$$

The first term and the last term in Eq. (1.57) cancel, and what is left is

$$\Delta\lambda = \frac{<(\Delta\mathbf{A})\mathbf{U};\mathbf{U}> - \lambda <(\Delta\mathbf{B})\mathbf{U};\mathbf{U}>}{<\mathbf{BU};\mathbf{U}>}, \tag{1.58}$$

which is the same as Eq. (1.54). Note that in this perturbation procedure, no assumptions regarding the self-adjointness of $\Delta\mathbf{A}$ and $\Delta\mathbf{B}$ were made.

1.3. Inertial Effect of a Mass Layer: Perturbation Integral

When a thin layer of another material is added to the surface of a crystal body, the resonant frequencies of the crystal change due to the inertia

and stiffness of the added layer. In the simplest description, the stiffness of the added layer can be neglected and the inertia of the layer lowers the resonant frequencies of the crystal. This effect has been used to make mass sensors for measuring the density and/or thickness of the layer. These mass sensors are also called quartz crystal microbalances (QCMs). They have applications in monitoring thin film deposition processes and in chemical and biological sensing. In this section we analyze frequency shifts in a crystal due to a thin layer of surface mass through a perturbation analysis [9].

1.3.1. Governing equations

Consider a piezoelectric body with a thin mass layer of thickness h' and density ρ' on part of its surface (see Fig. 1.2). Let the region occupied by the body be V and its boundary surface be S. The unit outward normal of S is **n**. The mass layer is assumed to be very thin. Only the inertial effect of the layer is to be considered; its stiffness is neglected.

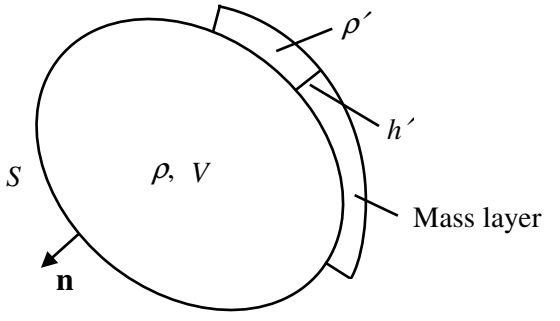

Fig. 1.2. A piezoelectric body with a surface mass layer.

For free vibration with a frequency ω, by Newton's second law, the traction boundary condition on the surface area with the mass layer is

$$-T_{ji}n_j = \rho' h' \ddot{u}_i = -\rho' h' \omega^2 u_i \,. \tag{1.59}$$

The eigenvalue problem for the resonant frequencies and modes of the crystal with the mass layer is:

$$\begin{aligned}
&\mathbf{AU} = \lambda \mathbf{BU} \quad \text{in} \quad V, \\
&u_i = 0 \quad \text{on} \quad S_u, \\
&T_{ji}(\mathbf{U}) n_j = \varepsilon \lambda \rho' h' u_i \quad \text{on} \quad S_T, \\
&\phi = 0 \quad \text{on} \quad S_\phi, \\
&D_i(\mathbf{U}) n_i = 0 \quad \text{on} \quad S_D,
\end{aligned} \tag{1.60}$$

where λ, $\mathbf{U}$, $\mathbf{A}$ and $\mathbf{B}$ are defined in Eq. (1.25). $T_{ji}(\mathbf{U})$ and $D_i(\mathbf{U})$ are the stress tensor and electric displacement vector in terms of the four-vector $\mathbf{U}$. In Eq. $(1.60)_3$ we have artificially introduced a dimensionless number ε to be used in our perturbation analysis. The real physical problem is represented by $\varepsilon = 1$.

1.3.2. Perturbation analysis

We make the following perturbation expansions:

$$\begin{aligned}
&\lambda \cong \lambda^{(0)} + \varepsilon \lambda^{(1)}, \\
&\mathbf{U} = \begin{Bmatrix} u_i \\ \phi \end{Bmatrix} \cong \begin{Bmatrix} u_i^{(0)} \\ \phi^{(0)} \end{Bmatrix} + \varepsilon \begin{Bmatrix} u_i^{(1)} \\ \phi^{(1)} \end{Bmatrix} = \mathbf{U}^{(0)} + \varepsilon \mathbf{U}^{(1)}.
\end{aligned} \tag{1.61}$$

Substituting Eq. (1.61) into Eq. (1.60), collecting terms of equal powers of ε, we obtain a series of perturbation problems of successive orders. We are interested in the lowest-order effect of the mass layer. Therefore we collect coefficients of terms with powers of ε^0 and ε^1 only. The zero-order problem is

$$\begin{aligned}
&-c_{jikl} u_{k,lj}^{(0)} - e_{kji} \phi_{,kj}^{(0)} = \rho \lambda^{(0)} u_i^{(0)} \quad \text{in} \quad V, \\
&-e_{ikl} u_{k,li}^{(0)} + \varepsilon_{ik} \phi_{,ki}^{(0)} = 0 \quad \text{in} \quad V, \\
&u_i^{(0)} = 0 \quad \text{on} \quad S_u, \\
&(c_{jikl} u_{k,l}^{(0)} + e_{kji} \phi_{,k}^{(0)}) n_j = 0 \quad \text{on} \quad S_T, \\
&\phi^{(0)} = 0 \quad \text{on} \quad S_\phi, \\
&(e_{ikl} u_{k,l}^{(0)} - \varepsilon_{ik} \phi_{,k}^{(0)}) n_i = 0 \quad \text{on} \quad S_D.
\end{aligned} \tag{1.62}$$

This represents free vibration of the body without the mass layer. The solution to the zero-order problem, $\lambda^{(0)}$ and $\mathbf{U}^{(0)}$, is assumed known as usual in a perturbation analysis. The following first-order problem is to be solved:

$$\begin{aligned}
&-c_{jikl}u^{(1)}_{k,lj} - e_{kji}\phi^{(1)}_{,kj} = \rho\lambda^{(1)}u^{(0)}_i + \rho\lambda^{(0)}u^{(1)}_i \quad \text{in} \quad V,\\
&-e_{ikl}u^{(1)}_{k,li} + \varepsilon_{ik}\phi^{(1)}_{,ki} = 0 \quad \text{in} \quad V,\\
&u^{(1)}_i = 0 \quad \text{on} \quad S_u,\\
&(c_{jikl}u^{(1)}_{k,l} + e_{kji}\phi^{(1)}_{,k})n_j = \rho' h' \lambda^{(0)}u^{(0)}_i \quad \text{on} \quad S_T,\\
&\phi^{(1)} = 0 \quad \text{on} \quad S_\phi,\\
&(e_{ikl}u^{(1)}_{k,l} - \varepsilon_{ik}\phi^{(1)}_{,k})n_i = 0 \quad \text{on} \quad S_D.
\end{aligned} \tag{1.63}$$

Equation $(1.63)_{1,2}$ can be written as

$$\mathbf{A}\mathbf{U}^{(1)} = \lambda^{(0)}\mathbf{B}\mathbf{U}^{(1)} + \lambda^{(1)}\mathbf{B}\mathbf{U}^{(0)}. \tag{1.64}$$

Multiplying both sides of Eq. (1.64) by $\mathbf{U}^{(0)}$ and integrating the resulting equation over V, we have

$$\begin{aligned}
&< \mathbf{A}\mathbf{U}^{(1)}; \mathbf{U}^{(0)} >\\
&\quad = \int_V [(-c_{jikl}u^{(1)}_{k,lj} - e_{kji}\phi^{(1)}_{,kj})u^{(0)}_i + (-e_{ikl}u^{(1)}_{k,li} + \varepsilon_{ik}\phi^{(1)}_{,ki})\phi^{(0)}]dV\\
&\quad = \lambda^{(0)} < \mathbf{B}\mathbf{U}^{(1)}; \mathbf{U}^{(0)} > + \lambda^{(1)} < \mathbf{B}\mathbf{U}^{(0)}; \mathbf{U}^{(0)} >,
\end{aligned} \tag{1.65}$$

where the inner product, $< ; >$, is defined in Eq. (1.28). With integration by parts, it can be shown that

$$\begin{aligned}
&< \mathbf{A}\mathbf{U}^{(0)}; \mathbf{U}^{(1)} >\\
&\quad = -\int_S [T_{ji}(\mathbf{U}^{(0)})n_j u^{(1)}_i + D_i(\mathbf{U}^{(0)})n_i\phi^{(1)}]dS\\
&\qquad + \int_S [T_{kl}(\mathbf{U}^{(1)})n_l u^{(0)}_k + D_k(\mathbf{U}^{(1)})n_k\phi^{(0)}]dS + < \mathbf{U}^{(0)}; \mathbf{A}\mathbf{U}^{(1)} >.
\end{aligned} \tag{1.66}$$

With the use of the boundary conditions in Eqs. $(1.62)_{3\text{-}6}$ and $(1.63)_{3\text{-}6}$, Eq. (1.66) becomes

$$\begin{aligned} &< \mathbf{A}\mathbf{U}^{(0)}; \mathbf{U}^{(1)} > \\ &\quad = \int_{S_T} \rho' h' \lambda^{(0)} u_k^{(0)} u_k^{(0)} dS + < \mathbf{U}^{(0)}; \mathbf{A}\mathbf{U}^{(1)} > . \end{aligned} \tag{1.67}$$

Substitution of Eq. (1.67) into Eq. (1.65) gives

$$\begin{aligned} &< \mathbf{A}\mathbf{U}^{(0)}; \mathbf{U}^{(1)} > - \int_{S_T} \rho' h' \lambda^{(0)} u_k^{(0)} u_k^{(0)} dS \\ &\quad = \lambda^{(0)} < \mathbf{B}\mathbf{U}^{(1)}; \mathbf{U}^{(0)} > + \lambda^{(1)} < \mathbf{B}\mathbf{U}^{(0)}; \mathbf{U}^{(0)} >, \end{aligned} \tag{1.68}$$

which can be further written as

$$\begin{aligned} &< \mathbf{A}\mathbf{U}^{(0)} - \lambda^{(0)} \mathbf{B}\mathbf{U}^{(0)}; \mathbf{U}^{(1)} > - \int_{S_T} \rho' h' \lambda^{(0)} u_k^{(0)} u_k^{(0)} dS \\ &\quad = \lambda^{(1)} < \mathbf{B}\mathbf{U}^{(0)}; \mathbf{U}^{(0)} > . \end{aligned} \tag{1.69}$$

With Eqs. $(1.62)_{1,2}$, we obtain, from Eq. (1.69),

$$\lambda^{(1)} = -\frac{\int_{S_T} \rho' h' \lambda^{(0)} u_k^{(0)} u_k^{(0)} dS}{< \mathbf{B}\mathbf{U}^{(0)}; \mathbf{U}^{(0)} >} = -\lambda^{(0)} \frac{\int_{S_T} \rho' h' u_k^{(0)} u_k^{(0)} dS}{\int_V \rho u_i^{(0)} u_i^{(0)} dV} . \tag{1.70}$$

The above perturbation procedure is for $\lambda = \omega^2$. For ω we make the following expansion:

$$\omega \cong \omega^{(0)} + \varepsilon \omega^{(1)} . \tag{1.71}$$

Then,

$$\lambda = \omega^2 \cong (\omega^{(0)} + \varepsilon \omega^{(1)})^2 \cong (\omega^{(0)})^2 + 2\varepsilon \omega^{(0)} \omega^{(1)} \cong \lambda^{(0)} + \varepsilon \lambda^{(1)} . \tag{1.72}$$

Hence,

$$\frac{\varepsilon \omega^{(1)}}{\omega^{(0)}} \cong \frac{1}{2(\omega^{(0)})^2} \varepsilon \lambda^{(1)} = -\frac{1}{2(\omega^{(0)})^2} \varepsilon \lambda^{(0)} \frac{\int_{S_T} \rho' h' u_k^{(0)} u_k^{(0)} dS}{\int_V \rho u_i^{(0)} u_i^{(0)} dV} . \tag{1.73}$$

Finally, setting $\varepsilon = 1$ in Eq. (1.73), we obtain

$$\frac{\omega - \omega^{(0)}}{\omega^{(0)}} \cong -\frac{1}{2}\frac{\int_{S_T} \rho' h' u_k^{(0)} u_k^{(0)} dS}{\int_V \rho u_i^{(0)} u_i^{(0)} dV}. \tag{1.74}$$

Equation (1.74) is linear in the density and thickness of the mass layer. It is negative, which shows that the inertia of the mass layer lowers the frequency, as expected. An example of the application of Eq. (1.74) will be given later in Section 2.4.

1.4. Effect of Mass Layer Stiffness: Perturbation Integral

In the previous section, only the inertial effect of the surface mass layer was considered; its stiffness was neglected. In this section we analyze frequency shifts due to a mass layer considering both the inertial and the stiffness effects of the layer [10].

1.4.1. Governing equations

Still consider the crystal body with a mass layer shown in Fig. 1.2. Denoting the interface traction on the crystal from the mass layer by t_i, we write the governing equations and boundary conditions of the crystal body as

$$\begin{aligned}
&c_{jikl} u_{k,lj} + e_{kji} \phi_{,kj} = \rho \ddot{u}_i, \quad \text{in} \quad V, \\
&-e_{ikl} u_{k,li} + \varepsilon_{ik} \phi_{,ki} = 0, \quad \text{in} \quad V, \\
&u_i = 0, \quad \text{on} \quad S_u, \\
&T_{ji} n_j = (c_{jikl} u_{k,l} + e_{kji} \phi_{,k}) n_j = t_i, \quad \text{on} \quad S_T, \\
&\phi = 0, \quad \text{on} \quad S_\phi, \\
&D_i n_i = (e_{ikl} u_{k,l} - \varepsilon_{ik} \phi_{,k}) n_i = 0, \quad \text{on} \quad S_D.
\end{aligned} \tag{1.75}$$

For the lowest-order effect of the stiffness of the mass layer, we use the membrane theory for a thin elastic shell in extension [11, 12] which describes a layer that does not resist bending. The shell displacement vector is given by $u_\beta = u_\beta(\alpha_1, \alpha_2)$, where α_1 and α_2 are the shell middle

surface principal coordinates, and α_3 is the shell thickness coordinate. β = 1, 2, 3 is associated with the shell principle coordinates (α_1, α_2, α_3). Then the shell membrane strains are

$$\begin{aligned} S_1 &= \frac{1}{A_1}\frac{\partial u_1}{\partial \alpha_1} + \frac{u_2}{A_1 A_2}\frac{\partial A_1}{\partial \alpha_2} + \kappa_1 u_3, \\ S_2 &= \frac{1}{A_2}\frac{\partial u_2}{\partial \alpha_2} + \frac{u_1}{A_1 A_2}\frac{\partial A_2}{\partial \alpha_1} + \kappa_2 u_3, \\ S_6 &= \frac{A_2}{A_1}\frac{\partial}{\partial \alpha_1}\left(\frac{u_2}{A_2}\right) + \frac{A_1}{A_2}\frac{\partial}{\partial \alpha_2}\left(\frac{u_1}{A_1}\right), \end{aligned} \tag{1.76}$$

where A_1 and A_2 are Lamé coefficients. κ_1 and κ_2 are the principal curvatures of the middle surface of the shell. The mass layer is assumed to be isotropic. The membrane stress resultants are given by the following membrane constitutive relations:

$$\begin{aligned} N_1 &= h'\gamma_{11} S_1 + h'\gamma_{12} S_2, \\ N_2 &= h'\gamma_{12} S_1 + h'\gamma_{11} S_2, \\ N_6 &= h'\gamma_{66} S_6, \end{aligned} \tag{1.77}$$

where γ_{11}, γ_{12} and γ_{66} are the shell membrane elastic constants. The shell membrane equations of motion are

$$\begin{aligned} &\frac{\partial}{\partial \alpha_1}(A_2 N_1) + \frac{\partial}{\partial \alpha_2}(A_1 N_6) \\ &\quad + N_6 \frac{\partial A_1}{\partial \alpha_2} - N_2 \frac{\partial A_2}{\partial \alpha_1} + A_1 A_2 F_1 = A_1 A_2 \rho' h' \ddot{u}_1, \\ &\frac{\partial}{\partial \alpha_1}(A_2 N_6) + \frac{\partial}{\partial \alpha_2}(A_1 N_2) \\ &\quad + N_6 \frac{\partial A_2}{\partial \alpha_1} - N_1 \frac{\partial A_1}{\partial \alpha_2} + A_1 A_2 F_2 = A_1 A_2 \rho' h' \ddot{u}_2, \\ &\quad - A_1 A_2 \kappa_1 N_1 - A_1 A_2 \kappa_2 N_2 + A_1 A_2 F_3 = A_1 A_2 \rho' h' \ddot{u}_3, \end{aligned} \tag{1.78}$$

where F_i is the load per unit middle surface area. With successive substitutions from Eqs. (1.76) and (1.77), Eq. (1.78) can be written in the following compact form

$$-L_\beta(\mathbf{u}) + F_\beta = \rho' h' \ddot{u}_\beta, \tag{1.79}$$

where L_β are linear differential operators. At every point of the shell, there exists a set of transformation coefficients $\Gamma_{i\beta}$ between the local shell principal coordinates and the global Cartesian coordinates. Multiplying Eq. (1.79) by the transformation coefficients we have

$$-L_i(\mathbf{u}) + F_i = \rho' h' \ddot{u}_i. \tag{1.80}$$

We note that the t_i in Eq. $(1.75)_4$ and the F_i in Eq. (1.80) are actions and reactions, equal in magnitude and opposite in directions ($F_i = -t_i$). Substituting Eq. (1.80) into Eq. $(1.75)_4$, considering time-harmonic motions with an exp($i\omega t$) factor, the eigenvalue problem for the free vibration of the body with the film can be written as

$$\begin{aligned}
&-c_{jikl}u_{k,lj} - e_{kji}\phi_{,kj} = \rho\lambda u_i, \quad \text{in} \quad V,\\
&-e_{ikl}u_{k,li} + \varepsilon_{ik}\phi_{,ki} = 0, \quad \text{in} \quad V,\\
&u_i = 0, \quad \text{on} \quad S_u,\\
&T_{ji}n_j = (c_{jikl}u_{k,l} + e_{kji}\phi_{,k})n_j\\
&\quad = \varepsilon[\rho' h' \lambda u_i - L_i(\mathbf{u})], \quad \text{on} \quad S_T,\\
&\phi = 0, \quad \text{on} \quad S_\phi,\\
&D_i n_i = (e_{ikl}u_{k,l} - \varepsilon_{ik}\phi_{,k})n_i = 0, \quad \text{on} \quad S_D,
\end{aligned} \tag{1.81}$$

where we have denoted $\lambda = \omega^2$. ε is an artificially introduced parameter for the perturbation analysis below. The original physical problem corresponds to $\varepsilon = 1$.

1.4.2. Perturbation analysis

For a perturbation solution of Eq. (1.81) we make the following expansions:

$$\begin{aligned} &\lambda \cong \lambda^{(0)} + \varepsilon \lambda^{(1)}, \\ &\mathbf{U} = \begin{Bmatrix} u_i \\ \phi \end{Bmatrix} \cong \begin{Bmatrix} u_i^{(0)} \\ \phi^{(0)} \end{Bmatrix} + \varepsilon \begin{Bmatrix} u_i^{(1)} \\ \phi^{(1)} \end{Bmatrix} = \mathbf{U}^{(0)} + \varepsilon \mathbf{U}^{(1)}, \end{aligned} \tag{1.82}$$

where $\omega^{(0)}$, $\mathbf{u}^{(0)}$ and $\phi^{(0)}$ are the frequency and modes when the mass layer is not present. Comparison of Eq. (1.81) with Eq. (1.60) shows that the only difference is the term with L_i. Therefore the perturbation procedure is very similar to that in the previous section, the only modification needed is the L_i term. The perturbation procedure will not be repeated. The result is

$$\lambda^{(1)} = \frac{\int_{S_T} [L_k(\mathbf{u}^{(0)}) u_k^{(0)} - \rho' h' \lambda^{(0)} u_k^{(0)} u_k^{(0)}] dS}{\int_V \rho u_i^{(0)} u_i^{(0)} dV}. \tag{1.83}$$

The above derivation is for the eigenvalue $\lambda = \omega^2$. For $\omega \cong \omega^{(0)} + \varepsilon\omega^{(1)}$, from Eq. (1.73) we have:

$$\frac{\varepsilon\omega^{(1)}}{\omega^{(0)}} \cong \frac{1}{2(\omega^{(0)})^2} \varepsilon\lambda^{(1)}. \tag{1.84}$$

Finally, substituting Eq. (1.83) into Eq. (1.84), setting $\varepsilon = 1$, we obtain

$$\begin{aligned} \frac{\omega - \omega^{(0)}}{\omega^{(0)}} \cong \frac{1}{2(\omega^{(0)})^2} \times \\ \frac{\int_{S_T} [L_k(\mathbf{u}^{(0)}) u_k^{(0)} - \rho' h' (\omega^{(0)})^2 u_k^{(0)} u_k^{(0)}] dS}{\int_V \rho u_i^{(0)} u_i^{(0)} dV}. \end{aligned} \tag{1.85}$$

The stiffness effect of the film is in L_k. When $L_k = 0$, Eq. (1.85) reduces to Eq. (1.74).

1.4.3. Example

The mass layer extensional stiffness does not affect thickness-shear modes of plates which are the main subject of later chapters. Therefore an example of the radial vibration of a thin elastic ring (see Fig. 1.3) is given here. The ring has a mean radius R, thickness h, Young's modulus E, Poisson's ratio ν, and mass density ρ. The mass layer has a thickness h', Young's modulus E' and mass density ρ'.

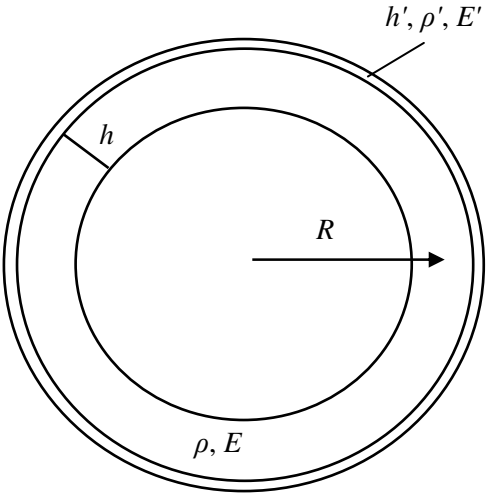

Fig. 1.3. An elastic ring with a mass layer.

When the mass layer is not present, in polar coordinates, the lowest radial mode of the ring is given by [3]

$$
\begin{aligned}
&(\omega^{(0)})^2 = \frac{E}{R^2\rho}, \\
&u_r^{(0)} = C, \quad u_\theta^{(0)} = 0, \quad u_z^{(0)} = -\nu\frac{C}{R}z \cong 0,
\end{aligned}
\tag{1.86}
$$

where C is an arbitrary constant. $u_z^{(0)}$ is due to Poisson's effect, which is neglected as an approximation. For the mass layer the equation of motion in the radial direction is

$$-\frac{h'E'}{R^2}u_r + F_r = \rho' h' \ddot{u}_r, \tag{1.87}$$

from which, by comparing with Eq. (1.79), we identify

$$L_r(\mathbf{u}) = \frac{h'E'}{R^2}u_r, \quad L_\theta(\mathbf{u}) = 0, \quad L_z(\mathbf{u}) = 0. \tag{1.88}$$

Substituting Eqs. (1.86) and (1.88) into Eq. (1.85), we obtain the frequency shift due to the mass layer as

$$\begin{aligned}\frac{\omega - \omega^{(0)}}{\omega^{(0)}} &\cong \frac{1}{2(\omega^{(0)})^2}\frac{1}{\rho h}\left[\frac{h'E'}{R^2} - \rho' h'(\omega^{(0)})^2\right] \\ &= \frac{1}{2(\omega^{(0)})^2}\frac{1}{\rho h}\left(\frac{h'E'}{R^2} - \rho' h'\frac{E}{R^2\rho}\right) \\ &= \frac{1}{2}\frac{h'}{h}\left(\frac{E'}{E} - \frac{\rho'}{\rho}\right).\end{aligned} \tag{1.89}$$

Equation (1.89) shows that the inertia of the mass layer lowers the frequency, and the stiffness of the mass layer raises the frequency as expected. It also shows that, compared to the inertial effect, the stiffness effect is not necessarily small depending on the materials involved, and should be considered in general. Following the procedure in [3] for obtaining Eq. (1.86), we can also obtain the frequency of the ring with the mass layer attached as

$$\omega^2 = \frac{Eh + E'h'}{R^2(\rho h + \rho' h')}. \tag{1.90}$$

It can be easily verified that for small h' Eq. (1.90) becomes Eq. (1.89). The mass layer stiffness considered in this section is the membrane

stiffness. The effect of the mass layer thickness-shear stiffness for the case of a layer on a crystal plates was studied in [13] using a higher-order shell theory for the mass layer and a perturbation procedure.

1.5. Frequency Perturbation Due to Contact with a Fluid

Vibrating crystals in contact with a viscous fluid can be used as fluid sensors based on frequency shifts due to the fluid viscosity and density. This is particularly convenient when the fluid density/viscosity is relatively low so that the fluid-induced frequency shifts are relatively small. For a fluid sensor we have a so-called fluid-structure interaction problem in mechanics over an unbounded, divided domain for the solid and the fluid, respectively (interior-exterior problem). In this case a perturbation analysis can also be used [14].

1.5.1. Governing equations

Consider an anisotropic elastic body in an unbounded region of a viscous, incompressible fluid (see Fig. 1.4). Let the interior region occupied by the crystal body be V and its boundary surface be S. The unit outward normal of S is **n**. Let the exterior region occupied by the fluid be $\overline{V}$.

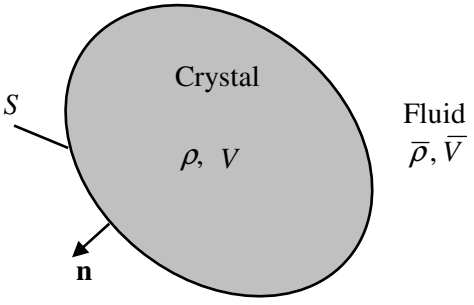

Fig. 1.4. A crystal in a fluid.

For free vibrations, the governing equations and boundary conditions of the elastic body and the fluid are

$$
\begin{aligned}
&T_{ji,j} = \rho \ddot{u}_i \quad \text{in} \quad V, \\
&T_{ji} = c_{jikl} u_{k,l} \quad \text{in} \quad V, \\
&\tau_{ji,j} - p_{,i} = \overline{\rho}\, \dot{v}_i \quad \text{in} \quad \overline{V}, \\
&v_{i,i} = 0 \quad \text{in} \quad \overline{V}, \\
&\tau_{ji} = \mu(v_{j,i} + v_{i,j}) \quad \text{in} \quad \overline{V}, \\
&T_{ji} n_j = \varepsilon(\tau_{ji} - p\delta_{ji}) n_j \quad \text{on} \quad S, \\
&\dot{u}_i = v_i \quad \text{on} \quad S.
\end{aligned}
\tag{1.91}
$$

where v_i is the velocity field, τ_{ij} is the viscous stress tensor, p is the pressure field, μ is the viscosity, and $\overline{\rho}$ is the mass density of the fluid. We consider small amplitude motions in which the material time derivative reduces to the partial derivative with respect to time, and Eq. (1.91) becomes linear. ε is an introduced parameter. The real physical problem is described by $\varepsilon = 1$. For the unbounded fluid region, some boundary conditions at infinity are also needed. For a viscous fluid the fields die out far away under the local disturbance from the crystal.

Consider time-harmonic motions. We use the usual complex notation. All fields are assumed to have an $\exp(i\omega t)$ factor which is canceled from all terms. Then Eq. (1.91) becomes

$$
\begin{aligned}
&-c_{jikl} u_{k,lj} = \rho \omega^2 u_i \quad \text{in} \quad V, \\
&\tau_{ji,j} - p_{,i} = \overline{\rho}\, i\omega v_i \quad \text{in} \quad \overline{V}, \\
&v_{i,i} = 0 \quad \text{in} \quad \overline{V}, \\
&\tau_{ji} = \mu(v_{j,i} + v_{i,j}) \quad \text{in} \quad \overline{V}, \\
&c_{jikl} u_{k,l} n_j = \varepsilon(\tau_{ji} - p\delta_{ji}) n_j \quad \text{on} \quad S, \\
&i\omega u_i = v_i \quad \text{on} \quad S.
\end{aligned}
\tag{1.92}
$$

1.5.2. Perturbation analysis

For a perturbation solution of Eq. (1.92) we make the following expansions:

$$\begin{aligned} &\omega \cong \omega^{(0)} + \varepsilon\, \omega^{(1)}, \quad \mathbf{u} \cong \mathbf{u}^{(0)} + \varepsilon\, \mathbf{u}^{(1)}, \\ &\mathbf{v} \cong \mathbf{v}^{(0)} + \varepsilon\, \mathbf{v}^{(1)}, \quad p \cong p^{(0)} + \varepsilon\, p^{(1)}, \\ &\tau_{ji} \cong \tau_{ji}^{(0)} + \varepsilon \tau_{ji}^{(1)}. \end{aligned} \tag{1.93}$$

Substituting Eq. (1.93) into Eq. (1.92), and collecting terms of equal powers of ε, we obtain a series of perturbation problems of successive orders. We are interested in the lowest-order effect of the fluid. Therefore, we collect coefficients of terms with powers of ε^0 and ε^1 only. The zero-order problem consists of

$$\begin{aligned} &-c_{jikl} u_{k,lj}^{(0)} = \rho (\omega^{(0)})^2 u_i^{(0)} \quad \text{in} \quad V, \\ &c_{jikl} u_{k,l}^{(0)} n_j = 0 \quad \text{on} \quad S, \end{aligned} \tag{1.94}$$

and

$$\begin{aligned} &\tau_{ji,j}^{(0)} - p_{,i}^{(0)} = \bar{\rho}\, i\omega^{(0)} v_i^{(0)} \quad \text{in} \quad \bar{V}, \\ &v_{i,i}^{(0)} = 0 \quad \text{in} \quad \bar{V}, \\ &\tau_{ji}^{(0)} = \mu (v_{j,i}^{(0)} + v_{i,j}^{(0)}) \quad \text{in} \quad \bar{V}, \\ &i\omega^{(0)} u_i^{(0)} = v_i^{(0)} \quad \text{on} \quad S. \end{aligned} \tag{1.95}$$

Equation (1.94) shows that $\omega^{(0)}$ and $\mathbf{u}^{(0)}$ represent the frequencies and modes when the fluid is not present, which can be written as real, nonnegative numbers and real functions, respectively. The zero-order problem is decoupled in the sense that the unperturbed frequency and modes of the crystal can be obtained from Eq. (1.94) by neglecting the fluid. Once $\omega^{(0)}$ and $\mathbf{u}^{(0)}$ of the crystal are determined, the corresponding fluid motion is determined from Eq. (1.95). The interface continuity conditions in Eqs. $(1.92)_{5,6}$ now become boundary conditions in Eqs. $(1.94)_2$ and $(1.95)_4$. The interior-exterior problem in Eq. (1.92) becomes an interior problem in Eq. (1.94) and an exterior problem in Eq. (1.95). The separation of the solid and the fluid is an important

simplification. The zero-order solution, $\omega^{(0)}$, $\mathbf{u}^{(0)}$, $v^{(0)}$, $p^{(0)}$ and $\tau_{ji}^{(0)}$, are assumed known as usual in a perturbation analysis.

For the first-order problem, for our purpose of determining the frequency shift $\varepsilon\omega^{(1)}$, only the following equations and boundary conditions for the crystal are needed:

$$\begin{aligned} -c_{jikl}u_{k,lj}^{(1)} &= \rho(\omega^{(0)})^2 u_i^{(1)} + \rho 2\omega^{(0)}\omega^{(1)}u_i^{(0)} \quad \text{in} \quad V, \\ c_{jikl}u_{k,l}^{(1)}n_j &= (\tau_{ji}^{(0)} - p^{(0)}\delta_{ji})n_j \quad \text{on} \quad S. \end{aligned} \tag{1.96}$$

A comparison of Eq. (1.96) with Eq. (1.63) shows that mathematically $(\tau_{ji}^{(0)} - p^{(0)}\delta_{ji})n_j$ in Eq. $(1.96)_2$ plays the role of $\rho' h' \lambda^{(0)} u_i^{(0)}$ in Eq. $(1.63)_4$. Therefore the perturbation procedure is very similar and will not be repeated here. The result is

$$\frac{\varepsilon\omega^{(1)}}{\omega^{(0)}} \cong -\frac{\varepsilon}{2(\omega^{(0)})^2} \frac{\int_S (\tau_{ji}^{(0)} - p^{(0)}\delta_{ji})n_j u_i^{(0)} dS}{\int_V \rho u_i^{(0)} u_i^{(0)} dV}. \tag{1.97}$$

Setting $\varepsilon = 1$, we obtain the first-order perturbation integral for the frequency shift as

$$\frac{\omega - \omega^{(0)}}{\omega^{(0)}} \cong -\frac{1}{2(\omega^{(0)})^2} \frac{\int_S (\tau_{ji}^{(0)} - p^{(0)}\delta_{ji})n_j u_i^{(0)} dS}{\int_V \rho u_i^{(0)} u_i^{(0)} dV}. \tag{1.98}$$

An example of using Eq. (1.98) will be given in Section 2.8.

1.6. Quartz and Langasite

Quartz (and langasite) belongs to the trigonal crystal class of 32 or D_3. It has one axis of trigonal symmetry and, in the plane at right angles, three digonal axes 120° apart. With respect to the crystallographic axes

(X, Y, Z) corresponding to (1, 2, 3) where Z is the trigonal or c axis and X a digonal axis, the material matrices have the following structures:

$$\begin{pmatrix} c_{11} & c_{12} & c_{13} & c_{14} & 0 & 0 \\ c_{21} & c_{11} & c_{13} & -c_{14} & 0 & 0 \\ c_{13} & c_{13} & c_{33} & 0 & 0 & 0 \\ c_{14} & -c_{14} & 0 & c_{44} & 0 & 0 \\ 0 & 0 & 0 & 0 & c_{44} & c_{14} \\ 0 & 0 & 0 & 0 & c_{14} & c_{66} \end{pmatrix},$$

$$\begin{pmatrix} e_{11} & -e_{11} & 0 & e_{14} & 0 & 0 \\ 0 & 0 & 0 & 0 & -e_{14} & -e_{11} \\ 0 & 0 & 0 & 0 & 0 & 0 \end{pmatrix}, \begin{pmatrix} \varepsilon_{11} & 0 & 0 \\ 0 & \varepsilon_{11} & 0 \\ 0 & 0 & \varepsilon_{33} \end{pmatrix}. \qquad (1.99)$$

The independent material constants are 6 + 2 + 2 = 10.

Quartz plates taken out of a bulk crystal at different orientations are referred to as plates of different cuts. A particular cut is specified by two angles, φ and θ, with respect to (X, Y, Z) (see Fig. 1.5) and is called a doubly-rotated cut in general. For example, the stress-compensated SC-cut has $(\varphi,\theta) = (22.4^{\circ},-33.88^{\circ})$. Plates of different cuts have different material matrices with respect to the coordinate system (x_1, x_2, x_3) in and normal to the plane of the plates.

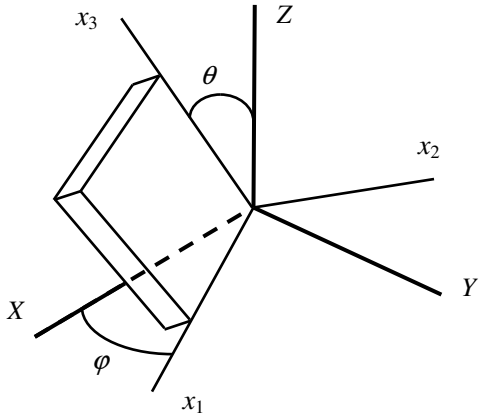

Fig. 1.5. A quartz plate cut from a bulk crystal (doubly-rotated cut).

One class of cuts of quartz plates, called rotated Y-cuts, is particularly useful in device applications. Rotated Y-cut quartz plates have $\varphi = 0$ (see Fig. 1.6) and they are called singly-rotated cuts.

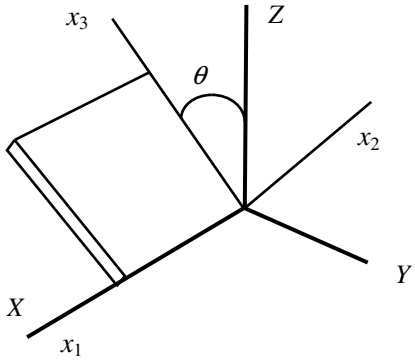

Fig. 1.6. A rotated Y-cut quartz plate (singly-rotated cut).

Rotated Y-cut quartz plates exhibit monoclinic symmetry of class 2 or C_2 in (x_1, x_2, x_3), with x_1 the diagonal axis. Rotated Y-cuts include a few common cuts, e.g., AT-cut with $(\varphi,\theta) = (0^o,-35^o)$ and BT-cut with $(\varphi,\theta) = (0^o,49^o)$ as special cases. Therefore we list the equations for monoclinic crystals of class 2 below which are useful for studying rotated Y-cut quartz plates in general. For these crystal plates, with the digonal axis along the x_1 axis, the material matrices are

$$\begin{pmatrix} c_{11} & c_{12} & c_{13} & c_{14} & 0 & 0 \\ c_{21} & c_{22} & c_{23} & c_{24} & 0 & 0 \\ c_{31} & c_{32} & c_{33} & c_{34} & 0 & 0 \\ c_{41} & c_{42} & c_{43} & c_{44} & 0 & 0 \\ 0 & 0 & 0 & 0 & c_{55} & c_{56} \\ 0 & 0 & 0 & 0 & c_{65} & c_{66} \end{pmatrix},$$

$$\begin{pmatrix} e_{11} & e_{12} & e_{13} & e_{14} & 0 & 0 \\ 0 & 0 & 0 & 0 & e_{25} & e_{26} \\ 0 & 0 & 0 & 0 & e_{35} & e_{36} \end{pmatrix}, \begin{pmatrix} \varepsilon_{11} & 0 & 0 \\ 0 & \varepsilon_{22} & \varepsilon_{23} \\ 0 & \varepsilon_{32} & \varepsilon_{33} \end{pmatrix}. \qquad (1.100)$$

The constitutive relations are

$$\begin{aligned}
T_{11} &= c_{11}u_{1,1} + c_{12}u_{2,2} + c_{13}u_{3,3} + c_{14}(u_{2,3} + u_{3,2}) + e_{11}\phi_{,1},\\
T_{22} &= c_{12}u_{1,1} + c_{22}u_{2,2} + c_{23}u_{3,3} + c_{24}(u_{2,3} + u_{3,2}) + e_{12}\phi_{,1},\\
T_{33} &= c_{13}u_{1,1} + c_{23}u_{2,2} + c_{33}u_{3,3} + c_{34}(u_{2,3} + u_{3,2}) + e_{13}\phi_{,1},\\
T_{23} &= c_{14}u_{1,1} + c_{24}u_{2,2} + c_{34}u_{3,3} + c_{44}(u_{2,3} + u_{3,2}) + e_{14}\phi_{,1},\\
T_{31} &= c_{55}(u_{3,1} + u_{1,3}) + c_{56}(u_{1,2} + u_{2,1}) + e_{25}\phi_{,2} + e_{35}\phi_{,3},\\
T_{12} &= c_{56}(u_{3,1} + u_{1,3}) + c_{66}(u_{1,2} + u_{2,1}) + e_{26}\phi_{,2} + e_{36}\phi_{,3},
\end{aligned} \tag{1.101}$$

and

$$\begin{aligned}
D_1 &= e_{11}u_{1,1} + e_{12}u_{2,2} + e_{13}u_{3,3} + e_{14}(u_{2,3} + u_{3,2}) - \varepsilon_{11}\phi_{,1},\\
D_2 &= e_{25}(u_{3,1} + u_{1,3}) + e_{26}(u_{1,2} + u_{2,1}) - \varepsilon_{22}\phi_{,2} - \varepsilon_{23}\phi_{,3},\\
D_3 &= e_{35}(u_{3,1} + u_{1,3}) + e_{36}(u_{1,2} + u_{2,1}) - \varepsilon_{23}\phi_{,2} - \varepsilon_{33}\phi_{,3}.
\end{aligned} \tag{1.102}$$

The equations of motion and charge are

$$\begin{aligned}
&c_{11}u_{1,11} + (c_{12} + c_{66})u_{2,12} + (c_{13} + c_{55})u_{3,13} + (c_{14} + c_{56})u_{2,13}\\
&\quad + (c_{14} + c_{56})u_{3,12} + 2c_{56}u_{1,23} + c_{66}u_{1,22} + c_{55}u_{1,33}\\
&\quad + e_{11}\phi_{,11} + e_{26}\phi_{,22} + (e_{36} + e_{25})\phi_{,23} + e_{35}\phi_{,33} = \rho\ddot{u}_1,\\
&c_{56}u_{3,11} + (c_{56} + c_{14})u_{1,13} + (c_{66} + c_{12})u_{1,12} + c_{66}u_{2,11}\\
&\quad + c_{22}u_{2,22} + (c_{23} + c_{44})u_{3,23} + 2c_{24}u_{2,23} + c_{24}u_{3,22}\\
&\quad + c_{34}u_{3,33} + c_{44}u_{2,33} + (e_{26} + e_{12})\phi_{,12} + (e_{36} + e_{14})\phi_{,13} = \rho\ddot{u}_2,\\
&c_{55}u_{3,11} + (c_{55} + c_{13})u_{1,13} + (c_{56} + c_{14})u_{1,12} + c_{56}u_{2,11}\\
&\quad + c_{24}u_{2,22} + 2c_{34}u_{3,23} + (c_{44} + c_{23})u_{2,23} + c_{44}u_{3,22}\\
&\quad + c_{33}u_{3,33} + c_{34}u_{2,33} + (e_{25} + e_{14})\phi_{,12} + (e_{35} + e_{13})\phi_{,13} = \rho\ddot{u}_3,
\end{aligned} \tag{1.103}$$

$$\begin{aligned}
&e_{11}u_{1,11} + (e_{12} + e_{26})u_{2,12} + (e_{13} + e_{35})u_{3,13} + (e_{14} + e_{36})u_{2,13}\\
&\quad + (e_{14} + e_{25})u_{3,12} + (e_{25} + e_{36})u_{1,23} + e_{26}u_{1,22}\\
&\quad + e_{35}u_{1,33} - \varepsilon_{11}\phi_{,11} - \varepsilon_{22}\phi_{,22} - 2\varepsilon_{23}\phi_{,23} - \varepsilon_{33}\phi_{,33} = 0.
\end{aligned} \tag{1.104}$$

In rotated Y-cut quartz, the following so-called shear-horizontal (SH) or antiplane motions with only one displacement component, u_1, are allowed and are useful in device applications. Consider

$$\begin{aligned} &u_1 = u_1(x_2, x_3, t), \quad u_2 = u_3 = 0, \\ &\phi = \phi(x_2, x_3, t). \end{aligned} \tag{1.105}$$

Equation (1.105) yields the following nonzero components of strain, electric field, stress, and electric displacement:

$$\begin{aligned} &S_5 = u_{1,3}, \quad S_6 = u_{1,2}, \\ &E_2 = -\phi_{,2}, \quad E_3 = -\phi_{,3}, \\ &T_{31} = c_{55}u_{1,3} + c_{56}u_{1,2} + e_{25}\phi_{,2} + e_{35}\phi_{,3}, \\ &T_{21} = c_{56}u_{1,3} + c_{66}u_{1,2} + e_{26}\phi_{,2} + e_{36}\phi_{,3}, \\ &D_2 = e_{25}u_{1,3} + e_{26}u_{1,2} - \varepsilon_{22}\phi_{,2} - \varepsilon_{23}\phi_{,3}, \\ &D_3 = e_{35}u_{1,3} + e_{36}u_{1,2} - \varepsilon_{23}\phi_{,2} - \varepsilon_{33}\phi_{,3}. \end{aligned} \tag{1.106}$$

The equations left to be satisfied by u_1 and ϕ are

$$\begin{aligned} &c_{66}u_{1,22} + c_{55}u_{1,33} + 2c_{56}u_{1,23} \\ &\quad + e_{26}\phi_{,22} + e_{35}\phi_{,33} + (e_{25} + e_{36})\phi_{,23} = \rho\ddot{u}_1, \\ &e_{26}u_{1,22} + e_{35}u_{1,33} + (e_{25} + e_{36})u_{1,23} \\ &\quad - \varepsilon_{22}\phi_{,22} - \varepsilon_{33}\phi_{,33} - 2\varepsilon_{23}\phi_{,23} = 0. \end{aligned} \tag{1.107}$$

1.7. Lithium Niobate and Lithium Tantalate

Lithium niobate and lithium tantalate have stronger piezoelectric coupling than quartz. For these two crystals the crystal class is $C_{3v} = 3m$, a different type of trigonal crystal than quartz. When x_3 is the trigonal axis like in quartz and x_1 is normal to a mirror plane in these crystals, the

material matrices are

$$\begin{pmatrix} c_{11} & c_{12} & c_{13} & c_{14} & 0 & 0 \\ c_{21} & c_{11} & c_{13} & -c_{14} & 0 & 0 \\ c_{13} & c_{13} & c_{33} & 0 & 0 & 0 \\ c_{14} & -c_{14} & 0 & c_{44} & 0 & 0 \\ 0 & 0 & 0 & 0 & c_{44} & c_{14} \\ 0 & 0 & 0 & 0 & c_{14} & c_{66} \end{pmatrix},$$

$$\begin{pmatrix} 0 & 0 & 0 & 0 & e_{15} & -e_{22} \\ -e_{22} & e_{22} & 0 & e_{15} & 0 & 0 \\ e_{31} & e_{32} & e_{33} & 0 & 0 & 0 \end{pmatrix}, \begin{pmatrix} \varepsilon_{11} & 0 & 0 \\ 0 & \varepsilon_{11} & 0 \\ 0 & 0 & \varepsilon_{33} \end{pmatrix}. \tag{1.108}$$

When a rotated Y-cut is formed by rotating about x_1, the material apparently has *m*-monoclinic symmetry with the following matrices

$$\begin{pmatrix} c_{11} & c_{12} & c_{13} & c_{14} & 0 & 0 \\ c_{21} & c_{22} & c_{23} & c_{24} & 0 & 0 \\ c_{31} & c_{32} & c_{33} & c_{34} & 0 & 0 \\ c_{41} & c_{42} & c_{43} & c_{44} & 0 & 0 \\ 0 & 0 & 0 & 0 & c_{55} & c_{56} \\ 0 & 0 & 0 & 0 & c_{65} & c_{66} \end{pmatrix},$$

$$\begin{pmatrix} 0 & 0 & 0 & 0 & e_{15} & e_{16} \\ e_{21} & e_{22} & e_{23} & e_{24} & 0 & 0 \\ e_{31} & e_{32} & e_{33} & e_{34} & 0 & 0 \end{pmatrix}, \begin{pmatrix} \varepsilon_{11} & 0 & 0 \\ 0 & \varepsilon_{22} & \varepsilon_{23} \\ 0 & \varepsilon_{32} & \varepsilon_{33} \end{pmatrix}. \tag{1.109}$$

The constitutive relations are

$$\begin{aligned} T_{11} &= c_{11}u_{1,1} + c_{12}u_{2,2} + c_{13}u_{3,3} + c_{14}(u_{2,3} + u_{3,2}) + e_{21}\phi_{,2} + e_{31}\phi_{,3}, \\ T_{22} &= c_{12}u_{1,1} + c_{22}u_{2,2} + c_{23}u_{3,3} + c_{24}(u_{2,3} + u_{3,2}) + e_{22}\phi_{,2} + e_{32}\phi_{,3}, \\ T_{33} &= c_{13}u_{1,1} + c_{23}u_{2,2} + c_{33}u_{3,3} + c_{34}(u_{2,3} + u_{3,2}) + e_{23}\phi_{,2} + e_{33}\phi_{,3}, \\ T_{23} &= c_{14}u_{1,1} + c_{24}u_{2,2} + c_{34}u_{3,3} + c_{44}(u_{2,3} + u_{3,2}) + e_{24}\phi_{,2} + e_{34}\phi_{,3}, \\ T_{31} &= c_{55}(u_{3,1} + u_{1,3}) + c_{56}(u_{1,2} + u_{2,1}) + e_{15}\phi_{,1}, \\ T_{12} &= c_{56}(u_{3,1} + u_{1,3}) + c_{66}(u_{1,2} + u_{2,1}) + e_{16}\phi_{,1}, \end{aligned} \tag{1.110}$$

and

$$
\begin{aligned}
D_1 &= e_{15}(u_{1,3} + u_{3,1}) + e_{16}(u_{1,2} + u_{2,1}) - \varepsilon_{11}\phi_{,1}, \\
D_2 &= e_{21}u_{1,1} + e_{22}u_{2,2} + e_{23}u_{3,3} + e_{24}(u_{2,3} + u_{3,2}) - \varepsilon_{22}\phi_{,2} - \varepsilon_{23}\phi_{,3}, \\
D_3 &= e_{31}u_{1,1} + e_{32}u_{2,2} + e_{33}u_{3,3} + e_{34}(u_{2,3} + u_{3,2}) - \varepsilon_{23}\phi_{,2} - \varepsilon_{33}\phi_{,3}.
\end{aligned} \tag{1.111}
$$

The equations of motion and charge are

$$
\begin{aligned}
&c_{11}u_{1,11} + (c_{12} + c_{66})u_{2,12} + (c_{13} + c_{55})u_{3,13} + (c_{14} + c_{56})u_{2,13} \\
&\quad + (c_{14} + c_{56})u_{3,12} + 2c_{56}u_{1,23} + c_{66}u_{1,22} + c_{55}u_{1,33} \\
&\quad + (e_{21} + e_{16})\phi_{,12} + (e_{31} + e_{15})\phi_{,13} = \rho\ddot{u}_1, \\
&c_{56}u_{3,11} + (c_{56} + c_{14})u_{1,13} + (c_{66} + c_{12})u_{1,12} + c_{66}u_{2,11} + c_{22}u_{2,22} \\
&\quad + (c_{23} + c_{44})u_{3,23} + 2c_{24}u_{2,23} + c_{24}u_{3,22} + c_{34}u_{3,33} + c_{44}u_{2,33} \\
&\quad + e_{16}\phi_{,11} + e_{22}\phi_{,22} + (e_{32} + e_{24})\phi_{,23} + e_{34}\phi_{,33} = \rho\ddot{u}_2, \\
&c_{55}u_{3,11} + (c_{55} + c_{13})u_{1,13} + (c_{56} + c_{14})u_{1,12} + c_{56}u_{2,11} + c_{24}u_{2,22} \\
&\quad + 2c_{34}u_{3,23} + (c_{44} + c_{23})u_{2,23} + c_{44}u_{3,22} + c_{33}u_{3,33} + c_{34}u_{2,33} \\
&\quad + e_{15}\phi_{,11} + e_{24}\phi_{,22} + (e_{34} + e_{23})\phi_{,23} + e_{33}\phi_{,33} = \rho\ddot{u}_3,
\end{aligned} \tag{1.112}
$$

$$
\begin{aligned}
&(e_{15} + e_{31})u_{1,31} + e_{15}u_{3,11} + (e_{16} + e_{21})u_{1,12} + e_{16}u_{2,11} + e_{22}u_{2,22} \\
&\quad + (e_{23} + e_{34})u_{3,23} + (e_{24} + e_{32})u_{2,23} + e_{24}u_{3,22} + e_{33}u_{3,33} + e_{34}u_{2,33} \\
&\quad - \varepsilon_{11}\phi_{,11} - \varepsilon_{22}\phi_{,22} - 2\varepsilon_{23}\phi_{,23} - \varepsilon_{33}\phi_{,33} = 0.
\end{aligned} \tag{1.113}
$$

1.8. Polarized Ceramics and Crystals in Class 6mm

Polarized ceramics are transversely isotropic. When the poling direction

is along x_3, the material matrices are

$$\begin{pmatrix} c_{11} & c_{12} & c_{13} & 0 & 0 & 0 \\ c_{21} & c_{11} & c_{13} & 0 & 0 & 0 \\ c_{31} & c_{31} & c_{33} & 0 & 0 & 0 \\ 0 & 0 & 0 & c_{44} & 0 & 0 \\ 0 & 0 & 0 & 0 & c_{44} & 0 \\ 0 & 0 & 0 & 0 & 0 & c_{66} \end{pmatrix},$$

$$\begin{pmatrix} 0 & 0 & 0 & 0 & e_{15} & 0 \\ 0 & 0 & 0 & e_{15} & 0 & 0 \\ e_{31} & e_{31} & e_{33} & 0 & 0 & 0 \end{pmatrix}, \begin{pmatrix} \varepsilon_{11} & 0 & 0 \\ 0 & \varepsilon_{11} & 0 \\ 0 & 0 & \varepsilon_{33} \end{pmatrix}, \tag{1.114}$$

where $c_{66} = (c_{11} - c_{12})/2$. With Eq. (1.114), the constitutive relations take the following form:

$$\begin{aligned} T_{11} &= c_{11}u_{1,1} + c_{12}u_{2,2} + c_{13}u_{3,3} + e_{31}\phi_{,3}, \\ T_{22} &= c_{12}u_{1,1} + c_{11}u_{2,2} + c_{13}u_{3,3} + e_{31}\phi_{,3}, \\ T_{33} &= c_{13}u_{1,1} + c_{13}u_{2,2} + c_{33}u_{3,3} + e_{33}\phi_{,3}, \\ T_{23} &= c_{44}(u_{2,3} + u_{3,2}) + e_{15}\phi_{,2}, \\ T_{31} &= c_{44}(u_{3,1} + u_{1,3}) + e_{15}\phi_{,1}, \\ T_{12} &= c_{66}(u_{1,2} + u_{2,1}), \end{aligned} \tag{1.115}$$

and

$$\begin{aligned} D_1 &= e_{15}(u_{3,1} + u_{1,3}) - \varepsilon_{11}\phi_{,1}, \\ D_2 &= e_{15}(u_{2,3} + u_{3,2}) - \varepsilon_{11}\phi_{,2}, \\ D_3 &= e_{31}(u_{1,1} + u_{2,2}) + e_{33}u_{3,3} - \varepsilon_{33}\phi_{,3}. \end{aligned} \tag{1.116}$$

The equations of motion and charge are

$$\begin{aligned}
&c_{11}u_{1,11}+(c_{12}+c_{66})u_{2,12}+(c_{13}+c_{44})u_{3,13}+c_{66}u_{1,22}\\
&\quad+c_{44}u_{1,33}+(e_{31}+e_{15})\phi_{,13}=\rho\ddot{u}_1,\\
&c_{66}u_{2,11}+(c_{12}+c_{66})u_{1,12}+c_{11}u_{2,22}+(c_{13}+c_{44})u_{3,23}\\
&\quad+c_{44}u_{2,33}+(e_{31}+e_{15})\phi_{,23}=\rho\ddot{u}_2,\\
&c_{44}u_{3,11}+(c_{44}+c_{13})u_{1,31}+c_{44}u_{3,22}+(c_{13}+c_{44})u_{2,23}\\
&\quad+c_{33}u_{3,33}+e_{15}(\phi_{,11}+\phi_{,22})+e_{33}\phi_{,33}=\rho\ddot{u}_3,
\end{aligned} \tag{1.117}$$

$$\begin{aligned}
&e_{15}u_{3,11}+(e_{15}+e_{31})u_{1,13}+e_{15}u_{3,22}+(e_{15}+e_{31})u_{2,32}\\
&\quad+e_{31}u_{3,33}-\varepsilon_{11}(\phi_{,11}+\phi_{,22})-\varepsilon_{33}\phi_{,33}=0.
\end{aligned} \tag{1.118}$$

The material matrices of hexagonal crystals in class 6mm or C_{6v} have the same structures as those in Eq. (1.114). Therefore, within the theory of linear piezoelectricity, crystals in class 6mm behave the same as polarized ceramics.

Polarized ceramics also allow SH or antiplane motions with

$$u_1=u_2=0\,,\quad u_3=u(x_1,x_2,t)\,,\quad \phi=\phi(x_1,x_2,t)\,. \tag{1.119}$$

These motions have been systematically discussed in [15].

This page intentionally left blank

Chapter 2

Thickness Modes in Plates: Elastic Analysis

Quartz is probably the most widely used crystal for acoustic wave resonators and sensors. Its piezoelectric coupling is very weak. Therefore, for free-vibration frequency analysis of quartz devices, the small piezoelectric coupling can be neglected for many applications. In this case the basic behaviors of quartz plates are governed by the equations of linear elasticity for anisotropic materials. In this chapter we collect a few results for vibrations of quartz plates based on anisotropic elasticity. For some of them, generalizations to include piezoelectric coupling can be found later in Chapter 3. For others the consideration of piezoelectric coupling may become mathematically complicated.

2.1. Equations of Anisotropic Elasticity

Our notation still follows that in [1] but the electric field and piezoelectric coupling are neglected. We first summarize the basic theory of linear elasticity for crystals with general anisotropy, and then specialize them to quartz.

2.1.1. General anisotropic crystals

The equations of motion are

$$T_{ji,j} + f_i = \rho \ddot{u}_i , \tag{2.1}$$

where **T** is the stress tensor, ρ is the mass density, **f** is the body force per unit volume, and **u** is the displacement vector. Constitutive relations are given by a strain energy density function

$$U(\mathbf{S}) = \frac{1}{2} c_{ijkl} S_{ij} S_{kl} \tag{2.2}$$

through

$$T_{ij} = \frac{\partial U}{\partial S_{ij}} = c_{ijkl} S_{kl} , \tag{2.3}$$

where the strain tensor, **S**, is related to the displacement, **u**, by

$$S_{ij} = (u_{j,i} + u_{i,j})/2 . \tag{2.4}$$

c_{ijkl} are the elastic stiffness. The elastic constants have the following symmetries:

$$c_{ijkl} = c_{jikl} = c_{klij} . \tag{2.5}$$

We also assume that the elastic constants are positive definite in the following sense:

$$\begin{aligned} &c_{ijkl} S_{ij} S_{kl} \geq 0 \quad \text{for any} \quad S_{ij} = S_{ji} , \\ &\quad \text{and} \quad c_{ijkl} S_{ij} S_{kl} = 0 \quad \Rightarrow \quad S_{ij} = 0. \end{aligned} \tag{2.6}$$

Equation (2.3) can be inverted to give

$$S_{ij} = s_{ijkl} T_{kl} , \tag{2.7}$$

where s_{ijkl} are the elastic compliance. With successive substitutions from Eqs. (2.3) and (2.4), Eq. (2.1) can be written as three equations for **u**:

$$c_{ijkl} u_{k,lj} + f_i = \rho \ddot{u}_i . \tag{2.8}$$

Typical boundary conditions are the prescription of surface displacement or traction on the boundary of a body. Typical initial conditions are the specification of initial displacement and velocity. With the compact matrix notation defined in Section 1.1, the constitutive relations can be written as

$$T_p = c_{pq} S_q , \tag{2.9}$$

or

$$\begin{Bmatrix} T_1 \\ T_2 \\ T_3 \\ T_4 \\ T_5 \\ T_6 \end{Bmatrix} = \begin{pmatrix} c_{11} & c_{12} & c_{13} & c_{14} & c_{15} & c_{16} \\ c_{21} & c_{22} & c_{23} & c_{24} & c_{25} & c_{26} \\ c_{31} & c_{32} & c_{33} & c_{34} & c_{35} & c_{36} \\ c_{41} & c_{42} & c_{43} & c_{44} & c_{45} & c_{46} \\ c_{51} & c_{52} & c_{53} & c_{54} & c_{55} & c_{56} \\ c_{61} & c_{62} & c_{63} & c_{64} & c_{65} & c_{66} \end{pmatrix} \begin{Bmatrix} S_1 \\ S_2 \\ S_3 \\ S_4 \\ S_5 \\ S_6 \end{Bmatrix}, \tag{2.10}$$

where $c_{pq} = c_{qp}$.

2.1.2. Rotated Y-cut Quartz

Quartz belongs to the trigonal crystal class of 32 or D_3. With respect to the crystallographic axes (*X*, *Y*, *Z*), the elastic stiffness are given by

$$[c_{pq}] = \begin{pmatrix} c_{11} & c_{12} & c_{13} & c_{14} & 0 & 0 \\ c_{21} & c_{11} & c_{13} & -c_{14} & 0 & 0 \\ c_{13} & c_{13} & c_{33} & 0 & 0 & 0 \\ c_{14} & -c_{14} & 0 & c_{44} & 0 & 0 \\ 0 & 0 & 0 & 0 & c_{44} & c_{14} \\ 0 & 0 & 0 & 0 & c_{14} & c_{66} \end{pmatrix}. \tag{2.11}$$

Rotated Y-cut quartz is effectively monoclinic with

$$[c_{pq}] = \begin{pmatrix} c_{11} & c_{12} & c_{13} & c_{14} & 0 & 0 \\ c_{21} & c_{22} & c_{23} & c_{24} & 0 & 0 \\ c_{31} & c_{32} & c_{33} & c_{34} & 0 & 0 \\ c_{41} & c_{42} & c_{43} & c_{44} & 0 & 0 \\ 0 & 0 & 0 & 0 & c_{55} & c_{56} \\ 0 & 0 & 0 & 0 & c_{65} & c_{66} \end{pmatrix}. \tag{2.12}$$

The corresponding constitutive relations are

$$\begin{aligned}
T_{11} &= c_{11}u_{1,1} + c_{12}u_{2,2} + c_{13}u_{3,3} + c_{14}(u_{2,3} + u_{3,2}),\\
T_{22} &= c_{12}u_{1,1} + c_{22}u_{2,2} + c_{23}u_{3,3} + c_{24}(u_{2,3} + u_{3,2}),\\
T_{33} &= c_{13}u_{1,1} + c_{23}u_{2,2} + c_{33}u_{3,3} + c_{34}(u_{2,3} + u_{3,2}),\\
T_{23} &= c_{14}u_{1,1} + c_{24}u_{2,2} + c_{34}u_{3,3} + c_{44}(u_{2,3} + u_{3,2}),\\
T_{31} &= c_{55}(u_{3,1} + u_{1,3}) + c_{56}(u_{1,2} + u_{2,1}),\\
T_{12} &= c_{56}(u_{3,1} + u_{1,3}) + c_{66}(u_{1,2} + u_{2,1}).
\end{aligned} \tag{2.13}$$

The equations of motion are

$$\begin{aligned}
&c_{11}u_{1,11} + (c_{12} + c_{66})u_{2,12} + (c_{13} + c_{55})u_{3,13} + (c_{14} + c_{56})u_{2,13}\\
&\quad + (c_{14} + c_{56})u_{3,12} + 2c_{56}u_{1,23} + c_{66}u_{1,22} + c_{55}u_{1,33} = \rho\ddot{u}_1,\\
&c_{56}u_{3,11} + (c_{56} + c_{14})u_{1,13} + (c_{66} + c_{12})u_{1,12} + c_{66}u_{2,11} + c_{22}u_{2,22}\\
&\quad + (c_{23} + c_{44})u_{3,23} + 2c_{24}u_{2,23} + c_{24}u_{3,22} + c_{34}u_{3,33} + c_{44}u_{2,33} = \rho\ddot{u}_2,\\
&c_{55}u_{3,11} + (c_{55} + c_{13})u_{1,13} + (c_{56} + c_{14})u_{1,12} + c_{56}u_{2,11} + c_{24}u_{2,22}\\
&\quad + 2c_{34}u_{3,23} + (c_{44} + c_{23})u_{2,23} + c_{44}u_{3,22} + c_{33}u_{3,33} + c_{34}u_{2,33} = \rho\ddot{u}_3.
\end{aligned} \tag{2.14}$$

2.2. Thickness Modes in a Quartz Plate

Consider a plate of monoclinic crystals as shown in Fig. 2.1. It has a uniform thickness $2b$ and is unbounded in the x_1 and x_3 directions. The two surfaces are traction free. Thickness modes depend on the plate thickness coordinate x_2 and time. They can exist in unbounded plates only [16]. These modes are often used in acoustic wave devices.

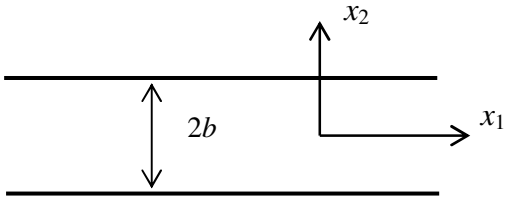

Fig. 2.1. A plate of monoclinic crystals.

For thickness modes, Eqs. (2.13) and (2.14) reduce to

$$\begin{aligned} T_{11} &= c_{12}u_{2,2} + c_{14}u_{3,2}, \\ T_{22} &= c_{22}u_{2,2} + c_{24}u_{3,2}, \\ T_{33} &= c_{23}u_{2,2} + c_{34}u_{3,2}, \\ T_{23} &= c_{24}u_{2,2} + c_{44}u_{3,2}, \\ T_{31} &= c_{56}u_{1,2}, \\ T_{12} &= c_{66}u_{1,2}, \end{aligned} \tag{2.15}$$

and

$$\begin{aligned} c_{66}u_{1,22} &= \rho\ddot{u}_1, \\ c_{22}u_{2,22} + c_{24}u_{3,22} &= \rho\ddot{u}_2, \\ c_{24}u_{2,22} + c_{44}u_{3,22} &= \rho\ddot{u}_3. \end{aligned} \tag{2.16}$$

The boundary conditions are

$$T_{2j} = 0, \quad x_2 = \pm b\,. \tag{2.17}$$

In this case the free vibration problem splits into two uncoupled problems. One is the x_1 thickness shear (TS_1) described by u_1 alone. The other is coupled x_3 thickness shear (TS_3) and thickness stretch (TSt) represented by u_3 and u_2. These two problems will be treated separately below.

2.2.1. TS_1 modes

The governing equation and boundary conditions are

$$\begin{aligned} &c_{66}u_{1,22} = \rho\ddot{u}_1, \quad -b < x_2 < b, \\ &T_{21} = 0, \quad x_2 = \pm b. \end{aligned} \tag{2.18}$$

Let

$$u_1 = A_1 \sin \eta x_2 \exp(i\omega t)\,. \tag{2.19}$$

Equation (2.19) is antisymmetric about $x_2 = 0$. The boundary conditions in Eq. $(2.18)_2$ imply that

$$\eta_n = \frac{n\pi}{2b}, \quad n = 1,3,5,\cdots. \tag{2.20}$$

Equation $(2.18)_1$ requires that

$$\omega_n = \sqrt{\frac{c_{66}}{\rho}}\,\eta = \sqrt{\frac{c_{66}}{\rho}}\,\frac{n\pi}{2b} = \sqrt{\frac{c_1}{\rho}}\,\frac{n\pi}{2b}, \quad n = 1,3,5,\cdots, \tag{2.21}$$

where we have denoted

$$c_1 = c_{66}. \tag{2.22}$$

n = 1 gives the fundamental frequency and mode. n>1 are the overtone frequencies and modes. The overtones are integral multiples of the fundamental and are called harmonic overtones or harmonics. If $\cos\eta x_2$ is used in Eq. (2.19), a different set of modes symmetric about $x_2 = 0$ with n = 0, 2, 4, … will be obtained. n = 0 represents a rigid-body displacement and is not of much interest. In applications, the antisymmetric modes are more useful. Static thickness-shear deformation and the first few thickness-shear modes in a plate are shown in Fig. 2.2.

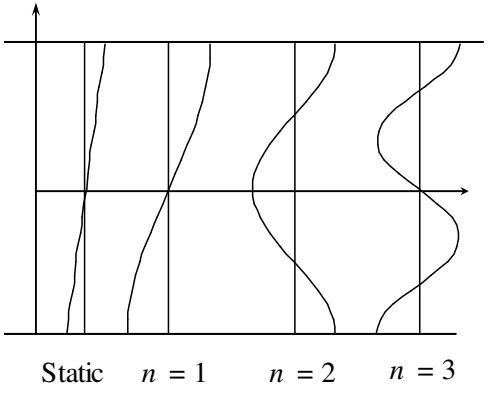

Fig. 2.2. TSh deformation and modes in a plate.

2.2.2. Coupled TS_3 and TT modes

The governing equations and boundary conditions are

$$\begin{aligned} &c_{22}u_{2,22} + c_{24}u_{3,22} = \rho\ddot{u}_2, \quad -b < x_2 < b, \\ &c_{24}u_{2,22} + c_{44}u_{3,22} = \rho\ddot{u}_3, \quad -b < x_2 < b, \\ &T_{23} = 0, \quad T_{22} = 0, \quad x_2 = \pm b. \end{aligned} \tag{2.23}$$

Let

$$\begin{aligned} u_2 &= A_2 \sin \eta x_2 \exp(i\omega t), \\ u_3 &= A_3 \sin \eta x_2 \exp(i\omega t). \end{aligned} \tag{2.24}$$

The boundary conditions in Eq. (2.23) still imply Eq. (2.20). Equations $(2.23)_{1,2}$ require that

$$\begin{aligned} c_{22}\eta^2 A_2 + c_{24}\eta^2 A_3 &= \rho\omega^2 A_2, \\ c_{24}\eta^2 A_2 + c_{44}\eta^2 A_3 &= \rho\omega^2 A_3. \end{aligned} \tag{2.25}$$

For nontrivial solutions of A_2 and/or A_3, the determinant of the coefficient matrix of Eq. (2.25) has to vanish, which leads to two sets of frequencies

$$\omega_n = \sqrt{\frac{c_2}{\rho}}\,\eta = \sqrt{\frac{c_2}{\rho}}\,\frac{n\pi}{2b}, \quad n = 1,3,5,\cdots, \tag{2.26}$$

and

$$\omega_n = \sqrt{\frac{c_3}{\rho}}\,\eta = \sqrt{\frac{c_3}{\rho}}\,\frac{n\pi}{2b}, \quad n = 1,3,5,\cdots, \tag{2.27}$$

where

$$\begin{aligned} c_2 &= \tfrac{1}{2}\{c_{22} + c_{44} + [(c_{22} - c_{44})^2 + 4c_{24}^2]^{1/2}\}, \\ c_3 &= \tfrac{1}{2}\{c_{22} + c_{44} - [(c_{22} - c_{44})^2 + 4c_{24}^2]^{1/2}\}. \end{aligned} \tag{2.28}$$

If the $\sin \eta x_2$ factor in Eq. (2.24) is replaced by $\cos \eta x_2$, a different set of modes symmetric about $x_2 = 0$ with n = 0, 2, 4, … will be obtained. We

note that if we set $c_{24}=0$ in Eq. (2.28), c_2 and c_3 become c_{22} and c_{44}, respectively, assuming that $c_{22}>c_{44}$. Therefore Eq. (2.26) is TT dominated and Eq. (2.27) is TS_3 dominated.

2.3. Inertial Effect of a Mass Layer: Sauerbrey Equation

Consider a quartz plate with a thin layer of a different material with density ρ' on its top surface (see Fig. 2.3). We are interested in the effect of the mass layer on the resonant frequencies of the thickness modes obtained in the previous section.

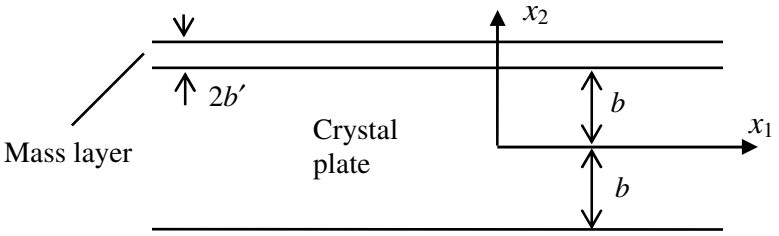

Fig. 2.3. A crystal plate with a mass layer.

Instead of analyzing the structure in Fig. 2.3 directly, we proceed as follows [17]. From Eqs. (2.21), (2.26) or (2.27), we write

$$\omega_n=\sqrt{\frac{c}{\rho}}\frac{n\pi}{2b},\quad n=1,3,5,\cdots, \tag{2.29}$$

where c may be c_1, c_2 or c_3. Imagine that the plate thickness has increased a little. The corresponding frequency shift is given by

$$\begin{aligned}\delta\omega_n&=-\sqrt{\frac{c}{\rho}}\frac{n\pi}{(2b)^2}\delta(2b)=-\sqrt{\frac{c}{\rho}}\frac{n\pi}{2b}\frac{\delta(2b)}{2b}\\&=-\sqrt{\frac{c}{\rho}}\frac{n\pi}{2b}\frac{\delta(\rho 2b)}{\rho 2b}=-\sqrt{\frac{c}{\rho}}\frac{n\pi}{2b}\frac{\delta m}{m},\end{aligned} \tag{2.30}$$

or

$$\frac{\delta\omega_n}{\omega_n} = -\frac{\delta m}{m} = -\frac{2\rho' b'}{2\rho b} = -R\,, \tag{2.31}$$

where R is the mass ratio between the incremental mass due to the increase of the plate thickness and the mass of the original plate. Note that once the frequency shift is written in the form of Eq. (2.31) in terms of the additional mass, Eq. (2.31) can be interpreted in a more general sense when the incremental mass is due to a layer of a different material as in Fig. 2.3.

2.4. Inertial Effect of a Mass Layer: Perturbation

Still consider the plate in Fig. 2.3. In this section we will obtain Eq. (2.31) using the perturbation integral in Eq. (1.74) [9]. As an example we consider the TS_1 modes in Section 2.2.1. When the surface mass is not present, the frequencies and modes are given by Eqs. (2.21) and (2.19) which, in the notation of Section 1.3, take the following form:

$$\begin{aligned} &\omega^{(0)} = \frac{n\pi}{2h}\sqrt{\frac{c_{66}}{\rho}}, \quad n = 1,3,5,\cdots, \\ &u_1^{(0)} = \sin\frac{n\pi x_2}{2h}, \quad u_2^{(0)} = u_3^{(0)} = 0. \end{aligned} \tag{2.32}$$

The effect of the mass layer is obtained by substituting Eq. (2.32) into Eq. (1.74):

$$\frac{\Delta\omega}{\omega^{(0)}} = -\frac{\rho' b'}{\rho b} = -R\,. \tag{2.33}$$

2.5. Inertial Effect of a Mass Layer: Differential Equation

For the plate in Fig. 2.3, the governing equation and boundary conditions are

$$\begin{aligned} &c_{66}u_{1,22} = \rho\ddot{u}_1 = -\rho\omega^2 u_1, \quad -b < x_2 < b, \\ &T_{21} = -2b'\rho'\ddot{u}_j = 2b'\rho'\omega^2 u_1, \quad x_2 = b, \\ &T_{21} = 0, \quad x_2 = -b. \end{aligned} \tag{2.34}$$

Equation $(2.34)_2$ is obtained by applying Newton's second law to a differential element of the mass layer. It has the mass layer inertial effect only and is valid for thin mass layers. For thick mass layers the effect of the mass layer shear stiffness may need to be considered [18, 13]. Thick mass layers will be treated later in Section 3.7. The general solution to Eq. $(2.34)_1$ and the corresponding expression for the stress component needed in the boundary conditions are

$$u_1 = B\cos\xi(x_2 + b)\,, \tag{2.35}$$

$$T_{21} = -c_{66}\xi B\sin\xi(x_2 + b)\,, \tag{2.36}$$

where B is an undetermined constant, and

$$\xi^2 = \frac{\rho}{c_{66}}\omega^2\,. \tag{2.37}$$

We note that the traction-free boundary condition $T_{21} = 0$ at $x_2 = -b$ is already satisfied by Eq. (2.36). For Eqs. (2.35) and (2.36) to satisfy the remaining boundary condition in Eq. $(2.34)_2$, we must have the following frequency equation:

$$\tan 2\xi b = -2\xi bR, \quad R = \rho' b'/(\rho b)\,. \tag{2.38}$$

Next we look for a perturbation solution of Eq. (2.38) in the case of thin mass layers with a small R. For the zero-order solution, we simply neglect the mass layer and set the right-hand side of Eq. (2.38) to zero. This results in two sets of resonant frequencies:

$$\sin\xi_n^{(0)}b = 0, \quad \xi_n^{(0)}b = n\pi/2, \quad n = 2,4,6,\cdots, \quad \omega_n^{(0)} = \frac{n\pi}{2b}\sqrt{\frac{c_{66}}{\rho}}\,, \tag{2.39}$$

$$\cos\xi_n^{(0)}b = 0, \quad \xi_n^{(0)}b = n\pi/2, \quad n = 1,3,5,\cdots, \quad \omega_n^{(0)} = \frac{n\pi}{2b}\sqrt{\frac{c_{66}}{\rho}}\,, \tag{2.40}$$

where the superscript (0) indicates that they are the zero-order approximation in the perturbation procedure. It can be identified that Eqs. (2.39) and (2.40) represent modes symmetric and antisymmetric

about $x_2 = 0$, respectively. We are mainly interested in the antisymmetric modes in Eq. (2.40) which can be conveniently excited by an electric field in the plate thickness direction. Therefore, in the following, we focus on the antisymmetric modes. For the first-order perturbation, we write [2]

$$\xi_n b = \frac{n\pi}{2} - \Delta_n, \quad n = 1,3,5,\cdots, \tag{2.41}$$

where Δ_n is small. Substituting Eq. (2.41) into Eq. (2.38), for small Δ_n and small R, we obtain

$$\Delta_n \cong \frac{n\pi}{2} R \tag{2.42}$$

Equation (2.42) implies the following relative frequency shift through Eqs. (2.41) and (2.37):

$$\Delta\Omega_n = \frac{\omega_n - \omega_n^{(0)}}{\omega_n^{(0)}} = -\frac{2}{n\pi}\Delta_n \cong -R\,. \tag{2.43}$$

2.6. Plate with Asymmetric Mass Layers

In the manufacturing of crystal resonators operating with thickness-shear modes of plates driven by a thickness electric field, an electrode is first deposited on one side of the plate with a pre-determined thickness. Then the electrode on the other side of the plate has a thickness that is determined by the electroded plate having a desired frequency. This usually results in a crystal plate with two electrodes of slightly different thickness (see Fig. 2.4). In this section we consider thickness modes in such a plate [19]. At the top and bottom of the plate there are two thin mass layers or electrodes with densities ρ' and ρ'', and thicknesses $2h'$ and $2h''$, respectively. They are assumed to be very thin. Their inertial effect will be considered, but their stiffness will be neglected. We will study the case when the plate is of general anisotropy first, and then specialize the result to the case of a quartz plate of Rotated Y-cut.

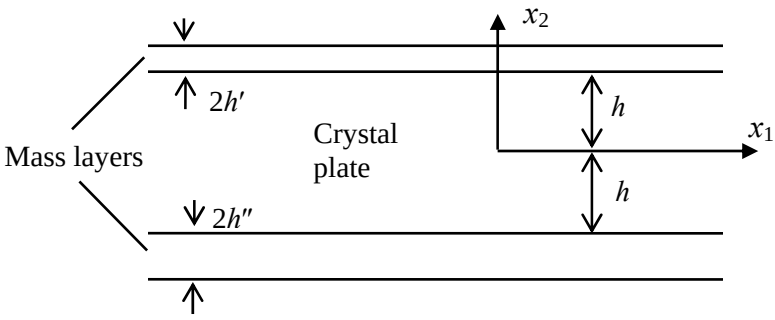

Fig. 2.4. A crystal plate with asymmetric mass layers.

2.6.1. General anisotropic crystals

The governing equations and boundary conditions are

$$T_{2j,2} = c_{2j2l}u_{l,22} = \rho\ddot{u}_j, \quad |x_2| < h, \tag{2.44}$$

$$\begin{aligned} T_{2j} &= -2h'\rho'\ddot{u}_j = 2h'\rho'\omega^2 u_j, \quad x_2 = h, \\ T_{2j} &= 2h''\rho''\ddot{u}_j = -2h''\rho''\omega^2 u_j, \quad x_2 = -h. \end{aligned} \tag{2.45}$$

We take

$$u_j = A_j \sin\eta x_2 \exp(i\omega t) \tag{2.46}$$

as the solution of Eq. (2.44). Substitution of Eq. (2.46) into Eq. (2.44) gives

$$(c_{2j2l}\eta^2 - \rho\omega^2\delta_{jl})A_l = 0. \tag{2.47}$$

For nontrivial solutions of A_l, we must have

$$|c_{2j2l} - c\delta_{jl}| = 0, \tag{2.48}$$

which is a cubic equation for

$$c = \frac{\rho\omega^2}{\eta^2}. \tag{2.49}$$

We denote the three roots of Eq. (2.48) by $c^{(n)}$ where the superscript "n" in the parentheses is not a tensor index and it assumes 1, 2, and 3. Then, from Eq. (2.49), three $\eta^{(n)}$ are determined. The corresponding nontrivial solutions of A_l from Eq. (2.47) are denoted by $\beta_l^{(n)}$. We normalize $\beta_l^{(n)}$ by

$$\beta_l^{(m)}\beta_l^{(n)} = \delta^{(mn)}. \tag{2.50}$$

Similarly, if

$$u_j = B_j \cos\eta x_2 \exp(i\omega t) \tag{2.51}$$

is considered, we still have the same $c^{(n)}$, $\eta^{(n)}$ and $\beta_l^{(n)}$ as in the above. Hence, for the general solution we take

$$u_j = \sum_{n=1}^{3} P^{(n)}\beta_j^{(n)} \sin\eta^{(n)} x_2 + Q^{(n)}\beta_j^{(n)} \cos\eta^{(n)} x_2, \tag{2.52}$$

where $P^{(n)}$ and $Q^{(n)}$ are undetermined constants. Equation (2.52) produces the following stress components relevant to boundary conditions:

$$\begin{aligned} T_{2j} &= c_{2j2l} u_{l,2} \\ &= c_{2j2l} \sum_{n=1}^{3} P^{(n)}\beta_l^{(n)}\eta^{(n)} \cos\eta^{(n)} x_2 - Q^{(n)}\beta_l^{(n)}\eta^{(n)} \sin\eta^{(n)} x_2. \end{aligned} \tag{2.53}$$

Substitution of Eqs. (2.52) and (2.53) into the boundary condition at $x_2 = h$ gives

$$\begin{aligned} & c_{2j2l} \sum_{n=1}^{3} P^{(n)}\beta_l^{(n)}\eta^{(n)} \cos\eta^{(n)} h - Q^{(n)}\beta_l^{(n)}\eta^{(n)} \sin\eta^{(n)} h \\ &= 2h'\rho'\omega^2 \sum_{n=1}^{3} P^{(n)}\beta_j^{(n)} \sin\eta^{(n)} h + Q^{(n)}\beta_j^{(n)} \cos\eta^{(n)} h, \end{aligned} \tag{2.54}$$

which can be further written as

$$\sum_{n=1}^{3} \left(c_{2j2l}\eta^{(n)}\cos\eta^{(n)}h - 2h'\rho'\omega^2\delta_{jl}\sin\eta^{(n)}h\right)\beta_l^{(n)}P^{(n)} + \left(-c_{2j2l}\eta^{(n)}\sin\eta^{(n)}h - 2h'\rho'\omega^2\delta_{jl}\cos\eta^{(n)}h\right)\beta_l^{(n)}Q^{(n)} = 0. \tag{2.55}$$

Similarly, the boundary condition at $x_2 = -h$ gives

$$\sum_{n=1}^{3} \left(c_{2j2l}\eta^{(n)}\cos\eta^{(n)}h - 2h''\rho''\omega^2\delta_{jl}\sin\eta^{(n)}h\right)\beta_l^{(n)}P^{(n)} + \left(c_{2j2l}\eta^{(n)}\sin\eta^{(n)}h + 2h''\rho''\omega^2\delta_{jl}\cos\eta^{(n)}h\right)\beta_l^{(n)}Q^{(n)} = 0. \tag{2.56}$$

Equations (2.55) and (2.56) are six linear homogeneous equations for $P^{(n)}$ and $Q^{(n)}$. For nontrivial solutions the determinant of the coefficient matrix has to vanish, which gives the frequency equation for determining ω.

2.6.2. Monoclinic crystals

For plates of monoclinic crystals, $c^{(1)}$ is the same as the c_1 in Eq. (2.22), and $c^{(2)}$ and $c^{(3)}$ are the same as the c_2 and c_3 in Eq. (2.28). The two lowest (fundamental) frequencies for thickness-shear modes (TS_1 and TS_3) are of primary interest. They were obtained in [19]:

$$\omega_a^2 = \frac{\pi^2 c_a}{4\rho h^2}\{1 - C_a R_S[1 - C_a R_S + \tfrac{1}{4}\pi^2 C_a^2(R_S^2 - R_D^2)]\}^2, \quad a = 1,3, \quad \text{not summed}, \tag{2.57}$$

where

$$R_S = (\rho'h' + \rho''h'')/\rho h, \quad R_D = (\rho'h' - \rho''h'')/\rho h, \tag{2.58}$$

$$\begin{aligned} c_1 &= c_{66}, \\ c_2 &= \tfrac{1}{2}\{c_{22} + c_{44} + [(c_{22} - c_{44})^2 + 4c_{24}^2]^{1/2}\}, \\ c_3 &= \tfrac{1}{2}\{c_{22} + c_{44} - [(c_{22} - c_{44})^2 + 4c_{24}^2]^{1/2}\}, \\ C_j &= c_j / c_{2j2j}. \end{aligned} \tag{2.59}$$

From Eq. (2.57) we can see that to the lowest order the effect of the mass layers is given by

$$\omega_a^2 = \frac{\pi^2 c_a}{4\rho h^2}(1-2C_a R_S), \tag{2.60}$$

which depends on the total mass of the two layers.

2.7. Plate in Contact with a Fluid: Differential Equation

In the section we analyze frequency shifts in a crystal plate due to contact with a viscous fluid [20]. Consider the plate in Fig. 2.5. All fields have the same $\exp(i\omega t)$ factor which will be dropped.

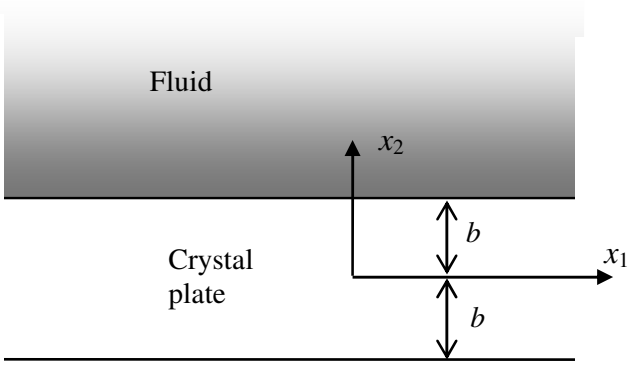

Fig. 2.5. A crystal plate in contact with a semi-infinite fluid.

2.7.1. Fields in the crystal plate

The governing equation and boundary condition at the plate bottom surface are

$$\begin{aligned} &c_{66}u_{1,22} = \rho\ddot{u}_1 = -\rho\omega^2 u_1, \quad -b < x_2 < b, \\ &T_{21} = 0, \quad x_2 = -b. \end{aligned} \tag{2.61}$$

The displacement and stress fields are the same as those in Eqs. (2.35)-(2.37):

$$u_1 = B\cos\xi(x_2 + b)\,, \tag{2.62}$$

$$T_{21} = -c_{66}\xi B\sin\xi(x_2 + b)\,, \tag{2.63}$$

$$\xi^2 = \frac{\rho}{c_{66}}\omega^2\,, \tag{2.64}$$

where B is an undetermined constant. We note that the traction-free boundary condition $T_{21} = 0$ at $x_2 = -b$ is already satisfied by Eq. (2.63).

2.7.2. Fields in the fluid

The equation of motion for the fluid is [21]

$$T_{21,2} = \rho_L \dot{v}_1\,, \tag{2.65}$$

where v_1 is the relevant velocity component and the shear stress T_{21} is related to the velocity gradient through

$$T_{21} = \mu\frac{\partial v_1}{\partial x_2}\ . \tag{2.66}$$

μ and ρ_L are the viscosity and mass density of the fluid. The velocity field in the fluid satisfying Eqs. (2.65) and (2.66) can be easily found as

$$v_1 = C\exp\left[-(1+i)\eta(x_2 - b)\right]\,, \tag{2.67}$$

where C is an undetermined constant and

$$\eta = \sqrt{\frac{\rho_L\omega}{2\mu}}\ . \tag{2.68}$$

Note that Eq. (2.67) decays from the plate surface into the fluid and thus also satisfies the boundary condition at $x_2 = +\infty$. The relevant stress component needed for boundary and continuity conditions is

$$T_{21} = -(1+i)\mu\eta C \exp[-(1+i)\eta(x_2 - b)]. \tag{2.69}$$

2.7.3. Continuity conditions and frequency equation

Continuity conditions at the plate top surface are

$$\begin{aligned} i\omega u_1(b^-) &= v_1(b^+), \\ T_{21}(b^-) &= T_{21}(b^+). \end{aligned} \tag{2.70}$$

Substitution of the relevant fields into Eq. (2.70) results in two linear homogeneous equations for B and C. For nontrivial solutions,

$$\tan 2\xi b = -(1-i)\sqrt{\frac{\omega\rho_L\mu}{2\rho c_{66}}}. \tag{2.71}$$

2.7.4. Perturbation solution of the frequency equation

We look for a perturbation solution of Eq. (2.71) in the case of a low density or low viscosity fluid so that the right-hand side of Eq. (2.71) is small. For the zero-order solution, we simply neglect the fluid and set the right-hand side of Eq. (2.71) to zero. This results in the same two sets of resonant frequencies as in Eqs. (2.39) and (2.40):

$$\xi_n^{(0)} b = n\pi/2, \quad \omega_n^{(0)} = \frac{n\pi}{2b}\sqrt{\frac{c_{66}}{\rho}}, \tag{2.72}$$

where the superscript (0) indicates that they are the zero-order approximation in the perturbation procedure. n = 1, 3, 5, … are modes antisymmetric about the plate middle plane. n = 2, 4, 6… are symmetric

modes. For the first-order perturbation, we write [2]

$$\xi_n b = \frac{n\pi}{2} - \Delta_n . \tag{2.73}$$

Substituting Eq. (2.73) into Eq. (2.71), for small Δ_n and small viscosity/density, we obtain

$$\Delta_n \cong \frac{1-i}{2}\sqrt{\frac{\rho_L \mu \omega_n^{(0)}}{2\rho c_{66}}} . \tag{2.74}$$

Equation (2.74) implies the following relative frequency shift:

$$\Delta\Omega_n = \frac{\omega_n - \omega_n^{(0)}}{\omega_n^{(0)}} = -\frac{2}{n\pi}\Delta_n \cong -\frac{1-i}{n\pi}\sqrt{\frac{\rho_L \mu \omega_n^{(0)}}{2\rho c_{66}}} . \tag{2.75}$$

The real part of $\Delta\Omega_n$ is negative, representing a frequency drop due to the drag of the fluid. The imaginary part of $\Delta\Omega_n$ is positive which, when combined with the $\exp(i\omega t)$ factor, describes damped motion due to the fluid viscosity. Higher-order modes with a larger *n* have smaller relative frequency shifts.

2.8. Plate in Contact with a Fluid: Perturbation

As an example of the perturbation analysis in Section 1.5, we apply the procedure to the problem in the previous section [14]. Still consider the plate in Fig. 2.5. For simplicity we focus on the fundamental thickness-shear mode. The unperturbed frequency and mode when the fluid is not present is:

$$\omega^{(0)} = \frac{\pi}{2b}\sqrt{\frac{c_{66}}{\rho}} , \quad u_1^{(0)} = \sin\frac{\pi x_2}{2b}, \quad u_2^{(0)} = u_3^{(0)} = 0 . \tag{2.76}$$

Then, from Eq. (1.95), the zero-order problem for the fluid motion is

$$\begin{aligned} &\tau_{21,2}^{(0)} = \rho_L i\omega^{(0)} v_1^{(0)}, \quad x_2 > b, \\ &\tau_{21}^{(0)} = \mu v_{1,2}^{(0)}, \quad x_2 > b, \\ &i\omega^{(0)} = v_1^{(0)}, \quad x_2 = b. \end{aligned} \tag{2.77}$$

$p^{(0)}$ has been taken to be zero. The solution to Eq. (2.77) is

$$\begin{aligned} &v_1^{(0)} = i\omega^{(0)} \exp[-\xi(x_2 - h)], \\ &\tau_{21}^{(0)} = \mu i\omega^{(0)}(-\xi)\exp[-\xi(x_2 - h)], \\ &\xi = \sqrt{\frac{\rho_L i\omega^{(0)}}{\mu}} = \sqrt{\frac{\rho_L \omega^{(0)}}{\mu}} \frac{1+i}{\sqrt{2}}. \end{aligned} \tag{2.78}$$

Substituting Eqs. (2.78) and (2.76) into Eq. (1.98), we obtain

$$\frac{\omega - \omega^{(0)}}{\omega^{(0)}} \cong \frac{1}{\pi}\sqrt{\omega^{(0)}} \sqrt{\frac{\rho_L \mu}{\rho c_{66}}} \frac{-1+i}{\sqrt{2}}, \tag{2.79}$$

which agrees with Eq. (2.75) when $n = 1$.

2.9. Plate with Particles

A crystal plate is sometimes loaded with small particles. These particles may be due to contamination. They affect resonant frequencies and usually appear as an undesirable effect. At the same time this effect may be explored for measuring particle properties. In fact, a mass layer on a crystal plate can be viewed as a plate loaded with a lot of particles interacting in a certain way. Therefore studying the effects of particles on a crystal plate is fundamental. Particles on a crystal plate may be sparse or dense and eventually form a thin film. They may be small compared with the thickness of the plate, or not so (as in biosensors for measuring cells). When the particle size is not infinitesimal compared to the plate thickness, the rotational degree of freedom and the rotatory inertia of the

particles may have effects that cannot be neglected. In this section we consider a plate loaded with finite particles (see Fig. 2.6) [22].

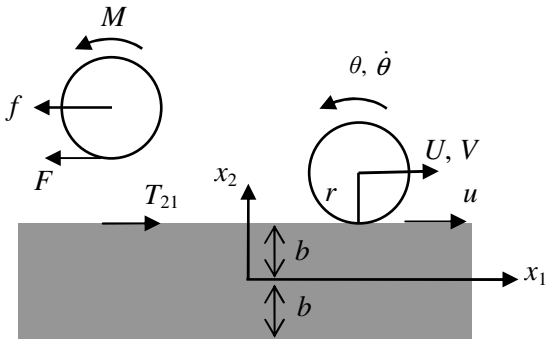

Fig. 2.6. A finite particle on a crystal plate.

2.9.1. Frequency equation

For the crystal plate, the governing equation is

$$T_{21,2} = c_{66} u_{1,22} = -\rho\omega^2 u_1 . \tag{2.80}$$

The general solution to Eq. (2.80) and the corresponding expression for the stress component needed in the relevant boundary conditions are

$$u_1 = A_1 \cos \xi x_2 + A_2 \sin \xi x_2 , \tag{2.81}$$

$$T_{21} = c_{66} \xi (-A_1 \sin \xi x_2 + A_2 \cos \xi x_2) , \tag{2.82}$$

where A_1 and A_2 are undetermined constants, and

$$\xi^2 = \frac{\rho}{c_{66}} \omega^2 . \tag{2.83}$$

The particles are represented by rigid spheres (or circular cylinders) with identical radius r and mass m. The moment of inertia about the

center of mass is *I*. For spheres $I = 2mr^2/5$ and for cylinders $I = mr^2/2$. The linear displacement and velocity of the particle center are U and $V = \dot{U}$, respectively. The angular displacement and angular velocity are θ and $\dot{\theta}$. We consider the case when the particles are rolling without slipping on the plate. In addition to the friction force *F* between the particles and plate surface, we assume that the particles can also interact with the plate surface elastically with an effective force *f* and an effective moment *M*. The particles are assumed to be sparse, without interactions among themselves. The equation of motion in the x_1 direction and the moment equation about the mass center of the particles are

$$-F - f = m\dot{V}, \tag{2.84}$$

$$M - Fr = I\ddot{\theta}. \tag{2.85}$$

The particle-plate interaction force *f* and moment *M* are described by linear and angular springs with

$$f = k(U - u), \tag{2.86}$$

$$M = -\beta\theta, \tag{2.87}$$

where $u = u_1(b)$ is the plate surface displacement. The non-slip condition of the particles for rolling without slipping with respect to the moving plate surface is given by

$$U - u = r(-\theta), \tag{2.88}$$

or, upon differentiation with respect to time,

$$V - \dot{u} = r(-\dot{\theta}). \tag{2.89}$$

From Eqs. (2.86) and (2.88), we have

$$f = -kr\theta. \tag{2.90}$$

Substituting Eq. (2.89) into Eq. (2.84), using $\ddot{u} = -\omega^2 u$ and $\ddot{\theta} = -\omega^2 \theta$ for harmonic motions, we obtain

$$-F - f = -m\omega^2 u + m\omega^2 r\theta \,. \tag{2.91}$$

Similarly, substitution of Eq. (2.87) into Eq. (2.85) and using $\ddot{\theta} = -\omega^2 \theta$ gives

$$-\beta\theta - Fr = -I\theta\omega^2 \,. \tag{2.92}$$

Eliminating θ from Eqs. (2.90)-(2.92), we obtain

$$F = \frac{\beta - I\omega^2}{kr^2} f \,, \tag{2.93}$$

$$-F - f = -m_e u\omega^2 \,, \tag{2.94}$$

where

$$m_e(\omega) = \frac{m}{1 + \dfrac{m\omega^2 r^2}{I\omega^2 - \beta - kr^2}} \tag{2.95}$$

is the effective mass of the particles.

The lower surface of the plate is traction free. At the upper surface of the plate, let the particle number density be *N*. The shear stress at the plate upper surface is completely determined by the interaction forces between the particles and the plate surface. Therefore the boundary conditions at the plate top and bottom surfaces are

$$T_{21}(b) = N(F + f) \,, \tag{2.96}$$

$$T_{21}(-b) = 0 \,. \tag{2.97}$$

With substitutions from Eqs. (2.82) and (2.94), we can write Eqs. (2.96) and (2.97) as two linear homogeneous equations for A_1 and A_2:

$$\begin{aligned} & c_{66}\xi(-A_1 \sin \xi b + A_2 \cos \xi b) \\ & \quad = Nm_e(A_1 \cos \xi b + A_2 \sin \xi b)\omega^2, \\ & A_1 \sin \xi b + A_2 \cos \xi b = 0. \end{aligned} \tag{2.98}$$

For nontrivial solutions, the determinant of the coefficient matrix of Eq. (2.98) has to vanish, which gives the following frequency equation that determines the resonant frequency ω:

$$\tan 2\xi b = -\frac{Nm_e\omega^2}{c_{66}\xi}. \tag{2.99}$$

In the special case when the particles are perfectly fixed to the plate surface without relative motion, the frequency equation can be reduced from Eq. (2.99) by setting $m_e = m$.

2.9.2. Approximate frequency solution

We look for a perturbation solution of Eq. (2.99) in the case of sparse and light particles representing small effects on the plate. In this case Nm_e is very small. For the lowest-order (zero-order) solution, we neglect the particles and set the right-hand side of Eq. (2.99) to zero. This results in the same two sets of resonant frequencies as in Eqs. (2.39) and (2.40):

$$\xi_n^{(0)} b = n\pi/2, \quad \omega_n^{(0)} = \frac{n\pi}{2b}\sqrt{\frac{c_{66}}{\rho}}, \tag{2.100}$$

where the superscript (0) indicates that they are the zero-order approximation in the perturbation procedure. n = 1, 3, 5, … are modes antisymmetric about the plate middle plane. n = 2, 4, 6, … are symmetric modes. For the first-order perturbation, we write [2]

$$\xi_n b = \frac{n\pi}{2} - \Delta_n, \tag{2.101}$$

where Δ_n is small. Substituting Eq. (2.101) into Eq. (2.99), for small Δ_n and small Nm_e, we obtain

$$\Delta_n \cong \frac{Nm_e^{(0)} \times (\omega_n^{(0)})^2}{2c_{66}\xi_n^{(0)}}, \tag{2.102}$$

where $m_e^{(0)} = m_e(\omega_n^{(0)})$. Equation (2.102) implies the follow frequency shift through Eqs. (2.101) and (2.83):

$$\Delta\Omega_n = \frac{\omega_n - \omega_n^{(0)}}{\omega_n^{(0)}} = -\frac{2}{n\pi}\Delta_n \cong -\frac{m_e^{(0)}}{m}\frac{Nm}{2b\rho} = -\frac{m_e^{(0)}}{m}R, \tag{2.103}$$

where

$$R = \frac{Nm}{2b\rho} \tag{2.104}$$

is the static mass ratio between the particles and the crystal plate. We note that the right-hand side of Eq. (2.103) does not depend on the unknown frequency ω_n now. Equation (2.103) shows that the frequency shift is a function of the geometric and physical parameters of the crystal plate and the particles. Therefore the frequency shift can be used to measure these parameters in a combination.

2.9.3. Discussion and numerical results

The difference between m_e and m is due to the finite size, the rotational degree of freedom, and the rotatory inertia of the particles. The following observations can be made from Eq. (2.95):

(i) When r = 0, from Eq. (2.95) we have $m_e = m$. In this case the rotational effects of the particles disappear and Eq. (2.103) reduces to the classical result of $\Delta\Omega_n = -R$ (the well-known Sauerbrey equation in a different form).

(ii) When

$$I\omega^2 - \beta - kr^2 = 0\,, \tag{2.105}$$

from Eq. (2.95) we have $m_e = 0$. In this case, from Eq. (2.94), we have $F + f = 0$. The net interaction force between the particles and the plate surface is zero. The acceleration of the mass center of the particles is zero. The plate does not feel the particles. Eq. (2.105) defines a frequency

$$\overline{\omega} = \sqrt{\frac{\beta + kr^2}{I}}\,. \tag{2.106}$$

Then Eq. (2.95) can be written as

$$m_e = \frac{m}{1 + \dfrac{m\omega^2 r^2}{I(\omega^2 - \overline{\omega}^2)}}\,. \tag{2.107}$$

(iii) When $\omega > \overline{\omega}$, the denominator of Eq. (2.017) is larger than one. We have $0 < m_e < m$. In this case the particles appear lighter.

(iv) When $\omega < \overline{\omega}$, there are two possibilities depending on whether the denominator of the right-hand side of Eq. (2.107) is positive or negative. Consider the case when it is positive first. The condition that the denominator of the right-hand side of Eq. (2.107) is positive is equivalent to

$$\beta + kr^2 > I\omega^2 + m\omega^2 r^2\,. \tag{2.108}$$

When the left and right-hand sides of Eq. (2.108) are equal, it defines another frequency $\hat{\omega}$ by

$$\hat{\omega} = \sqrt{\frac{\beta + kr^2}{I + mr^2}} < \overline{\omega}\,. \tag{2.109}$$

Physically, $\hat{\omega}$ is the frequency of the particle when it is rolling without sliding on a fixed surface with elastic constraints described by k and β. With Eq. (2.109), we can write Eq. (2.108) as $\omega < \hat{\omega}$ which automatically implies that $\omega < \bar{\omega}$. In this case the denominator of Eq. (2.107) is smaller than one and is positive. We have $m_e > m$. The particles appear heavier.

(v) When $\hat{\omega} < \omega < \bar{\omega}$, the denominator of Eq. (2.107) becomes negative and $m_e < 0$. In this case the particles appear to be with a negative mass and raise the plate resonant frequencies.

We summarize the behaviors of m_e as

$\omega < \hat{\omega}$	$\omega = \hat{\omega}$	$\hat{\omega} < \omega < \bar{\omega}$	$\omega = \bar{\omega}$	$\omega > \bar{\omega}$
$m_e > m$	Jump	$m_e < 0$	$m_e = 0$	$0 < m_e < m$

(2.110)

We plot m_e / m versus ω in Fig. 2.7 according to

$$\frac{m_e}{m} = \frac{1}{1 + \dfrac{mr^2}{I}\dfrac{\Omega^2}{\Omega^2 - 1}}, \tag{2.111}$$

where

$$\Omega = \omega / \bar{\omega}. \tag{2.112}$$

The behavior shown in the figure is complicated. The familiar situation of $m_e / m \cong 1$ happens only when $\Omega << 1$. In this case the rotational effects of the particles can be neglected, the plate feels the true inertia of the particles, and the Sauerbrey equation applies. As summarized in Eq. (2.110), Fig. 2.7 shows that m_e / m can be larger or smaller than one, and can even be negative.

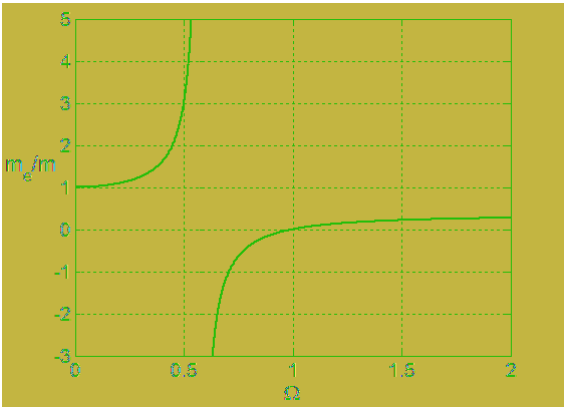

Fig. 2.7. Effective mass versus frequency ($mr^2 / I = 2$).

2.10. Plate with an Array of Rods in Extension

Consider a plate of hexagonal crystals in the 6mm class. The six-fold axis is indicated by an arrow labeled with "P" as shown in Fig. 2.8. The plate is loaded with an array of thin rods [23]. Under a thickness electric field, the plate can be driven into thickness-stretch vibration with the rods in extensional motion.

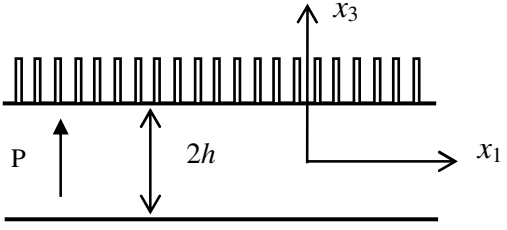

Fig. 2.8. A crystal plate with a micro-rod array.

2.10.1. Crystal plate

Thickness-stretch vibration is described by the following displacement field:

$$u_3 = u_3(x_3)\exp(i\omega t), \quad u_1 = u_2 = 0\,. \tag{2.113}$$

The nontrivial components of the strain and stress tensors are

$$S_{33} = u_{3,3}\,, \tag{2.114}$$

$$T_{11} = T_{22} = c_{13}u_{3,3}\,, \quad T_{33} = c_{33}u_{3,3}\,, \tag{2.115}$$

where the time-harmonic factor has been dropped. The relevant equation of motion is

$$T_{33,3} = c_{33}u_{3,33} = -\rho\omega^2 u_3\,. \tag{2.116}$$

The general solution to Eq. (2.116) and the corresponding expression for the stress component needed in the relevant boundary and continuity conditions are

$$u_3 = B\cos\xi(x_3 + h)\,, \tag{2.117}$$

$$T_{33} = -c_{33}\xi B\sin\xi(x_3 + h)\,, \tag{2.118}$$

where B is an undetermined constant, and

$$\xi^2 = \frac{\rho}{c_{33}}\omega^2\,. \tag{2.119}$$

Note that the traction-free boundary condition $T_{33} = 0$ at the plate bottom $x_3 = -h$ is already satisfied by Eq. (2.118).

2.10.2. Rod array

For the rods, we use the 1-D theory for longitudinal motions [24, 25]. Corresponding to the TSt vibration of the plate, for time-harmonic motions, all rods vibrate in phase. For a typical rod (see Fig. 2.9), let the longitudinal displacement be $w(z)\exp(i\omega t)$, and the axial force be P. We have

$$P' = \overline{\rho}A\ddot{w}\,, \tag{2.120}$$

$$P = EAw'\,, \tag{2.121}$$

where E is the Young's modulus, $\overline{\rho}$ is the mass density, and A is the area of the rod cross section. A prime indicates a derivative with respect to z. It can be found in a straightforward manner that the solution to Eqs. (2.120) and (2.121) that satisfies the free-end boundary conditions at the top of the rods, i.e., $P(L) = EA\, w'(L) = 0$, is given by

$$w = Df(z, E, \overline{\rho}, L, \omega), \tag{2.122}$$

where D is an undetermined constant and

$$f = \cos\alpha(z - L), \quad \alpha = \omega\sqrt{\frac{\overline{\rho}}{E}}\ . \tag{2.123}$$

From Eqs. (2.121) and (2.122) we calculate the axial force at the rod bottom as

$$P(z = 0) = EAD\, f'(0, E, \overline{\rho}, L, \omega)\ . \tag{2.124}$$

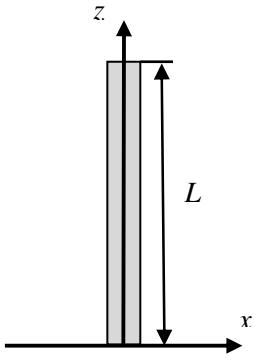

Fig. 2.9. A single rod and coordinate system.

2.10.3. Plate-rod interaction

Let the number density of the rods per unit area of the plate surface be N. The continuity conditions of the displacement and stress at $x_3 = h$ are

$$\begin{aligned} u_3(x_3 = h) &= w(z = 0), \\ T_{33}(x_3 = h) &= NP(z = 0). \end{aligned} \tag{2.125}$$

Substituting Eqs. (2.117), (2.118), (2.122) and (2.124) into Eq. (2.125), we obtain

$$\begin{aligned} B\cos 2\xi h &= Df(0, E, \overline{\rho}, L, \omega), \\ -c_{33}\xi B \sin 2\xi h &= NDEAf'(0, E, \overline{\rho}, L, \omega). \end{aligned} \tag{2.126}$$

Equation (2.126) is a system of linear homogeneous equations for B and D. For nontrivial solutions the determinant of the coefficient matrix has to vanish. This yields the following equation that determines the resonant frequencies:

$$\tan 2\xi h = -\frac{NEAf'(0, E, \overline{\rho}, L, \omega)}{c_{33}\xi f(0, E, \overline{\rho}, L, \omega)}, \tag{2.127}$$

where ξ is related to ω through Eq. (2.119).

2.10.4. Equivalent mass layer

For comparison, consider a related problem in which there is a thin mass layer with density ρ' and thickness $2h'$ attached to the top surface of the crystal plate at $x_3 = h$. In this case, according to Newton's second law, the boundary condition at $x_3 = h$ is $-T_{33} = \rho' 2h' \ddot{u}_3$ and the frequency equation can be obtained in a similar way as in the problem analyzed in Section 2.5. The result is (see Eq. (2.38)):

$$\tan 2\xi h = -R 2\xi h, \tag{2.128}$$

where $R = (\rho' h')/(\rho h)$ is the mass ratio between the mass layer and the crystal plate.

In our case of a rod array on a crystal plate, the frequency equation given by Eq. (2.127) can be written in the same form as Eq. (2.128), with an equivalent mass ratio defined by

$$R = \frac{NEAf'(0, E, \overline{\rho}, L, \omega)}{2c_{33}\xi^2 h f(0, E, \overline{\rho}, L, \omega)} = \frac{NEA\alpha \sin(\alpha L)}{2c_{33}\xi^2 h \cos(\alpha L)}. \tag{2.129}$$

Clearly, R depends on EA, $\overline{\rho}$ and L which are the material and geometric parameters of the rods. R also depends on N which is an array property. Note that R is frequency dependent through α in Eq. (2.123) and ξ in Eq. (2.119).

In the special case when $f(0, E, \overline{\rho}, L, \omega) = 0$, i.e., the rod bottoms have no displacements, R becomes infinite. In this case $f(0, E, \overline{\rho}, L, \omega) = 0$ determines a series of resonant frequencies for rods with fixed bottoms and free tops. We denote the resonant frequencies of these rods by ϖ_m, with m = 1, 2, 3, …. They can be easily determined as [25]:

$$\varpi_n = \frac{(2n-1)\pi}{2L}\sqrt{\frac{E}{\overline{\rho}}}, \qquad n = 1,2,3,\ldots. \tag{2.130}$$

For a numerical example we consider a ZnO plate with $h = 0.5$ mm. For the rods we also consider ZnO with $\overline{\rho} = 5665\,\text{kg/m}^3$, $E = 40$ GPa, diameter d = 0.1 μm, L = 10 μm, and N = $1\times10^8/\text{cm}^2$. In this case, $\varpi_1 = 0.41739757\times10^9$ rad/s and $\varpi_2 = 1.25219270\times10^9$ rad/s. We plot the frequency dependence of R in Fig. 2.10 where R is normalized by $R_0 = N\overline{\rho}AL/(2\rho h)$ which is the static mass ratio between the rod array and the crystal plate. Figure 2.10 shows that R is strongly frequency dependent. At the low frequency limit, R/R_0 approaches one which is the static mass ratio. R can be smaller or larger than one, and can even become negative. The frequency dependence of the effective mass ratio is due to the extensibility of the rods. Near the rod resonant frequencies ϖ_m (only the first two are shown in the frequency range in Fig. 2.10), R becomes large and is in fact unbounded because there is no damping in the idealized elastic structure we are analyzing.

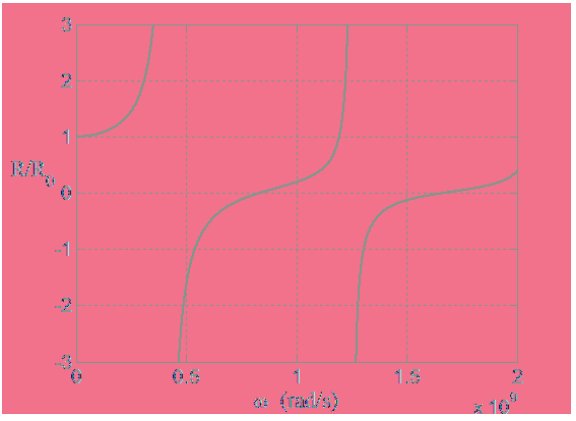

Fig. 2.10. Normalized effective mass ratio versus frequency.

2.10.5. Approximate frequency solution

To exhibit the relation between the resonant frequencies and the rod array parameters more explicitly, we look for a perturbation solution of Eq. (2.127) in the case of small R when the rods represent small effects on the crystal plate. For the zero-order solution, we neglect the rods and set the right-hand side of Eq. (2.127) to zero. This results in two sets of resonant frequencies:

$$\sin \xi_n^{(0)} h = 0, \quad \xi_n^{(0)} h = n\pi / 2, \quad n = 2,4,6,\cdots, \quad \omega_n^{(0)} = \frac{n\pi}{2h}\sqrt{\frac{c_{33}}{\rho}}, \tag{2.131}$$

$$\cos \xi_n^{(0)} h = 0, \quad \xi_n^{(0)} h = n\pi / 2, \quad n = 1,3,5,\cdots, \quad \omega_n^{(0)} = \frac{n\pi}{2h}\sqrt{\frac{c_{33}}{\rho}}, \tag{2.132}$$

where the superscript "(0)" indicates that they are the zero-order approximations in the perturbation procedure. Through Eq. (2.117), it can be identified that Eqs. (2.131) and (2.132) represent modes antisymmetric and symmetric about $x_3 = 0$, respectively. For the first-order perturbation, we write [2]

$$\xi_n h = \frac{n\pi}{2} - \Delta_n, \tag{2.133}$$

where Δ_n is a small perturbation. Substituting Eq. (2.133) into Eq. (2.128), for small Δ_n and small R, we obtain

$$\Delta_n \cong \frac{n\pi}{2} R_n^{(0)} = \frac{NEAf'(0, E, \overline{\rho}, L, \omega_n^{(0)})}{2c_{33}\xi_n^{(0)} f(0, E, \overline{\rho}, L, \omega_n^{(0)})}, \tag{2.134}$$

where

$$\xi_n^{(0)} = \sqrt{\frac{\rho}{c_{33}}}\ \omega_n^{(0)} = \frac{n\pi}{2h}. \tag{2.135}$$

Equation (2.134) implies the following frequency shift through Eqs. (2.133) and (2.119):

$$\begin{aligned}\Delta\Omega_n &= \frac{\omega_n - \omega_n^{(0)}}{\omega_n^{(0)}} = -\frac{2}{n\pi}\Delta_n \\ &\cong -R_n^{(0)} = -\frac{NEA\,\alpha_n^{(0)}\sin(\alpha_n^{(0)}L)}{2c_{33}(\xi_n^{(0)})^2 h\cos(\alpha_n^{(0)}L)},\end{aligned} \tag{2.136}$$

where

$$\alpha_n^{(0)} = \omega_n^{(0)}\sqrt{\frac{\overline{\rho}}{E}}\ . \tag{2.137}$$

We note that the right-hand side of Eq. (2.136) does not depend on the unknown frequency ω_n and instead it is a function of $\omega_n^{(0)}$ which is known. In the above derivation, since R has been assumed small, the special case when a particular plate resonant frequency $\omega_n^{(0)}$ is close to a particular beam resonant frequency ϖ_m has to be excluded. In such a case $f(0, E, \overline{\rho}, L, \omega_n^{(0)})$ approaches zero and $R_n^{(0)}$ becomes large.

The frequency shift in Eq. (2.136) is a function of the parameters of the rod array. This provides the theoretical foundation for determining the parameters of the array through frequency measurements. The procedure is as follows: $\omega_n^{(0)}$ are known theoretically. ω_n are measured from experiments. Then $\Delta\Omega_n$ are known, and Eq. (2.136) becomes a system of equations of the parameters of the rod array when several frequencies are used. These equations are complicated transcendental equations. It does not seem to be easy to measure all of the parameters of the array at the same time. A relatively simple situation is when some of the parameters of the array are already known and only one or two parameters are left to be determined. Then it may be convenient to solve Eq. (2.136).

2.10.6. Special cases

In the special case when the resonant frequencies of the rods are much higher than the fundamental thickness-stretch frequency of the

ZnO plate, the rods follow the surface of the plate in the so-called quasistatic manner. In this special case we show that our general result in the above analysis reduces to an expression that is equivalent to the Sauerbrey equation. From Eq. (2.117) we write the plate surface displacement as $B\cos 2\xi_n^{(0)}h$ and the plate surface acceleration as $-(\omega_n^{(0)})^2 B\cos 2\xi_n^{(0)}h$. In quasistatic motions the rod acceleration is taken to be the same as the plate surface acceleration, i.e.,

$$\begin{aligned} &w'' - \frac{\overline{\rho}}{E}\ddot{w} = w'' - \frac{\overline{\rho}}{E}\ddot{u}_3(b) \cong w'' + \frac{\overline{\rho}}{E}(\omega_n^{(0)})^2 B\cos 2\xi_n^{(0)}h = 0, \\ &w(0) = B\cos 2\xi_n^{(0)}h, \quad w'(L) = 0. \end{aligned} \tag{2.138}$$

Equation (2.138) determines

$$w = -B\cos(2\xi_n^{(0)}h)[\frac{\overline{\rho}}{2E}(\omega_n^{(0)})^2(z^2 - 2Lz) - 1], \tag{2.139}$$

or

$$f = \frac{\overline{\rho}}{2E}(\omega_n^{(0)})^2(z^2 - 2Lz) - 1. \tag{2.140}$$

Substituting Eq. (2.140) into Eq. (2.136), we obtain

$$\Delta\Omega_n = \frac{\omega_n - \omega_n^{(0)}}{\omega_n^{(0)}} = -\frac{N\overline{\rho}AL}{2\rho h} = -R_0, \tag{2.141}$$

which is the static mass ratio between the rods and the plate.

In Fig. 2.11 we plot the frequency shifts predicted by Eqs. (2.136) and (2.141) for the fundamental thickness-stretch mode with n = 1 by solid and dotted lines, respectively. Equation (2.141) (dotted line) predicts a simple linear relation, ideal for sensor application. This is true for relatively short rods whose first resonance is higher than the fundamental thickness-stretch frequency of the plate, i.e., $\varpi_1 > \omega_1^{(0)}$. As the rods become longer, when $L = 2.179\times10^{-4}$ m and the first resonant frequency of the rod approaches the fundamental TSt frequency of the

plate, i.e., $\varpi_1 \cong \omega_1^{(0)}$, Eq. (2.141) is no longer valid and Eq. (2.136) predicts a jump discontinuity. When the rod length is further increased, when $L = 6.537 \times 10^{-4}$ m and the second resonant frequency of the rod coincides with the fundamental plate TSt frequency, i.e., $\varpi_2 \cong \omega_1^{(0)}$, the second discontinuity appears.

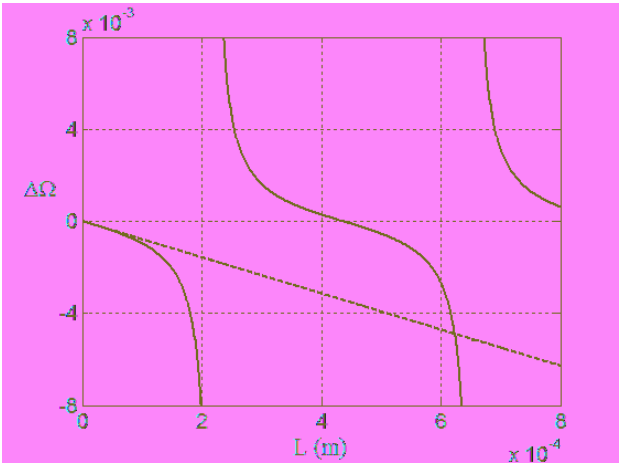

Fig. 2.11. Frequency shift versus rod length. Solid line: from Eq. (2.136). Dotted line: from Eq. (2.141).

Another special case is when the rods are very long ($L = \infty$). In this case the boundary condition at infinity requires that the disturbance propagating along the rods due to the vibration of the crystal plate should be outgoing for large z (radiation), i.e.,

$$w = C \exp(-i\alpha z), \tag{2.142}$$

which is subject to

$$w(0) = B \cos 2\xi h. \tag{2.143}$$

Equations (2.142) and (2.143) determine

$$w = B \cos(2\xi h) \exp(-i\alpha z), \tag{2.144}$$

or

$$f = \exp(-i\alpha z) . \tag{2.145}$$

Substitution of Eq. (2.145) into Eqs. (2.134) and (2.136) leads to

$$\Delta\Omega_n = \frac{\omega_n - \omega_n^{(0)}}{\omega_n^{(0)}} = \frac{iNA}{n\pi}\sqrt{\frac{\overline{\rho}E}{\rho c_{33}}} . \tag{2.146}$$

Equation (2.146) is imaginary, representing a damped motion of the crystal plate due to the radiation of energy through the propagation of extensional waves along the rods away from the plate.

2.11. Plate with an Array of Beams in Bending

Consider a quartz plate loaded with a beam array as shown in Fig. 2.12 [26]. Different from the previous section, this time the plate is in thickness-shear motion. The beams are in flexural motion correspondingly. We want to determine the effects of the beams on the resonant frequencies of the plate.

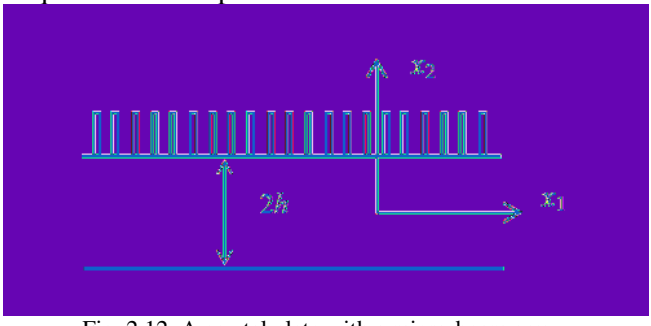

Fig. 2.12. A crystal plate with a micro-beam array.

2.11.1. Crystal plate

For the crystal plate we have

$$T_{21,2} = c_{66}u_{1,22} = -\rho\omega^2 u_1 . \tag{2.147}$$

The general solution to Eq. (2.147) and the corresponding expression for the stress component needed in the relevant boundary and continuity conditions are

$$u_1 = B\cos\xi(x_2 + h)\,, \tag{2.148}$$

$$T_{21} = -c_{66}\xi B\sin\xi(x_2 + h)\,, \tag{2.149}$$

where B is an undetermined constant, and

$$\xi^2 = \frac{\rho}{c_{66}}\omega^2\,. \tag{2.150}$$

We note that the traction-free boundary condition $T_{21} = 0$ at $x_2 = -h$ is already satisfied by Eq. (2.149).

2.11.2. Beam array

For the flexural motion of the beams, we use the Euler-Bernoulli theory of bending [24, 25]. Corresponding to the thickness-shear vibration of the plate, for time-harmonic motions, all beams vibrate in phase. For a typical beam in its own coordinate system (see Fig. 2.13), let the deflection curve be $v(x)$, the rotation or slope be θ, the bending moment be M, and the shear force be V. We have [25]

$$EIv'''' + \overline{\rho}A\ddot{v} = 0\,, \tag{2.151}$$

$$\theta = v'\,,\quad M = EIv''\,,\quad V = EIv'''\,, \tag{2.152}$$

where E is the Young's modulus, $\overline{\rho}$ is the mass density, and I and A are the moment of inertia and the area of the beam cross section. A prime indicates a derivative with respect to x. For time-harmonic motions with a frequency ω, it can be found in a straightforward manner that the solution to Eq. (2.151) that satisfies $M(L) = 0$, $V(L) = 0$, and $\theta(0) = 0$ is

$$v = Cf(x, EI, \overline{\rho}A, L, \omega)\,, \tag{2.153}$$

where C is an undetermined constant and

$$f = \cos\alpha(x-L) + \cosh\alpha(x-L) + \gamma[\sin\alpha(x-L) + \sinh\alpha(x-L)], \tag{2.154}$$

$$\alpha = \left(\frac{\bar{\rho}A\omega^2}{EI}\right)^{1/4}, \quad \gamma = \frac{\sinh\alpha L - \sin\alpha L}{\cosh\alpha L + \cos\alpha L}. \tag{2.155}$$

From Eqs. (2.152) and (2.153) we calculate the shear force at the beam bottom as

$$V(0) = CEIf'''(0, EI, \bar{\rho}A, L, \omega), \tag{2.156}$$

which will be needed in the continuity condition next.

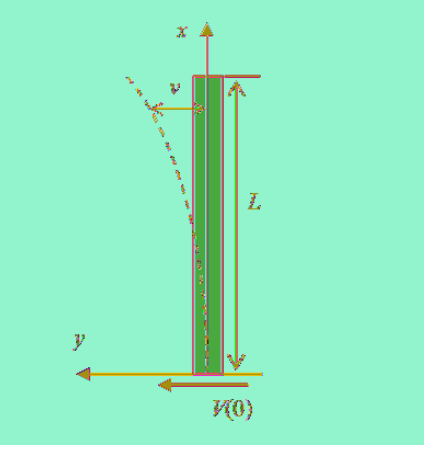

Fig. 2.13. Notation and coordinate system for beam bending.

2.11.3. Plate-beam interaction

Let the number density of the beams per unit area of the crystal surface be N. The continuity conditions of the displacement and shear stress

at $x_2 = h$ between the top surface of the plate and the bottoms of the beams are

$$\begin{aligned} u_1(x_2 = h) &= -v(x = 0), \\ T_{21}(x_2 = h) &= NV(x = 0). \end{aligned} \tag{2.157}$$

Substituting Eqs. (2.148), (2.149), (2.153) and (2.156) into Eq. (2.157), we obtain

$$\begin{aligned} B\cos 2\xi h &= -Cf(0, EI, \overline{\rho}A, L, \omega), \\ -c_{66}\xi B \sin 2\xi h &= NCEIf'''(0, EI, \overline{\rho}A, L, \omega). \end{aligned} \tag{2.158}$$

Equation (2.158) is a system of linear homogeneous equations for *B* and *C*. For nontrivial solutions the determinant of the coefficient matrix has to vanish. This yields the following frequency equation that determines the resonant frequencies of the plate carrying the beams:

$$\tan 2\xi h = \frac{NEIf'''(0, EI, \overline{\rho}A, L, \omega)}{c_{66}\xi f(0, EI, \overline{\rho}A, L, \omega)}, \tag{2.159}$$

where ξ is related to ω through Eq. (2.150), and

$$\begin{aligned} &f(0, EI, \overline{\rho}A, L, \omega) \\ &\quad = \cos(\alpha L) + \cosh(\alpha L) - \gamma[\sin(\alpha L) + \sinh(\alpha L)], \\ &f'''(0, EI, \overline{\rho}A, L, \omega) \\ &\quad = -\alpha^3 \sin(\alpha L) - \alpha^3 \sinh(\alpha L) + \alpha^3\gamma[-\cos(\alpha L) + \cosh(\alpha L)]. \end{aligned} \tag{2.160}$$

Therefore Eq. (2.159) is an equation for ω.

2.11.4. Equivalent mass layer

We can write the right-hand side of Eq. (2.159) in the same form as the frequency equation for a uniform mass layer on a crystal plate (see Eq. (2.38)):

$$\tan 2\xi h = -R2\xi h, \tag{2.161}$$

where R is the mass ratio between the mass layer and the crystal plate. In our case of a beam array,

$$\begin{aligned} R &= -\frac{NEIf'''(0, EI, \overline{\rho}A, L, \omega)}{(2\xi h)c_{66}\xi f(0, EI, \overline{\rho}A, L, \omega)} \\ &= -\frac{NEI\alpha^3}{2\xi^2 hc_{66}} \frac{-\sin(\alpha L) - \sinh(\alpha L) + \gamma[-\cos(\alpha L) + \cosh(\alpha L)]}{\cos(\alpha L) + \cosh(\alpha L) - \gamma[\sin(\alpha L) + \sinh(\alpha L)]}, \end{aligned} \tag{2.162}$$

which may be called the effective mass ratio between the beam array and the crystal plate or, equivalently, $R2\rho h$ is the effective mass of the beam array over unit area of the surface of the crystal plate. Clearly, R depends on EI, $\overline{\rho}A$ and L which are the material and geometric parameters of the beams. R also depends on N which is an array property. R is frequency dependent through α in Eq. (2.155) and ξ in Eq. (2.150).

We note that when $f(0, EI, \overline{\rho}A, L, \omega) = 0$, i.e., the beam bottoms have no displacements, R becomes infinite. $f(0, EI, \overline{\rho}A, L, \omega) = 0$ determines a series of resonant frequencies for cantilever beams with rigidly fixed bottoms and free tops. We denote their resonant frequencies by ϖ_m with $m = 1, 2, 3, \ldots$. For these cantilever beams ϖ_m are given in [25]:

$$\varpi_m = \beta_m^2 \sqrt{\frac{EI}{\overline{\rho}A}} = \beta_m^2 d \sqrt{\frac{E}{\overline{\rho}}}, \quad m = 1, 2, 3, \ldots, \tag{2.163}$$

where, for the first two resonances,

$$\beta_1 = \frac{1.875}{L}, \quad \beta_2 = \frac{4.694}{L}. \tag{2.164}$$

For a numerical example we consider an AT-cut quartz plate with $h = 0.5\text{mm}$. For the beams we consider ZnO with $\overline{\rho} = 5600 kg/\text{m}^3$, $E = 40\,\text{GPa}$, diameter $d = 0.1\,\mu\text{m}$, $L = 1\ \mu\text{m}$, and $N = 1\times 10^8/\text{cm}^2$. In this case

$$\varpi_1 = 0.234924\times 10^9, \quad \varpi_2 = 1.472241\times 10^9\ \text{rad/s}. \tag{2.165}$$

We plot the frequency dependence of R in Fig. 2.14 where R is normalized by $R_0 = N\overline{\rho}AL/(2\rho h)$ which is the static mass ratio between the beams and the crystal plate. Figure 2.14 shows that R is strongly frequency dependent. At the low frequency limit R/R_0 approaches one which is the static mass ratio. R can be smaller or larger than one, and can even become negative. This is not surprising for frequency dependent masses as often seen in the study of materials with internal structures and internal degrees of freedom. In the problem we are analyzing the frequency dependence of the effective mass layer is due to the flexibility of the beams. Near the beam resonant frequencies ϖ_m (only the first two are shown in the frequency range in Fig. 2.14), R becomes unbounded.

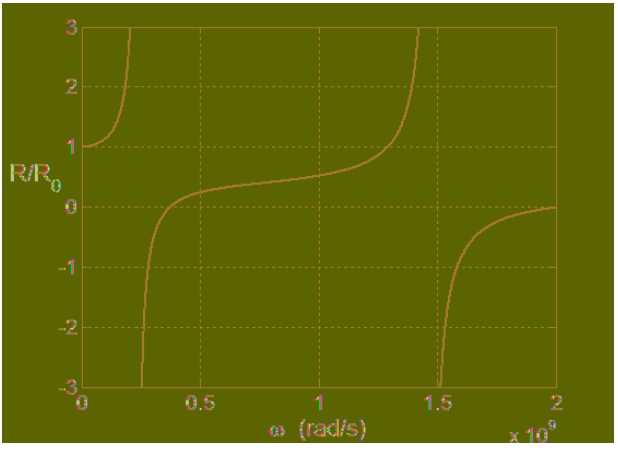

Fig. 2.14. Normalized effective mass ratio versus frequency.

2.11.5. Approximate frequency solution

We look for a perturbation solution of Eq. (2.161) in the case of small R. For the lowest-order (zero-order) solution, we neglect the beams and set the right-hand side of Eq. (2.161) to zero. This results in the same two sets of resonant frequencies as in Eqs. (2.39) and (2.40):

$$\xi_n^{(0)} b = n\pi/2, \quad \omega_n^{(0)} = \frac{n\pi}{2b}\sqrt{\frac{c_{66}}{\rho}}, \tag{2.166}$$

where the superscript (0) indicates that they are the zero-order approximation in the perturbation procedure. n = 1, 3, 5, … are modes antisymmetric about the plate middle plane. n = 2, 4, 6, … are symmetric modes. For the first-order perturbation, we write [2]

$$\xi_n h = \frac{n\pi}{2} - \Delta_n , \tag{2.167}$$

where Δ_n is a small perturbation. Substituting Eq. (2.167) into Eq. (2.161), for small Δ_n and small R, we obtain

$$\Delta_n \cong \frac{n\pi}{2} R_n^{(0)} = -\frac{n\pi}{2} \frac{NEIf'''(0, EI, \overline{\rho}A, L, \omega_n^{(0)})}{2(\xi_n^{(0)})^2 hc_{66} f(0, EI, \overline{\rho}A, L, \omega_n^{(0)})}, \tag{2.168}$$

$$\xi_n^{(0)} = \sqrt{\frac{\rho}{c_{66}}}\ \omega_n^{(0)} = \frac{n\pi}{2h}. \tag{2.169}$$

Equation (2.168) implies the following relative frequency shift through Eqs. (2.167) and (2.150):

$$\Delta\Omega_n = \frac{\omega_n - \omega_n^{(0)}}{\omega_n^{(0)}} = -\frac{2}{n\pi}\Delta_n \cong -R_n^{(0)} = -\frac{NEI(\alpha_n^{(0)})^3}{2(\xi_n^{(0)})^2 hc_{66}} \frac{F^{(0)}}{G^{(0)}}, \tag{2.170}$$

where

$$\begin{aligned} F^{(0)} &= -\sin(\alpha_n^{(0)} L) - \sinh(\alpha_n^{(0)} L) \\ &\quad + \gamma_n^{(0)}[-\cos(\alpha_n^{(0)} L) + \cosh(\alpha_n^{(0)} L)], \\ G^{(0)} &= \cos(\alpha_n^{(0)} L) + \cosh(\alpha_n^{(0)} L) \\ &\quad - \gamma_n^{(0)}[\sin(\alpha_n^{(0)} L) + \sinh(\alpha_n^{(0)} L)], \end{aligned} \tag{2.171}$$

$$\alpha_n^{(0)} = \left(\frac{\overline{\rho}A(\omega_n^{(0)})^2}{EI}\right)^{1/4}, \quad \gamma_n^{(0)} = \frac{\sinh \alpha_n^{(0)} L - \sin \alpha_n^{(0)} L}{\cosh \alpha_n^{(0)} L + \cos \alpha_n^{(0)} L}. \tag{2.172}$$

Note that the right-hand side of Eq. (2.170) does not depend on the unknown frequency ω_n and instead it is a function of $\omega_n^{(0)}$ which is known. In the above derivation, since R has been assumed to be small, the special case when a particular plate resonant frequency $\omega_n^{(0)}$ is close

to a particular beam resonant frequency ϖ_m has to be excluded. In such a case $f(0, EI, \overline{\rho}A, L, \omega^{(0)})$ approaches zero and $R_n^{(0)}$ becomes large.

2.11.6. Special case

When the beams are small and their resonant frequencies are much higher than the fundamental thickness-shear frequency of the plate, the beams follow the motion of the surface of the crystal plate quasistatically. In this case an approximation of Eq. (2.161) can be obtained as follows. From Eq. (2.148) we write the zero-order unperturbed plate surface displacement as $B\cos 2\xi_n^{(0)}h$ and the corresponding plate surface acceleration as $-(\omega_n^{(0)})^2 B\cos 2\xi_n^{(0)}h$. The beam acceleration is approximately taken to be the plate surface acceleration:

$$\begin{aligned} &EIv'''' + \overline{\rho}A\ddot{v} \cong EIv'''' + \overline{\rho}A(\omega_n^{(0)})^2 B\cos 2\xi_n^{(0)}h = 0, \\ &v(0) = -B\cos 2\xi_n^{(0)}h, \quad \theta(0) = 0, \quad M(L) = 0, \quad V(L) = 0. \end{aligned} \tag{2.173}$$

Equation (2.173) determines

$$\begin{aligned} v = &\frac{1}{24}\frac{\overline{\rho}A}{EI}(\omega_n^{(0)})^2 B\cos 2\xi_n^{(0)}h[L^4 - (x-L)^4 - 4xL^3] \\ &- B\cos 2\xi_n^{(0)}h, \end{aligned} \tag{2.174}$$

or

$$f = \frac{1}{24}\frac{\overline{\rho}A}{EI}(\omega_n^{(0)})^2[L^4 - (x-L)^4 - 4xL^3] - 1. \tag{2.175}$$

Substitutions of Eq. (2.174) into Eqs. (2.161) and (2.168) lead to

$$\tan 2\xi h = -R_0 2\xi h, \tag{2.176}$$

$$\Delta\Omega_n = \frac{\omega_n - \omega_n^{(0)}}{\omega_n^{(0)}} = -\frac{N\overline{\rho}AL}{2\rho h} = -R_0, \tag{2.177}$$

respectively. R_0 is the static mass ratio between the beams and the plate. Equation (2.177) shows that in the quasistatic case the beam inertia lowers the plate resonant frequencies as expected.

In Fig. 2.15 we plot the frequency shifts predicted by Eq. (2.170) and (2.177) for the fundamental thickness-shear mode with $n = 1$ by solid and dotted lines, respectively. For the plate we are considering, $\omega_1^{(0)} = 1.040 \times 10^7$ rad/s . Equation (2.177) (dotted line) predicts a simple linear relation, ideal for sensor application. This is true for relatively short beams whose first resonance is higher than the fundamental thickness-shear frequency of the plate, i.e., $\varpi_1 > \omega_1^{(0)}$. As the beam becomes longer, when $L = 4.752 \times 10^{-6}$ m and the first resonant frequency of the beam approaches the fundamental thickness-shear frequency of the plate, i.e., $\varpi_1 \cong \omega_1^{(0)}$, Eq. (2.177) is no longer valid and Eq. (2.170) predicts a jump discontinuity. When the beam length is further increased, when $L = 1.190 \times 10^{-5}$ m and the second resonant frequency of the beam coincides with the fundamental plate thickness-shear frequency, i.e., $\varpi_2 \cong \omega_1^{(0)}$, the second discontinuity appears.

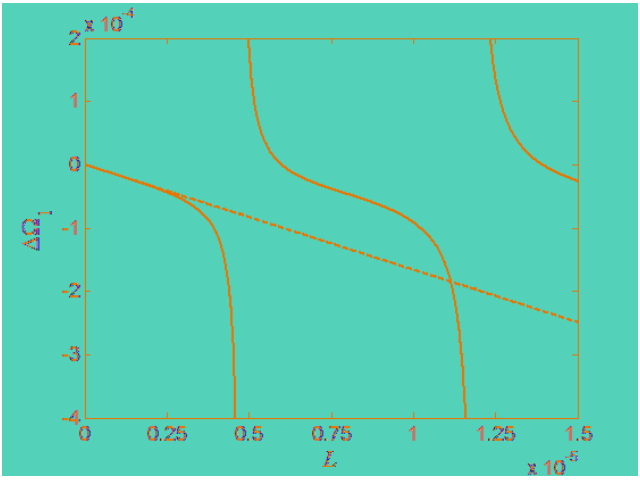

Fig. 2.15. Frequency shift versus beam length. Solid line: from Eq. (2.170). Dotted line: from Eq. (2.177).

2.12. Plate with Beams: Effect of Couple Stress

In the continuity conditions in Eq. (2.157) of the previous section, the bending moments at the beam bottoms effectively form a distribution of

moments or couples. This distributed couple was simply neglected because the theory of elasticity used to describe the crystal plate could not handle a distribution of couples on the plate surface. To take the beam bottom bending moments into consideration, a generalized theory of elasticity called the couple-stress theory [27] is needed. In this section we revisit [28] the problem in the previous section using the couple-stress theory for the plate which is assumed to be isotropic. Consider the elastic plate with surface beams in Fig. 2.16. Our notation follows that in [27] by Mindlin and Tiersten. Equations taken from [27] are indicated by "MT" and an equation number.

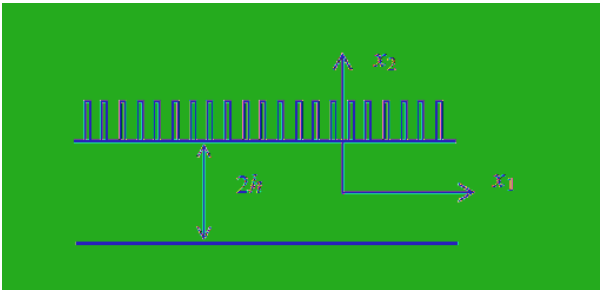

Fig. 2.16. An elastic plate with an array of rigid microbeams.

2.12.1. Equations and fields of the plate

For isotropic materials, scalar and vector displacement potentials of the couple-stress theory were introduced in [27]. For thickness-shear motions of a plate with its normal along x_2 or y and the only displacement component along x_1 or x, only the x_3 or z component of the vector potential H_z is needed which is a function of y and time. In [27], thickness-shear vibrations antisymmetric about the middle plane of an elastic plate were studied. Since the plate we are considering is loaded with an array of beams on its top surface, vibration modes cannot be separated into symmetric and antisymmetric ones. Therefore we generalize MT (8.4) accordingly and take the relevant displacement potential to be

$$\begin{aligned} H_z &= H_z' + H_z'', \\ H_z' &= A_1 \cos \beta_1 y + B_1 \sin \beta_1 y, \\ H_z'' &= A_2 \cosh \beta_2 y + B_2 \sinh \beta_2 y, \end{aligned} \tag{2.178}$$

where A_1, A_2, B_1 and B_2 are undetermined constants. From MT (7.5),

$$\begin{aligned}\beta_1 &= \frac{1}{\sqrt{2}\,l}[(1+4l^2\omega^2/c_2^2)^{1/2}-1]^{1/2},\\ \beta_2 &= \frac{1}{\sqrt{2}\,l}[(1+4l^2\omega^2/c_2^2)^{1/2}+1]^{1/2},\end{aligned} \tag{2.179}$$

and from MT (6.4),

$$\begin{aligned}c_2^2 &= \mu/\rho,\\ l^2 &= \eta/\mu.\end{aligned} \tag{2.180}$$

ρ and μ are the usual density and shear modulus of the material. η is a material constant introduced in the couple-stress theory. l has the dimension of length. The potential components in Eq. (2.178) already satisfy the equations of motion of the couple-stress theory [27]. The only displacement component is given by the displacement-potential relations in MT (7.6) as:

$$\begin{aligned}u_x &= \frac{\partial H_z}{\partial y} = \frac{\partial H_z'}{\partial y} + \frac{\partial H_z''}{\partial y}\\ &= -A_1\beta_1\sin\beta_1 y + B_1\beta_1\cos\beta_1 y + A_2\beta_2\sinh\beta_2 y + B_2\beta_2\cosh\beta_2 y.\end{aligned} \tag{2.181}$$

The nontrivial components of the strain tensor $\boldsymbol{\varepsilon}$, the rotation vector $\mathbf{w}$, and the curvature-twist tensor $\boldsymbol{\kappa}$ are given by MT (5.2) as:

$$\begin{aligned}\varepsilon_{xy} &= \frac{1}{2}\frac{\partial u_x}{\partial y} = \frac{1}{2}[-A_1\beta_1^2\cos\beta_1 y - B_1\beta_1^2\sin\beta_1 y\\ &\quad + A_2\beta_2^2\cosh\beta_2 y + B_2\beta_2^2\sinh\beta_2 y],\\ w_z &= -\frac{1}{2}\frac{\partial u_x}{\partial y} = -\frac{1}{2}[-A_1\beta_1^2\cos\beta_1 y - B_1\beta_1^2\sin\beta_1 y\\ &\quad + A_2\beta_2^2\cosh\beta_2 y + B_2\beta_2^2\sinh\beta_2 y],\\ \kappa_{yz} &= -\frac{1}{2}\frac{\partial^2 u_x}{\partial y^2} = -\frac{1}{2}[A_1\beta_1^3\sin\beta_1 y - B_1\beta_1^3\cos\beta_1 y\\ &\quad + A_2\beta_2^3\sinh\beta_2 y + B_2\beta_2^3\cosh\beta_2 y].\end{aligned} \tag{2.182}$$

The symmetric part of the relevant component of the stress tensor $\boldsymbol{\tau}$ and the relevant component of the couple stress tensor $\boldsymbol{\mu}$ are given by the following constitutive relations from MT (5.3) as:

$$\begin{aligned}
\tau_{xy}^{S} &= 2\mu\varepsilon_{xy} = \mu\frac{\partial u_x}{\partial y} \\
&= \mu[-A_1\beta_1^2\cos\beta_1 y - B_1\beta_1^2\sin\beta_1 y \\
&\quad + A_2\beta_2^2\cosh\beta_2 y + B_2\beta_2^2\sinh\beta_2 y], \\
\mu_{yz} &= 4\eta\kappa_{yz} = -2\eta\frac{\partial^2 u_x}{\partial y^2} \\
&= -2\eta[A_1\beta_1^3\sin\beta_1 y - B_1\beta_1^3\cos\beta_1 y \\
&\quad + A_2\beta_2^3\sinh\beta_2 y + B_2\beta_2^3\cosh\beta_2 y].
\end{aligned} \tag{2.183}$$

From MT (1.11) and MT (1.10), the relevant total stress component including the symmetric and antisymmetric parts is

$$\begin{aligned}
\tau_{xy} &= \tau_{xy}^{S} + \tau_{xy}^{A} = \tau_{xy}^{S} + \frac{1}{2}\frac{\partial\mu_{yz}}{\partial y} \\
&= \tau_{xy}^{S} - \eta[A_1\beta_1^4\cos\beta_1 y + B_1\beta_1^4\sin\beta_1 y \\
&\quad + A_2\beta_2^4\cosh\beta_2 y + B_2\beta_2^4\sinh\beta_2 y].
\end{aligned} \tag{2.184}$$

2.12.2. Equations of the beams

The microbeams are assumed to be rigid. They are moving in the horizontal direction following the plate surface and are also rotating (see Fig. 2.17). We assume that the beam bottoms are moving and rotating together with the infinitesimal material elements at the plate top surface, i.e., $u_x(h)$ and $w_z(h)$. Then the acceleration of the centers of mass of the beams and their rotations about their centers of mass can be expressed in terms of $u_x(h)$ and $w_z(h)$. The equation of motion of the centers of mass and the moment equation for the angular motion around the centers

of mass of the beams are

$$\begin{aligned} -F &= -\omega^2 m\left(u_x - w_z \frac{H}{2}\right), \\ -M - F\frac{H}{2} &= -\omega^2 I_G w_z, \end{aligned} \tag{2.185}$$

where

$$I_G = \frac{1}{12} m H^2 . \tag{2.186}$$

I_G is the moment of inertia of the beams about their centers of mass. In Section 2.11, the rotations of the beam bottoms were taken to be zero which is an approximation that makes the system too rigid. Since the beam bottoms are built into an elastic plate, some rotations of the beam bottoms may happen which is allowed in this section.

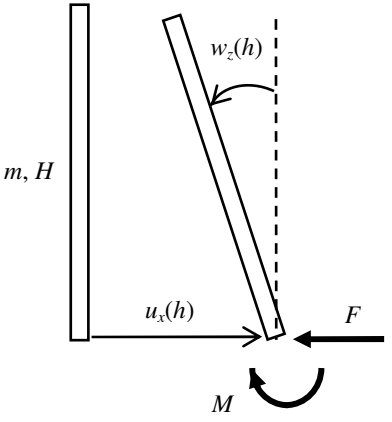

Fig. 2.17. Notation for the rigid-body motion of a beam with mass m and length H.

2.12.3. Continuity conditions and frequency equation

The bottom of the plate is free from any tractions or couples. Therefore, at $x_2 = -h$, we have the following boundary conditions (see MT (8.8)):

$$\begin{aligned} \tau_{xy} &= 0, \\ \mu_{yz} &= 0. \end{aligned} \tag{2.187}$$

At the top of the plate, let N be the number density of the beams, i.e., N beams per unit area of the plate surface. For many small beams the shear forces F and the bending moments M at the beam bottoms effectively act as a shear stress and a distribution of couples. Therefore, the boundary or continuity conditions at $x_2 = h$ are:

$$\begin{aligned} \tau_{xy} &= NF, \\ \mu_{yz} &= NM. \end{aligned} \tag{2.188}$$

Substitution of the relevant equations into Eqs. (2.187) and (2.188) results in the following four homogeneous equations for A_1, A_2, B_1 and B_2:

$$\begin{pmatrix} c_{11} & c_{12} & c_{13} & c_{14} \\ c_{21} & c_{22} & c_{23} & c_{24} \\ c_{31} & c_{32} & c_{33} & c_{34} \\ c_{41} & c_{42} & c_{43} & c_{44} \end{pmatrix} \begin{pmatrix} A_1 \\ A_2 \\ B_1 \\ B_2 \end{pmatrix} = 0, \tag{2.189}$$

where

$$\begin{aligned} c_{11} &= -(\mu\beta_1^2 + \eta\beta_1^4)\cos\beta_1 h, \\ c_{12} &= (\mu\beta_2^2 - \eta\beta_2^4)\cosh\beta_2 h, \\ c_{13} &= (\mu\beta_1^2 + \eta\beta_1^4)\sin\beta_1 h, \\ c_{14} &= -(\mu\beta_2^2 - \eta\beta_2^4)\sinh\beta_2 h, \end{aligned} \tag{2.190}$$

$$\begin{aligned} c_{21} &= \beta_1^3 \sin\beta_1 h, \\ c_{22} &= \beta_2^3 \sinh\beta_2 h, \\ c_{23} &= \beta_1^3 \cos\beta_1 h, \\ c_{24} &= -\beta_2^3 \cosh\beta_2 h, \end{aligned} \tag{2.191}$$

$$\begin{aligned} c_{31} &= -(\mu\beta_1^2 + \eta\beta_1^4)\cos\beta_1 h + N\omega^2 m(\beta_1 \sin\beta_1 h + \frac{H}{4}\beta_1^2 \cos\beta_1 h), \\ c_{32} &= (\mu\beta_2^2 - \eta\beta_2^4)\cosh\beta_2 h - N\omega^2 m(\beta_2 \sinh\beta_2 h + \frac{H}{4}\beta_2^2 \cosh\beta_2 h), \\ c_{33} &= -(\mu\beta_1^2 + \eta\beta_1^4)\sin\beta_1 h - N\omega^2 m(\beta_1 \cos\beta_1 h - \frac{H}{4}\beta_1^2 \sin\beta_1 h), \\ c_{34} &= (\mu\beta_2^2 - \eta\beta_2^4)\sinh\beta_2 h - N\omega^2 m(\beta_2 \cosh\beta_2 h + \frac{H}{4}\beta_2^2 \sinh\beta_2 h), \end{aligned} \tag{2.192}$$

$$
\begin{aligned}
c_{41} &= -2\eta\beta_1^3 \sin\beta_1 h \\
&\quad -\frac{N\omega^2}{2}(I_G\beta_1^2 \cos\beta_1 h + Hm\beta_1 \sin\beta_1 h + \frac{H^2}{4} m\beta_1^2 \cos\beta_1 h), \\
c_{42} &= -2\eta\beta_2^3 \sinh\beta_2 h \\
&\quad +\frac{N\omega^2}{2}(I_G\beta_2^2 \cosh\beta_2 h + Hm\beta_2 \sinh\beta_2 h + \frac{H^2}{4} m\beta_2^2 \cosh\beta_2 h), \\
c_{43} &= 2\eta\beta_1^3 \cos\beta_1 h \\
&\quad -\frac{N\omega^2}{2}(I_G\beta_1^2 \sin\beta_1 h - Hm\beta_1 \cos\beta_1 h + \frac{H^2}{4} m\beta_1^2 \sin\beta_1 h), \\
c_{44} &= -2\eta\beta_2^3 \cosh\beta_2 h \\
&\quad +\frac{N\omega^2}{2}(I_G\beta_2^2 \sinh\beta_2 h + Hm\beta_2 \cosh\beta_2 h + \frac{H^2}{4} m\beta_2^2 \sinh\beta_2 h).
\end{aligned}
\tag{2.193}
$$

For nontrivial solutions the determinant of the coefficient matrix of Eq. (2.189) has to vanish. This gives the frequency equation for determining the resonant frequency ω of the structure. The corresponding nontrivial solutions of A_1, A_2, B_1 and B_2 determine the vibration mode. The frequency equation will be very long if the determent of the coefficient matrix in Eq. (2.189) is expanded, which will not be pursued here. Instead, we examine a few special cases so that analytical work can be carried out further to bring out some of the underlying physics.

Specifically, in the following we examine three special cases with either a zero N (without beams) or a zero η (without couple stresses), or when both N and η are zero. Since η appears in the displacement equation of motion in MT (7.3) as the coefficient of the term with the fourth (the highest) derivative, the reduction to the case of $\eta = 0$ cannot be obtained in a standard perturbation procedure.

2.12.4. Case of $\eta = 0$ *and* $N = 0$

In this case, the microbeams and the couple stresses are both absent. We only need H_z' from Eq. (2.187) but not H_z''. Among the continuity conditions in Eqs. (2.187) and (2.188), Eqs. $(2.187)_2$ and $(2.188)_2$ have to be dropped. Equations $(2.187)_1$ and $(2.188)_1$ with $N = 0$ still remain. The

frequency equation is found to be:

$$\tan \beta_1 (2h) = 0 , \tag{2.194}$$

where $\beta_1 = \omega / c_2$ when $\eta = 0$. We denote the solution to Eq. (2.194) by a superscript "0" in parentheses, i.e.,

$$2\beta_1^{(0)} h = n\pi, \quad n = 0,1,2,3,\cdots , \tag{2.195}$$

which may be viewed as the zero-order solution of a perturbation procedure to be used later. Equation (2.195) implies that

$$\omega_n^{(0)} = \frac{n\pi}{2h}\sqrt{\frac{\mu}{\rho}} . \tag{2.196}$$

For convenience we normalize the frequencies as follows

$$\Omega_n^{(0)} = \omega_n^{(0)} \Big/ \frac{\pi}{2h}\sqrt{\frac{\mu}{\rho}} = n . \tag{2.197}$$

n = 0 is a rigid-body mode. It will be discarded because it is not useful in the sensor application we are considering. When n is odd or even the modes are antisymmetric or symmetric about the middle plane of the plate.

2.12.5. Case of $\eta = 0$ and $N \neq 0$

In this case, there are microbeams but the couple stresses in the plate are absent. We still have $H_z'' = 0$. The situation is similar to and simpler than what was treated in Section 2.11 where the microbeams are elastic. Instead of using the A_1 and B_1 terms in Eq. (2.181), equivalently, following Section 2.11 (see Eq. (2.148)), we write the displacement field as

$$u_x = B\cos \beta_1 (y + h) , \tag{2.198}$$

where B is an undetermined constant. Equation (2.198) already satisfies Eq. $(2.187)_1$. Substitution of Eq. (2.198) into Eq. $(2.188)_1$ leads to the following frequency equation

$$\tan \beta_1(2h) = -\frac{N\omega^2 m_e}{\mu\beta_1}, \tag{2.199}$$

where we have introduced an effective mass for the beams:

$$m_e = \frac{m}{1-\dfrac{N\omega^2 mH}{4\mu}} = \frac{m}{1-\omega^2/\phi^2}. \tag{2.200}$$

In Eq. (2.200) we have denoted

$$\phi^2 = \frac{4\mu}{NmH}. \tag{2.201}$$

Equation (2.199) cannot be reduced from the frequency equation in Section 2.11 where the bottoms of the elastic beams cannot rotate. ϕ has the dimension of frequency. It is involved with the parameters of both the plate and the beam array. Its physical interpretation is not obvious. We note that m_e is frequency dependent. It may be smaller or larger than m, or even become negative. In the case of small beams, ϕ is a relatively high frequency and $m_e \cong m$. Equation (2.199) can be further written as

$$\tan \beta_1(2h) = -R_e \beta_1 2h, \tag{2.202}$$

where R_e is the effective mass ratio between the beams and the plate:

$$R_e = \frac{Nm_e}{\rho 2h}. \tag{2.203}$$

When $m_e = 0$, Eqs. (2.199) and (2.202) reduce to Eq. (2.194). When the beams are present, the modes cannot be separated into symmetric and

antisymmetric ones about the plate middle plane. In dimensionless form, Eq. (2.199) or (2.202) becomes:

$$\tan(\pi\Omega) = -R_e \pi\Omega\,, \tag{2.204}$$

where

$$\begin{aligned} &\Omega = \omega \Big/ \frac{\pi}{2h}\sqrt{\frac{\mu}{\rho}}, \quad R_e = \frac{R}{1-\Omega^2/\Phi^2}, \\ &R = \frac{Nm}{\rho 2h}, \quad \Phi = \phi \Big/ \frac{\pi}{2h}\sqrt{\frac{\mu}{\rho}}. \end{aligned} \tag{2.205}$$

R is the static mass ratio between the beams and the elastic plate.

We look for an approximate solution to Eq. (2.202) when the effects of the beams or the right-hand side of Eq. (2.202) are small. We write the solution to Eq. (2.202) as a small perturbation of Eq. (2.195):

$$\beta_1 h = \frac{n\pi}{2} - \Delta\,, \tag{2.206}$$

where Δ is small. Substituting Eq. (2.206) into Eq. (2.202), we obtain, approximately,

$$\Delta \cong R_e^{(0)} \beta_1^{(0)} h\,, \tag{2.207}$$

where we have denoted

$$\beta_1^{(0)} = \frac{\omega_n^{(0)}}{c_2}, \quad R_e^{(0)} = \frac{Nm_e^{(0)}}{2\rho h}, \quad m_e^{(0)} = \frac{m}{1-(\omega_n^{(0)})^2/\phi^2}. \tag{2.208}$$

Equations (2.206) and (2.207) imply the following approximate expression for the resonant frequencies:

$$\omega_n = \omega_n^{(0)}\left(1 - \frac{2}{n\pi}\Delta\right) \cong \omega_n^{(0)}\left(1 - R_e^{(0)}\right), \tag{2.209}$$

or

$$\Omega_n = n(1-\frac{2}{n\pi}\Delta) \cong n(1-R_e^{(0)})$$
$$= n\left(1-\frac{R}{1-(\Omega_n^{(0)})^2/\Phi^2}\right) = n\left(1-\frac{R}{1-n^2/\Phi^2}\right). \tag{2.210}$$

For large Φ, Eq. (2.210) shows that small beams lower the resonant frequencies more than their static inertia R, especially for higher order modes with larger values of n.

We plot Ω versus Φ determined from Eqs. (2.204) (solid lines) and (2.210) (dotted lines) in Fig. 2.18 for the case of R = 0.1. We are mainly interested in the case of large Φ where Ω approaches $n(1-R)$ from below. In this case the inertia of the beams dominates, the effective mass is positive, and the beams lower the resonant frequencies of the plate which is a familiar situation. As Φ decreases, the curves deviate from $n(1-R)$ gradually. The approximated, dotted lines change more rapidly. When Φ is close to n, the solid lines are still continuous but the dotted lines have discontinuities and become unbounded. In fact, when Φ is close to n, Eq. (2.210) is not valid anymore because the frequency perturbation is no longer small. When $\Phi < n$, the curves are above $n(1-R)$ and approach n from above. In this case the effective mass is negative and the beams raise the resonant frequencies.

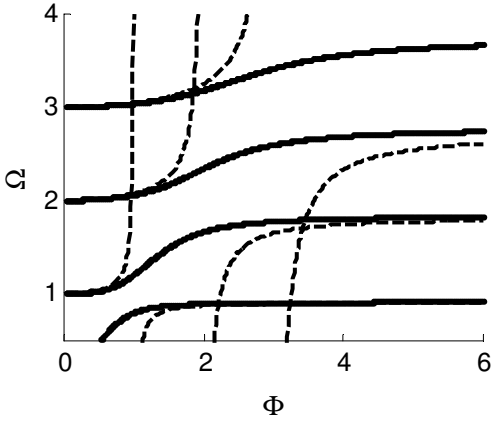

Fig. 2.18. Ω vs. Φ from Eqs. (2.204) (solid lines) and (2.210) (dotted lines). R = 0.1.

Figure 2.19 shows the effects of the beams on the fundamental thickness-shear mode (n = 1) of the plate determined from Eq. (2.198) where B is taken to be one. The approximate $\beta_1 h$ determined from Eq. (2.206) and (2.207) is used. Without the beams the mode would be a perfect sinusoidal curve with vertical tangents at the plate surfaces for zero shear stresses there. Because of the beams, at the plate top surface the modes no longer have a vertical tangent. When Φ decreases toward one from above, the modes deviate more from a sinusoidal curve.

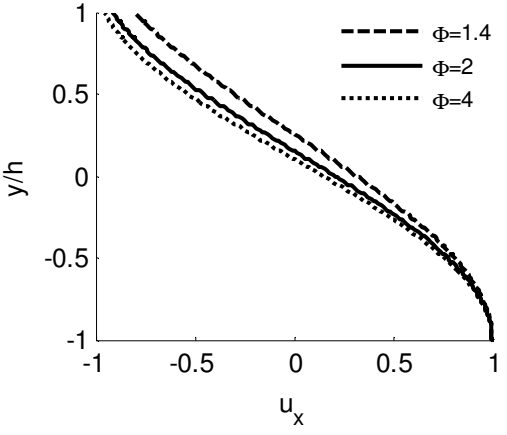

Fig. 2.19. Effect of the beams on the fundamental TSh mode.

The relative or normalized frequency shift caused by the beams can be written as

$$\frac{\omega-\omega_n^{(0)}}{\omega_n^{(0)}}=\frac{\Omega_n-\Omega_n^{(0)}}{\Omega_n^{(0)}}=\frac{\Delta\Omega_n}{\Omega_n^{(0)}}=\frac{\Delta\Omega_n}{n}=-\frac{2}{n\pi}\Delta\cong-R_e^{(0)}. \qquad (2.211)$$

The frequency shift in Eq. (2.211) is a function of the parameters of the beam array. This provides the theoretical foundation for determining the parameters of the beam array through frequency measurements.

Once the frequencies and modes are obtained, from Eq. $(2.185)_1$ we can calculate F, and from Eq. $(2.185)_2$ we can calculate M:

$$\begin{aligned} M &= \omega^2 I_G w_z - \omega^2 m\left(u_x - w_z \frac{H}{2}\right)\frac{H}{2} \\ &= -\frac{1}{2} mH\omega^2 B\left[\cos(2\beta_1 h) - \frac{1}{3}\beta_1 h \frac{H}{h}\sin(2\beta_1 h)\right]. \end{aligned} \tag{2.212}$$

This M is usually nonzero and it violates Eq. $(2.188)_2$ if there is no couple stress in the plate. This shows the inadequacy of the theory of elasticity when there are distributed couples and the necessity of the couple-stress theory. M is explicitly proportional to the beam mass m, height H and ω^2 or the acceleration. These are intuitively reasonable. M also depends on m and H implicitly through ω and β_1. We nondimensionalize M by $-mH\omega^2 B/2$ and plot in Fig. 2.20 the dimensionless couple, i.e., the two terms in the square brackets in Eq. (2.212), versus Φ where the approximate $\beta_1 h$ determined from Eq. (2.207) is used. $R = 0.1$ and $H/h = 0.1$. The normalized couple is clearly nonzero in general. It is essentially a constant except when Φ is close to one where the couple begins to change rapidly. Figure 2.20 is reliable when Φ is not close to one. Near $\Phi = 1$ the approximate solution given by Eq. (2.207) which is used in plotting Fig. 2.20 is not accurate.

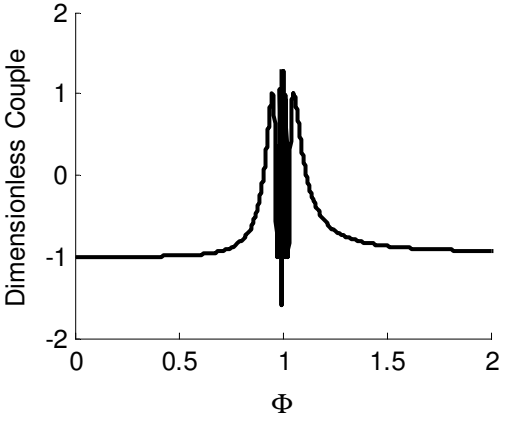

Fig. 2.20. Dimensionless couple versus Φ from Eq. (2.212). $R = 0.1$. $H/h = 0.1$.

It can be easily verified that if the beams follow the plate surface in translation only without rotation, the frequency equation is still formally given by Eq. (2.199) or (2.202) with

$$m^e = m \quad \text{or} \quad R^e = R\,. \tag{2.213}$$

In this case the relative frequency shift in Eq. (2.211) reduces to

$$\frac{\Delta\Omega_n}{n} = -R\,, \tag{2.214}$$

which is the well-known Sauerbrey equation [17] for mass induced frequency shifts. When there is no beam rotation, the moments at the bottoms of the beams in Eq. (2.212) reduces to

$$M = -F\frac{H}{2} = -\frac{1}{2}mH\omega^2 B\cos(2\beta_1 h)\,. \tag{2.215}$$

2.12.6. Case of $\eta \neq 0$ *and* $N = 0$

In this case there are couple stresses in the plate but the microbeams are absent. The modes can be separated into antisymmetric and symmetric ones. The determinant in Eq. (2.189) can be factored into two frequency equations for antisymmetric and symmetric modes, respectively:

$$(\beta_1\mu - \beta_1\beta_2^2\eta)\tan\beta_1 h + (\beta_2\mu + \beta_1^2\beta_2\eta)\tanh\beta_2 h = 0\,, \tag{2.216}$$

and

$$(\beta_2\mu + \beta_1^2\beta_2\eta)\tan\beta_1 h - (\beta_1\mu - \beta_1\beta_2^2\eta)\tanh\beta_2 h = 0\,. \tag{2.217}$$

It can be shown that Eqs. (2.216) and (2.217) can be written into the following form:

$$\tan\gamma = f^3\tanh f\gamma\,, \tag{2.218}$$

and

$$\cot\gamma = -f^3\coth f\gamma\,, \tag{2.219}$$

where

$$\gamma = \beta_1 h\,, \tag{2.220}$$

$$f = \frac{\beta_2}{\beta_1} = \frac{(1+g^2)^{1/2}+1}{g}, \tag{2.221}$$

$$g = \frac{2\gamma l}{h}\left(1+\frac{\gamma^2 l^2}{h^2}\right)^{1/2}. \tag{2.222}$$

Equations (2.216) and (2.218) for antisymmetric modes were obtained in [27]. With Eqs. (2.221) and (2.222), the frequency equations in Eqs. (2.218) and (2.219) can be viewed as equations for $\gamma = \beta_1 h$ with *l/h* as a parameter. For a given *l/h*, once γ is found from Eqs. (2.218) or (2.219), the normalized frequency can be obtained from

$$\Omega = \frac{\omega}{\pi c_2 / 2h} = \gamma\pi^{-1}\{2[(1+g^2)^{1/2}+1]\}^{1/2} = 2\gamma\pi^{-1}\left(1+\frac{\gamma^2 l^2}{h^2}\right)^{1/2} = \frac{gh}{\pi l}. \tag{2.223}$$

In the limit when η, and accordingly *l/h,* go to zero (absence of couple stress), *g* also goes to zero and *f* goes to infinity. In this case Eqs. (2.218), (2.219), and (2.223) reduce to

$$\cot\gamma = 0\,, \tag{2.224}$$

$$\tan\gamma = 0\,, \tag{2.225}$$

$$\Omega = n\,. \tag{2.226}$$

Equations (2.224) and (2.225) are equivalent to Eq. (2.194) as expected, and Eq. (2.226) is the same as Eq. (2.197).

In Fig. 2.21 we show the first few resonant frequencies versus *h/l*. (a) is for the lowest three antisymmetric modes determined by Eq. (2.218) which were obtained in [27] approximately, and (b) is for the lowest two symmetric modes from Eq. (2.219). For thickness-shear modes *h* may be viewed as the characteristic wavelength, especially for the first few modes of interest. When *h/l* is large, the curves become flat and approach their asymptotes of $\Omega = n$. In this case the effects of the couple stress on

resonant frequencies are negligible. When *h/l* is not very large, the curves begin to deviate from $\Omega = n$, indicating the failure of the theory of elasticity in predicting resonant frequencies. In particular, the curve of $n = 1$ for the fundamental antisymmetric mode is not sensitive to *h/l*. Therefore an acoustic wave resonator or sensor operating with this mode is less affected by the couple stress.

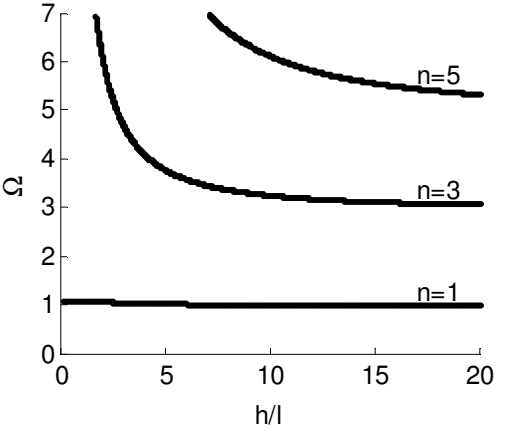

(a)

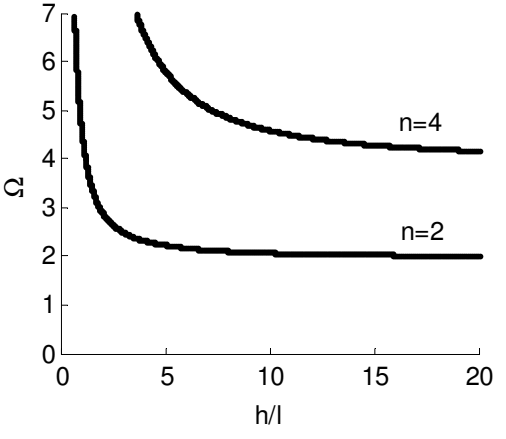

(b)

Fig. 2.21. Ω versus *h/l*. (a): from Eq. (2.218). (b): from Eq. (2.219).

Figure 2.22 shows the effect of the couple stress on the third ($n = 3$), thickness-shear mode (antisymmetric). The curve with $h/l = \infty$ or $\Omega = 3$ is from the theory of elasticity and is a pure sinusoidal curve with three nodal points. The two other modes are from the couple stress theory. As h/l decreases, the modes deviate more from the sinusoidal curve, mainly near the plate surfaces. This is because l appears as the coefficient of the highest (the fourth) derivative term of the differential equation of the couple stress theory (MT (7.3)). During the transition of $l \to 0$ from the couple stress theory to the theory of elasticity, the order of the differential equation drops from four to two. The boundary conditions associated with the couple stress have to be dropped or, in other words, are to be violated by the solution of the theory of elasticity. Therefore the solutions to the two theories differ mainly near the boundary where some boundary layer behavior causes the difference.

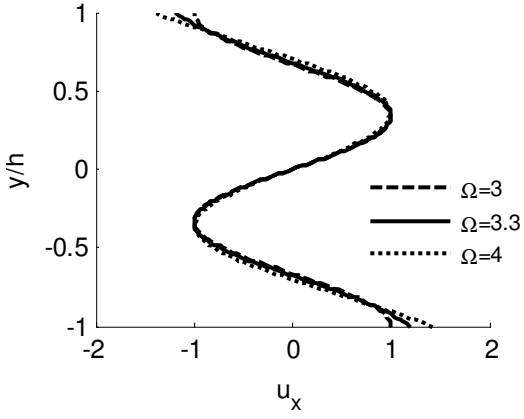

Fig. 2.22. Effect of couple stress on the third TSh mode.

2.13. Plate with an Inhomogeneous Layer of Finite Thickness

In this section we analyze thickness-shear vibration of an AT-cut quartz plate carrying a layer of a functionally graded material (FGM) whose density and stiffness vary along its thickness [29]. The effect of the material property gradient on the resonant frequencies of the two-layer plate as a compound resonator is examined. This effect may be used to

measure the material property gradient of the FGM. Consider time-harmonic free vibrations of the compound resonator in Fig. 2.23. We need to obtain solutions in the crystal plate and the FGM layer separately, and then join them by the interface continuity conditions.

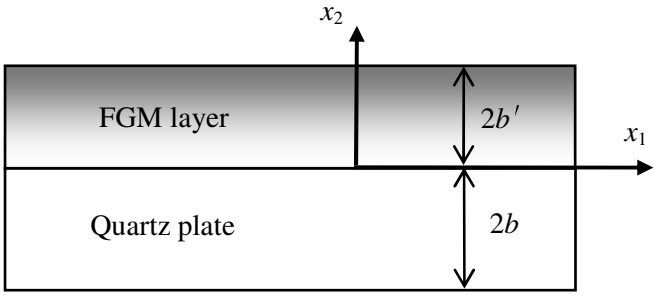

Fig. 2.23. A quartz plate with an FGM layer as a compound resonator.

For thickness-shear motions of the crystal plate, the relevant equations are

$$\begin{aligned} &T_{21,2} = c_{66}u_{1,22} = \rho\ddot{u}_1 = -\rho\omega^2 u_1, \quad -2b < x_2 < 0, \\ &T_{21} = c_{66}u_{1,2}, \quad -2b < x_2 < 0. \end{aligned} \tag{2.227}$$

For the FGM layer, when the material properties including density and stiffness are varying along x_2 only, the relevant equations are

$$\begin{aligned} &T_{21,2} = \overline{\rho}(x_2)\ddot{u}_1 = -\overline{\rho}(x_2)\omega^2 u_1, \quad 0 < x_2 < 2b', \\ &T_{21} = \overline{c}(x_2)u_{1,2}, \quad 0 < x_2 < 2b', \end{aligned} \tag{2.228}$$

where $\overline{\rho}$ is the density and $\overline{c}$ is the shear elastic constant of the FGM layer. As an FGM, $\overline{\rho}$ and $\overline{c}$ are functions of x_2. The boundary and interface continuity conditions are, from bottom to top,

$$T_{21}(-2b) = 0, \tag{2.229}$$

$$\begin{aligned} u_1\left(0^-\right) &= u_1(0^+), \\ T_{21}\left(0^-\right) &= T_{21}(0^+), \end{aligned} \tag{2.230}$$

$$T_{21}\left(2b'\right) = 0\,. \tag{2.231}$$

For the crystal plate governed by Eq. (2.227), the displacement and shear stress fields can be found as

$$\begin{aligned} u_1 &= C\cos\eta(x_2 + 2b), \\ T_{21} &= -c_{66}\eta C\sin\eta(x_2 + 2b), \end{aligned} \tag{2.232}$$

where C is an arbitrary constant and

$$\eta^2 = \frac{\rho}{c_{66}}\omega^2\,. \tag{2.233}$$

We note that the traction-free boundary condition in Eq. (2.229) is already satisfied by Eq. $(2.232)_2$. For the FGM layer, we proceed as follows. Substitution of Eq. $(2.228)_2$ into Eq. $(2.228)_1$ gives

$$\overline{c}_{,2}u_{1,2} + \overline{c}u_{1,22} = -\overline{\rho}\,\omega^2 u_1\,. \tag{2.234}$$

The spatially varying material properties of the FGM usually lead to differential equations with variable coefficients and present considerable mathematical challenges for which two common approaches are usually employed. One is to use the same exponential variation for all material properties, and the other is to divide an FGM layer into many sublayers of different but constant material properties. Here we follow the former approach. We assume that all material properties of the FGM layer have the same exponential variation along the x_2 direction, i.e.,

$$\overline{c} = c^0\exp(\beta x_2), \quad \overline{\rho} = \rho^0\exp(\beta x_2)\,, \tag{2.235}$$

where c^0, ρ^0 and β are constants. c^0 and ρ^0 represent the stiffness and the density of the FGM layer at the interface. Although FGMs cannot all be described by Eq. (2.235), the purpose this section is to get

the order of magnitude of effect of the material property variation (β) on resonant frequencies for which Eq. (2.235) is sufficient. Under Eq. (2.235), Eq. (2.234) becomes an equation with constant coefficients:

$$c^0 \beta u_{1,2} + c^0 u_{1,22} = -\rho^0 \omega^2 u_1 . \tag{2.236}$$

The general solution to Eq. (2.236) and the related shear stress can be written as

$$\begin{aligned} u_1 &= C_1 \exp(\lambda_1 x_2) + C_2 \exp(\lambda_2 x_2), \\ T_{21} &= c_{66} \lambda_1 C_1 \exp(\lambda_1 x_2) + c_{66} C_2 \lambda_2 \exp(\lambda_2 x_2), \end{aligned} \tag{2.237}$$

where C_1 and C_2 are arbitrary constants and

$$\lambda_{1,2} = \frac{1}{2}\left[-\beta \pm \sqrt{\beta^2 - 4\frac{\rho^0 \omega^2}{c^0}} \right]. \tag{2.238}$$

In the case of $\beta^2 - 4\rho^0 \omega^2 / c^0 < 0$, to avoid complex numbers, it is more convenient to write the solution to Eq. (2.236) in the following form:

$$\begin{aligned} u_1 &= C_1 \exp(r_1 x_2)\cos(r_2 x_2) + C_2 \exp(r_1 x_2)\sin(r_2 x_2), \\ T_{21} &= c_{66} C_1 [r_1 \exp(r_1 x_2)\cos(r_2 x_2) - r_2 \exp(r_1 x_2)\sin(r_2 x_2)] \\ &\quad + c_{66} C_2 [r_1 \exp(r_1 x_2)\sin(r_2 x_2) + r_2 \exp(r_1 x_2)\cos(r_2 x_2)], \end{aligned} \tag{2.239}$$

where

$$r_1 = -\frac{\beta}{2}, \quad r_2 = \frac{1}{2}\sqrt{4\frac{\rho^0 \omega^2}{c^0} - \beta^2} . \tag{2.240}$$

Substituting Eqs. (2.232) and (2.237) into Eqs. (2.230) and (2.231) results in

$$\begin{aligned} C\cos(2\eta b) &= C_1 + C_2, \\ -c_{66}\eta C \sin(2\eta b) &= c_{66}\lambda_1 C_1 + c_{66} C_2 \lambda_2, \\ c_{66}\lambda_1 C_1 \exp(2\lambda_1 b') &+ c_{66} C_2 \lambda_2 \exp(2\lambda_2 b') = 0. \end{aligned} \tag{2.241}$$

Equation (2.241) is a system of linear homogeneous equations for C, C_1 and C_2. For nontrivial solutions the determinant of the coefficient matrix has to vanish, which yields the frequency equation. The corresponding nontrivial solutions of C, C_1 and C_2 determine mode shapes. In the case of $\beta^2 - 4\rho^0\omega^2 / c^0 < 0$, using Eq. (2.239), the boundary and continuity conditions in Eqs. (2.230) and (2.231) lead to

$$\begin{aligned}
&C\cos(2\eta b) = C_1,\\
&-c_{66}\eta C\sin(2\eta b) = c_{66}C_1 + c_{66}C_2 r_2,\\
&c_{66}C_1[r_1\exp(2r_1 b')\cos(2r_2 b') - r_2\exp(2r_1 b')\sin(2r_2 b')]\\
&\quad + c_{66}C_2[r_1\exp(2r_1 b')\sin(2r_2 b') + r_2\exp(2r_1 b')\cos(2r_2 b')] = 0.
\end{aligned} \tag{2.242}$$

For a numerical example we consider the case when b = 2 mm, $b' = 2b$, $c^0 = 2c_{66}$, $\rho^0 = \rho$, and $\exp(\beta b') = 2$. In this case, the density and stiffness in the middle of the FGM layer are twice their values at the interface. The lowest three resonant frequencies are found to be ω= 0.94293, 2.2052, and 3.1609×10^7 1/s. The frequencies of the higher-order modes are not integral multiples of the fundamental frequency. The corresponding modes are shown in Fig. 2.24 (a), normalized by their values at the bottom surface of the compound resonator. The three modes have one, two, and three nodal points (zeros), respectively. They do not posses any symmetry or antisymmetry. Near the plate top surface where the material is stiffer than at the interface or near the bottom, the displacement changes more gradually. Since the material is stiffer near the top, the nodal points shift toward the bottom compared to the equally spaced nodal points of modes in a homogeneous plate.

Figure 2.24 (b) is for the first (or the fundamental) mode only. c^0 is varied according to $c^0 = 0.5c_{66}$, c_{66}, and $2c_{66}$. All other parameters are kept the same as those used for Fig. 2.24 (a). The corresponding frequencies are $\omega = 7.1366$, 8.2731, and 9.4293×10^6 1/s. They increase in correspondence to stiffer materials. As the material of the upper layer is becoming stiffer, the nodal point moves toward the lower layer.

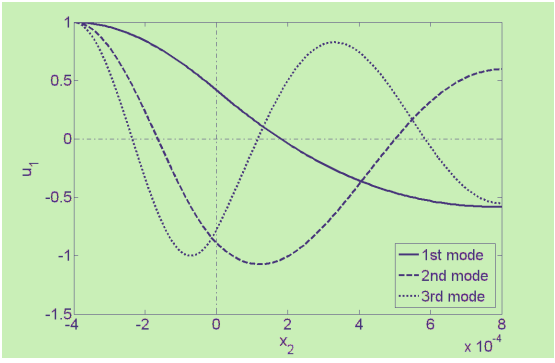

(a)

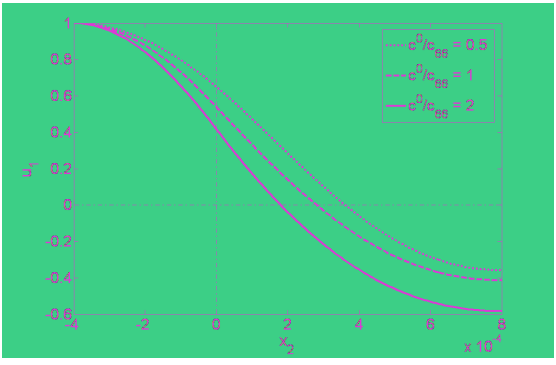

(b)

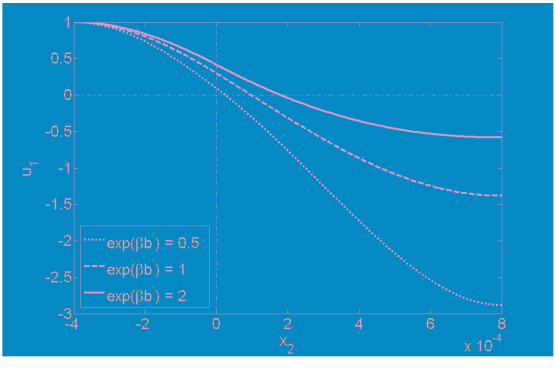

(c)

Fig. 2.24. (a) The first few TSh modes. (b) Effect of c^0 on the first mode. (c) Effect of β on the first mode.

When plotting Fig. 2.24 (c), β is varied according to $\exp(\beta b') = 0.5$, 1, and 2 while all other parameters are kept the same as those used for Fig. 2.24 (a). The corresponding frequencies are found to be $\omega = 1.2219$, 1.0471, and 0.94293×10^7 1/s. When $\exp(\beta b') = 0.5$, the material in the FGM layer becomes lighter and softer from the interface to the top. When $\exp(\beta b') = 1$, the material in the FGM layer is in fact uniform. When $\exp(\beta b') = 2$, the material in the FGM layer becomes heavier and stiffer from the interface to the top. Both the density and the stiffness affect the frequency. For the first mode the displacement is large near the plate top and bottom where the density of the material is felt most, and the shear strain is large near the middle part along the plate thickness where the stiffness is felt more. Since the density and stiffness vary mostly near the plate top surface, the frequency is dominated by the density variation there and becomes lower as β increases.

Our main interest is how the material inhomogeneity or β affects the frequency. Still consider a compound resonator with b = 2 mm and $\rho^0 = \rho$. Figure 2.25 shows the fundamental thickness-shear frequency versus $\beta b'$ for different values of c^0 in (a) or different values of b'/b in (b), respectively. The frequency decreases with β in most cases as explained in the discussion of Fig. 2.24 (c). The most important thing is that the frequency is sensitive to $\beta b'$. When $\beta b'$ ranges from -0.8 to 0.8, causing significant change of material properties in the FGM layer, the frequency change is of the order of ten per cent.

For crystal resonators, relative frequency shifts of the order of a few ppm (parts per million) can be detected. If we vary $\beta b'$ slightly with $\exp(2\beta b') = 1.1$, 1.01, 1.001, and 1.0001 such that the material properties in the FGM layer change by 10%, 1%, 0.1%, and 0.01% from the interface to the top, the corresponding relative frequency shifts are -9137.5, -969.25, -97.521, and -9.7581 ppm. Therefore the frequency is very sensitive to material inhomogeneity and may be used to characterize the material variation of FGMs.

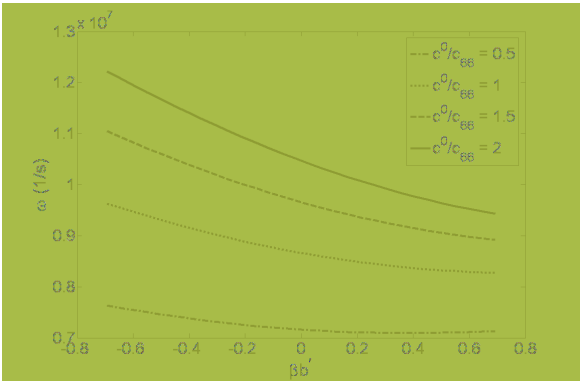

(a)

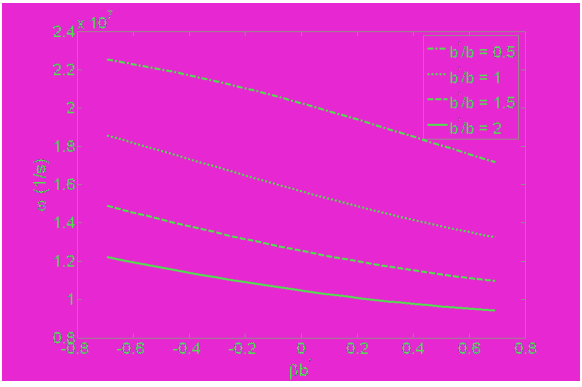

(b)

Fig. 2.25. Frequency of the first TSh mode versus $\beta b'$. (a) Effect of c^0 ($b' = 2b$). (b) Effect of b'/b ($c^0 = 2c_{66}$).

This page intentionally left blank

Chapter 3

Thickness Modes in Plates: Piezoelectric Analysis

Thickness vibrations of piezoelectric plates were analyzed in [2, 30, and 31] for anisotropic materials in general and monoclinic crystals in particular. In this chapter we will mainly study the special case of thickness-shear vibration of a rotated-Y-cut quartz plate. In addition to vibrations of a piezoelectric plate alone, effects of surface electrodes, air gaps, and contact with a fluid, etc., are also discussed. Further complications of the combined effects of electrodes and contact with a fluid, viscoelastic mass layers, multiple mass layers, and interface slips between a plate and a fluid can be found in [32–36].

3.1. Unelectroded Plate

Consider an unbounded, rotated Y-cut quartz plate (see Fig. 3.1). The two major surfaces are traction free and are unelectroded. The electric field in the surrounding free space is neglected. There are no external loads. We are interested in the free vibration eigenvalue problem.

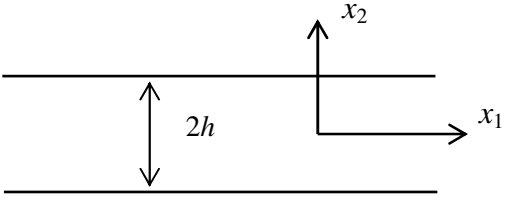

Fig. 3.1. An unelectroded quartz plate.

From the three-dimensional theory of linear piezoelectricity, the governing equations and boundary conditions are:

$$\begin{aligned} &T_{ji,j} = \rho\ddot{u}_i, \quad D_{i,i} = 0, \quad |\, x_2 \,| < h, \\ &T_{ij} = c_{ijkl}S_{kl} - e_{kij}E_k, \quad D_i = e_{ikl}S_{kl} + \varepsilon_{ik}E_k, \quad |\, x_2 \,| < h, \\ &S_{ij} = (u_{i,j} + u_{j,i})/2, \quad E_i = -\phi_{,i}, \quad |\, x_2 \,| < h, \end{aligned} \tag{3.1}$$

and

$$\begin{aligned} &T_{2j} = 0, \quad x_2 = \pm h, \\ &D_2 = 0, \quad x_2 = \pm h. \end{aligned} \tag{3.2}$$

Consider the possibility of the following displacement and potential fields:

$$u_1 = u_1(x_2)\exp(i\omega t), \quad u_2 = u_3 = 0, \quad \phi = \phi(x_2)\exp(i\omega t)\,. \tag{3.3}$$

The nontrivial components of strain, electric field, stress, and electric displacement are

$$2S_{12} = u_{1,2}, \quad E_2 = -\phi_{,2}, \tag{3.4}$$

and

$$\begin{aligned} &T_{31} = c_{56}u_{1,2} + e_{25}\phi_{,2}, \quad T_{12} = c_{66}u_{1,2} + e_{26}\phi_{,2}, \\ &D_2 = e_{26}u_{1,2} - \varepsilon_{22}\phi_{,2}, \quad D_3 = e_{36}u_{1,2} - \varepsilon_{23}\phi_{,2}, \end{aligned} \tag{3.5}$$

where the time-harmonic factor has been dropped. The equations of motion and the charge equation reduce to

$$\begin{aligned} &T_{21,2} = c_{66}u_{1,22} + e_{26}\phi_{,22} = \rho\ddot{u}_1 = -\rho\omega^2 u_1, \\ &D_{2,2} = e_{26}u_{1,22} - \varepsilon_{22}\phi_{,22} = 0. \end{aligned} \tag{3.6}$$

Equation $(3.6)_2$ can be integrated to yield

$$\phi = \frac{e_{26}}{\varepsilon_{22}}u_1 + B_1 x_2 + B_2\,, \tag{3.7}$$

where B_1 and B_2 are integration constants, and B_2 is immaterial. Substituting Eq. (3.7) into the expressions for T_{21}, D_2, and Eq. $(3.6)_1$, we obtain

$$\begin{aligned} T_{21} &= \bar{c}_{66} u_{1,2} + e_{26} B_1, \\ D_2 &= -\varepsilon_{22} B_1, \end{aligned} \tag{3.8}$$

and

$$\bar{c}_{66} u_{1,22} = -\rho \omega^2 u_1, \tag{3.9}$$

where

$$\bar{c}_{66} = c_{66}(1 + k_{26}^2), \quad k_{26}^2 = \frac{e_{26}^2}{\varepsilon_{22} c_{66}}. \tag{3.10}$$

We note from Eq. (3.10) that due to piezoelectric coupling we have $\bar{c}_{66} > c_{66}$, i.e., the material appears to be stiffer. This is the so-called piezoelectric stiffening effect. $\bar{c}_{66}$ is called a piezoelectrically stiffened elastic constant. The general solution to Eq. (3.9) and the corresponding expression for the electric potential are

$$\begin{aligned} u_1 &= A_1 \sin \xi x_2 + A_2 \cos \xi x_2, \\ \phi &= \frac{e_{26}}{\varepsilon_{22}} (A_1 \sin \xi x_2 + A_2 \cos \xi x_2) + B_1 x_2 + B_2, \end{aligned} \tag{3.11}$$

where A_1 and A_2 are integration constants, and

$$\xi^2 = \frac{\rho}{\bar{c}_{66}} \omega^2. \tag{3.12}$$

Then the expression for the stress component relevant to boundary conditions becomes

$$T_{21} = \bar{c}_{66} (A_1 \xi \cos \xi x_2 - A_2 \xi \sin \xi x_2) + e_{26} B_1. \tag{3.13}$$

The boundary conditions of $D_2 = 0$ at the plate surfaces imply through Eq. $(3.8)_2$ that $B_1 = 0$. The boundary conditions of $T_{21} = 0$ imply through

Eq. (3.13) the following two sets of modes: One may be called symmetric modes with $A_1 = 0$ and

$$u_1^{(n)} = \cos\frac{n\pi}{2h}x_2, \quad \omega^{(n)} = \frac{n\pi}{2h}\sqrt{\frac{\bar{c}_{66}}{\rho}}, \quad n = 2, 4, 6, \cdots. \tag{3.14}$$

The other may be called antisymmetric modes with $A_2 = 0$ and

$$u_1^{(n)} = \sin\frac{n\pi}{2h}x, \quad \omega^{(n)} = \frac{n\pi}{2h}\sqrt{\frac{\bar{c}_{66}}{\rho}}, \quad n = 1, 3, 5, \cdots. \tag{3.15}$$

Equations (3.14) and (3.15) show that piezoelectric coupling raises resonant frequencies. When $\bar{c}_{66}$ is replaced by c_{66}, Eqs. (3.14) and (3.15) reduce to Eqs. (2.39) and (2.40).

Finally, we point out that the solution obtained in this section is also valid for a plate electroded at its two surfaces, with the two electrodes open and without net charges on the open electrodes. In this case we also have $D_2 = 0$ on the plate surfaces as electrical boundary conditions.

3.2. Thickness Field Excitation

Consider the same plate as shown in Fig. 3.1 but now the two surfaces are electroded, with a driving voltage $V\exp(i\omega t)$ across the plate thickness. From Eq. (3.6), the governing equations are

$$\begin{aligned} T_{21,2} &= c_{66}u_{1,22} + e_{26}\phi_{,22} = \rho\ddot{u}_1 = -\rho\omega^2 u_1, \\ D_{2,2} &= e_{26}u_{1,22} - \varepsilon_{22}\phi_{,22} = 0. \end{aligned} \tag{3.16}$$

The boundary conditions for a traction-free and electroded plate are

$$\begin{aligned} &T_{2j} = 0, \quad x_2 = \pm h, \\ &\phi(x_2 = h) - \phi(x_2 = -h) = V\exp(i\omega t). \end{aligned} \tag{3.17}$$

The general solution is given by Eq. (3.11)

$$\begin{aligned} u_1 &= A_1 \sin \xi x_2 + A_2 \cos \xi x_2, \\ \phi &= \frac{e_{26}}{\varepsilon_{22}} (A_1 \sin \xi x_2 + A_2 \cos \xi x_2) + B_1 x_2 + B_2, \end{aligned} \tag{3.18}$$

where $\xi^2 = \rho\omega^2 / \bar{c}_{66}$. For boundary conditions we need the following fields from Eqs. $(3.8)_2$ and (3.13):

$$D_2 = -\varepsilon_{22} B_1, \tag{3.19}$$

$$T_{21} = \bar{c}_{66} (A_1 \xi \cos \xi x_2 - A_2 \xi \sin \xi x_2) + e_{26} B_1. \tag{3.20}$$

The boundary conditions in Eq. (3.17) require that

$$\begin{aligned} &\bar{c}_{66} A_1 \xi \cos \xi h - \bar{c}_{66} A_2 \xi \sin \xi h + e_{26} B_1 = 0, \\ &\bar{c}_{66} A_1 \xi \cos \xi h + \bar{c}_{66} A_2 \xi \sin \xi h + e_{26} B_1 = 0, \\ &2 \frac{e_{26}}{\varepsilon_{22}} A_1 \sin \xi h + 2 B_1 h = V. \end{aligned} \tag{3.21}$$

We add Eqs. $(3.21)_{1,2}$, and also subtract them from each other. Then Eq. (3.21) becomes:

$$\begin{aligned} &\bar{c}_{66} A_1 \xi \cos \xi h + e_{26} B_1 = 0, \\ &\bar{c}_{66} A_2 \xi \sin \xi h = 0, \\ &2 \frac{e_{26}}{\varepsilon_{22}} A_1 \sin \xi h + 2 B_1 h = V. \end{aligned} \tag{3.22}$$

We treat free vibration and forced vibration separately below.

3.2.1. Free vibration

First, consider free vibration with $V = 0$. Equation (3.22) decouples into two sets of equations. For symmetric modes, $A_1 = B_1 = 0$. Equation (3.22) reduces to

$$\bar{c}_{66} A_2 \xi \sin \xi h = 0. \tag{3.23}$$

Nontrivial solutions may exist if

$$\sin \xi h = 0 , \tag{3.24}$$

or

$$\xi^{(n)} h = \frac{n\pi}{2}, \quad n = 2, 4, 6, \cdots , \tag{3.25}$$

which determines the following resonant frequencies:

$$\omega^{(n)} = \frac{n\pi}{2h} \sqrt{\frac{\bar{c}_{66}}{\rho}}, \quad n = 2, 4, 6, \cdots . \tag{3.26}$$

The frequencies in Eq. (3.26) is the same as those in Eq. (3.14). The corresponding modes are

$$u_1^{(n)} = \cos \xi^{(n)} x_2 , \quad \phi^{(n)} = \frac{e_{26}}{\varepsilon_{22}} \cos \xi^{(n)} x_2 . \tag{3.27}$$

For antisymmetric modes, $A_2 = 0$. Equation (3.22) reduces to

$$\begin{aligned} &\bar{c}_{66} A_1 \xi \cos \xi h + e_{26} B_1 = 0, \\ &2 \frac{e_{26}}{\varepsilon_{22}} A_1 \sin \xi h + 2 B_1 h = 0. \end{aligned} \tag{3.28}$$

The resonance frequencies are determined by

$$\begin{vmatrix} \bar{c}_{66} \xi \cos \xi h & e_{26} \\ \dfrac{e_{26}}{\varepsilon_{22}} \sin \xi h & h \end{vmatrix} = \bar{c}_{66} \xi h \cos \xi h - \frac{e_{26}^2}{\varepsilon_{22}} \sin \xi h = 0 , \tag{3.29}$$

or

$$\cot \xi h = \frac{\bar{k}_{26}^2}{\xi h} , \tag{3.30}$$

where

$$\bar{k}_{26}^2 = \frac{e_{26}^2}{\varepsilon_{22}\bar{c}_{66}} = \frac{e_{26}^2}{\varepsilon_{22}c_{66}(1+k_{26}^2)} = \frac{k_{26}^2}{1+k_{26}^2}. \tag{3.31}$$

Equations (3.30) and (3.28) determine the resonant frequencies and modes.

For quartz, $\bar{k}_{26}^2$ is very small. Equation (3.30) can be solved approximately. For example, for the most widely used fundamental mode with $n = 1$, we can write [2]

$$\xi h = \frac{\pi}{2} - \Delta, \tag{3.32}$$

where Δ is a small number. Substituting Eq. (3.32) into Eq. (3.30), for small $\bar{k}_{26}^2$ and small Δ, we obtain

$$\Delta \cong \frac{2}{\pi}\bar{k}_{26}^2, \tag{3.33}$$

or

$$\begin{aligned}
\omega^{(1)} &\cong \frac{\pi}{2h}\sqrt{\frac{\bar{c}_{66}}{\rho}}\left(1-\frac{4}{\pi^2}\bar{k}_{26}^2\right) = \frac{\pi}{2h}\sqrt{\frac{c_{66}(1+k_{26}^2)}{\rho}}\left(1-\frac{4}{\pi^2}\bar{k}_{26}^2\right) \\
&\cong \frac{\pi}{2h}\sqrt{\frac{c_{66}}{\rho}}\left(1+\frac{1}{2}k_{26}^2\right)\left(1-\frac{4}{\pi^2}\bar{k}_{26}^2\right) \\
&\cong \frac{\pi}{2h}\sqrt{\frac{c_{66}}{\rho}}\left(1+\frac{1}{2}k_{26}^2-\frac{4}{\pi^2}k_{26}^2\right) > \frac{\pi}{2h}\sqrt{\frac{c_{66}}{\rho}}.
\end{aligned} \tag{3.34}$$

We note that the $\omega^{(1)}$ from Eq. (3.34) is lower than that from Eq. (3.15) because for an electroded plate with shorted electrodes there is less piezoelectric stiffening.

3.2.2. Forced vibration

For forced vibration we have $A_2 = 0$ and

$$A_1 = \frac{\begin{vmatrix} 0 & e_{26} \\ V & 2h \end{vmatrix}}{\begin{vmatrix} \bar{c}_{66}\xi\cos\xi h & e_{26} \\ 2\dfrac{e_{26}}{\varepsilon_{22}}\sin\xi h & 2h \end{vmatrix}} = \frac{-e_{26}V}{2\bar{c}_{66}\xi h\cos\xi h - 2\dfrac{e_{26}^2}{\varepsilon_{22}}\sin\xi h}, \tag{3.35}$$

$$B_1 = \frac{\begin{vmatrix} \bar{c}_{66}\xi\cos\xi h & 0 \\ 2\dfrac{e_{26}}{\varepsilon_{22}}\sin\xi h & V \end{vmatrix}}{\begin{vmatrix} \bar{c}_{66}\xi\cos\xi h & e_{26} \\ 2\dfrac{e_{26}}{\varepsilon_{22}}\sin\xi h & 2h \end{vmatrix}} = \frac{V\bar{c}_{66}\xi\cos\xi h}{2\bar{c}_{66}\xi h\cos\xi h - 2\dfrac{e_{26}^2}{\varepsilon_{22}}\sin\xi h}. \tag{3.36}$$

Hence

$$D_2 = -\varepsilon_{22}B_1 = -\varepsilon_{22}\frac{V}{2h}\frac{\xi h}{\xi h - \bar{k}_{26}^2\tan\xi h} = -\sigma, \tag{3.37}$$

where σ is the surface free charge per unit area on the electrode at $x_2 = h$. The capacitance per unit area is then

$$C = \frac{\sigma}{V} = \frac{\varepsilon_{22}}{2h}\frac{\xi h}{\xi h - \bar{k}_{26}^2\tan\xi h}. \tag{3.38}$$

Note the following limits:

$$\begin{aligned} &\lim_{e_{26}\to 0} C = \frac{\varepsilon_{22}}{2h}, \\ &\lim_{\omega\to 0} C = \frac{\varepsilon_{22}}{2h}\frac{1}{1-\dfrac{k_{26}^2}{1+k_{26}^2}} = \frac{\varepsilon_{22}}{2h}(1+k_{26}^2). \end{aligned} \tag{3.39}$$

3.3. Lateral Field Excitation

The plate in Fig. 3.1 can also be excited into thickness-shear vibration by a lateral electric field E_3 through the piezoelectric constant e_{36}. In the analysis below [37], we assume the presence of a spatially uniform driving electric field $E_3 = E$ and its time-harmonic factor is dropped as usual. We begin with the following trial fields. They will be shown to satisfy all governing equations and boundary conditions of the theory of piezoelectricity:

$$u_1 = u_1(x_2), \quad u_2 = u_3 = 0, \quad \phi = \varphi(x_2) - Ex_3 . \tag{3.40}$$

The nontrivial components of the strain, electric field, stress, and electric displacement components are, correspondingly,

$$2S_{12} = u_{1,2}, \quad E_2 = -\varphi_{,2} \quad E_3 = E , \tag{3.41}$$

$$\begin{aligned} T_{31} &= c_{56}u_{1,2} + e_{25}\varphi_{,2} - e_{35}E, \\ T_{21} &= c_{66}u_{1,2} + e_{26}\varphi_{,2} - e_{36}E, \\ D_2 &= e_{26}u_{1,2} - \varepsilon_{22}\varphi_{,2} + \varepsilon_{23}E, \\ D_3 &= e_{36}u_{1,2} - \varepsilon_{32}\varphi_{,2} + \varepsilon_{33}E. \end{aligned} \tag{3.42}$$

The equation of motion left to be satisfied by u_1 and φ and the charge equation of electrostatics are formally the same as Eq. (3.6):

$$\begin{aligned} T_{21,2} &= c_{66}u_{1,22} + e_{26}\varphi_{,22} = -\rho\omega^2 u_1 , \\ D_{2,2} &= e_{26}u_{1,22} - \varepsilon_{22}\varphi_{,22} = 0. \end{aligned} \tag{3.43}$$

The displacement and potential fields determined from Eq. (3.43) are formally the same as Eq. (3.11)

$$\begin{aligned} u_1 &= A_1 \sin \xi x_2 + A_2 \cos \xi x_2 , \\ \varphi &= \frac{e_{26}}{\varepsilon_{22}}(A_1 \sin \xi x_2 + A_2 \cos \xi x_2) + B_1 x_2 + B_2 , \end{aligned} \tag{3.44}$$

where $\xi^2 = \rho\omega^2 / \bar{c}_{66}$. Then the stress and electric displacement components needed for boundary conditions are

$$T_{21} = \bar{c}_{66}(A_1\xi\cos\xi x_2 - A_2\xi\sin\xi x_2) + e_{26}B_1 - e_{36}E\,, \tag{3.45}$$

$$D_2 = -\varepsilon_{22}B_1 + \varepsilon_{23}E\,. \tag{3.46}$$

For traction-free and unelectroded plate surfaces, we have

$$T_{21}(x_2 = h) = \bar{c}_{66}(A_1\xi\cos\xi h - A_2\xi\sin\xi h) + e_{26}B_1 - e_{36}E = 0\,, \tag{3.47}$$

$$T_{21}(x_2 = -h) = \bar{c}_{66}(A_1\xi\cos\xi h + A_2\xi\sin\xi h) + e_{26}B_1 - e_{36}E = 0\,, \tag{3.48}$$

$$D_2(x_2 = \pm h) = -\varepsilon_{22}B_1 + \varepsilon_{23}E = 0\,. \tag{3.49}$$

Equations (3.47)–(3.49) show that the lateral electric field E drives the plate as effective surface traction and charge. For free vibration, when $E = 0$, from Eq. (3.49) we have $B_1 = 0$. Then Eqs. (3.47) and (3.48) have frequencies and modes given by Eqs. (3.14) and (3.15). Lateral field excitation becomes more interesting when variations of the fields along x_3 are considered and the modes are no longer pure thickness modes.

3.4. Plate with Separated Electrodes

Surface deposited electrodes have a few undesirable effects including residual stress in the electrodes, the frequency effect of electrode irregularity in manufacturing, and the field concentration at electrode edges. In resonator applications, electrodes at some distance from the crystal surface are often used. Separated or unattached electrodes offer certain advantages. In this section we analyze a rotated Y-cut quartz resonator with separated electrodes (see Fig. 3.2) [38].

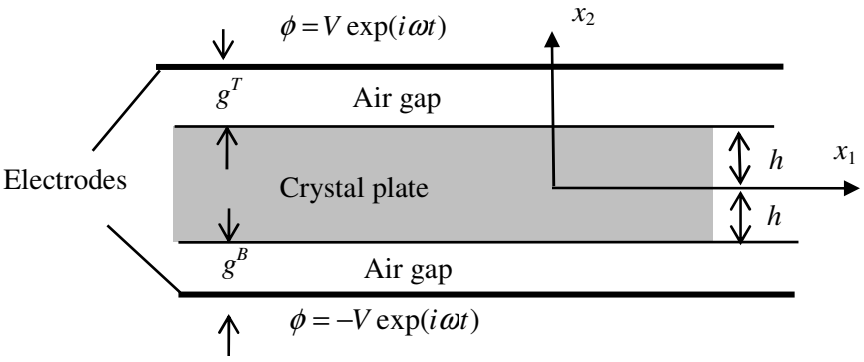

Fig. 3.2. A crystal plate with separated electrodes and air gaps.

The governing equations for the displacement and potential fields in the plate are given by Eq. (3.6)

$$\begin{aligned} T_{21,2} &= c_{66}u_{1,22} + e_{26}\phi_{,22} = \rho\ddot{u}_1 = -\rho\omega^2 u_1\,, \\ D_{2,2} &= e_{26}u_{1,22} - \varepsilon_{22}\phi_{,22} = 0. \end{aligned} \tag{3.50}$$

The general solution is given by Eq. (3.11)

$$\begin{aligned} u_1 &= A_1\sin\xi x_2 + A_2\cos\xi x_2\,, \\ \phi &= \frac{e_{26}}{\varepsilon_{22}}(A_1\sin\xi x_2 + A_2\cos\xi x_2) + B_1 x_2 + B_2\,, \end{aligned} \tag{3.51}$$

where $\xi^2 = \rho\omega^2 / \bar{c}_{66}$. For boundary and continuity conditions we need the following fields from Eqs. $(3.8)_2$ and (3.13):

$$D_2 = -\varepsilon_{22}B_1\,, \tag{3.52}$$

$$T_{21} = \bar{c}_{66}(A_1\xi\cos\xi x_2 - A_2\xi\sin\xi x_2) + e_{26}B_1\,. \tag{3.53}$$

In the upper air gap, we have

$$E_2 = -\phi_{,2}\,, \tag{3.54}$$

$$D_2 = \varepsilon_0 E_2 = -\varepsilon_0 \phi_{,2}\,, \tag{3.55}$$

$$D_{2,2} = -\varepsilon_0 \phi_{,22} = 0\,. \tag{3.56}$$

The general solution to Eq. (3.56) is

$$\phi = F_1 x_2 + G_1\,, \tag{3.57}$$

where F_1 and G_1 are undetermined constants. Substituting Eq. (3.57) into Eq. (3.55) gives

$$D_2 = \varepsilon_0 E_2 = -\varepsilon_0 F_1\,, \tag{3.58}$$

which is needed in the continuity condition at the plate surface. Similarly, for the bottom air gap,

$$\phi = F_2 x_2 + G_2\,, \tag{3.59}$$

$$D_2 = -\varepsilon_0 F_2\,, \tag{3.60}$$

where F_2 and G_2 are undetermined constants.

The quartz plate is under an applied voltage $2V$. We have the following boundary and continuity conditions:

$$\begin{aligned}
&\phi = V, \quad x_2 = h + g^T\,,\\
&\phi = -V, \quad x_2 = -h - g^B\,,\\
&T_{2j}(x_2 = h) = T_{2j}(x_2 = -h) = 0,\\
&\phi(x_2 = h^+) = \phi(x_2 = h^-),\\
&\phi(x_2 = -h^+) = \phi(x_2 = -h^-),\\
&D_2(x_2 = h^+) = D_2(x_2 = h^-),\\
&D_2(x_2 = -h^+) = D_2(x_2 = -h^-).
\end{aligned} \tag{3.61}$$

Substituting the relevant fields into Eq. (3.61), we obtain

$$
\begin{aligned}
&F_1(h+g^T)+G_1=V,\\
&F_2(-h-g^B)+G_2=-V,\\
&\bar{c}_{66}\xi(A_1\cos\xi h-A_2\sin\xi h)+e_{26}B_1=0,\\
&\bar{c}_{66}\xi(A_1\cos\xi h+A_2\sin\xi h)+e_{26}B_1=0,\\
&F_1h+G_1=\frac{e_{26}}{\varepsilon_{22}}(A_1\sin\xi h+A_2\cos\xi h)+B_1h+B_2,\\
&\frac{e_{26}}{\varepsilon_{22}}(-A_1\sin\xi h+A_2\cos\xi h)-B_1h+B_2=-F_2h+G_2,\\
&-\varepsilon_0F_1=-\varepsilon_{22}B_1,\\
&-\varepsilon_{22}B_1=-\varepsilon_0F_2.
\end{aligned}
\tag{3.62}
$$

Equation (3.62) is a system of linear equations for the undetermined constants. We are interested in free vibration resonant frequencies. Therefore we set the driving voltage $V = 0$ and require the determinant of the coefficient matrix to vanish. This yields the following equation that determines the resonant frequencies:

$$
\bar{c}_{66}\xi\sin\xi h\left\{\frac{2\sin\xi h e_{26}^2}{\varepsilon_{22}}-\bar{c}_{66}\xi\cos\xi h\left[2h+\frac{\varepsilon_{22}(g^T+g^B)}{\varepsilon_0}\right]\right\}=0. \tag{3.63}
$$

Equation (3.63) has two factors. $\sin\xi h=0$ gives the essentially symmetric modes not useful in applications. We are interested in the second factor which can be written as

$$
\cot\xi h=\frac{\bar{k}_{26}^2}{\xi[h+\frac{\varepsilon_{22}(g^T+g^B)}{2\varepsilon_0}]}. \tag{3.64}
$$

Equation (3.64) determines the frequencies of the essentially antisymmetric modes that can be electrically excited by a thickness electric field. A few observations can be made from Eq. (3.64). When there are no air gaps, Eq. (3.64) reduces to Eq. (3.30). It is the total

thickness of the air gaps that matters when frequency is concerned. The frequencies increase when the air gaps become thicker.

For the first root of equation (3.64), we can write

$$\xi h = \frac{\pi}{2} - \Delta, \tag{3.65}$$

where Δ is an unknown small number. Substituting Eq. (3.65) into Eq. (3.64), for small $\bar{k}_{26}^2$ and small Δ, we obtain

$$\Delta \cong \frac{2\bar{k}_{26}^2}{\pi[1 + \dfrac{\varepsilon_{22}(g^T + g^B)}{2\varepsilon_0 h}]}. \tag{3.66}$$

Then, from $\xi^2 = \rho\omega^2 / \bar{c}_{66}$, we obtain the following approximation of the fundamental thickness-shear frequency:

$$\omega^{(1)} \cong \frac{\pi}{2h}\sqrt{\frac{c_{66}}{\rho}}\left\{1 + \frac{1}{2}k_{26}^2 - \frac{4k_{26}^2}{\pi^2\left[1 + \dfrac{\varepsilon_{22}(g^T + g^B)}{2\varepsilon_0 h}\right]}\right\} \tag{3.67}$$

$$> \frac{\pi}{2h}\sqrt{\frac{c_{66}}{\rho}} = \omega_0,$$

or

$$\frac{\omega^{(1)} - \omega_0}{\omega_0} \cong 1 + \frac{1}{2}k_{26}^2 - \frac{4k_{26}^2}{\pi^2\left[1 + \dfrac{\varepsilon_{22}(g^T + g^B)}{2\varepsilon_0 h}\right]}, \tag{3.68}$$

where ω_0 is the fundamental thickness-shear frequency when piezoelectric coupling is neglected and is introduced as a reference.

In the special case of symmetric air gaps with $g^T = g^B = g$, we plot $(\omega^{(1)} - \omega_0)/\omega_0$ versus *g/h* from Eq. (3.68) in Fig. 3.3 for quartz plates of different cuts. The curves are simple increasing functions. The frequency is sensitive to air gaps when the gaps are small. Overall the effect of air gaps is of the order of 10^{-4} to 10^{-3}.

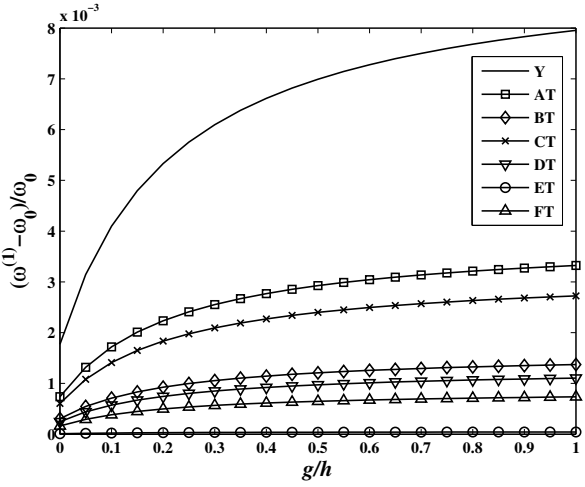

Fig. 3.3. Effect of air gaps on the fundamental TSh frequency.

Due to the dependence of frequency on air gaps, it is possible to use air gaps of varying thickness to create energy trapping in resonators (see Fig. 3.4). When the electrodes are attached to a crystal plate, energy trapping is due to the inertial effect of the electrodes, and the effect of the electrodes on the electric field in the crystal plate and its related piezoelectric stiffening effect. When the electrodes are not attached to the crystal surface, the inertial effect disappears but the effect of the electrodes on the electric field still exists. The effects of electric field and piezoelectric coupling on energy trapping are more pronounced in materials with relatively strong piezoelectric coupling (like langasite) and may be considered for energy trapping creation or enhancement.

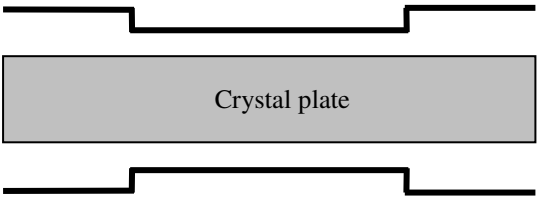

Fig. 3.4. Energy trapping by varying air gaps.

3.5. Effect of Electrode Inertia

Electrodes on piezoelectric plates affect the resonant frequencies both electrically and mechanically. The electrodes on the crystal plate in Section 3.2 were assumed to be very thin. Their mechanical effects were neglected. The most basic mechanical effect of electrodes is their inertia [2, 39]. In this section we study the inertial effect of the electrodes only. Consider a plate of monoclinic crystals with electrodes of unequal thickness as shown in Fig. 3.5. The electrodes are shorted.

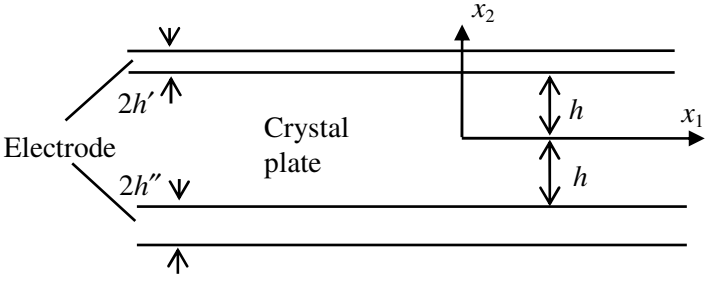

Fig. 3.5. A crystal plate with electrodes of different thickness.

3.5.1. General analysis

From Eq. (3.6), the governing equations are

$$\begin{aligned} T_{21,2} &= c_{66}u_{1,22} + e_{26}\phi_{,22} = \rho\ddot{u}_1 = -\rho\omega^2 u_1, \\ D_{2,2} &= e_{26}u_{1,22} - \varepsilon_{22}\phi_{,22} = 0. \end{aligned} \tag{3.69}$$

The boundary conditions for a traction-free and electroded plate are

$$\begin{aligned} -T_{2j} &= 2\rho' h' \ddot{u}_j, \quad x_2 = h, \\ T_{2j} &= 2\rho' h'' \ddot{u}_j, \quad x_2 = -h, \\ \phi(x_2 = h) &= \phi(x_2 = -h), \end{aligned} \tag{3.70}$$

where ρ' is the electrode mass density. The general solution To Eq. (3.69) is given by Eq. (3.11):

$$\begin{aligned} u_1 &= A_1 \sin \xi x_2 + A_2 \cos \xi x_2, \\ \phi &= \frac{e_{26}}{\varepsilon_{22}} (A_1 \sin \xi x_2 + A_2 \cos \xi x_2) + B_1 x_2 + B_2, \end{aligned} \tag{3.71}$$

where $\xi^2 = \rho\omega^2 / \bar{c}_{66}$. For boundary conditions we need the following fields from Eqs. $(3.8)_2$ and (3.13):

$$D_2 = -\varepsilon_{22} B_1, \tag{3.72}$$

$$T_{21} = \bar{c}_{66} (A_1 \xi \cos \xi x_2 - A_2 \xi \sin \xi x_2) + e_{26} B_1. \tag{3.73}$$

Substituting Eqs. (3.71) and (3.73) into the boundary conditions in Eq. (3.70), we obtain

$$\begin{aligned} &-\bar{c}_{66} \xi (A_1 \cos \xi h - A_2 \sin \xi h) - e_{26} B_1 \\ &\quad = -\omega^2 2\rho' h' (A_1 \sin \xi h + A_2 \cos \xi h), \\ &\bar{c}_{66} \xi (A_1 \cos \xi h + A_2 \sin \xi h) + e_{26} B_1 \\ &\quad = -\omega^2 2\rho' h'' (-A_1 \sin \xi h + A_2 \cos \xi h), \\ &\frac{e_{26}}{\varepsilon_{22}} A_1 \sin \xi h + B_1 h = 0. \end{aligned} \tag{3.74}$$

For nontrivial solutions of the undetermined constants, the determinant of the coefficient matrix of Eq. (3.74) has to vanish. This results in the

following frequency equation:

$$\begin{vmatrix} -\bar{c}_{66}\xi\cos\xi h + \omega^2 2\rho' h'\sin\xi h & \bar{c}_{66}\xi\sin\xi h + \omega^2 2\rho' h'\cos\xi h & -e_{26} \\ \bar{c}_{66}\xi\cos\xi h - \omega^2 2\rho' h''\sin\xi h & \bar{c}_{66}\xi\sin\xi h + \omega^2 2\rho' h''\cos\xi h & e_{26} \\ \dfrac{e_{26}}{\varepsilon_{22}}\sin\xi h & 0 & h \end{vmatrix} = 0 . \tag{3.75}$$

3.5.2. Identical electrodes

We examine the special case of symmetric electrodes where $h'' = h'$. The modes can be separated into symmetric and antisymmetric and Eq. (3.75) splits into two factors. For symmetric modes $A_1 = 0$ and $B_1 = 0$. The frequency equation is

$$\tan\xi h = -R\xi h , \tag{3.76}$$

where *R* is the electrode-plate mass ratio given by

$$R = \frac{2\rho' h'}{\rho h} . \tag{3.77}$$

For antisymmetric modes $A_2 = 0$. The frequency equation is

$$\cot\xi h - \frac{\bar{k}_{26}^2}{\xi h} = R\xi h . \tag{3.78}$$

For the fundamental antisymmetric mode, if we write [2]

$$\xi h = \frac{\pi}{2} - \Delta , \tag{3.79}$$

we obtain, for small Δ, small $\bar{k}_{26}^2$, and small *R*,

$$\Delta \cong \frac{2}{\pi}\bar{k}_{26}^2 + \frac{\pi}{2}R , \tag{3.80}$$

which implies that

$$\omega^{(1)} \cong \frac{\pi}{2h}\sqrt{\frac{\bar{c}_{66}}{\rho}}\,(1-\frac{4}{\pi^2}\bar{k}_{26}^2 - R)\,. \tag{3.81}$$

Obviously, R lowers the frequency. When $R = 0$, Eq. (3.81) reduces to Eq. (3.34).

3.6. Imperfectly Bonded Electrodes

The electrodes in the previous section follow the crystal surfaces perfectly with the same displacements. In this section, we analyze the thickness-shear vibration of a crystal plate with imperfectly bonded electrodes [40]. The interfaces between the crystal and the electrodes are described by the so-called shear-slip model. Consider the plate of monoclinic crystals shown in Fig. 3.6 where the electrodes are not perfectly bonded to the plate surfaces.

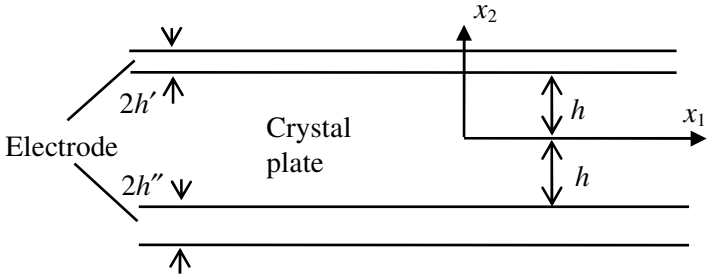

Fig. 3.6. A crystal plate with imperfectly boned electrodes.

3.6.1. General analysis

For free vibrations we have the following equations and boundary conditions:

$$\begin{aligned} T_{21,2} &= c_{66}u_{1,22} + e_{26}\phi_{,22} = \rho\ddot{u}_1 = -\rho\omega^2 u_1\,, \\ D_{2,2} &= e_{26}u_{1,22} - \varepsilon_{22}\phi_{,22} = 0. \end{aligned} \tag{3.82}$$

$$
\begin{aligned}
&-T_{21} = 2\rho' h' \ddot{u}_1', \quad x_2 = h, \\
&T_{21} = 2\rho'' h'' \ddot{u}_1'', \quad x_2 = -h, \\
&\phi(x_2 = h) = \phi(x_2 = -h),
\end{aligned} \tag{3.83}
$$

where ρ' and ρ'' are the mass densities of the top and bottom electrodes. u_j' and u_j'' are the displacements of the top and bottom electrodes. According to the shear-slip model, u_j' and u_j'' may be different from the crystal surface displacements and the following constitutive relations describe the behavior of the interfaces between the crystal plate and the electrodes:

$$
\begin{aligned}
&T_{21} = k'(u_1' - u_1), \quad x_2 = h, \\
&T_{21} = k''(u_1 - u_1''), \quad x_2 = -h,
\end{aligned} \tag{3.84}
$$

where k' and k'' are the elastic constants of the interfaces. With k' and k'', the interfaces are allowed to possess strain energy. Substituting Eq. (3.84) into the boundary conditions in Eq. $(3.83)_{1,2}$, we have

$$
\begin{aligned}
&-k'(u_1' - u_1) = 2\rho' h' \ddot{u}_1', \quad x_2 = h, \\
&k''(u_1 - u_1'') = 2\rho'' h'' \ddot{u}_1'', \quad x_2 = -h.
\end{aligned} \tag{3.85}
$$

The general solution To Eq. (3.82) is given by Eq. (3.11):

$$
\begin{aligned}
&u_1 = A_1 \sin \xi x_2 + A_2 \cos \xi x_2, \\
&\phi = \frac{e_{26}}{\varepsilon_{22}}(A_1 \sin \xi x_2 + A_2 \cos \xi x_2) + B_1 x_2 + B_2,
\end{aligned} \tag{3.86}
$$

where $\xi^2 = \rho\omega^2 / \bar{c}_{66}$. For boundary conditions we need the following fields from Eqs. $(3.8)_2$ and (3.13):

$$
D_2 = -\varepsilon_{22} B_1, \tag{3.87}
$$

$$
T_{21} = \bar{c}_{66}(A_1 \xi \cos \xi x_2 - A_2 \xi \sin \xi x_2) + e_{26} B_1. \tag{3.88}
$$

We write the mass later displacements as

$$u_1' = A' \exp(i\omega t), \quad u_1'' = A'' \exp(i\omega t). \tag{3.89}$$

Substituting Eqs. (3.86)–(3.89) into Eqs. (3.84), (3.85) and $(3.83)_3$, we obtain

$$\begin{aligned}
&\bar{c}_{66}\xi(A_1 \cos\xi h - A_2 \sin\xi h) + e_{26}B_1 \\
&\quad = k'[A' - (A_1 \sin\xi h + A_2 \cos\xi h)], \\
&\bar{c}_{66}\xi(A_1 \cos\xi h + A_2 \sin\xi h) + e_{26}B_1 \\
&\quad = k''[-A_1 \sin\xi h + A_2 \cos\xi h - A''], \\
&-k'[A' - (A_1 \sin\xi h + A_2 \cos\xi h)] = -\omega^2 2\rho' h' A', \\
&k''[-A_1 \sin\xi h + A_2 \cos\xi h - A''] = -\omega^2 2\rho'' h'' A'', \\
&\frac{e_{26}}{\varepsilon_{22}} A_1 \sin\xi h + B_1 h = 0.
\end{aligned} \tag{3.90}$$

For nontrivial solutions of the undetermined constants, the determinant of the coefficient matrix of Eq. (3.90) has to vanish. This results in the following frequency equation:

$$\begin{vmatrix}
\bar{c}_{66}\xi \cos\xi h + k' \sin\xi h & -\bar{c}_{66}\xi \sin\xi h + k' \cos\xi h & e_{26} & -k' & 0 \\
\bar{c}_{66}\xi \cos\xi h + k'' \sin\xi h & \bar{c}_{66}\xi \sin\xi h - k'' \cos\xi h & e_{26} & 0 & k'' \\
k' \sin\xi h & k' \cos\xi h & 0 & \omega^2 2\rho' h' - k' & 0 \\
-k'' \sin\xi h & k'' \cos\xi h & 0 & 0 & \omega^2 2\rho'' h'' - k'' \\
\frac{e_{26}}{\varepsilon_{22}} \sin\xi h & 0 & h & 0 & 0
\end{vmatrix} = 0 . \tag{3.91}$$

3.6.2. Identical electrodes

We examine the special case of symmetric electrodes. In this case $h'' = h'$, $\rho'' = \rho'$, and $k'' = k'$.

3.6.2.1. Identical electrodes in general

The modes can be classified as symmetric and antisymmetric and Eq. (3.91) has two factors. For symmetric modes $A_1 = B_1 = 0$ and $A'' = A'$. The frequency equation is

$$\bar{c}_{66}\xi h \tan \xi h = k'h + \frac{k'^2 h}{2\rho' h' \omega^2 - k'}. \tag{3.92}$$

For antisymmetric modes $A_2 = 0$ and $A'' = -A'$. The frequency equation is

$$\bar{c}_{66}\xi h(\cot \xi h - \frac{\bar{k}_{26}^2}{\xi h}) = -k'h - \frac{k'^2 h}{2\rho' h' \omega^2 - k'}. \tag{3.93}$$

With

$$X = \xi h, \quad \alpha = \frac{\bar{c}_{66}}{k'h}, \tag{3.94}$$

Equations (3.92) and (3.93) can be written as

$$\tan X = \frac{1}{\alpha X}\left(1 + \frac{1}{\alpha R X^2 - 1}\right), \tag{3.95}$$

and

$$\cot X = \frac{\bar{k}_{26}^2}{X} - \frac{1}{\alpha X}\left(1 + \frac{1}{\alpha R X^2 - 1}\right), \tag{3.96}$$

where

$$R = \frac{2\rho' h'}{\rho h}. \tag{3.97}$$

The roots of Eq. (3.95) are determined by the intersections of the following two families of curves:

$$Y_1 = \tan X, \quad Y_2 = \frac{1}{\alpha X}\left(1 + \frac{1}{\alpha R X^2 - 1}\right), \tag{3.98}$$

which are shown in Fig. 3.7 for Y-cut quartz.

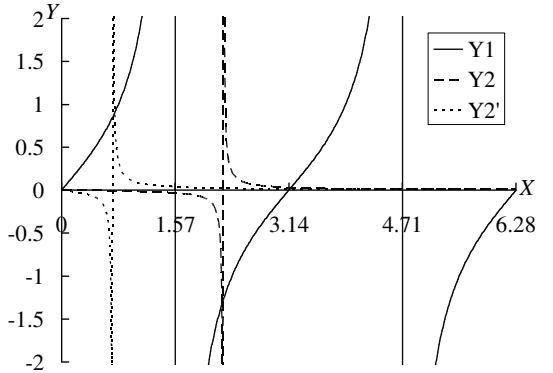

Fig. 3.7. Roots of Eq. (3.95) for symmetric modes, $\alpha = 20$. Y2: $R = 0.01$. Y2′: $R = 0.1$.

Equation (3.96) can be treated in the same way with

$$Y_1 = \cot X, \quad Y_2 = \frac{\bar{k}_{26}^2}{X} - \frac{1}{\alpha X}\left(1 + \frac{1}{\alpha R X^2 - 1}\right), \tag{3.99}$$

and is plotted in Fig. 3.8 for Y-cut quartz.

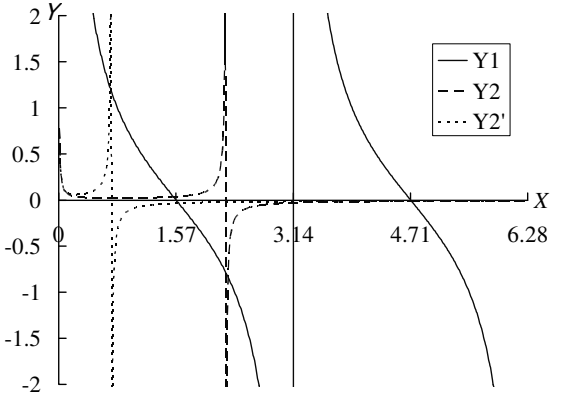

Fig. 3.8. Roots of Eq. (3.96) for antisymmetric modes, $\alpha = 20$. Y2: $R = 0.01$. Y2′: $R = 0.1$.

3.6.2.2. Large k' limit

We examine Eqs. (3.95) and (3.96) for large k' with $\alpha \to 0$. To the lowest order, Eqs. (3.95) and (3.96) are asymptotic to

$$\tan X = -RX \tag{3.100}$$

and

$$\cot X - \frac{\bar{k}_{26}^2}{X} = RX\,, \tag{3.101}$$

which are the results for perfectly bonded electrodes in Eqs. (3.76) and (3.78).

3.6.2.3. Small k' limit

Next we examine another limit case of Eqs. (3.95) and (3.96). For loosely bonded electrodes, in the limit of $k' \to 0$ or $\alpha \to \infty$, to the lowest order, Eqs. (3.95) and (3.96) are asymptotic to

$$\tan X = \frac{1}{\alpha X}\,, \tag{3.102}$$

and

$$\cot X = \frac{\bar{k}_{26}^2 - \dfrac{1}{\alpha}}{X}\,, \tag{3.103}$$

respectively. If α is set to infinity, Eqs. (3.102) and (3.103) reduce to Eqs. (3.24) and (3.30) for a plate with very thin electrodes of negligible mass, as expected.

The roots of Eq. (3.102) are determined by the intersections of the curves in Fig. 3.9 (for two values of α). Compared to the frequencies of $\alpha = \infty$ which are determined by $\sin X = 0$, from the figure it can be seen that a reduction of α raises the resonant frequencies. This is because for small k' the mass layers do not follow the crystal surface

much and the interface shear acts as a restoring force on the vibrating crystal. From the energy point of view, the resonant frequencies are determined by the Rayleigh quotient of strain energy over kinetic energy. For small k' the mass layers do not move much and contribute little to the kinetic energy. At the same time the interfaces are in large shears with considerable strain energy. Therefore the change of strain energy dominates and the resonant frequencies of the crystal become higher.

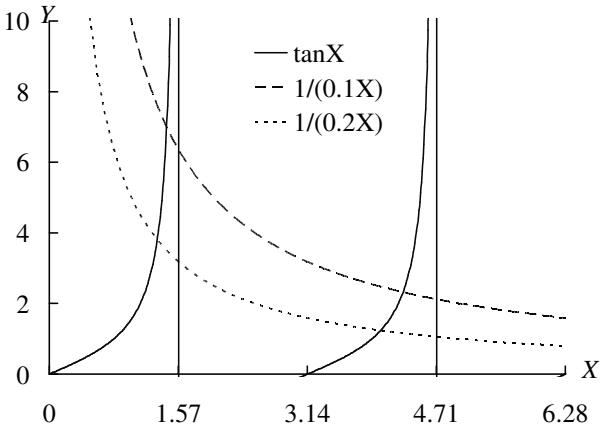

Fig. 3.9. Roots of Eq. (3.102) for symmetric modes.

The roots of Eq. (3.103) are determined by the intersections of the two families of curves in Fig. 3.10. This case is more complicated due to piezoelectric coupling. There are two types of curves and intersections depending on the sign of $\bar{k}_{26}^2 - 1/\alpha$. Numerical results show that it is easier to plot the curves for Y-cut langasite with a larger electromechanical coupling coefficient $\bar{k}_{26}^2 \cong 0.0268$ than Y-cut quartz with $\bar{k}_{26}^2 \cong 0.0078$. The case of $\bar{k}_{26}^2 - 1/\alpha < 0$ is shown in Fig. 3.10. For the case of $\bar{k}_{26}^2 - 1/\alpha > 0$, two curves corresponding to two different

values of α are shown in Figs. 3.11 and 3.12 respectively. The curve for $\alpha = 5000$ is slightly higher than the curve for $\alpha = 500$. In this case it can be concluded that a larger α leads to a lower frequency.

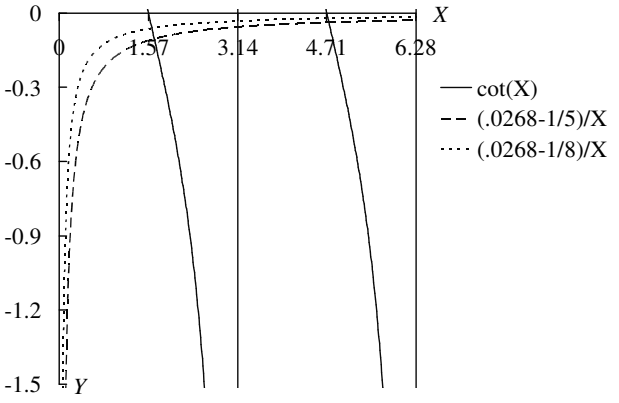

Fig. 3.10. Roots of Eq. (3.103) for antisymmetric modes (langasite, $\bar{k}_{26}^2 - 1/\alpha < 0$).

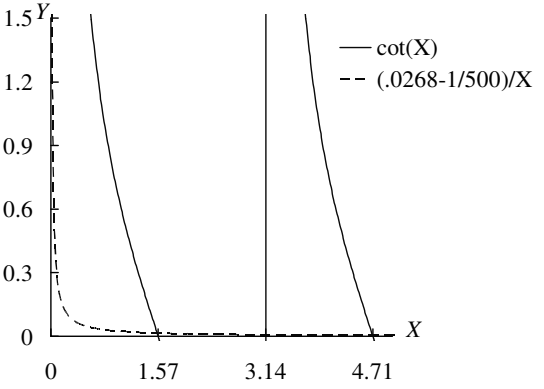

Fig. 3.11. Roots of Eq. (3.103) for antisymmetric modes (langasite, $\bar{k}_{26}^2 - 1/\alpha > 0$).

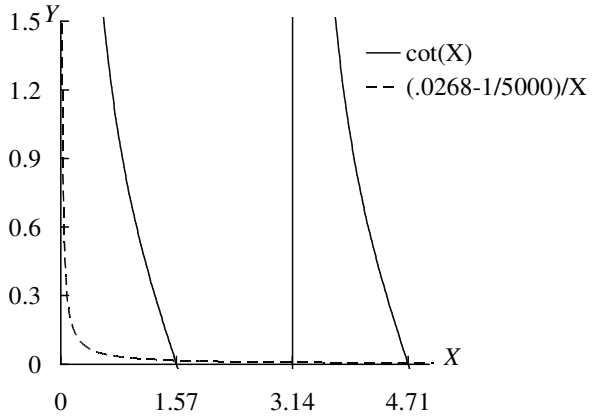

Fig. 3.12. Roots of Eq. (3.103) for antisymmetric modes (langasite, $\bar{k}_{26}^2 - 1/\alpha > 0$).

3.7. Effect of Electrode Shear Stiffness

When the electrodes are not thin compared to the crystal plate, the shear stiffness of the electrodes may need to be considered. In this section we analyze the thickness-shear vibration of a crystal plate with consideration of both the inertia and the shear stiffness of the electrodes [41-43]. Consider a plate of monoclinic crystals with thick and shorted electrodes as shown in Fig. 3.13. The electrodes are modeled by the equations of elasticity.

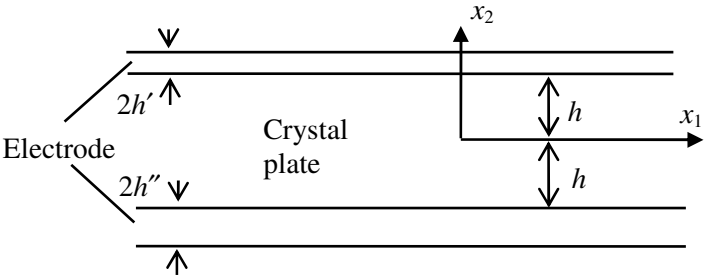

Fig. 3.13. A crystal plate with thick electrodes.

3.7.1. General analysis

For the fields in the crystal plate, from Eq. (3.6), the governing equations are

$$\begin{aligned} T_{21,2} &= c_{66}u_{1,22} + e_{26}\phi_{,22} = \rho\ddot{u}_1 = -\rho\omega^2 u_1, \\ D_{2,2} &= e_{26}u_{1,22} - \varepsilon_{22}\phi_{,22} = 0. \end{aligned} \tag{3.104}$$

We still have

$$\begin{aligned} &\xi^2 = \rho\omega^2 / \bar{c}_{66}, \\ &u_1 = A_1 \sin\xi x_2 + A_2 \cos\xi x_2, \\ &\phi = \frac{e_{26}}{\varepsilon_{22}}(A_1 \sin\xi x_2 + A_2 \cos\xi x_2) + B_1 x_2 + B_2, \\ &T_{21} = \bar{c}_{66}(A_1\xi \cos\xi x_2 - A_2\xi \sin\xi x_2) + e_{26}B_1, \\ &D_2 = -\varepsilon_{22}B_1. \end{aligned} \tag{3.105}$$

The electrodes are isotropic, elastic, and perfect conductors. Consider the upper electrode first. We have

$$T_{21,2} = c'_{66}u_{1,22} = -\rho'\omega^2 u_1, \tag{3.106}$$

$$u_1 = A'_1 \sin\xi'(x_2 - h) + A'_2 \cos\xi'(x_2 - h), \tag{3.107}$$

$$T_{21} = c'_{66}[A'_1\xi' \cos\xi'(x_2 - h) - A'_2\xi' \sin\xi'(x_2 - h)], \tag{3.108}$$

where A'_1 and A'_2 are undetermined constants, ρ' and c'_{66} are the density and shear constant of the electrodes, and

$$(\xi')^2 = \frac{\rho'}{c'_{66}}\omega^2. \tag{3.109}$$

Similarly, for the lower electrode we have

$$u_1 = A''_1 \sin\xi'(x_2 + h) + A''_2 \cos\xi'(x_2 + h), \tag{3.110}$$

$$T_{21} = c'_{66}[A''_1\xi' \cos\xi'(x_2 + h) - A''_2\xi' \sin\xi'(x_2 + h)], \tag{3.111}$$

where A''_1 and A''_2 are undetermined constants.

We have the following boundary and continuity conditions:

$$\begin{aligned}
&T_{2j} = 0, \quad x_2 = h + 2h', \quad x_2 = -h - 2h'', \\
&u_j(x_2 = h^-) = u_j(x_2 = h^+), \\
&T_{2j}(x_2 = h^-) = T_{2j}(x_2 = h^+), \\
&u_j(x_2 = -h^+) = u_j(x_2 = -h^-), \\
&T_{2j}(x_2 = -h^+) = T_{2j}(x_2 = -h^-), \\
&\phi(x_2 = h) = \phi(x_2 = -h).
\end{aligned} \tag{3.112}$$

Substituting the relevant fields into Eq. (3.112), we have

$$\begin{aligned}
&A_1 \sin \xi h + A_2 \cos \xi h = A'_2, \\
&-A_1 \sin \xi h + A_2 \cos \xi h = A''_2, \\
&\bar{c}_{66} \xi (A_1 \cos \xi h - A_2 \sin \xi h) + e_{26} B_1 = c'_{66} \xi' A'_1, \\
&\bar{c}_{66} \xi (A_1 \cos \xi h + A_2 \sin \xi) h + e_{26} B_1 = c'_{66} \xi' A''_1, \\
&A'_1 \cos \xi' 2h' - A'_2 \sin \xi 2h' = 0, \\
&A''_1 \cos \xi 2h'' + A''_2 \sin \xi 2h'' = 0, \\
&\frac{e_{26}}{\varepsilon_{22}} A_1 \sin \xi h + B_1 h = 0.
\end{aligned} \tag{3.113}$$

For nontrivial solutions of the undetermined constants, the determinant of the coefficient matrix of Eq. (3.113) has to vanish. This results in the following frequency equation:

$$\begin{aligned}
&\left(1 - \bar{k}_{26}^2 \frac{\tan \xi h}{\xi h}\right)\left[2 \tan \xi h + \sqrt{\frac{\rho' c'_{66}}{\rho \bar{c}_{66}}} \left(\tan \xi' 2h' + \tan \xi' 2h''\right)\right] \\
&= \sqrt{\frac{\rho' c'_{66}}{\rho \bar{c}_{66}}} \tan \xi h \Bigg[\tan \xi h \left(\tan \xi' 2h' + \tan \xi' 2h''\right) \\
&\qquad + 2 \sqrt{\frac{\rho' c'_{66}}{\rho \bar{c}_{66}}} \tan \xi' 2h' \tan \xi' 2h'' \Bigg].
\end{aligned} \tag{3.114}$$

3.7.2. Special cases

We examine the following special cases of Eq. (3.114).

3.7.2.1. Very thin electrodes without mechanical effects

When $h' = 0$ and $h'' = 0$, i.e., the mechanical effects of the electrodes are neglected, Eq. (3.114) reduces to

$$\left(1 - \bar{k}_{26}^2 \frac{\tan \xi h}{\xi h}\right) \tan \xi h = 0, \tag{3.115}$$

which is the frequency equation of both the symmetric and antisymmetric modes in Eqs. (3.24) and (3.30).

3.7.2.2. Identical electrodes

When $h' = h''$, i.e., the electrodes are of the same thickness, Eq. (3.114) reduces to

$$\begin{aligned} &\left(1 - \bar{k}_{26}^2 \frac{\tan \xi h}{\xi h} - \sqrt{\frac{\rho' c'_{66}}{\rho \bar{c}_{66}}} \tan \xi h \tan \xi' 2h'\right) \\ &\quad \times \left(\tan \xi h + \sqrt{\frac{\rho' c'_{66}}{\rho \bar{c}_{66}}} \tan \xi' 2h'\right) = 0. \end{aligned} \tag{3.116}$$

The first factor of Eq. (3.116) is the frequency equation for the antisymmetric modes treated in [42]. The second factor is for symmetric modes.

For small h', i.e., thin and equal electrodes, we approximately have

$$\tan \xi' 2h' \cong \xi' 2h', \quad \sqrt{\frac{\rho' c'_{66}}{\rho \bar{c}_{66}}} \tan \xi' 2h' \cong R \xi h, \quad R = \frac{\rho' 2h'}{\rho h}. \tag{3.117}$$

In this case Eq. (3.116) reduces to

$$\tan \xi h = -R\xi h, \quad \tan \xi h = \frac{\xi h}{\bar{k}_{26}^2 + R(\xi h)^2}, \tag{3.118}$$

which are Eqs. (3.76) and (3.78).

3.7.2.3. Electrode inertia

When h' and h'' are both small, i.e., thin and unequal electrodes, Eq. (3.114) reduces to

$$\begin{aligned} &\left(1 - \bar{k}_{26}^2 \frac{\tan \xi h}{\xi h}\right)\left[2 \tan \xi h + (R' + R'')\xi h\right] \\ &\quad = \xi h \tan \xi h\left[(R' + R'') \tan \xi h + 2R'R''\xi h\right], \end{aligned} \tag{3.119}$$

where we have denoted

$$R' = \frac{\rho' 2h'}{\rho h}, \quad R'' = \frac{\rho' 2h''}{\rho h}. \tag{3.120}$$

To the lowest (the first) order of the mass effect, the $R'R''$ term on the right-hand side of Eq. (3.119) can be dropped. Then it can be seen that it is the total mass ratio $R' + R''$ that matters.

3.7.2.4. Nonpiezoelectric plates

For a three-layered elastic plate, $k_{26} = 0$. Equation (3.114) reduces to

$$\begin{aligned} &2 \tan \xi h + \sqrt{\frac{\rho' c'_{66}}{\rho \bar{c}_{66}}}\left(\tan \xi' 2h' + \tan \xi' 2h''\right) = \sqrt{\frac{\rho' c'_{66}}{\rho \bar{c}_{66}}} \tan \xi h \\ &\times \left[\tan \xi h\left(\tan \xi' 2h' + \tan \xi' 2h''\right) + 2\sqrt{\frac{\rho' c'_{66}}{\rho \bar{c}_{66}}} \tan \xi' 2h' \tan \xi' 2h''\right]. \end{aligned} \tag{3.121}$$

For a two-layered elastic plate, we set $h'' = 0$ in Eq. (3.121) and obtain

$$2\tan\xi h + \sqrt{\frac{\rho' c'_{66}}{\rho \bar{c}_{66}}}\tan\xi' 2h' = \sqrt{\frac{\rho' c'_{66}}{\rho \bar{c}_{66}}}\tan\xi h \tan\xi h \tan\xi' 2h'. \quad (3.122)$$

3.7.3. Numerical results

Introduce a normalized frequency

$$\Omega = \frac{\omega}{\bar{\omega}_0}, \quad \bar{\omega}_0^2 = \frac{\pi^2 \bar{c}_{66}}{\rho h^2}. \quad (3.123)$$

Then Eq. (3.114) can be written as an equation for Ω:

$$\left(1 - \bar{k}_{26}^2 \frac{\tan\frac{\pi}{2}\Omega}{\frac{\pi}{2}\Omega}\right)\left[2\tan\frac{\pi}{2}\Omega + \alpha\left(\tan\beta'\Omega + \tan\beta''\Omega\right)\right]$$
$$= \alpha\tan\frac{\pi}{2}\Omega\left[\tan\frac{\pi}{2}\Omega\left(\tan\beta'\Omega + \tan\beta''\Omega\right)\right. \quad (3.124)$$
$$\left. + 2\alpha\tan\beta'\Omega\tan\beta''\Omega\right],$$

where

$$\alpha = \sqrt{\frac{\rho' c'_{66}}{\rho \bar{c}_{66}}}, \quad \beta' = \sqrt{\frac{\rho' c'_{66}}{\rho \bar{c}_{66}}}\frac{2h'}{h}\frac{\pi}{2}, \quad \beta'' = \sqrt{\frac{\rho' c'_{66}}{\rho \bar{c}_{66}}}\frac{2h''}{h}\frac{\pi}{2}. \quad (3.125)$$

Consider an AT-cut quartz plate. For the electrodes we consider the following common materials:

	$\rho'(\text{kg/m}^3)$	$c'_{66}\ (10^{10}\ \text{N/m}^2)$
Gold	19,300	2.85
Silver	10,490	2.7

We plot the normalized fundamental thickness-shear frequency from Eq. (3.124) in Figs. 3.14 and 3.15 as function a of β' for different values

of β''. For gold or silver electrodes the inertial effect dominates. It tends to lower the resonant frequencies as expected. Gold is heavier than silver and has a larger effect on frequencies.

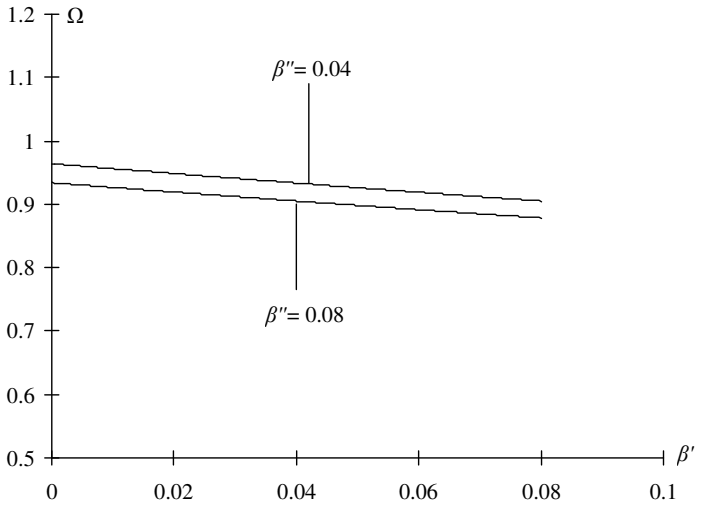

Fig. 3.14. Effect of gold electrodes on resonant frequency.

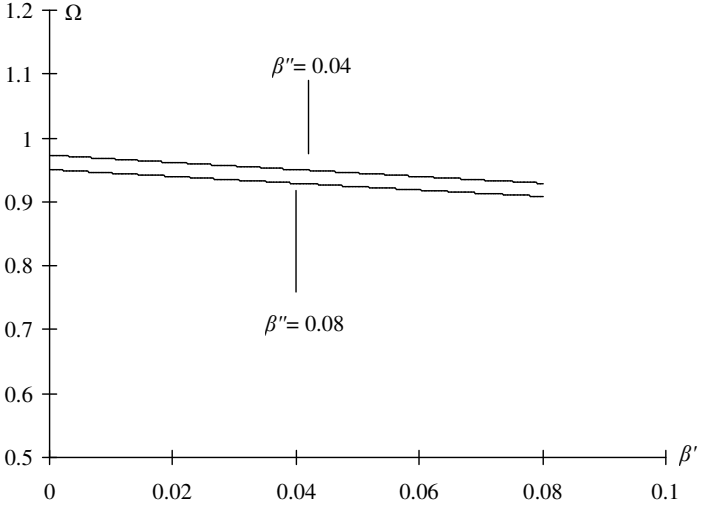

Fig. 3.15. Effect of silver electrodes on resonant frequency.

3.8. Plate in Contact with a Fluid under a Separated Electrode

Consider the plate with a fluid layer shown in Fig. 3.16 [44]. One electrode is at the top of the fluid layer, separated from the crystal plate. Another electrode is at the bottom of the plate. A time-harmonic driving voltage $V\exp(i\omega t)$ is applied across the electrodes.

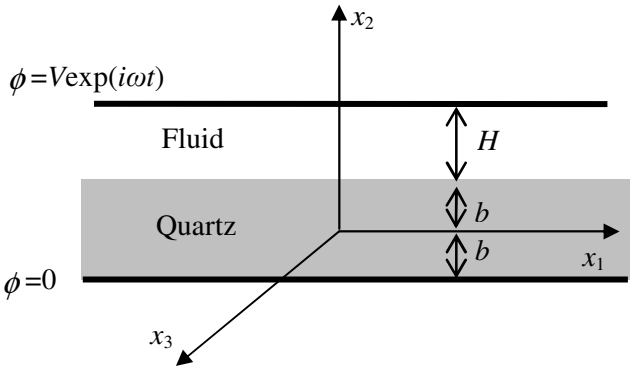

Fig. 3.16. A plate with a fluid under a separated electrode.

3.8.1. Governing equations and fields

The fluid is assumed to be without electromechanical coupling. For motions independent of x_1 and x_3, its electric and mechanical fields are governed by

$$D_{2,2} = 0, \quad D_2 = \varepsilon E_2, \quad E_2 = -\phi_{,2}, \tag{3.126}$$

and [21]

$$T_{21,2} = \rho_L \dot{v}_1, \quad T_{21} = \mu \frac{\partial v_1}{\partial x_2}, \tag{3.127}$$

respectively. ε, μ, and ρ_L are the dielectric constant, viscosity, and mass density of the fluid. v_1 and T_{21} are the relevant velocity and shear stress

components. Equations (3.126) and (3.127) allow the following fields:

$$\begin{aligned} \phi &= C_1(x_2 - b) + C_2, \\ D_2 &= -\varepsilon C_1, \end{aligned} \tag{3.128}$$

$$\begin{aligned} v_1 &= \{C_3 \sinh[(1+i)\eta(x_2 - b)] + C_4 \cosh[(1+i)\eta(x_2 - b)]\}, \\ T_{21} &= (1+i)\mu\eta\{C_3 \cosh[(1+i)\eta(x_2 - b)] + C_4 \sinh[(1+i)\eta(x_2 - b)]\}, \end{aligned} \tag{3.129}$$

where C_1 through C_4 are undetermined constants, and

$$\eta = \sqrt{\frac{\rho_L \omega}{2\mu}}\,. \tag{3.130}$$

For the crystal plate, the equation of motion and the charge equation of electrostatics take the following form (see Eq. (3.6)):

$$\begin{aligned} T_{21,2} &= c_{66} u_{1,22} + e_{26}\phi_{,22} = -\rho\omega^2 u_1\,, \\ D_{2,2} &= e_{26} u_{1,22} - \varepsilon_{22}\phi_{,22} = 0. \end{aligned} \tag{3.131}$$

The general solution to Eq. (3.131) and the relevant shear stress and electric displacement components are

$$u_1 = C_5 \sin[\xi(x_2 - b)] + C_6 \cos[\xi(x_2 - b)]\,, \tag{3.132}$$

$$\phi = \frac{e_{26}}{\varepsilon_{22}}\{C_5 \sin[\xi(x_2 - b)] + C_6 \cos[\xi(x_2 - b)]\} + C_7(x_2 - b) + C_8\,, \tag{3.133}$$

$$T_{21} = \bar{c}_{66}\xi\{C_5 \cos[\xi(x_2 - b)] - C_6 \sin[\xi(x_2 - b)]\} + e_{26}C_7\,, \tag{3.134}$$

$$D_2 = -\varepsilon_{22}C_7\,, \tag{3.135}$$

where C_5 through C_8 are undetermined constants, and

$$\xi^2 = \frac{\rho}{\bar{c}_{66}}\omega^2\,, \tag{3.136}$$

$$\bar{c}_{66} = c_{66}(1+k_{26}^2), \quad k_{26}^2 = \frac{e_{26}^2}{\varepsilon_{22}c_{66}}. \tag{3.137}$$

The top of the fluid layer is traction free and has the prescribed electric potential

$$T_{21}(b+H)=0, \quad \phi(b+H)=V\,. \tag{3.138}$$

At the interface between the fluid and the crystal plate, we have the continuity of velocity, electric potential, shear stress, and normal electric displacement:

$$\begin{aligned} &\dot{u}_1(b^-)=v_1(b^+), \quad \phi(b^-)=\phi(b^+),\\ &T_{21}(b^-)=T_{21}(b^+), \quad D_2(b^-)=D_2(b^+). \end{aligned} \tag{3.139}$$

The bottom of the crystal plate is traction free and is grounded electrically:

$$\phi(-b)=0, \quad T_{21}(-b)=0\,. \tag{3.140}$$

Substitution of the relevant fields into Eqs. (3.138)–(3.140) gives the following eight equations for C_1 through C_8:

$$\begin{aligned} &HC_1 + C_2 = V,\\ &\cosh[(1+i)\eta H]C_3 + \sinh[(1+i)\eta H]C_4 = 0,\\ &C_4 - i\omega C_6 = 0,\\ &C_2 - \frac{e_{26}}{\varepsilon_{22}}C_6 - C_8 = 0,\\ &(1+i)\mu\eta C_3 - \bar{c}_{66}\xi C_5 - e_{26}C_7 = 0,\\ &\varepsilon C_1 - \varepsilon_{22}C_7 = 0,\\ &\frac{e_{26}}{\varepsilon_{22}}\sin(-2b\xi)C_5 + \frac{e_{26}}{\varepsilon_{22}}\cos(-2b\xi)C_6 - 2bC_7 + C_8 = 0,\\ &\bar{c}_{66}\xi\cos(-2b\xi)C_5 - \bar{c}_{66}\xi\sin(-2b\xi)C_6 + e_{26}C_7 = 0. \end{aligned} \tag{3.141}$$

3.8.2. Free vibration

For free vibrations we set $V = 0$ and Eq. (3.141) becomes homogeneous. For nontrivial solutions the determinant of the coefficient matrix of Eq. (3.141) has to vanish, which gives the following frequency equation:

$$\begin{aligned}&\xi(H\frac{\varepsilon_{22}}{\varepsilon}+2b)\sin(2b\xi)+2\bar{k}_{26}{}^{2}[\cos(2b\xi)-1]\\&=\frac{(1-i)\mu\eta\omega}{\bar{c}_{66}\ \xi}[\bar{k}_{26}{}^{2}\sin(2b\xi)\\&-\xi(H\frac{\varepsilon_{22}}{\varepsilon}+2b)\cos(2b\xi)]\tanh[(1+i)\eta H],\end{aligned}\tag{3.142}$$

where $\bar{k}_{26}^2 = e_{26}{}^2/(\varepsilon_{22}\bar{c}_{66})$.

Consider a special case of Eq. (3.142) first. If we neglect the piezoelectric coupling in Eq. (3.142) by setting $\bar{k}_{26}^2 = 0$ (in this case $\bar{c}_{66} = c_{66}$) and consider the limit when $H \to \infty$, Eq. (3.142) reduces to Eq. (2.71):

$$\tan\left(2b\omega\sqrt{\frac{\rho}{c_{66}}}\right) = -(1-i)\sqrt{\frac{\omega\rho_L\mu}{2\rho c_{66}}}\,,\tag{3.143}$$

which is the frequency equation in [20].

Next we consider another special case of Eq. (3.142). If we neglect the drag due to fluid viscosity by setting $\mu = 0$, the right-hand side of Eq. (3.142) vanishes and the left-hand side can be factored into two equations. One is simply

$$\sin(\xi b) = 0\,,\tag{3.144}$$

which is not of interest because in the special case of $H = 0$ this equation determines modes that are symmetric about $x_2 = 0$ which cannot be excited by a thickness electric field. What is useful in device applications is the other equation which can be written as

$$\cot(\xi b) = \frac{\bar{k}_{26}^2}{\left(\frac{\varepsilon_{22}H}{2\varepsilon}+b\right)\xi}\,.\tag{3.145}$$

Equation (3.145) agrees with Eq. (3.64) for a crystal plate with an air gap when $\varepsilon = \varepsilon_0$, the dielectric constant of free space. Equation (3.145) shows that, although the fluid viscosity is neglected, the fluid dielectric constant and thickness still affect the resonant frequencies of the crystal plate. Modes determined by Eq. (3.145) are essentially antisymmetric about $x_2 = 0$ and can be excited by a thickness electric field. We will focus on these modes in the following. For small piezoelectric coupling, if the small $\bar{k}_{26}^2$ is neglected, Eq. (3.145) has approximate roots of $\xi b = n\pi/2$ with n = 1, 3, 5, … These approximate roots will be the base for obtaining an approximate solution to Eq. (3.142) next.

We now return to the general frequency equation in Eq. (3.142). Consider the case of small piezoelectric coupling (small $\bar{k}_{26}^2$) and a low viscosity (small μ) fluid. We look for approximate roots of Eq. (3.142) by letting

$$\xi b \cong \frac{n\pi}{2} - \Delta^{(n)}, \tag{3.146}$$

where $\Delta^{(n)}$ is a small perturbation. Substituting Eq. (3.146) into Eq. (3.142), for small piezoelectric coupling and small viscosity, we obtain

$$\Delta^{(n)} \cong \frac{4\bar{k}_{26}^2}{\left(\frac{\varepsilon_{22}}{\varepsilon}\frac{H}{2b}+1\right)2n\pi} + \frac{1-i}{2}\sqrt{\frac{\rho_L \mu \omega_0^{(n)}}{2\rho c_{66}}}\tanh[(1+i)\eta_0^{(n)}H], \tag{3.147}$$

where

$$\begin{aligned} \omega_0^{(n)} &= \frac{n\pi}{2b}\sqrt{\frac{\bar{c}_{66}}{\rho}}, \quad n = 1,3,5,\cdots, \\ \eta_0^{(n)} &= \sqrt{\rho_L \omega_0^{(n)}/(2\mu)}. \end{aligned} \tag{3.148}$$

With $\Delta^{(n)}$ given by Eq. (3.147), from Eqs. (3.146) and (3.136) we obtain the relative frequency shift as

$$\Delta\Omega^{(n)} = \frac{\omega^{(n)} - \omega_0^{(n)}}{\omega_0^{(n)}} = -\frac{2}{n\pi}\Delta^{(n)} = \Delta\Omega_1^{(n)} + \Delta\Omega_2^{(n)}, \tag{3.149}$$

where

$$\Delta\Omega_1^{(n)} = -\frac{4\bar{k}_{26}^2}{\left(\dfrac{\varepsilon_{22}}{\varepsilon}\dfrac{H}{2b}+1\right)n^2\pi^2},$$
$$\Delta\Omega_2^{(n)} = -\frac{1-i}{n\pi}\sqrt{\frac{\rho_L\mu\omega_0^{(n)}}{2\rho c_{66}}}\tanh[(1+i)\eta_0^{(n)}H]. \tag{3.150}$$

$\Delta\Omega_1^{(n)}$ is due to the piezoelectric coupling in the crystal plate and the dielectric effect of the fluid. $\Delta\Omega_2^{(n)}$ is due to the density and viscosity of the fluid.

Equation $(3.150)_2$ is more general than the classical result in [20] by including the effect of the finite H. When $H = \infty$, Eq. $(3.150)_2$ reduces to Eq. (2.75):

$$\Delta\omega^{(n)} = \omega^{(n)} - \omega_0^{(n)} = -\frac{1-i}{n\pi}\omega_0^{(n)}\sqrt{\frac{\rho_L\mu\omega_0^{(n)}}{2\rho c_{66}}}\,. \tag{3.151}$$

When $n = 1$, the real part of Eq. (3.151) gives the classical result of [20] for the frequency shift of the fundamental thickness-shear mode in a crystal plate resonator due to contact with a viscous fluid. From Eq. (3.151), higher-order modes with larger values of n have smaller frequency shifts.

3.8.3. Forced vibration

For forced vibrations Eq. (3.141) is inhomogeneous. Under a real driving frequency the coefficient matrix does not vanish. A solution always exists, is unique, and can be obtained using a computer. The free charge Q_e per unit area of the electrode at $x_2 = b + H$, the current I per unit area that flows into this electrode, and the admittance Y per unit electrode area of the plate are given by

$$Q_e = -D_2 = \varepsilon C_1, \quad I = \dot{Q}_e = i\omega Q_e, \quad Y = I/V\,. \tag{3.152}$$

3.8.4. Numerical results

Consider a plate with $\omega_0^{(1)} = 9\times10^6$ 1/s and $H = 2b$ unless otherwise stated. We will consider several mixed fluids including ethanol with density ρ_L = 0.78522 g/cm^3 and viscosity μ = 1.04 mPa·s, and toluene with ρ_L = 0.8669 g/cm^3 and μ = 0.5503 mPa·s. For the viscosity and the dielectric constant of mixed fluids, we use the following formulas from [45] and [46], respectively:

$$\begin{aligned} \mu &= X_1^2\mu_1 + X_2^2\mu_2 + X_1X_2\mu', \\ \mu' &= \mu_1 + \mu_2, \\ \varepsilon &= \varepsilon_1 p_1 + \varepsilon_2 p_2, \end{aligned} \tag{3.153}$$

where X_1 and X_2 are mole fractions, and p_i are relative volume fractions. The mass density of the mixture is based on the ratio between the mass sum over the volume sum.

Figure 3.17 is for the case when the fluid is 100% ethanol. To examine the effect of the fluid dielectric constant individually, we artificially vary the parameter and plot the result. The fluid dielectric constant lowers the frequency monotonically. The frequency is more sensitive to the fluid dielectric constant when it is small.

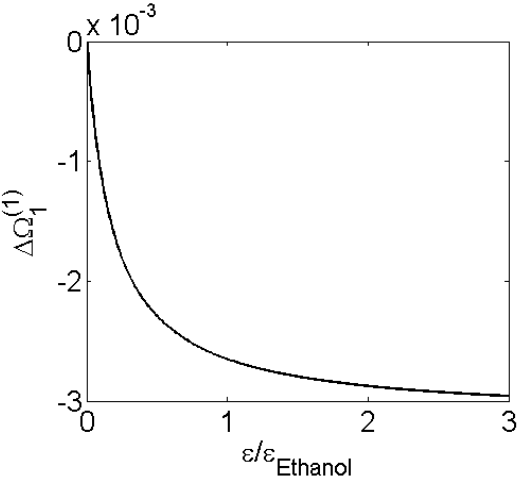

Fig. 3.17. Effect of fluid dielectric constant on $\Delta\Omega_1^{(1)}$.

Figure 3.18 is also for the case when the fluid is 100% ethanol. We artificially vary the fluid's viscosity. It lowers the frequency as expected. The effect of the fluid mass density is similar.

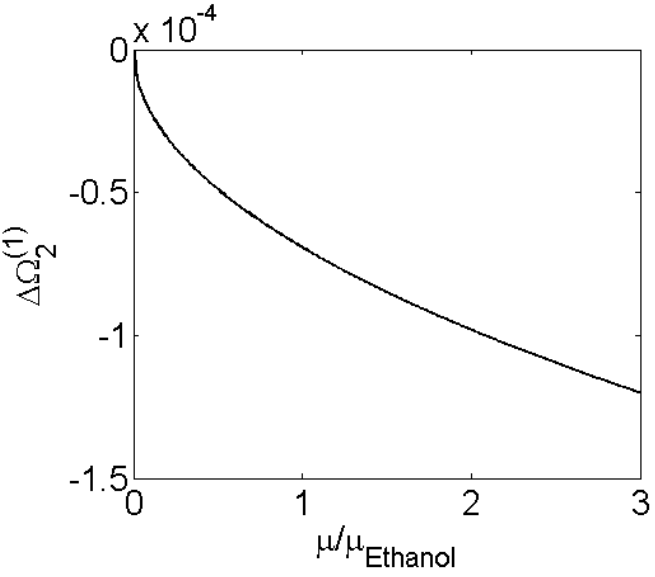

Fig. 3.18. Effect of fluid viscosity on $\Delta\Omega_2^{(1)}$.

Figure 3.19 shows the effect of the fluid layer thickness for different volume fractions of ethanol in ethylene glycol. $\Delta\Omega_1^{(1)}$ in (a) approaches a constant for large *H*. It is not sensitive to the volume fraction. $\Delta\Omega_2^{(1)}$ approaches a constant quicker and it is sensitive to the volume fraction. For small *H*, $|\Delta\Omega_2^{(1)}|$ increases with *H* essentially linearly. Before it saturates, it reaches a maximum that is slightly larger than the saturation value.

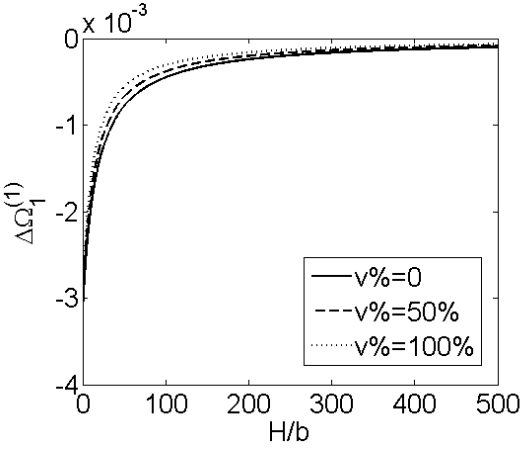

(a)

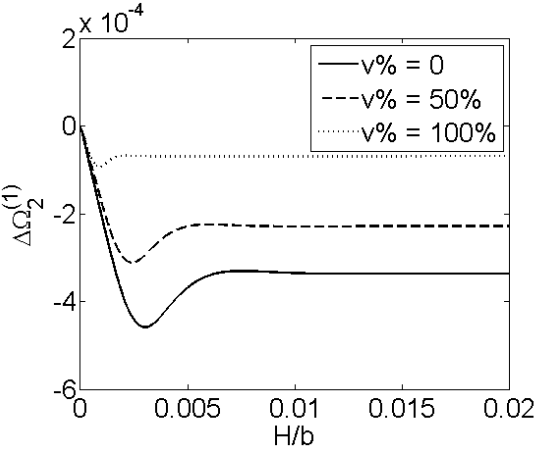

(b)

Fig. 3.19. Effect of fluid layer thickness on $\Delta\Omega_1^{(1)}$ (a) and $\Delta\Omega_2^{(1)}$ (b) for different volume fractions of ethanol in ethylene glycol.

Figure 3.20 is from the forced vibration analysis. It shows the admittance per unit plate surface area for different volume fractions of ethanol in toluene. When the volume fraction of ethanol increases from 0 to 100%, the corresponding frequency change is of the order of 10^{-3}.

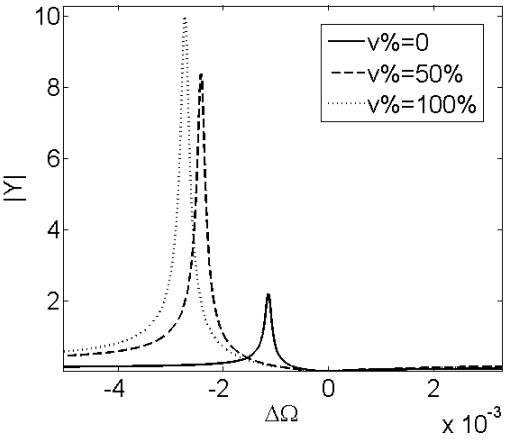

Fig. 3.20. Admittance for different volume fraction of ethanol in toluene.

3.9. Plate in Contact with a Fluid: Lateral Field Excitation

Consider the plate shown in Fig. 3.21 which is unbounded in the x_1 direction [37]. There are two edge electrodes at $x_3 = \pm c$. On these electrodes a driving voltage of $\phi = \pm V \exp(i\omega t)/2$ is applied. We assume thin plates with *c*>>*b* so that edge effects can be neglected and pure thickness-shear modes exist.

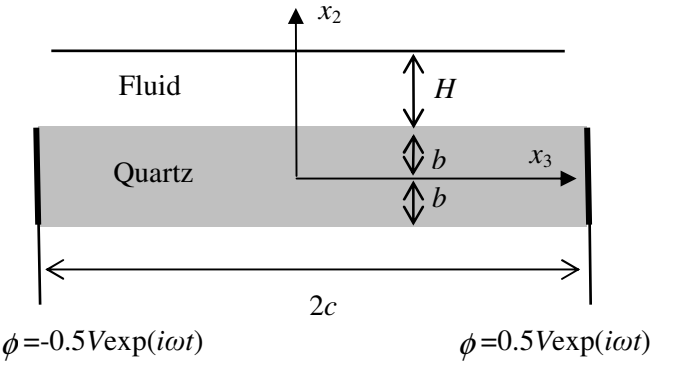

Fig. 3.21. A plate in contact with a fluid under a lateral electric field.

3.9.1. Governing equations and fields

For thickness-shear modes independent of x_1 and x_3 in the plate, the corresponding governing equations of the electric field in the upper free space are

$$D_{2,2} = 0, \quad D_2 = \varepsilon_0 E_2, \quad E_2 = -\phi_{,2}. \tag{3.154}$$

We consider the case when $x_2 = \pm\infty$ are electrically open and $D_2 = 0$. Since D_2 is a constant in the free space as dictated by Eq. $(3.154)_1$, $D_2 \equiv 0$. The free-space electric potential is simply

$$\phi = -Ex_3 + C_1, \tag{3.155}$$

where $E = -V/2c$ is a constant. C_1 is an arbitrary constant. Equation (3.155) implies that $E_3 = E$ and $D_2 = 0$. The open circuit condition at $x_2 = +\infty$ is satisfied.

The fluid is assumed to be without electromechanical coupling. The electric field in the fluid is still governed by Eq. (3.154) but the free-space permittivity ε_0 needs to be replaced by the fluid permittivity ε. The equation of motion for the fluid is [21]

$$T_{21,2} = \rho_L \dot{v}_1, \quad T_{21} = \mu \frac{\partial v_1}{\partial x_2}. \tag{3.156}$$

μ and ρ_L are the viscosity and mass density of the fluid. v_1 and T_{21} are the relevant velocity and shear stress components. The potential and velocity fields in the fluid are

$$\begin{aligned} &\phi = -Ex_3 + C_1, \\ &v_1 = C_3 \sinh\left[(1+i)\eta(x_2 - b)\right] + C_4 \cosh\left[(1+i)\eta(x_2 - b)\right], \end{aligned} \tag{3.157}$$

where C_3 and C_4 are undetermined constants, and $\eta = \sqrt{\rho_L \omega/(2\mu)}$. The relevant stress and electric displacement components needed for

boundary and continuity conditions are

$$\begin{aligned} T_{21} &= (1+i)\mu\eta\{C_3\cosh[(1+i)\eta(x_2-b)] \\ &\quad + C_4\sinh[(1+i)\eta(x_2-b)]\}, \\ D_2 &= 0. \end{aligned} \tag{3.158}$$

We note that the continuity of ϕ and D_2 between the upper free space and the fluid are already satisfied.

In the crystal plate, due to the presence of E_3, we consider (see Eq. (3.40)):

$$u_1 = u_1(x_2), \quad u_2 = u_3 = 0, \quad \phi = \varphi(x_2) - Ex_3 + C_2, \tag{3.159}$$

where C_2 is an undetermined constant. The nontrivial components of the strain, electric field, stress, and electric displacement components are, correspondingly,

$$2S_{12} = u_{1,2}, \quad E_2 = -\varphi_{,2} \quad E_3 = E, \tag{3.160}$$

$$\begin{aligned} T_{31} &= c_{56}u_{1,2} + e_{25}\varphi_{,2} - e_{35}E, \\ T_{21} &= c_{66}u_{1,2} + e_{26}\varphi_{,2} - e_{36}E, \\ D_2 &= e_{26}u_{1,2} - \varepsilon_{22}\varphi_{,2} + \varepsilon_{23}E, \\ D_3 &= e_{36}u_{1,2} - \varepsilon_{32}\varphi_{,2} + \varepsilon_{33}E. \end{aligned} \tag{3.161}$$

The equation of motion and the charge equation of electrostatics take the following form (see Eq. (3.43)):

$$\begin{aligned} T_{21,2} &= c_{66}u_{1,22} + e_{26}\varphi_{,22} = -\rho\omega^2 u_1, \\ D_{2,2} &= e_{26}u_{1,22} - \varepsilon_{22}\varphi_{,22} = 0. \end{aligned} \tag{3.162}$$

The displacement and potential fields are

$$u_1 = C_5\sin[\xi(x_2-b)] + C_6\cos[\xi(x_2-b)], \tag{3.163}$$

$$\begin{aligned}\phi = \frac{e_{26}}{\varepsilon_{22}}\{C_5 \sin[\xi(x_2 - b)] + C_6 \cos[\xi(x_2 - b)]\} \\ + C_7(x_2 - b) - Ex_3 + C_2,\end{aligned} \tag{3.164}$$

where C_5, C_6 and C_7 are undetermined constants, and

$$\xi^2 = \frac{\rho}{\bar{c}_{66}}\omega^2. \tag{3.165}$$

The stress and electric displacement components are

$$\begin{aligned}T_{21} = \bar{c}_{66}\xi\{C_5 \cos[\xi(x_2 - b)] - C_6 \sin[\xi(x_2 - b)]\} \\ + e_{26}C_7 - e_{36}E,\end{aligned} \tag{3.166}$$

$$D_2 = -\varepsilon_{22}C_7 + \varepsilon_{23}E, \tag{3.167}$$

$$\begin{aligned}D_3 = \left(e_{36} - \frac{\varepsilon_{32}}{\varepsilon_{22}}e_{26}\right)\xi\{C_5 \cos[\xi(x_2 - b)] - C_6 \sin[\xi(x_2 - b)]\} \\ - \varepsilon_{32}C_7 + \varepsilon_{33}E,\end{aligned} \tag{3.168}$$

where $\bar{c}_{66} = c_{66}(1 + k_{26}^2)$ and $k_{26}^2 = e_{26}^2/(\varepsilon_{22}c_{66})$.

For the lower free space we have

$$\phi = -Ex_3 + C_8, \tag{3.169}$$

where C_8 is an arbitrary constant. The open circuit condition $D_2 = 0$ at $x_2 = -\infty$ is satisfied.

The top of the fluid layer is traction free, i.e.,

$$T_{21}(b + H) = 0. \tag{3.170}$$

At the interface between the fluid and the top of the crystal plate, we have the continuity of velocity, electric potential, shear stress, and normal electric displacement:

$$\begin{aligned} &\dot{u}_1\left(b^-\right)=v_1\left(b^+\right), \quad \phi\left(b^-\right)=\phi\left(b^+\right), \\ &T_{21}\left(b^-\right)=T_{21}\left(b^+\right), \quad D_2\left(b^-\right)=0. \end{aligned} \tag{3.171}$$

At the interface between the bottom of the crystal plate and the free space below it, we have:

$$\phi\left(-b^-\right)=\phi\left(-b^+\right), \quad D_2\left(-b^-\right)=0, \quad T_{21}\left(-b^-\right)=0. \tag{3.172}$$

We note that although there are eight equations in Eqs. (3.170)–(3.172), they are effectively seven because D_2 in the crystal plate as given in Eq. (3.167) is a constant and $D_2(\pm b^-)=0$ are effectively one condition. Substitution of the relevant fields into Eqs. (3.170)–(3.172) gives the following seven equations for C_1 through C_8:

$$\begin{aligned} &C_3\cosh\left[(1+i)\eta H\right]+C_4\sinh\left[(1+i)\eta H\right]=0, \\ &C_1-\frac{e_{26}}{\varepsilon_{22}}C_6=C_2, \\ &\varepsilon_{22}C_7=\varepsilon_{23}E, \\ &C_4-i\omega C_6=0, \\ &-(1+i)\mu\eta C_3+\bar{c}_{66}\xi C_5+e_{26}C_7=e_{36}E, \\ &\bar{c}_{66}\xi\left[C_5\cos(2\xi b)+C_6\sin(2\xi b)\right]+e_{26}C_7=e_{36}E, \\ &\frac{e_{26}}{\varepsilon_{22}}\left[C_5\sin(2\xi b)-C_6\cos(2\xi b)\right]+C_7(2b)+C_8=C_2. \end{aligned} \tag{3.173}$$

Effectively C_1-C_2 and C_8-C_2 are two constants. Therefore the unknown constants in Eq. (3.173) are also seven.

3.9.2. Free vibration

For free vibration we set $E = 0$. Equation (3.173) becomes homogeneous. For nontrivial solutions the determinant of the coefficient matrix of Eq. (3.173) has to vanish, which gives the following frequency equation:

$$\tan\left(2b\omega\sqrt{\frac{\rho}{\bar{c}_{66}}}\right) = -(1-i)\sqrt{\frac{\omega\rho_L\mu}{2\rho\bar{c}_{66}}}\tanh\left[(1+i)\eta H\right]. \tag{3.174}$$

If we neglect the small piezoelectric coupling by setting $e_{26} = 0$ (in this case $\bar{c}_{66} = c_{66}$) and consider the limit when $H \to \infty$, Eq. (3.174) reduces to Eq. (2.71):

$$\tan\left(2b\omega\sqrt{\frac{\rho}{c_{66}}}\right) = -(1-i)\sqrt{\frac{\omega\rho_L\mu}{2\rho c_{66}}}, \tag{3.175}$$

which is the frequency equation in [20].

On the other hand, if we neglect the drag due to the fluid viscosity in Eq. (3.174) by setting μ = 0, the right-hand side of Eq. (3.174) vanishes and the left-hand side can be factored into two equations. One is $\sin(\xi b) = 0$ which is not of interest because it determines modes that are essentially symmetric about x_2 = 0. What is useful in device applications is the other equation $\cos(\xi b) = 0$ which determines modes antisymmetric about $x_2 = 0$ for which

$$\xi b = n\pi/2\,,\ n = 1, 3, 5, \ldots \tag{3.176}$$

Corresponding to Eq. (3.176), from Eq. (3.165) we obtain the following frequencies for antisymmetric thickness-shear modes when the fluid is not present as our reference frequencies:

$$\omega_0^{(n)} = \frac{n\pi}{2b}\sqrt{\frac{\bar{c}_{66}}{\rho}}\,. \tag{3.177}$$

We now return to the general frequency equation in Eq. (3.174). Consider the case of a low viscosity fluid. We look for approximate roots of Eq. (3.174) by letting [2]

$$\xi b \cong \frac{n\pi}{2} - \Delta^{(n)}, \tag{3.178}$$

where $\Delta^{(n)}$ is small. Substituting Eq. (3.178) into Eq. (3.174), for small viscosity, we obtain

$$\Delta^{(n)} \cong \frac{1-i}{2}\sqrt{\frac{\rho_L \mu \omega_0^{(n)}}{2\rho \bar{c}_{66}}}\tanh[(1+i)\eta_0^{(n)} H] \ , \tag{3.179}$$

where $\eta_0^{(n)} = \sqrt{\rho_L \omega_0^{(n)}/(2\mu)}$. With $\Delta^{(n)}$ given by Eq. (3.179), from Eq. (3.165) we obtain the relative frequency shift as

$$\begin{aligned} \Delta\Omega^{(n)} &= \frac{\omega^{(n)} - \omega_0^{(n)}}{\omega_0^{(n)}} = -\frac{2}{n\pi}\Delta^{(n)} \\ &= -\frac{1-i}{n\pi}\sqrt{\frac{\rho_L \mu \omega_0^{(n)}}{2\rho \bar{c}_{66}}}\tanh[(1+i)\eta_0^{(n)} H]. \end{aligned} \tag{3.180}$$

When $e_{26} = 0$ and $H = \infty$, Eq. (3.180) reduces to Eq. (2.75):

$$\Delta\omega^{(n)} = \omega^{(n)} - \omega_0^{(n)} = -\frac{1-i}{n\pi}\omega_0^{(n)}\sqrt{\frac{\rho_L \mu \omega_0^{(n)}}{2\rho c_{66}}} \ . \tag{3.181}$$

When $n = 1$, the real part of Eq. (3.181) gives the classical result of [20] for the frequency shift of the fundamental thickness-shear mode in a crystal plate due to contact with a viscous fluid. The real part of Eq. (3.181) is negative, indicating that the fluid drag lowers the frequency.

From Eq. (3.181), higher-order modes with larger values of n have smaller frequency shifts. The imaginary part of Eq. (3.181) represents the damping effect due to the fluid viscosity.

3.9.3. Forced vibration

For forced vibration, Eq. (3.173) is inhomogeneous. Under a real driving frequency the coefficient matrix does not vanish. A solution always exists, is unique, and can be obtained using a computer. The free charge Q_e on the edge electrode at $x_3 = c$ per unit length along x_1, the current I that flows into this electrode, and the admittance Y of the structure are given by

$$Q_e = \int_{-b}^{b} -D_3 dx_2, \quad I = \dot{Q}_e = i\omega Q_e, \quad Y = I/V. \tag{3.182}$$

3.9.4. Numerical results

Consider a plate of AT-cut quartz with b = 0.58 mm so that $\omega_0^{(1)} = 9\times10^6$ 1/s. The fluid layer thickness is $H = 2b$ except in Figs. 3.22 and 3.23. For the fluid we use ethanol, toluene, and chloroform. For ethanol and toluene the relevant material constants are in the previous section. For chloroform ρ_L = 1.483 g/cm^3 and μ = 0.542 mPa·s.

Figure 3.22 shows the effect of the fluid layer thickness H on frequency shifts due to different fluids for the fundamental mode with n = 1. The fluid lowers the frequency as expected. For small H the frequency shift is proportional to H. There is a maximal frequency shift of the order of 10^{-4} when H is somewhat less than b, half the thickness of the crystal plate. This is considered a strong and clear signal because typical thermal noise in quartz resonators is of the order of 10^{-6}. When $H>2b$ the frequency shift becomes constant. In this case the fluid layer can in fact be treated as a half space. Figure 3.23 shows similar behaviors of the third overtone mode with n = 3, with smaller frequency shifts and quicker decay of fields in the fluids (smaller penetration depth).

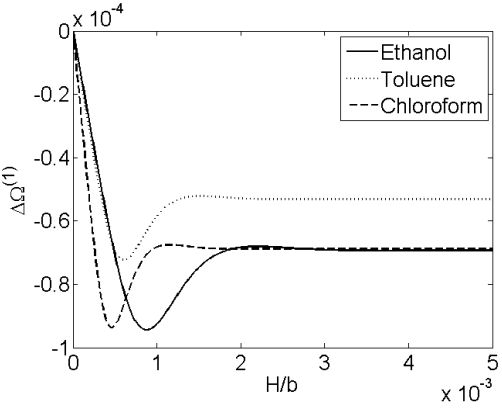

Fig. 3.22. $\Delta\Omega^{(1)}$ versus fluid layer thickness.

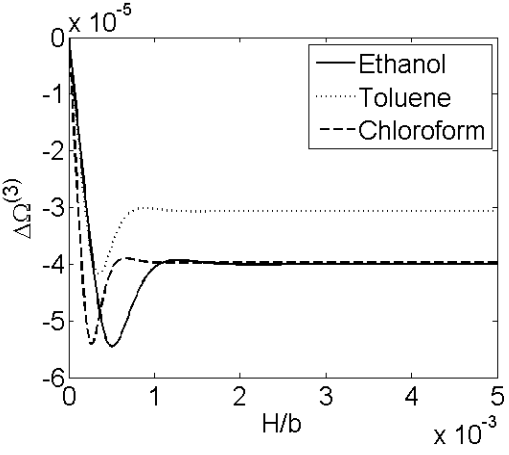

Fig. 3.23. $\Delta\Omega^{(3)}$ versus fluid layer thickness.

Figure 3.24 is from the forced vibration analysis. It shows the admittance per unit length of the plate in the x_1 direction. At resonance the admittance assumes maximum.

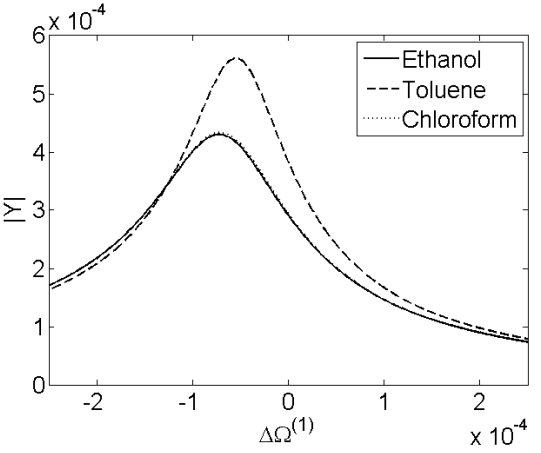

Fig. 3.24. Admittance versus driving frequency.

3.10. Plate with Surface Load Described by Acoustic Impedance

In time-harmonic motions, various mechanical effects on a crystal plate through surface interactions can be described by acoustic impedance. In this section such an analysis is given. Unelectroded and electroded plates are treated separately.

3.10.1. Unelectroded plates

Consider an unelectroded plate first (see Fig. 3.1). The governing equations are still given by Eq. (3.6):

$$\begin{aligned} T_{21,2} &= c_{66}u_{1,22} + e_{26}\phi_{,22} = \rho\ddot{u}_1 = -\rho\omega^2 u_1, \\ D_{2,2} &= e_{26}u_{1,22} - \varepsilon_{22}\phi_{,22} = 0. \end{aligned} \tag{3.183}$$

The boundary conditions are

$$\begin{aligned} T_{21} &= -Z(\omega)\dot{u}_1, \quad D_2 = 0, \quad x_2 = h, \\ T_{21} &= Z(\omega)\dot{u}_1, \quad D_2 = 0, \quad x_2 = -h, \end{aligned} \tag{3.184}$$

where $Z(\omega)$ is the impedance of the surface load and we have assumed the same impedance at the plate's top and bottom. We look for antisymmetric modes in the following form:

$$\begin{aligned} u_1 &= A\sin(\eta x_2)\exp(i\omega t), \\ \phi &= \frac{e_{26}}{\varepsilon_{22}} A\sin(\eta x_2)\exp(i\omega t), \end{aligned} \tag{3.185}$$

which makes $D_2 = 0$ and thus satisfies Eq. $(3.183)_2$ and the boundary conditions for D_2. Substituting Eq. (3.185) into Eq. $(3.183)_1$, we have

$$\eta = \sqrt{\frac{\rho\omega^2}{\bar{c}_{66}}}, \tag{3.186}$$

where $\bar{c}_{66}$ is given by Eq. (3.10). When Eq. (3.185) is substituted into the stress boundary conditions in Eq. (3.184), it gives the frequency equation as

$$\tan(\eta h) = -\frac{\bar{c}_{66}\eta h}{Z(\omega) i\omega h}. \tag{3.187}$$

For small impedance, we write

$$\eta_n h = \frac{n\pi}{2} - \Delta_n, \quad n = 1,3,5,\cdots. \tag{3.188}$$

Substituting Eq. (3.188) into Eq. (3.187), for small Δ_n and small $Z(\omega)$, we obtain, approximately,

$$\Delta_n \cong -\frac{2hi\omega}{n\pi\bar{c}_{66}} Z(\omega). \tag{3.189}$$

Hence,

$$\eta_n h \cong \frac{n\pi}{2} + \frac{2hi\omega}{n\pi\bar{c}_{66}} Z(\omega), \tag{3.190}$$

and

$$\omega_n \cong \sqrt{\frac{\bar{c}_{66}}{\rho}}\frac{n\pi}{2h}\left(1+\frac{4hi\omega}{n^2\pi^2\bar{c}_{66}}Z(\omega)\right). \tag{3.191}$$

In Eqs. (3.189)–(3.191), the frequency in $Z(\omega)$ is understood to be the unperturbed frequency when there is no surface impedance. Then Eq. (3.191) gives an approximation of the perturbed frequency showing the small effect of $Z(\omega)$.

3.10.2. Electroded plates

For electroded plates we consider electrically forced vibration. It can also lead to the frequency equation which is usually obtained from a free vibration analysis. The boundary conditions are

$$\begin{aligned} T_{21} &= -2\rho' h'\ddot{u}_1 - Z(\omega)\dot{u}_1, \quad \phi = V, \quad x_2 = h, \\ T_{21} &= 2\rho' h'\ddot{u}_1 + Z(\omega)\dot{u}_1, \quad \phi = -V, \quad x_2 = -h, \end{aligned} \tag{3.192}$$

where ρ' and $2h'$ are the density and the thickness of the electrodes. We look for solutions in the following form:

$$\begin{aligned} u_1 &= \left[-\frac{e_{26}V}{c_{22}h}x_2 + \sum_{n=1,3,5,\cdots} A_n \sin(\eta_n x_2)\right]\exp(i\omega t), \\ \phi &= \left\{\frac{V}{h}x_2 + \sum_{n=1,3,5,\cdots}\frac{e_{26}}{\varepsilon_{22}}A_n\left[\sin(\eta_n x_2) - \frac{x_2}{h}\sin(\eta_n h)\right]\right\}\exp(i\omega t). \end{aligned} \tag{3.193}$$

Equation (3.193) satisfies Eq. (3.183) and the electrical boundary conditions in Eq. (3.192). Substituting Eq. (3.193) into the stress boundary conditions in Eq. (3.192), we determine forced vibration amplitude as

$$A_n \cong \frac{(-1)^{\frac{n-1}{2}}}{1-\frac{\omega_n^2}{\omega^2}}\frac{2e_{26}V}{c_{66}}\frac{4}{n^2\pi^2}\left[1+R+\left(\frac{12}{n^2\pi^2}-1\right)\bar{k}_{26}^2+\left(\frac{6}{n\pi}-n\pi\right)\frac{iZ(\omega)}{\sqrt{\bar{\rho}c_{66}}}\right]. \tag{3.194}$$

For the frequency equation of free vibration, we let the denominator of the right-hand side of Eq. (3.194) vanish and obtain

$$\tan(\eta_n h) = \frac{\eta_n h}{\bar{k}_{26}^2 + R\eta_n^2 h^2 + \dfrac{Z(\omega_n) i\omega_n h}{\bar{c}_{66}}}, \tag{3.195}$$

where $\bar{k}_{26}^2 = e_{26}^2/(\varepsilon_{22}\bar{c}_{66})$. $R = 2\rho' h'/(\rho h)$ is the mass ratio between the electrodes and the crystal plate. For small impedance, we approximately have

$$\eta_n h = \frac{n\pi}{2} - \Delta_n, \tag{3.196}$$

$$\Delta_n \cong \frac{n\pi}{2} R + \frac{2\bar{k}_{26}^2}{n\pi} - \frac{2hi\omega}{n\pi\bar{c}_{66}} Z(\omega), \tag{3.197}$$

$$\eta_n h \cong \frac{n\pi}{2} - \frac{n\pi}{2} R - \frac{2\bar{k}_{26}^2}{n\pi} + \frac{2hi\omega}{n\pi\bar{c}_{66}} Z(\omega), \tag{3.198}$$

$$\omega_n \cong \sqrt{\frac{\bar{c}_{66}}{\rho}} \frac{n\pi}{2h} \left(1 - R - \frac{4\bar{k}_{26}^2}{n^2\pi^2} + \frac{4hi\omega}{n^2\pi^2\bar{c}_{66}} Z(\omega) \right). \tag{3.199}$$

In Eqs. (3.197)–(3.199), the frequency in $Z(\omega)$ is understood to be the unperturbed frequency when there is no surface impedance. Then Eq. (3.199) gives an approximation of the perturbed frequency showing the small effect of $Z(\omega)$.

3.11. Transient Thickness-shear Vibration

The analyses in the previous sections were all for time-harmonic vibrations. In real applications there are various transient effects that affect resonator operations. These include the startup of a device from rest, the fluctuation of the amplitude and the frequency of the driving voltage source, thermal and mechanical shocks, etc. There have been

studies of transient processes in piezoelectric ceramic plates [47, 48]. In this section we analyze the transient thickness-shear vibrations of a quartz plate [49] using the standard method of separation of variables for partial differential equations.

3.11.1. Governing equations

Consider the unbounded plate shown in Fig. 3.25. The two surfaces are traction free and are electroded, with a driving voltage $V(t)$.

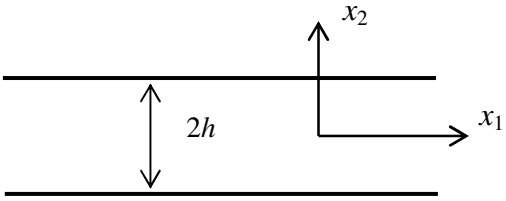

Fig. 3.25. An electroded plate.

We introduce some damping in the constitutive relations through viscoelasticity:

$$\begin{aligned} T_{31} &= c_{56}u_{1,2} + c'_{56}\dot{u}_{1,2} + e_{25}\phi_{,2}, \\ T_{21} &= c_{66}u_{1,2} + c'_{66}\dot{u}_{1,2} + e_{26}\phi_{,2}, \end{aligned} \tag{3.200}$$

$$\begin{aligned} D_2 &= e_{26}u_{1,2} - \varepsilon_{22}\phi_{,2}, \\ D_3 &= e_{36}u_{1,2} - \varepsilon_{23}\phi_{,2}, \end{aligned} \tag{3.201}$$

where c'_{pq} are the viscoelastic constants. Substitution of Eqs. (3.200) and (3.201) into the relevant equations of motion and electrostatics results in the following two equations for u_1 and ϕ:

$$T_{21,2} = c_{66}u_{1,22} + c'_{66}\dot{u}_{1,22} + e_{26}\phi_{,22} = \rho\ddot{u}_1, \tag{3.202}$$

$$D_{2,2} = e_{26}u_{1,22} - \varepsilon_{22}\phi_{,22} = 0. \tag{3.203}$$

The boundary conditions for thickness-shear motions are

$$T_{21} \cong c_{66}u_{1,2} + e_{26}\phi_{,2} = 0, \quad x_2 = \pm h, \tag{3.204}$$

$$\phi = \pm V(t)/2, \quad x_2 = \pm h, \tag{3.205}$$

where, in the mechanical boundary conditions in Eq. (3.204), we have made an approximation of neglecting the viscous damping term. Under Eq. (3.205) which is antisymmetric in x_2, the crystal plate is driven into antisymmetric thickness-shear vibrations with u_1 as an odd function of x_2. There are two initial conditions for Eq. (3.202):

$$u_1 = p(x_2), \quad t = 0, \tag{3.206}$$

$$\dot{u}_1 = q(x_2), \quad t = 0. \tag{3.207}$$

We limit ourselves to the case when $p(x_2)$ and $q(x_2)$ are odd functions of x_2. In order to homogenize the electrical boundary conditions in Eq. (3.205), we introduce a transformation of the unknown fields from u_1 and ϕ into $\hat{u}$ and $\hat{\phi}$ by [31]:

$$u_1 = \hat{u} - \frac{e_{26}}{c_{66}}\frac{V}{2h}x_2, \tag{3.208}$$

$$\phi = \hat{\phi} + \frac{V}{2h}x_2. \tag{3.209}$$

Then Eqs. (3.202)–(3.207) become:

$$c_{66}\hat{u}_{,22} + c'_{66}\dot{\hat{u}}_{,22} + e_{26}\hat{\phi}_{,22} = \rho\left(\ddot{\hat{u}} - \frac{e_{26}}{c_{66}}\frac{\ddot{V}}{2h}x_2\right), \tag{3.210}$$

$$e_{26}\hat{u}_{,22} - \varepsilon_{22}\hat{\phi}_{,22} = 0, \tag{3.211}$$

$$T_{21} \cong c_{66}\hat{u}_{,2} + e_{26}\hat{\phi}_{,2} = 0, \quad x_2 = \pm h, \tag{3.212}$$

$$\hat{\phi} = 0, \quad x_2 = \pm h, \tag{3.213}$$

$$\hat{u} = p(x_2) + \frac{e_{26}}{c_{66}} \frac{V}{2h} x_2, \quad \dot{\hat{u}} = q(x_2) + \frac{e_{26}}{c_{66}} \frac{\dot{V}}{2h} x_2, \quad t = 0. \tag{3.214}$$

Equation (3.211) can be integrated with respect to x_2 twice to give

$$\hat{\phi} = \frac{e_{26}}{\varepsilon_{22}} \hat{u} + B(t) x_2 + B'(t), \tag{3.215}$$

where B' and B are integration constants which may still depend on time. Since $\hat{\phi}$ is an odd function, $B' = 0$. Substitution of Eq. (3.215) into Eqs. (3.210), (3.212) and (3.213) results in

$$\bar{c}_{66} \hat{u}_{,22} + c'_{66} \dot{\hat{u}}_{,22} = \rho \ddot{\hat{u}} - \rho \frac{e_{26}}{c_{66}} \frac{\ddot{V}}{2h} x_2, \tag{3.216}$$

$$T_{21} \cong \bar{c}_{66} \hat{u}_{,2} + e_{26} B = 0, \quad x_2 = \pm h, \tag{3.217}$$

$$\hat{\phi} = \frac{e_{26}}{\varepsilon_{22}} \hat{u} + B x_2 = 0, \quad x_2 = \pm h, \tag{3.218}$$

where

$$\bar{c}_{66} = c_{66} + \frac{e_{26}^2}{\varepsilon_{22}}. \tag{3.219}$$

Due to the antisymmetry in x_2, for Eqs. (3.217) and (3.218) we only need to consider $x_2 = h$:

$$\begin{aligned} &\bar{c}_{66} \hat{u}_{,2}(h) + e_{26} B = 0, \\ &\frac{e_{26}}{\varepsilon_{22}} \hat{u}(h) + Bh = 0. \end{aligned} \tag{3.220}$$

Eliminating B, we obtain

$$\bar{c}_{66}\hat{u}_{,2}(h) - \frac{1}{h}\frac{e_{26}^2}{\varepsilon_{22}}\hat{u}(h) = 0\,. \tag{3.221}$$

Our mathematical problem has reduced to solving Eq. (3.216) for an antisymmetric solution under Eqs. (3.221) and (3.214).

3.11.2. Free vibration solution

We look for free vibration modes first when there is no damping. These modes will be used later as base functions for the series solution of the electrically forced vibration. The antisymmetric free vibration modes are governed by Eq. (3.216) with $V = 0$:

$$\bar{c}_{66}\hat{u}_{,22} = \rho\ddot{\hat{u}}\,, \tag{3.222}$$

and the boundary condition in Eq. (3.221). The solution to this problem is well known [31]. The modes are given by

$$\hat{u}_n = \sin\eta_n x_2, \quad n = 1,2,3,\cdots, \tag{3.223}$$

where η_n is related to the resonant frequency ω_n through Eq. (3.222) which takes the following form:

$$\bar{c}_{66}\eta_n^2 = \rho\omega_n^2\,. \tag{3.224}$$

The frequency equation determined by Eq. (3.221) is

$$\cot\eta_n h = \frac{\bar{k}_{26}^2}{\eta_n h}\,, \tag{3.225}$$

where

$$\bar{k}_{26}^2 = \frac{e_{26}^2}{\bar{c}_{66}\varepsilon_{22}}\,. \tag{3.226}$$

For AT-cut quartz $\bar{k}_{26}^2 \cong 0.008$ which is very small. Equation (3.225) has the following approximate solution [31]:

$$\eta_n h \cong \frac{(2n-1)\pi}{2}\left(1-\frac{4\bar{k}_{26}^2}{(2n-1)^2\pi^2}\right). \tag{3.227}$$

Correspondingly,

$$\omega_n \cong \frac{(2n-1)\pi}{2h}\sqrt{\frac{\bar{c}_{66}}{\rho}}\left(1-\frac{4\bar{k}_{26}^2}{(2n-1)^2\pi^2}\right). \tag{3.228}$$

3.11.3. Forced vibration solution

For the forced vibration problem defined by Eq. (3.216) under Eqs. (3.221) and (3.214), we expand the unknown displacement into the following series:

$$\hat{u} = \sum_{n=1}^{\infty} T_n(t)\sin(\eta_n x_2)\,. \tag{3.229}$$

Equation (3.229) satisfies the boundary condition in Eq. (3.221). We also expand the known linear function of x_2 in Eq. (3.216) and the initial fields $p(x_2)$ and $q(x_2)$ in Eq. (3.214) into

$$\begin{aligned} x_2 &= \sum_{n=1}^{\infty} A_n \sin\eta_n x_2, \\ p(x_2) &= \sum_{n=1}^{\infty} P_n \sin\eta_n x_2, \\ q(x_2) &= \sum_{n=1}^{\infty} Q_n \sin\eta_n x_2, \end{aligned} \tag{3.230}$$

where

$$\begin{aligned} A_n &= \int_{-h}^{h} x_2 \sin(\eta_n x_2)dx_2 \Big/ \int_{-h}^{h} \sin^2(\eta_n x_2)dx_2\,, \\ P_n &= \int_{-h}^{h} p(x_2)\sin(\eta_n x_2)dx_2 \Big/ \int_{-h}^{h} \sin^2(\eta_n x_2)dx_2\,, \\ Q_n &= \int_{-h}^{h} q(x_2)\sin(\eta_n x_2)dx_2 \Big/ \int_{-h}^{h} \sin^2(\eta_n x_2)dx_2\,. \end{aligned} \tag{3.231}$$

Substitution of Eqs. (3.229) and (3.230) into Eq. (3.216) leads to a system of ordinary differential equations for $T_n(t)$:

$$\ddot{T}_n + \lambda_n'^2 \dot{T}_n + \lambda_n^2 T_n = \frac{e_{26}}{c_{66}} \frac{\ddot{V}}{2h} A_n, \tag{3.232}$$

where

$$\lambda_n = \eta_n \sqrt{\bar{c}_{66} / \rho}\,, \quad \lambda_n' = \eta_n \sqrt{c_{66}' / \rho}\,. \tag{3.233}$$

For the specific applications we are interested in, we consider a time-harmonic driving voltage and use the usual complex notation with the real parts representing the physical fields of interest:

$$V = -iV_0 \exp(i\omega t). \tag{3.234}$$

In this case the general solution to Eq. (3.232) is

$$\begin{aligned} T_n &= C_{1n} \exp(\beta_n t) + C_{2n} \exp(\beta_n^* t) \\ &+ \frac{e_{26}}{c_{66}} \frac{V_0 \omega^2}{2h} \frac{A_n}{(\beta_n - \beta_n^*)} \left[\frac{\omega - i\beta_n}{\beta_n^2 + \omega^2} - \frac{\omega - i\beta_n^*}{(\beta_n^*)^2 + \omega^2} \right] \exp(i\omega t), \end{aligned} \tag{3.235}$$

where C_{1n} and C_{2n} are undetermined constants, and

$$\beta_n = \frac{-\lambda_n'^2 + i\sqrt{4\lambda_n^2 - \lambda_n'^4}}{2}, \quad \beta_n^* = \frac{-\lambda_n'^2 - i\sqrt{4\lambda_n^2 - \lambda_n'^4}}{2}. \tag{3.236}$$

With $T_n(t)$ given by Eq. (3.235), we substitute Eqs. (3.229) and (3.230) into the initial conditions in Eq. (3.214), multiply the resulting equations by $\sin(\eta_m x_2)$, and integrate them through the plate thickness. With the orthogonality among $\sin(\eta_m x_2)$, we arrive at the following system of

linear equations for C_{1n} and C_{2n}:

$$\begin{aligned} T_n(0) &= C_{1n} + C_{2n} \\ &\quad + \frac{e_{26}}{c_{66}} \frac{V_0 \omega^2}{2h} \frac{A_n}{(\beta_n - \beta_n^*)} \left[\frac{\omega - i\beta_n}{\beta_n^2 + \omega^2} - \frac{\omega - i\beta_n^*}{(\beta_n^*)^2 + \omega^2} \right] \\ &= P_n - i \frac{e_{26}}{c_{66}} \frac{V_0}{2h} A_n, \\ \dot{T}_n(0) &= C_{1n}\beta_n + C_{2n}\beta_n^* \\ &\quad + i \frac{e_{26}}{c_{66}} \frac{V_0 \omega^3}{2h} \frac{A_n}{(\beta_n - \beta_n^*)} \left[\frac{\omega - i\beta_n}{\beta_n^2 + \omega^2} - \frac{\omega - i\beta_n^*}{(\beta_n^*)^2 + \omega^2} \right] \\ &= Q_n + \frac{e_{26}}{c_{66}} \frac{V_0 \omega}{2h} A_n. \end{aligned} \tag{3.237}$$

Solving Eq. (3.237) completes the solution procedure. This is done numerically on a computer.

3.11.4. Numerical results

For numerical examples we consider a plate of AT-cut quartz with $2h$ = 1 mm which is typical for a resonator. Quartz has very little damping. We choose $(\omega c_{66}')/c_{66} \cong 10^{-5}$. Twenty terms in the series are kept in the calculation with eleven significant figures for the displacement field. The plate is essentially vibrating in the fundamental mode with just a little contribution from the higher-order modes. Therefore twenty terms can produce very high accuracy.

3.11.4.1. Resonator startup

In this example we examine the sudden application of a time-harmonic driving voltage (see Eq. (3.234)) to a resonator at rest with $p(x_2) = 0$ and $q(x_2) = 0$. The amplitude of the driving voltage V_0 = 1 volt. The frequency of the driving voltage is the same as the resonator fundamental thickness-shear frequency, i.e., $\omega = \omega_1$ = 1.655869767 MHz. The

corresponding period is 6.039×10^{-7} s. Figure 3.26 shows the displacement of the plate top surface versus time, i.e., $u_1(h,t)$. During the time interval shown, the resonator goes through many cycles. The curve of $u_1(h,t)$ makes many turns and effectively fills an area in the figure. It can be seen that the amplitude of the surface displacement starts from zero, increases monotonically, and then reaches saturation in about 0.1 s. This translates into 1.656×10^{5} cycles.

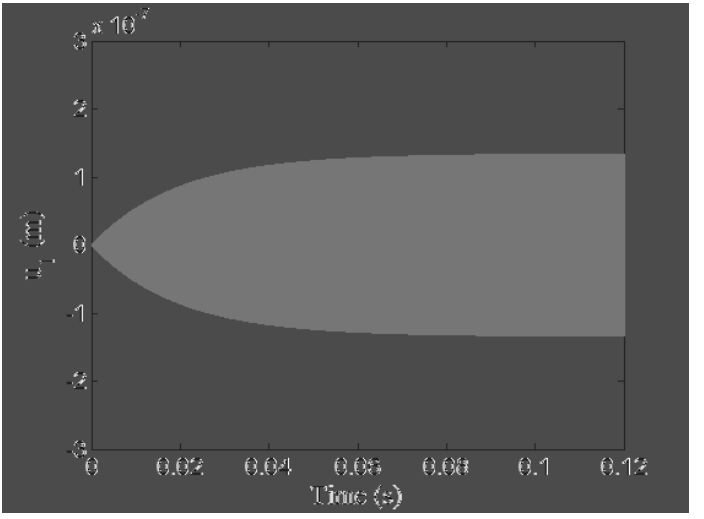

Fig. 3.26. Resonator startup.

3.11.4.2. Driving voltage amplitude rise

Next we study the effect of a sudden rise of the amplitude of the driving voltage on a resonator that is already in time-harmonic motion. $V_0 = 1$ volt and $\omega = \omega_1$. The voltage change is described by

$$V = \begin{cases} -iV_0 \exp(i\omega_1 t), & t < t_0, \\ -i(V_0 + \Delta V)\exp(i\omega_1 t), & t_0 < t, \end{cases} \tag{3.238}$$

where, in order to show the effect more clearly, we use a relatively large ΔV =1 volt. In this case, separate solutions in the form of Eq. (3.229) exist in the two time intervals of $(0, t_0)$ and (t_0, ∞). The displacement and velocity fields at the end of the first interval serve as the initial conditions for the second interval. This is implemented numerically. The results are shown in Fig. 3.27. t_0 = 0.3 s. The behavior in the figure is as expected. The displacement amplitude is doubled as it should in a linear theory. The transition zone between the old and new amplitudes is about 0.1 s.

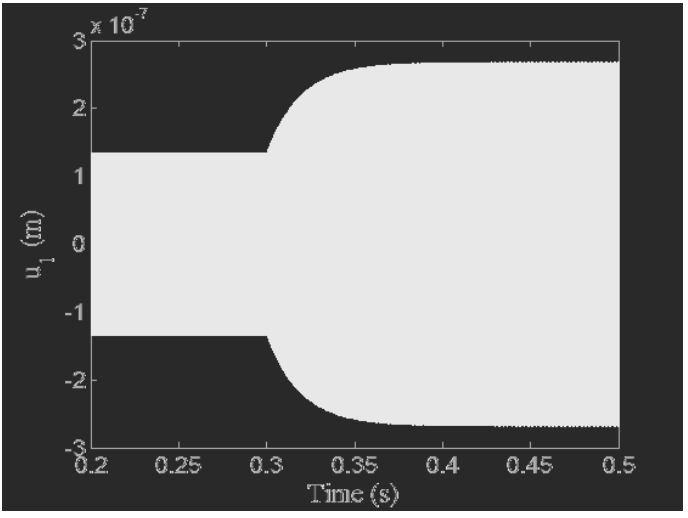

Fig. 3.27. Effect of a driving voltage amplitude rise. t_0= 0.3 s.

3.11.4.3. Driving voltage amplitude pulse

We now examined the effect of a sudden and temporary rise (pulse) of the amplitude of the driving voltage. The driving voltage changes its amplitude according to

$$V = \begin{cases} -iV_0 \exp(i\omega_1 t), & t < t_0 \\ -i(V_0 + \Delta V)\exp(i\omega_1 t), & t_0 < t < t_0 + \Delta t, \\ -iV_0 \exp(i\omega_1 t), & t_0 + \Delta t < t. \end{cases} \tag{3.239}$$

In this case three series solutions during the three time periods are needed, with continuity conditions among them. $t_0 = 0.3$ s and $\Delta t = 0.1$ s are used. The results are shown in Fig. 3.28. It takes about 0.1 s for the motion of the plate to become stead-state.

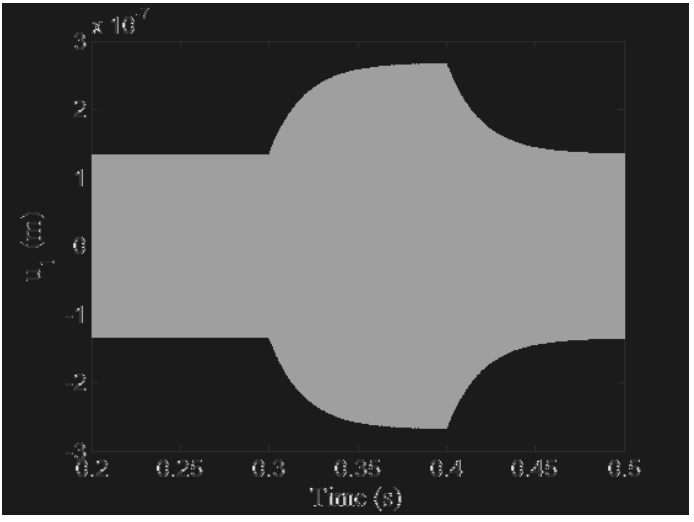

Fig. 3.28. Effect of a driving voltage amplitude pulse. $t_0 = 0.3$ s, $\Delta t = 0.1$ s.

3.11.4.4. Driving voltage frequency rise

Suppose at t_0 there is a sudden change of the frequency of the driving voltage:

$$V = \begin{cases} -iV_0 \exp(i\omega_1 t), & t < t_0, \\ -iV_0 \exp[i(\omega_1 + \Delta\omega)t], & t_0 < t. \end{cases} \tag{3.240}$$

Since a resonator has very little damping, its resonant peaks are very narrow. The frequency requirement of a crystal resonator is usually in terms of ppm (parts per million). We consider a small frequency deviation with $\Delta\omega = 10$ Hz at t_0=0.3 s. The corresponding $u_1(h,t)$ is shown in Fig. 3.29. It can be seen that $u_1(h,t)$ is very sensitive to this

small frequency deviation. With 10 Hz off the resonance, the displacement amplitude drops significantly.

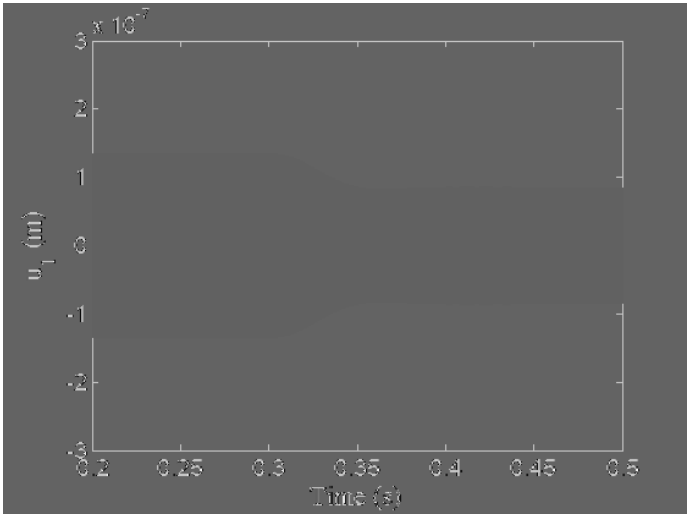

Fig. 3.29. Effect of a driving voltage frequency rise. $t_0 = 0.3$ s.

3.11.4.5. Driving voltage frequency pulse

Finally we consider the effect of a pulse fluctuation in the driving frequency during $(t_0, t_0 + \Delta t)$:

$$V = \begin{cases} -iV_0 \exp(i\omega_1 t), & t < t_0 \\ -iV_0 \exp[i(\omega_1 + \Delta\omega)t], & t_0 < t < t_0 + \Delta t, \\ -iV_0 \exp(i\omega_1 t), & t_0 + \Delta t < t. \end{cases} \tag{3.241}$$

The numerical results for the case of $t_0 = 0.3$ s, $\Delta t = 0.1$ s, and $\Delta\omega = 10$ Hz are shown in Fig. 3.30. The behavior is as expected.

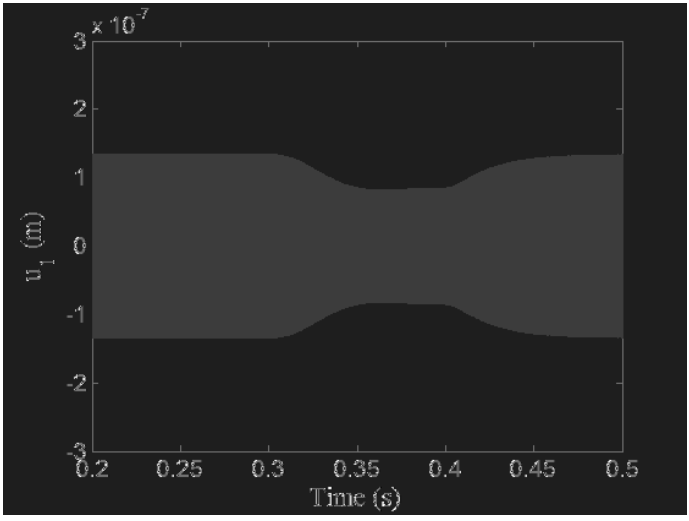

Fig. 3.30. Effect of a driving voltage frequency pulse. $t_0 = 0.3$ s, $\Delta t = 0.1$ s.

This page intentionally left blank

Chapter 4

Shear-horizontal Waves in Unbounded Plates

Shear-horizontal or antiplane motions with one displacement component u_1 are allowed in quartz and langasite by the equations of linear piezoelectricity. These motions include thickness-shear, face-shear, and thickness-twist modes which are important in devices. This chapter is mainly on elastic analysis. Piezoelectric shear-horizontal motions in quartz and langasite plates as governed by Eq. (1.107) are discussed in Section 4.12 only. For piezoelectric shear-horizontal motions in polarized ceramics, many results can be found in a recent book [15].

4.1. Governing Equations

From the relevant equations in Section 2.1.2, for rotated Y-cut quartz or langasite which are monoclinic crystals, the following shear-horizontal motions governed by the equations of anisotropic elasticity are possible:

$$u_1 = u_1(x_2, x_3, t), \quad u_2 = u_3 = 0. \tag{4.1}$$

Equation (4.1) yields the following nonzero components of strain and stress:

$$S_5 = u_{1,3}, \quad S_6 = u_{1,2}, \tag{4.2}$$

$$\begin{aligned} T_5 &= T_{31} = c_{55}u_{1,3} + c_{56}u_{1,2}, \\ T_6 &= T_{21} = c_{56}u_{1,3} + c_{66}u_{1,2}. \end{aligned} \tag{4.3}$$

The equation of motion to be satisfied by u_1 is

$$T_{21,2} + T_{31,3} = c_{66}u_{1,22} + c_{55}u_{1,33} + 2c_{56}u_{1,23} = \rho\ddot{u}_1. \tag{4.4}$$

Equation (4.4) is not as simple as it appears because of the mixed derivative term. By a proper coordinate transformation, the mixed

derivative term can be removed. Then the equation becomes separable and some solutions can be constructed.

4.2. Face-shear Wave

Consider a plate of monoclinic crystals as shown in Fig. 4.1. The plate is homogeneous with a thickness $2b$ and is unbounded. The plate surfaces are traction free.

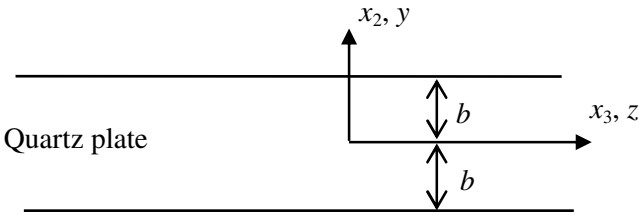

Fig. 4.1. A quartz plate and coordinate system.

The simplest wave that can propagate in such a plate is the so-called face-shear wave obtained by Mindlin [50]. Let

$$u_1 = A\sin\zeta\left(z - \frac{c_{56}}{c_{66}}y - ct\right). \tag{4.5}$$

The displacement in Eq. (4.5) produces the following nonzero strains:

$$\begin{aligned} S_5 &= u_{1,3} = A\zeta\cos\zeta\left(z - \frac{c_{56}}{c_{66}}y - ct\right), \\ S_6 &= u_{1,2} = -A\zeta\frac{c_{56}}{c_{66}}\cos\zeta\left(z - \frac{c_{56}}{c_{66}}y - ct\right). \end{aligned} \tag{4.6}$$

There is only one nonzero stress component given by

$$T_5 = A\zeta\left(\frac{c_{55}c_{66} - c_{56}^2}{c_{66}}\right)\cos\zeta\left(z - \frac{c_{56}}{c_{66}}y - ct\right). \tag{4.7}$$

For Eq. (4.5) to satisfy the equation of motion in Eq. (4.4), we must have

$$c = c_Q , \tag{4.8}$$

where we have denoted

$$c_Q = \left(\frac{\gamma_{55}}{\rho} \right)^{1/2}, \quad \gamma_{55} = c_{55} - \frac{c_{56}^2}{c_{66}} . \tag{4.9}$$

Since $T_6 \equiv 0$, the traction-free boundary conditions are trivially satisfied. The wave is called a face-shear wave because T_5 is the only nonzero stress component.

4.3. Thickness-twist Wave

For the same plate as in Fig. 4.1, other shear-horizontal motions called thickness-twist waves are also possible [51, 52]. This section is based on [52].

4.3.1. Antisymmetric waves

Consider

$$u_1 = A \sin \eta y \cos \zeta \left(\frac{c_{56}}{c_{66}} y - z \right) \exp(i\omega t) , \tag{4.10}$$

where the time-harmonic factor will be dropped in the following. It produces the following nonzero strains:

$$\begin{aligned} S_5 &= u_{1,3} = A\zeta \sin \eta y \sin \zeta \left(\frac{c_{56}}{c_{66}} y - z \right), \\ S_6 &= u_{1,2} = A\eta \cos \eta y \cos \zeta \left(\frac{c_{56}}{c_{66}} y - z \right) \\ &\quad - A\zeta \frac{c_{56}}{c_{66}} \sin \eta y \sin \zeta \left(\frac{c_{56}}{c_{66}} y - z \right). \end{aligned} \tag{4.11}$$

The stress component relevant to boundary conditions is

$$T_6 = c_{66} A \eta \cos \eta y \cos \zeta \left(\frac{c_{56}}{c_{66}} y - z \right). \tag{4.12}$$

For Eq. (4.10) to satisfy the equation of motion in Eq. (4.4), we must have

$$\rho \omega^2 = c_{66} \eta^2 + \gamma_{55} \zeta^2, \tag{4.13}$$

where γ_{55} is given by Eq. (4.9). For Eq. (4.12) to satisfy the boundary conditions of $T_6 = 0$ at the plate surfaces, we must have

$$\cos \eta b = 0, \quad \eta b = m\pi / 2, \quad m = 1,3,5,\cdots. \tag{4.14}$$

Equations (4.13) and (4.14) imply the following dispersion relations of the waves:

$$\omega^2 = \frac{c_{66}}{\rho} \left(\frac{\pi}{2b} \right)^2 \left[m^2 + \frac{\gamma_{55}}{c_{66}} \left(\frac{2\zeta b}{\pi} \right)^2 \right]. \tag{4.15}$$

4.3.2. Symmetric waves

Similarly, if

$$u_1 = C \cos \eta y \cos \zeta \left(\frac{c_{56}}{c_{66}} y - z \right) \exp(i\omega t) \tag{4.16}$$

is considered, we have the following nonzero strains:

$$\begin{aligned} S_5 &= u_{1,3} = C\zeta \cos \eta y \sin \zeta \left(\frac{c_{56}}{c_{66}} y - z \right), \\ S_6 &= u_{1,2} = -C\eta \sin \eta y \cos \zeta \left(\frac{c_{56}}{c_{66}} y - z \right) \\ &\quad - C\zeta \frac{c_{56}}{c_{66}} \cos \eta y \sin \zeta \left(\frac{c_{56}}{c_{66}} y - z \right). \end{aligned} \tag{4.17}$$

The stress component relevant to boundary conditions is

$$T_6 = -c_{66} C\eta \sin\eta y \cos\zeta\left(\frac{c_{56}}{c_{66}} y - z\right). \tag{4.18}$$

For Eq. (4.16) to satisfy the equation of motion in Eq. (4.4), we still have Eq. (4.13). For Eq. (4.18) to satisfy the boundary conditions of $T_6 = 0$ at the plate surfaces, we must have

$$\sin\eta b = 0, \quad \eta b = m\pi/2, \quad m = 0,2,4,\cdots. \tag{4.19}$$

Equation (4.19) still implies Eq. (4.15) but m = 0,2,4,$\cdots$. When m = 0, Eq. (4.15) reduces to Eq. (4.8) with the identification of $\omega = c\zeta$. When $\zeta = 0$, Eqs. (4.10) and (4.16) reduce to thickness-shear modes antisymmetric and symmetric about the middle plane of the plate. Therefore, loosely speaking, the waves in Eqs. (4.10) and (4.16) may be called antisymmetric and symmetric waves, respectively, although they are exactly so only when $\zeta = 0$. In most applications, we are interested in long waves with a small ζ. Because of their antisymmetry when $\zeta = 0$, the modes described by Eq. (4.10) are more useful than those in Eq. (4.16).

4.3.3. Dispersion curves

We introduce the following dimensionless frequency and dimensionless wave number:

$$\Omega = \frac{\omega}{\omega_s}, \quad Z = \sqrt{\frac{\gamma_{55}}{c_{66}}}\frac{2\zeta b}{\pi}, \tag{4.20}$$

where

$$\omega_s = \frac{\pi}{2b}\sqrt{\frac{c_{66}}{\rho}}, \tag{4.21}$$

which is the fundamental thickness-shear frequency of the plate. Then Eqs. (4.13) and (4.15) can be written as

$$\Omega^2 = \left(\frac{2\eta b}{\pi}\right)^2 + Z^2, \tag{4.22}$$

and

$$\Omega^2 = m^2 + Z^2, \tag{4.23}$$

respectively. When Ω is real, the corresponding Z from Eq. (4.23) is either real or purely imaginary. Equation (4.23) is plotted in Fig. 4.2. The case of $m = 0$ is the face-shear wave. It is a straight line going through the origin and is nondispersive. The waves corresponding to the curves of $m>0$ are the thickness-twist waves. They are dispersive. The finite intercepts with the Ω axis are the cutoff frequencies below which the wave number becomes pure imaginary and corresponding waves cannot propagate.

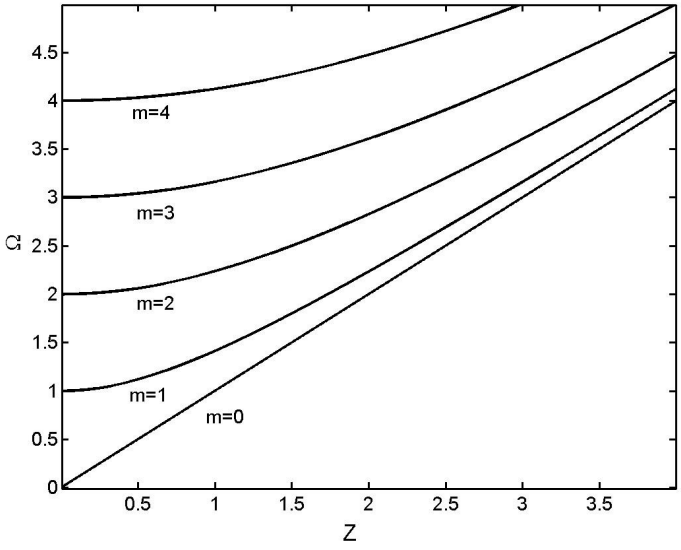

Fig. 4.2. Dispersion curves of face-shear ($m = 0$) and thickness-twist ($m>0$) waves.

4.4. Symmetric Mass Layers

Next consider the case when a crystal plate is symmetrically covered by identical mass layers or electrodes (see Fig. 4.3). The mass layers are assumed to be thin. Their inertia will be considered, but their stiffness will be neglected.

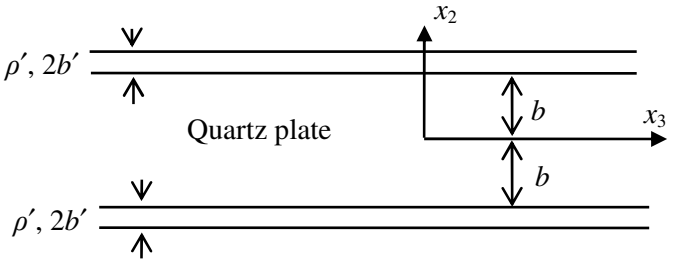

Fig. 4.3. A crystal plate with identical thin mass layers.

4.4.1. Antisymmetric waves

Following [52], consider the following displacement (see Eq. (4.10)):

$$u_1 = A \sin \eta y \cos \zeta \left(\frac{c_{56}}{c_{66}} y - z \right) \exp(i\omega t) . \tag{4.24}$$

The equation of motion (Eq. (4.4)) still requires that (see Eq. (4.13))

$$\rho \omega^2 = c_{66} \eta^2 + \gamma_{55} \zeta^2 . \tag{4.25}$$

The stress component needed for boundary conditions is given by Eq. (4.12)

$$T_6 = c_{66} A \eta \cos \eta y \cos \zeta \left(\frac{c_{56}}{c_{66}} y - z \right). \tag{4.26}$$

With the mass layers, the boundary conditions at the plate surfaces take the following form:

$$T_6 = \mp 2 \rho' b' \ddot{u}_1 = \pm 2 \rho' b' \omega^2 u_1, \quad y = \pm b . \tag{4.27}$$

Substitution of Eqs. (4.24) and (4.26) into Eq. (4.27) results in two identical equations. For nontrivial solutions of A we find that

$$\tan \eta b = \frac{c_{66}\eta}{2\rho' b' \omega^2}. \tag{4.28}$$

With

$$\Omega = \frac{\omega}{\omega_s}, \quad \omega_s = \frac{\pi}{2b}\sqrt{\frac{c_{66}}{\rho}}, \quad R = \frac{2\rho' b'}{\rho b}, \tag{4.29}$$

Eq. (4.29) can be written as

$$\tan \eta b = \frac{4\eta b}{\pi^2 \Omega^2 R}. \tag{4.30}$$

4.4.2. Symmetric waves

Similarly, corresponding to Eqs. (4.16) and (4.18), we have

$$u_1 = C \cos \eta y \cos \zeta \left(\frac{c_{56}}{c_{66}} y - z \right) \exp(i\omega t), \tag{4.31}$$

$$T_6 = -c_{66} C \eta \sin \eta y \cos \zeta \left(\frac{c_{56}}{c_{66}} y - z \right). \tag{4.32}$$

For Eq. (4.31) to satisfy the equation of motion we still have Eq. (4.25). The boundary conditions in Eq. (4.27) imply that

$$\tan \eta b = -\frac{2\rho' b' \omega^2}{c_{66}\eta}, \tag{4.33}$$

or

$$\tan \eta b = -\frac{\Omega^2 R}{4\eta b \pi^2}. \tag{4.34}$$

4.4.3. Dispersion curves

Dispersion curves determined by Eqs. (4.30) and (4.34) are shown in Fig. 4.4. in dotted lines for R = 3% in comparison to those determined by Eq. (4.23) when R = 0. It can be seen that the inertia of the mass layers lowers the frequency as expected. The two curves corresponding to m = 0 essentially coincide with each other in the figure.

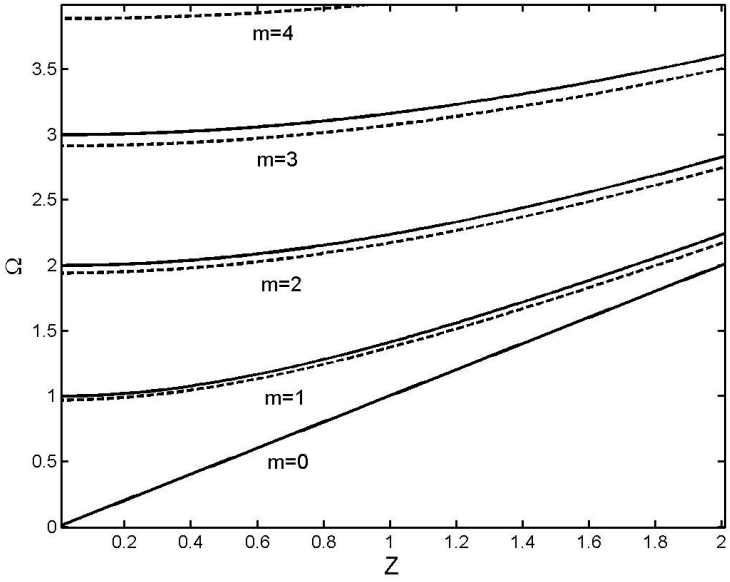

Fig. 4.4. Effect of mass layer inertia on dispersion relation. Solid lines: R = 0. Dotted lines: R = 3%.

4.4.4. Approximate dispersion relation

As R is usually small compared to unity, we look for an approximate solution to Eq. (4.30) mainly based on the smallness of R. The solution for the special case when R=0 is given by Eq. (4.14) or $\cos \eta b = 0$, $\eta b = m\pi/2$, $m = 1,3,5,\cdots$. For small and nonzero values of R, let

$$\eta b = m\pi/2 - \Delta, \tag{4.35}$$

where Δ is small. Substituting Eq. (4.35) into Eq. (4.30), we obtain

$$\cot\Delta = \frac{2m\pi - 4\Delta}{m^2\pi^2 R}, \tag{4.36}$$

where $\Omega^2 \cong m^2$ has been used in the denominator of the right-hand side of Eq. (4.36). This approximation is valid for small R and small Z or long waves. For small Δ, Eq. (4.36) can be approximated by

$$\tan\Delta \cong \Delta = \frac{m\pi}{2} R. \tag{4.37}$$

Then, from Eq. (4.35),

$$\eta b \cong \frac{m\pi}{2}(1-R). \tag{4.38}$$

Substitution of Eq. (4.38) into Eq. (4.25) yields the following approximate dispersion relation:

$$\omega^2 = \frac{c_{66}}{\rho}\left(\frac{\pi}{2b}\right)^2\left[m^2(1-R)^2 + \frac{\gamma_{55}}{c_{66}}\left(\frac{2\zeta b}{\pi}\right)^2\right], \tag{4.39}$$

or

$$\begin{aligned}\Omega^2 &= m^2(1-R)^2 + Z^2 \\ &\cong m^2(1-2R) + Z^2.\end{aligned} \tag{4.40}$$

Similarly, for the symmetric waves determined by Eq. (4.34), when m assumes $2,4,6,\cdots$, for small R, formally we still obtain Eqs. (4.39) and (4.40). However, the above approximation procedure does not work for the case of $m = 0$ which needs a separate treatment. When $m = 0$, the approximate dispersion relation is given by

$$\Omega^2 = (1-R)Z^2. \tag{4.41}$$

From Eq. (4.40) it can be seen that the mass layer lowers the cutoff frequencies of the thickness-twist waves when $Z = 0$. Equation (4.41) shows that the face-shear wave is still nondispersive.

4.5. Partial Mass Layers and Bechmann's Number

In this section we determine the so-called Bechmann's number for thickness-twist modes [52]. Consider a crystal plate with partial electrodes (mass layers) as shown in Fig. 4.5.

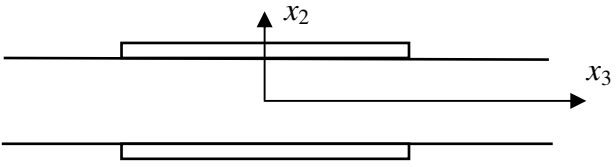

Fig. 4.5. A crystal plate with partial electrodes.

In such a plate there may exist the so-called trapped modes that have oscillatory behavior in the electroded central region and decay exponentially out of the electrode edges. Thus vibration energy is essentially trapped in the central region of the plate under the electrodes. This phenomenon is called energy trapping. Since the vibration essentially vanishes at a distance of a few times of the plate thickness away from the electrode edges, mounting of the crystal plate can be designed at such a distance without affecting the vibration of the plate.

The reason why trapped modes may exist in a partially electroded plate can be qualitatively explained as follows. Figure 4.6 shows the dispersion curves of thickness-twist waves in an infinite plate, either unelectroded or fully electroded. Consider long waves with a small wave number ζ which may be either real or purely imaginary. ω_1 and ω_2 are the cutoff frequencies of the waves. The inertia of the electrodes lowers the frequency. Therefore we have $\omega_2 < \omega_1$. If the plate in Fig. 4.5 has resonances between ω_2 and ω_1, then the wave number in the electroded region is real but in the unelectroded region it is purely imaginary (see the intersections of the horizontal line with the dispersion curves in Fig. 4.6). Therefore the modes have oscillatory behavior under the electrodes and decay exponentially away from the electrode edges in the unelectroded region.

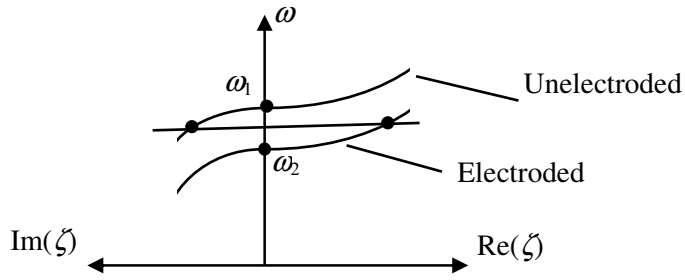

Fig. 4.6. Dispersion curves of thickness-twist waves in electroded and unelectroded plates.

There may be several trapped modes between ω_2 and ω_1, with different numbers of nodal points in the electroded region along the x_3 direction. The frequencies of these modes are closely distributed. In applications usually only the first mode without a nodal point in the x_3 direction is desired. Bechmann observed that reduction of the electrode length eliminates the undesirable modes one by one until only the desired mode remains. Bechmann's number is defined as the ratio of the electrode length over the plate thickness below which only one trapped mode without a nodal point in the x_3 direction exists. Quantitatively Bechmann's number of a wave is equal to the ratio of the wavelength in an electroded plate at the cutoff frequency of the same wave in an unelectroded plate to the plate thickness [52]. Therefore, to calculate Bechmann's number, we do not have to solve a vibration problem for the partially electroded plate in Fig. 4.5. The dispersion relations obtained in the previous two sections for unelectroded and symmetrically electroded plates will be sufficient. From Eq. (4.15), the cutoff frequencies of thickness-twist waves in an unelectroded plate can be found as

$$\omega^2 = \frac{c_{66}}{\rho}\left(\frac{\pi}{2b}\right)^2 m^2 . \tag{4.42}$$

Setting the frequency in the dispersion relation of thickness-twist waves in an electroded plate in Eq. (4.39) to the frequency in Eq. (4.42) gives

$$\frac{c_{66}}{\rho}\left(\frac{\pi}{2b}\right)^2 m^2 = \frac{c_{66}}{\rho}\left(\frac{\pi}{2b}\right)^2 \left[m^2 (1-R)^2 + \frac{\gamma_{55}}{c_{66}}\left(\frac{2\zeta b}{\pi}\right)^2 \right], \tag{4.43}$$

which implies that Bechmann's number for thickness-twist waves is given by

$$B_{TT} = \frac{2\pi}{\zeta}\frac{1}{2b} = \frac{1}{m}\sqrt{\frac{2\gamma_{55}}{Rc_{66}}}\,. \tag{4.44}$$

Equation (4.44) shows that Bechmann's number is inversely proportional to m and $\sqrt{R}$.

4.6. Asymmetric Mass Layers

The effects of asymmetric mass layers were studied in [53]. In this section we present a different treatment of the same problem. Consider a crystal plate with two different mass layers as shown in Fig. 4.7.

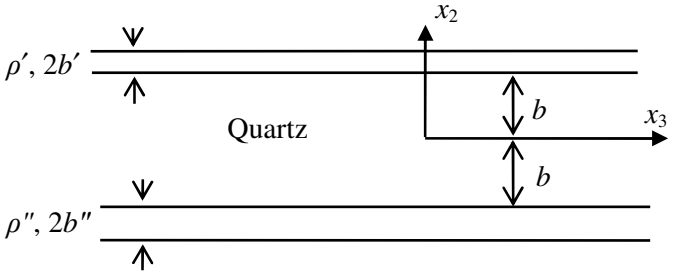

Fig. 4.7. A crystal plate with asymmetric mass layers.

4.6.1. Dispersion relation

When the mass layers are not symmetric, the modes cannot be separated into antisymmetric and symmetric ones. We need to combine the antisymmetric fields in Eqs. (4.10) and (4.12) with the symmetric fields in Eqs. (4.16) and (4.18), i.e.,

$$u_1 = (A\sin\eta y + C\cos\eta y)\cos\zeta\left(\frac{c_{56}}{c_{66}}y - z\right), \tag{4.45}$$

$$T_6 = c_{66}\eta(A\cos\eta y - C\sin\eta y)\cos\zeta\left(\frac{c_{56}}{c_{66}}y - z\right). \tag{4.46}$$

For Eq. (4.45) to satisfy the equation of motion in Eq. (4.4), we still have Eq. (4.13):

$$\rho\omega^2 = c_{66}\eta^2 + \gamma_{55}\zeta^2. \tag{4.47}$$

The boundary conditions at the plate surfaces are

$$\begin{aligned} T_6 &= -2\rho' b'\ddot{u}_1 = 2\rho' b'\omega^2 u_1, \quad y = b, \\ T_6 &= 2\rho'' b''\ddot{u}_1 = -2\rho'' b''\omega^2 u_1, \quad y = -b. \end{aligned} \tag{4.48}$$

Substitution of Eqs. (4.45) and (4.46) into Eq. (4.48) gives two linear homogeneous equations for A and C. For nontrivial solutions the determinant of the coefficient matrix has to vanish, which yields

$$\tan 2\eta b = \frac{\lambda' + \lambda''}{\lambda'\lambda'' - 1}, \tag{4.49}$$

where

$$\lambda' = \frac{2\rho' b'\omega^2}{c_{66}\eta}, \quad \lambda'' = \frac{2\rho'' b''\omega^2}{c_{66}\eta}, \tag{4.50}$$

which are small for thin mass layers. Equation (4.49) shows that the first-order effect of the inertia of asymmetric mass layers is the total mass layer inertia. In the special case of symmetric mass layers, $\rho'' b'' = \rho' b'$ and $\lambda'' = \lambda'$. In this case, with the following trigonometric identity:

$$\tan 2\alpha = \frac{2\tan\alpha}{1 - (\tan\alpha)^2}, \tag{4.51}$$

it can be shown that Eq. (4.49) reduces to

$$\tan\eta b = \frac{1}{\lambda'} = \frac{c_{66}\eta}{2\rho' b'\omega^2}, \tag{4.52}$$

$$\tan \eta b = -\lambda' = -\frac{2\rho' b' \omega^2}{c_{66}\eta}, \tag{4.53}$$

which are Eqs. (4.28) and (4.33).

4.6.2. Special case: one mass layer

Consider the special case when there is one mass at the top of the plate, i.e., $\rho'' b'' = 0$. In this case Eq. (4.49) reduces to

$$\tan 2\eta b = -\lambda' = -\frac{2\rho' b' \omega^2}{c_{66}\eta}. \tag{4.54}$$

We look for an approximate solution of Eq. (4.54) when $\rho' b'$ is small. We will call the mass layer effect described by Eq. (4.54) the exact effect, to distinguish it from the approximate effect to be determined next. As the lowest order of approximation, we set b' to zero. Then Eq. (4.54) implies that $\tan(2\eta b) = 0$. We have

$$\eta = \frac{m\pi}{2b}, \quad m = 0,1,2,3\cdots, \tag{4.55}$$

and

$$\omega^2 = \frac{c_{66}}{\rho}\left(\frac{\pi}{2b}\right)^2\left[m^2 + \frac{\gamma_{55}}{c_{66}}\left(\frac{2\zeta b}{\pi}\right)^2\right], \tag{4.56}$$

or

$$\Omega^2 = m^2 + Z^2. \tag{4.57}$$

where

$$\Omega = \frac{\omega}{\omega_s}, \quad Z = \sqrt{\frac{\gamma_{55}}{c_{66}}}\frac{2\zeta b}{\pi}, \quad \omega_s = \frac{\pi}{2b}\sqrt{\frac{c_{66}}{\rho}}. \tag{4.58}$$

When b' is nonzero and is small, for a given ω, we expect that the corresponding ζ determined by Eq. (4.54) is perturbed a little from the ζ given in Eq. (4.56). Therefore we write

$$\zeta^2 = \frac{\rho\omega^2}{\gamma_{55}} - \frac{c_{66}m^2\pi^2}{4\gamma_{55}b^2} + \Delta, \tag{4.59}$$

where Δ is small. From Eq. (4.47),

$$\eta = \sqrt{\frac{m^2\pi^2}{4b^2} - \frac{\gamma_{55}}{c_{66}}\Delta}\ . \tag{4.60}$$

Substituting Eq. (4.60) into Eq. (4.54), for small Δ, we obtain

$$\Delta = \frac{2\rho' b'\omega^2}{\gamma_{55}bm\pi}, \quad m>0. \tag{4.61}$$

Then, from Eq. (4.59),

$$\zeta^2 = \frac{\rho\omega^2}{\gamma_{55}} - \frac{c_{66}m^2\pi^2}{4\gamma_{55}b^2} + \frac{2\rho' b'\omega^2}{\gamma_{55}bm\pi}, \quad m>0. \tag{4.62}$$

Equation (4.62) is not valid when $m = 0$ which needs a separate and similar treatment. The result for the case of $m = 0$ is

$$\Delta = \frac{\rho' b'\omega^2}{\gamma_{55}b}, \quad m=0, \tag{4.63}$$

$$\zeta^2 = \frac{\rho\omega^2}{\gamma_{55}} + \frac{\rho' b'\omega^2}{\gamma_{55}b}, \quad m=0. \tag{4.64}$$

In terms of the dimensionless variables in Eq. (4.58), with $R = \rho' b' / (\rho b)$, we write Eq. (4.54), (4.62) and (4.64) as

$$\tan(2\eta b) = -\frac{\pi^2 R}{2\eta b}\Omega^2, \quad R = \frac{\rho' b'}{\rho b}. \tag{4.65}$$

$$\Omega^2 = \frac{m\pi}{m\pi + 2R}(m^2 + Z^2), \quad m>0, \tag{4.66}$$

$$\Omega^2 = \frac{1}{1+R}Z^2 \cong (1-R)Z^2, \quad m=0. \tag{4.67}$$

Equation (4.67) is the same as Eq. (4.41). Figure 4.8 shows the comparison between the exact mass layer effect from Eq. (4.65) (solid lines) with the approximate mass layer effect from Eqs. (4.66) and (4.67) (dotted lines).

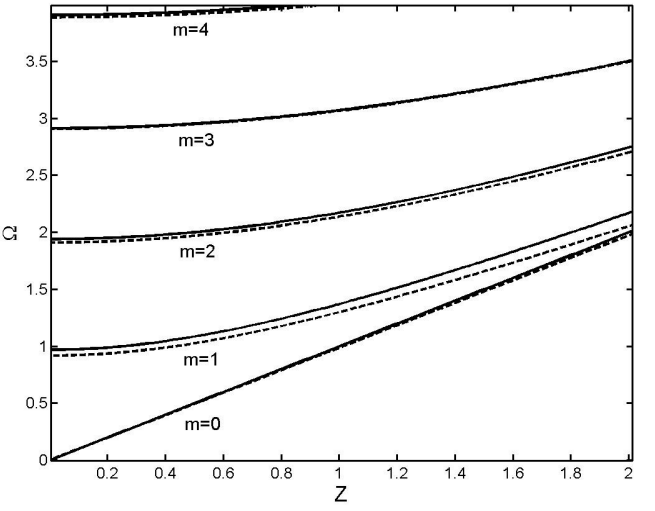

Fig. 4.8. Dispersion curves when R=3%. Solid line: from Eq. (4.65). Dotted lines: from Eqs. (4.66) and (4.67).

4.7. Imperfectly Bonded Mass Layer

Propagation of face-shear and thickness-twist waves in a crystal plate with an imperfectly bonded mass layer was analyzed in [54]. Consider such a plate as shown in Fig. 4.9.

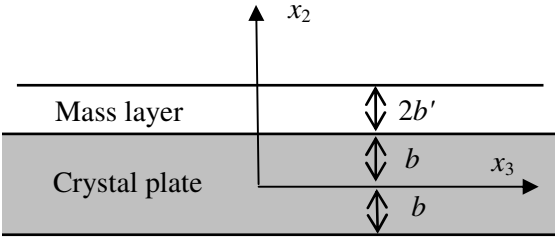

Fig. 4.9. A crystal plate with an imperfectly bonded thin mass layer.

4.7.1. Dispersion relation

Due to the asymmetry about the middle plane of the plate, the waves cannot be separated into antisymmetric and symmetric ones. We consider (see Eq. (4.45))

$$u_1 = (A\sin\eta y + C\cos\eta y)\cos\zeta\left(\frac{c_{56}}{c_{66}}y - z\right). \tag{4.68}$$

For Eq. (4.68) to satisfy the equation of motion in Eq. (4.4), we still have Eq. (4.13):

$$\rho\omega^2 = c_{66}\eta^2 + \gamma_{55}\zeta^2. \tag{4.69}$$

The stress component relevant to boundary conditions is (see Eq. (4.46))

$$T_6 = c_{66}\eta(A\cos\eta y - C\sin\eta y)\cos\zeta\left(\frac{c_{56}}{c_{66}}y - z\right). \tag{4.70}$$

The boundary conditions at the plate top and bottom are

$$\begin{aligned} -T_{21} &= 2\rho' b' \ddot{u}_1', \quad x_2 = b, \\ T_{21} &= 0, \quad x_2 = -b, \end{aligned} \tag{4.71}$$

where u_1' is the displacement of the mass layer. According to the shear-slip interface model, u_1' may be different from the plate surface displacement and the following constitutive relation describes the behavior of the interface:

$$T_{21} = k(u_1' - u_1), \quad x_2 = b\,, \tag{4.72}$$

where k is the elastic constant of the interface. Corresponding to Eq. (4.68), we let

$$u_1' = A' \cos\left[\zeta\left(\frac{c_{56}}{c_{66}}b - z\right)\right]\exp(i\omega t)\,, \tag{4.73}$$

where A' is an undetermined constant. Substitution of Eqs. (4.68), (4.70) and (4.73) into Eqs. (4.71) and (4.72) yields three linear homogeneous equations for A, C, and A':

$$\begin{aligned} &A\cos(\eta b) - C\sin(\eta b) - A'\frac{2\rho' b'\omega^2}{c_{66}\eta} = 0, \\ &A\cos(\eta b) + C\sin(\eta b) = 0, \\ &A[c_{66}\eta\cos(\eta b) + k\sin(\eta b)] + C[k\cos(\eta b) - c_{66}\eta\sin(\eta b)] - A'k = 0. \end{aligned} \tag{4.74}$$

For nontrivial solutions the determinant of the coefficient matrix of Eq. (4.74) has to vanish, which leads to

$$\tan(2\eta b) = \frac{\pi^2 R}{2\eta b}\frac{\omega^2}{\omega_s^2}\left[\frac{c_{66}}{k2b}(2\eta b)\tan(2\eta b) - 1\right], \tag{4.75}$$

where

$$R = \frac{\rho' b'}{\rho b}, \quad \omega_s^2 = \frac{\pi^2 c_{66}}{4\rho b^2}. \tag{4.76}$$

With Eq. (4.69), Eq. (4.75) determines the dispersion relation of ω versus ζ. When $k \to \infty$, Eq. (4.75) becomes Eq. (4.65).

4.7.2. Approximate dispersion relation (small R)

We try to obtain approximate dispersion relations from Eq. (4.75) under the assumption of thin mass layers with a small R. For a given ω, we still write the corresponding ζ by Eq. (4.59) and we still have Eq. (4.60). Substituting Eq. (4.60) into Eq. (4.75), for small Δ, we obtain

$$\Delta = \frac{2k\rho' b' \omega^2}{\gamma_{55} bm\pi \left(k - 2\rho' b' \omega^2\right)}, \quad m > 0, \tag{4.77}$$

$$\Delta = \frac{k\rho' b' \omega^2}{b\gamma_{55} \left(k - 2\rho' b' \omega^2\right)}, \quad m=0. \tag{4.78}$$

Equations (4.77) and (4.78) lead to

$$\zeta^2 = \frac{\rho\omega^2}{\gamma_{55}} - \frac{c_{66} m^2 \pi^2}{4\gamma_{55} b^2} + \frac{2k\rho' b' \omega^2}{\gamma_{55} bm\pi (k - 2\rho' b' \omega^2)}, \quad m>0, \tag{4.79}$$

$$\zeta^2 = \frac{\rho\omega^2}{\gamma_{55}} + \frac{k\rho' b' \omega^2}{\gamma_{55} b (k - 2\rho' b' \omega^2)}, \quad m=0, \tag{4.80}$$

which can be further written as

$$\Omega^2 = m^2 + Z^2 + \frac{2}{m\pi} \frac{R\Omega^2 K}{R\Omega^2 - K}, \quad m>0, \tag{4.81}$$

$$\Omega^2 = Z^2 + \frac{R\Omega^2 K}{R\Omega^2 - K}, \quad m=0, \tag{4.82}$$

where

$$\Omega = \frac{\omega}{\omega_s}, \quad Z = \sqrt{\frac{\gamma_{55}}{c_{66}}}\frac{2\zeta b}{\pi}, \quad \omega_s = \frac{\pi}{2b}\sqrt{\frac{c_{66}}{\rho}}, \quad K = \frac{2bk}{\pi^2 c_{66}}. \tag{4.83}$$

The last term in Eq. (4.81) or (4.82) represents the effect of the small R. The Ω^2 in this term may be approximately replaced by $m^2 + Z^2$ from Eq. (4.23) which is the dispersion relation when the mass layer is not present, or simply by m^2 for long waves near cutoff with a small Z. When $K \to \infty$, Eqs. (4.81) and (4.82) reduce to Eqs. (4.66) and (4.67).

The last term in Eq. (4.81) or (4.82) may be positive or negative. To examine this term further we introduce

$$\omega_l^2 = \frac{k}{2\rho' b'}, \quad K/R = \Omega_l^2 = \omega_l^2/\omega_s^2, \tag{4.84}$$

where ω_l may be considered as the resonance frequency of the mass layer under the action of the interface stiffness.

When $K > R\Omega^2$ or $\Omega_l^2 > \Omega^2$, i.e. the interface stiffness dominates the mass layer inertia, the last term in Eq. (4.81) or (4.82) is negative and the resonant frequency of the plate is lowered by the mass layer because the mass layer follows the plate surface motion well and the inertia of the mass layer is felt by the plate.

When $K < R\Omega^2$ or $\Omega_l^2 < \Omega^2$, the interface stiffness is relatively small, the last term in Eq. (4.81) or (4.82) is positive and the resonant frequency of the plate is raised by the mass layer because the mass layer does not follow the plate surface motion much and the interface stiffness raises the plate frequency. Near $K = R\Omega^2$ Eq. (4.81) and (4.82) are not valid. These observations agree with what is shown in Fig. 4.10 where, depending on the material parameters, the transition from a frequency drop to a frequency rise may occur in the face-shear mode with $m = 0$ (see Fig. 4.10 (a)) or a thickness-twist mode for which the case of $m = 1$ is shown in Fig. 4.10 (b).

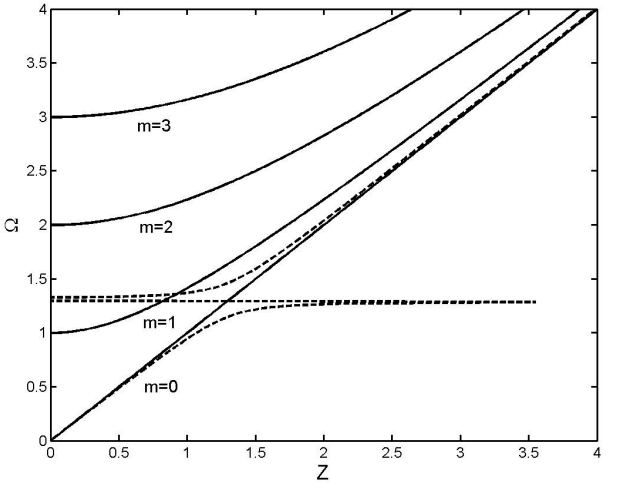

(a)

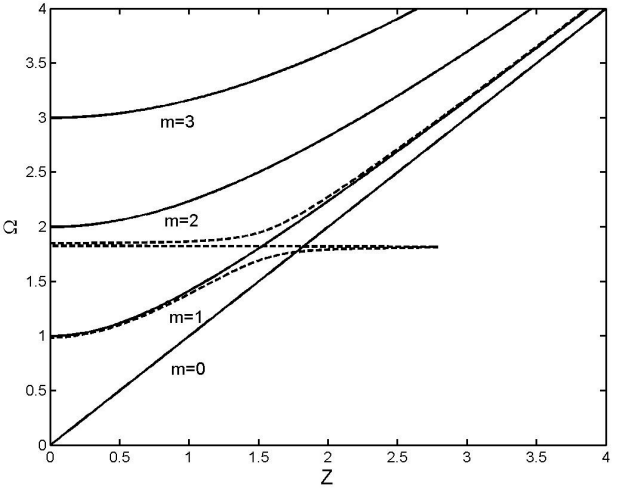

(b)

Fig. 4.10. Dispersion curves when K=10%. Solid lines: R = 0. Dotted lines: loosely bonded mass layer from Eqs. (4.81) and (4.82). (a) R = 6%. (b) R = 3%.

4.7.3. Approximate dispersion relation (large k)

Consider the special case when k is large and $1/k$ is nonzero and small. This case describes a plate with a nearly perfectly bonded mass layer. Using the frequencies of a plate with a perfectly bonded mass layer ($1/k = 0$) as a starting point, our goal is to obtain a modification of these frequencies by a small amount of the order of $1/k$. An approximate analysis similar to that in previous subsection is used. It turns out that the leading term of the frequency modification is of the order of $(b')^2/k$. Since b' is also a small parameter, we keep up to $(b')^3$ in the analysis and obtain

$$\zeta^2 = \frac{\rho\omega^2}{\gamma_{55}} - \frac{c_{66}m^2\pi^2}{4\gamma_{55}b^2} + \frac{2\rho' b'\omega^2}{\gamma_{55}bm\pi} - \frac{4}{\gamma_{55}c_{66}}\left(\frac{\rho' b'\omega^2}{m\pi}\right)^2 - \frac{32b}{3\gamma_{55}c_{66}^{\,2}}\left(\frac{\rho' b'\omega^2}{m\pi}\right)^3 + \frac{4\left(\rho' b'\omega^2\right)^2}{\gamma_{55}m\pi b}\frac{1}{k}, \quad m > 0, \tag{4.85}$$

$$\zeta^2 = \frac{\rho\omega^2}{\gamma_{55}} + \frac{\rho' b'\omega^2}{\gamma_{55}b} + \frac{4\left(\rho' b'\omega^2\right)^2}{3\gamma_{55}c_{66}} + \frac{32b\left(\rho' b'\omega^2\right)^3}{9\gamma_{55}c_{66}^{\,2}} + \frac{2\left(\rho' b'\omega^2\right)^2}{\gamma_{55}b}\frac{1}{k}, \quad m = 0. \tag{4.86}$$

In dimensionless form, according to Eq. (4.83), Eqs. (4.85) and (4.86) become

$$Z^2 = \Omega^2 - m^2 + \frac{2R\Omega^2}{m\pi} - \frac{\left(R\Omega^2\right)^2}{m^2} - \frac{2\pi\left(R\Omega^2\right)^3}{3m^3} + \frac{2\left(R\Omega^2\right)^2}{m\pi K}, \ m>0, \tag{4.87}$$

$$Z^2 = (1+R)\Omega^2 + \frac{\pi^2\left(R\Omega^2\right)^2}{3} + \frac{2\pi^4\left(R\Omega^2\right)^3}{9} + \frac{\left(R\Omega^2\right)^2}{K}, \quad m = 0. \tag{4.88}$$

A few observations can be made from Eqs. (4.87) and (4.88). When $K = \infty$, Eqs. (4.87) and (4.88) reduce to Eqs. (4.66) and (4.67) with additional higher-order terms of R. The effect of $1/K$ is together with R^2 and therefore is a higher-order effect. If only linear effects of R and $1/K$ are wanted, then $1/K$ has no contribution. Equations (4.87) and (4.88) are plotted in Fig. 4.11 (dotted lines) in comparison with the case without a mass layer (solid lines). A nearly perfectly bonded mass layer follows the crystal plate surface motion well and lowers the wave frequencies.

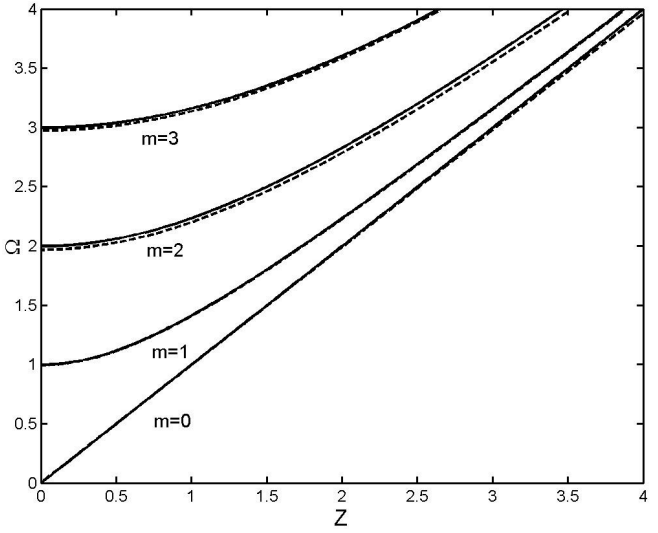

Fig. 4.11. Dispersion curves when the mass layer is nearly perfectly bonded, K = 100. Solid lines: R = 0. Dotted lines: From Eqs. (4.87) and (4.88) with R = 1%.

4.8. Mass Layer Stiffness

In this section we study the stiffness effect of thin mass layers on a crystal plate [55]. Consider the crystal plate with two elastic mass layers in Fig. 4.12.

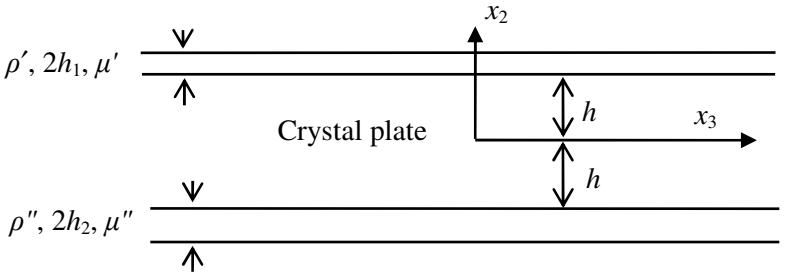

Fig. 4.12. A crystal plate with two elastic layers.

4.8.1. Dispersion relation

The procedure below is different from that in [55]. The displacement field in the crystal plate is (see Eq. (4.45))

$$u_1 = (A\sin\eta y + C\cos\eta y)\cos\zeta\left(\frac{c_{56}}{c_{66}}y - z\right). \tag{4.89}$$

For Eq. (4.89) to satisfy the equation of motion in Eq. (4.4), we still have Eq. (4.13):

$$\rho\omega^2 = c_{66}\eta^2 + \gamma_{55}\zeta^2. \tag{4.90}$$

The stress component relevant to boundary conditions is given by Eq. (4.46)

$$T_6 = c_{66}\eta(A\cos\eta y - C\sin\eta y)\cos\zeta\left(\frac{c_{56}}{c_{66}}y - z\right). \tag{4.91}$$

The boundary conditions to be satisfied are

$$\begin{aligned} &2h_1\mu' u_{1,33} - T_{21} = \rho' 2h_1\ddot{u}_1, \quad x_2 = h, \\ &2h_2\mu'' u_{1,33} + T_{21} = \rho'' 2h_2\ddot{u}_1, \quad x_2 = -h, \end{aligned} \tag{4.92}$$

where μ (μ' or μ'') is the shear elastic constant of the mass layers. Physically, the above boundary conditions at $x_2 = \pm h$ state that the stress

gradients, $2h_1\mu' u_{1,33}$ and $2h_2\mu'' u_{1,33}$, in the mass layers and the interface stress, T_{21}, between the mass layers and the crystal plate are responsible for the mass layer accelerations according to Newton's law. Equation (4.92) is in fact the same as the equations of the plane-stress theory of elasticity. Substitutions of Eqs. (4.89) and (4.91) into Eq. (4.92) give two linear homogeneous equations for *A* and *C*. For nontrivial solutions the determinant of the coefficient matrix has to vanish, which gives

$$\tan 2\eta b = \frac{\lambda' + \lambda''}{\lambda'\lambda'' - 1}, \tag{4.93}$$

where

$$\lambda' = \frac{2\rho' h_1 \omega^2 - \mu' \zeta^2}{c_{66}\eta}, \quad \lambda'' = \frac{2\rho'' h_2 \omega^2 - \mu'' \zeta^2}{c_{66}\eta}, \tag{4.94}$$

which are small for thin mass layers and long waves. When μ = 0, Eq. (4.94) reduces to Eq. (4.50) with the identification of $h_1 = b'$ and $h_2 = b''$. Hence the discussion for the special case of identical mass layers also follows that in Section 4.6, i.e., for identical mass layers with $\lambda' = \lambda''$ Eq. (4.93) reduces to the following two equations (see Eqs. (4.52) and (4.53)):

$$\tan \eta b = \frac{1}{\lambda'}, \tag{4.95}$$

$$\tan \eta b = -\lambda', \tag{4.96}$$

for antisymmetric and symmetric waves, respectively.

4.8.2. Numerical example

We denote the dispersion relations for a plate without mass layers by (see Eq. 4.15)

$$\omega_0^2 = \omega_s^2 [m^2 + \frac{\gamma_{55}}{c_{66}} (\frac{2h\zeta}{\pi})^2], \quad m = 0,1,2,3,\cdots. \tag{4.97}$$

We focus on the fundamental thickness-twist wave (m = 1). Identical aluminum mass layers with $\mu' = 26$ GPa and $\rho' = 2700\,\text{kg/m}^3$ are used as an example. In Fig. 4.13, we plot the frequency shift which is defined as

$$\Delta\omega = \omega - \omega_0\,, \tag{4.98}$$

where ω and ω_0 are obtained from Eq. (4.93) and Eq. (4.97) respectively. Equation (4.93) is solved numerically in two different ways. In one we set the mass layer shear elastic constant $\mu = 0$ so that only the mass layer inertia is considered (the curves with square markers). In the other both the mass layer inertia and stiffness are considered (the curves with circular markers). Two cases of different mass layer thickness are shown. The figure shows that the mass layer inertia lowers the frequency as expected. It also shows that the mass layer stiffness raises the wave frequency. This stiffness effect is more pronounced for short waves with relatively large wave numbers. This is not surprising because for long waves the mass layers do not deform much and only their inertial effect is felt. Therefore, for mass sensors whose sensitivity is predicted by the mass layer inertial effect only, their actual sensitivity will be lower if the mass layer stiffness gets involved. This reduction of sensitivity may be significant for relatively short waves. The stiffness effect is also more pronounced when the mass layers are thicker.

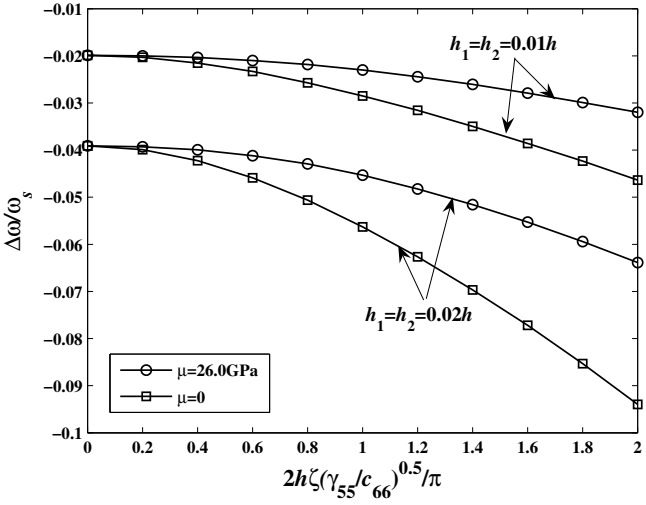

Fig. 4.13. Effect of elastic layer stiffness (m = 1).

4.9. Thick Mass Layer

This section is concerned with thick mass layers described by the equations of elasticity [56]. Obviously both the mass layer inertia and stiffness are involved. Consider an elastic layer on a crystal plate as shown in Fig. 4.14. No assumptions are made regarding the relative magnitude between b' and b.

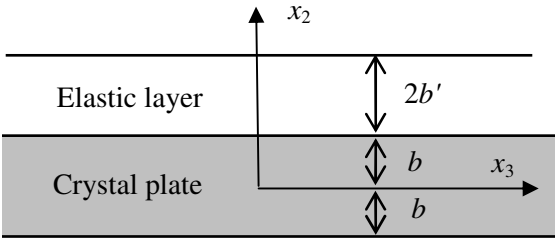

Fig. 4.14. A crystal plate with an isotropic elastic layer of finite thickness.

4.9.1. Dispersion relation

The displacement field in the crystal plate is still from Eq. (4.45):

$$u_1 = (A\sin\eta y + C\cos\eta y)\cos\zeta\left(\frac{c_{56}}{c_{66}}y - z\right). \tag{4.99}$$

For Eq. (4.99) to satisfy the equation of motion in Eq. (4.4), we still have Eq. (4.13):

$$\rho\omega^2 = c_{66}\eta^2 + \gamma_{55}\zeta^2. \tag{4.100}$$

The stress component relevant to boundary and interface conditions is given by Eq. (4.46):

$$T_6 = c_{66}\eta(A\cos\eta y - C\sin\eta y)\cos\zeta\left(\frac{c_{56}}{c_{66}}y - z\right). \tag{4.101}$$

The displacement field in the elastic layer is governed by:

$$\mu\nabla^2 u_1 = \bar{\rho}\ddot{u}_1, \tag{4.102}$$

where μ is the shear elastic constant of the elastic layer. $\bar{\rho}$ is its mass density. $\nabla^2 = \partial_1^2 + \partial_2^2$ is the two-dimensional Laplacian. The nonzero stress components are

$$T_{21} = \mu u_{1,2}, \quad T_{31} = \mu u_{1,3}. \tag{4.103}$$

Consider the following displacement field for the elastic layer:

$$u_1 = [\bar{A}\sin(\bar{\eta}y) + \bar{C}\cos(\bar{\eta}y)]\cos\left[\zeta\left(\frac{c_{56}}{c_{66}}b - z\right)\right]\exp(i\omega t), \tag{4.104}$$

where $\bar{A}$ and $\bar{C}$ are undetermined constants. $\bar{\eta}$ is the wave number in the *y* direction. Equation (4.104) satisfies Eq. (4.102) provided that

$$\bar{\rho}\omega^2 = \mu(\bar{\eta}^2 + \zeta^2). \tag{4.105}$$

The shear stress component needed in boundary and continuity conditions is given by

$$T_{21} = \mu\bar{\eta}[\bar{A}\cos(\bar{\eta}y) - \bar{C}\sin(\bar{\eta}y)]\cos\left[\zeta\left(\frac{c_{56}}{c_{66}}b - z\right)\right]\exp(i\omega t). \tag{4.106}$$

The top of the elastic layer is traction free. At the interface between the elastic layer and the crystal plate, the continuity of the displacement and the shear stress component T_{21} must be maintained. The bottom of the crystal plate is also traction free. Therefore, we impose the following boundary and continuity conditions:

$$\begin{aligned} &T_{21}(b + 2b') = 0, \\ &u_1(b^+) = u_1(b^-), \\ &T_{21}(b^+) = T_{21}(b^-), \\ &T_{21}(-b) = 0. \end{aligned} \tag{4.107}$$

Substitution of Eqs. (4.99), (4.101), (4.104) and (4.106) into Eq. (4.107) results in four linear and homogeneous equations for A, C, $\bar{A}$ and $\bar{C}$:

$$\begin{aligned}
&\bar{A}\cos[\bar{\eta}(b+2b')]-\bar{C}\sin[\bar{\eta}(b+2b')]=0,\\
&\bar{A}\sin(\bar{\eta}b)+\bar{C}\cos(\bar{\eta}b)=A\sin(\eta b)+C\cos(\eta b),\\
&\mu\bar{\eta}[\bar{A}\cos(\bar{\eta}b)-\bar{C}\sin(\bar{\eta}b)]=c_{66}\eta[A\cos(\eta b)-C\sin(\eta b)],\\
&A\cos(\eta b)+C\sin(\eta b)=0.
\end{aligned} \tag{4.108}$$

For nontrivial solutions the determinant of the coefficient matrix of Eq. (4.108) has to vanish, which leads to the following frequency equation:

$$c_{66}\eta\tan(2\eta b)+\mu\bar{\eta}\tan(2\bar{\eta}b')=0\,. \tag{4.109}$$

Together with Eqs. (4.100) and (4.105), Eq. (4.109) determines the dispersion relation of ω versus ζ.

With the introduction of the following dimensionless frequency Ω and dimensionless wave number Z:

$$\Omega=\frac{\omega}{\omega_s},\quad \omega_s=\frac{\pi}{2b}\sqrt{\frac{c_{66}}{\rho}},\quad Z=\sqrt{\frac{\gamma_{55}}{c_{66}}}\frac{2\zeta b}{\pi}, \tag{4.110}$$

Equation (4.109) becomes

$$\begin{aligned}
&\sqrt{\Omega^2-Z^2}\tan\left[\sqrt{\left(\Omega^2-Z^2\right)}\pi\right]\\
&+\frac{\sqrt{RR_s\Omega^2-R_s{}^2Z^2}}{R_b}\tan\left(\frac{R_b\sqrt{RR_s\Omega^2-R_s{}^2Z^2}}{R_s}\pi\right)=0,
\end{aligned} \tag{4.111}$$

where

$$R=\frac{\bar{\rho}b'}{\rho b},\quad R_s=\frac{\mu b'}{\gamma_{55}b},\quad R_b=\sqrt{\frac{c_{66}}{\gamma_{55}}}\frac{b'}{b}. \tag{4.112}$$

The special case when the elastic layer is not present can be obtained from Eq. (4.111) by setting $b'=0$, In this case the roots of

Eq. (4.111) are given by $\Omega^2 = m^2 + Z^2$ (see Eq. (4.23)). When the elastic layer is present, both its inertia and stiffness affect the dispersion relations. One tends to lower the wave frequencies while the other tends to raise them. The combined effect may vary from material to material depending on whether the material is light or heavy, and stiff or compliant. The case of $R = R_s = R_b = 5\%$ is shown in Fig. 4.15. The solid lines are from $\Omega^2 = m^2 + Z^2$ when the elastic layer is not present and are plotted for comparison. The dotted lines are according to Eq. (4.111) and show the effect of the elastic layer. For $m = 0$ the solid and dotted lines essentially coincide. The wave frequencies are lowered except when $m = 0$ which cannot be seen clearly. The frequency shift is larger for higher-order modes with a larger m, and for long waves with a small Z.

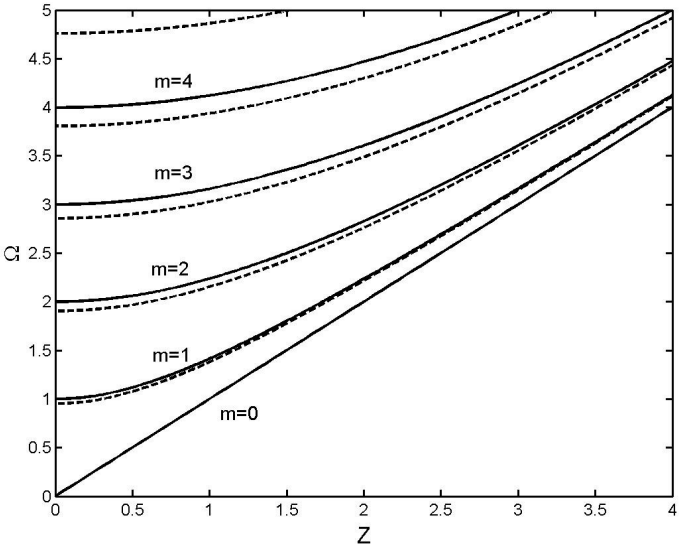

Fig. 4.15. Effect of a mass layer. Solid lines: without a mass layer. Dotted lines: with a mass layer.

4.9.2. Long-wave approximation

We now try to obtain an approximate solution to Eq. (4.109) or (4.111) for long waves with a small ζ, which is the case used often in device

applications. The face-shear wave and the thickness-twist waves need to be treated separately.

Consider the face-shear wave first. From Fig. 4.15, it can be seen that when ζ is small ω is also small and is of the same order as ζ. Then, from Eqs. (4.100) and (4.105), η and $\bar{\eta}$ are also small. In this case, Eq. (4.109) can be approximated by

$$\omega = \sqrt{\frac{\gamma_{55} b + \mu b'}{\rho b + \bar{\rho} b'}}\, \zeta \,. \tag{4.113}$$

Equation (4.113) shows that the speed of the face-shear wave is simply determined by the effective mass density and the effective stiffness according to the volume fraction of the two materials. From Eq. (4.113), clearly, the stiffness of the elastic layer raises the frequency and the inertia of the elastic layer lowers the frequency.

For thickness-twist waves, when ζ approaches zero, ω approaches nonzero cutoff frequencies. In this case, for small ζ, from Eqs. (4.100) and (4.105), we have

$$\eta \cong \sqrt{\frac{\rho\omega^2}{c_{66}}}\left(1 - \frac{\gamma_{55}\zeta^2}{2\rho\omega^2}\right), \quad \bar{\eta} \cong \sqrt{\frac{\bar{\rho}\omega^2}{\mu}}\left(1 - \frac{\mu\zeta^2}{2\bar{\rho}\omega^2}\right). \tag{4.114}$$

Then it can be shown that Eq. (4.109) can be approximated by

$$A(\omega) - B(\omega)\zeta^2 = 0 \tag{4.115}$$

where

$$\begin{aligned} A(\omega) &= \sqrt{\rho\omega^2 c_{66}} \tan\left(2b\sqrt{\frac{\rho\omega^2}{c_{66}}}\right) + \sqrt{\bar{\rho}\omega^2\mu} \tan\left(2b'\sqrt{\frac{\bar{\rho}\omega^2}{\mu}}\right), \\ B(\omega) &= \gamma_{55} b \sec^2\left(2b\sqrt{\frac{\rho\omega^2}{c_{66}}}\right) + \frac{\gamma_{55}}{2}\sqrt{\frac{c_{66}}{\rho\omega^2}} \tan\left(2b\sqrt{\frac{\rho\omega^2}{c_{66}}}\right) \\ &\quad + b'\mu \sec^2\left(2b'\sqrt{\frac{\bar{\rho}\omega^2}{\mu}}\right) + \frac{1}{2}\sqrt{\frac{\mu^3}{\bar{\rho}\omega^2}} \tan\left(2b'\sqrt{\frac{\bar{\rho}\omega^2}{\mu}}\right). \end{aligned} \tag{4.116}$$

According to Eqs. (4.110) and (4.112), in dimensionless form, Eqs. (4.113) and (4.116) can be written as

$$\Omega = \sqrt{\frac{1+R_s}{1+R}}\, Z\,, \tag{4.117}$$

$$\begin{aligned}
&\Omega \tan\left(\Omega\pi\right) + \frac{\sqrt{RR_s}}{R_b}\Omega \tan\left(R_b\sqrt{\frac{R}{R_s}}\Omega\pi\right) - \frac{\pi Z^2}{2}\sec^2\left(\Omega\pi\right) \\
&-\frac{Z^2}{2\Omega}\tan\left(\Omega\pi\right) - \frac{\pi R_s Z^2}{2}\sec^2\left(R_b\sqrt{\frac{R}{R_s}}\Omega\pi\right) \\
&-\frac{R_s Z^2}{2R_b\Omega}\sqrt{\frac{R_s}{R}}\tan\left(R_b\sqrt{\frac{R}{R_s}}\Omega\pi\right) = 0.
\end{aligned} \tag{4.118}$$

In Eq. (4.118), we further make the following two approximations. One is that, for small Z, in the terms associated with Z^2 in Eq. (4.118) we set $\Omega \cong m$. The other is that, in those terms of Eq. (4.118) that are independent of Z, we write

$$\Omega \cong m + \Delta\Omega\,. \tag{4.119}$$

Then, from Eq. (4.118), for small $\Delta\Omega$, we can determine an expression of $\Delta\Omega$ which, when substituted into Eq. (4.119), gives the following expression of the long-wave approximation for m>0:

$$\begin{aligned}
&\Omega = m + \frac{P}{Q}, \\
&P = \left(R_s\sqrt{\frac{R_s}{R}}Z^2 - 2\sqrt{RR_s}\,m^2\right)\tan\left(R_b\sqrt{\frac{R}{R_s}}m\pi\right) \\
&\quad + m\pi R_b R_s Z^2 \sec^2\left(R_b\sqrt{\frac{R}{R_s}}m\pi\right) + m\pi R_b Z^2, \\
&Q = 2\sqrt{RR_s}\,m\tan\left(R_b\sqrt{\frac{R}{R_s}}m\pi\right) \\
&\quad + 2RR_b m^2\pi\sec^2\left(R_b\sqrt{\frac{R}{R_s}}m\pi\right) + 2R_b m^2\pi.
\end{aligned} \tag{4.120}$$

For the case of $R = R_s = R_b = 10\%$, Eqs. (4.117) and (4.120) are plotted in Fig. 4.16. The dark dotted lines show the exact effect of the elastic layer from Eq. (4.111). The light dotted lines are from the long-wave approximation given by Eqs. (4.117) and (4.120). For a specific branch of the dispersion curves, the long-wave approximation agrees with Eq. (4.111) for small *Z*. For large *Z* the long-wave approximation deviates from Eq. (4.111). The range of validity of the long-wave approximation varies with *m*.

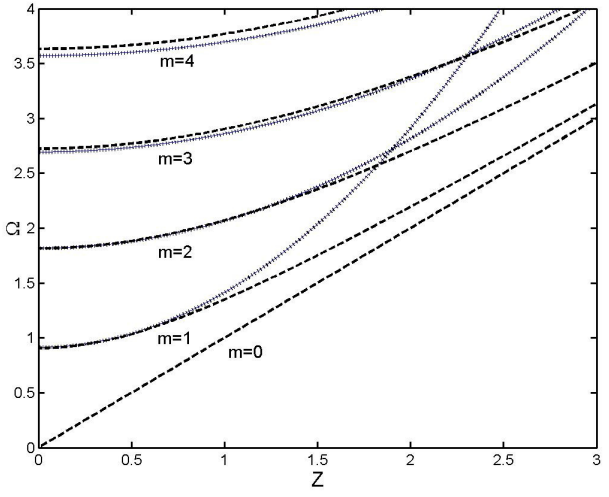

Fig. 4.16. Long-wave approximation. Dark dotted lines: exact mass layer effect from Eq. (4.111). Light dotted lines: approximate mass layer effect from Eqs. (4.117) and (4.120).

4.9.3. Thin-film approximation

When the elastic layer is thin, b' is small. In such a situation we expect the solution to Eq. (4.109) to be slightly different from $2\eta b = m\pi$ which is for the case of $b' = 0$. Therefore we write

$$2\eta b = m\pi + \Delta\,, \tag{4.121}$$

where Δ is a small unknown. We substitute Eq. (4.121) into the first term of Eq. (4.109). For the second term of Eq. (4.109), since it effectively has the small b' as a factor, we substitute the following equivalence of $\Omega^2 = m^2 + Z^2$ for ζ versus ω:

$$\zeta^2 = \frac{\rho\omega^2}{\gamma_{55}} - \frac{c_{66}m^2\pi^2}{4\gamma_{55}b^2}. \tag{4.122}$$

Then Eq. (4.109) becomes an equation for Δ from which we find

$$\Delta = \frac{\left(\dfrac{4\rho\mu bb'}{\gamma_{55}c_{66}} - \dfrac{4\bar{\rho}bb'}{c_{66}}\right)\omega^2 - \dfrac{m^2\pi^2\mu b'}{\gamma_{55}b}}{m\pi}, \tag{4.123}$$

which leads to

$$\zeta^2 = (1 + 2R - 2R_s)\frac{\rho\omega^2}{\gamma_{55}} + (2R_s - 1)\frac{c_{66}m^2\pi^2}{4\gamma_{55}b^2}. \tag{4.124}$$

The case of $m = 0$ needs a special treatment. The result is

$$\Delta^2 = \left(\frac{4\rho\mu bb'}{\gamma_{55}c_{66}} - \frac{4\bar{\rho}bb'}{c_{66}}\right)\omega^2, \tag{4.125}$$

$$\zeta^2 = \left(\frac{\rho}{\gamma_{55}} + \frac{\bar{\rho}}{\gamma_{55}b}b' - \frac{\rho\mu}{\gamma_{55}{}^2b}b'\right)\omega^2. \tag{4.126}$$

In dimensionless form, Eqs. (4.124) and (4.126) are

$$\Omega^2 = \frac{1}{1 + R - R_s}Z^2 \cong (1 - R + R_s)Z^2, \quad m = 0, \tag{4.127}$$

$$\begin{aligned}\Omega^2 &= \frac{1 - 2R_s}{1 + 2R - 2R_s}m^2 + \frac{1}{1 + 2R - 2R_s}Z^2 \\ &\cong (1 - 2R)m^2 + (1 - 2R + 2R_s)Z^2, \quad m > 0.\end{aligned} \tag{4.128}$$

The case of $R = R_s = R_b = 12.5\%$ is shown in Fig. 4.17. These values are larger than what are normally encountered in mass sensor applications. They are so chosen to show the difference among different cases more clearly. The solid lines are from $\Omega^2 = m^2 + Z^2$ for the case when the elastic layer is not present and are plotted for comparison. The dark dotted lines show the exact effect of the elastic layer from Eq. (4.111). The light dotted lines are from the thin-film approximation given by Eqs. (4.127) and (4.128). For m = 0 the three lines essentially coincide. The thin-film approximation predicts slightly lower frequencies but overall it agrees with the exact solution well. If a common value of 5% for R, R_s and R_b is used, the thin-film approximation is almost indistinguishable graphically from the exact solution.

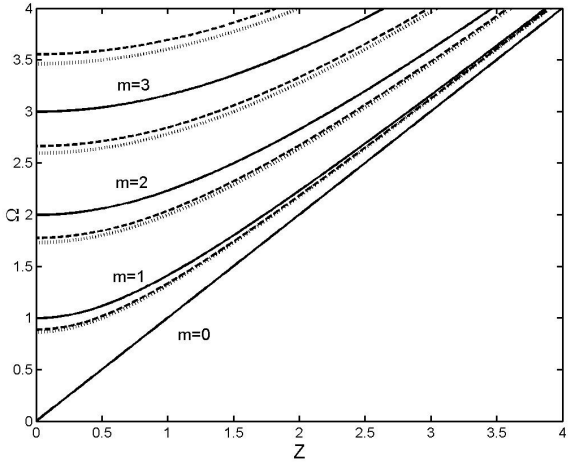

Fig. 4.17. Thin-film approximation. Solid lines: $\Omega^2 = m^2 + Z^2$. Dark dotted lines: exact mass layer effect from Eq. (4.111). Light dotted lines: approximate mass layer effect from Eqs. (4.127) and (4.128).

4.10. Plate on a Substrate

We now consider waves in a crystal plate on an isotropic elastic half space (see Fig. 4.18) [57]. Both the crystal plate and the elastic half space are governed by the equations of elasticity.

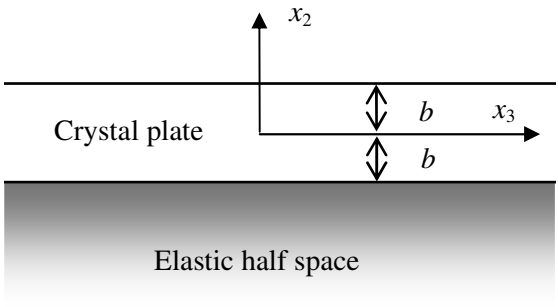

Fig. 4.18. A rotated Y-cut quartz plate on an isotropic elastic half space.

4.10.1. Dispersion relation

The displacement field in the crystal plate is (see Eq. (4.45))

$$u_1 = (A\sin\eta y + C\cos\eta y)\cos\zeta\left(\frac{c_{56}}{c_{66}}y - z\right). \tag{4.129}$$

For Eq. (4.129) to satisfy the equation of motion in Eq. (4.4), we still have Eq. (4.13):

$$\rho\omega^2 = c_{66}\eta^2 + \gamma_{55}\zeta^2. \tag{4.130}$$

The stress component relevant to boundary and interface conditions is (see Eq. (4.46))

$$T_6 = c_{66}\eta(A\cos\eta y - C\sin\eta y)\cos\zeta\left(\frac{c_{56}}{c_{66}}y - z\right). \tag{4.131}$$

The displacement in the elastic half space is governed by

$$\mu\nabla^2 u_1 = \rho' \ddot{u}_1, \tag{4.132}$$

where $\nabla^2 = \partial_1^2 + \partial_2^2$ is the two-dimensional Laplacian, ρ' is the mass density of the half space, and μ is its shear elastic constant. The nonzero stress components are

$$T_{21} = \mu u_{1,2}, \quad T_{31} = \mu u_{1,3}. \tag{4.133}$$

Specifically, consider the following displacement field:

$$u_1 = \bar{A} \exp(\bar{\eta} y) \cos\left[\zeta\left(\frac{c_{56}}{c_{66}} b + z\right)\right] \exp(i\omega t), \tag{4.134}$$

where $\bar{A}$ is an undetermined constant. Equation (4.134) is a solution to Eq. (4.132) provided that $\bar{\eta}$ satisfies

$$\rho'\omega^2 = \mu(-\bar{\eta}^2 + \zeta^2) \quad \text{or} \quad \bar{\eta} = \sqrt{\zeta^2 - \frac{\rho'\omega^2}{\mu}}, \tag{4.135}$$

where, for a surface wave solution, we have chosen the positive root for $\bar{\eta}$. For $\bar{\eta}$ to be real and positive we must have $\zeta^2 > \rho'\omega^2/\mu$. The shear stress component needed in boundary and continuity conditions is given by

$$T_{21} = \bar{A}\mu\bar{\eta} \exp(\bar{\eta} y) \cos\left[\zeta\left(\frac{c_{56}}{c_{66}} b + z\right)\right] \exp(i\omega t). \tag{4.136}$$

The top of the crystal plate is traction-free. At the interface between the crystal plate and the elastic half space, the continuity of the displacement and the shear stress component T_{21} must be met. Therefore, we impose the following boundary and continuity conditions:

$$\begin{aligned} &T_{21}(b) = 0, \\ &u_1(-b^-) = u_1(-b^+), \\ &T_{21}(-b^-) = T_{21}(-b^+). \end{aligned} \tag{4.137}$$

Substitution of Eqs. (4.129), (4.131), (4.134) and (4.136) into Eq. (4.137) results in three linear and homogeneous equations for A, C, and $\bar{A}$:

$$\begin{aligned} &c_{66}\eta[A\cos(\eta b) - C\sin(\eta b)] = 0, \\ &-A\sin(\eta b) + C\cos(\eta b) - \bar{A}\exp(-\bar{\eta} b) = 0, \\ &c_{66}\eta[A\cos(\eta b) + C\sin(\eta b)] - \bar{A}\mu\bar{\eta}\exp(-\bar{\eta} b) = 0. \end{aligned} \tag{4.138}$$

For nontrivial solutions the determinant of the coefficient matrix of Eq. (4.138) has to vanish, which leads to

$$\tan(2\eta b) = \frac{\mu\bar{\eta}}{c_{66}\eta}. \tag{4.139}$$

With the use of Eqs. (4.130) and (4.135), Eq. (4.139) can be written as

$$\tan\left[\left(\frac{\rho\omega^2 - \gamma_{55}\zeta^2}{c_{66}}\right)^{1/2} 2b\right] = \frac{\mu\left(\zeta^2 - \dfrac{\rho'\omega^2}{\mu}\right)^{1/2}}{c_{66}\left(\dfrac{\rho\omega^2 - \gamma_{55}\zeta^2}{c_{66}}\right)^{1/2}}, \tag{4.140}$$

which determines the dispersion relation of ω versus ζ. We denote

$$\frac{\gamma_{55}}{\rho} = c_Q^2, \quad \frac{\mu}{\rho'} = c_T^2, \quad \frac{\omega}{\zeta} = c\ , \tag{4.141}$$

where c_Q is the face-shear wave speed in a rotated Y-cut quartz plate defined in Eq. (4.9), c_T is the speed of plane shear waves in the half space, and c is the speed of the shear-horizontal waves we are considering. Then Eq. (4.140) can be written into the following form as an equation for c:

$$\tan\left[\left(\frac{c^2}{c_Q^2} - 1\right)^{1/2} 2b\zeta\left(\frac{\gamma_{55}}{c_{66}}\right)^{1/2}\right] - \left(\frac{\gamma_{55}}{c_{66}}\right)^{1/2} \frac{\mu\left(1 - \dfrac{c^2}{c_T^2}\right)^{1/2}}{\gamma_{55}\left(\dfrac{c^2}{c_Q^2} - 1\right)^{1/2}} = 0\ . \tag{4.142}$$

Equation (4.142) reduces to the well-known frequency equation for Love waves in the theory of isotropic elasticity if the anisotropy of the crystal plate is removed by setting $\gamma_{55} = c_{66}$ because for isotropic materials $c_{56} = 0$ and $c_{55} = c_{66}$. Due to the presence of ζ in Eq. (4.142), c is a function of ζ and the waves are dispersive. When $c \to c_T$ the left-hand side of Eq. (4.142) is positive. When $c \to c_Q$ the left-hand side of Eq. (4.142) is negative. Therefore at least one real root exists in the interval of (c_Q, c_T) when $c_T > c_Q$. We expect that the roots to Eq. (4.142) are not unique because of the presence of trigonometric functions. This agrees with the fact that even for waves in a plate alone there are infinitely many branches of dispersion curves. Once a root to Eq. (4.142) is found, from Eq. (4.138) we can determine the ratios among *A*, *C*, and $\overline{A}$, and thus the displacement field of the corresponding wave.

4.10.2. Numerical result

For numerical examples we consider the most widely used AT-cut quartz plate. For AT-cut quartz $c_Q = 5089$ m/s and $\gamma_{55}/c_{66} = 2.3644$. Consider the case when the material constants of the half space, μ and ρ', are determined from

$$\frac{c_Q}{c_T} = 0.89, \quad \frac{\mu}{\gamma_{55}} = 1.4. \tag{4.143}$$

We also introduce a dimensionless wave number $Z = 2\zeta b/\pi$. Equation (4.142) is solved using MATLAB. The first two dispersion curves with low frequencies are shown in Fig. 4.19 (a). The waves are clearly dispersive. When $Z = 2$, the corresponding displacement fields of the two waves are shown in Fig. 4.19 (b). The displacement distribution is normalized by the maximal displacement at the top surface. The wave with a higher frequency has a nodal point along the plate thickness.

Next we consider a different material for the elastic half space whose density and shear constant are defined by

$$\frac{c_Q}{c_T} = 0.78, \quad \frac{\mu}{\gamma_{55}} = 1.8. \tag{4.144}$$

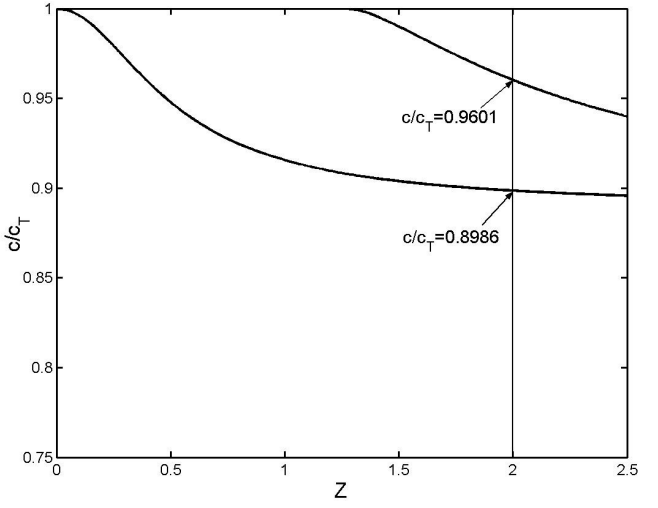

(a)

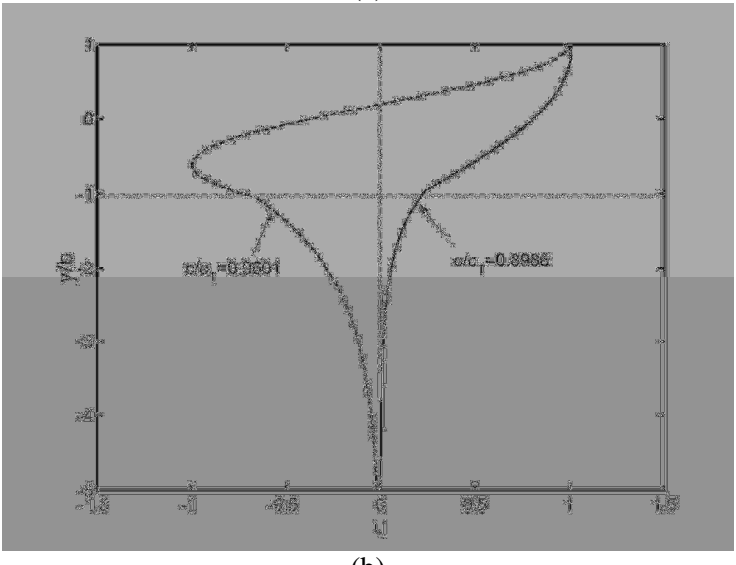

(b)

Fig. 4.19. Dispersion curves and mode shapes when $c_Q = 0.89c_T$ and $\mu = 1.4\gamma_{55}$. $u = u_1(x_2)/u_1$ (b).

In this case, in the same frequency and wave number range as in Fig. 4.19 (a), there are three branches of dispersion curves as shown in Fig. 4.20 (a). When $Z = 2$, the corresponding displacement fields of the first three waves are shown in Fig. 4.20 (b). The three waves have zero, one and two nodal points along the plate thickness, respectively.

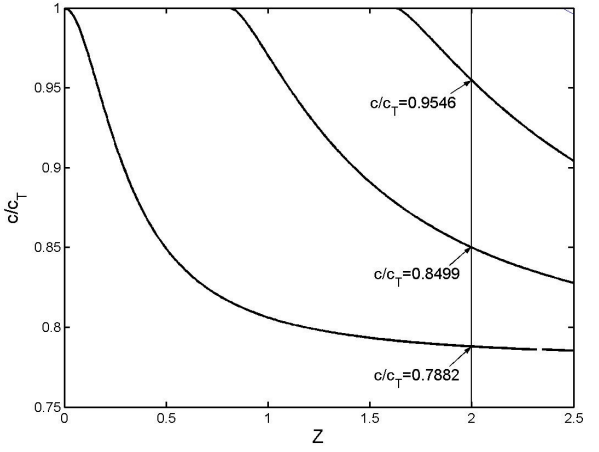

(a)

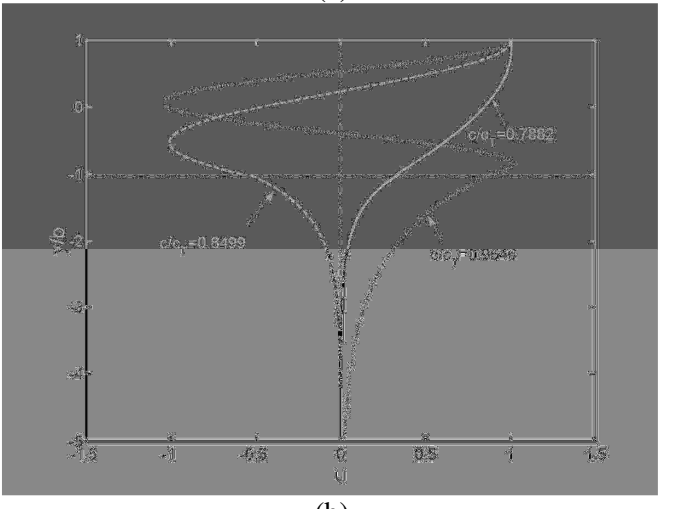

(b)

Fig. 4.20. Dispersion curves and mode shapes when when $c_Q = 0.78c_T$ and $\mu = 1.8\gamma_{55}$. $u = u_1(x_2)/u_1$ (b).

4.11. Plate in Contact with a Fluid

Propagation of face-shear and thickness-twist waves in a crystal plate in contact with a semi-infinite viscous fluid (see Fig. 4.21) was analyzed in [58].

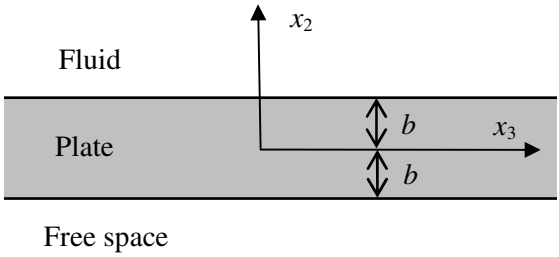

Fig. 4.21. A crystal plate in contact with a semi-infinite viscous fluid.

4.11.1. Dispersion relation

The displacement field in the crystal plate is (see Eq. (4.45)):

$$u_1 = (A\sin\eta y + C\cos\eta y)\cos\zeta\left(\frac{c_{56}}{c_{66}}y - z\right). \tag{4.145}$$

For Eq. (4.145) to satisfy the equation of motion in Eq. (4.4), we still have Eq. (4.13):

$$\rho\omega^2 = c_{66}\eta^2 + \gamma_{55}\zeta^2. \tag{4.146}$$

The stress component relevant to boundary and interface conditions is (see Eq. (4.46)):

$$T_6 = c_{66}\eta(A\cos\eta y - C\sin\eta y)\cos\zeta\left(\frac{c_{56}}{c_{66}}y - z\right). \tag{4.147}$$

The shear-horizontal velocity component in the fluid is governed by [21]

$$T_{21,2} + T_{31,3} = \rho_L \dot{v}_1 , \tag{4.148}$$

where ρ_L is the mass density of the fluid. v_1, T_{21}, and T_{31} are the relevant velocity and shear stress components. The shear stresses are related to the velocity gradients through [21]

$$T_{21} = \mu \frac{\partial v_1}{\partial x_2}, \quad T_{31} = \mu \frac{\partial v_1}{\partial x_3} , \tag{4.149}$$

where μ is the viscosity of the fluid. Substitution of the stresses in Eq. (4.149) into Eq. (4.148) gives

$$\mu(v_{1,22} + v_{1,33}) = \rho_L \dot{v}_1 . \tag{4.150}$$

Consider the following wave:

$$v_1 = \bar{C} \exp\left[-\lambda(y-b)\right] \cos\left[\zeta\left(\frac{c_{56}}{c_{66}} b - z\right)\right] \exp(i\omega t) , \tag{4.151}$$

where $\bar{C}$ is an undetermined constant. Equation (4.151) satisfies Eq. (4.150) provided that λ is determined from

$$\mu(\lambda^2 - \zeta^2) = i\omega\rho_L . \tag{4.152}$$

There are two complex roots for λ from Eq. (4.152). The one with a positive real part is taken so that the shear velocity field decays for large y. The stress component needed in the interface condition is given by

$$T_{21} = \mu \frac{\partial v_1}{\partial x_2} = -\mu\lambda\bar{C} \exp\left[-\lambda(y-b)\right] \cos\left[\zeta\left(\frac{c_{56}}{c_{66}} b - z\right)\right] \exp(i\omega t) . \tag{4.153}$$

At the interface between the fluid and the crystal plate the continuity of the velocity component v_1 and the shear stress component T_{21} must be

satisfied. The bottom of the crystal plate is traction-free. Therefore, we impose the following boundary and continuity conditions:

$$\begin{aligned} &v_1(b^+) = i\omega u_1(b^-), \\ &T_{21}(b^+) = T_{21}(b^-), \\ &T_{21}(-b) = 0. \end{aligned} \tag{4.154}$$

Substitution of Eqs. (4.145), (4.147), (4.151) and (4.153) into Eq. (4.154) results in three linear homogeneous equations for A, C and $\bar{C}$:

$$\begin{aligned} &\bar{C} = i\omega[A\sin(\eta b) + C\cos(\eta b)], \\ &-\mu\lambda\bar{C} = c_{66}\eta[A\cos(\eta b) - C\sin(\eta b)], \\ &A\cos(\eta b) + C\sin(\eta b) = 0. \end{aligned} \tag{4.155}$$

For nontrivial solutions the determinant of the coefficient matrix of Eq. (4.155) has to vanish, which leads to

$$\tan(2\eta b) = i\frac{\mu\lambda\omega}{c_{66}\eta}. \tag{4.156}$$

Together with Eqs. (4.146) and (4.152), Eq. (4.156) determines the dispersion relation of ω versus ζ. We consider the case when ω is real. The corresponding ζ determined from Eq. (4.156) will be complex in general.

4.11.2. Special case: a plate without fluid

For comparison we begin with the case when the fluid is not present or when the fluid viscosity $\mu = 0$ in a way more general than that in Sections 4.2 and 4.3 with consideration of imaginary wave numbers. When $\mu = 0$ the roots of Eq. (4.156) are determined by $\sin(2\eta b) = 0$ or $2\eta b = m\pi$, $m = 0, 1, 2, \cdots$. Then from Eq. (4.146) we obtain the following dispersion relation:

$$\rho\omega^2 = \rho m^2\omega_s^2 + \gamma_{55}\zeta^2, \quad \omega_s^2 = \frac{\pi^2 c_{66}}{4\rho b^2}. \tag{4.157}$$

With the introduction of the following dimensionless frequency Ω and dimensionless wave number Z:

$$\Omega = \frac{\omega}{\omega_s}, \quad Z = \sqrt{\frac{\gamma_{55}}{c_{66}}} \frac{2\zeta b}{\pi}, \tag{4.158}$$

Equation (4.157) can be written as

$$\Omega^2 = m^2 + Z^2 . \tag{4.159}$$

Equation (4.159) is plotted in Fig. 4.22 as a reference. When Ω is real, the dispersion curves are piecewise planar, either in the real plane with Im(Z) = 0 or in the imaginary plane with Re(Z) = 0.

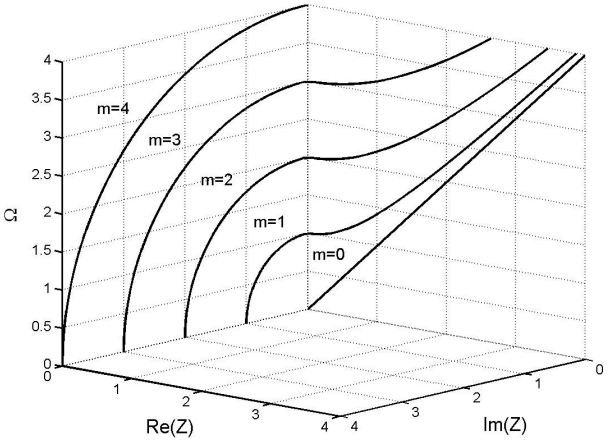

Fig. 4.22. Dispersion curves of FS and TT waves when the fluid is not present.

4.11.3. Low viscosity fluid

When the viscosity of the fluid is small, the effect of the fluid is a small perturbation of the dispersion relations of the plate itself without

the fluid. For a given ω, the corresponding ζ is slightly perturbed from what is given in Eq. (4.157) due to the small viscosity. We write

$$\zeta^2 = \frac{\rho}{\gamma_{55}}\left(\omega^2 - m^2\omega_s^2\right) + \Delta, \tag{4.160}$$

where Δ is small. We try to determine Δ next. First, from Eqs. (4.146) and (4.152), using Eq. (4.160), we obtain

$$\eta \cong \frac{m\pi}{2b}\left(1 - \frac{2\gamma_{55}b^2}{c_{66}m^2\pi^2}\Delta\right), \tag{4.161}$$

$$\lambda \cong \sqrt{\frac{i\omega\rho_L}{\mu} + \frac{\rho\omega^2}{\gamma_{55}} - \frac{\rho m^2\omega_s^2}{\gamma_{55}}}\left(1 + \frac{\Delta}{2\left(\frac{i\omega\rho_L}{\mu} + \frac{\rho\omega^2}{\gamma_{55}} - \frac{\rho m^2\omega_s^2}{\gamma_{55}}\right)}\right). \tag{4.162}$$

Substitution of Eqs. (4.161) and (4.162) into Eq. (4.156), for small Δ, we obtain

$$\Delta \cong -\frac{i\omega^{3/2}}{b\gamma_{55}}\sqrt{i\mu\rho_L}\,. \tag{4.163}$$

With Δ given by Eq. (4.163), from Eq. (4.160) we obtain the following approximate dispersion relation for small μ:

$$\zeta^2 = \frac{\rho}{\gamma_{55}}\left(\omega^2 - m^2\omega_s^2\right) - \frac{i\omega^{3/2}}{b\gamma_{55}}\sqrt{i\mu\rho_L}\,. \tag{4.164}$$

Equation (4.164) shows that the fluid makes the dispersion relation complex, causing both wave attenuation and additional dispersion.

For the special case of $m = 0$, a separate treatment is needed. The result is

$$\Delta \cong -\frac{i\omega^{3/2}}{2b\gamma_{55}}\sqrt{i\mu\rho_L}\,, \tag{4.165}$$

$$\zeta^2 = \frac{\rho\omega^2}{\gamma_{55}} - \frac{i\omega^{3/2}}{2b\gamma_{55}}\sqrt{i\mu\rho_L}\ . \tag{4.166}$$

Equations (4.164) and (4.166) can be written in the following dimensionless form:

$$Z^2 = \Omega^2 + \frac{A}{2}\Omega^{3/2}, \quad m=0, \tag{4.167}$$

$$Z^2 = \Omega^2 - m^2 + A\Omega^{3/2}, \quad m>0, \tag{4.168}$$

where

$$A = \frac{\sqrt{2}}{\pi}(1-i)\left(\frac{\mu\rho_L\omega_s}{c_{66}\rho}\right)^{1/2}. \tag{4.169}$$

A is a dimensionless combination of geometric and physical parameters. The low-viscosity approximation is valid when A is small and the $\Omega^{3/2}$ term associated with A represents small modifications in Eqs. (4.167) and (4.168). Equations (4.167) and (4.168) are convenient for calculating Z given Ω. Since A is very small for a low viscosity fluid, as an approximation, we can use Eq. (4.159) to express the $\Omega^{3/2}$ term on the right-hand side of Eq. (4.167) or (4.168) in terms of Z and m. The resulting equations will be convenient for calculating Ω given Z.

Consider a numerical example. The crystal plate is made of AT-cut quartz. For the fluid we choose chloroform with $\rho_L = 1.489\times10^3$ kg/m^3 and a relatively low viscosity of μ = 0.542 mPa·s which is smaller than the viscosity of water. The corresponding $A = 6.1433\times10^{-6}(1-i)/\sqrt{2}$ which is indeed very small and its effect on the dispersion curves is not visible if plotted in a manner similar to Fig. 4.22. To see the effect qualitatively we artificially enlarge A by a factor of 10^5 and use the resulting $A = 6.1433\times10^{-1}(1-i)/\sqrt{2}$ to plot the dispersion curves determined by Eqs. (4.167) and (4.168) in Fig. 4.23. Figure 4.23 (a) is viewed from the same angle as in Fig. 4.22. If we rotate Fig. 4.23 (a) into Fig. 4.23 (b), it shows clearly that the dispersion curves are three-dimensional spatial curves, showing wave attenuation or damped waves.

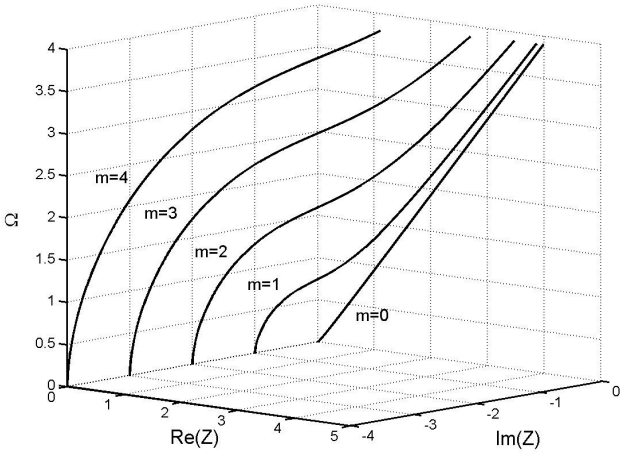

(a)

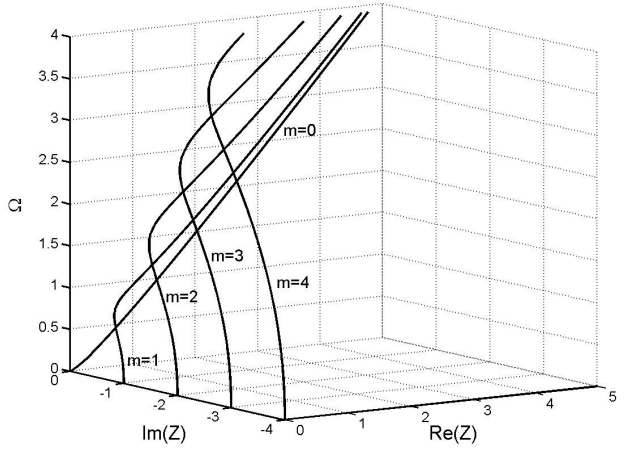

(b)

Fig. 4.23. Effect of fluid on dispersion relation viewed from different angles (exaggerated).

Figure 4.24 shows the effect of the fluid on wave frequencies for chloroform using the true $A = 6.1433\times10^{-6}(1-i)/\sqrt{2}$. In the figure, for a

real Z, $\Delta\Omega$ is the difference between the real part of the complex frequency from Eq. (4.167) or (4.168) and the real frequency from Eq. (4.159), normalized by the real frequency from Eq. (4.159). Therefore Fig. 4.24 shows the relative frequency shift caused by the fluid. The frequency shift is negative, showing that the fluid viscosity lowers the frequency as expected. The frequency shift is not sensitive to Z except in the case of $m = 0$ for which $\Omega \to 0$ when $Z \to 0$. The frequency shift is of the order of 10^{-6}.

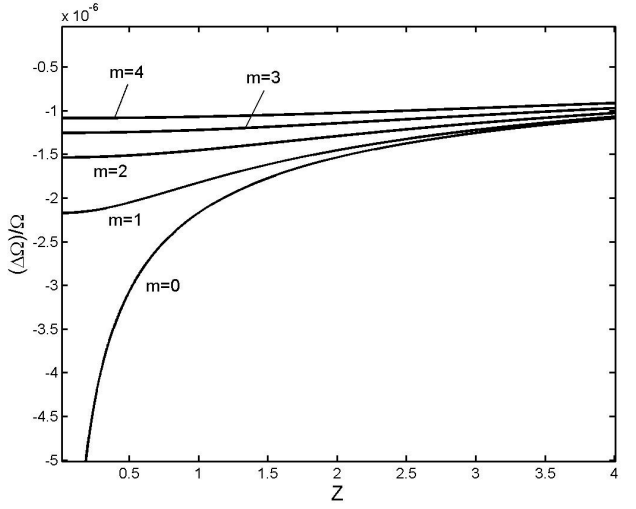

Fig. 4.24. Effect of fluid on wave frequency.

4.11.4. Long-wave approximation

Next we try to obtain an approximate solution to Eq. (4.156) for long waves with a small ζ. The face-shear wave and the thickness-twist waves need to be treated separately.

Consider the face-shear wave first. From Fig. 4.22 it can be seen that when ζ is small, ω is also small and is of the same order as ζ. Then from Eq. (4.146) η is also small. In this case, it can be shown that

Eq. (4.156) can be approximated by

$$\left(2b\gamma_{55}+\frac{\mu^{3/2}}{2}\sqrt{\frac{i\omega}{\rho_L}}\right)\zeta^2=2b\rho\omega^2-i\omega\sqrt{i\mu\omega\rho_L}\,. \tag{4.170}$$

For thickness-twist waves, when ζ approaches zero, ω approaches nonzero cutoff frequencies. In this case, it can be shown that that Eq. (4.156) can be approximated by

$$\begin{aligned}&\left[\frac{\gamma_{55}}{2}\sqrt{\frac{c_{66}}{\rho\omega^2}}\tan\left(2b\sqrt{\frac{\rho\omega^2}{c_{66}}}\right)+\frac{b\gamma_{55}}{\cos^2\left(2b\sqrt{\frac{\rho\omega^2}{c_{66}}}\right)}+\frac{\mu^{3/2}}{2}\sqrt{\frac{i\omega}{\rho_L}}\right]\zeta^2\\&=\sqrt{c_{66}\rho\omega^2}\tan\left(2b\sqrt{\frac{\rho\omega^2}{c_{66}}}\right)-i\omega\sqrt{i\mu\omega\rho_L}\,.\end{aligned} \tag{4.171}$$

When ζ = 0, Eq. (4.171) reduces to Eq. (2.71). In Eqs. (4.170) and (4.171), we further make the following two approximations. One is that since ζ is small, in the terms associated with ζ^2 we set $\omega\cong m\omega_s$. The other is that in those terms that are independent of ζ we write

$$\omega\cong m\omega_s+\Delta\omega\,. \tag{4.172}$$

Then, from Eqs. (4.170) and (4.171), for small $\Delta\omega$, we can determine an expression of $\Delta\omega$ which gives the following expressions of the long-wave approximation:

$$\zeta^2=\frac{2\rho}{\gamma_{55}}\omega^2-i^{3/2}\frac{\sqrt{\mu\rho_L}}{b\gamma_{55}}\omega^{3/2}\,,\quad m=0, \tag{4.173}$$

$$\omega=m\omega_s+\frac{\left(b\gamma_{55}+\frac{1}{2}\mu^{3/2}\sqrt{\frac{im\omega_s}{\rho_L}}\right)\zeta^2+(im\omega_s)^{3/2}(\mu\rho_L)^{1/2}}{2bm\omega_s\rho-\frac{3}{2}i^{3/2}\sqrt{\mu\rho_L m\omega_s}}, \tag{4.174}$$

$m>0$.

Dispersion curves determined by Eqs. (4.173) and (4.174) are plotted in Fig. 4.25. Since the viscosity of chloroform is small, we use Eq. (4.159) for the case when the fluid is not present for comparison as shown by the dotted lines. The figure shows that for $m>0$ the long wave approximation represented by the solid lines agree with the dotted lines for small Z and the range of agreement increases with m. In the special case of $m = 0$ the long-wave approximation in Eq. (4.173) has a different slope from Eq. (4.159). This is because the viscosity term in Eq. (4.173) has a power of $\omega^{3/2}$ which dominates the ω^2 term for small ω, causing the difference when $m = 0$.

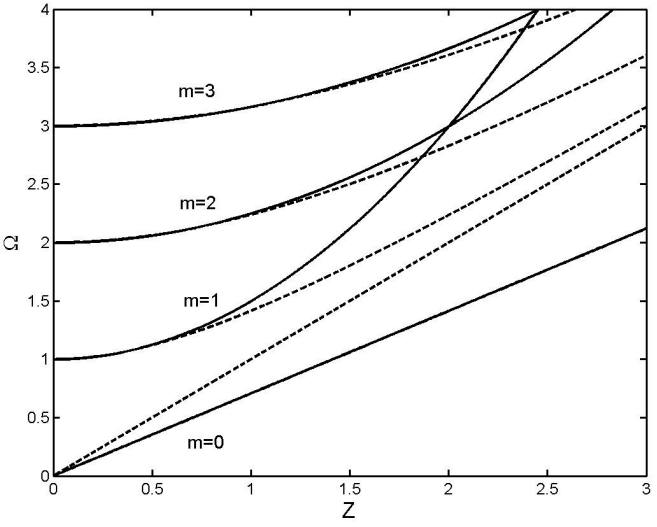

Fig. 4.25. Long-wave approximation (solid lines).

4.12. Effect of Piezoelectric Coupling

In all of the previous sections of this chapter, the theory of anisotropic elasticity was used because of the weak piezoelectric coupling in quartz. In this section we use the theory of linear piezoelectricity to study the propagation of face-shear and thickness-twist waves in piezoelectric plates of monoclinic crystals [59].

4.12.1. Governing equations

Consider the following fields in the plate of monoclinic crystals shown in Fig. 4.26:

$$\begin{aligned} &u_1 = u_1(x_2, x_3, t), \quad u_2 = u_3 = 0, \\ &\phi = \phi(x_2, x_3, t). \end{aligned} \tag{4.175}$$

The equations to be satisfied by u_1 and ϕ are (see Eq. (1.107)):

$$\begin{aligned} &c_{66}u_{1,22} + c_{55}u_{1,33} + 2c_{56}u_{1,23} \\ &\quad + e_{26}\phi_{,22} + e_{35}\phi_{,33} + (e_{25} + e_{36})\phi_{,23} = \rho\ddot{u}_1, \\ &e_{26}u_{1,22} + e_{35}u_{1,33} + (e_{25} + e_{36})u_{1,23} \\ &\quad - \varepsilon_{22}\phi_{,22} - \varepsilon_{33}\phi_{,33} - 2\varepsilon_{23}\phi_{,23} = 0. \end{aligned} \tag{4.176}$$

Once u_1 and ϕ are known, the nonzero components of the strain tensor **S**, the electric field vector **E**, the stress tensor **T**, and the electric displacement vector **D** can be calculated from (see Eq. (1.106)):

$$\begin{aligned} &S_5 = u_{1,3}, \quad S_6 = u_{1,2}, \\ &E_2 = -\phi_{,2}, \quad E_3 = -\phi_{,3}, \\ &T_{31} = c_{55}u_{1,3} + c_{56}u_{1,2} + e_{25}\phi_{,2} + e_{35}\phi_{,3}, \\ &T_{21} = c_{56}u_{1,3} + c_{66}u_{1,2} + e_{26}\phi_{,2} + e_{36}\phi_{,3}, \\ &D_2 = e_{25}u_{1,3} + e_{26}u_{1,2} - \varepsilon_{22}\phi_{,2} - \varepsilon_{23}\phi_{,3}, \\ &D_3 = e_{35}u_{1,3} + e_{36}u_{1,2} - \varepsilon_{23}\phi_{,2} - \varepsilon_{33}\phi_{,3}. \end{aligned} \tag{4.177}$$

The two surfaces of the plate are assumed to be traction free. For an electroded plate with shorted electrodes, we have

$$T_{21} = 0, \quad \phi = 0, \quad x_2 = \pm h. \tag{4.178}$$

When the plate is unelectroded, Eq. (4.178) is replaced by

$$T_{21} = 0, \quad D_2 = 0, \quad x_2 = \pm h. \tag{4.179}$$

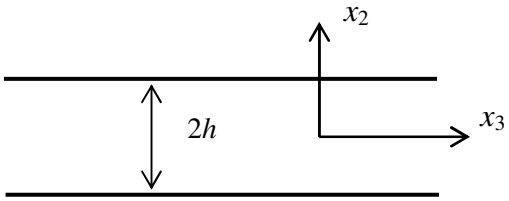

Fig. 4.26. A piezoelectric plate and coordinate system.

4.12.2. Propagating wave solution

We study the following waves propagating in the x_3 direction:

$$\begin{aligned} u_1 &= A\exp(i\eta y)\exp[i(\varsigma z - \omega t)], \\ \phi &= B\exp(i\eta y)\exp[i(\varsigma z - \omega t)], \end{aligned} \tag{4.180}$$

where $y = x_2$ and $z = x_3$. Substitution of Eq. (4.180) into Eq. (4.176) gives

$$\begin{aligned} &-(c_{66}\eta^2 + c_{55}\varsigma^2 + 2c_{56}\eta\varsigma)A \\ &\quad -[e_{26}\eta^2 + e_{35}\varsigma^2 + (e_{25} + e_{36})\eta\varsigma]B = -\rho\omega^2 A, \\ &-[e_{26}\eta^2 + e_{35}\varsigma^2 + (e_{25} + e_{36})\eta\varsigma]A \\ &\quad +(\varepsilon_{22}\eta^2 + \varepsilon_{33}\varsigma^2 + 2\varepsilon_{23}\eta\varsigma)B = 0. \end{aligned} \tag{4.181}$$

Equation (4.181) is a system of linear homogeneous equations of A and B. For nontrivial solutions of A and/or B, the determinant of the coefficient matrix of Eq. (4.181) has to vanish, which implies that

$$\begin{aligned} &(c_{66}\eta^2 + c_{55}\varsigma^2 + 2c_{56}\eta\varsigma - \rho\omega^2) \\ &\quad \times(\varepsilon_{22}\eta^2 + \varepsilon_{33}\varsigma^2 + 2\varepsilon_{23}\eta\varsigma) \\ &\quad = -[e_{26}\eta^2 + e_{35}\varsigma^2 + (e_{25} + e_{36})\eta\varsigma]^2. \end{aligned} \tag{4.182}$$

Equation (4.182) determines four roots for $\eta = \eta(\omega, \varsigma)$, which are denoted by $\eta_{(m)}$ with m = 1, 2, 3, and 4. The corresponding amplitude ratios are obtained from Eq. $(4.181)_2$ as

$$\beta = \frac{B}{A} = \frac{e_{26}\eta^2 + e_{35}\varsigma^2 + (e_{25} + e_{36})\eta\varsigma}{\varepsilon_{22}\eta^2 + \varepsilon_{33}\varsigma^2 + 2\varepsilon_{23}\eta\varsigma}. \tag{4.183}$$

Then the general solution to Eq. (4.176) in the form of Eq. (4.180) can be written as

$$\begin{aligned} u_1 &= \sum_{m=1}^{4} A_{(m)} \exp[i\eta_{(m)} y]\exp[i(\varsigma z - \omega t)], \\ \phi &= \sum_{m=1}^{4} A_{(m)}\beta_{(m)} \exp[i\eta_{(m)} y]\exp[i(\varsigma z - \omega t)], \end{aligned} \tag{4.184}$$

where $A_{(m)}$ are undetermined constants, and $\beta_{(m)}$ is obtained by substituting $\eta_{(m)}$ into Eq. (4.183).

For an electroded plate, we substitute Eq. (4.184) into Eq. (4.178) and obtain

$$\begin{aligned} &\sum_{m=1}^{4} (c_{56}\varsigma + c_{66}\eta_{(m)} + e_{26}\eta_{(m)}\beta_{(m)} + e_{36}\beta_{(m)}\varsigma) \\ &\quad \times A_{(m)} \exp[i\eta_{(m)} h] = 0, \\ &\sum_{m=1}^{4} (c_{56}\varsigma + c_{66}\eta_{(m)} + e_{26}\eta_{(m)}\beta_{(m)} + e_{36}\beta_{(m)}\varsigma) \\ &\quad \times A_{(m)} \exp[-i\eta_{(m)} h] = 0, \\ &\sum_{m=1}^{4} A_{(m)}\beta_{(m)} \exp[i\eta_{(m)} h] = 0, \\ &\sum_{m=1}^{4} A_{(m)}\beta_{(m)} \exp[-i\eta_{(m)} h] = 0. \end{aligned} \tag{4.185}$$

For nontrivial solutions of $A_{(m)}$, the determinant of the coefficient matrix of Eq. (4.185) has to vanish, which yields the frequency equation that determines the dispersion relations of ω versus ς.

Similarly, for an unelectroded plate, we substitute Eq. (4.184) into Eq. (4.179) and obtain four equations similar to Eq. (4.185) from which the corresponding dispersion relations can be determined.

4.12.3. Numerical results and discussion

We plot the dispersion relations of face-shear and thickness-twist waves determined from Eq. (4.185) in an electroded AT-cut quartz plate in Fig. 4.27 (a) by dotted lines where the normalized frequency and wave number are defined by:

$$\Omega = \frac{\omega}{\omega_s}, \quad \omega_s^2 = \frac{c_{66}}{\rho}\left(\frac{\pi}{2h}\right)^2, \qquad Z = \sqrt{\frac{\gamma_{55}}{c_{66}}}\frac{2\varsigma h}{\pi}, \quad \gamma_{55} = c_{55} - \frac{c_{56}^2}{c_{66}}. \tag{4.186}$$

In Fig. 4.27 (a), for comparison, we also plot using solid lines the dispersion relations of the same waves determined from the elastic analyses in Sections 4.2 and 4.3. The dotted lines and the solid lines almost coincide with each other. The dotted lines are slightly higher because of the piezoelectric stiffening effect. The number of branches of the dispersion relations is infinite. Only the lowest five branches are shown. The one that goes through the origin is the face-shear wave and is called a low-frequency wave. The rest are thickness-twist waves. They have finite intercepts with the frequency axis and are classified as high-frequency waves. The intercepts are called cutoff frequencies below which the corresponding waves cannot propagate. The requirements on the resonant frequencies of crystal resonators are usually in terms of ppm (parts per million). Although the dotted lines in Fig. 4.27 (a) from a piezoelectric analysis and the solid lines from an elastic analysis seem to be very close, we want to examine them in more detail quantitatively. Therefore, in Fig. 4.27 (b), we plot the normalized difference between the exact and approximate dispersion relations. As $\Delta\Omega$ increases from zero, the five curves in Fig. 4.27 (b) are in the same sequence as the corresponding curves in Fig. 4.27 (a). In other words, lower-order waves have smaller normalized frequency difference. The normalized frequency

difference is of the order of 1%. For a typical resonator with a resonant frequency of 10 MHz, this translates into 10^5 Hz and is a very large frequency difference.

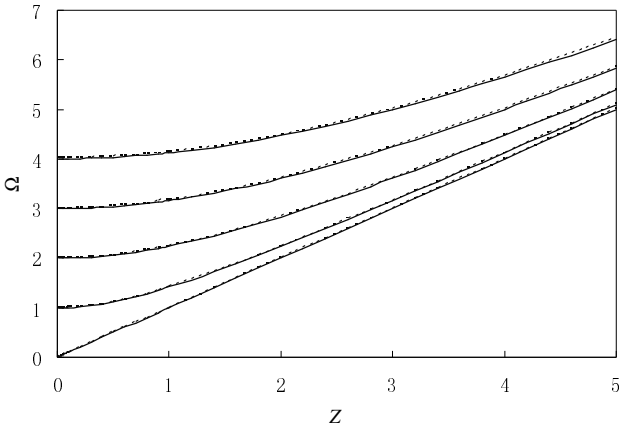

(a)

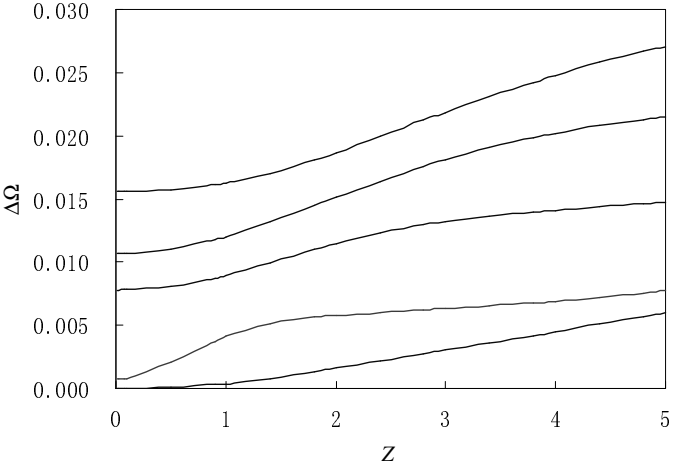

(b)

Fig. 4.27. Waves in an electroded AT-cut quartz plate. (a) Dispersion relations. (b) Difference between piezoelectric and elastic analyses.

The case of an unelectroded quartz plate is shown in Fig. 4.28, which is similar to Fig. 4.27.

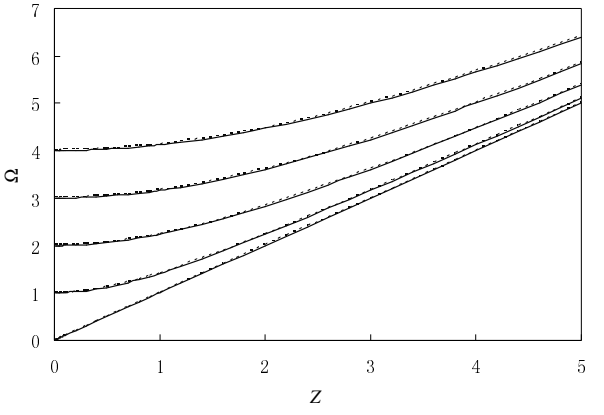

(a)

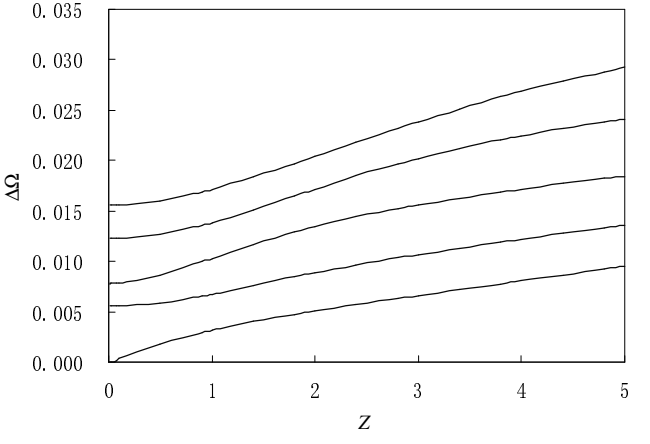

(b)

Fig. 4.28. Waves in an unelectroded AT-cut quartz plate. (a) Dispersion relations. (b) Difference between piezoelectric and elastic analyses.

Figures 4.29 and 4.30 show the corresponding results for Y-cut langasite plates. The dispersion relations in Figs. 4.29 (a) and 4.30 (a) are qualitatively the same as those in Figs. 4.27 (a) and 4.28 (a). Since langasite has stronger piezoelectric couplings than quartz, the frequency difference between the piezoelectric and elastic analyses in Figs. 4.29 (b) and 4.30 (b) is a few times larger than those in Figs. 4.27 (b) and 4.28 (b) for long waves with small values of *Z*. In Figs. 4.29 (b) and 4.30 (b) the curves for the face-shear waves almost coincide with the horizontal axis.

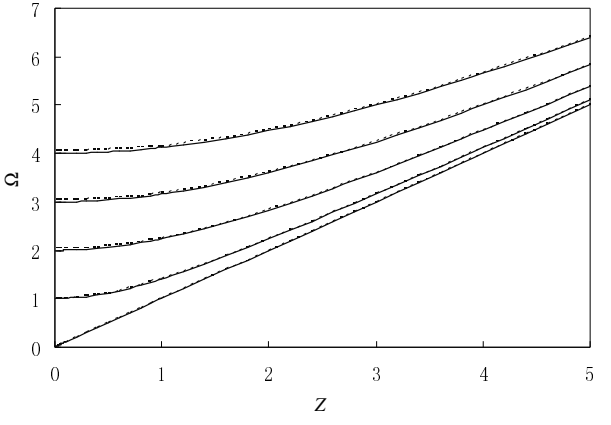

(a)

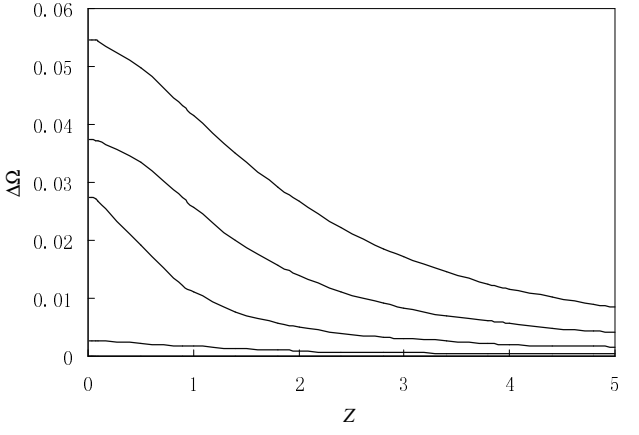

(b)

Fig. 4.29. Waves in an electroded Y-cut langasite plate. (a) Dispersion relations. (b) Difference between piezoelectric and elastic analyses.

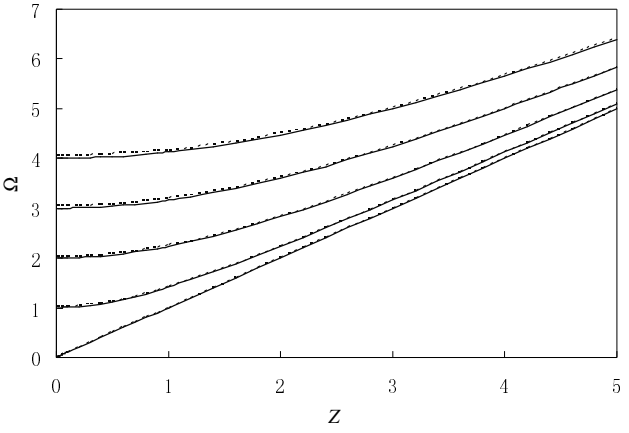

(a)

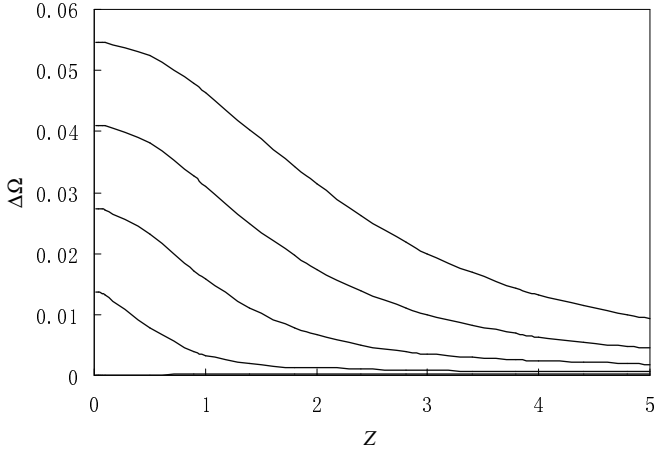

(b)

Fig. 4.30. Waves in an unelectroded Y-cut langasite plate. (a) Dispersion relations. (b) Difference between piezoelectric and elastic analyses.

Chapter 5

Shear-horizontal Vibrations of Finite Plates

In this chapter, we will be analyzing the shear-horizontal vibrations of finite plates. The first section presents an exact solution of the equations of anisotropic elasticity for a plate with tilted edges. For AT-cut quartz plates, $c_{55} = 68.81$, $c_{56} = 2.53$, and $c_{66} = 29.01 \times 10^9$ N/m^2. c_{56} is very small compared to c_{55} and c_{66}. Therefore, in Sections 5.2–5.9, 5.11 and 5.12, the small c_{56} is neglected which is a common approximation in the analysis of AT-cut quartz plates. There are other theoretical results in the literature with additional approximations [60-62]. Section 5.10 is on plates of isotropic materials.

5.1. Plate with Tilted Edges

For a monoclinic crystal plate finite in the x_3 direction, exact modes can be obtained when the plate has a pair of tilted edges (see Fig. 5.1) [63].

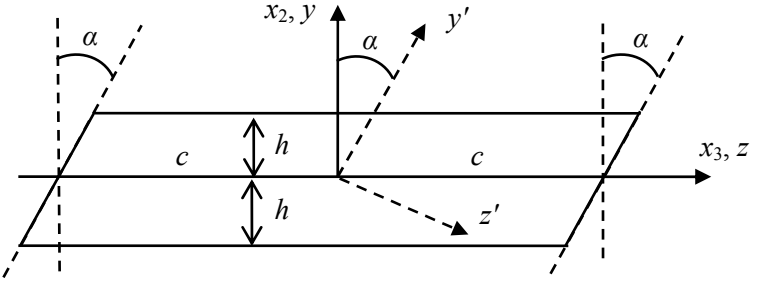

Fig. 5.1. A crystal plate with tilted edges.

Consider the following displacement field:

$$\begin{aligned} u_1 = & A\sin\eta y\cos\zeta\left(\frac{c_{56}}{c_{66}}y - z\right) + B\sin\eta y\sin\zeta\left(\frac{c_{56}}{c_{66}}y - z\right) \\ & + C\cos\eta y\cos\zeta\left(\frac{c_{56}}{c_{66}}y - z\right) + D\cos\eta y\sin\zeta\left(\frac{c_{56}}{c_{66}}y - z\right). \end{aligned} \tag{5.1}$$

For Eq. (5.1) to satisfy the equation of motion in Eq. (4.4), we still have Eq. (4.13):

$$\rho\omega^2 = c_{66}\eta^2 + \gamma_{55}\zeta^2 . \tag{5.2}$$

The stress components corresponding to Eq. (5.1) are

$$\begin{aligned} T_5 = & \gamma_{55}\zeta A\sin\eta y\sin\zeta\left(\frac{c_{56}}{c_{66}}y - z\right) + c_{56}\eta A\cos\eta y\cos\zeta\left(\frac{c_{56}}{c_{66}}y - z\right) \\ & - \gamma_{55}\zeta B\sin\eta y\cos\zeta\left(\frac{c_{56}}{c_{66}}y - z\right) + c_{56}\eta B\cos\eta y\sin\zeta\left(\frac{c_{56}}{c_{66}}y - z\right) \\ & + \gamma_{55}\zeta C\cos\eta y\sin\zeta\left(\frac{c_{56}}{c_{66}}y - z\right) - c_{56}\eta C\sin\eta y\cos\zeta\left(\frac{c_{56}}{c_{66}}y - z\right) \\ & - \gamma_{55}\zeta D\cos\eta y\cos\zeta\left(\frac{c_{56}}{c_{66}}y - z\right) - c_{56}\eta D\sin\eta y\sin\zeta\left(\frac{c_{56}}{c_{66}}y - z\right), \end{aligned} \tag{5.3}$$

$$\begin{aligned} T_6 = & c_{66}\eta A\cos\eta y\cos\zeta\left(\frac{c_{56}}{c_{66}}y - z\right) + c_{66}\eta B\cos\eta y\sin\zeta\left(\frac{c_{56}}{c_{66}}y - z\right) \\ & - c_{66}\eta C\sin\eta y\cos\zeta\left(\frac{c_{56}}{c_{66}}y - z\right) - c_{66}\eta D\sin\eta y\sin\zeta\left(\frac{c_{56}}{c_{66}}y - z\right). \end{aligned} \tag{5.4}$$

For Eq. (5.4) to satisfy the traction-free boundary conditions at $y = \pm h$, we have

$$\eta h = m\pi/2 , \tag{5.5}$$

where m is an odd integer for solutions A and B and an even integer (including zero which corresponds to a face-shear mode) for solutions C and D. For the boundary conditions at the tiled edges, we transform the relevant stress components into the (y',z') system in which the tilted edges are at $z' = \pm c\cos\alpha$:

$$\begin{aligned} &T_1' = T_2' = T_3' = T_4' = 0, \\ &T_5' = T_5\cos\alpha - T_6\sin\alpha, \\ &T_6' = T_5\sin\alpha + T_6\cos\alpha. \end{aligned} \tag{5.6}$$

The boundary conditions at $z' = \pm c\cos\alpha$ are $T_5' = 0$. Substitution of Eqs. (5.3) and (5.4) into Eq. $(5.6)_2$ gives

$$\begin{aligned} T_5' = {} & A\eta(c_{56}\cos\alpha - c_{66}\sin\alpha)\cos\eta y\cos\zeta\left(\frac{c_{56}}{c_{66}}y - z\right) \\ & + A\zeta\gamma_{55}\cos\alpha\sin\eta y\sin\zeta\left(\frac{c_{56}}{c_{66}}y - z\right) \\ & + B\eta(c_{56}\cos\alpha - c_{66}\sin\alpha)\cos\eta y\sin\zeta\left(\frac{c_{56}}{c_{66}}y - z\right) \\ & - B\zeta\gamma_{55}\cos\alpha\sin\eta y\cos\zeta\left(\frac{c_{56}}{c_{66}}y - z\right) \\ & - C\eta(c_{56}\cos\alpha - c_{66}\sin\alpha)\sin\eta y\cos\zeta\left(\frac{c_{56}}{c_{66}}y - z\right) \\ & + C\zeta\gamma_{55}\cos\alpha\cos\eta y\sin\zeta\left(\frac{c_{56}}{c_{66}}y - z\right) \\ & - D\eta(c_{56}\cos\alpha - c_{66}\sin\alpha)\sin\eta y\sin\zeta\left(\frac{c_{56}}{c_{66}}y - z\right) \\ & - D\zeta\gamma_{55}\cos\alpha\cos\eta y\cos\zeta\left(\frac{c_{56}}{c_{66}}y - z\right). \end{aligned} \tag{5.7}$$

Consider the special case when the tilted edges are at a particular angle α determined by

$$\tan\alpha = \frac{c_{56}}{c_{66}}. \tag{5.8}$$

Then Eq. (5.7) simplifies into

$$\begin{aligned} T_5' = {} & A\zeta\gamma_{55}\cos\alpha\sin\eta y\sin\zeta\left(\frac{c_{56}}{c_{66}}y - z\right) \\ & - B\zeta\gamma_{55}\cos\alpha\sin\eta y\cos\zeta\left(\frac{c_{56}}{c_{66}}y - z\right) \\ & + C\zeta\gamma_{55}\cos\alpha\cos\eta y\sin\zeta\left(\frac{c_{56}}{c_{66}}y - z\right) \\ & - D\zeta\gamma_{55}\cos\alpha\cos\eta y\cos\zeta\left(\frac{c_{56}}{c_{66}}y - z\right). \end{aligned} \tag{5.9}$$

At the tilted edges where $z' = \pm c\cos\alpha$, we have

$$z = y\tan\alpha \pm c = \frac{c_{56}}{c_{66}}y \pm c. \tag{5.10}$$

Therefore, the traction-free boundary conditions at the tilted edges are

$$\begin{aligned} T_5' = {} & A\zeta\gamma_{55}\cos\alpha\sin\eta y\sin\zeta(\mp c) \\ & - B\zeta\gamma_{55}\cos\alpha\sin\eta y\cos\zeta(\mp c) \\ & + C\zeta\gamma_{55}\cos\alpha\cos\eta y\sin\zeta(\mp c) \\ & - D\zeta\gamma_{55}\cos\alpha\cos\eta y\cos\zeta(\mp c) = 0. \end{aligned} \tag{5.11}$$

Hence, it is apparent that $T_5' = 0$ at the tilted edges if

$$\zeta c = n\pi/2, \tag{5.12}$$

where n is an even integer (including zero which gives simple thickness-shear modes) for solutions A and C, and an odd integer for solutions B and D.

Upon substituting Eqs. (5.5) and (5.12) into Eqs. (5.1) and (5.2), we find the following simple solutions:

$$u_1 = A\sin\frac{m\pi y}{2h}\cos\frac{n\pi}{2c}\left(\frac{c_{56}}{c_{66}}y - z\right) + B\sin\frac{m\pi y}{2h}\sin\frac{n\pi}{2c}\left(\frac{c_{56}}{c_{66}}y - z\right)$$
$$+ C\cos\frac{m\pi y}{2h}\cos\frac{n\pi}{2c}\left(\frac{c_{56}}{c_{66}}y - z\right) + D\cos\frac{m\pi y}{2h}\sin\frac{n\pi}{2c}\left(\frac{c_{56}}{c_{66}}y - z\right), \tag{5.13}$$

with frequencies given by

$$\omega = \frac{m\pi}{2h}\left(\frac{c_{66}}{\rho}\right)^{1/2}\left(1 + \frac{\gamma_{55}n^2h^2}{c_{66}m^2c^2}\right)^{1/2}, \tag{5.14}$$

where m and n are odd or even integers, for solutions A, B, C, and D, according to

$$\begin{aligned} &A: \quad m \quad \text{odd}, \quad n \quad \text{even}, \\ &B: \quad m \quad \text{odd}, \quad n \quad \text{odd}, \\ &C: \quad m \quad \text{even}, \quad n \quad \text{even}, \\ &D: \quad m \quad \text{even}, \quad n \quad \text{odd}. \end{aligned} \tag{5.15}$$

For AT-cut quartz, from Eq. (5.8), $\alpha \cong 5^{\circ}$.

5.2. Unelectroded Plate

If the small c_{56} is neglected, $\alpha = 0$ from Eq. (5.8). Then the solution in the previous section is approximately valid for a rectangular plate (see Fig. 5.2) [64].

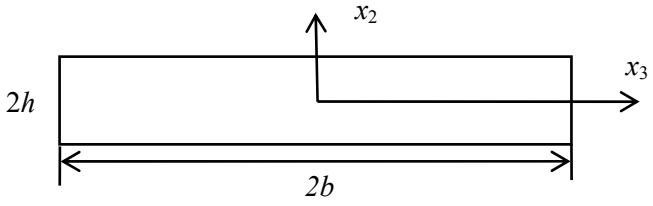

Fig. 5.2. An unelectroded plate.

When c_{56} is neglected the governing equation (see Eq. (4.4)) reduces to

$$c_{66}u_{1,22} + c_{55}u_{1,33} \cong \rho \ddot{u}_1 . \tag{5.16}$$

The approximate stress-strain relations are

$$T_{31} \cong c_{55}u_{1,3}, \quad T_{21} \cong c_{66}u_{1,2} . \tag{5.17}$$

For a traction-free plate, the boundary conditions are

$$T_{21} = 0, \quad x_2 = \pm h, \quad |x_3| < b , \tag{5.18}$$

$$T_{31} = 0, \quad x_3 = \pm b, \quad |x_2| < h . \tag{5.19}$$

The modes and frequencies can be obtained by setting $c_{56} \cong 0$ and $\gamma_{55} \cong c_{55}$ in Eqs. (5.13) and (5.14)

$$\begin{aligned} u_1 = {} & A \sin\frac{m\pi y}{2h}\cos\frac{n\pi z}{2b} + B \sin\frac{m\pi y}{2h}\sin\frac{n\pi z}{2b} \\ & + C \cos\frac{m\pi y}{2h}\cos\frac{n\pi z}{2b} + D \cos\frac{m\pi y}{2h}\sin\frac{n\pi z}{2b}, \end{aligned} \tag{5.20}$$

$$\omega = \frac{m\pi}{2h}\left(\frac{c_{66}}{\rho}\right)^{1/2}\left(1 + \frac{c_{55}n^2h^2}{c_{66}m^2b^2}\right)^{1/2}, \tag{5.21}$$

where m and n are odd or even integers according to Eq. (5.15). The first term on the right-hand side of Eq. (5.21) determines the cutoff frequencies of thickness-twist modes of different orders which are modes of unbounded plates. The second term on the right-hand side of Eq. (5.21) shows the effect of the finite size of the plate in the x_3 direction which raises the frequencies and disappears when $b \to \infty$.

5.3. Fully Electroded Plate

Consider the fully electroded crystal plate in Fig. 5.3 [64]. The two electrodes are identical. The density and thickness of the electrodes are ρ' and $2h'$.

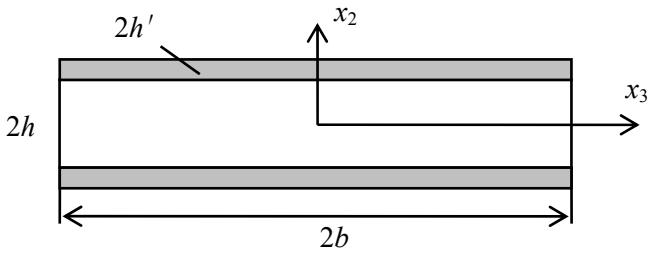

Fig. 5.3. A fully electroded plate.

The governing equation and boundary conditions are

$$c_{66}u_{1,22} + c_{55}u_{1,33} \cong \rho \ddot{u}_1, \quad |x_3| < b, \quad |x_2| < h, \tag{5.22}$$

$$T_{21} = \mp 2\rho' h' \ddot{u}_1, \quad x_2 = \pm h, \quad |x_3| < b, \tag{5.23}$$

$$T_{31} = 0, \quad x_3 = \pm b, \quad |x_2| < h. \tag{5.24}$$

The plate in Fig. 5.3 is symmetric in both x_2 and x_3. For resonator applications, we are interested in modes that are antisymmetric about the x_3 axis and symmetric about the x_2 axis. Therefore we construct the following solution that is odd in x_2 and even in x_3 from separation of

variables based on Eqs. (5.22) and (5.24):

$$u_1 = B_0 \sin(\eta_0 x_2) + \sum_{m=1}^{\infty} B_m \sin(\eta_m x_2) \cos\frac{m\pi x_3}{b}, \tag{5.25}$$

where B_0 and B_m are undetermined constants, and

$$\eta_m^2 = \frac{\rho\omega^2}{c_{66}} - \frac{c_{55}}{c_{66}}\left(\frac{m\pi}{b}\right)^2 = \frac{\pi^2}{4h^2}\left[\frac{\omega^2}{\omega_s^2} - \frac{c_{55}}{c_{66}}\left(m\frac{2h}{b}\right)^2\right], \tag{5.26}$$
$$m = 0,1,2,3,\cdots.$$

Equation (5.25) already satisfies Eqs. (5.22) and (5.24). It describes certain modes of interest for the symmetric structure in Fig. 5.3, but not all possible modes of the structure. Quartz resonators are usually with large length/thickness ratios, i.e., *b*>>*h*. In this case, for an *m* that is not large, η_m^2 is positive. We are interested in the first few face-shear and thickness-twist modes with no more than a couple of nodal points along the x_3 direction for which a large *m* is not needed. In the case when η_m^2 is nonpositive, the construction of the solution in Eq. (5.25) will be different. To apply the boundary conditions at the plate top and bottom, we need

$$\begin{aligned} T_{21} &= c_{66}u_{1,2} = c_{66}B_0\eta_0 \cos(\eta_0 x_2) \\ &+ c_{66}\sum_{m=1}^{\infty} B_m\eta_m \cos(\eta_m x_2)\cos\frac{m\pi x_3}{b}. \end{aligned} \tag{5.27}$$

Substitution of Eqs. (5.25) and (5.27) into Eq. (5.23) gives

$$\begin{aligned} &c_{66}B_0\eta_0 \cos(\eta_0 h) + c_{66}\sum_{m=1}^{\infty} B_m\eta_m \cos(\eta_m h)\cos\frac{m\pi x_3}{b} \\ &= 2\rho' h'\omega^2[B_0 \sin(\eta_0 h) + \sum_{m=1}^{\infty} B_m \sin(\eta_m h)\cos\frac{m\pi x_3}{b}]. \end{aligned} \tag{5.28}$$

Due to the antisymmetry involved, the boundary conditions at $x_2 = \pm h$ lead to the same equation as in Eq. (5.28). We multiply both sides of

Eq. (5.28) by $\cos(n\pi x_3/b)$ (n = 0, 1, 2, …) and integrate the resulting expression over (-b, b) to obtain

$$c_{66}B_n\eta_n\cos(\eta_n h)=2\rho' h'\omega^2 B_n\sin(\eta_n h),\quad n=0,1,2,\cdots. \tag{5.29}$$

For nontrivial solutions of B_n we must have

$$\cot(\eta_m h)=\frac{\pi^2}{4}\frac{R}{\eta_m h}\frac{\omega^2}{\omega_s^2},\quad m=0,1,2,\cdots, \tag{5.30}$$

where

$$\omega_s=\frac{\pi}{2h}\sqrt{\frac{c_{66}}{\rho}},\quad R=\frac{2\rho' h'}{\rho h}. \tag{5.31}$$

Solutions to Eq. (5.30) will be called "exact" in the rest of this section. We look for an approximate solution to Eq. (5.30) when the electrodes are thin and R is small. The lowest-order approximation when R = 0 is given by $\eta_m h=n\pi+\pi/2$, $n=0,1,2,\cdots$. For the next order of approximation we write [2]

$$\eta_m h=n\pi+\frac{\pi}{2}-\Delta_n,\quad n=0,1,2,\cdots, \tag{5.32}$$

where Δ_n is small. Substitution of Eq. (5.32) into Eq. (5.30), for small Δ_n and small R, we obtain

$$\Delta_n=\frac{\pi^2}{4}\frac{R}{n\pi+\dfrac{\pi}{2}}\left[(2n+1)^2+\frac{c_{55}}{c_{66}}\left(m\frac{2h}{b}\right)^2\right]. \tag{5.33}$$

Substitution of Eq. (5.33) into Eq. (5.32), with the use of Eq. (5.26), we have, approximately,

$$\frac{\omega_{mn}^2}{\omega_s^2}=(1-2R)\left[(2n+1)^2+\frac{c_{55}}{c_{66}}\left(m\frac{2h}{b}\right)^2\right]. \tag{5.34}$$

Equation (5.34) shows that the electrode inertia lowers the frequencies. When $R = 0$, Eq. (5.34) reduces to Eq. (5.21) for the frequencies of the A term in Eq. (5.20).

We plot the exact frequency ω_{mn}/ω_s determined by Eq. (5.30) and its approximation in Eq. (5.34) versus the plate aspect ratio h/b in Fig. 5.4. $n = 0$ is fixed. The thickness-shear mode ($m = 0$) and the first two thickness-twist modes ($m = 1, 2$) are shown when $R = 0.1$. In real applications R is much smaller. It is exaggerated so that the difference can be seen. The exact and the approximate solutions are very close and the frequency axis has to be stretched considerably to see the difference.

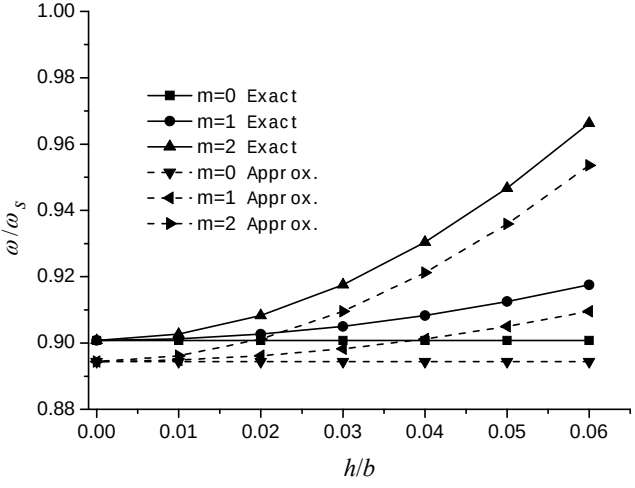

Fig. 5.4. Frequency versus plate aspect ratio: comparison between exact and approximate solutions ($n = 0$, $R = 0.1$).

In Fig. 5.5 we plot ω_{mn}/ω_s versus h/b from the approximate solution in Eq. (5.34) for different values of R. R lowers the frequencies as expected. The frequencies increase with h/b because shorter plates with a smaller b have higher frequencies when h is fixed. In the special case of $m = 0$ the frequency is independent of h/b. A larger m means shorter waves and hence higher frequencies.

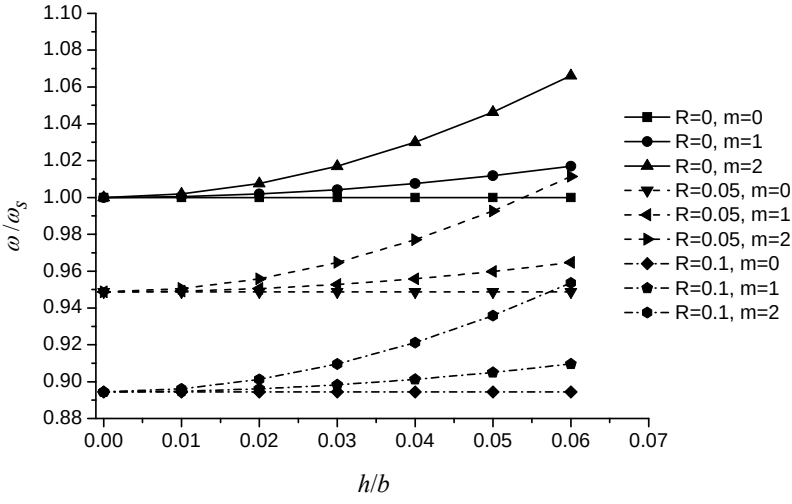

Fig. 5.5. Frequency versus plate aspect ratio: approximate solutions for different mass ratios ($n = 0$).

5.4. Partially Electroded Plate

Next, consider the case when the crystal plate is partially electroded with identical electrodes (see Fig. 5.6) [64].

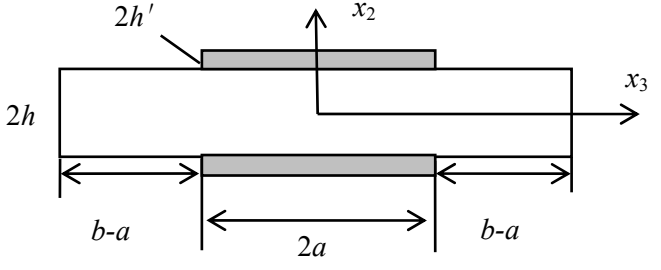

Fig. 5.6. A partially electroded crystal plate.

5.4.1. Fourier series solution

The governing equation and boundary conditions are

$$c_{66}u_{1,22} + c_{55}u_{1,33} \cong \rho \ddot{u}_1, \quad |x_3| < b, \quad |x_2| < h, \tag{5.35}$$

$$T_{21} = \begin{cases} \mp 2\rho' h' \ddot{u}_1, & x_2 = \pm h, \quad |x_3| < a, \\ 0, & x_2 = \pm h, \quad a < |x_3| < b, \end{cases} \tag{5.36}$$

$$T_{31} = 0, \quad x_3 = \pm b, \quad |x_2| < h. \tag{5.37}$$

Consider the following displacement field (see Eq. (5.25)):

$$u_1 = B_0 \sin(\eta_0 x_2) + \sum_{m=1}^{\infty} B_m \sin(\eta_m x_2) \cos\frac{m\pi x_3}{b}, \tag{5.38}$$

where (see Eq. (5.26))

$$\begin{aligned} \eta_m^2 &= \frac{\rho\omega^2}{c_{66}} - \frac{c_{55}}{c_{66}}\left(\frac{m\pi}{b}\right)^2 = \frac{\pi^2}{4h^2}\left[\frac{\omega^2}{\omega_s^2} - \frac{c_{55}}{c_{66}}\left(m\frac{2h}{b}\right)^2\right], \\ m &= 0,1,2,3,\cdots, \\ \omega_s &= \frac{\pi}{2h}\sqrt{\frac{c_{66}}{\rho}}. \end{aligned} \tag{5.39}$$

Equations (5.35) and (5.37) are already satisfied by Eq. (5.38). Equation (5.38) is antisymmetric about $x_2 = 0$ and symmetric about $x_3 = 0$. The stress component needed for the boundary conditions in Eq. (5.36) is (see Eq. (5.27))

$$\begin{aligned} T_{21} &= c_{66}u_{1,2} = c_{66}B_0\eta_0 \cos(\eta_0 x_2) \\ &\quad + c_{66}\sum_{m=1}^{\infty} B_m\eta_m \cos(\eta_m x_2)\cos\frac{m\pi x_3}{b}. \end{aligned} \tag{5.40}$$

Substitution of Eqs. (5.38) and (5.40) into Eq. (5.36) gives

$$c_{66}B_0\eta_0\cos(\eta_0 h)+c_{66}\sum_{m=1}^{\infty}B_m\eta_m\cos(\eta_m h)\cos\frac{m\pi x_3}{b}$$
$$=\begin{cases}2\rho' h'\omega^2[B_0\sin(\eta_0 h)+\sum_{m=1}^{\infty}B_m\sin(\eta_m h)\cos\frac{m\pi x_3}{b}], & |x_3|<a,\\ 0, & a<|x_3|<b.\end{cases} \tag{5.41}$$

The boundary conditions at $x_2=\pm h$ lead to the same equation as in Eq. (5.41). We multiply both sides of Eq. (5.41) by $\cos(n\pi x_3/b)$ (n = 0, 1, 2, …) and integrate the resulting expression over (-b, b) to obtain

$$c_{66}B_0\eta_0\cos(\eta_0 h)2b$$
$$=2\rho' h'\omega^2[B_0\sin(\eta_0 h)2a+\sum_{m=1}^{\infty}B_m\sin(\eta_m h)\frac{2b}{m\pi}\sin\frac{m\pi a}{b}], \tag{5.42}$$
$$n=0,$$

$$c_{66}B_n\eta_n\cos(\eta_n h)b$$
$$=2\rho' h'\omega^2[B_0\sin(\eta_0 h)\frac{2b}{n\pi}\sin\frac{n\pi a}{b}+\sum_{m=1}^{\infty}B_m\sin(\eta_m h)C_{nm}], \tag{5.43}$$
$$n=1,2,3,\cdots,$$

where

$$C_{nm}=\int_{-a}^{a}\cos\frac{n\pi x_3}{b}\cos\frac{m\pi x_3}{b}dx_3=C_{mn},\quad m,n=1,2,3,\cdots. \tag{5.44}$$

Equations (5.42) and (5.43) are linear homogeneous equations for B_0 and B_m. For nontrivial solutions the determinant of the coefficient matrix has to vanish, which determines the resonant frequencies. The nontrivial solutions of B_0 and B_m determine the corresponding modes. This is a complicated eigenvalue problem because the eigenvalue or the resonant

frequency is present in every η_m. The eigenvalue problem is solved on a computer using MATLAB.

5.4.2. Numerical result

We examine the effects of partial electrodes on energy trapping systematically. We introduce

$$\bar{\omega}_s = \omega_s(1-R), \qquad R = \frac{2\rho' h'}{\rho h}, \tag{5.45}$$

where $\bar{\omega}_s$ is the resonant frequency of the fundamental thickness-shear mode in an unbounded quartz plate fully covered by electrodes. The resonant frequencies of the modes we are interested in are within $\bar{\omega}_s < \omega < \omega_s$. We fix the plate thickness $2h$ = 1 mm and the plate length $2b$ = 40 mm.

We begin with the case when the electrode length $2a$ = 15 mm and the mass ratio R = 3%. In this case two resonant frequencies are found within $\bar{\omega}_s < \omega < \omega_s$. When using 9, 10 and 11 terms in the series, the two frequencies are always found to be ω_1/ω_s = 0.9740 and ω_2/ω_s = 0.9961. The corresponding modes also converge very well, without noticeable differences. Therefore all calculations below are based on using 11 terms in the series. In this case η_m^2 is positive. More terms will make η_m^2 negative. The modes corresponding to the two frequencies are shown in Fig. 5.7 which is not drawn to scale. The first mode has no nodal points along the x_3 direction which is the mode of interest and the one most useful in applications. It is a transversely varying thickness-shear mode. The second mode has two nodal points along the x_3 direction and is a thickness-twist mode. For both of the modes in Fig. 5.7, the vibration is large in the central region and small near the plate edges. In other words the vibration is mainly under the electrodes and decays outside them. This is the so-called energy trapping of thickness-shear and thickness-twist modes.

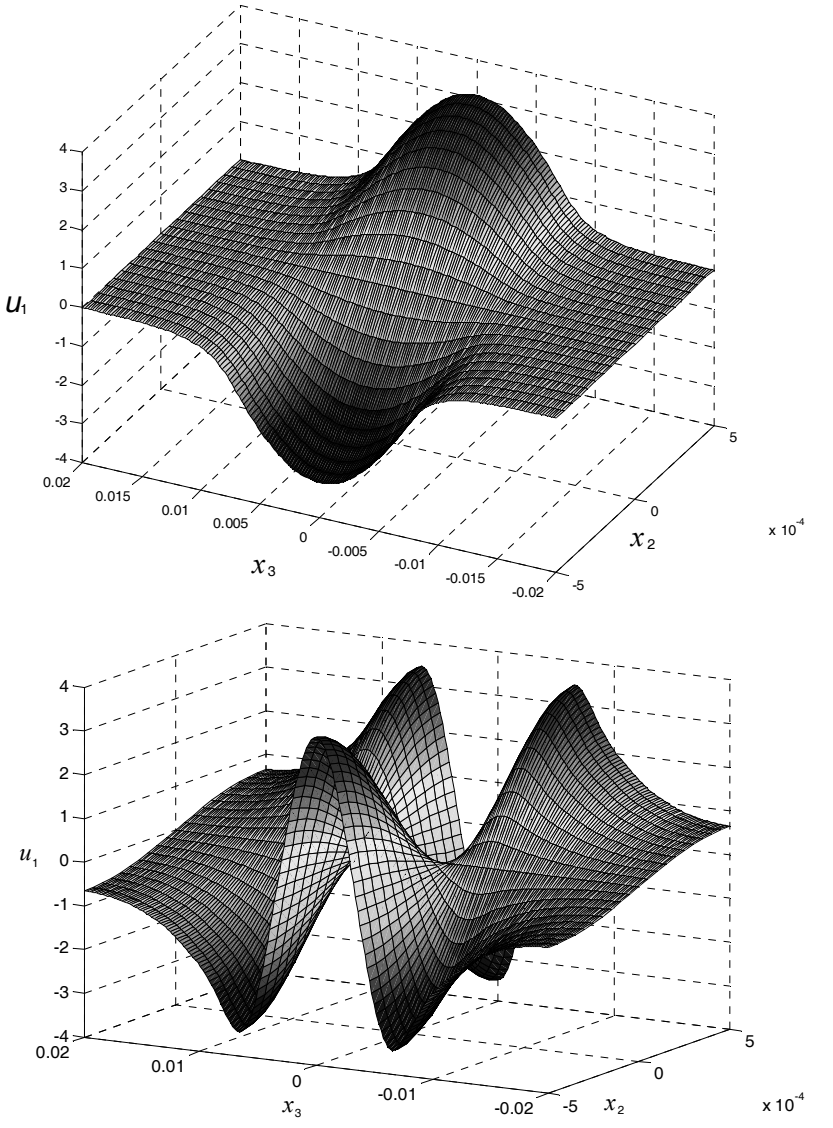

Fig. 5.7. Two trapped modes when $2a$ = 15 mm and R = 3%.

Next we keep R = 3% and increase the electrode length to $2a$ = 23 mm. Then, within $\bar{\omega}_s < \omega < \omega_s$, there still exist two frequencies with ω_1/ω_s = 0.9725 and ω_2/ω_s = 0.9845, slightly lower than the previous case because of the longer electrodes and increased inertia. The two modes are qualitatively similar to the two in Fig. 5.7 but have wider distributions along the x_3 direction because of the longer electrodes.

If we still keep R = 3% and increase the electrode length further to $2a$ = 26 mm, then three resonant frequencies appear within $\bar{\omega}_s < \omega < \omega_s$: ω_1/ω_s = 0.9722, ω_2/ω_s = 0.9820 and ω_3/ω_s = 0.9988. The first two are slightly lower than the previous case as expected. The displacements at the plate top surface of the three modes are shown in Fig. 5.8. The first two modes are similar to those in Fig. 5.7. The third mode is new and is a thickness-twist mode with four nodal points along the x_3 direction. We note that the second mode is not as well trapped as the first mode, and that the third mode is essentially no longer trapped.

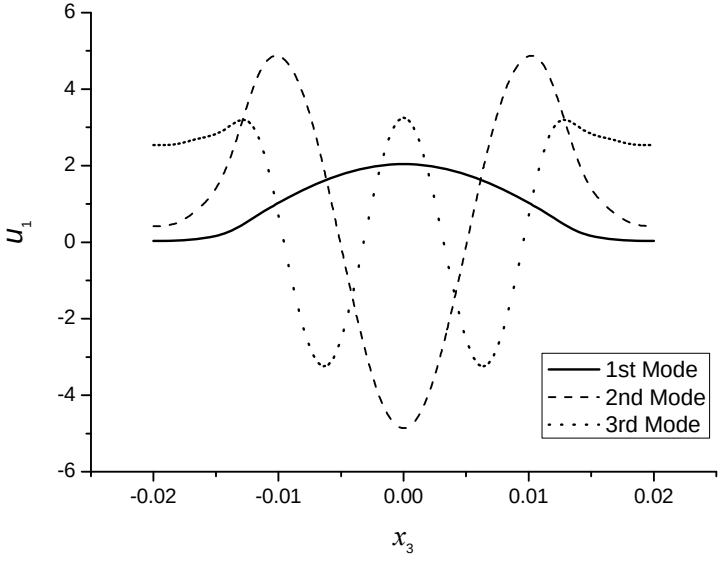

Fig. 5.8. Three trapped modes when $2a$ = 26 mm and R = 3%.

On the other hand, if we keep R = 3% and reduce the electrode length to $2a$ = 12 mm, there exists only one frequency within

$\bar{\omega}_s < \omega < \omega_s$ with $\omega_1 / \omega_s = 0.9753$ — slightly higher than the case of R = 3% and $2a$ = 15 mm. The corresponding mode has no nodal points along the x_3 direction.

In Fig. 5.9 we summarize the effects of electrode length on the first mode when R = 3% is fixed and $2a$ = 15, 23 and 26 mm, respectively. Clearly, the vibration distribution becomes wider when the electrodes become longer. In the case of $2a$ = 26 mm, the length of the unelectroded portions is b-a = 20-13 = 7 mm, seven times the plate thickness $2h$ = 1 mm. In this case the mode still decays to essentially zero at the plate edges and we still have good energy trapping.

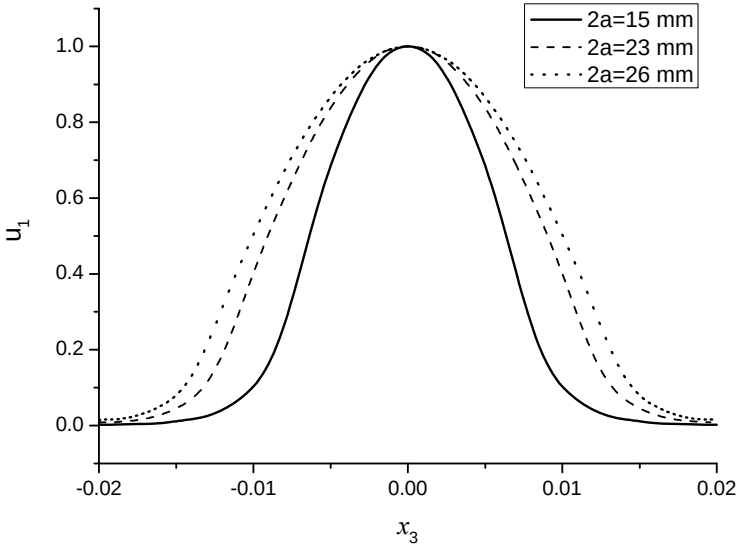

Fig. 5.9. Effect of electrode size on energy trapping of the first mode.

In the following we examine the effect of the mass ratio R. Consider the case when $2a$ = 23 mm. We choose different values of R = 3%, 6%, and 10% and examine the corresponding modes. For these three values of R there exist 2, 3, and 3 trapped modes correspondingly. We focus on the first trapped mode for each value of R. The frequencies of these three first modes are ω_1 / ω_s = 0.9725, 0.9452 and 0.9113. They decrease as R

increases as expected. The corresponding modes are shown in Fig. 5.10. A larger R leads to better energy trapping, but the effect is not as strong as that in Fig. 5.9 by reducing the electrode length.

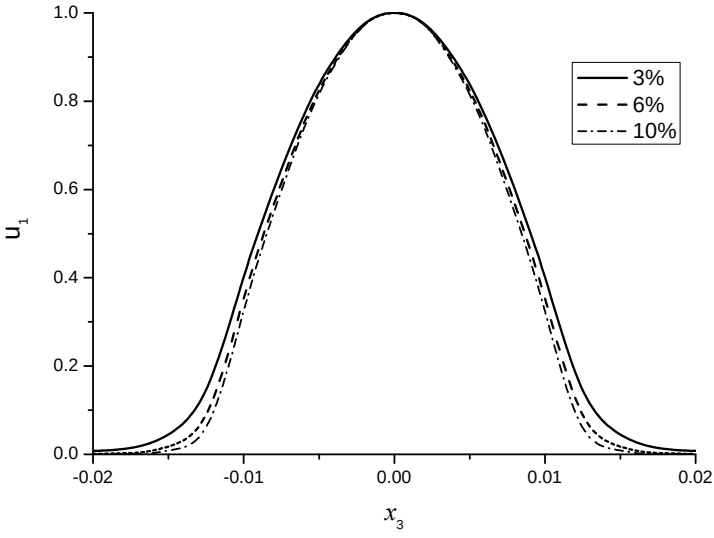

Fig. 5.10. Effect of electrode thickness on energy trapping of the first mode.

5.5. Plate with a Partial Mass Layer

Consider the crystal plate with one partial mass layer as shown in Fig. 5.11 [65].

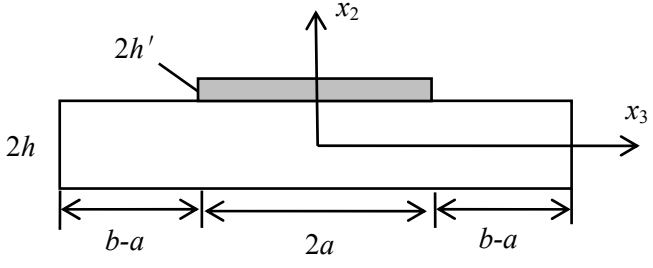

Fig. 5.11. An AT-cut quartz plate with a partial mass layer.

The governing equation and boundary conditions are

$$c_{66}u_{1,22} + c_{55}u_{1,33} \cong \rho \ddot{u}_1, \quad |x_3| < b, \quad |x_2| < h, \tag{5.46}$$

$$T_{21} = \begin{cases} -2\rho' h' \ddot{u}_1, & x_2 = h, \quad |x_3| < a, \\ 0, & x_2 = h, \quad a < |x_3| < b, \end{cases} \tag{5.47}$$

$$T_{21} = 0, \quad x_2 = -h, \quad |x_3| < b, \tag{5.48}$$

$$T_{31} = 0, \quad x_3 = \pm b, \quad |x_2| < h. \tag{5.49}$$

Due to the loss of symmetry of the structure about the x_3 axis, the following displacement field, which is more general than Eq. (5.38), is needed:

$$\begin{aligned} u_1 = {} & A_0 \cos(\eta_0 x_2) + B_0 \sin(\eta_0 x_2) \\ & + \sum_{m=1}^{\infty} [A_m \cos(\eta_m x_2) + B_m \sin(\eta_m x_2)] \cos \frac{m\pi x_3}{b}, \end{aligned} \tag{5.50}$$

where A_0, B_0, A_m and B_m are undetermined constants, and

$$\eta_m^2 = \frac{\rho\omega^2}{c_{66}} - \frac{c_{55}}{c_{66}}\left(\frac{m\pi}{b}\right)^2 = \frac{\pi^2}{4h^2}\left[\frac{\omega^2}{\omega_s^2} - \frac{c_{55}}{c_{66}}\left(m\frac{2h}{b}\right)^2\right], \quad m = 0,1,2,3,\cdots. \tag{5.51}$$

Equation (5.50) is symmetric about $x_2 = 0$. Equations (5.46) and (5.49) are already satisfied by Eq. (5.50). The stress component needed for the boundary conditions in Eqs. (5.47) and (5.48) is

$$\begin{aligned} T_{21} = c_{66}u_{1,2} = {} & -c_{66}A_0\eta_0 \sin(\eta_0 x_2) + c_{66}B_0\eta_0 \cos(\eta_0 x_2) \\ & + c_{66}\sum_{m=1}^{\infty} [-A_m\eta_m \sin(\eta_m x_2) + B_m\eta_m \cos(\eta_m x_2)] \cos \frac{m\pi x_3}{b}. \end{aligned} \tag{5.52}$$

Substituting Eqs. (5.50) and (5.52) into Eqs. (5.47) and (5.48), multiplying the resulting equations by $\cos(n\pi x_3/b)$ (n = 0, 1, 2, …) and integrating them over (-b, b), we obtain linear homogeneous equations for the undetermined constants. These equations represent an eigenvalue problem. It is somewhat more complicated than the eigenvalue problem in the previous section and can be solved in a similar way. We introduce

$$\bar{\omega}_s = \omega_s(1-R), \quad \omega_s = \frac{\pi}{2h}\sqrt{\frac{c_{66}}{\rho}}, \quad R = \frac{\rho' h'}{\rho h}. \tag{5.53}$$

The resonant frequencies of the modes we are interested in are within $\bar{\omega}_s < \omega < \omega_s$. We fix the plate thickness $2h$ = 1 mm and the plate length $2b$ = 40 mm.

When the film length $2a$ = 15 mm and the mass ratio R = 3%, two resonant frequencies are found within $\bar{\omega}_s < \omega < \omega_s$. When using 9 and 10 terms in the series, the two frequencies are always found to be ω_1/ω_s = 0.974089 and ω_2/ω_s = 0.996126. Numerical tests show that A_0, B_0, A_n and B_n are very sensitive to the frequencies. Six significant figures are used to ensure sufficient accuracy of the frequencies. Then the corresponding modes converge very well, without noticeable differences. They are trapped modes similar to those in Fig. 5.7 although there is only one mass layer. All calculations below are with 10 terms in the series. In this case η_m^2 is positive. 12 or more terms will make η_m^2 negative.

To show the effect of R on displacement distributions graphically we exaggerate the mass ratio a little and consider the case with $2a$ = 15 mm and R = 10%. In this case there are three trapped modes: ω_1/ω_s = 0.914855, ω_2/ω_s = 0.942886 and ω_3/ω_s = 0.992584. For the first mode, Fig. 5.12 shows the displacement magnitude distributions at the plate top $x_2 = h$ and bottom $x_2 = -h$. The modes are exactly even in x_3 but are not exactly odd in x_2 due to the fact that the mass layer is on one side of the plate only. At the plate bottom there is no mass layer and the vibration amplitude is slightly larger than that at the top.

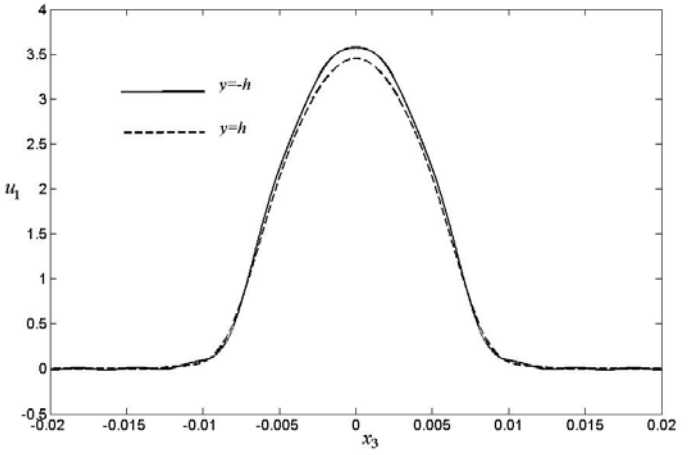

Fig. 5.12. Displacement distribution at the plate top and bottom surfaces. a = 7.5 mm and R =10%.

When 2a = 15 mm, for two values of R = 3% and 10%, we plot the displacement distributions at the plate middle cross section $x_3 = 0$ in Fig. 5.13. The figure shows that, because of the mass layer and the related loss of symmetry about $x_2 = 0$, the nodal point along the plate thickness deviates slightly from the plate middle plane toward the plate top where the mass layer is attached. The deviation is larger for a larger R.

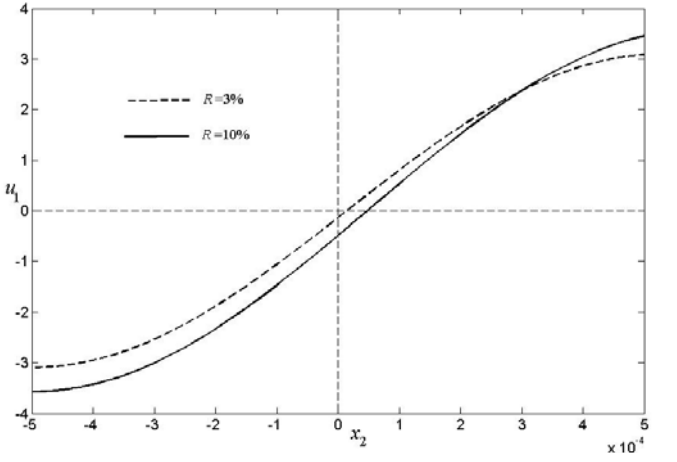

Fig. 5.13. Displacement distribution at the plate middle cross section. $x_3 = 0$. a = 7.5 mm.

5.6. Plate with Misaligned Electrodes

In resonator manufacturing, the top and bottom electrodes on a plate maybe slightly unequal or mismatched (see Fig. 5.14). For face-shear and thickness-twist modes this problem was analyzed in [66].

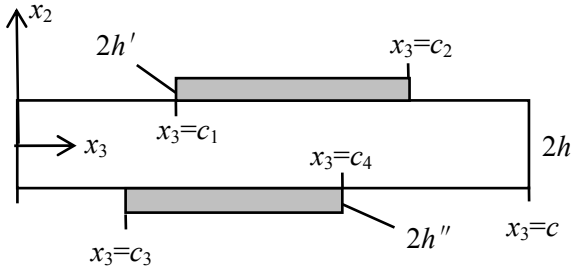

Fig. 5.14. A plate with mismatched and unequal electrodes.

The governing equation and boundary conditions are

$$c_{66}u_{1,22} + c_{55}u_{1,33} \cong \rho\ddot{u}_1, \quad 0 < x_3 < c, \quad |x_2| < h, \tag{5.54}$$

$$T_{21} = \begin{cases} -2\rho' h'\ddot{u}_1, & x_2 = h, \quad c_1 < x_3 < c_2, \\ 0, & x_2 = h, \quad 0 < x_3 < c_1 \quad \text{or} \quad c_2 < x_3 < c, \end{cases} \tag{5.55}$$

$$T_{21} = \begin{cases} 2\rho'' h''\ddot{u}_1, & x_2 = -h, \quad c_3 < x_3 < c_4, \\ 0, & x_2 = -h, \quad 0 < x_3 < c_3 \quad \text{or} \quad c_4 < x_3 < c, \end{cases} \tag{5.56}$$

$$T_{31} = 0, \quad x_3 = 0,\ c, \quad |x_2| < h. \tag{5.57}$$

Due to the complete loss of symmetry, the following general displacement field from separation of variables is necessary:

$$\begin{aligned} u_1 &= A_0 \cos(\eta_0 x_2) + B_0 \sin(\eta_0 x_2) \\ &\quad + \sum_{m=1}^{\infty} [A_m \cos(\eta_m x_2) + B_m \sin(\eta_m x_2)] \cos\frac{m\pi x_3}{c}, \end{aligned} \tag{5.58}$$

where A_0, B_0, A_m and B_m are undetermined constants, and

$$\eta_m^2 = \frac{\rho\omega^2}{c_{66}} - \frac{c_{55}}{c_{66}}\left(\frac{m\pi}{c}\right)^2 = \frac{\pi^2}{4h^2}\left[\frac{\omega^2}{\omega_s^2} - \frac{c_{55}}{c_{66}}\left(m\frac{2h}{c}\right)^2\right], \quad m = 0,1,2,3,\cdots. \tag{5.59}$$

Equations (5.54) and (5.57) are already satisfied by Eq. (5.58). To apply the boundary conditions at the plate top and bottom, we need

$$T_{21} = c_{66}u_{1,2} = -c_{66}A_0\eta_0 \sin(\eta_0 x_2) + c_{66}B_0\eta_0 \cos(\eta_0 x_3) + c_{66}\sum_{m=1}^{\infty}\left[-A_m\eta_m \sin(\eta_m x_2) + B_m\eta_m \cos(\eta_m x_2)\right]\cos\frac{m\pi x_3}{c}. \tag{5.60}$$

Substituting Eqs. (5.58) and (5.60) into Eqs. (5.55) and (5.56), multiplying the resulting equations by $\cos(n\pi x_3 / c)$ (n = 0, 1, 2, …) and integrating them over (0, c), we obtain linear homogeneous equations for the undetermined constants. These equations represent an eigenvalue problem and are solved using MATLAB.

We introduce

$$\bar{\omega}_s = \omega_s(1-R), \quad \omega_s = \frac{\pi}{2h}\sqrt{\frac{c_{66}}{\rho}}, \quad R = \frac{\rho' h' + \rho'' h''}{\rho h}. \tag{5.61}$$

The resonant frequencies of the modes we are interested in are within $\bar{\omega}_s < \omega < \omega_s$. We consider a resonator with c = 40 mm and $2h$ = 1 mm.

First we consider the case of two identical electrodes without a mismatch as a reference. Both electrodes are 15 mm in length, located at the center with c_1 = 12.5 mm, c_2 = 27.5 mm, c_3 = 12.5 mm, and c_4 = 27.5 mm. R = 3%. In this case there are three frequencies in the interval of $\bar{\omega}_s < \omega < \omega_s$. When using 17 ($n$ = 16) and 18 (n = 17) terms in the series, the three frequencies are always found to be:

$$\omega_1/\omega_s = 0.974032, \quad \omega_2/\omega_s = 0.983082, \quad \omega_3/\omega_s = 0.996098, \tag{5.62}$$

with six significant figures. The corresponding modes converge very well, without noticeable differences. Therefore all calculations below are based on 18 terms in the series. In this case η_n^2 is positive. 27 (n = 26) or more terms will make η_n^2 negative. The modes corresponding to the first and the third frequencies are the same as those in Fig. 5.7. These two modes are symmetric about $x_3 = c/2$. Since in Eq. (5.58) we have included functions antisymmetric about $x_3 = c/2$, the mode corresponding to the second frequency is antisymmetric about $x_3 = c/2$ and is shown in Fig. 5.15.

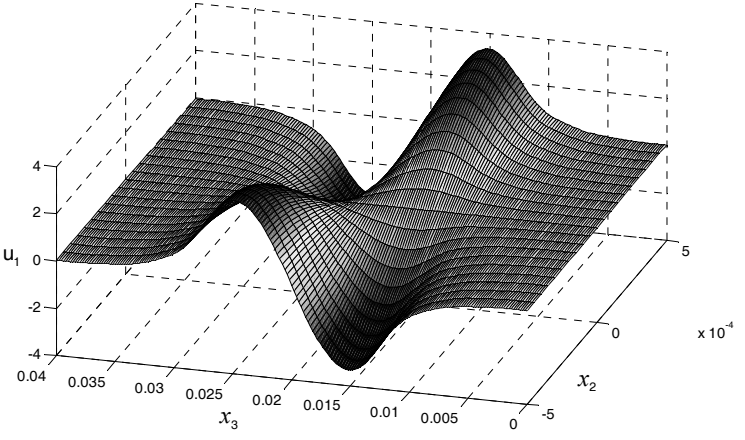

Fig. 5.15. The second trapped mode antisymmetric about $x_3 = c/2$.

Next consider the case when the two electrodes are identical (15 mm in length) but the top electrode is shifted to the right from the center by 2.5 mm while the bottom electrode is shifted to the left by 2.5 mm. In this case c_1 = 15 mm, c_2 = 30 mm, c_3 = 10 mm, and c_4 = 25. We still use R = 3%. The following three frequencies are found:

$$\omega_1 / \omega_s = 0.975396, \quad \omega_2 / \omega_s = 0.986455, \quad \omega_3 / \omega_s = 0.996121, \quad (5.63)$$

which are slightly higher than those in Eq. (5.62). The corresponding modes look essentially the same as those corresponding to Eq. (5.62)

(see Figs. 5.7 and 5.15), although from the numerical data small differences can be detected. Basically the mode shapes are not very sensitive to small shifts of the electrodes.

Finally we examine electrodes with different lengths. Consider the case when the top electrode is 10 mm long and the bottom electrode is 20 mm long. The total length of the two electrodes is 30 mm, the same as those in the two previous cases. Both electrodes are at the centers of the plate surfaces. In this case $c_1 = 15$ mm, $c_2 = 25$ mm, $c_3 = 10$ mm, and $c_4 = 30$ mm. For the same $R = 3\%$, the three resonant frequencies found are exactly the same as those in Eq. (5.63). Again the corresponding modes look essentially the same as those corresponding to Eq. (5.62).

In Fig. 5.16 we compare the plate top surface displacement of the first mode for the three electrode configurations considered in the above. The case of mismatched electrodes and the case of electrodes with unequal length are indistinguishable. It can be seen that the displacement is slightly more confined to the center when the electrodes are mismatched or with unequal length.

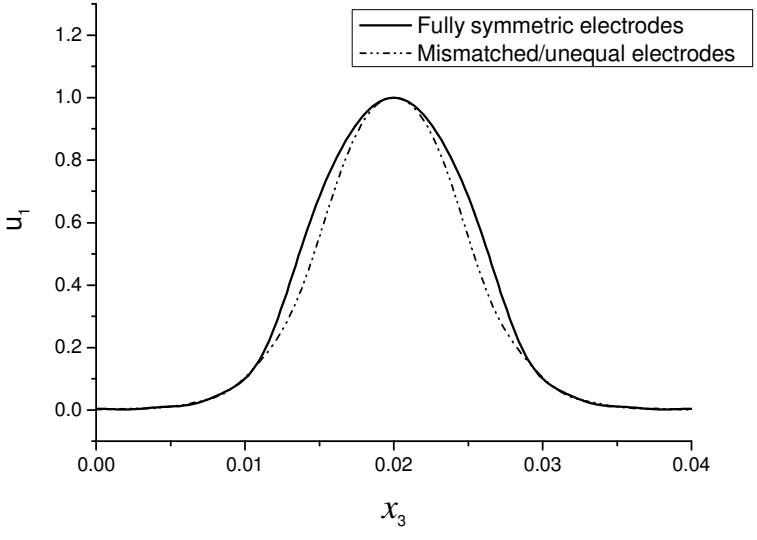

Fig. 5.16. Plate top surface displacements of the first mode in different cases.

5.7. Plate with a Mass Layer Array

Mass sensor arrays are with different receptors for multicomponent sensing. This usually leads to nonperiodic arrays in which the vibration may vary from one element to another. In this section we study face-shear and thickness-twist vibrations of a crystal plate with an array of mass layers (see Fig. 5.17) [67]. There are K different mass layers at the top surface of the plate. The case of K = 5 is shown. The kth layer is within $a_k < x_3 < b_k$. It has a density ρ_k and thickness $2h_k$.

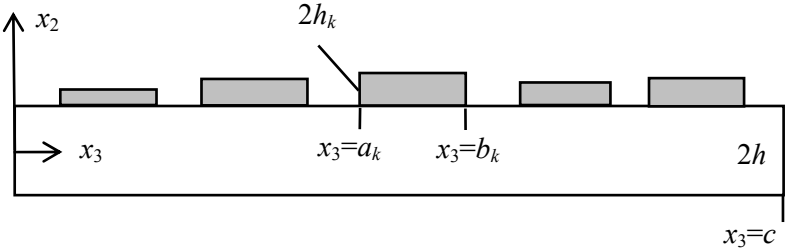

Fig. 5.17. A plate with a nonperiodic array of mass layers.

5.7.1. Governing equations and series solution

The equation to be satisfied by u_1 is:

$$c_{66}u_{1,22} + c_{55}u_{1,33} \cong \rho \ddot{u}_1 . \tag{5.64}$$

The boundary condition at the plate top surface is

$$T_{21} = \begin{cases} -2\rho_k h_k \ddot{u}_1, & x_2 = h, \quad a_k < x_3 < b_k, \quad k = 1,2,\cdots,K, \\ 0, & x_2 = h, \quad \text{elsewhere.} \end{cases} \tag{5.65}$$

The boundary condition at the plate bottom surface is simply

$$T_{21} = 0 . \tag{5.66}$$

The edge conditions at the left and right ends are

$$T_{31} = 0, \quad x_3 = 0,\ c, \quad |\, x_2 \,| < h\,. \tag{5.67}$$

The series for u_1 is still given by Eq. (5.58) which leads to the same series for T_{21} in Eq. (5.60). They already satisfy Eqs. (5.64) and (5.67). We substitute them into Eqs. (5.65) and (5.66), multiply the resulting equations by $\cos(n\pi x_3 / c)$ with n = 0, 1, 2, …, and integrate them over (0, c) to obtain linear equations for the undetermined constants in the series. These equations are solved numerically. We introduce

$$\omega_s = \frac{\pi}{2h}\sqrt{\frac{c_{66}}{\rho}}\,, \quad \bar{\omega}_s = \omega_s(1-R)\,, \quad R = \underset{k}{\text{Max}}\{R_k\}\,, \quad R_k = \frac{\rho_k h_k}{\rho h}\,. \tag{5.68}$$

R_k is the mass ratio between the kth mass layers and the plate. $\bar{\omega}_s$ is the resonant frequency of the fundamental thickness-shear mode in an unbounded quartz plate fully covered by a mass layer with the largest mass ratio. The resonant frequencies of the modes we are interested in are within $\bar{\omega}_s < \omega < \omega_s$.

5.7.2. Effect of mass layer thickness

Consider an array of two mass layers with the one on the right a little thicker than the one on the left (see Fig. 5.18). The exact dimensions are $a_1 = 3.75$ mm, $b_1 = 8.75$ mm, $a_2 = 11.25$ mm, $b_2 = 16.25$ mm, $c = 20$ mm and $h = 0.25$ mm. Twenty-one terms of the series are used in the calculation. The first resonant frequency calculated from using nineteen and twenty-one terms are ω_1 = 19095208 rad/s and 19095215 rad/s, respectively, which is considered sufficiently accurate. If twenty-four or more terms are used in the series, the η_m^2 in Eq. (5.59) will become negative. Six modes are found within $\bar{\omega}_s < \omega < \omega_s$ (see Fig. 5.19). The first mode has vibration under the thicker film on the right only. This mode has no nodal points (zeros) along the x_3 direction. The thicker film has more inertia and lowers the cutoff frequency ω_s of the

crystal plate more than the thinner film. Therefore the vibration occurs under the thicker film first. At a higher frequency the second mode appears which has vibration under the thinner film on the left only, and it does not have a nodal point. The third and fourth modes have vibration mainly under the thicker and thinner films, respectively. Each mode has one nodal point under the film with the main vibration. Similarly, the fifth and six modes have two nodal points each under the film with the main vibration.

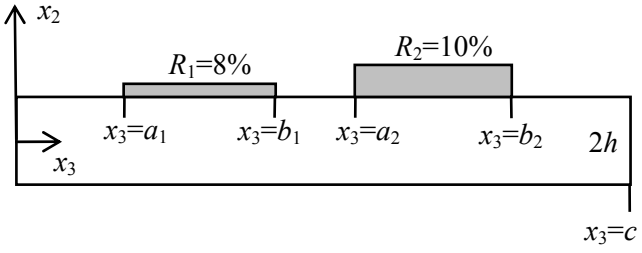

Fig. 5.18. Two mass layers with different thickness.

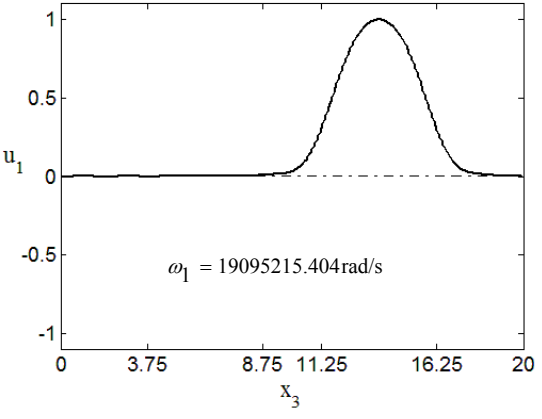

Fig. 5.19. Vibration distribution of trapped modes.

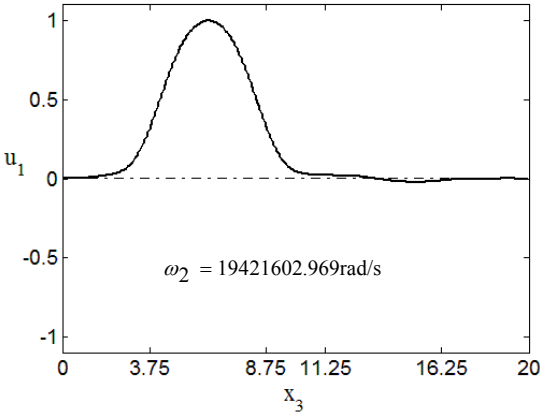

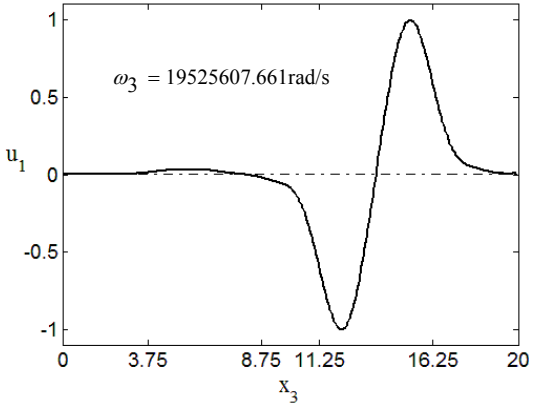

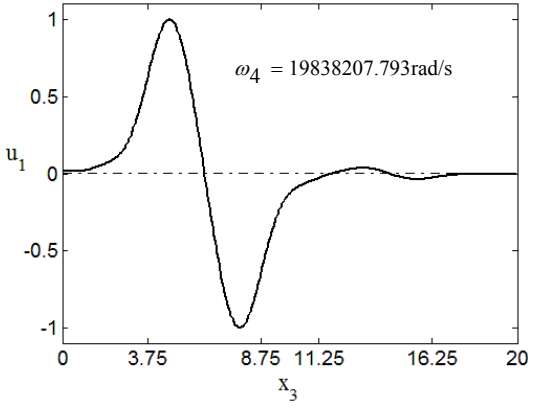

Fig. 5.19. (*Continued*)

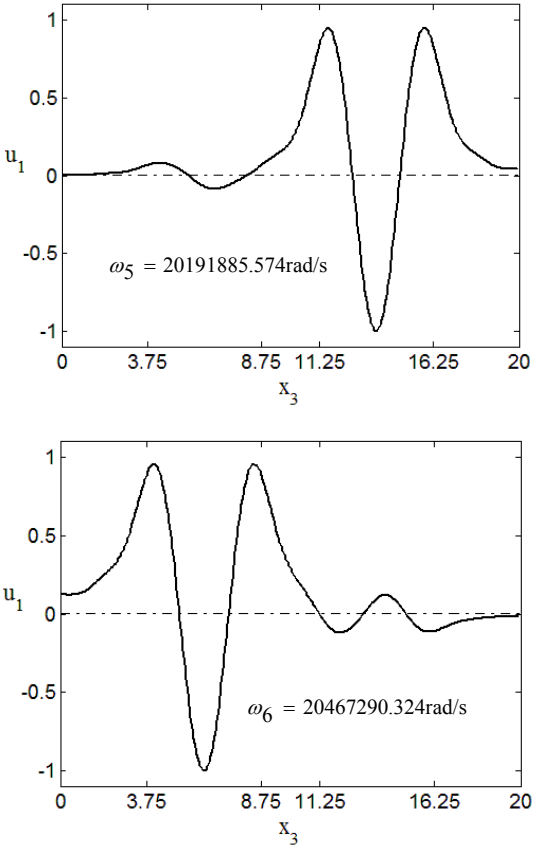

Fig. 5.19. (*Continued*)

5.7.3. Effect of mass layer length

Figure 5.20 shows two mass layers with the one on the right slightly longer than the one on the left. The geometric parameters are $a_1 = 2.5$ mm, $b_1 = 7.5$ mm, $a_2 = 10$ mm, $b_2 = 17.5$ mm, $c = 20$ mm and $h = 0.25$ mm. Again twenty-one terms of the series are used in the calculation. Seven modes are found within $\bar{\omega}_s < \omega < \omega_s$. Except the sixth mode, the other six modes are similar to the six modes in Fig. 5.29. Roughly, a longer film has more mass and affects the vibration in a way similar to a thicker film.

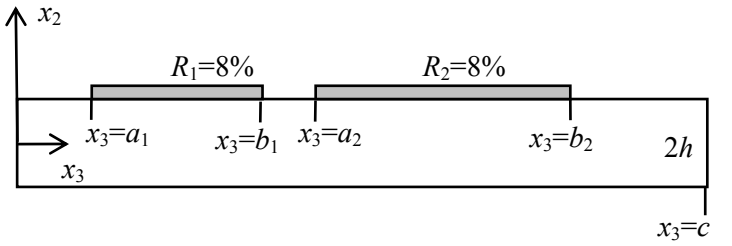

Fig. 5.20. Two mass layers with different length.

5.7.4. An array of four mass layers

In Fig. 5.21 we have an array of four mass layers among which two are identical (the first and the third from left), one is slightly thicker (the second from left), and one is slightly longer (the fourth from left). They are with $a_1 = 3.75$ mm, $b_1 = 8.75$ mm, $a_2 = 13.75$ mm, $b_2 = 18.75$ mm, $a_3 = 23.75$ mm, $b_3 = 28.75$ mm, $a_4 = 33.75$ mm, $b_4 = 41.25$ mm, $c = 45$ mm and $h = 0.25$ mm. This is a longer crystal plate than those in the previous examples and forty-nine terms in the series are used in the calculation to ensure sufficient accuracy. Twelve modes are found within $\bar{\omega}_s < \omega < \omega_s$. The first four modes are shown in Fig. 5.22. It can be seen that the plate can vibrate in complicated manners. The vibration may be under one or two films, with different numbers of nodal points.

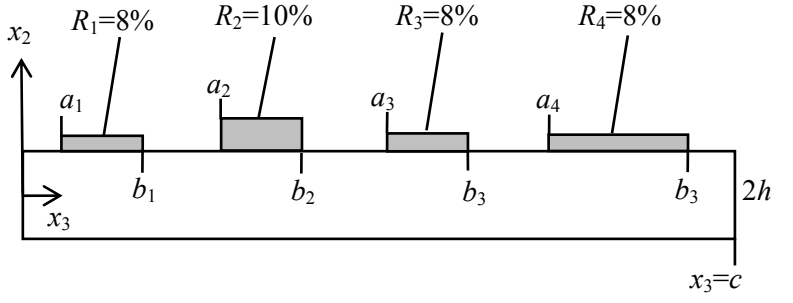

Fig. 5.21. A plate with four mass layers.

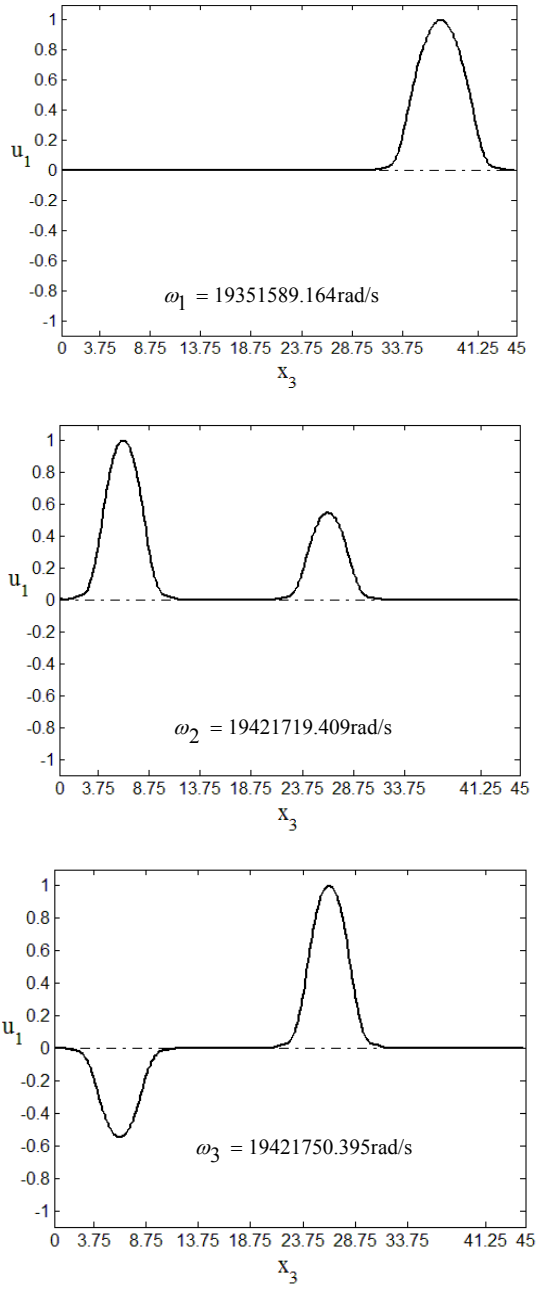

Fig. 5.22. Vibration distribution of the first four modes.

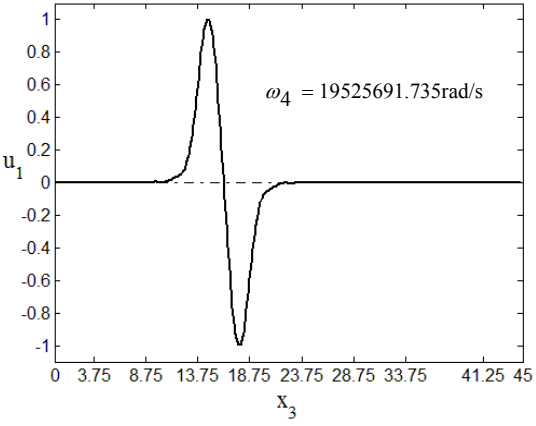

Fig. 5.22. (*Continued*)

5.8. Mesa Resonator

In this section we study thickness-shear and thickness-twist vibrations of an AT-cut quartz plate mesa resonator with stepped thickness (see Fig. 5.23) [68]. The changing plate thickness in mesa resonators usually leads to stronger energy trapping than the inertia of partial electrodes. At the same time, due to the change of plate thickness, analytical modeling of mesa resonators is complicated. We divide the resonator into three rectangular regions. For each rectangular region a Fourier series solution can be constructed with undetermined coefficients. Then solutions of different regions are substituted into the interface continuity conditions among different regions to obtain linear algebraic equations for the undetermined coefficients. Specifically, in the vertical (x_2) direction, we artificially divide the plate cross section into three rectangular regions by the two dotted lines in the figure and call them the top region ($h < x_2 < h + H$), the middle region ($-h < x_2 < h$), and the bottom region ($-(h + H) < x_2 < -h$), respectively. The above division is for solving the problem mathematically. For convenience, in the horizontal (x_3) direction, we call the thicker shaded region ($|x_3| < a$) the inner region, and the unshaded thinner regions with $a < |x_3| < b$ the outer regions.

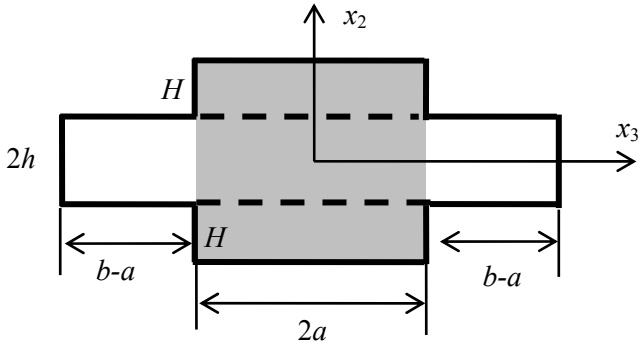

Fig. 5.23. A mesa resonator of AT-cut quartz.

5.8.1. Governing equations

The equation governing u_1 is

$$c_{66}u_{1,22} + c_{55}u_{1,33} \cong \rho \ddot{u}_1 , \tag{5.69}$$

which is valid in every rectangular region in Fig. 1. The boundary condition at the top of the inner region ($|x_3| < a$) of the plate is

$$T_{21}(x_3, h+H) = 0, \quad |x_3| < a . \tag{5.70}$$

The continuity and boundary conditions at the interface between the top and middle rectangular regions are

$$\begin{aligned} &u_1(x_3, h^-) = u_1(x_3, h^+), \quad |x_3| < a, \\ &T_{21}(x_3, h^-) = \begin{cases} T_{21}(x_3, h^+), & |x_3| < a, \\ 0, & a < |x_3| < b. \end{cases} \end{aligned} \tag{5.71}$$

The right edges of the top and middle rectangular regions are traction free, with

$$T_{31}(a, x_2) = 0, \quad h < |x_2| < h+H , \tag{5.72}$$

$$T_{31}(b, x_2) = 0, \quad |x_2| < h . \tag{5.73}$$

The plate in Fig. 5.23 is symmetric in both x_2 and x_3. For the applications we are considering, we are interested in modes that are symmetric in x_3 and antisymmetric in x_2. Due to symmetry and antisymmetry, the boundary and continuity conditions at the lower interface $x_2 = -h$, the bottom surface $x_2 = -(h+H)$, and the left edges are not needed.

5.8.2. Fourier series solution

For the middle region, the following solution can be constructed from standard separation of variables (see Eq. (5.25)):

$$u_1 = B_0 \sin(\eta_0 x_2) + \sum_{m=1}^{\infty} B_m \sin(\eta_m x_2) \cos\frac{m\pi x_3}{b}, \tag{5.74}$$

where B_0 and B_m are undetermined constants, and

$$\eta_m^2 = \frac{\rho\omega^2}{c_{66}} - \frac{c_{55}}{c_{66}}\left(\frac{m\pi}{b}\right)^2 = \frac{\pi^2}{4h^2}\left[\frac{\omega^2}{\omega_s^2} - \frac{c_{55}}{c_{66}}\left(m\frac{2h}{b}\right)^2\right], \tag{5.75}$$
$$m = 0,1,2,3,\cdots,$$

$$\omega_s = \frac{\pi}{2h}\sqrt{\frac{c_{66}}{\rho}}. \tag{5.76}$$

Equation (5.74) satisfies Eqs. (5.69) and (5.73). To apply boundary and continuity conditions, we need (see Eq. (5.27)):

$$\begin{aligned} T_{21} &= c_{66}u_{1,2} = c_{66}B_0\eta_0 \cos(\eta_0 x_2) \\ &\quad + c_{66}\sum_{m=1}^{\infty} B_m\eta_m \cos(\eta_m x_2)\cos\frac{m\pi x_3}{b}. \end{aligned} \tag{5.77}$$

Similarly, for the top rectangular region we construct the following solution from separation of variables:

$$\begin{aligned} u_1 &= C_0 \cos(\xi_0 x_2) + D_0 \sin(\xi_0 x_2) \\ &\quad + \sum_{m=1}^{\infty} [C_m \cos(\xi_m x_2) + D_m \sin(\xi_m x_2)]\cos\frac{m\pi x_3}{a}, \end{aligned} \tag{5.78}$$

where C_0, D_0, C_m and D_m are undetermined constants, and

$$\xi_m^2 = \frac{\rho\omega^2}{c_{66}} - \frac{c_{55}}{c_{66}}\left(\frac{m\pi}{a}\right)^2 = \frac{\pi^2}{4h^2}\left[\frac{\omega^2}{\omega_s^2} - \frac{c_{55}}{c_{66}}\left(m\frac{2h}{a}\right)^2\right], \quad m = 0,1,2,3,\cdots. \tag{5.79}$$

Equation (5.78) satisfies Eqs. (5.69) and (5.72). To apply boundary and continuity conditions, we need:

$$\begin{aligned} T_{21} = c_{66}u_{1,2} &= -c_{66}C_0\xi_0 \sin(\xi_0 x_2) + c_{66}D_0\xi_0 \cos(\xi_0 x_2) \\ &+ c_{66}\sum_{m=1}^{\infty} [-C_m\xi_m \sin(\xi_m x_2) + D_m\xi_m \cos(\xi_m x_2)]\cos\frac{m\pi x_3}{a}. \end{aligned} \tag{5.80}$$

5.8.3. Boundary and continuity conditions

Substitution of Eqs. (5.74), (5.77), (5.78) and (5.80) into Eqs. (5.70) and (5.71) yields the following three equations:

$$\begin{aligned} &-c_{66}C_0\xi_0 \sin[\xi_0(h+H)] + c_{66}D_0\xi_0 \cos[\xi_0(h+H)] \\ &+ c_{66}\sum_{m=1}^{\infty} \{-C_m\xi_m \sin[\xi_m(h+H)] \\ &+ D_m\xi_m \cos[\xi_m(h+H)]\}\cos\frac{m\pi x_3}{a} = 0, \quad |x_3| < a, \end{aligned} \tag{5.81}$$

$$\begin{aligned} &B_0 \sin(\eta_0 h) + \sum_{m=1}^{\infty} B_m \sin(\eta_m h)\cos\frac{m\pi x_3}{b} \\ &= C_0 \cos(\xi_0 h) + D_0 \sin(\xi_0 h) \\ &+ \sum_{m=1}^{\infty} [C_m \cos(\xi_m h) + D_m \sin(\xi_m h)]\cos\frac{m\pi x_3}{a}, \quad |x_3| < a, \end{aligned} \tag{5.82}$$

$$c_{66}B_0\eta_0\cos(\eta_0 h)+c_{66}\sum_{m=1}^{\infty}B_m\eta_m\cos(\eta_m h)\cos\frac{m\pi x_3}{b}$$
$$=\begin{cases}-c_{66}C_0\xi_0\sin(\xi_0 h)+c_{66}D_0\xi_0\cos(\xi_0 h)\\ \quad+c_{66}\sum_{m=1}^{\infty}[-C_m\xi_m\sin(\xi_m h)+D_m\xi_m\cos(\xi_m h)]\cos\frac{m\pi x_3}{a}, & (5.83)\\ \quad |x_3|<a,\\ 0, \quad a<|x_3|<b.\end{cases}$$

We multiply both sides of Eqs. (5.81) and (5.82) by $\cos n\pi x/a$ (n = 0, 1, 2, …) and integrate the resulting expressions over (-a, a), and multiply both sides of Eq. (5.83) by $\cos n\pi x/b$ (n = 0, 1, 2, …) and integrate the resulting expression over (-b, b). This leads to a system of linear homogeneous equations for the undetermined coefficients in the Fourier series, representing an eigenvalue problem. These equations are solved using a computer.

5.8.4. Numerical result

As an example consider a mesa resonator with the following dimensions: a = 5 mm, b = 8 mm, 2h = 0.3 mm, and H = 0.08 mm. The modes we are interested in have slow variations in the x_3 direction, with no more than a few nodal points. Numerical tests show that to describe such a slow variation we do not need many terms in the series. The top region with $|x_3|<a$ is shorter than the middle region with $|x_3|<b$. Therefore we use fewer terms for the top region than the middle region. A few thickness-shear and thickness-twist modes can be found in the frequency range of interest. The mode we are most interested in is the first trapped mode (transversely varying thickness shear) with the lowest frequency. Calculations show that when using 11 terms for the series of the middle region and 7 terms for the series of the top region, the frequency of the first mode is 2.264783×10^7 rad/s. When using 12 terms for the middle region and 8 terms for the top region, the frequency of the first mode is 2.264773×10^7 rad/s. There are five significant figures. In this case η_m^2 and ξ_m^2 are both positive.

Figure 5.24 shows the lowest four trapped modes of interest in the order of increasing frequency. 12 terms are used in the series for the middle region and 8 terms for the top region. $\omega_1 = 2.264773 \times 10^7$ rad/s, $\omega_2 = 2.302294 \times 10^7$ rad/s, $\omega_3 = 2.377118 \times 10^7$ rad/s, and $\omega_4 = 2.487805 \times 10^7$ rad/s. The modes are normalized in such a way that the maximal displacement at the plate top surface $x_2 = h + H$ is equal to one. The first mode is a transversely varying thickness-shear mode. The others are thickness-twist modes. For all of these modes the vibration is large in the inner region of the plate ($|x_3| < a$) and small in the outer regions, especially near the plate edges where the vibration is essentially zero. This is the so-called energy trapping in mesa resonators.

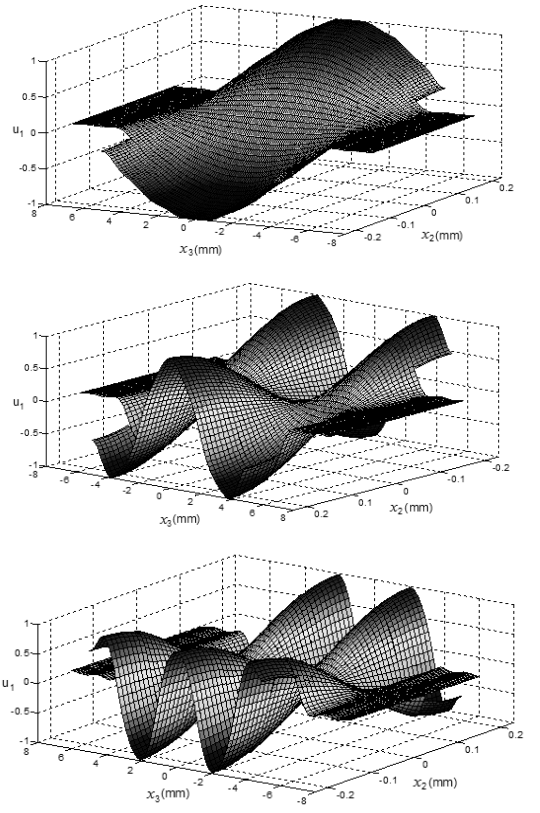

Fig. 5.24. The lowest four trapped modes.

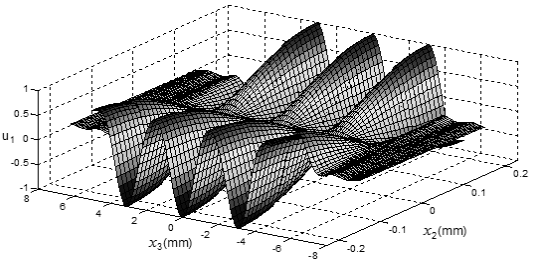

Fig. 5.24. (*Continued*)

Figure 5.25 shows the effect of a, the length of the thick inner region, on the first trapped mode. The curves are for u_1 versus x_3 at $x_2 = h$. Calculations show that larger values of a are associated with lower frequencies due to the additional inertia. For the three modes shown, $\omega_1 = 2.267035 \times 10^7$ rad/s, 2.264773×10^7 rad/s, and 2.262611×10^7 rad/s, respectively. The vibration distribution follows a and is sensitive to a. A larger a has a wider vibration distribution.

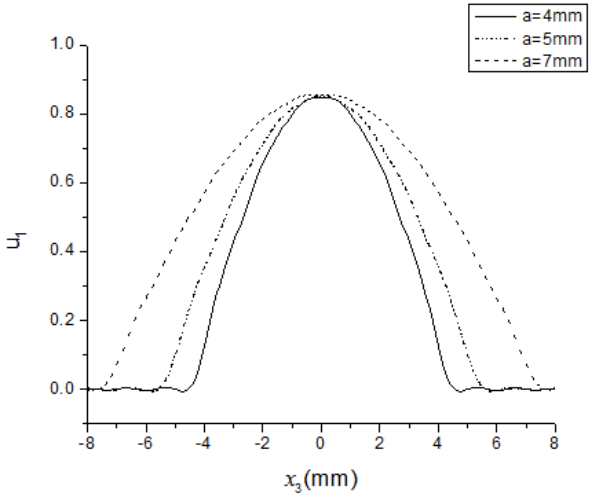

Fig. 5.25. Effect of a on the first mode.

Figure 5.26 shows the effect of H on the first trapped mode. Numerical results show that larger values of H lead to lower frequencies.

For the three modes shown, $\omega_1 = 2.479719 \times 10^7$ rad/s, 2.264773×10^7 rad/s and 2.084216×10^7 rad/s, respectively. The mode shape is not very sensitive to H. The width of the vibration distribution is essentially unaffected by H. For larger values of H, u_1 at $x_2 = h$ becomes slightly smaller.

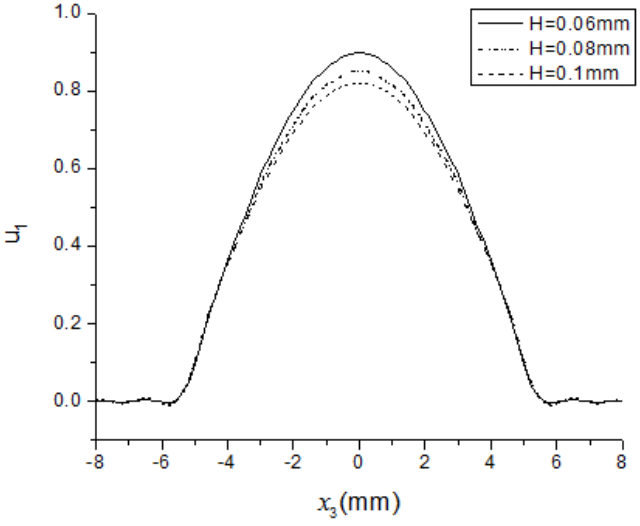

Fig. 5.26. Effect of H on the first mode.

5.9. Filter

In this section we analyze free vibrations of a crystal plate with two pairs of electrodes [69]. Such a structure represents a typical acoustic wave filter. One pair of electrodes is for time-harmonic electrical input and the other pair for output. Significant output is possible only at a few resonances.

5.9.1. Governing equations

Consider an AT-cut quartz plate as shown in Fig. 5.27. It carries two pairs of electrodes (left pair and right pair) at the top and bottom surfaces, symmetric about the middle plane of the plate. The two electrodes within

the left or right pair are identical, but the left pair and the right pair may be different. The electrodes are assumed to be very thin. Their inertia will be considered but their stiffness will be neglected. The equation governing u_1 is:

$$c_{66}u_{1,22} + c_{55}u_{1,33} \cong \rho\ddot{u}_1 . \tag{5.84}$$

The boundary condition at the plate top and bottom are

$$T_{21} = \begin{cases} \mp 2\rho' h'\ddot{u}_1, & x_2 = \pm h, \quad c_1 < x_3 < c_2, \\ \mp 2\rho' h''\ddot{u}_1, & x_2 = \pm h, \quad c_3 < x_3 < c_4, \\ 0, & x_2 = \pm h, \quad 0 < x_3 < c_1, \\ & c_2 < x_3 < c_3, \quad \text{or} \quad c_4 < x_3 < c. \end{cases} \tag{5.85}$$

The boundary conditions at the left and right edges are

$$T_{31} = 0, \quad x_3 = 0,\ c, \quad |x_2| < h . \tag{5.86}$$

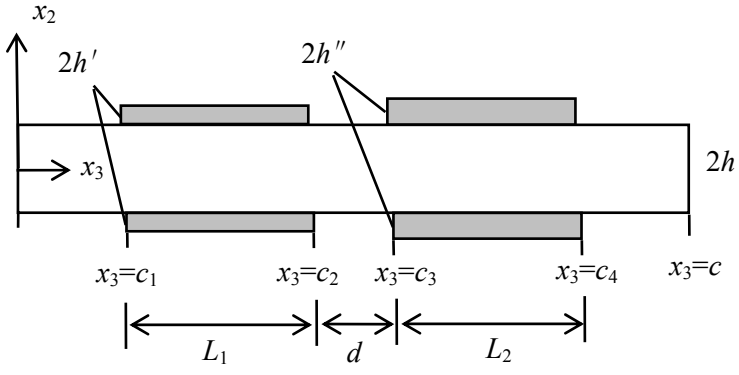

Fig. 5.27. A monolithic acoustic wave filter.

5.9.2. Fourier Series solution

We construct the following series solution from separation of variables:

$$u_1 = B_0 \sin(\eta_0 x_3) + \sum_{m=1}^{\infty} B_m \sin(\eta_m x_2) \cos\frac{m\pi x_3}{c}, \tag{5.87}$$

where B_0 and B_m are undetermined constants,

$$\eta_m^2 = \frac{\rho\omega^2}{c_{66}} - \frac{c_{55}}{c_{66}}\left(\frac{m\pi}{c}\right)^2 = \frac{\pi^2}{4h^2}\left[\frac{\omega^2}{\omega_s^2} - \frac{c_{55}}{c_{66}}\left(m\frac{2h}{c}\right)^2\right], \qquad (5.88)$$
$$m = 0,1,2,3,\cdots,$$

and

$$\omega_s = \frac{\pi}{2h}\sqrt{\frac{c_{66}}{\rho}}. \qquad (5.89)$$

Equation (5.87) satisfies Eqs. (5.84) and (5.86). To apply the boundary conditions at the plate top and bottom, we need

$$\begin{aligned} T_{21} &= c_{66}u_{1,2} = c_{66}B_0\eta_0\cos(\eta_0 x_3) \\ &\quad + c_{66}\sum_{m=1}^{\infty} B_m\eta_m\cos(\eta_m x_2)\cos\frac{m\pi x_3}{c}. \end{aligned} \qquad (5.90)$$

Due to the antisymmetry of the modes about the plate middle plane, the boundary conditions at $x_2 = -h$ do not provide equations independent to the boundary conditions at $x_2 = h$. Substitution of Eqs. (5.87) and (5.90) into to the boundary conditions at $x_2 = h$ in Eq. (5.85) leads to

$$\begin{aligned} &c_{66}B_0\eta_0\cos(\eta_0 h) + c_{66}\sum_{m=1}^{\infty} B_m\eta_m\cos(\eta_m h)\cos\frac{m\pi x_3}{c} \\ &= \begin{cases} 2\rho' h'\omega^2[B_0\sin(\eta_0 h) + \sum_{m=1}^{\infty} B_m\sin(\eta_m h)\cos\frac{m\pi x_3}{c}], \\ \qquad c_1 < x_3 < c_2, \\ 2\rho' h''\omega^2[B_0\sin(\eta_0 h) + \sum_{m=1}^{\infty} B_m\sin(\eta_m h)\cos\frac{m\pi x_3}{c}], \\ \qquad c_3 < x_3 < c_4, \\ 0, \\ \qquad 0 < x_3 < c_1, \quad c_2 < x_3 < c_3, \quad \text{or} \quad c_4 < x_3 < c. \end{cases} \end{aligned} \qquad (5.91)$$

We multiply both sides of Eq. (5.91) by $\cos(n\pi x_3/c)$ (n = 0, 1, 2, …) and integrate the resulting expression over (0, c) to obtain

$$\begin{aligned}
&c_{66}B_0\eta_0\cos(\eta_0 h)c = 2\rho' h'\omega^2 B_0\sin(\eta_0 h)(c_2 - c_1)\\
&\quad + 2\rho' h'\omega^2\sum_{m=1}^{\infty} B_m\sin(\eta_m h)\frac{c}{m\pi}\left(\sin\frac{m\pi c_2}{c} - \sin\frac{m\pi c_1}{c}\right)\\
&\quad + 2\rho' h''\omega^2 B_0\sin(\eta_0 h)(c_4 - c_3)\\
&\quad + 2\rho' h''\omega^2\sum_{m=1}^{\infty} B_m\sin(\eta_m h)\frac{c}{m\pi}\left(\sin\frac{m\pi c_4}{c} - \sin\frac{m\pi c_3}{c}\right),\\
&n = 0,
\end{aligned} \tag{5.92}$$

and

$$\begin{aligned}
&\frac{c}{2}c_{66}B_n\eta_n\cos(\eta_n h) = 2\rho' h'\omega^2 B_0\sin(\eta_0 h)\frac{c}{n\pi}\left(\sin\frac{n\pi c_2}{c} - \sin\frac{n\pi c_1}{c}\right)\\
&\quad + 2\rho' h'\omega^2\sum_{m=1}^{\infty} B_m\sin(\eta_m h)C_{nm}\\
&\quad + 2\rho' h''\omega^2 B_0\sin(\eta_0 h)\frac{c}{n\pi}\left(\sin\frac{n\pi c_4}{c} - \sin\frac{n\pi c_3}{c}\right)\\
&\quad + 2\rho' h''\omega^2\sum_{m=1}^{\infty} B_m\sin(\eta_m h)D_{nm}, \quad n = 1,2,3,\cdots,
\end{aligned} \tag{5.93}$$

where

$$\begin{aligned}
&C_{nm} = \int_{c_1}^{c_2}\cos\frac{n\pi x_3}{c}\cos\frac{m\pi x_3}{c}dx_3 = C_{mn},\\
&D_{nm} = \int_{c_3}^{c_4}\cos\frac{n\pi x_3}{c}\cos\frac{m\pi x_3}{c}dx_3 = D_{mn},\\
&n = 1,2,3,\cdots.
\end{aligned} \tag{5.94}$$

Equations (5.92) and (5.93) are linear homogeneous equations for B_0 and B_m. For nontrivial solutions the determinant of the coefficient matrix has to vanish, which determines the resonant frequencies.

5.9.3. Symmetric filter ($L_1 = L_2$, $R_1 = R_2$)

As an example we first consider a filter with four identical electrodes. $L_1 = L_2 = L = 5$ mm and $R_1 = R_2 = R = 2.5\%$. The distance between the two pairs of electrodes is $d = 1$ mm. The geometric parameters are $c = 20$ mm, $c_1 = 4.5$ mm, $c_2 = 9.5$ mm, $c_3 = 10.5$ mm, $c_4 = 15.5$ mm, and $2h = 0.3$ mm. $\omega_s = 3.46546489 \times 10^7$ rad/s. The frequencies of the modes we are interested in are within $\omega_s(1-R) < \omega < \omega_s$. The structure is symmetric about $x_3 = c/2$. Accordingly modes can be separated into symmetric ones and antisymmetric ones about $x_3 = c/2$.

Three modes antisymmetric about $x_3 = c/2$ are found and are shown in Fig. 5.28 in the order of increasing frequency. $\omega_1 = 3.39064675 \times 10^7$ rad/s, $\omega_2 = 3.41890214 \times 10^7$ rad/s, and $\omega_3 = 3.46086051 \times 10^7$ rad/s. The modes have slow variations in the x_3 direction, with no more than a few nodal points or lines (zeros). Numerical tests show that to describe such a slow variation we do not need many terms in the series. When using 20 terms in the series, $\omega_1 = 3.39064675 \times 10^7$ rad/s. When using 19 terms, $\omega_1 = 3.39064680 \times 10^7$ rad/s. There are 8 significant figures. The corresponding modes also show good agreement. Therefore all calculations below are with 20 terms in the series. In this case the η_m^2 in Eq. (5.88) is positive. For all of the modes in Fig. 5.28, the vibration is small near the plate edges at $x_3 = 0$, c, showing energy trapping. In the first mode, there is one nodal point along the x_3 direction in the middle between the two pairs of electrodes. The vibrations under the two pairs of electrodes are with opposite signs (out of phase). Such a mode can be driven by opposite voltages on the two pairs of electrodes. The other modes have more nodal points.

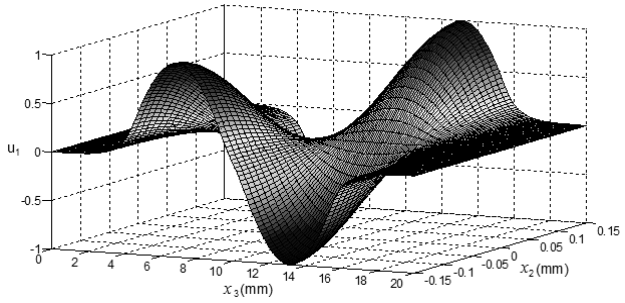

(a)

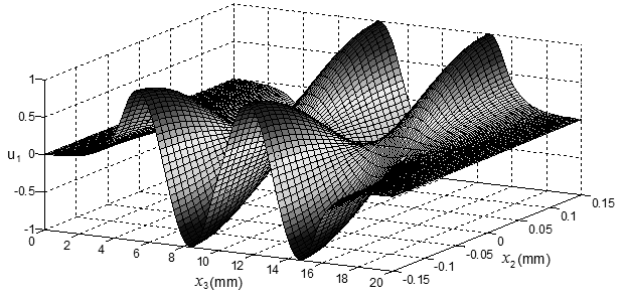

(b)

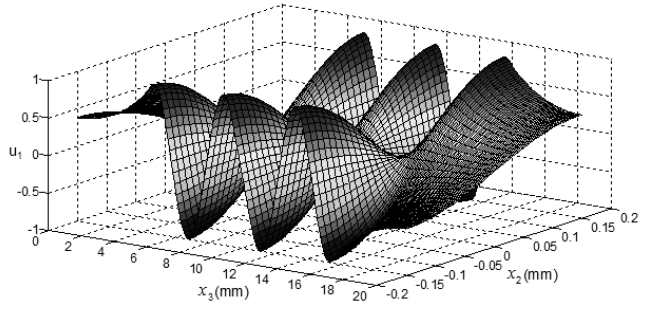

(c)

Fig. 5.28. Antisymmetric trapped modes.

Figure 5.29 shows the effects of various parameters of the electrodes on the lowest antisymmetric mode. In Fig. 5.29 (a) only the electrode length is varied (L or c_1 and c_4). When L = 4 mm, there are two trapped modes. When L = 5 or 6 mm, there are three trapped modes. As the electrodes become longer, the frequency of the first mode becomes lower due to more inertia from longer electrodes. When L = 4, 5, and 6 mm, ω_1 = 3.39476548, 3.39064675, and 3.38812666$\times 10^7$ rad/s, respectively. When the electrodes become longer, the vibration distribution becomes wider.

In Fig. 5.29 (b) only the electrode thickness is varied. The case of R = 2% has two trapped modes. The cases of R = 2.5% and 3% have 3 trapped modes. As R increases, the frequency of the first mode decreases as expected: ω_1 = 3.40695776, 3.39064675, and 3.37444052$\times 10^7$ rad/s, respectively. The vibration distribution is not sensitive to R.

In Fig. 5.29 (c) only the distance d between the two pairs of electrodes is varied. The frequency is not sensitive to d as expected: ω_1 = 3.39064675, 3.39009008, and 3.38993846$\times 10^7$ rad/s, respectively. The vibration distribution is sensitive to d. When d = 1 mm, the solid line in the figure is smooth. When d=2 and 3 mm, the dotted lines in the figure show the effect of the distance between the electrodes.

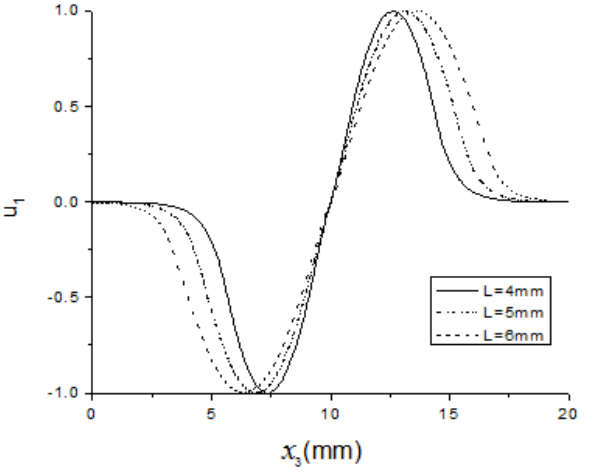

(a)

Fig. 5.29. Effects of electrode parameters.

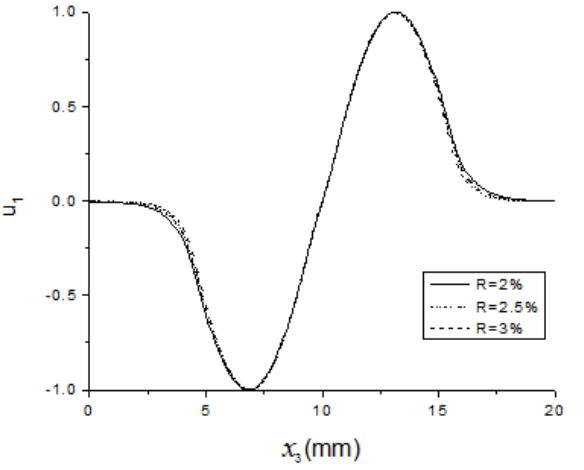

(b)

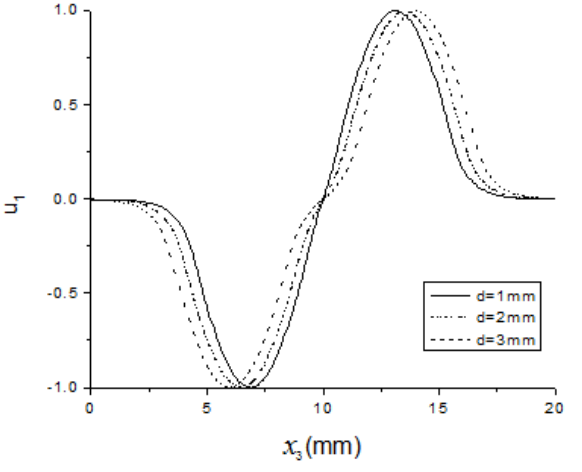

(c)

Fig. 5.29. (*Continued*)

For the same symmetric filter whose antisymmetric modes are in Fig. 5.28, there also exist three trapped modes symmetric about $x_3 = c/2$ which are shown in Fig. 5.30 in the order of increasing frequency. These modes can be excited by applying the same voltage

on the two pairs of electrodes. $\omega_1 = 3.38893137 \times 10^7$ rad/s, $\omega_2 = 3.41240560 \times 10^7$ rad/s, and $\omega_3 = 3.44943502 \times 10^7$ rad/s. These three frequencies are slightly below the frequencies of the three modes in Fig. 5.28. When symmetric and antisymmetric modes are considered together, there are six trapped modes. The lowest mode is symmetric, followed by the first antisymmetric mode, and so on.

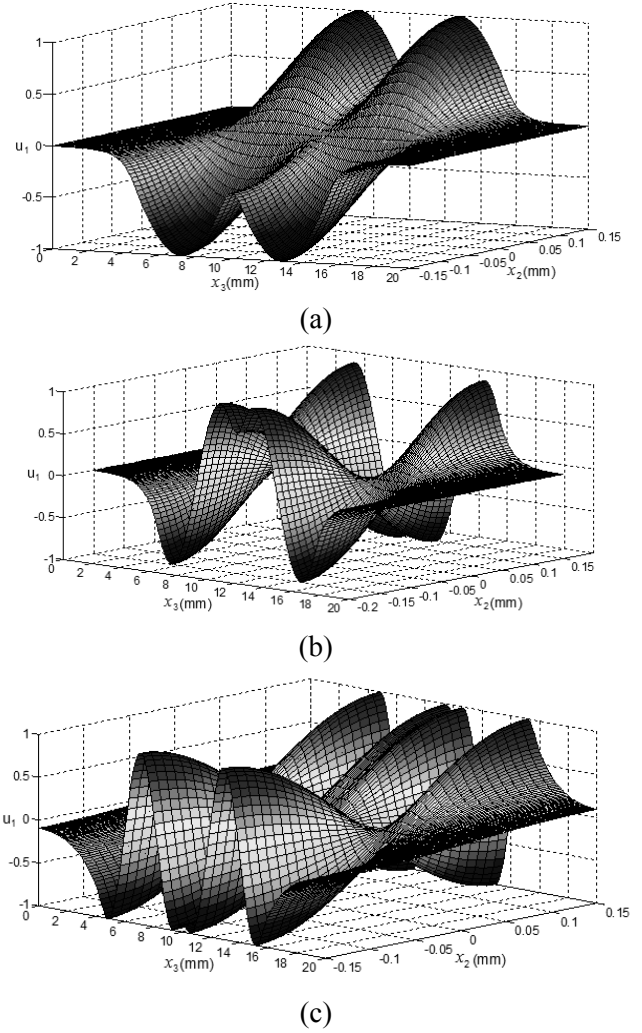

Fig. 5.30. Symmetric trapped modes.

5.9.4. Asymmetric filter

Figure 5.31 shows the effects of the electrode parameters when the thickness or length of the right pair of electrodes is varied. In this case

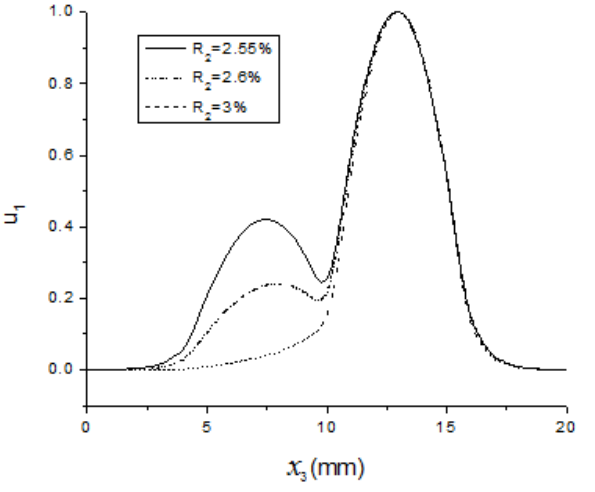

(a)

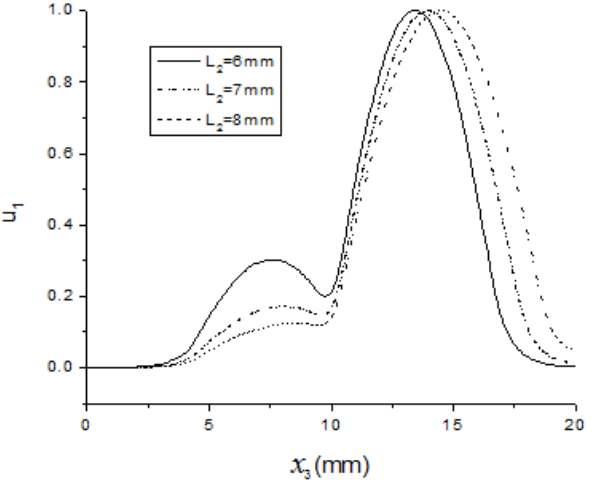

(b)

Fig. 5.31. Effects of electrode parameters.

the structure loses its symmetry about $x_3 = c/2$. For filters, even if the structure of the crystal plate and electrodes are symmetric about $x_3 = c/2$, the input and output electrical circuits may cause loss of symmetry about $x_3 = c/2$ when piezoelectric coupling is considered. Therefore the examination of the effects of some small asymmetry is fundamental. In Fig. 5.31 (a) R_1 is fixed to be 2.5%. R_2 is varied. When R_2 = 2.55%, 2.6%, and 3%, there are always 6 trapped modes which can no longer be separated into symmetric and antisymmetric modes. As R_2 increases, the frequency of the first mode decreases as expected: ω_1 = 3.38781680, 3.38637123, and 3.37371241×10^7 rad/s, respectively. At the same time the vibration distribution is more and more under the thicker electrodes.

Figure 5.31 (b) shows the effect of L_2. When L_2 = 6 mm, there are six trapped modes. When L_2 = 7 and 8 mm, there are seven trapped modes. As the right pair of electrodes become longer, the frequency of the first mode becomes lower: ω_1 = 3.38738566, 3.38602462, and 3.38501809×10^7 rad/s, respectively. At the same time the vibration is more and more under the longer electrodes

5.10. Contoured Resonator

An important property of thickness-shear and thickness-twist modes is their energy trapping behavior in a partially electroded plate in which vibrations are confined near the electroded central region of the plate (see Section 5.4). Near the edges of the plate there is essentially no vibration where the plate can be mounted without affecting its vibration. Energy trapping is due to the inertial effect of the electrodes on an elastic plate. Contoured plates with varying thickness (thick in the central region and thin near the edges) can also produce strong energy trapping. A cylinder with an oblate elliptical cross section (see Fig. 5.32) may be viewed as a contoured resonator. In this section we study shear-horizontal vibrations in such an elastic cylinder [70].

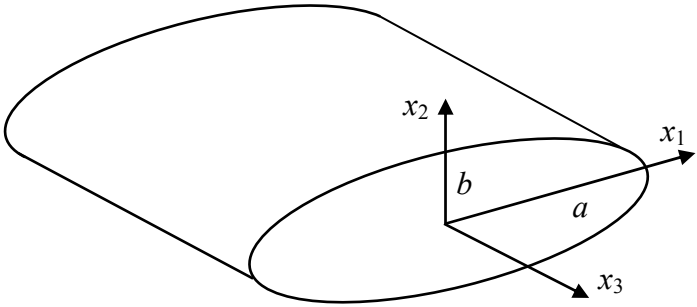

Fig. 5.32. An oblate elliptical cylinder and coordinate system.

5.10.1. Governing equation

Consider the long cylinder with an elliptical cross-section shown in Fig. 5.32. The semi-major and semi-minor axes are denoted by a and b. We are interested in the case when $a>>b$. For resonator applications we consider the case when the surface of the cylinder is traction free. The cylinder is made of an isotropic elastic material. The three-dimensional theory of elasticity allows for the following shear-horizontal motions described by:

$$u_1 = u_2 = 0, \quad u_3 = u_3(x_1, x_2, t), \tag{5.95}$$

which depends on time and two spatial variables only. The nonzero components of the strain tensor S_{ij} and the stress tensor T_{ij} are

$$\begin{aligned} &S_4 = 2S_{32} = u_{3,2}, \quad S_5 = 2S_{31} = u_{3,1}, \\ &T_4 = \mu u_{3,2}, \quad T_5 = \mu u_{3,1}. \end{aligned} \tag{5.96}$$

μ is the shear elastic constant. The nontrivial one of the equations of motion takes the following form:

$$c_2^2 \nabla^2 u_3 = \ddot{u}_3, \tag{5.97}$$

where ∇^2 is the two-dimensional Laplacian. c_2 is the speed of plane shear waves given by

$$c_2^2 = \mu / \rho . \tag{5.98}$$

We consider time-harmonic free vibrations for which all fields have the same $\exp(i\omega t)$ factor which will be dropped for simplicity. For harmonic motions, Eq. (5.97) reduces to the Helmholtz equation:

$$c_2^2 \nabla^2 u_3 = -\omega^2 u_3 . \tag{5.99}$$

We introduce elliptical coordinates (ξ, η) defined by

$$x_1 = h \cosh \xi \cos \eta , \quad x_2 = h \sinh \xi \sin \eta , \tag{5.100}$$

where h is half the focal distance of the ellipses associated with Eq. (5.100). Then Eq. (5.99) takes the following form:

$$\frac{\partial^2 u_3}{\partial \xi^2} + \frac{\partial^2 u_3}{\partial \eta^2} + 2k^2 (\cosh 2\xi - \cos 2\eta) u_3 = 0 , \tag{5.101}$$

where

$$2k = \frac{\omega}{c_2} h . \tag{5.102}$$

The stress components in the elliptic coordinates are

$$T_{\xi z} = \frac{\mu}{hJ} \frac{\partial u_3}{\partial \xi} , \quad T_{\eta z} = \frac{\mu}{hJ} \frac{\partial u_3}{\partial \eta} , \tag{5.103}$$

where

$$J = \frac{\sqrt{2}}{2} \sqrt{\cosh 2\xi - \cos 2\eta} . \tag{5.104}$$

5.10.2. Solutions of the Helmholtz equation

By the method of separation of variables, we write u_3 as:

$$u_3(\xi, \eta) = U(\xi) V(\eta) . \tag{5.105}$$

Substitution of Eq. (5.105) into Eq. (5.101) results in the following two ordinary differential equations:

$$\frac{d^2V(\eta)}{d\eta^2} + (\lambda - 2q\cos(2\eta))V(\eta) = 0\,, \tag{5.106}$$

$$\frac{d^2U(\xi)}{d\xi^2} + (2q\cosh(2\xi) - \lambda)U(\xi) = 0\,, \tag{5.107}$$

where λ is the separation constant and

$$q = \frac{\omega^2 h^2}{4c_2^2}\,. \tag{5.108}$$

Equations (5.106) and (5.107) are known as the angular and radial Mathieu equations, respectively.

5.10.2.1. Solutions of the angular Mathieu equation

Equation (5.106) has four kinds of periodic solutions with period 2π :

$$se_{2m+1}(\eta, q) = \sum_{r=0}^{\infty} A_{2r+1}^{(2m+1)}(q)\sin(2r+1)\eta\,, \tag{5.109}$$

$$se_{2m+2}(\eta, q) = \sum_{r=0}^{\infty} A_{2r+2}^{(2m+2)}(q)\sin(2r+2)\eta\,, \tag{5.110}$$

$$ce_{2m}(\eta, q) = \sum_{r=0}^{\infty} B_{2r}^{(2m)}(q)\cos(2r\eta), \tag{5.111}$$

$$ce_{2m+1}(\eta, q) = \sum_{r=0}^{\infty} B_{2r+1}^{(2m+1)}(q)\cos(2r+1)\eta\,, \tag{5.112}$$

where m = 0, 1, 2, 3, …. $A_r^{(m)}(q)$ and $B_r^{(m)}(q)$ are coefficients for the series of η. They are solutions of the following equations obtained by substituting Eqs. (5.109)–(5.112) into Eq. (5.106):

$$\begin{bmatrix} 1-q-\lambda & q & 0 & 0 & 0 & 0 & \cdots \\ q & 3^2-\lambda & q & 0 & 0 & 0 & \cdots \\ 0 & q & 5^2-\lambda & q & 0 & 0 & \cdots \\ 0 & 0 & q & 7^2-\lambda & q & 0 & \cdots \\ \cdots & \cdots & \cdots & \cdots & \cdots & \cdots & \cdots \end{bmatrix} \begin{bmatrix} A_1^{(2m+1)} \\ A_3^{(2m+1)} \\ A_5^{(2m+1)} \\ A_7^{(2m+1)} \\ \cdots \end{bmatrix} = \begin{bmatrix} 0 \\ 0 \\ 0 \\ 0 \\ 0 \\ \cdots \end{bmatrix}, \quad (5.113)$$

$$\begin{bmatrix} 2^2-\lambda & q & 0 & 0 & 0 & 0 & \cdots \\ q & 4^2-\lambda & q & 0 & 0 & 0 & \cdots \\ 0 & q & 6^2-\lambda & q & 0 & 0 & \cdots \\ 0 & 0 & q & 8^2-\lambda & q & 0 & \cdots \\ \cdots & \cdots & \cdots & \cdots & \cdots & \cdots & \cdots \end{bmatrix} \begin{bmatrix} A_2^{(2m+2)} \\ A_4^{(2m+2)} \\ A_6^{(2m+2)} \\ A_8^{(2m+2)} \\ \cdots \end{bmatrix} = \begin{bmatrix} 0 \\ 0 \\ 0 \\ 0 \\ 0 \\ \cdots \end{bmatrix}, \quad (5.114)$$

$$\begin{bmatrix} -\lambda & q & 0 & 0 & 0 & 0 & \cdots \\ 2q & 2^2-\lambda & q & 0 & 0 & 0 & \cdots \\ 0 & q & 4^2-\lambda & q & 0 & 0 & \cdots \\ 0 & 0 & q & 6^2-\lambda & q & 0 & \cdots \\ \cdots & \cdots & \cdots & \cdots & \cdots & \cdots & \cdots \end{bmatrix} \begin{bmatrix} B_0^{(2m)} \\ B_2^{(2m)} \\ B_4^{(2m)} \\ B_6^{(2m)} \\ \cdots \end{bmatrix} = \begin{bmatrix} 0 \\ 0 \\ 0 \\ 0 \\ 0 \\ \cdots \end{bmatrix}, \quad (5.115)$$

$$\begin{bmatrix} 1+q-\lambda & q & 0 & 0 & 0 & 0 & \cdots \\ q & 3^2-\lambda & q & 0 & 0 & 0 & \cdots \\ 0 & q & 5^2-\lambda & q & 0 & 0 & \cdots \\ 0 & 0 & q & 7^2-\lambda & q & 0 & \cdots \\ \cdots & \cdots & \cdots & \cdots & \cdots & \cdots & \cdots \end{bmatrix} \begin{bmatrix} B_1^{(2m+1)} \\ B_3^{(2m+1)} \\ B_5^{(2m+1)} \\ B_7^{(2m+1)} \\ \cdots \end{bmatrix} = \begin{bmatrix} 0 \\ 0 \\ 0 \\ 0 \\ 0 \\ \cdots \end{bmatrix}. \quad (5.116)$$

λ is obtained by setting the determinants of the coefficient matrices of Eqs. (5.113)–(5.116) to zero. $se_{2m+1}(\eta,q)$ and $se_{2m+2}(\eta,q)$ correspond to modes antisymmetric about the major axis x_1. $ce_{2m}(\eta,q)$ and $ce_{2m+1}(\eta,q)$ correspond to symmetric modes. $ce_m(\eta,q)$ and $se_m(\eta,q)$ are orthogonal functions satisfying the following condition:

$$\int_0^{2\pi} ce_m(\eta,q)ce_n(\eta,q)=\int_0^{2\pi} se_m(\eta,q)se_n(\eta,q)=\begin{cases}\pi, & \text{if } m=n,\\ 0, & \text{if } m\neq n.\end{cases} \tag{5.117}$$

In accordance with Eq. (5.117), we have the following normalization conditions:

$$\begin{aligned}&\sum_{r=0}^{\infty}\left(A_{2r+1}^{(2m+1)}\right)^2=1,\quad \sum_{r=0}^{\infty}\left(A_{2r+2}^{(2m+2)}\right)^2=1,\\ &2(B_0^{(2m)})^2+\sum_{r=1}^{\infty}\left(B_{2r}^{(2m)}\right)^2=1,\quad \sum_{r=0}^{\infty}\left(B_{2r+1}^{(2m+1)}\right)^2=1.\end{aligned} \tag{5.118}$$

5.10.2.2. Solutions of the radial Mathieu equation

The four kinds of radial Mathieu functions corresponding to the above angular Mathieu functions are:

$$\begin{aligned}Se_{2m+1}(\xi,q)=&\frac{se'_{2m+1}(0,q)se_{2m+1}\left(\frac{\pi}{2},q\right)}{\sqrt{q}\left(A_1^{(2m+1)}\right)^2}\\ &\times\sum_{r=0}^{\infty}(-1)^m A_{2r+1}^{(2m+1)}\left[J_m(v_1)J_{m+1}(v_2)-J_m(v_2)J_{m+1}(v_1)\right],\end{aligned} \tag{5.119}$$

$$\begin{aligned}Se_{2m+2}(\xi,q)=&-\frac{se'_{2m+2}(0,q)se'_{2m+2}\left(\frac{\pi}{2},q\right)}{q\left(A_2^{(2m+2)}\right)^2}\\ &\times\sum_{r=0}^{\infty}(-1)^m A_{2r+2}^{(2m+2)}\left[J_m(v_1)J_{m+2}(v_2)-J_m(v_2)J_{m+2}(v_1)\right],\end{aligned} \tag{5.120}$$

$$Ce_{2m}(\xi,q)=\frac{ce_{2m}(0,q)ce_{2m}\left(\frac{\pi}{2},q\right)}{\left(B_0^{(2m)}\right)^2}\times\sum_{r=0}^{\infty}(-1)^m B_{2r}^{(2m)}(q)J_m(v_1)J_m(v_2), \tag{5.121}$$

$$Ce_{2m+1}(\xi,q)=-\frac{ce_{2m+1}(0,q)ce_{2m+1}\left(\frac{\pi}{2},q\right)}{\sqrt{q}\left(B_1^{(2m+1)}\right)^2}\times\sum_{r=0}^{\infty}(-1)^m B_{2r+1}^{(2m+1)}(q)\left[J_m(v_1)J_{m+1}(v_2)+J_m(v_2)J_{m+1}(v_1)\right], \tag{5.122}$$

where $v_1=\sqrt{q}\,\exp(-\xi)$ and $v_2=\sqrt{q}\,\exp(\xi)$. J_m are Bessel functions of the first kind.

5.10.3. Shear-horizontal modes

We discuss modes antisymmetric and symmetric about the major axis of the oblate elliptical cross section separately.

5.10.3.1. Antisymmetric modes

The displacement field of these modes is

$$u_3(\xi,\eta,t)=\sum_{m=1}^{\infty}S_m Se_m(\xi,q)se_m(\eta,q)\,, \tag{5.123}$$

where S_m are undetermined constants. Substitution of Eq. (5.123) into Eq. (5.103) gives

$$T_{\xi z}=\frac{\mu}{hJ}\sum_{m=1}^{\infty}S_m Se'_m(\xi,q)se_m(\eta,q),$$
$$T_{\eta z}=\frac{\mu}{hJ}\sum_{m=1}^{\infty}S_m Se_m(\xi,q)se'_m(\eta,q), \tag{5.124}$$

where a prime indicates differentiation with respect to ξ in Eq. $(5.124)_1$ or η in Eq. $(5.124)_2$. Let the elliptical boundary of the cross section of the cylinder be at $\xi = \xi_0$. The traction-free boundary condition is

$$T_{\xi z} = \frac{\mu}{hJ} \sum_{m=1}^{\infty} S_m Se'_m(\xi_0, q) se_m(\eta, q) = 0, \tag{5.125}$$

which implies that

$$Se'_m(\xi_0, q) = 0. \tag{5.126}$$

Equation (5.126) determines q. Then ω can be determined from Eq. (5.108).

5.10.3.2. Symmetric modes

Similarly, the symmetric modes are given by

$$u_3 = \sum_{m=0}^{\infty} C_m Ce_m(\xi, q) ce_m(\eta, q), \tag{5.127}$$

$$\begin{aligned} T_{\xi z} &= \frac{\mu}{hJ} \sum_{m=0}^{\infty} C_m Ce'_m(\xi, q) ce_m(\eta, q), \\ T_{\eta z} &= \frac{\mu}{hJ} \sum_{m=0}^{\infty} C_m Ce_m(\xi, q) ce'_m(\eta, q), \end{aligned} \tag{5.128}$$

$$Ce'_m(\xi_0, q) = 0. \tag{5.129}$$

5.10.4. Numerical result and discussion

As an example, for the elastic material we consider Glass-7950 with $\rho = 2180\ \text{kg/m}^3$ and $\mu = 2.7815 \times 10^{10}\ \text{N/m}^2$. The elliptical boundary is oblate with a = 10b = 5 mm, which is typical for a resonator. $\xi_0 =$ 0.10033 from calculation. We use the first thirty terms of each series to calculate the displacement field. For the most widely used fundamental thickness-shear mode, the number of significant figures for its frequency is sixteen when thirty terms are kept in the series. In the figures shown in the following, the maximal displacement is normalized to one. The

figures are not drawn to scale. The ellipses are in fact much more oblate than what is shown in the figures. We discuss thickness-shear and thickness-twist modes separately below.

5.10.4.1. Thickness-shear modes

The fundamental thickness-shear mode is the one most widely used in acoustic wave devices and therefore its displacement distribution over a cross section is shown alone in Fig. 5.33. The upper picture is two-dimensional where darker areas represent larger displacements. The lower picture is three-dimensional. This mode has one nodal line with zero displacement at $x_2 = 0$ or along the x_1 axis. When the upper half of the cross section is moving in one direction, the lower half moves in the opposite direction or vise versa. The top and bottom of the cylinder are moving with the largest displacement. The left and right edges are essentially not moving. This is the so-called energy trapping phenomenon. With energy trapping, the cylinder can be mounted at the left and/or right edges without affecting the vibration in the central region.

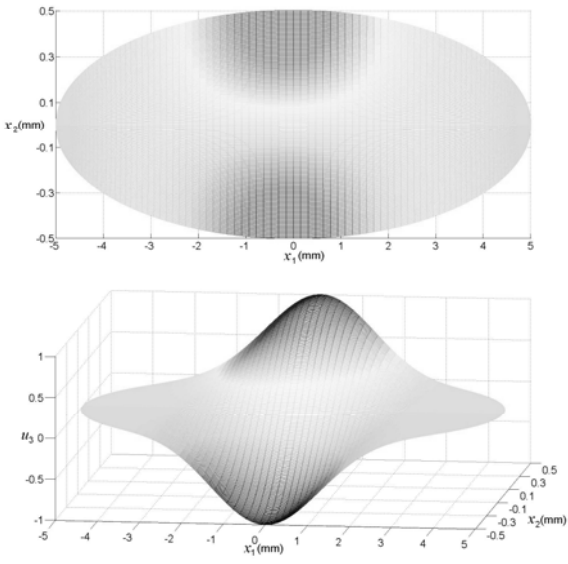

Fig. 5.33. Fundamental thickness-shear mode. 1st mode when $u_3 = Se_1(q,\xi)se_1(q,\eta)$. $\omega = 1.1567271\times10^7$ rad/s.

Figures 5.34 (a), (b), and (c) show three higher-order thickness-shear modes. They have two, three, and four nodal lines roughly parallel to the x_1 axis, respectively. The frequencies of the thickness-shear modes in Fig. 5.33 and Figs. 5.34 (a), (b), and (c) are roughly equally spaced although not exactly so. The modes in Fig. 5.33 and Fig. 5.34 (b) are antisymmetric about the x_1 axis. The other two modes are symmetric. Higher-order modes are better trapped, i.e., with narrower vibration distributions in the x_1 direction.

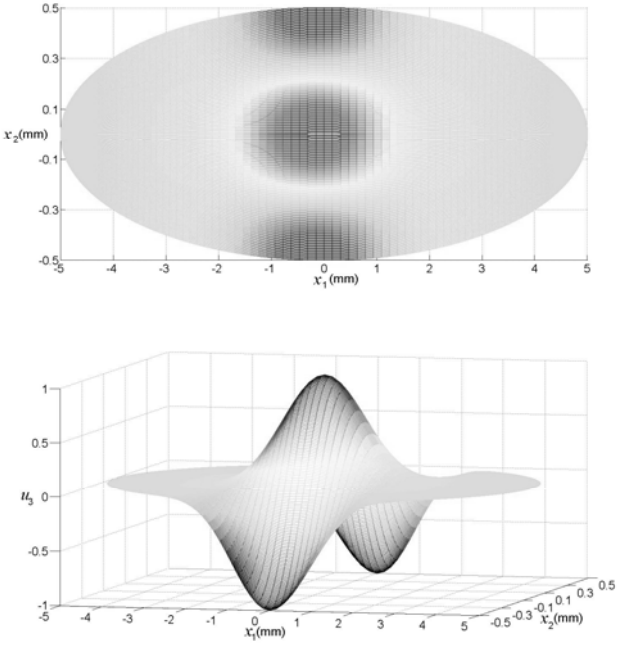

(a)

Fig. 5.34. Higher-order thickness-shear modes. (a) 1st mode when $u_3 = Ce_0(q,\xi)ce_0(q,\eta)$. $\omega = 2.2795427\times10^7$ rad/s. (b) 2nd mode when $u_3 = Se_1(q,\xi)se_1(q,\eta)$. $\omega = 3.4019209\times10^7$ rad/s. (c) 3rd mode when $u_3 = Ce_0(q,\xi)ce_0(q,\eta)$. $\omega = 4.5241962\times10^7$ rad/s.

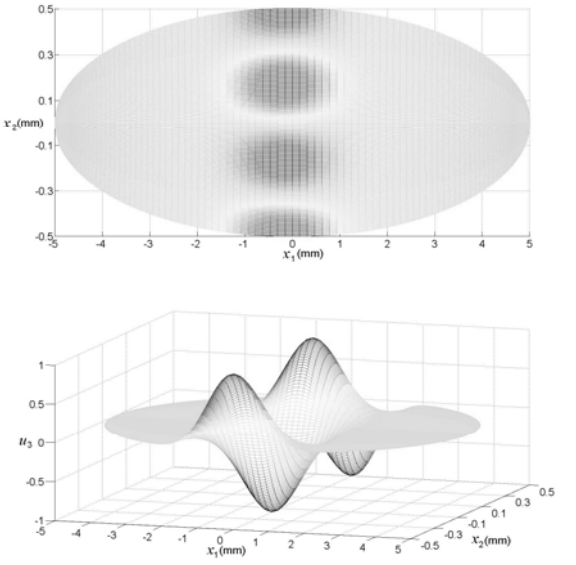

(b)

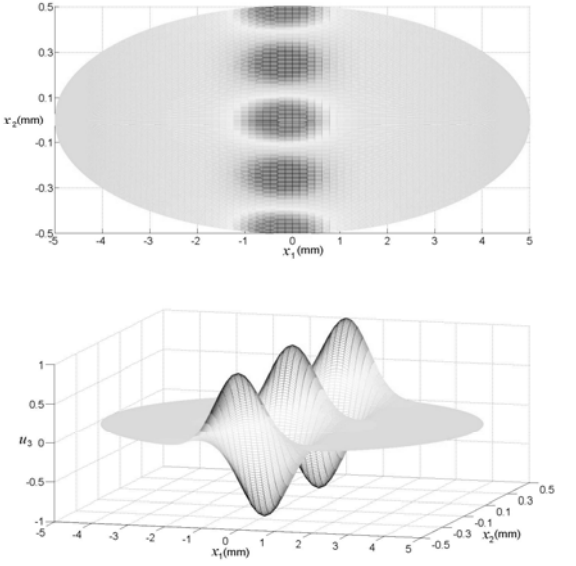

(c)

Fig. 5.34. (*Continued*)

5.10.4.2. Thickness-twist modes

Corresponding to the fundamental thickness-shear mode in Fig. 5.33 with a horizontal nodal line at $x_2 = 0$, there are higher-order modes with roughly vertical nodal lines as shown in Figs. 5.35 (a), (b) and (c) with an increasing number of one, two, and three vertical nodal lines, respectively. These are called thickness-twist modes for the obvious reason as shown in the figure. The distribution of the modes in Figs. 5.35 (a), (b) and (c) in the x_1 direction becomes wider and wider, or higher-order modes are less trapped. At the same time, the frequencies of the modes in Figs. 5.35 (a), (b) and (c) increase only slightly.

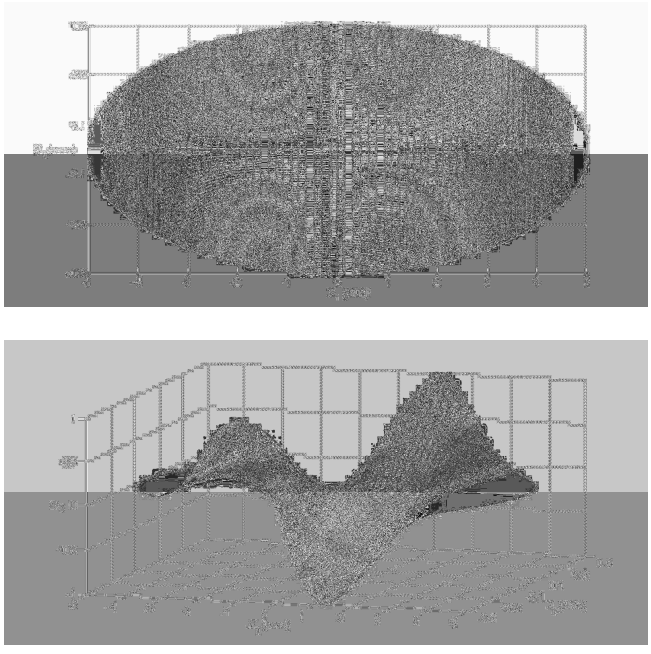

(a)

Fig. 5.35. TT modes associated with the fundamental TSh mode. (a) 1st mode when $u_3 = Se_2(q,\xi)se_2(q,\eta)$. $\omega = 1.2303289\times10^7$ rad/s. (b) 1st mode when $u_3 = Se_3(q,\xi)se_3(q,\eta)$. $\omega = 1.3060256\times10^7$ rad/s. (c) 1st mode when $u_3 = Se_4(q,\xi)se_4(q,\eta)$. $\omega = 1.3837045\times10^7$ rad/s.

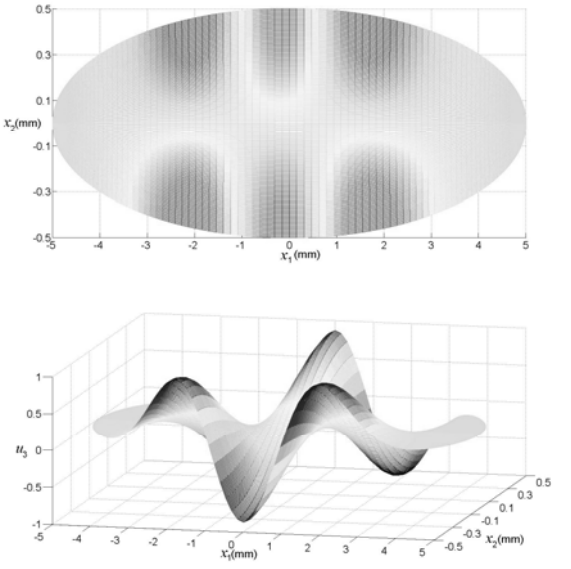

(b)

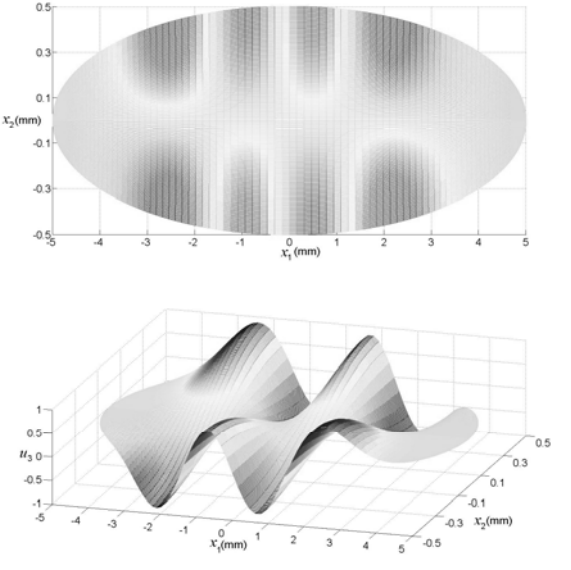

(c)

Fig. 5.35. (*Continued*)

Similarly, Figs. 5.36 (a), (b) and (c) show three thickness-twist modes corresponding to the higher-order thickness-shear mode in Fig. 5.34 (a). Figures 5.36 (d) and (e) are thickness-twist modes corresponding to the thickness-shear modes in Figs. 5.34 (b) and (c), respectively.

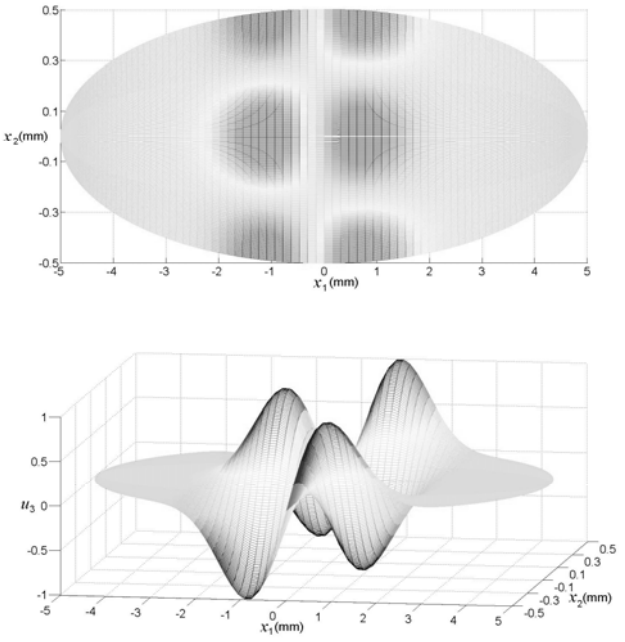

(a)

Fig. 5.36. Some other thickness-twist modes. (a) 1st mode when $u_3 = Ce_1(q,\xi)ce_1(q,\eta)$. $\omega = 2.3521836\times10^7$ rad/s. (b) 1st mode when $u_3 = Ce_2(q,\xi)ce_2(q,\eta)$. $\omega = 2.4259184\times10^7$ rad/s. (c) 1st mode when $u_3 = Ce_3(q,\xi)ce_3(q,\eta)$. $\omega = 2.5007192\times10^7$ rad/s. (d) 2nd mode when $u_3 = Se_2(q,\xi)se_2(q,\eta)$. $\omega = 3.4742139\times10^7$ rad/s. (e) 2nd mode when $u_3 = Ce_1(q,\xi)ce_1(q,\eta)$. $\omega = 4.5963106\times10^7$ rad/s.

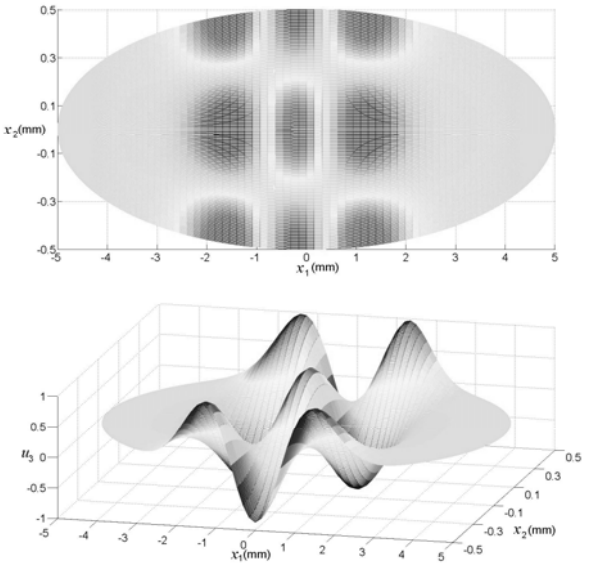

(b)

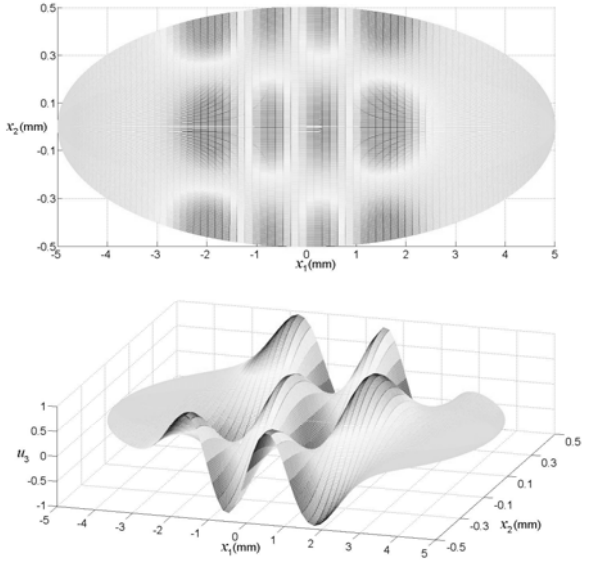

(c)

Fig. 5.36. (*Continued*)

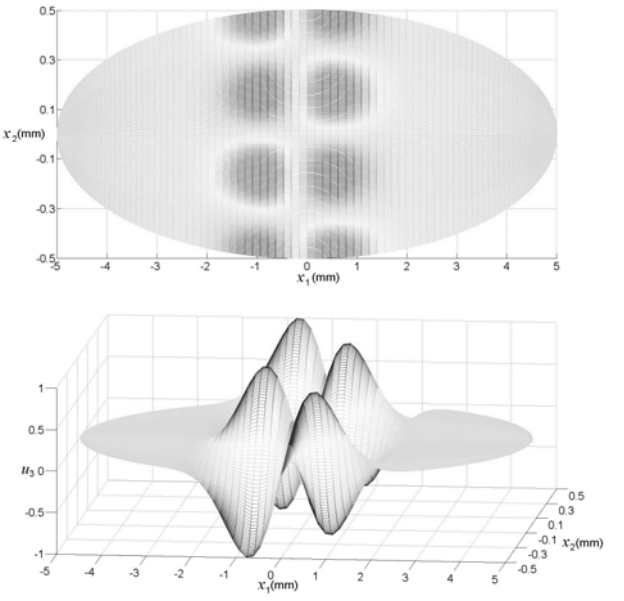

(d)

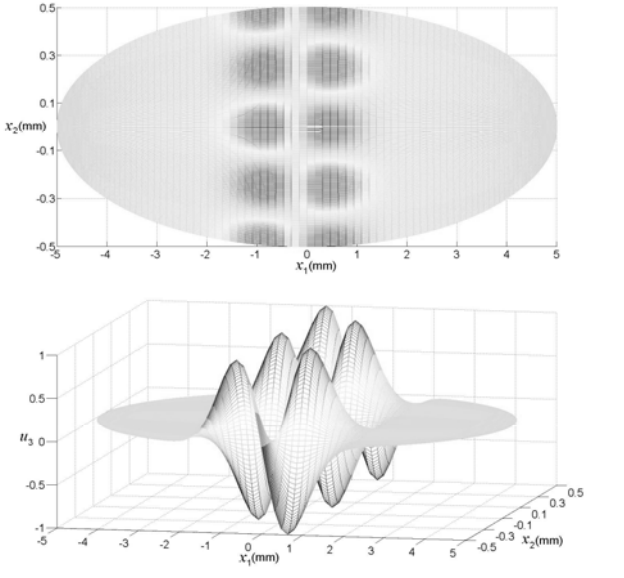

(e)

Fig. 5.36. (*Continued*)

5.11. Plate with a Nonuniform Mass Layer

In real applications of quartz crystal microbalances the mass layer may be nonuniform with a varying thickness. It may also be asymmetric in the in-plane x_1 and x_3 coordinates. In this section we address the issue of asymmetric and nonuniform mass layers (see Fig. 5.37) [71].

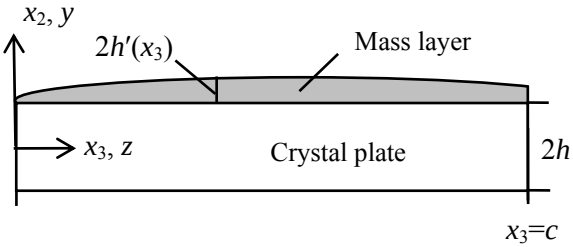

Fig. 5.37. An AT-cut quartz plate with a nonuniform mass layer.

5.11.1. Fourier series solution

The governing equations and boundary conditions are

$$c_{66}u_{1,22} + c_{55}u_{1,33} \cong \rho\ddot{u}_1, \quad 0 < x_3 < c, \quad |x_2| < h, \tag{5.130}$$

$$T_{21} = -2\rho' h'(x_3)\ddot{u}, \quad x_2 = h, \quad 0 < x_3 < c, \tag{5.131}$$

$$T_{21} = 0, \quad x_2 = -h, \quad 0 < x_3 < c, \tag{5.132}$$

$$T_{31} = 0, \quad x_3 = 0,\ c, \quad |x_2| < h, \tag{5.133}$$

where

$$\begin{aligned} 2h'(x_3) &= 2h_0\left[1 - a\left(\frac{x_3}{c} - b\right)^2\right] = 2h_0 f(x_3), \\ f(x_3) &= 1 - a\left(\frac{x_3}{c} - b\right)^2. \end{aligned} \tag{5.134}$$

h_0, a and b are positive constants. $2h_0$ is the maximal thickness. a and b are dimensionless. f is the normalized mass layer thickness. f versus $x_3 = z$ for different values of a and b are shown in Figs. 5.38 (a) and (b),

respectively. It can be seen that f can describe various nonuniform and asymmetric mass layers with different choices of a and b. a describes nonuniformity, and b is related to asymmetry. When $a = 0$ the mass layer is uniform. When $b = 0.5$ the mass layer is symmetric about $x_3 = c/2$. For symmetric mass layers ($b = 0.5$), the mass layer edge thickness at $z = 0$ or c becomes zero when $a = 4$.

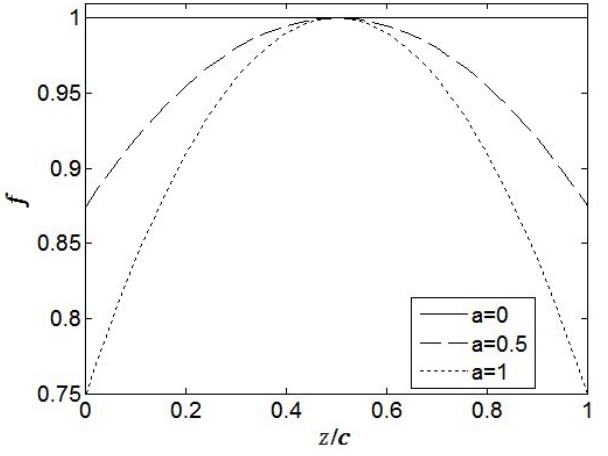

(a)

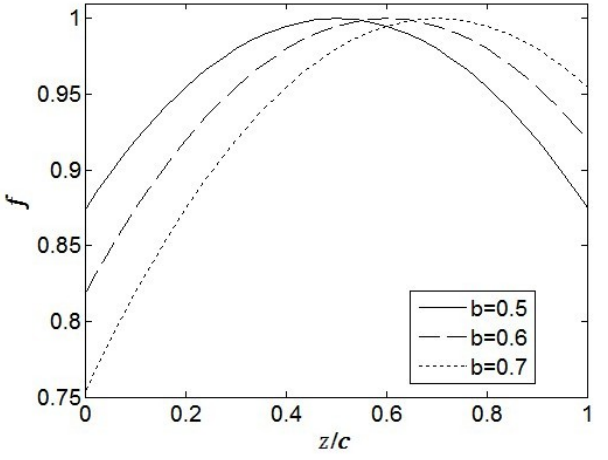

(b)

Fig. 5.38. Normalized mass layer thickness. (a) Effect of a on nonuniformity (b=0.5). (b) Effect of b on asymmetry (a=0.5).

Consider the following displacement field (see Eq. (5.58)):

$$u_1 = A_0 \cos(\eta_0 x_2) + B_0 \sin(\eta_0 x_2) + \sum_{m=1}^{\infty} [A_m \cos(\eta_m x_2) + B_m \sin(\eta_m x_2)] \cos\frac{m\pi x_3}{c}, \tag{5.135}$$

where A_0, B_0, A_m and B_m are undetermined constants, and

$$\eta_m^2 = \frac{\rho\omega^2}{c_{66}} - \frac{c_{55}}{c_{66}}\left(\frac{m\pi}{c}\right)^2 = \frac{\pi^2}{4h^2}\left[\frac{\omega^2}{\omega_s^2} - \frac{c_{55}}{c_{66}}\left(m\frac{2h}{c}\right)^2\right], \quad m = 0,1,2,3,\cdots. \tag{5.136}$$

$$\omega_s = \frac{\pi}{2h}\sqrt{\frac{c_{66}}{\rho}}. \tag{5.137}$$

Equations (5.130) and (5.133) are already satisfied by Eq. (5.135). To apply the boundary conditions at the plate top and bottom, we need

$$T_{21} = c_{66}u_{1,2} = -c_{66}A_0\eta_0 \sin(\eta_0 x_2) + c_{66}B_0\eta_0 \cos(\eta_0 x_3) + c_{66}\sum_{m=1}^{\infty} [-A_m\eta_m \sin(\eta_m x_2) + B_m\eta_m \cos(\eta_m x_2)] \cos\frac{m\pi x_3}{c}. \tag{5.138}$$

We then substitute Eqs. (5.135), (5.138) and (5.134) into Eqs. (5.131) and (5.132), multiply both sides of the resulting equations by $\cos(n\pi x_3 / c)$ (n = 0, 1, 2, …) and integrate them over (0, c). This gives linear homogeneous equations for A_0, B_0, A_m and B_m. For nontrivial solutions the determinant of the coefficient matrix has to vanish, which determines the resonant frequencies. The nontrivial solutions of A_0, B_0, A_m and B_m determine the corresponding modes.

5.11.2. Numerical result

We introduce another frequency

$$\bar{\omega}_s = \omega_s(1-R), \quad R = \frac{\rho' h_0}{\rho h}. \tag{5.139}$$

The resonant frequencies of the modes we are interested in are within $\bar{\omega}_s < \omega < \omega_s$. We begin with the case when a = 4, b = 0.5 (symmetric mass layer with zero edge thickness), and R = 5%. Twenty three terms are used in the calculations below. In this case five resonant frequencies are found within $\bar{\omega}_s < \omega < \omega_s$. The first mode is a slowly varying thickness-shear mode. The other modes all have nodal points along the x_3 direction and are thickness-twist modes. The first two modes are trapped. The third, fourth and fifth modes are not trapped.

In Fig. 5.39 we show the effect of R on energy trapping of the thickness-shear mode by plotting the plate bottom surface displacement at x_2 =- h. When R = 3%, 5%, and 9%, the corresponding resonant frequencies are ω/ω_s = 0.975662, 0.958367, and 0.925828, respectively, gradually decreasing. A larger value of R means a thicker mass layer with more inertia and hence a lower resonant frequency as expected. A larger R also corresponds to stronger energy trapping with the vibration distribution pushed more toward the central portion of the plate.

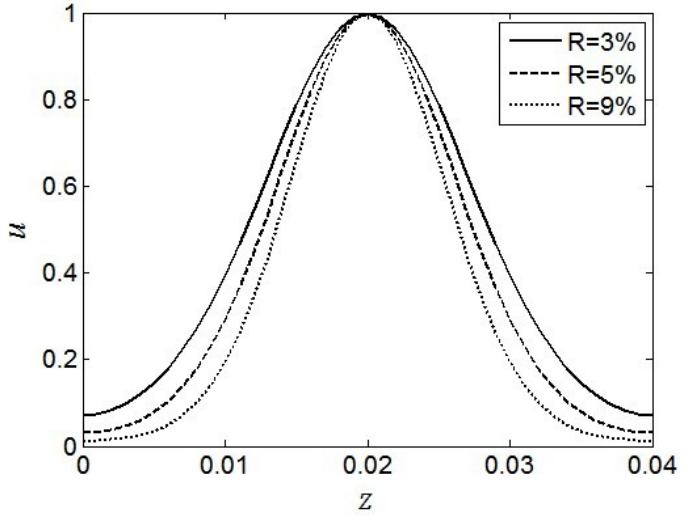

Fig. 5.39. Effect of mass layer thickness on energy trapping (a = 4, b = 0.5). u = $u_1(x_2 = -h, x_3)$.

Figure 5.40 shows the effect of a on energy trapping. When a = 2, 3, and 4, the corresponding resonant frequencies are ω/ω_s = 0.956929, 0.957726, and 0.958367, respectively, increasing slightly. A larger a means a more drastically changing mass layer thickness and less mass, and hence a higher frequency. A larger a also results in stronger energy trapping.

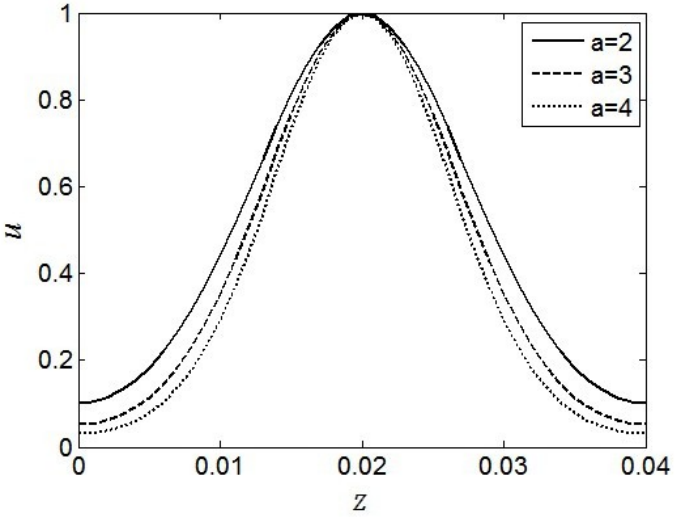

Fig. 5.40. Effect of mass layer nonuniformity on energy trapping (b = 0.5, R = 5%). u = $u_1(x_2 = -h, x_3)$.

In Fig. 5.41 we vary b so that the mass layer becomes asymmetric about $x_3 = c/2$ except when b = 0.5. Corresponding to b = 0.5, 0.55, and 0.6, the resonant frequencies are ω/ω_s = 0.922830, 0.922804, and 0.922721, respectively, changing very little. However, the mode shape is very sensitive to b.

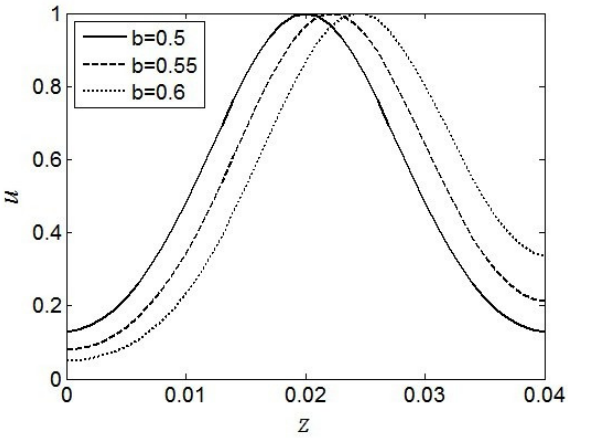

Fig. 5.41. Effect of mass layer asymmetry on energy trapping (a = 1, R = 9%). $u = u_1(x_2 = -h, x_3)$.

5.12. Plate with an Imperfectly Bonded Mass Layer

In this section we study free vibrations of a crystal plate of AT-cut quartz carrying an imperfectly bonded mass layer [72]. The interface is described by the shear-slip model which allows a discontinuity of the interface displacement. The effect of mass layer stiffness is also considered.

5.12.1. Fourier series solution

Consider an AT-cut quartz plate as shown in Fig. 5.42. It carries a thin mass layer at the central portion of its top surface.

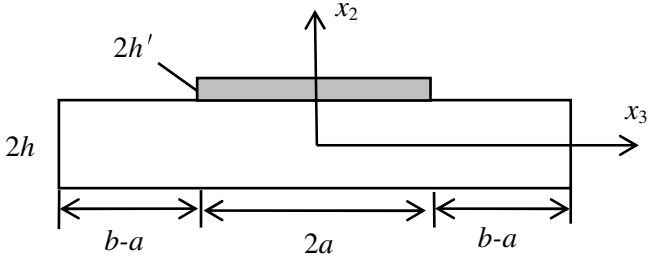

Fig. 5.42. An AT-cut quartz plate with a mass layer.

The governing equation for the crystal plate is:

$$c_{66}u_{1,22} + c_{55}u_{1,33} \cong \rho \ddot{u}_1, \quad |x_3| < b, \quad |x_2| < h. \tag{5.140}$$

The mass layer is modeled by the planes-stress equations in elasticity. For shear-horizontal motions, the plane-stress equation for the mass layer takes the following form (see Eq. (4.92)):

$$2h'\mu u'_{1,33} - T_{21} = \rho' 2h' \ddot{u}'_1, \quad |x_3| < a, \tag{5.141}$$

where $u'_1(x_3, t)$ is the displacement of the mass layer, $2h'$ its thickness, ρ' its density, and μ its shear modulus. T_{21} is the interface shear stress between the mass layer and the crystal plate. Physically, Eq. (5.141) states that the stress gradient $2h'\mu u'_{1,33}$ in the mass layer and the interface stress are responsible for the mass layer acceleration according to Newton's law. The boundary conditions at the plate left and right edges are

$$T_{31} = 0, \quad x_3 = \pm b, \quad |x_2| < h. \tag{5.142}$$

The plate bottom surface is traction free with

$$T_{21} = 0, \quad x_2 = -h, \quad |x_3| < b. \tag{5.143}$$

According to the shear-slip model, u'_1 of the mass layer may be different from the plate top surface displacement and the following constitutive relation describes the behavior of the interface:

$$T_{21} = k(u'_1 - u_1), \quad x_2 = h, \tag{5.144}$$

where k is the interface elastic constant. With Eq. (5.141), the stress boundary condition at the plate top surface can be written as

$$T_{21} = \begin{cases} 2h'\mu u'_{1,33} - \rho' 2h' \ddot{u}'_1, & x_2 = h, \quad |x_3| < a, \\ 0, & x_2 = h, \quad a < |x_3| < b. \end{cases} \tag{5.145}$$

Instead of using Eq. (5.144) directly, equivalently, we eliminate T_{21} from Eqs. (5.141) and (5.144) to obtain

$$2h'\mu u'_{1,33} - k(u'_1 - u_1) = 2\rho' h' \ddot{u}'_1, \quad x_2 = h. \tag{5.146}$$

We need to solve Eq. (5.140) with the boundary conditions in Eqs. (5.142), (5.143), (5.145) and (5.146). We construct the following solution for the plate from the method of separation of variables in partial differential equations (see Eq. (5.50):

$$\begin{aligned} u_1 &= A_0 \cos(\eta_0 x_2) + B_0 \sin(\eta_0 x_2) \\ &\quad + \sum_{m=1}^{\infty} [A_m \cos(\eta_m x_2) + B_m \sin(\eta_m x_2)] \cos\frac{m\pi x_3}{b}, \end{aligned} \tag{5.147}$$

where A_0, B_0, A_m and B_m are undetermined constants, and

$$\begin{aligned} &\eta_m^2 = \frac{\rho\omega^2}{c_{66}} - \frac{c_{55}}{c_{66}}\left(\frac{m\pi}{b}\right)^2 = \frac{\pi^2}{4h^2}\left[\frac{\omega^2}{\omega_s^2} - \frac{c_{55}}{c_{66}}\left(m\frac{2h}{b}\right)^2\right], \\ &m = 0,1,2,3,\cdots. \end{aligned} \tag{5.148}$$

$$\omega_s = \frac{\pi}{2h}\sqrt{\frac{c_{66}}{\rho}}. \tag{5.149}$$

ω_s is the resonant frequency of the fundamental thickness-shear mode in an unbounded quartz plate without mass layers. Equation (5.147) already satisfies Eqs. (5.140) and (5.142). To apply the remaining boundary conditions at the plate top and bottom, we need the following expression for the relevant stress component T_{21} in the plate:

$$\begin{aligned} T_{21} &= c_{66}u_{1,2} = -c_{66}A_0\eta_0 \sin(\eta_0 x_2) + c_{66}B_0\eta_0 \cos(\eta_0 x_2) \\ &\quad + c_{66}\sum_{m=1}^{\infty} [-A_m\eta_m \sin(\eta_m x_2) + B_m\eta_m \cos(\eta_m x_2)] \cos\frac{m\pi x_3}{b}. \end{aligned} \tag{5.150}$$

Since u_1' of the mass layer may be different from the plate top surface displacement, we write

$$u_1' = C_0 + \sum_{m=1}^{\infty} C_m \cos\frac{m\pi x_3}{a}, \tag{5.151}$$

where C_0 and C_m are undetermined constants. Substitution of Eqs. (5.147), (5.150) and (5.151) into Eqs. (5.143), (5.145) and (5.146) gives

$$\begin{aligned} &c_{66}A_0\eta_0 \sin(\eta_0 h) + c_{66}B_0\eta_0 \cos(\eta_0 h) \\ &\quad + c_{66}\sum_{m=1}^{\infty} \left[A_m\eta_m \sin(\eta_m h) + B_m\eta_m \cos(\eta_m h)\right]\cos\frac{m\pi x_3}{b} = 0, \end{aligned} \tag{5.152}$$

$$\begin{aligned} &-c_{66}A_0\eta_0 \sin(\eta_0 h) + c_{66}B_0\eta_0 \cos(\eta_0 h) \\ &\quad + c_{66}\sum_{m=1}^{\infty} \left[-A_m\eta_m \sin(\eta_m h) + B_m\eta_m \cos(\eta_m h)\right]\cos\frac{m\pi x_3}{b} \end{aligned} \tag{5.153}$$

$$= \begin{cases} -2h'\mu\sum_{m=1}^{\infty} \left(\frac{m\pi}{a}\right)^2 C_m \cos\frac{m\pi x_3}{a} \\ \quad + 2\rho' h'\omega^2\left(C_0 + \sum_{m=1}^{\infty} C_m \cos\frac{m\pi x_3}{a}\right), \quad |x_3| < a, \\ 0, \quad a < |x_3| < b, \end{cases}$$

$$\begin{aligned} &-2h'\mu\sum_{m=1}^{\infty} \left(\frac{m\pi}{a}\right)^2 C_m \cos\frac{m\pi x_3}{a} + k\{A_0 \cos(\eta_0 h) + B_0 \sin(\eta_0 h) \\ &\quad + \sum_{m=1}^{\infty} \left[A_m \cos(\eta_m h) + B_m \sin(\eta_m h)\right]\cos\frac{m\pi x_3}{b}\Big\} \\ &\quad - k\left(C_0 + \sum_{m=1}^{\infty} C_m \cos\frac{m\pi x_3}{a}\right) \\ &\quad = -2\rho' h'\omega^2\left(C_0 + \sum_{m=1}^{\infty} C_m \cos\frac{m\pi x_3}{a}\right). \end{aligned} \tag{5.154}$$

We then multiply both sides of Eqs. (5.152) and (5.153) by $\cos(n\pi x_3/b)$ (n = 0, 1, 2, …) and integrate the resulting equation over

(-*b*, *b*), and multiply both sides of Eq. (5.154) by $\cos(n\pi x/a)$ (n = 0, 1, 2, …) and integrate the resulting equation over (-*a*, *a*). This results in linear homogeneous equations for A_0, B_0, C_0, A_m, B_m and C_m. For nontrivial solutions the determinant of the coefficient matrix of the linear equations has to vanish, which determines the resonant frequencies. The nontrivial solutions of A_0, B_0, C_0, A_m, B_m and C_m determine the corresponding modes of the plate and the mass layer.

5.12.2. Numerical result

We introduce

$$\bar{\omega}_s = \omega_s(1-R), \quad R = \frac{\rho' h'}{\rho h}. \tag{5.155}$$

$\bar{\omega}_s$ is the resonant frequency of the fundamental thickness-shear mode in an unbounded quartz plate fully covered by a perfectly bonded mass layer with zero stiffness at the plate top surface. The resonant frequencies of the modes we are interested in are within $\bar{\omega}_s < \omega < \omega_s$. In this narrow frequency range we have trapped modes. We fix the plate thickness 2*h* = 1 mm and the plate length *b* = 20 mm. In the following we mainly examine the effects of the interface stiffness *k* and the mass layer stiffness μ. For convenience we introduced $r = kh/c_{66}$ and $s = \mu/c_{66}$ to describe the interface stiffness and the mass layer stiffness.

We begin with the case when *a* = 7.52 mm so that *a*/*b* is not equal to some *m*/*n* when *m* and *n* are not very large, and *R* = 3%. The mass layer shear stiffness μ (or *s*) is set to zero first which will be varied later. The interface stiffness is *r* = 0.5. The present case will be used as a reference case for later comparisons. In this case two resonant frequencies are found within $\bar{\omega}_s < \omega < \omega_s$. When using eleven (*m* = 10) and twelve (*m* = 11) terms in the series, the first resonant frequency has six significant figures. Therefore twelve terms are used in the calculations below. The corresponding η_m^2 are always positive. The two modes corresponding to the two frequencies in increasing order are shown in Fig. 5.43 (a) and (b), respectively, normalized by their maximal values. The two modes are symmetric about $x_3 = 0$. Our formulation does not include antisymmetric modes from the very beginning. The first mode does not have any nodal

points (zeros) along the x_3 direction and is a slowly varying thickness-shear mode. The second mode has two nodal points and is a thickness-twist mode. For both modes the vibration is large in the central region near $x_3 = 0$ and is essentially zero near the plate edges at $x_3 = -b$ and b. In other words the vibration is mainly under the mass layer. This is the so-called energy trapping of thickness-shear and thickness-twist modes.

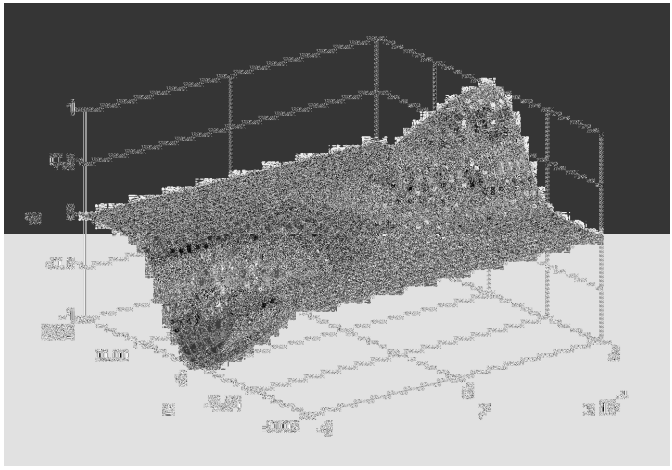

(a)

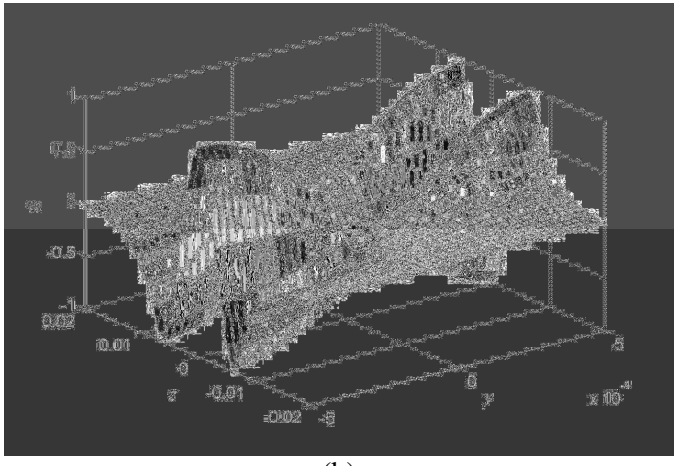

(b)

Fig. 5.43. Thickness-shear and thickness-twist modes ($u = u_1$, $r = 0.5$, $s = 0$). (a) The first mode, $\omega/\omega_s = 0.963758$. (b) The second mode, $\omega/\omega_s = 0.987605$.

Figure 5.44 shows the displacements of the mass layer and the top surface of the crystal plate for different values of r, while keeping all other parameters the same as those for Fig. 5.43. The mass

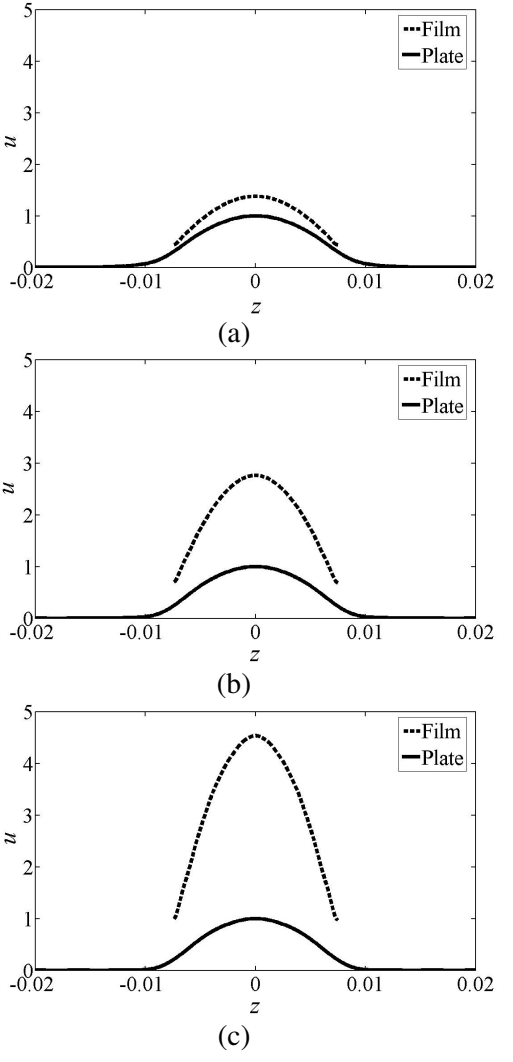

Fig. 5.44. Effect of interface stiffness on the displacements of the mass layer (film) and the plate top surface. (a) r = 0.5, ω/ω_s = 0.963758. (b) r = 0.2, ω/ω_s = 0.928352. (c) r = 0.15, ω/ω_s = 0.888607.

layer displacement is defined over (-*a*, *a*) only. The plate top surface displacement is defined over (-*b*, *b*). The maximal plate surface displacement is normalized to one. For a perfectly or rigidly bonded mass layer, the two displacements are the same within (-*a*, *a*). In Fig. 5.44 (a) they are different because of the imperfect interface described by r = 0.5. In Fig. 5.44 (b) the difference becomes larger because of a smaller r = 0.2 or weaker interface bonding. This trend continues when the interface bonding or r is further decreased till r = 0.15 as shown in Fig. 5.44 (c). When r is reduced from 0.5 to 0.15, the frequency decreases because of less stiffness in the entire structure of the plate and the mass layer. If a very large r is used, our results approach those for a perfectly bonded mass layer, which is as expected.

Figure 5.45 presents the effect of the interface stiffness on energy trapping by showing the plate top surface displacement for different r. Overall, within the range of the values of r considered, a smaller r leads to stronger energy trapping. This is not obvious and, for an explanation, we plot in Fig. 5.46 the distribution of the interface shear stress T_{21} under

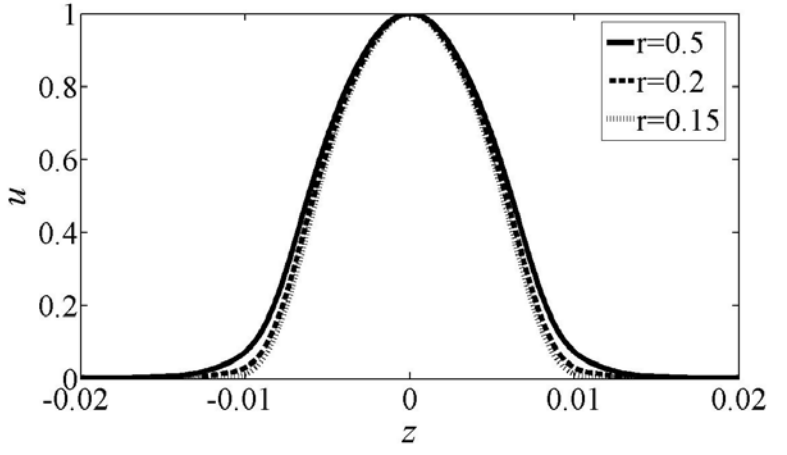

Fig. 5.45. Effect of interface stiffness on energy trapping.

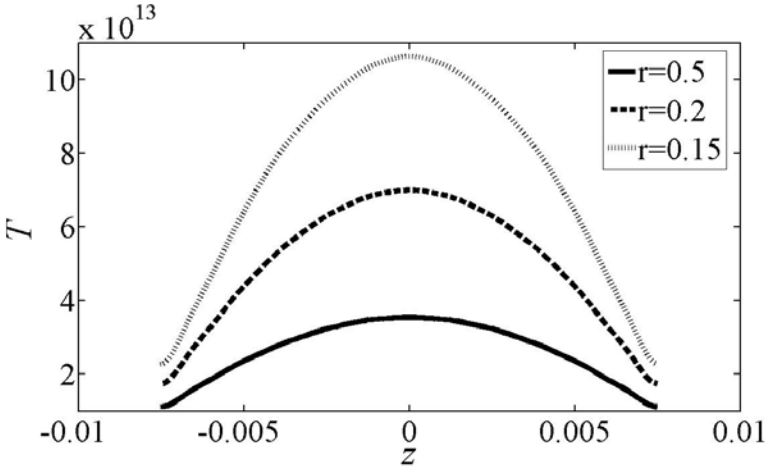

Fig. 5.46. Effect of interface stiffness on interface shear stress ($T = T_{21}$ in N/m^2).

the mass layer. When r becomes smaller, the difference between the mass layer and plate top surface displacements becomes significantly larger. As a consequence, the interface shear stress as described by Eq. (5.144) becomes larger which results in stronger energy trapping.

Figure 5.47 shows the displacements of the mass layer and the top surface of the crystal plate for different values of s, while keeping all other parameters the same as those for Fig. 5.43. For a thin mass layer whose stiffness can be neglected, $s = 0$ and the corresponding mass layer and plate surface displacements are given in Fig. 5.44 (a) when $r = 0.5$. Figure 5.47 shows the case when $s>0$. We vary s from 5 to 100 to show its effects clearly. When s increases, the frequency increases too as expected. At the same time, the mass layer and plate top surface displacement distributions both become wider due to more rigid mass layers. For Fig. 5.47 (c) the curve representing the plate surface displacement is slightly wavy in the central portion. This may be caused by the relatively more abrupt changes in the curve near $x_3 = \pm a$. More terms in the Fourier series may improve this but what is shown is sufficient to indicate the trend.

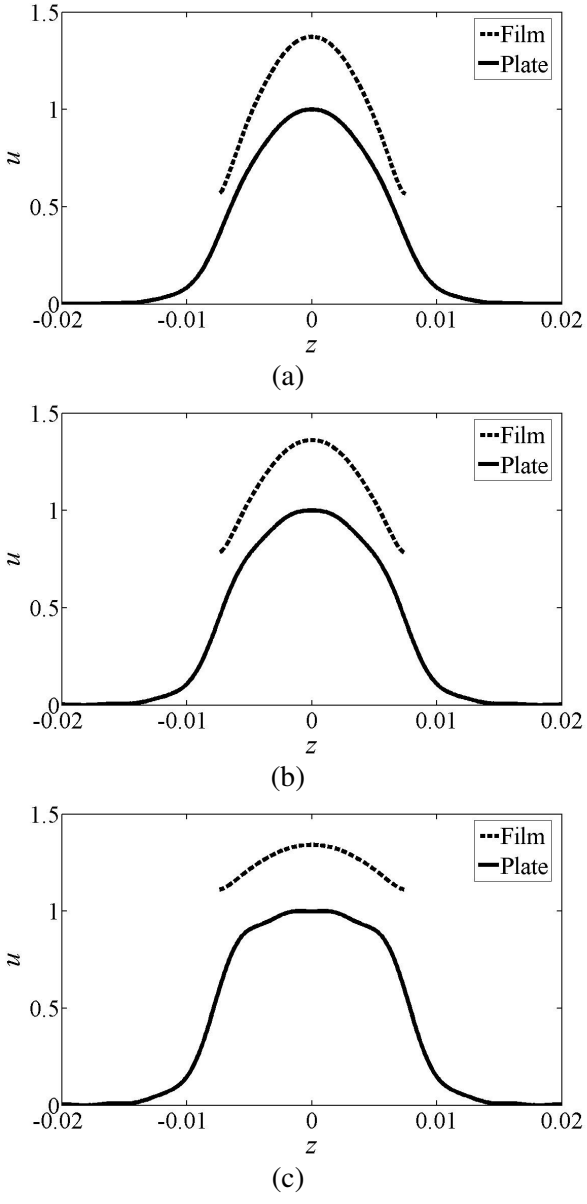

Fig. 5.47. Effect of mass layer stiffness on the displacements of the mass layer (film) and the plate top surface. (a) s = 5, ω/ω_s = 0.964150. (b) s = 20, ω/ω_s = 0.964816. (c) s = 100, ω/ω_s = 0.965694.

For a closer look at the effect of the mass layer stiffness on energy trapping, we plot the plate top surface displacement of different cases together in Fig. 5.48. Clearly, a stiffer mass layer makes the displacement distribution wider or less trapped. While under the central portion of the mass layer the interface shear stress is smaller for a stiffer mass layer as shown in Fig. 5.49, a stiffer mass layer causes stress concentration near the mass layer edges.

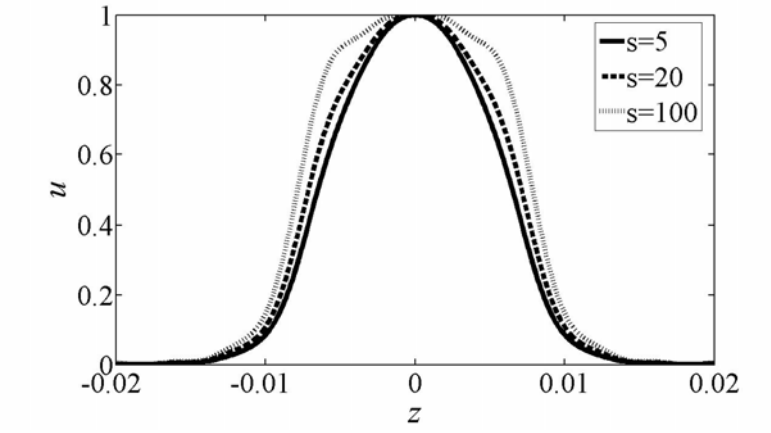

Fig. 5.48. Effect of mass layer stiffness on energy trapping.

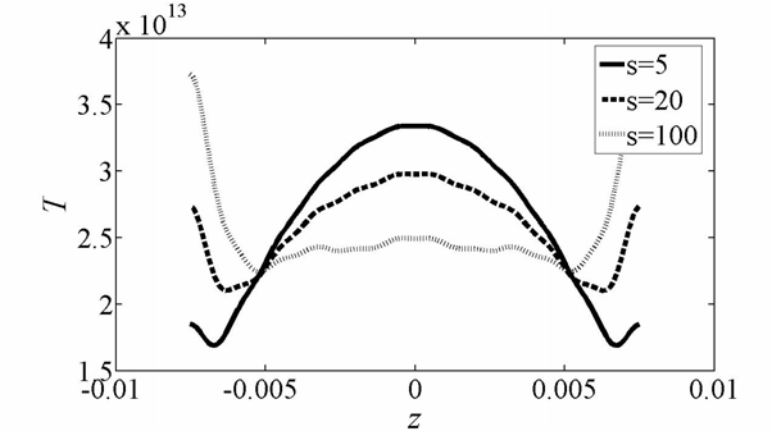

Fig. 5.49. Effect of mass layer stiffness on interface shear stress ($T = T_{21}$ in N/m^2).

5.13. Frequency Spectra

In this section we perform an exact analysis [73] of couple face-shear and thickness-twist vibrations in a rectangular plate without the omission of the small elastic constant c_{56}. We plot frequency spectra which are resonant frequencies versus the plate aspect ratio. Consider the plate in Fig. 5.50. The exact equation to be satisfied by u_1 is (see Eq. (4.4)):

$$c_{66}u_{1,22} + c_{55}u_{1,33} + 2c_{56}u_{1,23} = \rho\ddot{u}_1 . \tag{5.156}$$

For a traction-free plate, the boundary conditions are

$$T_{21} = 0, \quad x_2 = \pm b, \quad |\, x_3 \,| < c , \tag{5.157}$$

$$T_{31} = 0, \quad x_3 = \pm c, \quad |\, x_2 \,| < b . \tag{5.158}$$

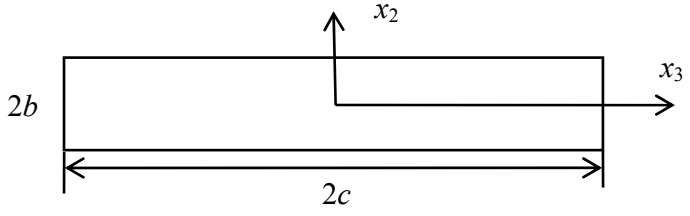

Fig. 5.50. An AT-cut quartz resonator and coordinate system.

The modes in Eqs. (5.1)–(5.5) are for unbounded plates. They satisfy Eqs. (5.156) and (5.157) for each value of m. For the finite plate in Fig. 5.50, a superposition of modes corresponding to different values of m is needed. Specifically, to satisfy the remaining boundary conditions in

Eq. (5.158), we write

$$
\begin{aligned}
T_5 = & \sum_{m=1,3,5,\cdots}^{\infty} \gamma_{55}\zeta_m A_m \sin\eta_m y \sin\zeta_m\left(\frac{c_{56}}{c_{66}}y - z\right) \\
& + c_{56}\eta_m A_m \cos\eta_m y \cos\zeta_m\left(\frac{c_{56}}{c_{66}}y - z\right) \\
& - \gamma_{55}\zeta_m B_m \sin\eta_m y \cos\zeta_m\left(\frac{c_{56}}{c_{66}}y - z\right) \\
& + c_{56}\eta_m B_m \cos\eta_m y \sin\zeta_m\left(\frac{c_{56}}{c_{66}}y - z\right) \\
& + \sum_{m=0,2,4,\cdots}^{\infty} \gamma_{55}\zeta_m C_m \cos\eta_m y \sin\zeta_m\left(\frac{c_{56}}{c_{66}}y - z\right) \\
& - c_{56}\eta_m C_m \sin\eta_m y \cos\zeta_m\left(\frac{c_{56}}{c_{66}}y - z\right) \\
& - \gamma_{55}\zeta_m D_m \cos\eta_m y \cos\zeta_m\left(\frac{c_{56}}{c_{66}}y - z\right) \\
& - c_{56}\eta_m D_m \sin\eta_m y \sin\zeta_m\left(\frac{c_{56}}{c_{66}}y - z\right),
\end{aligned}
\tag{5.159}
$$

where A_m, B_m, C_m and D_m are undetermined constants, and

$$
\eta_m = \frac{m\pi}{2b}, \tag{5.160}
$$

$$
\zeta_m^2 = \frac{1}{\gamma_{55}}(\rho\omega^2 - c_{66}\eta_m^2). \tag{5.161}
$$

We note that ζ_m^2 may become negative. In that case it is more convenient to rewrite Eq. (5.159) using real hyperbolic functions of $(c_{56}y/c_{66} - z)$. Even with the superposition of modes, the boundary

conditions in Eq. (5.158) cannot be satisfied by Eq. (5.159) conveniently pointwise. Instead they are satisfied in the following integral sense (the so-called weak form):

$$\begin{aligned} &\int_{-b}^{b} T_5(z=\pm c)\cos\eta_m y dy = 0, \quad m = 0,2,4,\cdots, \\ &\int_{-b}^{b} T_5(z=\pm c)\sin\eta_m y dy = 0, \quad m = 1,3,5,\cdots. \end{aligned} \tag{5.162}$$

This way of satisfying end condition in an integral sense is called Saint Venant's principle in elasticity and is a widely used technique. Equation (5.162) leads to linear homogeneous equations for A_m, B_m, C_m and D_m. Corresponding to each m, there are two undetermined constants in Eq. (5.159) and two linear equations from Eq. (5.162). Equations corresponding to different values of m are coupled. For nontrivial solutions the determinant of the coefficient matrix of Eq. (5.162) has to vanish, which gives the frequency equation that determines ω. The frequency spectra are obtained by plotting ω versus the plate aspect ration c/b. For common third or fifth-overtone resonators, it is expected that a few terms in the summation in Eq. (5.159) will be sufficient.

As an example, consider the most widely used AT-cut quartz plates. We introduce the following dimensionless frequency:

$$\Omega = \frac{\omega}{\omega_s}, \quad \omega_s = \frac{\pi}{2b}\sqrt{\frac{c_{66}}{\rho}}. \tag{5.163}$$

When Ω is real, the corresponding ζ_m from Eq. (5.161) may be either real or pure imaginary.

Figures 5.51–5.53 show the frequency spectra for the fundamental mode near $\Omega = 1$, the third-overtone mode near $\Omega = 3$, and the fifth-overtone mode near $\Omega = 5$, respectively. For the case of $\Omega = 3$, using ten, fifteen or twenty terms in the series in Eq. (5.159) does not make any visible difference in the figure. Small numerical differences in the numerical data can be found when using less than five terms in the series. Therefore ten terms in the series are used when plotting Figs. 5.51–5.53 to ensure sufficient accuracy.

The curves in Figs. 5.51–5.53 are in fact formed by data points without connecting them. They seem to automatically fall on some

curves. Each data point represents the frequency of a mode under a given *c/b*. Corresponding to a particular value of *c/b*, there exits an infinite number of modes. A few can be seen in the frequency range shown. The curves may be classified into two families. The relatively steep or vertical family represents face shear dominated modes. The relative gradual or horizontal family is for thickness twist dominated modes. The relatively flat portions of the thickness-twist family represent modes with little coupling to face-shear. They are related to the operating thickness-shear modes of plate resonators. When the flat portions of the thickness-twist family begin to bend near their ends or seem to be intersecting with the face-shear family, strong coupling to face-shear occurs which is undesirable to device operation and should be avoided. The usefulness of the frequency spectra is that it excludes a series of discrete values of *c/b*.

Clearly, from Fig. 5.51 to Fig. 5.53, the modes become more crowded and show more couplings. This makes the design and operation of overtone-mode resonators more difficult than fundamental-mode resonators. For overtone-mode resonators, more values of *c/b* have to be excluded to avoid mode coupling.

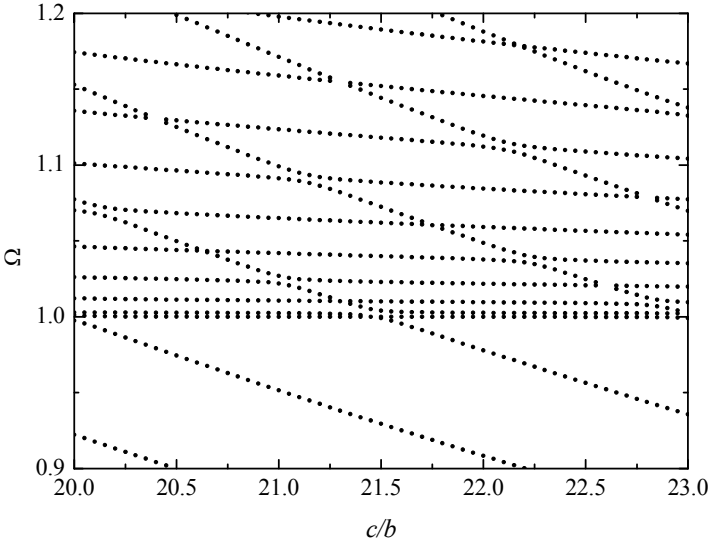

Fig. 5.51. Frequency spectra of coupled FS and TT modes near Ω = 1.

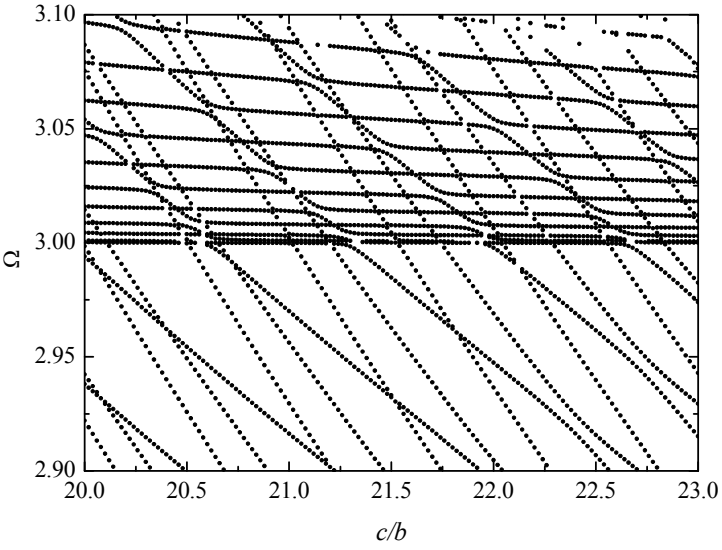

Fig. 5.52. Frequency spectra of coupled FS and TT modes near Ω = 3.

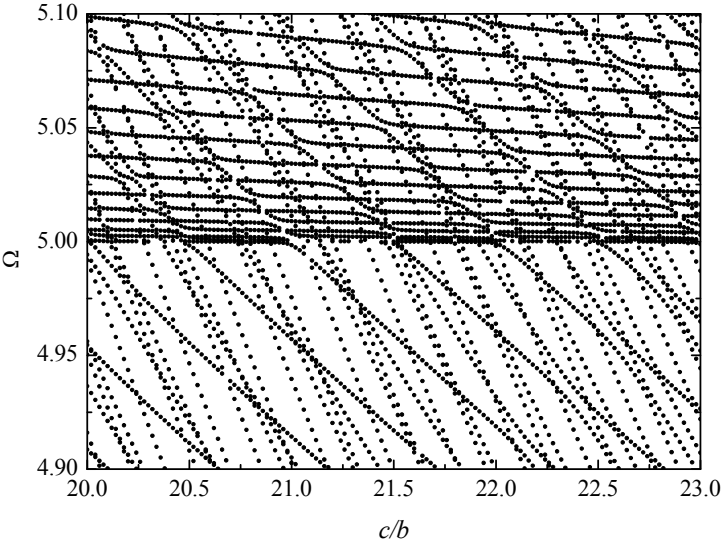

Fig. 5.53. Frequency spectra of coupled FS and TT modes near Ω = 5.

Chapter 6

Waves Propagating along Digonal Axis

In Chapters 4 and 5, shear-horizontal waves and modes of u_1 with in-plane variation along the x_3 direction were systematically studied. In this chapter we consider in-plane variation along the x_1 direction, the digonal axis of rotated Y-cut quartz plates. More complicated than Chapters 4 and 5 which were for u_1 only, when there is x_1 dependence, all three displacement components are involved and they are coupled. Historically, solutions for straight-crested waves in quartz plates varying along the x_1 direction were obtained in [74] first. The properties of these waves were explored later in great detail in [75–77].

6.1. Governing Equations

Consider an infinite plate of rotated Y-cut quartz as shown in Fig. 6.1. The plate surfaces are traction free. All fields are independent of x_3.

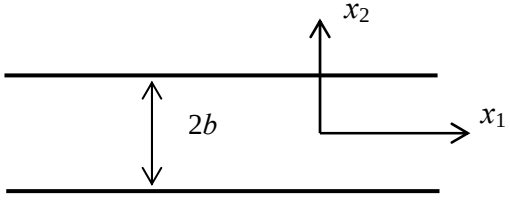

Fig. 6.1. A plate of monoclinic crystals.

The equations of motion are obtained by setting the derivative with respect to x_3 to zero in Eq. (2.14):

$$\begin{aligned} &c_{11}u_{1,11}+(c_{12}+c_{66})u_{2,12}+(c_{14}+c_{56})u_{3,12}+c_{66}u_{1,22}=\rho\ddot{u}_1,\\ &c_{56}u_{3,11}+(c_{66}+c_{12})u_{1,12}+c_{66}u_{2,11}+c_{22}u_{2,22}+c_{24}u_{3,22}=\rho\ddot{u}_2,\\ &c_{55}u_{3,11}+(c_{56}+c_{14})u_{1,12}+c_{56}u_{2,11}+c_{24}u_{2,22}+c_{44}u_{3,22}=\rho\ddot{u}_3, \end{aligned} \tag{6.1}$$

which are clearly very much coupled. Similarly, the corresponding constitutive relations are obtained from Eq. (2.13) by dropping all x_3 derivatives:

$$\begin{aligned} T_{11} &= c_{11}u_{1,1} + c_{12}u_{2,2} + c_{14}u_{3,2}, \\ T_{22} &= c_{12}u_{1,1} + c_{22}u_{2,2} + c_{24}u_{3,2}, \\ T_{33} &= c_{13}u_{1,1} + c_{23}u_{2,2} + c_{34}u_{3,2}, \\ T_{23} &= c_{14}u_{1,1} + c_{24}u_{2,2} + c_{44}u_{3,2}, \\ T_{31} &= c_{55}u_{3,1} + c_{56}(u_{1,2} + u_{2,1}), \\ T_{12} &= c_{56}u_{3,1} + c_{66}(u_{1,2} + u_{2,1}). \end{aligned} \tag{6.2}$$

The boundary conditions at the plate surfaces are

$$T_{2j} = 0, \quad x_2 = \pm b\,. \tag{6.3}$$

6.2. Wave Solution

For resonator applications, we are mainly interested in thickness-shear modes for which u_1 is an odd function of x_2. Therefore we consider the possibility of the following fields [75]

$$\begin{aligned} u_1 &= A_1 \cos\xi x_1 \sin\eta x_2 \exp(i\omega t), \\ u_2 &= A_2 \sin\xi x_1 \cos\eta x_2 \exp(i\omega t), \\ u_3 &= A_3 \sin\xi x_1 \cos\eta x_2 \exp(i\omega t). \end{aligned} \tag{6.4}$$

For convenience we will call these modes antisymmetric. There also exist symmetric modes described by

$$\begin{aligned} u_1 &= A_1 \sin\xi x_1 \cos\eta x_2 \exp(i\omega t), \\ u_2 &= A_2 \cos\xi x_1 \sin\eta x_2 \exp(i\omega t), \\ u_3 &= A_3 \cos\xi x_1 \sin\eta x_2 \exp(i\omega t). \end{aligned} \tag{6.5}$$

Consider the antisymmetric modes in Eq. (6.4). The symmetric modes in Eq. (6.5) can be treated similarly. Substitution of Eq. (6.4) into Eq. (6.1)

yields three linear homogeneous equations for A_i:

$$\begin{aligned}(a_1 - V^2)A_1 + a_6 A_2 + a_5 A_3 = 0,\\ a_6 A_1 + (a_2 - V^2)A_2 + a_4 A_3 = 0,\\ a_5 A_1 + a_4 A_2 + (a_3 - V^2)A_3 = 0,\end{aligned} \tag{6.6}$$

where

$$\begin{aligned}a_1 = 1 + c_{66}\alpha^2 / c_{11}, \quad a_4 = (c_{56} + c_{24}\alpha^2)/c_{11},\\ a_2 = (c_{66} + c_{22}\alpha^2)/c_{11}, \quad a_5 = (c_{14} + c_{56})\alpha / c_{11},\\ a_3 = (c_{55} + c_{44}\alpha^2)/c_{11}, \quad a_6 = (c_{12} + c_{66})\alpha / c_{11},\end{aligned} \tag{6.7}$$

and

$$\alpha = \frac{\eta}{\xi}, \quad V^2 = \frac{\rho\omega^2}{c_{11}\xi^2}. \tag{6.8}$$

The compatibility of Eq. (6.6) implies the following characteristic equation:

$$\begin{vmatrix} a_1 - V^2 & a_6 & a_5 \\ a_6 & a_2 - V^2 & a_4 \\ a_5 & a_4 & a_3 - V^2 \end{vmatrix} = 0. \tag{6.9}$$

Equation (6.9) may be viewed as a bicubic equation for α or η, or a cubic equation for η^2 which has three roots. We denote the three roots by $(\eta^{(i)})^2$, i = 1, 2, 3. When determining $\eta^{(i)}$ from $(\eta^{(i)})^2$, it does not matter which of the two roots differing by a sign is taken because of the form of Eq. (6.4). Corresponding to each $\eta^{(i)}$, Eq. (6.6) also determines a set of amplitude ratios

$$A_1 : A_2 : A_3 = \beta_1^{(i)} : \beta_2^{(i)} : \beta_3^{(i)}, \tag{6.10}$$

where $\beta_j^{(i)}$ may be normalized in some way if wanted. The general antisymmetric solution satisfying Eq. (6.1) can be written as

$$\begin{aligned} u_1 &= \sum_{i=1}^{3} C^{(i)} \beta_1^{(i)} \sin \eta^{(i)} x_2 \cos \xi x_1 \exp(i\omega t), \\ u_2 &= \sum_{i=1}^{3} C^{(i)} \beta_2^{(i)} \cos \eta^{(i)} x_2 \sin \xi x_1 \exp(i\omega t), \\ u_3 &= \sum_{i=1}^{3} C^{(i)} \beta_3^{(i)} \cos \eta^{(i)} x_2 \sin \xi x_1 \exp(i\omega t), \end{aligned} \tag{6.11}$$

where $C^{(i)}$ are undetermined constants. Equation (6.11) is substituted into the constitutive relations in Eq. (6.2) and then into the boundary conditions in Eq. (6.3). Due to the antisymmetry involved, the boundary conditions at the plate top surface yield the same three linear homogeneous equations for $C^{(i)}$ as the boundary conditions at the plate bottom surface. For nontrivial solutions of $C^{(i)}$, the determinant of the coefficient matrix of these three equations has to vanish. This yields a frequency equation containing ξ and ω, which determines the dispersion relation of ω versus ξ. The algebra involved is complicated. Due to the presence of trigonometric functions in the frequency equation, the dispersion relation is expected to be multivalued, with many branches.

6.3. Dispersion Curves

The final frequency equation needs to be solved numerically on a computer. The result for an AT-cut quartz plate is shown in Fig. 6.2 where we have introduced the following dimensionless wave number and frequency:

$$X = \frac{\xi}{\pi / 2b}, \quad \Omega = \frac{\omega}{\omega_s}, \quad \omega_s = \frac{\pi}{2b}\sqrt{\frac{c_{66}}{\rho}}. \tag{6.12}$$

Figure 6.2 in fact has many dots representing pairs of (ξ,ω) satisfying the frequency equation. These dots are not connected. They seem to form many curves representing different branches of the dispersion relation.

For real and small X, when Ω increases from zero, the first three branches are flexure mainly described by u_2, face-shear described by u_3, and the fundamental thickness-shear described by u_1. The dispersion curves of the symmetric modes in Eq. (6.5) form a figure similar to Fig. 6.2.

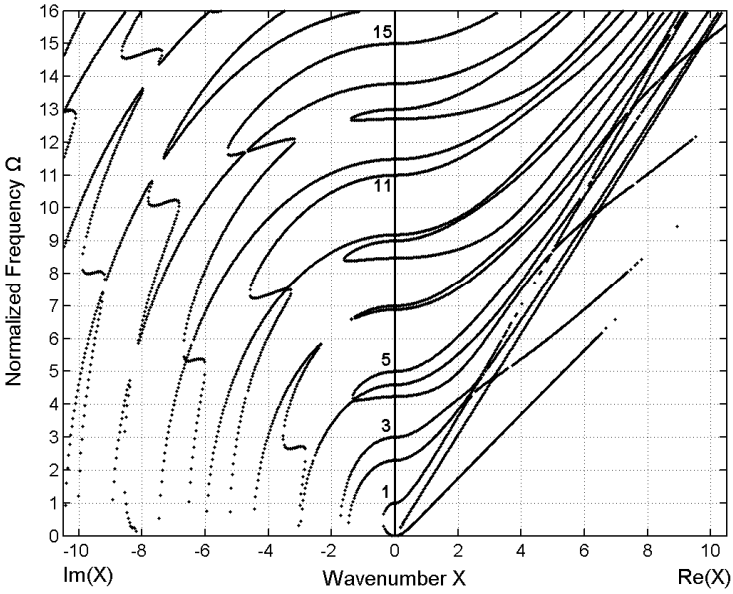

Fig. 6.2. Dispersion curves of antisymmetric waves in a quartz plate [78].

6.4. Long Wavelength Limit

For long wavelength and low frequency, ξ, η and ω all go to zero. Equation (6.1) degenerates to Cauchy's equation (see the Refs. in [75]):

$$\begin{aligned} &\gamma_{11}u_{1,11} = \rho\ddot{u}_1, \\ &-\frac{b^2}{3}\gamma_{11}u_{2,1111} = \rho\ddot{u}_2, \\ &\gamma_{55}u_{3,11} = \rho\ddot{u}_3, \end{aligned} \tag{6.13}$$

where

$$\gamma_{11} = c_{11} - \frac{c_{12}^2 c_{44} + c_{14}^2 c_{22} - 2c_{12}c_{24}c_{14}}{c_{22}c_{44} - c_{24}^2}, \qquad \gamma_{55} = c_{55} - c_{56}^2 / c_{66}. \tag{6.14}$$

Equations $(6.13)_1$, $(6.13)_2$, and $(6.13)_3$ are for extensional, flexural, and face-shear motions, respectively. The flexural and face-shear motions are antisymmetric and their dispersion curves are in Fig. 6.2. The extensional motion is symmetric and its dispersion curve is not in Fig. 6.2. Upon substituting the following waves into Eq. (6.13):

$$\begin{aligned} u_1 &= A_1 \sin \xi x_1 \exp(i\omega t), \\ u_2 &= A_2 \sin \xi x_1 \exp(i\omega t), \\ u_3 &= A_3 \sin \xi x_1 \exp(i\omega t), \end{aligned} \tag{6.15}$$

we find, for the extensional mode:

$$\Omega = \frac{2\xi b}{\pi}\sqrt{\frac{c_{11}}{c_{66}}}\ , \tag{6.16}$$

for the flexural mode:

$$\Omega = \frac{2\xi^2 b^2}{\pi}\sqrt{\frac{\gamma_{11}}{3c_{66}}}\ , \tag{6.17}$$

and, for the face-shear mode:

$$\Omega = \frac{2\xi b}{\pi}\sqrt{\frac{\gamma_{55}}{c_{66}}}\ . \tag{6.18}$$

In the region of long wavelengths and high frequencies, there are three families of modes in which the predominant displacement are thickness shear in the direction of the digonal axis of symmetry,

thickness shear at right angles to the digonal axis, and thickness stretch, respectively. Explicit formulas for the ordinates, slopes, and curvatures of the dispersion curves at infinite wavelength were given in [76]. These formulas are useful in the establishment of approximate, two-dimensional equations of motion that can be solved for high-frequency vibrations of bounded plates.

6.5. Other Results

In [79], propagation of straight-crested waves along the x_1 direction in a quartz plate with symmetric electrodes was studied. Dispersion relations and their asymptotic approximations for long waves were obtained from which Bechmann's number for a partially electroded plate was determined. Approximate solutions for coupled thickness-shear, flexure, and face-shear vibration frequencies and modes in a finite plate bounded by $|x_1| < l$ were given in [80]. The solution of straight-crested waves propagating in a plate of triclinic crystals was obtained in [81] in general.

6.6. Approximate Equations for u_1 and u_2

In this section we consider modes that have variations along both of the x_1 and x_3 directions. The situation is much more complicated than that in previous chapters/sections. As a consequence, more approximations are needed in order to obtain analytical results. Some of the approximations are valid for AT-cut quartz plates only. These approximations were introduced in [82–86] for quartz as a piezoelectric crystal. Since quartz is a material with very weak piezoelectric coupling, for free vibration frequency analysis we neglect the small piezoelectric coupling and present an elastic treatment. Following [82–86], we also neglect the relatively small elastic constants c_{14}, c_{24} and c_{56}. In finite plate thickness-shear resonators, the operating thickness-shear mode u_1 may be coupled to other displacement components. The main coupling is with the plate flexural motion described by u_2. Therefore we also neglect the less coupled displacement u_3 and drop the equation of motion for u_3

accordingly [82–86]. With the above approximations, the remaining displacement equations of motion from Eq. (2.14) are

$$\begin{aligned} &c_{11}u_{1,11} + (c_{12} + c_{66})u_{2,12} + c_{66}u_{1,22} + c_{55}u_{1,33} = \rho\ddot{u}_1, \\ &(c_{66} + c_{12})u_{1,12} + c_{66}u_{2,11} + c_{22}u_{2,22} + c_{44}u_{2,33} = \rho\ddot{u}_2. \end{aligned} \tag{6.19}$$

Under the above approximations, the constitutive relations in Eq. (2.13) for the stress components in terms of the displacement gradients become

$$\begin{aligned} T_{11} &= c_{11}u_{1,1} + c_{12}u_{2,2}, \\ T_{22} &= c_{12}u_{1,1} + c_{22}u_{2,2}, \\ T_{33} &= c_{13}u_{1,1} + c_{23}u_{2,2} + c_{34}u_{2,3}, \\ T_{23} &= c_{44}u_{2,3}, \\ T_{31} &= c_{55}u_{1,3}, \\ T_{12} &= c_{66}(u_{1,2} + u_{2,1}). \end{aligned} \tag{6.20}$$

The corresponding equations in [82–86] are piezoelectric. When piezoelectric coupling is neglected, Eqs. (6.19) and (6.20) are essentially the same as the corresponding equations in [82–86]. The only difference is that Eq. $(6.19)_2$ has a term related to c_{44} which was not in [82–86]. A few useful solutions to the piezoelectric form of Eq. (6.19) were obtained in [82–86].

6.7. Straight-crested Waves of u_1 and u_2

Consider the propagation of straight-crested waves in the x_1 direction of a quartz plate of thickness $2h$ [87]. The waves are governed by Eq. (6.19) in which the face-shear displacement u_3 is neglected. We have coupled thickness shear u_1 and flexure u_2. For straight-crested waves along the x_1 direction, we set the derivatives with respect to x_3 to zero. Then Eqs. (6.19) and (6.20) become

$$\begin{aligned} &c_{11}u_{1,11} + (c_{12} + c_{66})u_{2,12} + c_{66}u_{1,22} = \rho\ddot{u}_1, \\ &(c_{66} + c_{12})u_{1,12} + c_{66}u_{2,11} + c_{22}u_{2,22} = \rho\ddot{u}_2, \end{aligned} \tag{6.21}$$

$$
\begin{aligned}
T_{11} &= c_{11}u_{1,1} + c_{12}u_{2,2},\\
T_{22} &= c_{12}u_{1,1} + c_{22}u_{2,2},\\
T_{33} &= c_{13}u_{1,1} + c_{23}u_{2,2},\\
T_{23} &= 0,\\
T_{31} &= 0,\\
T_{12} &= c_{66}(u_{1,2} + u_{2,1}).
\end{aligned}
\tag{6.22}
$$

As solutions of Eq. (6.21), we start with

$$
\begin{aligned}
u_1 &= C_1 \cos\xi x_1 \sin\alpha x_2 \exp(i\omega t),\\
u_2 &= C_2 \sin\xi x_1 \cos\alpha x_2 \exp(i\omega t).
\end{aligned}
\tag{6.23}
$$

Upon substituting Eq. (6.23) into Eq. (6.21), we find

$$
\frac{C_2}{C_1} = \frac{\rho\omega^2 - c_{11}\xi^2 - c_{66}\alpha^2}{(c_{12}+c_{66})\xi\alpha} = \frac{(c_{12}+c_{66})\xi\alpha}{\rho\omega^2 - c_{66}\xi^2 - c_{22}\alpha^2}. \tag{6.24}
$$

Equation (6.24) represents two equations. The second of Eq. (6.24) may be regarded as a quadratic in α^2 for given ξ and ω. Call α_1^2, α_2^2 the two roots. Then Eq. (6.23) becomes, omitting the time dependence here and in the sequel,

$$
\begin{aligned}
u_1 &= (B_1 \sin\alpha_1 x_2 + B_2 \sin\alpha_2 x_2)\cos\xi x_1,\\
u_2 &= (B_1\gamma_1 \cos\alpha_1 x_2 + B_2\gamma_2 \cos\alpha_2 x_2)\sin\xi x_1,
\end{aligned}
\tag{6.25}
$$

where

$$
\gamma_i = \frac{\rho\omega^2 - c_{11}\xi^2 - c_{66}\alpha_i^2}{(c_{12}+c_{66})\xi\alpha_i} = \frac{(c_{12}+c_{66})\xi\alpha_i}{\rho\omega^2 - c_{66}\xi^2 - c_{22}\alpha_i^2}, \quad i = 1,2. \tag{6.26}
$$

For traction-free boundary conditions we have

$$
T_{21} = T_{22} = T_{23} = 0, \quad x_2 = \pm h, \tag{6.27}
$$

among which $T_{23} = 0$ is automatically satisfied. Upon substituting Eq. (6.25) in Eq. (6.22) and the result in Eq. (6.27), we find

$$\frac{B_2}{B_1} = -\frac{(c_{12}\xi + c_{22}\gamma_1\alpha_1)\sin\alpha_1 h}{(c_{12}\xi + c_{22}\gamma_2\alpha_2)\sin\alpha_2 h} = -\frac{(\alpha_1 + \gamma_1\xi)\cos\alpha_1 h}{(\alpha_2 + \gamma_2\xi)\cos\alpha_2 h}. \tag{6.28}$$

The second of Eq. (6.28) is the transcendental equation

$$\frac{\tan\alpha_1 h}{\tan\alpha_2 h} = \frac{(c_{12}\xi + c_{22}\gamma_2\alpha_2)(\alpha_1 + \gamma_1\xi)}{(c_{12}\xi + c_{22}\gamma_1\alpha_1)(\alpha_2 + \gamma_2\xi)}, \tag{6.29}$$

which, along with the quadratic in Eq. (6.24) in α^2, is the dispersion relation, ω versus ξ, for waves in the infinite plate. The approximation made in obtaining the above solution is the decoupling from face-shear, i.e.,

$$c_{14} = c_{24} = c_{56} = 0, \quad u_3 = 0. \tag{6.30}$$

For orthotropic, hexagonal, and isotropic materials Eq. (6.30) is exactly true. Approximate solutions for coupled thickness-shear and flexural vibrations of finite plates were also obtained in [87].

Chapter 7

Vibration of Rectangular Plates

In this chapter we analyze modes in rectangular plates with spatial variations in both of the x_1 and x_3 directions. Unelectroded, fully electroded, and partially electroded plates with energy trapping are all considered. The contoured plates with nonuniform thickness treated in Section 7.5 are unbounded.

7.1. Approximate Equation for u_1

Equation (6.19) is for coupled thickness shear u_1 and flexure u_2. The coupling between thickness shear and flexure in a finite plate depends on the plate dimensions and is strong only for certain aspect ratios of the plate. For thin plates with large aspect ratios, the coupling to flexure is weak and is less likely to happen. We assume that the coupling to flexure has been avoided through proper design. This allows us to neglect the flexural displacement u_2 and consider transversely varying thickness-shear modes with one displacement component $u_1(x_1, x_2, x_3, t)$ only. In this case Eqs. (6.19) and (6.20) reduce to [88]

$$c_{11}u_{1,11} + c_{66}u_{1,22} + c_{55}u_{1,33} = \rho\,\ddot{u}_1, \tag{7.1}$$

$$\begin{aligned} &T_{11} = c_{11}u_{1,1}, \quad T_{22} = c_{12}u_{1,1}, \quad T_{33} = c_{13}u_{1,1}, \\ &T_{23} = 0, \quad T_{31} = c_{55}u_{1,3}, \quad T_{12} = c_{66}u_{1,2}. \end{aligned} \tag{7.2}$$

When a plate is vibrating in transversely varying thickness-shear modes, $u_{1,2}$ is the major displacement gradient. Derivatives with respect to the in-plane coordinates x_1 and x_3 are small.

7.2. Unelectroded Plate

Consider an unelectroded AT-cut quartz plate as shown in Fig. 7.1 [88].

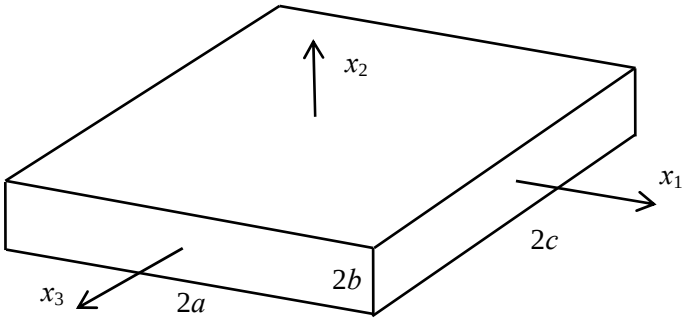

Fig. 7.1. Three-dimensional view of an AT-cut quartz plate

At the plate top and bottom, T_{21} is the major stress component. Therefore the traction-free boundary conditions are

$$T_{21} = 0, \quad x_2 = \pm b, \quad |x_1| < a, \quad |x_3| < c\,. \tag{7.3}$$

At $x_1 = \pm a$ the major stress component is T_{12}. At $x_3 = \pm c$ the major stress component is T_{31}. Therefore traction-free boundary conditions at the plate edges are [86]:

$$\begin{aligned} &T_{12} = 0, \quad x_1 = \pm a, \quad |x_2| < b, \quad |x_3| < c, \\ &T_{31} = 0, \quad x_3 = \pm c, \quad |x_2| < b, \quad |x_1| < a. \end{aligned} \tag{7.4}$$

Following the standard procedure of separation of variables. let

$$u_1(x_1, x_2, x_3, t) = F_1(x_1)F_2(x_2)F_3(x_3)\exp(i\omega t)\,. \tag{7.5}$$

Substitution of Eq. (7.5) into Eq. (7.1) yields

$$c_{11}F_{1,11}F_2F_3 + c_{66}F_1F_{2,22}F_3 + c_{55}F_1F_2F_{3,33} = -\rho\omega^2 F_1F_2F_3\,. \tag{7.6}$$

Dividing both sides of Eq. (7.6) by $F_1F_2F_3$, we obtain

$$c_{11}\frac{F_{1,11}}{F_1}+c_{66}\frac{F_{2,22}}{F_2}+c_{55}\frac{F_{3,33}}{F_3}=-\rho\omega^2. \tag{7.7}$$

This implies that

$$\frac{F_{1,11}}{F_1}=-\xi^2,\quad \frac{F_{2,22}}{F_2}=-\eta^2,\quad \frac{F_{3,33}}{F_3}=-\zeta^2, \tag{7.8}$$

or

$$F_{1,11}+\xi^2F_1=0,\quad F_{2,22}+\eta^2F_2=0,\quad F_{3,33}+\zeta^2F_3=0, \tag{7.9}$$

where the separation constants ξ, η and ζ must satisfy

$$\rho\omega^2=c_{11}\xi^2+c_{66}\eta^2+c_{55}\zeta^2. \tag{7.10}$$

For resonator applications we are interested in modes antisymmetric in x_2 and symmetric in x_1 and x_3. Solutions to Eq. (7.9) satisfying the corresponding boundary conditions with the desired symmetry can be easily found as

$$\xi_m=\frac{m\pi}{2a},\quad F_1=\cos\frac{m\pi x_1}{2a},\quad m=1,3,5,\cdots, \tag{7.11}$$

$$\eta_l=\frac{l\pi}{2b},\quad F_2=\sin\frac{l\pi x_2}{2b},\quad l=1,3,5,\cdots, \tag{7.12}$$

$$\zeta_n=\frac{n\pi}{2c},\quad F_3=\cos\frac{n\pi x_3}{2c},\quad n=0,2,4,\cdots. \tag{7.13}$$

Therefore u_1 can be written as:

$$u_1=A\sin\frac{l\pi x_2}{2b}\cos\frac{m\pi x_1}{2a}\cos\frac{n\pi x_3}{2c}\exp(i\omega t), \tag{7.14}$$

where A is an arbitrary constant. Substitution of Eq. (7.14) into Eq. (7.1) (or Eqs. (7.11)–(7.13) into Eq. (7.10)) determines the resonant

frequencies as

$$\rho\omega_{lmn}^2 = c_{66}\left(\frac{l\pi}{2b}\right)^2 + c_{11}\left(\frac{m\pi}{2a}\right)^2 + c_{55}\left(\frac{n\pi}{2c}\right)^2 . \tag{7.15}$$

It can be further written as

$$\frac{\omega_{lmn}^2}{\omega_s^2} = l^2 + \frac{c_{11}}{c_{66}}\left(m\frac{b}{a}\right)^2 + \frac{c_{55}}{c_{66}}\left(n\frac{b}{c}\right)^2 , \tag{7.16}$$

where

$$\omega_s = \frac{\pi}{2b}\sqrt{\frac{c_{66}}{\rho}} . \tag{7.17}$$

ω_s is the resonant frequency of the fundamental thickness mode in an unbounded quartz plate without electrodes. The modes in Eq. (7.14) are the same as those in [86], but the frequencies in Eq. (7.16) are different from those in [86] because of different approximations. The frequencies in [86] are more accurate.

7.3. Fully Electroded Plate

Consider a fully electroded plate as shown in Fig. 7.2 [89]. The top and bottom electrodes are identical.

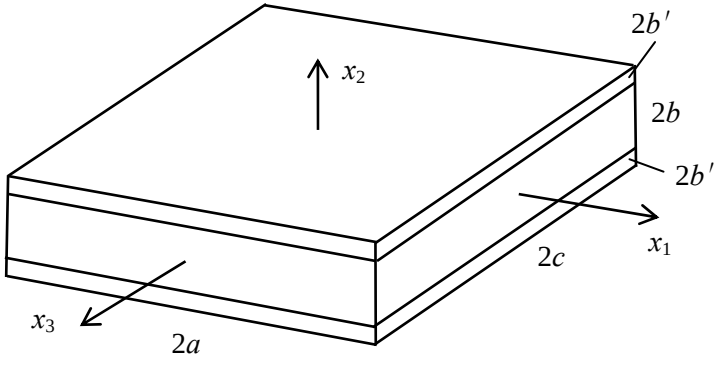

Fig. 7.2. A plate fully electroded symmetrically.

The boundary condition at the plate top and bottom are

$$T_{21} = \mp 2\rho' b' \ddot{u}_1, \quad x_2 = \pm b, \quad |x_1| < a, \quad |x_3| < c, \tag{7.18}$$

where ρ' and $2b'$ are the density and thickness of the electrodes. Equation (7.18) represents Newton's second law applied to the electrodes. The governing equation for u_1 is still given by Eq. (7.1) and the edge conditions are still given by Eq. (7.4). We consider the possibility of the following fields:

$$u_1 = A \sin \eta_{mn} x_2 \cos \frac{m\pi x_1}{2a} \cos \frac{n\pi x_3}{2c} \exp(i\omega t), \tag{7.19}$$

where m = 1, 3, 5, … and n = 0, 2, 4, …. Equation (7.19) satisfies the edge conditions in Eq. (7.4). For Eq. (7.19) to satisfy Eq. (7.1), we must have

$$\eta_{mn}^2 = \frac{1}{c_{66}} \left[\rho \omega^2 - c_{11} \left(\frac{m\pi}{2a} \right)^2 - c_{55} \left(\frac{n\pi}{2c} \right)^2 \right]. \tag{7.20}$$

Quartz resonators are made from thin plates with large a and c (a, c>>b). In this case, for m and n that are not large, η_{mn}^2 is positive. We are interested in the first few thickness-shear modes with no more than a couple of nodal points along the x_1 and x_3 directions described by a small m or n. In this case η_{mn}^2 is positive. Substitution of Eq. (7.19) into the plate top and bottom boundary conditions in Eq. (7.18) gives

$$\cot(\eta_{mn} b) = \frac{\pi^2}{4} \frac{R}{\eta_{mn} b} \frac{\omega^2}{\omega_s^2}, \quad m = 1,3,5,\cdots; \quad n = 0,2,4,\cdots, \tag{7.21}$$

where

$$R = \frac{2\rho' b'}{\rho b}. \tag{7.22}$$

R is the mass ratio between the electrodes and the crystal plate. We look for an approximate solution to Eq. (7.21) when the electrodes are thin and R is small. The lowest-order approximation when R = 0 is given by

$\eta_{mn}b = l\pi/2$ or Eq. (7.12). For the next order of approximation we write

$$\eta_{mn}b = \frac{l\pi}{2} - \Delta_l, \quad l = 1,3,5,\cdots, \tag{7.23}$$

where Δ_l is small. Substituting Eq. (7.23) into Eq. (7.21), for small Δ_l and small R, we obtain

$$\Delta_l = \frac{\pi R}{2l}\left[l^2 + \frac{c_{11}}{c_{66}}\left(m\frac{b}{a} \right)^2 + \frac{c_{55}}{c_{66}}\left(n\frac{b}{c} \right)^2 \right]. \tag{7.24}$$

Substitution of Eq. (7.24) into Eq. (7.23), with the use of Eq. (7.20), we have, approximately,

$$\frac{\omega_{lmn}^2}{\omega_s^2} = (1-2R)\left[l^2 + \frac{c_{11}}{c_{66}}\left(m\frac{b}{a} \right)^2 + \frac{c_{55}}{c_{66}}\left(n\frac{b}{c} \right)^2 \right]. \tag{7.25}$$

Equation (7.25) shows that the electrode inertia lowers the frequencies. When $R = 0$, Eq. (7.25) reduces to Eq. (7.16).

7.4. Partially Electroded Plate

Now we consider a partially electroded quartz plate (see Fig. 7.3) [89]. The electrodes at the plate top and bottom are identical and symmetric.

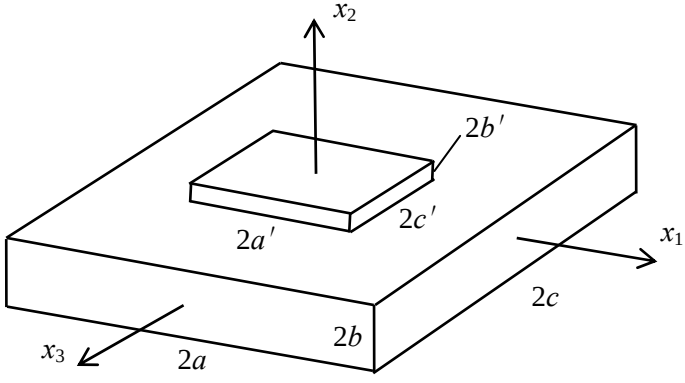

Fig. 7.3. A partially electroded rectangular plate.

7.4.1. Series solution

In this case the boundary condition at the plate top and bottom are piecewise:

$$T_{21} = \begin{cases} \mp 2\rho' b' \ddot{u}_1, & x_2 = \pm b, \quad |x_1| < a', \quad |x_3| < c', \\ 0, & x_2 = \pm b, \quad \text{elsewhere.} \end{cases} \tag{7.26}$$

The governing equation for u_1 is still given by Eq. (7.1) and the edge conditions are still given by Eq. (7.4). A single term like Eq. (7.14) or Eq. (7.19) is insufficient and a series representation of the displacement field is needed. We construct the following general solution:

$$u_1 = \sum_{m,n} A_{mn} \sin(\eta_{mn} x_2) \cos\frac{m\pi x_1}{2a} \cos\frac{n\pi x_3}{2c} \exp(i\omega t), \tag{7.27}$$

where m = 1, 3, 5, …, n = 0, 2, 4, …, A_{mn} are undetermined constants, and η_{mn} is still given by Eq. (7.20). Equation (7.27) satisfies Eqs. (7.1) and (7.4). To apply the boundary conditions at the plate top and bottom in Eq. (7.26), from Eq. (7.2) we calculate

$$T_{21} = c_{66} u_{1,2} = \sum_{m,n} c_{66} \eta_{mn} A_{mn} \cos(\eta_{mn} x_2) \cos\frac{m\pi x_1}{2a} \cos\frac{n\pi x_3}{2c} \exp(i\omega t). \tag{7.28}$$

Substitution of Eqs. (7.27) and (7.28) into Eq. (7.26) gives

$$\sum_{m,n} c_{66} \eta_{mn} A_{mn} \cos(\eta_{mn} b) \cos\frac{m\pi x_1}{2a} \cos\frac{n\pi x_3}{2c} = \begin{cases} 2\rho' b' \omega^2 \sum_{m,n} A_{mn} \sin(\eta_{mn} b) \cos\frac{m\pi x_1}{2a} \cos\frac{n\pi x_3}{2c}, & |x_1| < a', \quad |x_3| < c', \\ 0, & \text{elsewhere.} \end{cases} \tag{7.29}$$

Due to the antisymmetry involved, the boundary conditions at $x_2 = \pm b$ lead to the same equation as in Eq. (7.29). We multiply both sides of Eq. (7.29) by $\cos(p\pi x_1/2a)\cos(q\pi x_3/2c)$ with p = 1, 3, 5, … and q = 0, 2, 4, …, and integrate the resulting expression over the area of $|x_1| < a$, $|x_3| < c$ to obtain

$$\begin{aligned} & c_{66}\eta_{mn}A_{mn}\cos(\eta_{mn}b)\int_{-a}^{a}\cos^2\frac{p\pi x_1}{2a}dx_1\int_{-c}^{c}\cos^2\frac{q\pi x_3}{2c}dx_3 \\ & \quad = 2\rho' b'\omega^2\sum_{m,n}A_{mn}\sin(\eta_{mn}b)C_{mp}D_{nq}, \\ & m,p = 1,3,5...; \quad n,q = 0,2,4,.... \end{aligned} \tag{7.30}$$

where we have denoted

$$\begin{aligned} C_{mp} &= \int_{-a'}^{a'}\cos\frac{m\pi x_1}{2a}\cos\frac{p\pi x_1}{2a}dx_1 = C_{pm}, \quad m,p = 1,3,5,\cdots, \\ D_{nq} &= \int_{-c'}^{c'}\cos\frac{n\pi x_3}{2c}\cos\frac{q\pi x_3}{2c}dx_3 = D_{qn}, \quad n,q = 0,2,4,\cdots. \end{aligned} \tag{7.31}$$

Equation (7.30) is a system of linear homogeneous equations for A_{mn}. For nontrivial solutions the determinant of the coefficient matrix has to vanish, which determines the resonant frequencies together with Eq. (7.20). The nontrivial solutions of A_{mn} determine the corresponding modes.

7.4.2. Numerical result

We introduce

$$\bar{\omega}_s = \omega_s(1-R), \quad \omega_s = \frac{\pi}{2b}\sqrt{\frac{c_{66}}{\rho}}, \quad R = \frac{2\rho' b'}{\rho b}. \tag{7.32}$$

$\bar{\omega}_s$ is the resonant frequency of the fundamental thickness-shear mode in a fully electroded, unbounded plate. R is the mass ratio between the

electrodes and the plate. The resonant frequencies of the modes we are interested in are within $\bar{\omega}_s < \omega < \omega_s$.

Consider a resonator with $2a$ = 12.5 mm, $2a'$ = 7.5 mm, $2c$ = 10 mm, $2c'$ = 5 mm, and $2h$ = 0.25 mm. The mass ratio R = 3%. Five frequencies are found in $\bar{\omega}_s < \omega < \omega_s$. When using eight terms in the series for each of the x_1 and x_3 directions, the five frequencies are the same as those obtained when using nine terms in each of the x_1 and x_3 directions within six significant figures. Therefore eight terms are used in each direction for the numerical results below. The total number of terms in the series is sixty four.

Figure 7.4 shows the five trapped modes found in the order of increasing frequency. $\omega_1 = 4.049652 \times 10^7$ rad/s, $\omega_2 = 4.0725961 \times 10^7$ rad/s, $\omega_3 = 4.113085 \times 10^7$ rad/s, $\omega_4 = 4.134699 \times 10^7$ rad/s, and $\omega_5 = 4.154118 \times 10^7$ rad/s. For all of the five modes the vibration is large in the central region and small near the plate edges. In other words the vibration is mainly under the electrodes and decays outside them. This is the so-called energy trapping by electrodes. In the first mode, the whole plate is vibrating in phase. In the second mode and the third mode, there is a nodal line. In such a case the charges on an electrode produced by the shear strain tend to cancel with each other and thus reduce the capacitance of the resonator. This may be undesirable or desirable depending on the specific application. For higher order modes there are more nodal lines.

In Fig. 7.5 we vary the electrode dimensions. When $2a'$ = 5 mm and $2c'$ = 3 mm, 2 trapped modes are found with $\omega_1 = 4.070822 \times 10^7$ rad/s. When $2a'$ = 7.5 mm and $2c'$ = 5 mm, 5 trapped modes are found with $\omega_1 = 4.049652 \times 10^7$ rad/s. When $2a'$ = 10 mm and $2c'$ = 7 mm, 7 trapped modes are found with $\omega_1 = 4.023059 \times 10^7$ rad/s. The figure shows the effect of the electrode dimension on energy trapping of the first mode in each of the x_1 and x_3 directions. Small electrodes are associated with fewer trapped modes with higher frequencies. It can be seen that the vibration distribution follows the electrodes. For smaller electrodes the vibration is more trapped near the center.

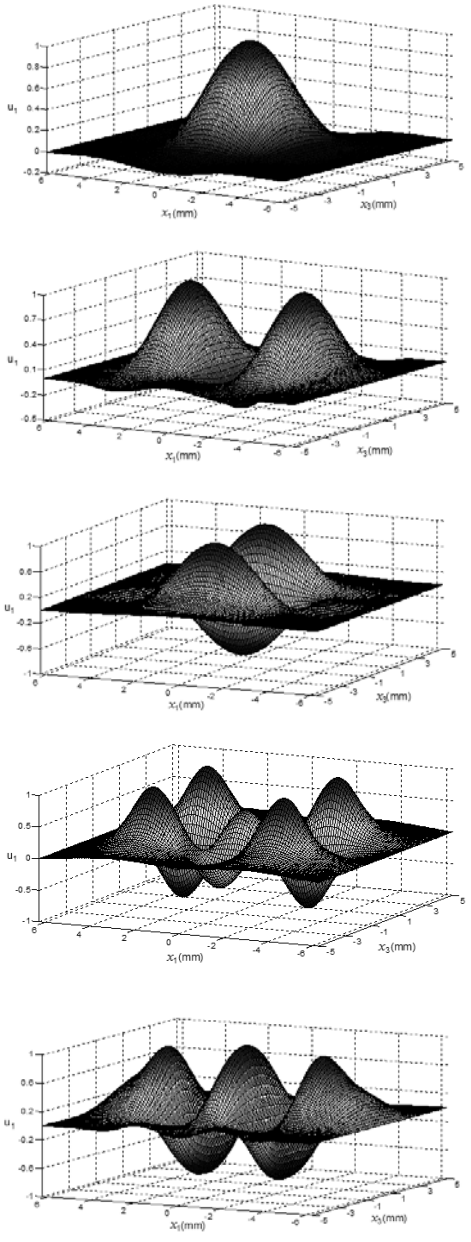

Fig. 7.4. Five trapped modes.

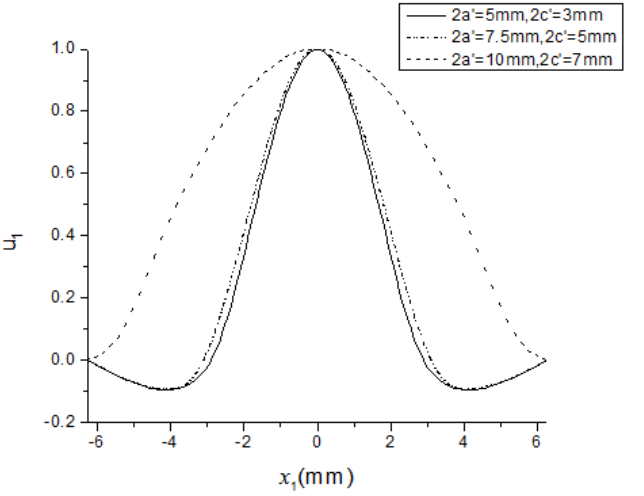

(a)

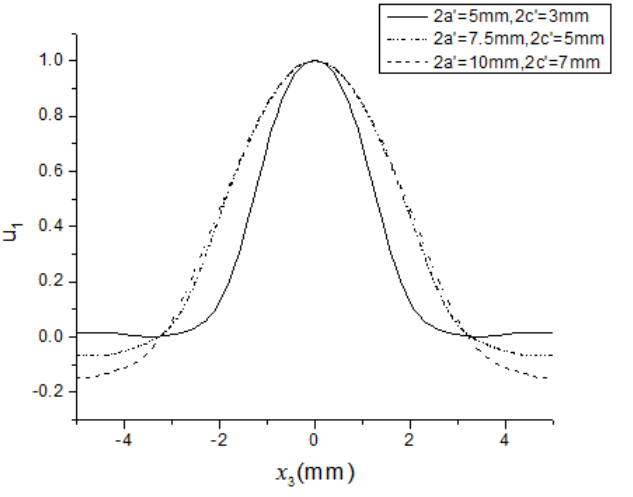

(b)

Fig. 7.5. Effect of electrode size on energy trapping. R = 3%. (a) Variation along x_1. (b) Variation along x_3.

In Fig. 7.6 we vary the electrode thickness. When R = 1%, 2 trapped modes are found with $\omega_1 = 4.130107 \times 10^7$ rad/s. When R = 3%, 5 trapped modes are found with $\omega_1 = 4.049652 \times 10^7$ rad/s. When R = 5%,

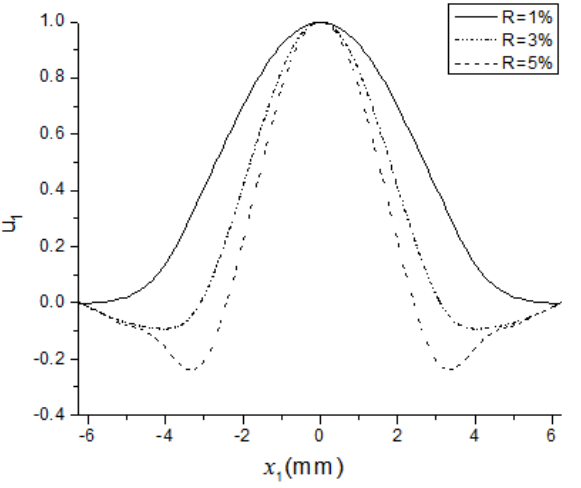

(a)

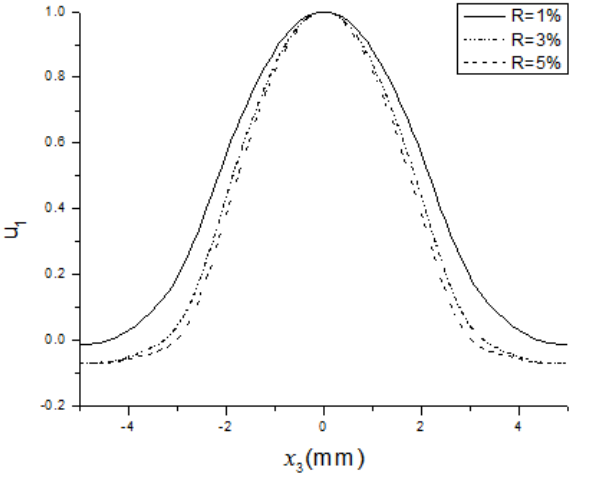

(b)

Fig. 7.6. Effect of electrode thickness on energy trapping. $2a'$ = 7.5mm, $2c'$ = 5mm. (a) Variation along x_1. (b) Variation along x_3.

7 trapped modes are found with $\omega_1 = 3.966399 \times 10^7$ rad/s. The figure shows the effect of the mass ratio R on the first mode. The frequency of this mode decreases as R increases, as expected. For larger values of R the mode is pushed further toward the center with better energy trapping. Larger values of R also increase the number of trapped mode.

7.5. Contoured Plate

The partially electroded plate in Fig. 7.3 with energy trapping can be considered as a plate that is a little thicker in the central region. Then it can be expected that a plate with a varying thickness (called contoured resonators), thicker in the central region (see Fig. 7.7), can also produce energy trapping. This is indeed true — in fact, contoured plates can lead to strong energy trapping. In this section we analyze such a plate [90].

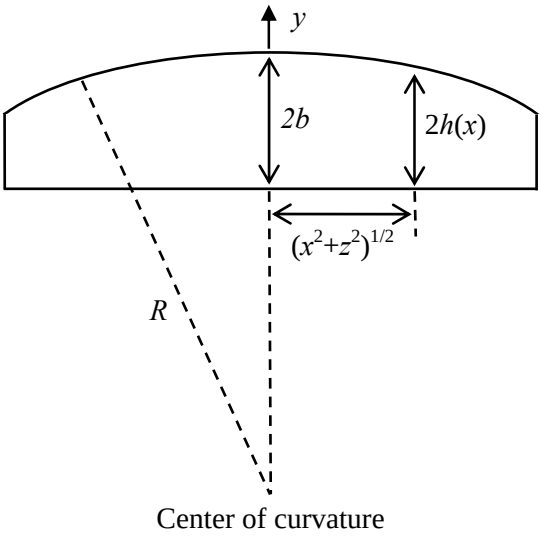

Fig. 7.7. A plate with varying thickness.

We use Eq. (7.1) for u_1:

$$c_{11}u_{1,11} + c_{66}u_{1,22} + c_{55}u_{1,33} = \rho\,\ddot{u}_1\,. \tag{7.33}$$

Consider the following displacement field:

$$u_1 = u = A(x,z)\sin\eta y \exp(i\omega t)\,, \tag{7.34}$$

where

$$\eta(x,z) = \frac{m\pi}{2h(x,z)}, \quad m = 1,3,5,\cdots. \tag{7.35}$$

Equation (7.34) satisfies the traction-free boundary conditions at the plate top and bottom surfaces approximately. Substitution of Eq. (7.34) in Eq. (7.33) leads to an equation for A:

$$c_{11}\frac{\partial^2 A}{\partial x^2} + c_{55}\frac{\partial^2 A}{\partial z^2} + (\rho\omega^2 - c_{66}\eta^2)A = 0\,. \tag{7.36}$$

To be specific we consider

$$2h = 2b\left(1 - \frac{x^2+z^2}{4Rb}\right). \tag{7.37}$$

In Eq. (7.37), for a thin plate with a slow thickness variation, we have $R>>b$. In addition, since we are considering modes trapped in the central region, $(x^2+z^2)^{1/2}$ is also small, usually of the order of a few times of the plate center thickness $2b$. Then the second term in the parentheses in Eq. (7.37) is much smaller than one. We have, approximately,

$$(2h)^2 \cong (2b)^2\left(1 - \frac{x^2+z^2}{2Rb}\right), \tag{7.38}$$

$$\frac{1}{(2h)^2} \cong \frac{1}{(2b)^2}\left(1 + \frac{x^2+z^2}{2Rb}\right). \tag{7.39}$$

With the use of Eqs. (7.35) and (7.39), Eq. (7.36) becomes

$$c_{11}\frac{\partial^2 A}{\partial x^2} + c_{55}\frac{\partial^2 A}{\partial z^2} + \left[\rho\omega^2 - c_{66}\left(\frac{m\pi}{2b}\right)^2\left(1 + \frac{x^2+z^2}{2Rb}\right)\right]A = 0\,. \tag{7.40}$$

As a partial differential equation, Eq. (7.40) is separable. Let

$$A(x,z) = F(x)G(z). \tag{7.41}$$

Substituting Eq. (7.41) in Eq. (7.40), we obtain

$$\begin{aligned} &c_{11}\frac{\partial^2 F}{\partial x^2}\frac{1}{F} + c_{55}\frac{\partial^2 G}{\partial z^2}\frac{1}{G} \\ &\quad + \rho\omega^2 - c_{66}\left(\frac{m\pi}{2b}\right)^2\left(1+\frac{x^2+z^2}{2Rb}\right) = 0. \end{aligned} \tag{7.42}$$

Following the standard argument in the method of separation of variables, Eq. (7.42) implies that

$$c_{11}\frac{\partial^2 F}{\partial x^2}\frac{1}{F} - c_{66}\left(\frac{m\pi}{2b}\right)^2\frac{x^2}{2Rb} = -\rho\omega_1^2, \tag{7.43}$$

$$c_{55}\frac{\partial^2 G}{\partial z^2}\frac{1}{G} - c_{66}\left(\frac{m\pi}{2b}\right)^2\frac{z^2}{2Rb} = -\rho\omega_3^2, \tag{7.44}$$

$$\rho\omega^2 = c_{66}\left(\frac{m\pi}{2b}\right)^2 + \rho\omega_1^2 + \rho\omega_3^2, \tag{7.45}$$

where ω_1 and ω_3 are separation constants. Equations (7.43) and (7.44) are ordinary differential equations. They can be written as

$$\frac{c_{11}}{\rho}\frac{\partial^2 F}{\partial x^2} + \left[\omega_1^2 - \frac{c_{66}}{\rho}\left(\frac{m\pi}{2b}\right)^2\frac{x^2}{2Rb}\right]F = 0, \tag{7.46}$$

$$\frac{c_{55}}{\rho}\frac{\partial^2 G}{\partial z^2} + \left[\omega_3^2 - \frac{c_{66}}{\rho}\left(\frac{m\pi}{2b}\right)^2\frac{z^2}{2Rb}\right]G = 0. \tag{7.47}$$

We introduce the following coordinate transformation between (x,z) and (ξ_1,ξ_3):

$$x=\alpha_1\xi_1,\quad z=\alpha_3\xi_3, \tag{7.48}$$

where

$$\alpha_1^4=\frac{R(2b)^3}{(m\pi)^2}\frac{c_{11}}{c_{66}},\quad \alpha_3^4=\frac{R(2b)^3}{(m\pi)^2}\frac{c_{55}}{c_{66}}. \tag{7.49}$$

With Eq. (7.48), Eqs. (7.46) and (7.47) take the following form:

$$\frac{\partial^2 F}{\partial\xi_1^2}+(\lambda_1-\xi_1^2)F=0, \tag{7.50}$$

$$\frac{\partial^2 G}{\partial\xi_3^2}+(\lambda_3-\xi_3^2)G=0, \tag{7.51}$$

where

$$\lambda_1=\frac{\omega_1^2\rho\alpha_1^2}{c_{11}},\quad \lambda_3=\frac{\omega_3^2\rho\alpha_3^2}{c_{55}}. \tag{7.52}$$

Equations (7.50) and (7.51) are both in the form of the well-known Weber's equation. Let

$$F(\xi_1)=\exp(-\xi_1^2/2)f(\xi_1), \tag{7.53}$$

$$G(\xi_3)=\exp(-\xi_3^2/2)g(\xi_3). \tag{7.54}$$

Equations (7.50) and (7.51) can be further written as

$$\frac{d^2 f}{d\xi_1^2}-2\xi_1\frac{df}{d\xi_1}+(\lambda_1-1)f=0, \tag{7.55}$$

$$\frac{d^2 g}{d\xi_3^2}-2\xi_3\frac{dg}{d\xi_3}+(\lambda_3-1)g=0. \tag{7.56}$$

The solutions for Eqs. (7.55) and (7.56) are known. For odd integers of λ_1 or λ_3, the bounded solutions of Eqs. (7.55) and (7.56) are the Hermite polynomials, i.e.,

$$\lambda_1 = 2p+1, \quad f(\xi_1) = H_p(\xi_1), \quad p = 0,1,2,3,\cdots, \tag{7.57}$$

$$\lambda_3 = 2q+1, \quad g(\xi_3) = H_q(\xi_3), \quad q = 0,1,2,3,\cdots, \tag{7.58}$$

where

$$\begin{aligned} &H_0(\xi) = 1, \\ &H_1(\xi) = 2\xi, \\ &H_2(\xi) = 4\xi^2 - 2, \\ &H_3(\xi) = 8\xi^3 - 12\xi, \\ &\cdots. \end{aligned} \tag{7.59}$$

With λ_1 or λ_3 given by Eqs. (7.57) and (7.58), from Eq. (7.52) we determine ω_1 and ω_3 as

$$\begin{aligned} \rho\omega_1^2 &= \frac{c_{11}\lambda_1}{\alpha_1^2} = c_{11}(2p+1)\frac{m\pi}{R^{1/2}(2b)^{3/2}}\sqrt{\frac{c_{66}}{c_{11}}}, \\ \rho\omega_3^2 &= \frac{c_{55}\lambda_3}{\alpha_3^2} = c_{55}(2q+1)\frac{m\pi}{R^{1/2}(2b)^{3/2}}\sqrt{\frac{c_{66}}{c_{55}}}. \end{aligned} \tag{7.60}$$

Finally, substituting Eq. (7.60) into Eq. (7.45), we obtain the resonant frequencies as

$$\begin{aligned} \rho\omega^2 = {} & c_{66}\left(\frac{m\pi}{2b}\right)^2 \\ & + c_{11}(2p+1)\frac{m\pi}{R^{1/2}(2b)^{3/2}}\sqrt{\frac{c_{66}}{c_{11}}} \\ & + c_{55}(2q+1)\frac{m\pi}{R^{1/2}(2b)^{3/2}}\sqrt{\frac{c_{66}}{c_{55}}}. \end{aligned} \tag{7.61}$$

This page intentionally left blank

Chapter 8

Scalar Equation for Thickness Modes

Due to material anisotropy and electromechanical coupling, analysis of crystal devices is mathematically challenging. In addition to using approximate techniques for solving differential equations, people have also tried to obtain approximate differential equations. These approximate equations are usually valid for certain modes only, within a certain frequency and/or wave number range of interest. For long or slowly varying thickness-shear or thickness-stretch modes in quartz plates, a single scalar differential equation can be derived. This chapter collects results from these approximate scalar differential equations.

8.1. Scalar Equation for AT-cut Quartz Plates

The piezoelectric version of Eqs. (6.19) and (6.20) is [82–86]

$$\begin{aligned} &c_{11}u_{1,11} + (c_{12} + c_{66})u_{2,12} \\ &\quad + c_{66}u_{1,22} + c_{55}u_{1,33} + e_{26}\phi_{,22} = \rho\ddot{u}_1, \\ &(c_{66} + c_{12})u_{1,12} + c_{66}u_{2,11} + c_{22}u_{2,22} = \rho\ddot{u}_2, \\ &e_{26}u_{1,22} - \varepsilon_{22}\phi_{,22} = 0, \end{aligned} \tag{8.1}$$

and

$$\begin{aligned} T_{11} &= c_{11}u_{1,1} + c_{12}u_{2,2}, \\ T_{22} &= c_{12}u_{1,1} + c_{22}u_{2,2}, \\ T_{31} &= c_{55}u_{1,3} + e_{25}\phi_{,2}, \\ T_{12} &= c_{66}(u_{1,2} + u_{2,1}) + e_{26}\phi_{,2}, \\ D_2 &= e_{26}u_{1,2} - \varepsilon_{22}\phi_{,2}. \end{aligned} \tag{8.2}$$

8.1.1. Unelectroded plate

For an unelectroded plate, the boundary conditions at the plate top and bottom surfaces are

$$T_{2j} = 0, \quad D_2 = 0, \quad x_2 = \pm h\,. \tag{8.3}$$

Consider time-harmonic vibration. The time-harmonic factor will be dropped in the sequel. We are only interested in modes that are antisymmetric about $x_2 = 0$. Consider u_1^n as defined by

$$u_1(x_1, x_2, x_3) = \sum_{n=1,3,5,\cdots}^{\infty} u_1^n(x_1, x_3) \sin \eta_n x_2\,, \tag{8.4}$$

where

$$\eta_n \cong \frac{n\pi}{2h}, \quad n \quad \text{odd}\,. \tag{8.5}$$

By studying the propagation of long u_1 waves in the (x_1, x_3) plane, from the approximate dispersion relations of these waves accurate to the second order of the small in-plane wave numbers, it was shown in [82–86] that u_1^n is governed by the following scalar equation which is two-dimensional:

$$M_n \frac{\partial^2 u_1^n}{\partial x_1^2} + c_{55} \frac{\partial^2 u_1^n}{\partial x_3^2} - \frac{n^2\pi^2}{4h^2} \bar{c}_{66} u_1^n - \rho \ddot{u}_1^n = 0\,, \tag{8.6}$$

where

$$M_n = c_{11} + (c_{12} + c_{66})r + \frac{4(r\bar{c}_{66} - c_{66})(rc_{22} + c_{12})}{c_{22} n\pi\kappa} \cot\frac{\kappa n\pi}{2}\,, \tag{8.7}$$

$$\bar{c}_{66} = c_{66} + \frac{e_{26}^2}{\varepsilon_{22}}\,, \tag{8.8}$$

$$\kappa = \left(\frac{\bar{c}_{66}}{c_{22}}\right)^{1/2}, \quad r = \frac{c_{12} + c_{66}}{\bar{c}_{66} - c_{22}}\,. \tag{8.9}$$

8.1.2. Electroded plate

For an electroded plate with shorted electrodes, the boundary conditions at the plate top and bottom surfaces are

$$\begin{aligned} &T_{2j} = \mp 2\rho' h' \ddot{u}_j, \quad x_2 = \pm h, \\ &\phi = 0, \quad x_2 = \pm h, \end{aligned} \tag{8.10}$$

Consider u_1^n defined by

$$u_1(x_1, x_2, x_3) = \sum_{n=1,3,5,\cdots}^{\infty} u_1^n(x_1, x_3) \sin \eta_n x_2 \ , \tag{8.11}$$

where

$$\eta_n \cong \frac{n\pi}{2h}, \quad n \quad \text{odd} \, . \tag{8.12}$$

It was shown in [82–86] that u_1^n is governed by the following equation:

$$\begin{aligned} &M_n \frac{\partial^2 u_1^n}{\partial x_1^2} + c_{55} \frac{\partial^2 u_1^n}{\partial x_3^2} - \frac{n^2 \pi^2}{4h^2} \hat{c}_{66} u_1^n - \rho \ddot{u}_1^n \\ &\quad = \rho \omega^2 \frac{e_{26} V x_2}{c_{66} 2h} \exp(i\omega t), \end{aligned} \tag{8.13}$$

where

$$\hat{c}_{66} = \bar{c}_{66} \left(1 - \frac{8\bar{k}_{26}^2}{n^2 \pi^2} - 2R\right), \quad \bar{k}_{26}^2 = \frac{e_{26}^2}{\bar{c}_{66} \varepsilon_{22}}, \tag{8.14}$$

$$R = \frac{2\rho' h'}{\rho h} . \tag{8.15}$$

Equations (8.6) and (8.13) can usually produce more refined and more accurate results than Eq. (7.1), but Eq. (7.1) is three-dimensional.

8.2. Rectangular Plate

Consider an unelectroded, rectangular AT-cut quartz plate as shown in Fig. 8.1 [86].

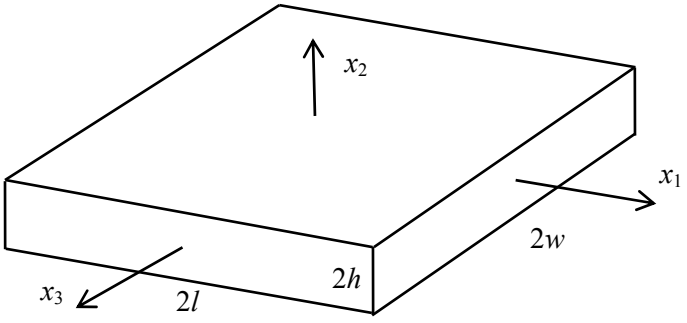

Fig. 8.1. Three-dimensional view of an AT-cut quartz plate.

The scalar equation for an unelectroded AT-cut quartz plate is given by Eq. (8.6):

$$M_n \frac{\partial^2 u_1^n}{\partial x_1^2} + c_{55} \frac{\partial^2 u_1^n}{\partial x_3^2} - \frac{n^2 \pi^2}{4h^2} \bar{c}_{66} u_1^n - \rho \ddot{u}_1^n = 0\,, \quad n=1, 3, 5, \ldots. \tag{8.16}$$

At the plate top and bottom, the traction-free boundary conditions are

$$T_{2j} = 0, \quad x_2 = \pm h, \quad |x_1| < l, \quad |x_3| < w\,, \tag{8.17}$$

which are approximately satisfied when deriving Eq. (8.16). At $x_1 = \pm l$ the major stress component is T_{12}. At $x_3 = \pm w$ the major stress component is T_{31}. Therefore, the traction-free boundary conditions at the plate edges are [86]:

$$\begin{aligned} &T_{12} = 0, \quad x_1 = \pm l, \quad |x_3| < w, \quad |x_2| < h, \\ &T_{31} = 0, \quad x_3 = \pm w, \quad |x_1| < l, \quad |x_2| < h, \end{aligned} \tag{8.18}$$

which are equivalent to

$$\begin{aligned} &u_1 = 0, \quad x_1 = \pm l, \quad |x_3| < w, \quad |x_2| < h, \\ &u_{1,3} = 0, \quad x_3 = \pm w, \quad |x_1| < l, \quad |x_2| < h. \end{aligned} \tag{8.19}$$

There are four independent solutions to Eqs. (8.16) and (8.19). They may be written as

$$\begin{aligned} u_1 &= B \sin \frac{n\pi x_2}{2h} \cos \xi x_1 \cos \nu x_3, \\ u_1 &= C \sin \frac{n\pi x_2}{2h} \cos \xi x_1 \sin \nu x_3, \\ u_1 &= D \sin \frac{n\pi x_2}{2h} \sin \xi x_1 \cos \nu x_3, \\ u_1 &= E \sin \frac{n\pi x_2}{2h} \sin \xi x_1 \sin \nu x_3, \end{aligned} \tag{8.20}$$

each of which satisfies

$$\omega^2 = \frac{1}{\rho}\left(\bar{c}_{66} \frac{n^2\pi^2}{4h^2} + M_n \xi^2 + c_{55} \nu^2 \right). \tag{8.21}$$

Each of Eq. (8.20) satisfies the edge conditions in Eq. (8.19) provided that

$$\xi = \frac{m\pi}{2l}, \quad m = 1,3,5,\cdots, \quad \nu = \frac{p\pi}{2w}, \quad p = 0,2,4,\cdots, \tag{8.22}$$

$$\xi = \frac{m\pi}{2l}, \quad m = 1,3,5,\cdots, \quad \nu = \frac{p\pi}{2w}, \quad p = 1,3,5,\cdots, \tag{8.23}$$

$$\xi = \frac{m\pi}{2l}, \quad m = 2,4,6,\cdots, \quad \nu = \frac{p\pi}{2w}, \quad p = 0,2,4,\cdots, \tag{8.24}$$

$$\xi = \frac{m\pi}{2l}, \quad m = 2,4,6,\cdots, \quad \nu = \frac{p\pi}{2w}, \quad p = 1,3,5,\cdots. \tag{8.25}$$

Clearly, the substitution of Eqs. (8.22)–(8.25) into Eq. (8.21) yields

$$\omega^2 = \frac{1}{\rho}\left(\bar{c}_{66}\frac{n^2\pi^2}{4h^2} + M_n\frac{m^2\pi^2}{4l^2} + c_{55}\frac{p^2\pi^2}{4w^2}\right), \tag{8.26}$$
$$n = 1,3,5,\cdots, \quad m = 1,2,3,\cdots, \quad p = 0,1,2,3,\cdots.$$

A few other solutions to Eq. (8.6) and/or Eq. (8.13) were obtained in [83–85]. These include a partially electroded plate (a trapped energy resonator) [83], a plate with two pairs of electrodes (a monolithic filter) [84], and a plate with varying thickness (a contoured resonator) [85]. Unelectroded circular plates were analyzed in [86] using perturbation method.

8.3. Elliptical Plate

Due to the in-plane anisotropy of AT-cut quartz plates, to obtain resonant frequencies and modes for a circular plate is not simple. This problem was analyzed in [86] where a perturbation procedure based on weak anisotropy was used. It is useful to note that Eq. (8.6) in fact allows simple solutions for curtain special elliptical plates. Consider an elliptical plate of AT-cut quartz as shown in Fig. 8.2.

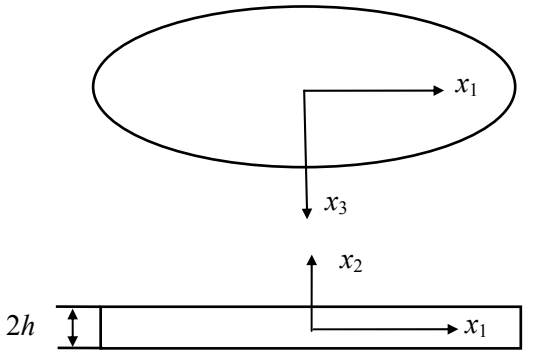

Fig. 8.2. Top and side views of an elliptical plate.

Time-harmonic motions of the plate are governed by Eq. (8.6):

$$M_n \frac{\partial^2 u_1^n}{\partial x_1^2} + c_{55} \frac{\partial^2 u_1^n}{\partial x_3^2} - \frac{n^2 \pi^2}{4h^2} \bar{c}_{66} u_1^n + \rho \omega^2 u_1^n = 0\,,\ n=1, 3, 5, \ldots. \quad (8.27)$$

Specifically, we consider the special case when the elliptical boundary of the plate is given by

$$\frac{x_1^2}{a^2 M_n / c_{55}} + \frac{x_3^2}{a^2} = 1\,. \quad (8.28)$$

In the (x_1, x_3) plane, we introduce a new coordinate system (ξ_1, ξ_3) by

$$x_1 = \xi_1 \sqrt{M_n / c_{55}}\,, \quad x_3 = \xi_3\,. \quad (8.29)$$

The transformation in Eq. (8.29) changes the elliptical boundary in Eq. (8.28) into a circle described by

$$\frac{\xi_1^2}{a^2} + \frac{\xi_3^2}{a^2} = 1\,. \quad (8.30)$$

At the same time, in the new coordinate system, Eq. (8.27) becomes

$$\frac{\partial^2 u_1^n}{\partial \xi_1^2} + \frac{\partial^2 u_1^n}{\partial \xi_3^2} + \alpha^2 u_1^n = 0\,, \quad (8.31)$$

where

$$\alpha^2 = \frac{1}{c_{55}} \left(\rho \omega^2 - \frac{n^2 \pi^2}{4h^2} \bar{c}_{66} \right). \quad (8.32)$$

We further introduce a polar coordinate system (r, θ) defined by

$$\xi_3 = r \cos\theta, \quad \xi_1 = r \sin\theta\,. \quad (8.33)$$

Then Eq. (8.31) takes the following form:

$$\frac{\partial^2 u_1^n}{\partial r^2} + \frac{1}{r}\frac{\partial^2 u_1^n}{\partial r} + \frac{1}{r^2}\frac{\partial^2 u_1^n}{\partial \theta^2} + \alpha^2 u_1^n = 0. \tag{8.34}$$

Consider modes that are independent of θ for which Eq. (8.34) reduces to

$$\frac{\partial^2 u_1^n}{\partial r^2} + \frac{1}{r}\frac{\partial^2 u_1^n}{\partial r} + \alpha^2 u_1^n = 0. \tag{8.35}$$

The general solution to Eq. (8.35) can be written as

$$u_1^n = AJ_0(\alpha r) + BY_0(\alpha r), \tag{8.36}$$

where A and B are undetermined constants. J_0 and Y_0 are the zero-order Bessel functions of the first kind and the second kind, respectively. Since Y_0 is unbounded when $r = 0$, we must have $B = 0$ and

$$u_1^n = AJ_0(\alpha r). \tag{8.37}$$

Equation (8.37) still needs to satisfy the boundary condition at the plate edge, which leads to a frequency equation for determining ω.

8.4. Circular Plate

Since the scalar differential equation (see Eq. (8.6)) is separable in Cartesian coordinates, free vibration frequencies and modes can be readily obtained for rectangular plates (see Section 8.2). For circular resonators, however, the situation is different. This is because Eq. (8.6) is not separable in polar coordinates due to the in-plane material anisotropy. A perturbation procedure by writing the coefficients of the scalar differential equation as the sum of a mean or isotropic part plus a deviation due to anisotropy was proposed in [86]. The perturbation

procedure is valid for weak in-plane anisotropy. For the most widely used fundamental mode AT-cut quartz resonator, the ratio between the deviation and the mean of the coefficients of the scalar differential equation is 0.231 [86] which is not very small. It is natural to wonder what the error or inaccuracy of the perturbation procedure is. This can be best answered by a direct comparison with the exact solution of the scalar differential equation, which is obtained in this section [91]. We also make comparisons with available experimental results.

8.4.1. Governing Equation

Consider the circular AT-cut quartz resonator in Fig. 8.3. Its radius is R and its thickness is $2h$.

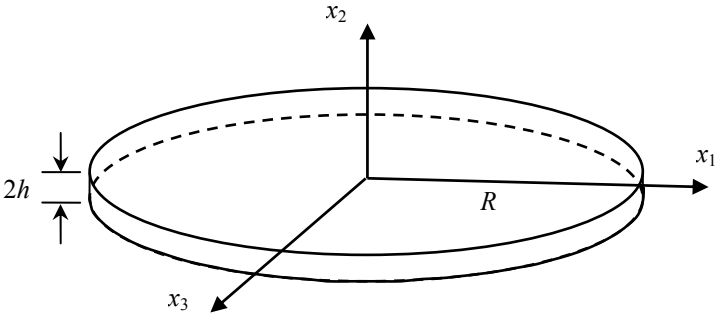

Fig. 8.3. A circular AT-cut quartz plate and coordinate system.

For time-harmonic free vibrations, Eq. (8.6) becomes

$$M_n \frac{\partial^2 u_1^n}{\partial x_1^2} + c_{55} \frac{\partial^2 u_1^n}{\partial x_3^2} - \frac{n^2 \pi^2}{4h^2} \bar{c}_{66} u_1^n + \rho \omega^2 u_1^n = 0 . \tag{8.38}$$

Introduce the following coordinate transformation from (x_1,x_3) to (y_1,y_3):

$$x_1 = \lambda y_1 , \quad x_3 = \mu y_3 , \tag{8.39}$$

where λ and μ are parameters to be specified later. Equation (8.39) transforms Eq. (8.38) into:

$$\frac{M_n}{\lambda^2}\frac{\partial^2 u_1^n}{\partial y_1^2}+\frac{c_{55}}{\mu^2}\frac{\partial^2 u_1^n}{\partial y_3^2}-\frac{n^2\pi^2}{4h^2}\bar{c}_{66}u_1^n+\rho\omega^2 u_1^n=0\,. \tag{8.40}$$

We choose

$$\lambda=\frac{1}{\omega_0}\sqrt{\frac{M_n}{\rho}}\,,\quad \mu=\frac{1}{\omega_0}\sqrt{\frac{c_{55}}{\rho}}\,, \tag{8.41}$$

where

$$\omega_0=\frac{n\pi}{2h}\sqrt{\frac{\bar{c}_{66}}{\rho}}\,. \tag{8.42}$$

Then Eq. (8.40) becomes the following Helmholtz equation:

$$\frac{\partial^2 u_1^n}{\partial y_1^2}+\frac{\partial^2 u_1^n}{\partial y_3^2}+\left(\frac{\omega^2}{\omega_0^2}-1\right)u_1^n=0\,. \tag{8.43}$$

Let the boundary of the circular resonator be defined by

$$x_1^2+x_3^2=R^2\,. \tag{8.44}$$

In the transformed plane the boundary of the resonator is

$$\lambda^2 y_1^2+\mu^2 y_3^2=R^2\,, \tag{8.45}$$

which represents an ellipse. For n = 1 and n = 3, we have $\lambda>\mu$. Therefore the semi-major and semi-minor axes are R/μ and R/λ, respectively.

We introduce elliptical coordinates (ξ,η) defined by

$$y_1=c\sinh\xi\sin\eta\,,\quad y_3=c\cosh\xi\cos\eta\,, \tag{8.46}$$

where c is a parameter and $2c$ is the focal distance of the ellipses associated with Eq. (8.46). Then Eq. (8.43) takes the following form:

$$\frac{\partial^2 u_1^n}{\partial \xi^2} + \frac{\partial^2 u_1^n}{\partial \eta^2} + 2q(\cosh 2\xi - \cos 2\eta)u_1^n = 0\,, \tag{8.47}$$

where

$$q = \frac{c^2}{4}\left(\frac{\omega^2}{\omega_0^2} - 1\right), \quad J = \frac{\sqrt{2}}{2}\sqrt{\cosh 2\xi - \cos 2\eta}\,. \tag{8.48}$$

8.4.2. Solution

The solution procedure of Eq. (8.47) is the same as that in Section 5.10 and will not be repeated here. We call modes odd or even in x_1 by antisymmetric or symmetric modes. For antisymmetric modes, the displacement can be written as

$$u_1^n(\xi, \eta, t) = \sum_{m=1}^{\infty} S_m Se_m(\xi, q) se_m(\eta, q)\,, \tag{8.49}$$

where S_m are undetermined constants. Let the elliptical boundary of the plate in the transformed plane be at $\xi = \xi_0$. The boundary condition is

$$u_1^n = \sum_{m=1}^{\infty} S_m Se_m(\xi_0, q) se_m(\eta, q) = 0\,, \tag{8.50}$$

or

$$Se_m(\xi_0, q) = 0\,. \tag{8.51}$$

Equation (8.51) determines q. Then ω can be determined from Eq. (8.48).

Similarly, the symmetric modes are given by

$$u_1^n = \sum_{m=0}^{\infty} C_m Ce_m(\xi_0, q) ce_m(\eta, q) = 0\,, \tag{8.52}$$

or

$$Ce_m(\xi_0, q) = 0. \tag{8.53}$$

8.4.3. Numerical Result

As an example, consider a circular plate resonator whose diameter $2R$ = 7.874 mm and thickness $2h$ = 1.10236 mm. This determines ω_0 = 9.467803×10^7 rad/s or f_0 = 1.506848×10^7 Hz, and ξ_0 = 0.10033. We use the first thirty terms of each series to calculate the displacement field. For the most widely used fundamental thickness-shear mode, the number of significant figures for its frequency is sixteen when thirty terms are kept in the series.

Figure 8.4 (a) and (b) show the distributions of $u_1^{(1)}$ for the fundamental thickness-shear mode with n = 1 and $u_1^{(3)}$ for the third overtone thickness-shear mode with n = 3, respectively. Darker areas have larger $u_1^{(1)}$ or $u_1^{(3)}$. When the plate is vibrating in the fundamental mode, all particles at the plate top surface vibrate in phase. The bottom surface has a 180° phase difference from the top surface. The plate's middle plane is a nodal plane without motion. The third overtone mode has three nodal planes parallel to the plate surfaces. Because of the in-plane material anisotropy of the plate, the vibration distributions are not exactly circular in Fig. 8.4. They are slightly longer along x_1 and narrower along x_3. The distribution in Fig. 8.4 (b) is more confined to the center than that in Fig. 8.4 (a). The frequency of the third overtone is roughly three times that of the fundamental.

We compare theoretical results with experimental measurements in Table 8.1, where the experimental results are the averages of ten repeated measurements for each of the two cases of n = 1 and 3 [86]. In both cases, the solution in this section is closer to the experimental result than the perturbation solution. For n = 1 and 3, the differences between the solution in this section and the perturbation solution are 68600 Hz and 206000 Hz, respectively. The relative difference is about 0.45–0.46% for both cases.

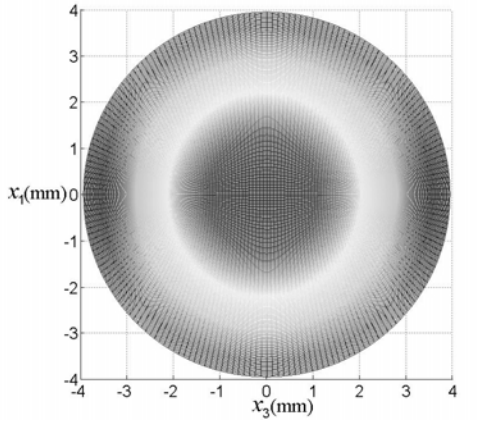

(a)

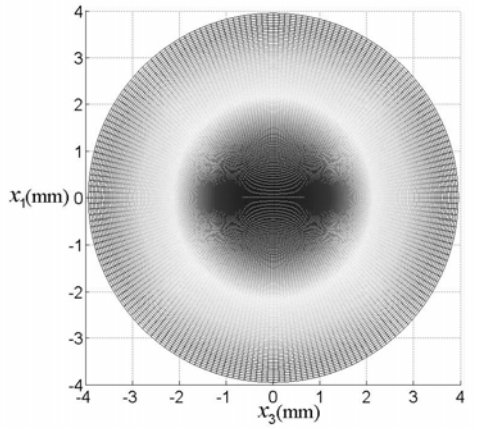

(b)

Fig. 8.4. (a) Fundamental thickness-shear mode. n = 1. 1st mode of Ce_0 = 0. f = 1.5079038×10^7 Hz. (b) Third overtone thickness-shear mode. n = 3. 1st mode of Ce_0 = 0. f = 4.5208283×10^7 Hz.

Table 8.1. Frequencies of thickness-shear modes: the fundamental (n = 1) and the third overtone (n = 3).

	$n = 1$	$n = 3$
Experiment [86]	1.50677×10^7 Hz	4.51776×10^7 Hz
Perturbation [86]	1.50104×10^7 Hz	4.50023×10^7 Hz
Exact	1.50790×10^7 Hz	4.52083×10^7 Hz

When n = 1, in addition to the mode in Fig. 8.4 (a), there other modes whose frequencies are slightly higher than the mode in Fig. 8.4 (a), with nodal lines roughly parallel to the x_3 axis in the (x_1,x_3) plane. They are also called thickness-shear modes. Three of these modes are shown in Fig. 8.5.

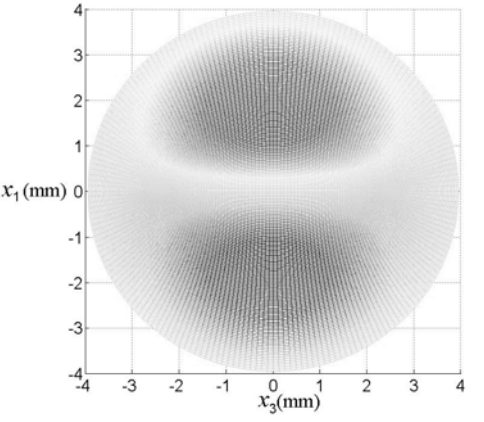

(a)

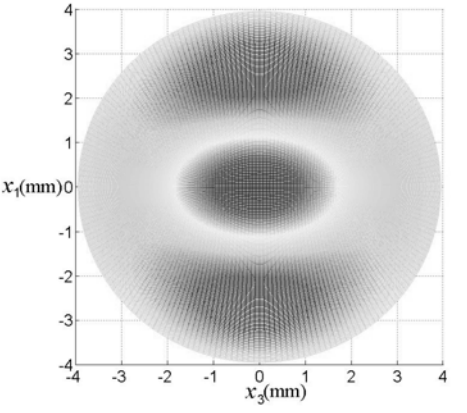

(b)

Fig. 8.5. Other thickness-shear modes (n = 1). (a) 1st mode of $Se_1 = 0$. f = 1.5098337×10^7 Hz. (b) 2nd mode of $Ce_0 = 0$. f = 1.5129323×10^7 Hz. (c) 2nd mode of $Se_1 = 0$. f = 1.5171146×10^7 Hz.

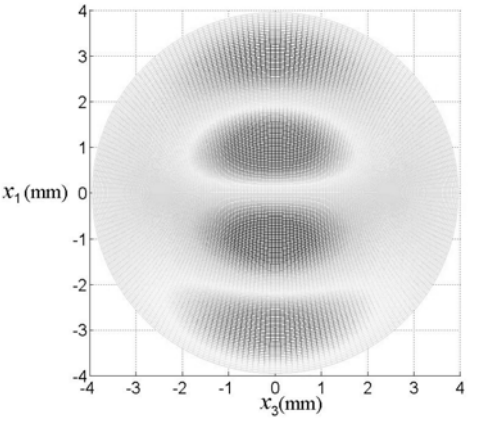

(c)

Fig. 8.5. (*Continued*)

Still for the case of $n = 1$, there also exist modes with nodal lines roughly parallel to the x_1 axis. They are called thickness-twist modes. Four of such modes are shown in Fig. 8.6. Their frequencies are only slightly different, increasing slowly when there are more nodal lines.

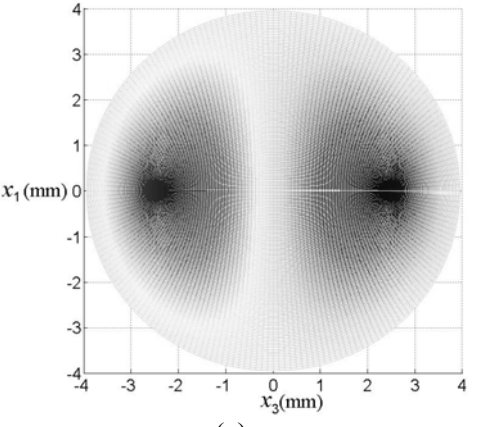

(a)

Fig. 8.6. Thickness-twist modes ($n = 1$). (a) 1st mode of $Ce_1 = 0$. $f = 1.5092173\times10^7$ Hz. (b) 1st mode of $Se_2 = 0$. $f = 1.5116458\times10^7$ Hz. (c) 2nd mode of $Ce_1 = 0$. $f = 1.5154326\times10^7$ Hz. (d) 2nd mode of $Se_2 = 0$. $f = 1.5202202\times10^7$ Hz.

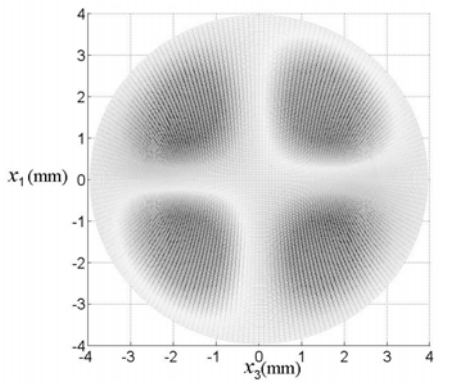

(b)

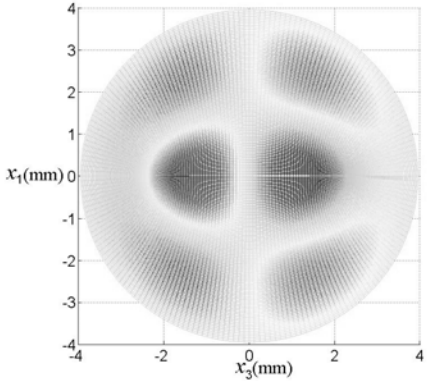

(c)

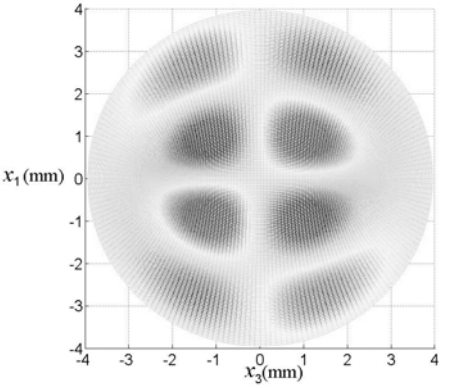

(d)

Fig. 8.6. (*Continued*)

8.5. Unbounded Plate with Parabolic Contour

When the plate thickness $2h$ in Eq. (8.6) depends on x_1 and x_3 slowly, Eq. (8.6) can describe contoured resonators with nonuniform thickness (see Fig. 7.7). In Cartesian coordinates, the scalar equation for an unbounded resonator with a parabolic contour can be solved in a way similar to Section 7.5 [85].

8.5.1. Governing equation and solution

We write Eq. (8.6) as

$$M_n \frac{\partial^2 u_1^{n_y}}{\partial x^2} + c_{55} \frac{\partial^2 u_1^{n_y}}{\partial z^2} - \frac{n_y^2 \pi^2}{4h^2} \bar{c}_{66} u_1^{n_y} - \rho \ddot{u}_1^{n_y} = 0, \tag{8.54}$$

where n_y is the n in Eq. (8.6). Let the resonator thickness be

$$2h = 2h_0[1 - f'(x) - g'(z)], \quad f'(x) = \gamma x^2, \quad g'(z) = \zeta z^2, \tag{8.55}$$

where γ and ζ are two small parameters. f' and g' are two small functions. For small f' and g',

$$\frac{1}{(2h)^2} \cong \frac{1}{(2h_0)^2}\left(1 + 2f' + 2g'\right). \tag{8.56}$$

We look for solutions with separated variables:

$$u_1^{n_y}(x, z) = E(x)G(z). \tag{8.57}$$

Substituting Eqs. (8.56) and (8.57) into Eq. (8.54), for harmonic motions, we obtain

$$M_n \frac{d^2 E}{dx^2}\frac{1}{E} + c_{55} \frac{d^2 G}{dz^2}\frac{1}{G} + \rho\omega^2 - \bar{c}_{66} \frac{n_y^2 \pi^2}{4h_0^2}\left(1 + 2\gamma x^2 + 2\zeta z^2\right) = 0. \tag{8.58}$$

From the standard argument in the method of separation of variables for partial differential equations, we have

$$M_n \frac{d^2E}{dx^2} + (\rho\omega_1^2 - \frac{\overline{c}_{66} n_y^2 \pi^2 \gamma}{2h_0^2} x^2)E = 0, \tag{8.59}$$

$$c_{55} \frac{d^2G}{dz^2} + (\rho\omega_3^2 - \frac{\overline{c}_{66} n_y^2 \pi^2 \zeta}{2h_0^2} z^2)G = 0, \tag{8.60}$$

$$\omega^2 = \frac{\overline{c}_{66}}{\rho} \frac{n_y^2 \pi^2}{4h_0^2} + \omega_1^2 + \omega_3^2, \tag{8.61}$$

where ω_1^2 and ω_3^2 are separation constants. Equations (8.59) and (8.60) have the same mathematical structure. We solve Eq. (8.59) in the following. The solution to Eq. (8.60) is similar. Introduce the following change of variable:

$$x = m_x X. \tag{8.62}$$

Then Eq. (8.59) is transformed into

$$\frac{d^2E(X)}{dX^2} + (\lambda_x - X^2)E(X) = 0, \tag{8.63}$$

where

$$m_x = \left(\frac{2h_0^2 M_n}{\gamma \overline{c}_{66} n_y^2 \pi^2} \right)^{1/4}, \quad \lambda_x = \frac{\rho\omega_1^2 m_x^2}{M_n}. \tag{8.64}$$

Equation (8.63) is the well-known Weber's equation. Let

$$E(X) = B_x \exp(-X^2/2) H(X), \tag{8.65}$$

where B_x is an undetermined constant. Equation (8.63) becomes

$$\frac{d^2H(X)}{dX^2} - 2X \frac{dH(X)}{dX} + (\lambda_x - 1)H(X) = 0. \tag{8.66}$$

For odd integers of λ_x, the solutions of Eq. (8.66) are the Hermite polynomials, i.e.,

$$\lambda_x = 2n_x + 1, \; H(X) = H_{n_x}(X), \; n_x = 0,1,2,3,\cdots, \tag{8.67}$$

where

$$H_0(X)=1,\quad H_1(X)=2X,$$
$$H_2(X)=4X^2-2,\quad H_3(X)=8X^3-12X,\quad \cdots. \tag{8.68}$$

Similarly, in the z direction,

$$z=m_z Z\ ,\quad m_z=\left(\frac{2h_0^2 c_{55}}{\zeta \overline{c}_{66} n_y^2 \pi^2}\right)^{1/4}\ ,\quad \lambda_z=\frac{\rho\omega_1^2 m_z^2}{c_{55}}\ , \tag{8.69}$$

$$G(Z)=B_z \exp(-Z^2/2)H(Z)\,, \tag{8.70}$$

$$\frac{d^2H(Z)}{dZ^2}-2Z\frac{dH(Z)}{dZ}+(\lambda_z-1)H(Z)=0\,, \tag{8.71}$$

$$\lambda_z=2n_z+1\,,\ H(Z)=H_{n_z}(Z)\,,\ \ n_z=0,1,2,3,\cdots. \tag{8.72}$$

Then the frequency can be obtained from Eq. (8.61) as

$$\omega^2=\frac{\overline{c}_{66}}{\rho}\frac{n_y^2\pi^2}{4h_0^2}+\frac{\lambda_x M_n}{\rho m_x^2}+\frac{\lambda_z c_{55}}{\rho m_z^2}\,. \tag{8.73}$$

8.5.2. Numerical result

Consider the two resonators shown in Fig. 8.7. Resonator 1 has a contour determined by $\gamma=\zeta=14252$ m^{-2}. The contour of Resonator 2 is given by $\gamma=\zeta=22166$ m^{-2}. The two resonators have the same thickness at the center.

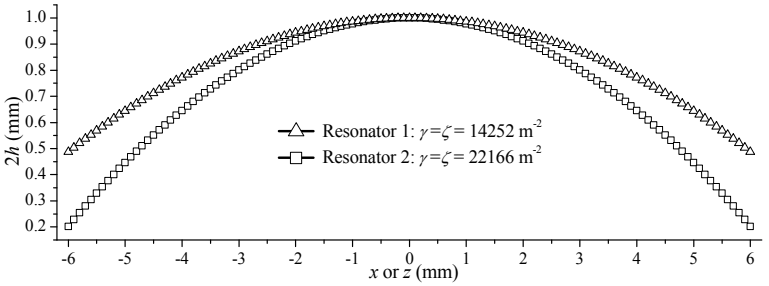

Fig. 8.7. Thickness variation of the two resonators.

Figure 8.8 shows the comparison of two modes of the two resonators along x. Since Resonator 2 is thinner than resonator 1, Resonator 2 has stronger energy trapping and higher frequencies.

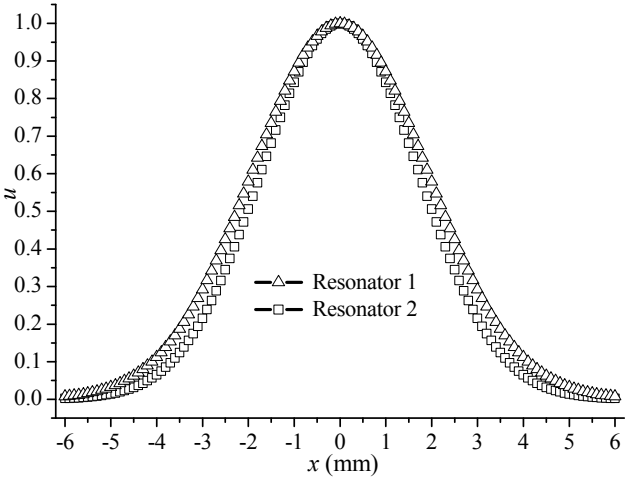

(a)

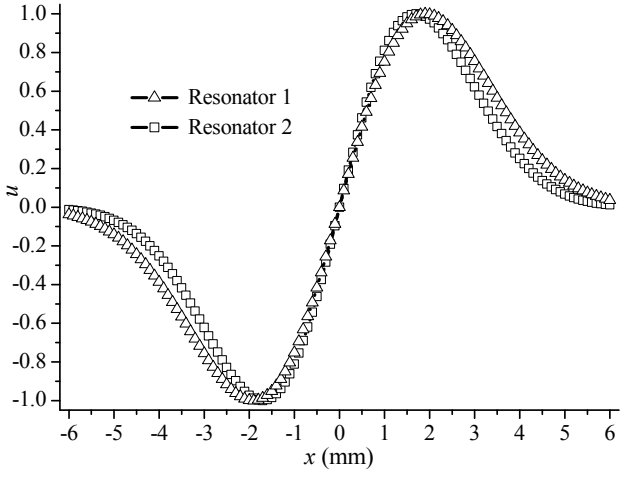

(b)

Fig. 8.8. Distribution of $u(x, 0)$ ($n_z = 0$). (a) The first mode (ω = 11.3694 MHz, 11.5882 MHz). (b) The second mode (ω = 12.3275 MHz, 12.7516 MHz).

Figure 8.9 shows the frequency dependence on n_x or n_z, respectively. Resonator 2 is thinner and therefore has higher frequencies. The frequency difference between the two resonators is much more sensitive to n_x than n_z.

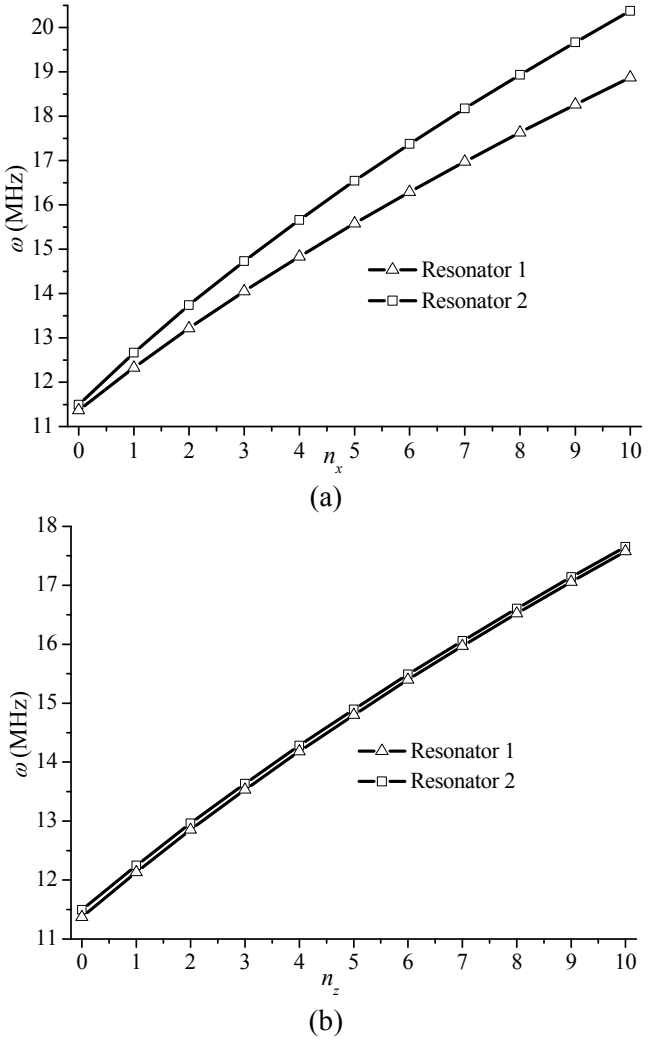

Fig. 8.9. Frequencies of the two resonators. (a) Dependence on n_x (n_z = 0). (b) Dependence on n_z (n_x = 0).

8.6. Unbounded Plate with Hyperbolic Contour

The contoured resonators analyzed in Sections 7.5 and 8.5 have a quadratic thickness variation. Far away from the resonator center, a quadratically varying thickness may become zero or even negative. This usually does not present a problem for a well-designed resonator because the modes are supposed to be trapped near the center and die out quickly away from the center. However, as resonators are made smaller and smaller, the behavior of the modes near the resonator edge becomes more important. It is desirable to have solutions for contoured resonators with other thickness variations. Analyzing contoured resonators using the scalar differential equation given in Eq. (8.6) requires solving equations with variable coefficients. Exact solutions can be obtained in special cases only. In this section we present another solution of the scalar equation for a resonator with a hyperbolic thickness variation [92] which does not lead to a zero or negative thickness far way from the resonator center.

8.6.1. Governing equation

From Eq. (8.6),

$$M_n \frac{\partial^2 u_1^n}{\partial x^2} + c_{55} \frac{\partial^2 u_1^n}{\partial z^2} - \frac{n_y^2 \pi^2}{4h^2} \overline{c}_{66} u_1^n - \rho \ddot{u}_1^n = 0 . \tag{8.74}$$

Consider a resonator with the following hyperbolic contour:

$$\begin{aligned} &2h = 2h_0[1 - f(x) - g(z)], \\ &f(x) = \alpha\left(1 - \frac{1}{\cosh^2 \xi x}\right), \quad g(z) = \beta\left(1 - \frac{1}{\cosh^2 \eta z}\right), \end{aligned} \tag{8.75}$$

where α, β, ξ and η are parameters. α and β are assumed to be small. Note that $f(0) = 0$, $g(0) = 0$, $f(\infty) = \alpha$, and $g(\infty) = \beta$. When β = 0, for different values of α and ξ, $2h$ as a function of x is shown in Fig. 8.10 (a) and (b), respectively. By adjusting the values of these parameters, Eq. (8.75) can describe resonators with different contours. A larger α or a larger ξ represents a more rapidly changing contour.

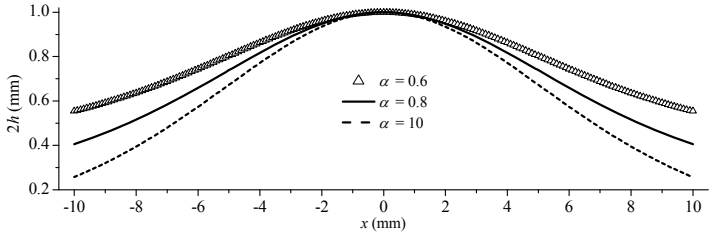

(a)

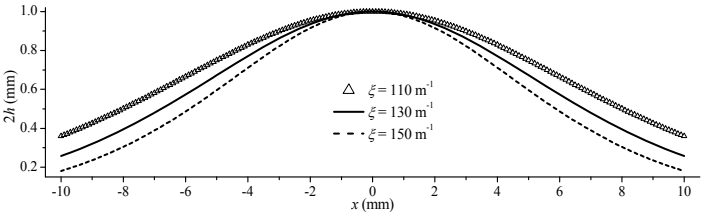

(b)

Fig. 8.10. (a) Effect of α on resonator contour. ξ = 130 m^{-1}. β = 0. (b) Effect of ξ on resonator contour. $\alpha = 1$. $\beta = 0$.

Near the resonator center where x and z are small, f or g can be expanded into power series of x or z in which the two leading terms are a constant and a quadratic term, resulting in a parabolic contour. These expansions are not necessary and will not be made. For small f and g, we have, approximately,

$$(2h)^2 \cong (2h_0)^2 \left(1 - 2f - 2g\right), \tag{8.76}$$

$$\frac{1}{(2h)^2} \cong \frac{1}{(2h_0)^2}\left(1 + 2f + 2g\right). \tag{8.77}$$

Substituting Eq. (8.77) into Eq. (8.74), we obtain, for time-harmonic motion with a frequency ω,

$$\begin{aligned} &M_n \frac{\partial^2 u_1^n}{\partial x^2} + c_{55} \frac{\partial^2 u_1^n}{\partial z^2} + \rho\omega^2 u_1^n \\ &- \overline{c}_{66} \frac{n^2\pi^2}{4h_0^2}\left(1 + 2\alpha + 2\beta - \frac{2\alpha}{\cosh^2 \xi x} - \frac{2\beta}{\cosh^2 \eta z}\right) u_1^n = 0, \end{aligned} \tag{8.78}$$

which has variable coefficients.

8.6.2. Analytical solution

As a partial differential equation, Eq. (8.78) is separable. Let

$$u_1^n(x,z) = E(x)G(z)\,. \tag{8.79}$$

Substitution of Eq. (8.79) into Eq. (8.78) gives

$$\begin{aligned} &M_n \frac{\partial^2 E}{\partial x^2}\frac{1}{E} + c_{55}\frac{\partial^2 G}{\partial z^2}\frac{1}{G} + \rho\omega^2 \\ &\quad - \bar{c}_{66}\frac{n^2\pi^2}{4h_0^2}\left(1 + 2\alpha + 2\beta - \frac{2\alpha}{\cosh^2 \xi x} - \frac{2\beta}{\cosh^2 \eta z}\right) = 0. \end{aligned} \tag{8.80}$$

Following the standard argument in the method of separation of variables of partial differential equations, we obtain, from Eq. (8.80), the following three equations:

$$M_n \frac{\partial^2 E}{\partial x^2}\frac{1}{E} + \bar{c}_{66}\frac{n^2\pi^2}{4h_0^2}\frac{2\alpha}{\cosh^2 \xi x} = \rho\omega_1^2\,, \tag{8.81}$$

$$c_{55}\frac{\partial^2 G}{\partial z^2}\frac{1}{G} + \bar{c}_{66}\frac{n^2\pi^2}{4h_0^2}\frac{2\beta}{\cosh^2 \eta z} = \rho\omega_3^2\,, \tag{8.82}$$

$$\omega^2 = \frac{\bar{c}_{66}}{\rho}\frac{n^2\pi^2}{4h_0^2}(1 + 2\alpha + 2\beta) - \omega_1^2 - \omega_3^2\,, \tag{8.83}$$

where ω_1 and ω_3 are separation constants. Equations (8.81) and (8.82) are ordinary differential equations. They can be further written as

$$M_n \frac{\partial^2 E}{\partial x^2} + \left(-\rho\omega_1^2 + \bar{c}_{66}\frac{n^2\pi^2}{4h_0^2}\frac{2\alpha}{\cosh^2 \xi x}\right)E = 0\,, \tag{8.84}$$

$$c_{55}\frac{\partial^2 G}{\partial z^2} + \left(-\rho\omega_3^2 + \bar{c}_{66}\frac{n^2\pi^2}{4h_0^2}\frac{2\beta}{\cosh^2 \eta z}\right)G = 0\,. \tag{8.85}$$

Equations (8.84) and (8.85) have the same structure. We provide a detailed solution to Eq. (8.84) in the following. For Eq. (8.85) the solution is similar.

For Eq. (8.84), introduce a new spatial variable X through

$$X = \tanh(\xi x). \tag{8.86}$$

Then Eq. (8.84) becomes the well-known Legendre equation:

$$\frac{d}{dX}\left[(1-X^2)\frac{dE}{dX}\right] + \left[q_x(q_x+1) - \frac{p_x}{1-X^2}\right]E = 0, \tag{8.87}$$

where we have denoted

$$U_0 = \alpha\frac{\overline{c}_{66}n^2\pi^2}{2h_0^2}, \quad p_x = \frac{1}{\xi}\sqrt{\frac{\rho\omega_1^2}{M_n}}, \quad q_x = \frac{1}{2}\left(-1+\sqrt{\frac{4U_0}{\xi^2 M_n}}\right). \tag{8.88}$$

We also introduce a new function H which is related to E by

$$E = (1-X^2)^{p_x/2}H(X). \tag{8.89}$$

With Eq. (8.89), we can write Eq. (8.87) into the hypergeometric equation:

$$J(1-J)\frac{d^2H}{dX^2} + (p_x+1)(1-2J)\frac{dH}{dX} - (p_x-q_x)(p_x+q_x+1)H = 0, \tag{8.90}$$

where

$$J(X)=(1-X)/2. \tag{8.91}$$

The solution to Eq. (8.90) finite at $X = 1$ or $x = \infty$ is

$$E = A(1-X^2)^{p_x/2}F\left[p_x - q_x, p_x + q_x + 1, p_x + 1, (1-X)/2\right], \tag{8.92}$$

where A is an undetermined constant. F is the hypergeometric function. For E to remain finite at $X = -1$ or $x = -\infty$, we must have

$$p_x - q_x = -n_x, \quad n_x = 0,1,2,\cdots. \tag{8.93}$$

In this case E is a polynomial of degree n_x. Equation (8.93) determines, through Eq. (8.88), that

$$\omega_1 = 2\xi\sqrt{\frac{M_n}{\rho}}\left[-(1+2n_x)+\sqrt{1+\frac{4U_0}{\xi^2 M_n}}\right]. \tag{8.94}$$

A finite number of ω_1 can be determined by the condition that $p_x > 0$ or $n_x < q_x$.

Similarly, for Eq. (8.85), we have

$$Z = \tanh(\xi z), \tag{8.95}$$

$$W_0 = \beta\frac{\bar{c}_{66}n^2\pi^2}{2h_0^2}, \quad p_z = \frac{1}{\eta}\sqrt{\frac{\rho\omega_3^2}{c_{55}}}, \quad q_z = \frac{1}{2}\left(-1+\sqrt{\frac{4W_0}{\eta^2 c_{55}}}\right), \tag{8.96}$$

$$G = B(1-Z^2)^{p_z/2}F\left[p_z - q_z, p_z + q_z + 1, p_z + 1, (1-Z)/2\right], \tag{8.97}$$

$$p_z - q_z = -n_z, \quad n_z = 0,1,2,\cdots, \tag{8.98}$$

$$\omega_3 = 2\eta\sqrt{\frac{c_{55}}{\rho}}\left[-(1+2n_z)+\sqrt{1+\frac{4W_0}{\eta^2 c_{55}}}\right], \tag{8.99}$$

where B is an undetermined constant. Substitution of Eqs. (8.94) and (8.99) into Eq. (8.83) determines the resonant frequencies.

8.6.3. Numerical result

As a numerical example, consider an AT-cut quartz resonator with $2h_0 = 1$ mm. We are interested in the fundamental mode with $n = 1$. In

Fig. 8.11 we show the first four modes in the order of increasing frequency. The first and the third modes are symmetric. The second and the fourth are antisymmetric and vanish at the center. The four modes shown all decay near the resonator edge (energy trapping). Since an AT-cut quartz resonator is anisotropic in the *x*-*z* plane, the decay rates of the modes in the *x* and *z* directions are different, faster in the *z* direction. Higher-order modes seem to decay more slowly near the edge.

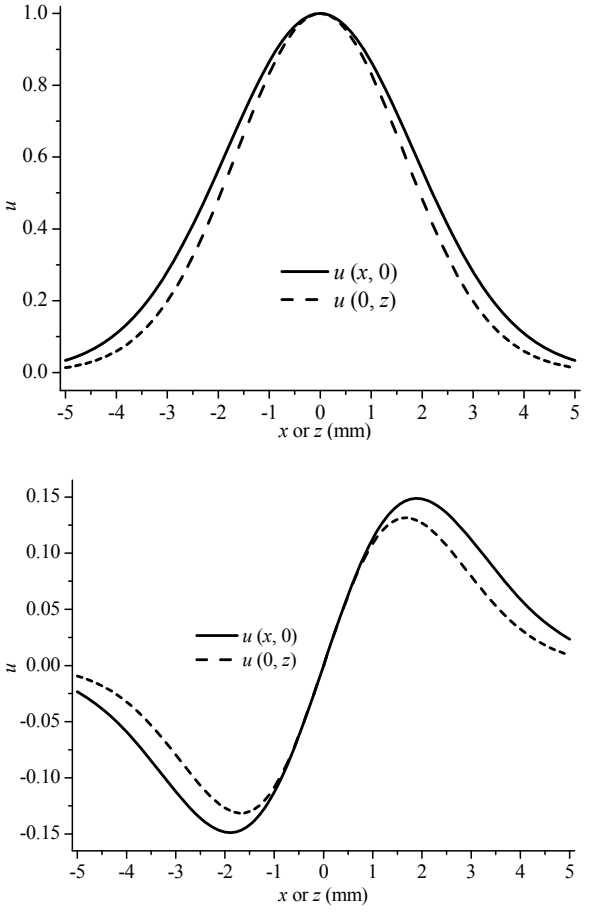

Fig. 8.11. The first four modes. $\alpha = \beta = 1$. $\xi = \eta = 130$ m^{-1}.

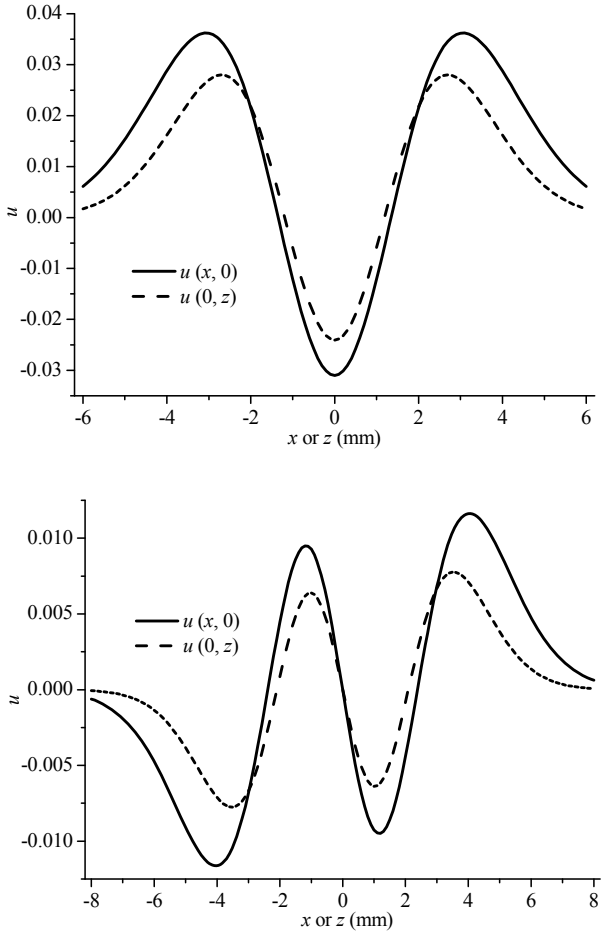

Fig. 8.11. (*Continued*)

Figure 8.12 shows the effects of the contour parameters on the first mode. The mode shapes are sensitive to the parameters. A larger α or a larger ξ with a more rapidly varying contour leads to stronger energy trapping and higher frequencies as expected.

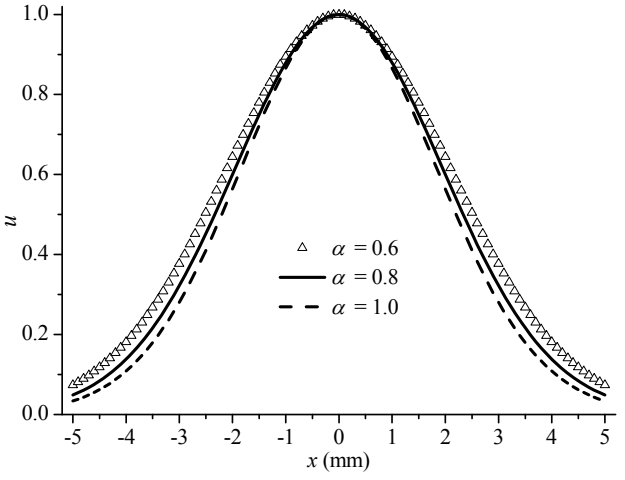

(a)

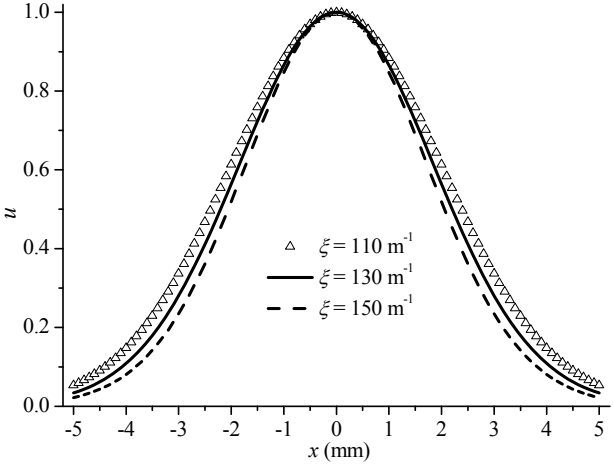

(b)

Fig. 8.12. (a) Effect of α on the first mode. $\xi = 130$ m^{-1}. (b) Effect of ξ on the first mode. $\alpha = 1$.

8.7. Elliptical Plate with Parabolic Contour

Because of the in-plane anisotropy of AT-cut quartz resonators, the scalar differential equation in Eq. (8.6) is not separable in polar coordinates. This makes it difficult to obtain solutions for circular resonators. However, as seen in Section 8.3, solutions for elliptical resonators with a particular ratio between the semi-major and semi-minor axes can be obtained relatively easily. In this section we generalize the result of Section 8.3 to contoured elliptical resonators with nonuniform thickness [93].

8.7.1. Governing equation and solution

Consider a resonator with nonuniform thickness as shown in Fig. 7.7. From Eq. (8.6),

$$M_n \frac{\partial^2 u_1^n}{\partial x_1^2} + c_{55} \frac{\partial^2 u_1^n}{\partial x_3^2} - \frac{n^2 \pi^2}{4h^2} \bar{c}_{66} u_1^n - \rho \ddot{u}_1^n = 0 . \tag{8.100}$$

Specifically, let the plate thickness variation be:

$$2h = 2h_0 \left(1 - \alpha x_1^2 - \beta x_3^2\right). \tag{8.101}$$

In Eq. (8.101), the resonator thickness is allowed to vary differently in the x_1 and x_3 directions. α and β are related to the principal curvatures of the contour. We consider small and slowly varying contours such that the second and the third terms in the parentheses in Eq. (8.101) are much smaller than one. We have, approximately,

$$(2h)^2 \cong (2h_0)^2 \left(1 - 2\alpha x_1^2 - 2\beta x_3^2\right), \tag{8.102}$$

$$\frac{1}{(2h)^2} \cong \frac{1}{(2h_0)^2} \left(1 + 2\alpha x_1^2 + 2\beta x_3^2\right). \tag{8.103}$$

Substituting Eq. (8.103) into Eq. (8.100), for time-harmonic free vibrations with an unknown frequency ω, we obtain

$$\frac{M_n}{\rho}\frac{\partial^2 u_1^n}{\partial x_1^2}+\frac{c_{55}}{\rho}\frac{\partial^2 u_1^n}{\partial x_3^2}-\omega_0^2\left(1+2\alpha x_1^2+2\beta x_3^2\right)u_1^n+\omega^2 u_1^n=0, \quad (8.104)$$

where we have denoted

$$\omega_0^2=\frac{n^2\pi^2\overline{c}_{66}}{(2h_0)^2\rho}. \quad (8.105)$$

Consider a special class of elliptical resonators in the (x_1, x_3) plane. Their exact shape and size will be specified later. These elliptical resonators become circular in the transformed (ξ_1, ξ_3) plane defined by:

$$x_1=\lambda\xi_1, \quad x_3=\mu\xi_3, \quad (8.106)$$

where λ and μ are undetermined parameters. Under Eq. (8.106), the scalar equation in Eq. (8.104) becomes

$$\begin{aligned}&\frac{M_n}{\rho}\frac{\partial^2 u_1^n}{\lambda^2\partial\xi_1^2}+\frac{c_{55}}{\rho}\frac{\partial^2 u_1^n}{\mu^2\partial\xi_3^2}\\&\quad-\omega_0^2(1+2\alpha\lambda^2\xi_1^2+2\beta\mu^2\xi_3^2)u_1^n+\omega^2 u_1^n=0.\end{aligned} \quad (8.107)$$

We choose λ, μ, α and β such that they satisfy

$$\frac{M_n}{\lambda^2}=\frac{c_{55}}{\mu^2}, \quad \alpha\lambda^2=\beta\mu^2, \quad (8.108)$$

so that Eq. (8.107) becomes effectively isotropic. Equation (8.108) determines the following ratios

$$\frac{\lambda}{\mu}=\sqrt{\frac{M_n}{c_{55}}}, \quad \frac{\alpha}{\beta}=\frac{\mu^2}{\lambda^2}=\frac{c_{55}}{M_n}. \quad (8.109)$$

Equation (8.109) defines two relationships with which λ, μ, α and β are still not unique. We choose

$$\lambda = \frac{1}{\omega_0}\sqrt{\frac{M_n}{\rho}}, \quad \mu = \frac{1}{\omega_0}\sqrt{\frac{c_{55}}{\rho}}, \qquad \alpha = \varepsilon\rho c_{55}\omega_0^2, \quad \beta = \varepsilon\rho M_n\omega_0^2, \tag{8.110}$$

so that Eq. (8.109) is satisfied. λ and μ have the dimension of length. Therefore ξ_1 and ξ_3 are dimensionless. Equation (8.110) determines the ratio between the semi-major and semi-minor axes of the elliptical resonator, and the ratio between the principal curvatures of the contour. ε is a small and arbitrary parameter. Using Eq. (8.110), we can write Eq. (8.107) as

$$\frac{\partial^2 u_1^n}{\partial \xi_1^2} + \frac{\partial^2 u_1^n}{\partial \xi_3^2} - \left(1 + 2\varepsilon c_{55} M_n \xi_1^2 + 2\varepsilon M_n c_{55} \xi_3^2\right) u_1^n + \frac{\omega^2}{\omega_0^2} u_1^n = 0, \tag{8.111}$$

which allows us to introduce the Laplacian operator

$$\nabla^2 = \frac{\partial^2}{\partial \xi_1^2} + \frac{\partial^2}{\partial \xi_3^2}, \quad \bar{\varepsilon} = 2\varepsilon c_{55} M_n, \quad \frac{\omega^2}{\omega_0^2} - 1 = \delta^2. \tag{8.112}$$

Then Eq. (8.111) can be written as

$$\nabla^2 u_1^n + \delta^2 u_1^n - \bar{\varepsilon}(\xi_1^2 + \xi_3^2) u_1^n = 0. \tag{8.113}$$

In polar coordinates defined by

$$\xi_3 = r\cos\theta, \quad \xi_1 = r\sin\theta, \tag{8.114}$$

Eq. (8.113) takes the following form:

$$\frac{\partial^2 u_1^n}{\partial r^2} + \frac{1}{r}\frac{\partial u_1^n}{\partial r} + \frac{1}{r^2}\frac{\partial^2 u_1^n}{\partial \theta^2} + \delta^2 u_1^n - \bar{\varepsilon} r^2 u_1^n = 0. \tag{8.115}$$

Let

$$u_1^n(r,\theta) = \begin{cases} u_1^n(r)\cos m\theta, \\ u_1^n(r)\sin m\theta, \end{cases} \tag{8.116}$$

where m = 0, 1, 2, …. Substitution of Eq. (8.116) into Eq. (8.115) gives the following ordinary differential equation for $u_1^n(r)$:

$$\frac{d^2u_1^n}{dr^2} + \frac{1}{r}\frac{du_1^n}{dr} + \delta^2 u_1^n - \frac{m^2}{r^2}u_1^n - \bar{\varepsilon} r^2 u_1^n = 0 . \tag{8.117}$$

The frequencies we are interested in satisfy $\delta^2 > 0$. We introduce another coordinate transformation from r to R:

$$R = \delta r . \tag{8.118}$$

Then Eq. (8.117) becomes

$$\frac{d^2u_1^n}{dR^2} + \frac{1}{R}\frac{du_1^n}{dR} + \left(1 - \frac{m^2}{R^2}\right)u_1^n = \bar{\varepsilon}\delta^{-4} R^2 u_1^n . \tag{8.119}$$

Equation (8.119) differs from the Bessel equation of order m by the $\bar{\varepsilon}$ term on the right-hand side. It can be solved by the well-known Frobenius method for power series solutions of ordinary differential equations. Let

$$u_1^n = \sum_{k=0}^{\infty} a_k R^{k+s} , \tag{8.120}$$

where a_k and s are to be determined. Substituting of Eq. (8.120) into Eq. (8.119), collecting coefficients of terms of like powers of R, we have

$$s = \pm m , \tag{8.121}$$

$$\begin{aligned} &a_0 = 1, \quad a_1 = 0, \\ &a_2 = -\frac{1}{4+4m}a_0, \quad a_3 = 0, \end{aligned} \tag{8.122}$$

$$a_k = \frac{\bar{\varepsilon}\delta^{-4} a_{k-4} - a_{k-2}}{k^2 + 2mk}, \quad (k \geq 4), \tag{8.123}$$

$s = -m$ determines a function that is singular at the resonator center and therefore it has to be discarded. $s = m$ determines a function which is denoted by $\tilde{J}_m(R)$. The form of the recurrence relation in Eq. (8.123) indicates that a_k has a factorial-type dependence on k^2. This suggests fast convergence like what happens in the power series of Bessel functions. With $\tilde{J}_m(R)$, the general solution of Eq. (8.119) bounded at the origin can be written as

$$u_1^n = C\tilde{J}_m(R) = C\tilde{J}_m(\delta r), \tag{8.124}$$

where C is an arbitrary constant. Let the boundary of a circular resonator in the (ξ_1, ξ_3) plane or the related polar coordinate system be $r = r_0$, the boundary condition for a free resonator is, approximately,

$$u_1^n = C\tilde{J}_m(\delta r_0) = 0. \tag{8.125}$$

Equation (8.125) is the frequency equation to be solved for free vibration frequencies. Denoting the pth root of $\tilde{J}_m(R) = 0$ by R_{mp}, we can write

$$\delta_{mp} r_0 = R_{mp}. \tag{8.126}$$

Then, from Eq. (8.112), we have

$$\omega_{nmp}^2 = \omega_0^2(1 + \delta_{mp}^2) = \frac{n^2\pi^2\bar{c}_{66}}{(2h_0)^2\rho}\left(1 + \frac{R_{mp}^2}{r_0^2}\right). \tag{8.127}$$

The corresponding modes are

$$u_{1mp}^n = C\tilde{J}_m(R_{mp}\frac{r}{r_0})\begin{Bmatrix}\cos m\theta \\ \sin m\theta\end{Bmatrix}. \tag{8.128}$$

8.7.2. Numerical result

Consider an AT-cut quartz resonator operating with the fundamental mode (n = 1). For AT-cut quartz, we have $c_{55} = 0.6881 \times 10^{11}$ Pa, and $M_1 = 1.099505 \times 10^{11}$ Pa. In this case $\sqrt{M_1 / c_{55}} = 1.2641$. The semi-major axis exceeds the semi-minor axis by about 26%. Let the resonator center thickness be $2h_0$ = 1 mm. Then we have $\omega_0 = 1.043684 \times 10^7$ 1/s, $\lambda = 0.6172888$ mm, and $\mu = 0.4883326$ mm. With these values of λ and μ, Eq. (8.106) transforms a circular resonator with a dimensionless radius of r_0 = 20 in the (ξ_1, ξ_3) plane to an elliptical resonator with a semi-major axis of 12.34578 mm along x_1 and a semi-minor axis of 9.766652 mm along x_3. We also need to choose a value of ε. This is done by specifying the edge thickness $h(r_0)$ of the resonator.

The numerical procedure for searching the resonant frequencies goes like follows. For a given m, we begin with a trial value of $\omega > \omega_0$ with which δ becomes known. Then $\tilde{J}_m(\delta r_0)$ can be calculated by summing the series in Eq. (8.120). If $\tilde{J}_m(\delta r_0) = 0$, then ω is a root of Eq. (8.125) or a resonant frequency. If $\tilde{J}_m(\delta r_0) \neq 0$, we try another value of ω and repeat the above procedure until a root is found, and then proceed to find the next root. In the numerical calculation, one hundred and twenty terms are used in the series to ensure twelve significant figures in the frequency solution.

When n = 1 and m = 0, Fig. 8.13 shows the first three trapped modes for different values of ε which determine different ratios of $h(r_0)/h_0$. The vibration is confined to the central portion of the plate (energy trapping). The three modes have an increasing number of nodal points (zeros) in the radial direction. Higher-order modes are less trapped. A larger ε represents a more drastic change of the thickness of the resonator and hence stronger energy trapping. A larger ε also leads to thinner plate edges and therefore higher frequencies.

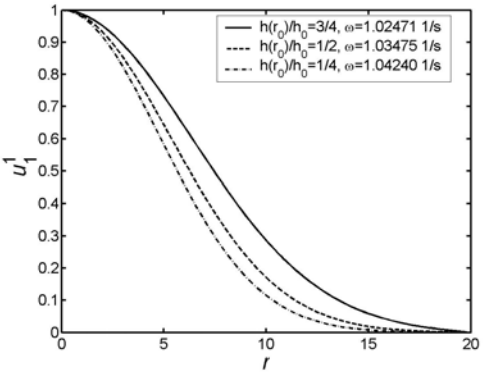

(a)

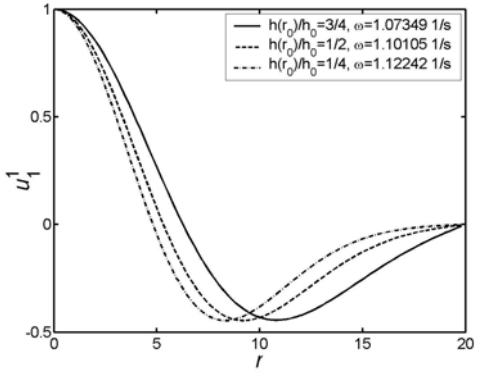

(b)

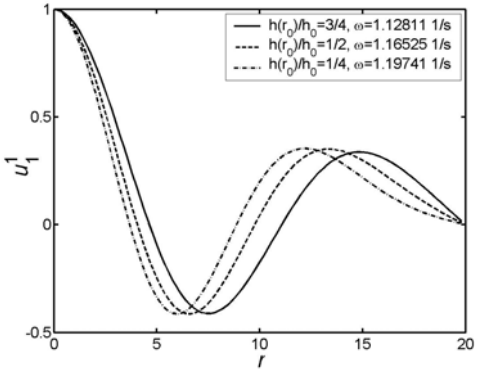

(c)

Fig. 8.13. Radial distribution of the first three trapped modes and the effect of ε when $n = 1$ and $m = 0$. (a) $p = 1$. (b) $p = 2$. (c) $p = 3$.

To see the modes in Fig. 8.13 more visually, we plot the first three modes when $n = 1$, $m = 0$, and $h(r_0)/h_0 = ½$ in Fig. 8.14 by three-dimensional figures. In the figure, the amplitude of the modes represents the magnitude of the thickness-shear deformation. These modes have no angular or θ dependence in polar coordinates. They have roughly circular nodal lines only where the shear deformation vanishes.

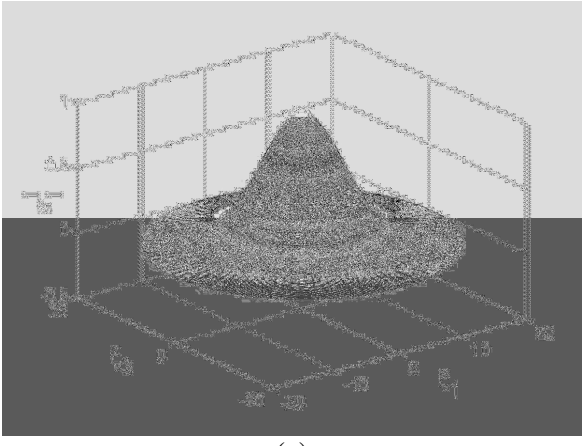

(a)

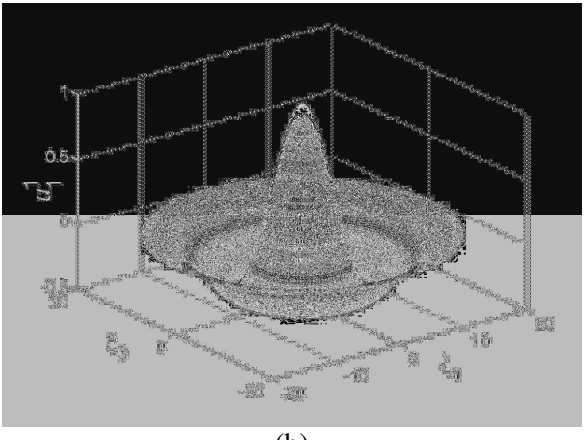

(b)

Fig. 8.14. Three-dimensional views of the first three trapped modes when $n = 1$ and $m = 0$. $h(r_0)/h_0 = ½$. (a) $p = 1$. $\omega = 1.034752$ 1/s. (b) $p = 2$. $\omega = 1.101053$ 1/s. (c) $p = 3$. $\omega = 1.165248$ 1/s.

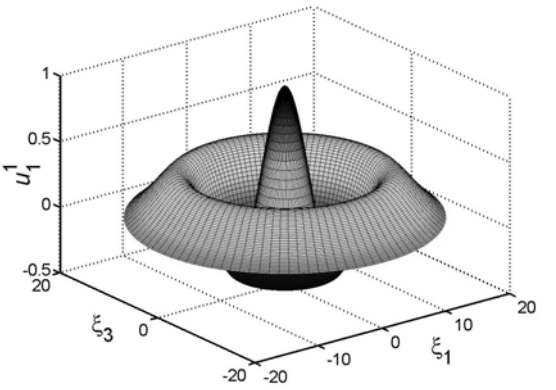

(c)

Fig. 8.14. (*Continued*)

Similar modes when m = 1 and 2 are plotted in Figs. 8.15 and 8.16, respectively. These modes have both radial and angular dependence. Because of the complicated nodal curves in these modes, they are not used very often in devices.

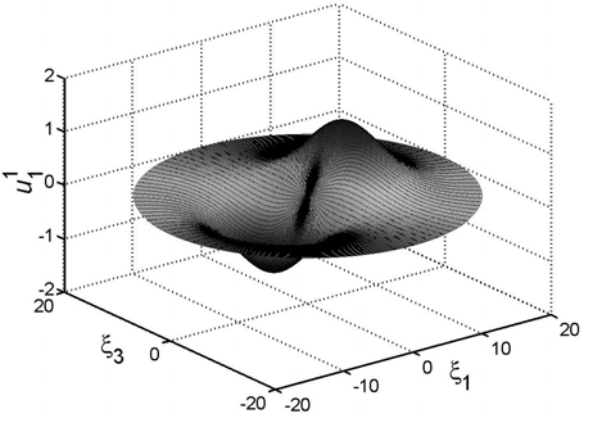

(a)

Fig. 8.15. Three-dimensional views of the first three trapped modes when n = 1 and m = 1. $h(r_0)/h_0$ = ½. (a) p = 1. ω = 1.068381 1/s. (b) p = 2. ω = 1.133062 1/s. (c) p = 3. ω = 1.198474 1/s.

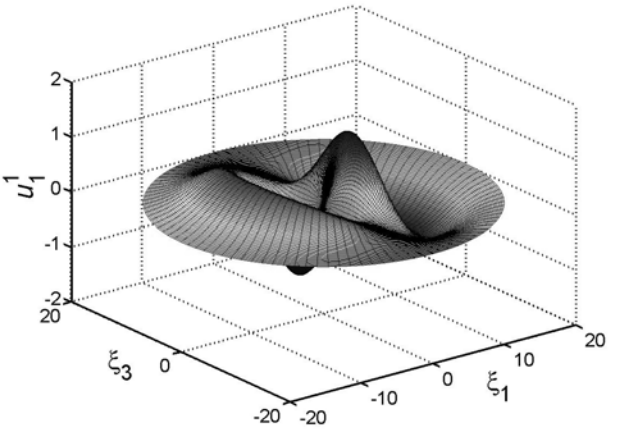

(b)

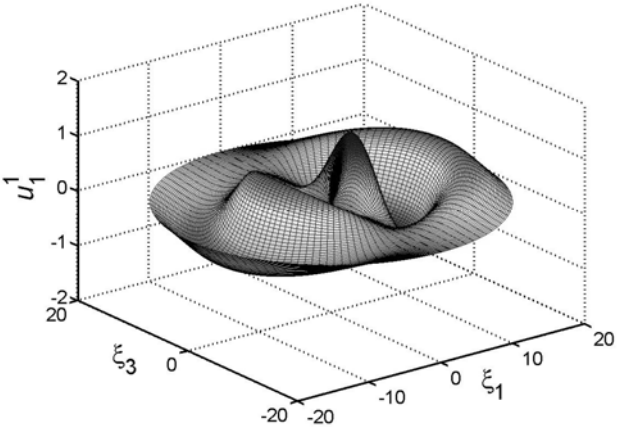

(c)

Fig. 8.15. (*Continued*)

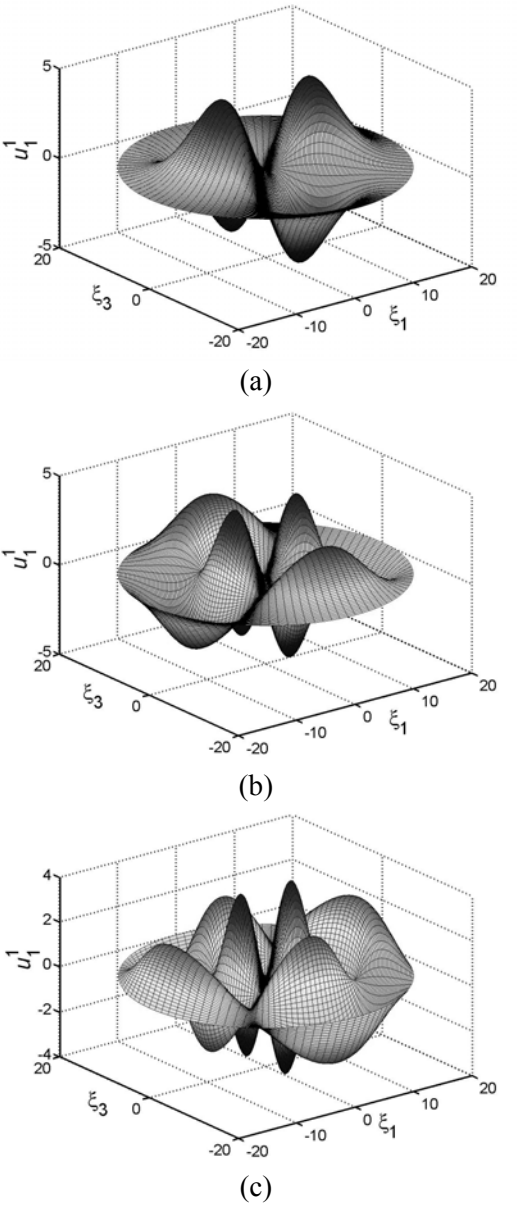

Fig. 8.16. Three-dimensional views of the first three trapped modes when n = 1 and m = 2. $h(r_0)/h_0$ = ½. (a) p = 1. ω = 1.101019 1/s. (b) p = 2. ω = 1.164882 1/s. (c) p = 3. ω = 1.233355 1/s.

8.8. Scalar Equation for SC-cut Quartz Plates

Doubly-rotated quartz plates, e.g., the well-known SC-cut (stress compensated cut) plates, are often used to make crystal resonators. Doubly-rotated crystal plates typically exhibit general material anisotropy (triclinic). The situation is much more complicated than AT-cut quartz plates which are singly-rotated and are effectively monoclinic in the plate coordinate system. Similar to Eqs. (8.6) and (8.13) which are for AT-cut quartz plates, two-dimensional equations for slowly varying thickness-shear modes in doubly-rotated, unelectroded and electroded plates were derived in [94]. We begin this section with pure thickness waves in doubly-rotated plates, followed by slowly varying thickness modes in unelectroded and electroded plates.

8.8.1. Pure thickness waves

Consider a doubly rotated quartz plate (see Fig. 8.17). The coordinate axes are so oriented with x_2 normal to the surfaces of the plate, which are at $x_2 = \pm h$, and x_1 directed along the axis of the second rotation (see Fig. 1.5).

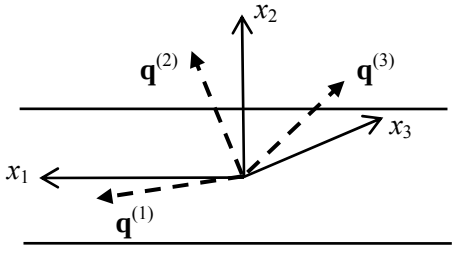

Fig. 8.17. A doubly rotated plate and the eigenvectors of thickness modes.

Let the elastic, piezoelectric, and dielectric constants in the plate coordinate system x_i be $\hat{c}_{ijkl}$, $\hat{e}_{ijk}$, and ε_{ij}. The displacement vector in the x_i system is denoted by $\hat{u}_i$. The equations of motion and electrostatics take the following form:

$$\begin{aligned} &\hat{c}_{mnrs}\hat{u}_{r,sm} + \hat{e}_{rmn}\phi_{,rm} = \rho\ddot{\hat{u}}_n, \\ &\hat{e}_{mrs}\hat{u}_{r,sm} - \varepsilon_{mn}\phi_{,mn} = 0. \end{aligned} \tag{8.129}$$

For pure thickness modes depending on x_2 and t only, Eq. (8.129) becomes

$$\begin{aligned} &\hat{c}_{2nr2}\hat{u}_{r,22} + \hat{e}_{22n}\phi_{,22} = \rho\ddot{\hat{u}}_n, \\ &\hat{e}_{2r2}\hat{u}_{r,22,} - \varepsilon_{22}\phi_{,22} = 0. \end{aligned} \tag{8.130}$$

Eliminating the electric potential, from Eq. (8.130) we obtain

$$\bar{\hat{c}}_{2nr2}\hat{u}_{r,22} = \rho\ddot{\hat{u}}_n, \tag{8.131}$$

where

$$\bar{\hat{c}}_{2nr2} = \hat{c}_{2nr2} + \frac{\hat{e}_{22n}e_{22r}}{\varepsilon_{22}}. \tag{8.132}$$

Let

$$\hat{u}_r = A_r \sin\eta x_2 \exp(i\omega t). \tag{8.133}$$

Substitution of Eq. (8.133) into Eq. (8.131) results in the following characteristic equation:

$$(\bar{\hat{c}}_{2nr2} - \bar{c}\delta_{nr})A_r = 0, \tag{8.134}$$

where

$$\bar{c} = \frac{\rho\omega^2}{\eta}. \tag{8.135}$$

For nontrivial solutions of A_r we must have

$$|\bar{\hat{c}}_{2nr2} - \bar{c}\delta_{nr}| = 0. \tag{8.136}$$

We denote the three real, positive roots of Eq. (8.136) by $\bar{c}^{(i)}$ and the three corresponding orthonormal eigenvectors from Eq. (8.134) by $\mathbf{q}^{(i)}$ with i = 1, 2, 3. For a doubly-rotated plate, $\mathbf{q}^{(i)}$ are not exactly parallel or perpendicular to the plate surfaces (see the dotted arrows in Fig. 8.17). We have quasi-TSh ($\mathbf{q}^{(1)}$ and $\mathbf{q}^{(3)}$) and quasi-TSt ($\mathbf{q}^{(2)}$) modes. $\mathbf{q}^{(i)}$

may be used as a set of base vectors. We transform the components of the mechanical displacement vector $\hat{u}_i$ in the original plate coordinate system to the components u_i in the thickness solution eigenvector system, i.e.,

$$u_i = Q_{ir}\hat{u}_r, \quad \hat{u}_r = Q_{ir}u_i, \tag{8.137}$$

where Q_{ir} is a 3×3 orthogonal matrix formed by $\mathbf{q}^{(i)}$. Substitution of Eq. (8.137) into Eq. (8.131) gives the equations for u_i.

8.8.2. Unelectroded plate

We are mainly interested in u_1. Let

$$u_1(x_1, x_2, x_3) \cong \sum_{n=1,3,5,\cdots}^{\infty} u_1^n(x_1, x_3) \sin\frac{n\pi}{2h} x_2 . \tag{8.138}$$

Through rather lengthy derivations, approximate dispersion relations of transversely varying thickness-shear modes of u_1^n with slow in-plane variations accurate to the second order of the small in-plane wave numbers can be obtained. Then an approximate equation governing u_1^n can be constructed from the approximate dispersion relations. The resulting equation is

$$M_n \frac{\partial^2 u_1^n}{\partial x_1^2} + Q_n \frac{\partial^2 u_1^n}{\partial x_1 \partial x_3} + P_n \frac{\partial^2 u_1^n}{\partial x_3^2} - \frac{n^2\pi^2 \bar{c}^{(1)}}{4h^2} u_1^n - \rho \ddot{u}_1^n = 0, \tag{8.139}$$

where

$$\begin{aligned} M_n &= c_{11} - \frac{c_{16}^{(2)}}{\bar{c}^{(1)}} + r_2(c_{12} + c_{66}) + r_5(c_{17} + c_{86}) \\ &\quad + \frac{4(r_2\bar{c}^{(1)} - c_{66})(r_2\bar{c}^{(2)} + c_{12})}{\bar{c}^{(2)}\kappa_2 n\pi} \cot\kappa_2 \frac{n\pi}{2} \\ &\quad + \frac{4(r_5\bar{c}^{(1)} - c_{86})(r_5\bar{c}^{(3)} + c_{17})}{\bar{c}^{(3)}\kappa_3 n\pi} \cot\kappa_3 \frac{n\pi}{2}, \end{aligned} \tag{8.140}$$

$$
\begin{aligned}
Q_n &= 2c_{51} - \frac{2c_{16}c_{56}}{\bar{c}^{(1)}} + r_2(c_{52}+c_{76}) + r_4(c_{12}+c_{66}) \\
&\quad + r_3(c_{17}+c_{86}) + r_5(c_{36}+c_{57}) \\
&\quad + 4\frac{(r_2\bar{c}^{(1)}-c_{66})(r_4\bar{c}^{(2)}+c_{52}) + (r_2\bar{c}^{(2)}+c_{12})(r_4\bar{c}^{(1)}-c_{76})}{\bar{c}^{(2)}\kappa_2 n\pi}\cot\kappa_2\frac{n\pi}{2} \\
&\quad + 4\frac{(r_5\bar{c}^{(1)}-c_{86})(r_3\bar{c}^{(3)}+c_{57}) + (r_5\bar{c}^{(3)}+c_{17})(r_3\bar{c}^{(1)}-c_{36})}{\bar{c}^{(3)}\kappa_3 n\pi}\cot\kappa_3\frac{n\pi}{2},
\end{aligned}
\tag{8.141}
$$

$$
\begin{aligned}
P_n &= c_{58} - \frac{2c_{56}^2}{\bar{c}^{(1)}} + r_4(c_{52}+c_{76}) + r_3(c_{36}+c_{57}) \\
&\quad + \frac{4(r_4\bar{c}^{(1)}-c_{76})(r_4\bar{c}^{(2)}+c_{52})}{\bar{c}^{(2)}\kappa_2 n\pi}\cot\kappa_2\frac{n\pi}{2} \\
&\quad \frac{4(r_3\bar{c}^{(1)}-c_{36})(r_3\bar{c}^{(3)}+c_{57})}{\bar{c}^{(3)}\kappa_3 n\pi}\cot\kappa_3\frac{n\pi}{2},
\end{aligned}
\tag{8.142}
$$

$$
\kappa_2 = \sqrt{\frac{\bar{c}^{(1)}}{\bar{c}^{(2)}}}, \quad \kappa_3 = \sqrt{\frac{\bar{c}^{(1)}}{\bar{c}^{(3)}}}
\tag{8.143}
$$

$$
\begin{aligned}
r_2 &= \frac{c_{12}+c_{66}}{\bar{c}^{(1)}-\bar{c}^{(2)}}, \quad r_3 = \frac{c_{36}+c_{57}}{\bar{c}^{(1)}-\bar{c}^{(3)}}, \\
r_4 &= \frac{c_{52}+c_{76}}{\bar{c}^{(1)}-\bar{c}^{(2)}}, \quad r_5 = \frac{c_{17}+c_{86}}{\bar{c}^{(1)}-\bar{c}^{(3)}}.
\end{aligned}
\tag{8.144}
$$

Similar equations governing modes of different orders of u_2 and u_3 can be found in [95, 96].

8.8.3. Electroded plate

For electroded plates with shorted electrodes, it was shown in [94] that

$$
u_1(x_1,x_2,x_3) \cong \sum_{n=1,3,5,\cdots}^{\infty} u_1^n(x_1,x_3)\sin\frac{n\pi}{2h}x_2\ ,
\tag{8.145}
$$

$$M_n \frac{\partial^2 u_1^n}{\partial x_1^2} + Q_n \frac{\partial^2 u_1^n}{\partial x_1 \partial x_3} + P_n \frac{\partial^2 u_1^n}{\partial x_3^2} - \frac{n^2 \pi^2 \hat{c}^{(1)}}{4h^2} u_1^n - \rho \ddot{u}_1^n = 0\,, \quad (8.146)$$

where

$$\hat{c}^{(1)} = \bar{c}^{(1)}(1 - \frac{8k_1^2}{n^2\pi^2} - 2R), \quad c^{(1)} = \bar{c}^{(1)}(1 - k_1^2)\,, \quad (8.147)$$

$$k_1^2 = \frac{e_{26}^2}{\bar{c}^{(1)}\varepsilon_{22}}, \quad R = \frac{2\rho' h'}{\rho h}. \quad (8.148)$$

The corresponding equation in [94] also has a driving term from an applied voltage across the electrodes. The driving term in [94] has some error that was later corrected in [31]. Similar equations for u_2 and u_3 were derived in [95, 96].

8.8.4. Canonical form

It is well-known that the mixed derivative terms in Eqs. (8.139) and (8.146) may be removed by an appropriate planar transformation of the independent coordinates x_1 and x_3. In this case we have

$$x_i' = R_{ij} x_j\,, \quad x_j = R_{ij} x_i'\,, \quad (8.149)$$

where

$$[R_{ij}] = \begin{bmatrix} \cos\hat{\beta}_n & 0 & -\sin\hat{\beta}_n \\ 0 & 1 & 0 \\ \sin\hat{\beta}_n & 0 & \cos\hat{\beta}_n \end{bmatrix}, \quad (8.150)$$

$$\hat{\beta}_n = \frac{1}{2}\tan^{-1}\left(\frac{-Q_n}{M_n - P_n}\right). \quad (8.151)$$

Thus R_{ij} represents a rotation about the x_2 axis by the angle $\hat{\beta}_n$. Note that $\hat{\beta}_n$ is dependent on the particular mode being considered. The resulting

transformed equation for Eq. (8.146) now takes the very convenient separable form

$$M_n' \frac{\partial^2 u^n}{\partial x_1'^2} + P_n' \frac{\partial^2 u^n}{\partial x_3'^2} - \frac{n^2\pi^2}{4h^2}\hat{c}^{(1)}u^n - \rho\ddot{u}^n = 0 \ , \tag{8.152}$$

where

$$\begin{aligned} M_n' &= M_n \cos^2\hat{\beta}_n - Q_n \sin\hat{\beta}_n \cos\hat{\beta}_n + P_n \sin^2\hat{\beta}_n \ , \\ P_n' &= M_n \sin^2\hat{\beta}_n + Q_n \sin\hat{\beta}_n \cos\hat{\beta}_n + P_n \cos^2\hat{\beta}_n . \end{aligned} \tag{8.153}$$

8.9. Optimal Electrode Shape and Size

Due to the need of resonator miniaturization, there has been a growing interest in the effect of electrode configurations that include electrode thickness, shape, and size. Electrodes of varying thickness have been shown to be effective in producing strong energy trapping. At present, circular and rectangular electrodes are routinely used in manufacturing. It has also been shown that electrodes with corners cause field concentration and should be avoided in general. An important known theoretical result on electrode shape was given in [97] with a formula for the optimal electrode shape and size of singly rotated AT-cut quartz resonators. The optimal electrodes defined in [97] satisfy Bechmann's number in every direction. Based on the theoretical result of [97], some numerical and graphical results were obtained in [98] where it was shown that the commonly used rectangular and circular electrodes deviate significantly from the optimal electrodes, and therefore significant improvement in resonator performance may be expected using the optimal electrodes. The results in [97, 98] were only for singly rotated crystal resonators. In this section we study electrode shape and size optimization in doubly rotated resonators [99].

To determine the optimal electrodes in SC-cut plates, in the spirit of [97], we consider the propagation of the following wave in an electroded plate in a direction described by ψ with a wavelength λ

$$u_1^n = A\exp\left[i\frac{2\pi}{\lambda}(x_1\cos\psi + x_3\sin\psi)\right]\exp(-i\omega t) . \tag{8.154}$$

Upon substitution of Eq. (8.154) into Eq. (8.146), there results the following dispersion relation:

$$\rho\omega^2 = \left(\frac{2\pi}{\lambda}\right)^2 (M_n \cos^2\psi + Q_n \sin\psi\cos\psi + P_n \sin^2\psi) + \frac{n^2\pi^2\hat{c}^{(1)}}{4h^2}. \tag{8.155}$$

A similar dispersion relation holds for an unelectroded plate when $\hat{c}^{(1)}$ is replaced by $\bar{c}^{(1)}$. The optimal dimension L of the electrode in the direction ψ is [97] the wavelength of the wave in the same direction in an electroded plate at the cutoff frequency of the same wave in an unelectroded plate, i.e., L is determined by the following equation as a function of ψ:

$$\begin{aligned}\frac{n^2\pi^2\bar{c}^{(1)}}{4h^2} &= \frac{n^2\pi^2\hat{c}^{(1)}}{4h^2} \\ &+ \left(\frac{2\pi}{L}\right)^2 (M_n \cos^2\psi + Q_n \sin\psi\cos\psi + P_n \sin^2\psi).\end{aligned} \tag{8.156}$$

An explicit expression of the normalized L can be obtained as

$$l = \frac{L}{2h} = \frac{2}{n}\left(\frac{M_n \cos^2\psi + Q_n \sin\psi\cos\psi + P_n \sin^2\psi}{\bar{c}^{(1)} - \hat{c}^{(1)}}\right)^{1/2}. \tag{8.157}$$

As a numerical example we consider an SC-cut quartz plate. The plate thickness is $2h$ = 1mm. We calculate $r = l/2$ versus ψ and plot r in the direction of ψ in Fig. 8.18 for n = 1, 3 and 5. The figure shows that the optimal electrodes are close to but not exact the same as ellipses. The major or minor axes of the nearly elliptical electrodes are not along any coordinate axis. Note that the major axis rotates by 90 degrees as n progresses from n = 1 to n = 3, 5. This depends on the relative magnitude of M_n and P_n in Eq. (8.146) in the principal direction where Q_n = 0. The electrode size decreases as n increases.

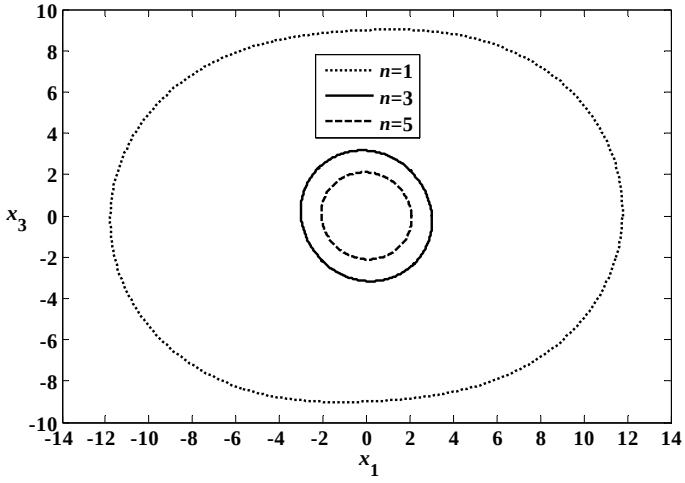

Fig. 8.18. Optimal electrodes for the fundamental mode (n = 1) and different overtones (n = 3, 5) of an SC-cut quartz resonator (R = 0.01).

In Fig. 8.19 we fix n = 1 and plot the optimal electrodes for different values of R, the electrode/plate mass ratio. For thicker or heavier electrodes with a larger R, the optimal electrodes become smaller.

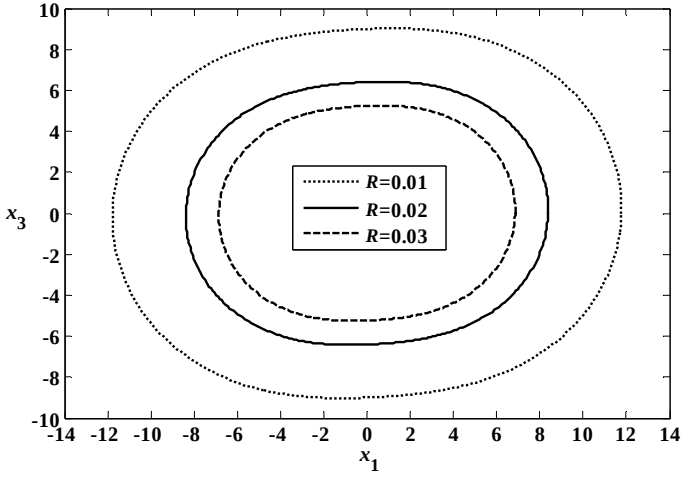

Fig. 8.19. Optimal electrodes for the fundamental mode (n = 1) of an SC-cut quartz resonator for different values of the mass ratio R.

Appendix 1

Notation

i – Imaginary unit
x_k – Reference position vector of a material point
u_k – Mechanical displacement vector
v_i – Velocity vector
S_{kl} – Strain tensor
T_{kl} – Stress tensor
f_j – Mechanical body force vector
t_k – Mechanical surface traction vector
ϕ – Electrostatic potential (except in Section 2.12)
E_i – Electric field vector
D_i – Electric displacement vector
H – Electric enthalpy
ε_0 – Permittivity of free space
Q_e – Free charge on an electrode (a scalar)
σ – Surface free charge density
I – Current
V – Voltage
Y – Admittance
Z – Impedance
Q – Material quality factor
R – Mass ratio
ρ – Mass density
$k_{26}^2 - e_{26}^2/(\varepsilon_{22}c_{66})$
$\bar{k}_{26}^2 - k_{26}^2/(1+k_{26}^2)$
0 D – Zero dimensional
1 D – One dimensional
2 D – Two dimensional
3 D – Three dimensional
BAW – Bulk acoustic wave

E – Extension
F – Flexure
FGM – Functionally graded material
FS – Face shear
LFE – Lateral field excitation
QCM – Quartz crystal microbalance
QCR – Quartz crystal resonator
SAW – Surface acoustic wave
SH – Shear horizontal or antiplane
TFE – Thickness field excitation
TSh – Thickness shear
TS_1 or TSh_1 – Thickness shear with u_1 as the main displacement
TS_3 or TSh_3 – Thickness shear with u_3 as the main displacement
TSt – Thickness stretch
TT – Thickness twist
Z – Impedance

Appendix 2

Material Constants

The permittivity of free space $\varepsilon_0 = 8.854 \times 10^{-12}$ F/m. Material constants for a few common piezoelectric crystals are summarized below. When referred to the crystallographic axes, the second-order material constants for left-hand quartz have the following values [100, 101]:

$$\rho = 2649 \text{ kg/m}^3,$$

$$[c_{pq}] = \begin{pmatrix} 86.74 & 6.99 & 11.91 & -17.91 & 0 & 0 \\ 6.99 & 86.74 & 11.91 & 17.91 & 0 & 0 \\ 11.91 & 11.91 & 107.2 & 0 & 0 & 0 \\ -17.91 & 17.91 & 0 & 57.94 & 0 & 0 \\ 0 & 0 & 0 & 0 & 57.94 & -17.91 \\ 0 & 0 & 0 & 0 & -17.91 & 39.88 \end{pmatrix} \times 10^9 \text{ N/m}^2,$$

$$[e_{ip}] = \begin{pmatrix} 0.171 & -0.171 & 0 & -0.0406 & 0 & 0 \\ 0 & 0 & 0 & 0 & 0.0406 & -0.171 \\ 0 & 0 & 0 & 0 & 0 & 0 \end{pmatrix} \text{C/m}^2,$$

$$[\varepsilon_{ij}] = \begin{pmatrix} 39.21 & 0 & 0 \\ 0 & 39.21 & 0 \\ 0 & 0 & 41.03 \end{pmatrix} \times 10^{-12} \text{C/Vm}.$$

AT-cut quartz is a special case of rotated Y-cut quartz (θ = 35.25°) whose material constants are [2]

$$[c_{pq}]=\begin{pmatrix} 86.74 & -8.25 & 27.15 & -3.66 & 0 & 0 \\ -8.25 & 129.77 & -7.42 & 5.7 & 0 & 0 \\ 27.15 & -7.42 & 102.83 & 9.92 & 0 & 0 \\ -3.66 & 5.7 & 9.92 & 38.61 & 0 & 0 \\ 0 & 0 & 0 & 0 & 68.81 & 2.53 \\ 0 & 0 & 0 & 0 & 2.53 & 29.01 \end{pmatrix} \times 10^9 \text{ N/m}^2,$$

$$[e_{ip}] = \begin{pmatrix} 0.171 & -0.152 & -0.0187 & 0.067 & 0 & 0 \\ 0 & 0 & 0 & 0 & 0.108 & -0.095 \\ 0 & 0 & 0 & 0 & -0.0761 & 0.067 \end{pmatrix} \text{C/m}^2,$$

$$[\varepsilon_{ij}] = \begin{pmatrix} 39.21 & 0 & 0 \\ 0 & 39.82 & 0.86 \\ 0 & 0.86 & 40.42 \end{pmatrix} \times 10^{-12} \text{C/Vm}.$$

The second-order material constants of langasite ($La_3Ga_5SiO_{14}$) are [102]

$$\rho = 5743 \text{ kg/m}^3,$$

$$[c_{pq}]=\begin{pmatrix} 18.875 & 10.475 & 9.589 & -1.412 & 0 & 0 \\ 10.475 & 18.875 & 9.589 & 1.412 & 0 & 0 \\ 9.589 & 9.589 & 26.14 & 0 & 0 & 0 \\ -1.412 & 1.412 & 0 & 5.35 & 0 & 0 \\ 0 & 0 & 0 & 0 & 5.35 & -1.412 \\ 0 & 0 & 0 & 0 & -1.412 & 4.2 \end{pmatrix}$$

$\times 10^{10} \text{ N/m}^2$,

$$[e_{ip}] = \begin{pmatrix} -0.44 & 0.44 & 0 & -0.08 & 0 & 0 \\ 0 & 0 & 0 & 0 & 0.08 & 0.44 \\ 0 & 0 & 0 & 0 & 0 & 0 \end{pmatrix} \mathrm{C/m^2},$$

$$[\varepsilon_{ij}] = \begin{pmatrix} 18.92\varepsilon_0 & 0 & 0 \\ 0 & 18.92\varepsilon_0 & 0 \\ 0 & 0 & 50.7\varepsilon_0 \end{pmatrix}$$

$$= \begin{pmatrix} 167.5 & 0 & 0 \\ 0 & 167.5 & 0 \\ 0 & 0 & 448.9 \end{pmatrix} \times 10^{-12}\,\mathrm{C/Vm}.$$

Material constants are also available for laganate [103] and langatate [104, 105].

The second-order material constants for lithium niobate are [106, 107]

$$\rho = 4700\ \mathrm{kg/m^3},$$

$$[c_{pq}] = \begin{pmatrix} 2.03 & 0.53 & 0.75 & 0.09 & 0 & 0 \\ 0.53 & 2.03 & 0.75 & -0.09 & 0 & 0 \\ 0.75 & 0.75 & 2.45 & 0 & 0 & 0 \\ 0.09 & -0.09 & 0 & 0.60 & 0 & 0 \\ 0 & 0 & 0 & 0 & 0.60 & 0.09 \\ 0 & 0 & 0 & 0 & 0.09 & 0.75 \end{pmatrix} \times 10^{11}\,\mathrm{N/m^2},$$

$$[e_{ip}] = \begin{pmatrix} 0 & 0 & 0 & 0 & 3.70 & -2.50 \\ -2.50 & 2.50 & 0 & 3.70 & 0 & 0 \\ 0.20 & 0.20 & 1.30 & 0 & 0 & 0 \end{pmatrix} \mathrm{C/m^2},$$

$$[\varepsilon_{ij}] = \begin{pmatrix} 38.9 & 0 & 0 \\ 0 & 38.9 & 0 \\ 0 & 0 & 25.7 \end{pmatrix} \times 10^{-11}\,\mathrm{C/Vm}.$$

The second-order material constants for lithium tantalate are [106, 107]

$$\rho = 7450 \text{ kg/m}^3,$$

$$[c_{pq}] = \begin{pmatrix} 2.33 & 0.47 & 0.80 & -0.11 & 0 & 0 \\ 0.47 & 2.33 & 0.80 & 0.11 & 0 & 0 \\ 0.80 & 0.80 & 2.45 & 0 & 0 & 0 \\ -0.11 & -0.11 & 0 & 0.94 & 0 & 0 \\ 0 & 0 & 0 & 0 & 0.94 & -0.11 \\ 0 & 0 & 0 & 0 & -0.11 & 0.93 \end{pmatrix} \times 10^{11} \text{N/m}^2,$$

$$[e_{ip}] = \begin{pmatrix} 0 & 0 & 0 & 0 & 2.6 & -1.6 \\ -1.6 & 1.6 & 0 & 2.6 & 0 & 0 \\ 0 & 0 & 1.9 & 0 & 0 & 0 \end{pmatrix} \text{C/m}^2,$$

$$[\varepsilon_{ij}] = \begin{pmatrix} 36.3 & 0 & 0 \\ 0 & 36.3 & 0 \\ 0 & 0 & 38.2 \end{pmatrix} \times 10^{-11} \text{C/Vm}.$$

For PZT-5H, $\rho = 7500\ kg/m^3$. When the poling direction is along the x_3 axis, the material matrices are [101]

$$[c_{pq}] = \begin{pmatrix} 12.6 & 7.95 & 8.41 & 0 & 0 & 0 \\ 7.95 & 12.6 & 8.41 & 0 & 0 & 0 \\ 8.41 & 8.41 & 11.7 & 0 & 0 & 0 \\ 0 & 0 & 0 & 2.3 & 0 & 0 \\ 0 & 0 & 0 & 0 & 2.3 & 0 \\ 0 & 0 & 0 & 0 & 0 & 2.325 \end{pmatrix} \times 10^{10} \text{N/m}^2,$$

$$[e_{ip}] = \begin{pmatrix} 0 & 0 & 0 & 0 & 17 & 0 \\ 0 & 0 & 0 & 17 & 0 & 0 \\ -6.5 & -6.5 & 23.3 & 0 & 0 & 0 \end{pmatrix} \text{C/m}^2,$$

$$[\varepsilon_{ij}]=\begin{pmatrix}1700\varepsilon_0 & 0 & 0\\ 0 & 1700\varepsilon_0 & 0\\ 0 & 0 & 1470\varepsilon_0\end{pmatrix}$$
$$=\begin{pmatrix}1.505 & 0 & 0\\ 0 & 1.505 & 0\\ 0 & 0 & 1.302\end{pmatrix}\times 10^{-8}\,\text{C/(V - m)}.$$

For PZT-5H, an equivalent set of material constants are

$$s_{11}=16.5,\quad s_{33}=20.7,\quad s_{44}=43.5,$$
$$s_{12}=-4.78,\quad s_{13}=-8.45\times 10^{-12}\,\text{m}^2/\text{N},$$
$$d_{31}=-274,\quad d_{15}=741,\quad d_{33}=593\times 10^{-12}\,\text{C/N},$$
$$\varepsilon_{11}=3130\varepsilon_0,\quad \varepsilon_{33}=3400\varepsilon_0.$$

When poling is along other directions, the material matrices can be obtained by tensor transformations. For PZT-5H, when poling is along the x_1 axis, we have

$$[c_{pq}]=\begin{pmatrix}11.7 & 8.41 & 8.41 & 0 & 0 & 0\\ 8.41 & 12.6 & 7.95 & 0 & 0 & 0\\ 8.41 & 7.95 & 12.6 & 0 & 0 & 0\\ 0 & 0 & 0 & 2.325 & 0 & 0\\ 0 & 0 & 0 & 0 & 2.3 & 0\\ 0 & 0 & 0 & 0 & 0 & 2.3\end{pmatrix}\times 10^{10}\,\text{N/m}^2,$$

$$[e_{ip}]=\begin{pmatrix}23.3 & -6.5 & -6.5 & 0 & 0 & 0\\ 0 & 0 & 0 & 0 & 0 & 17\\ 0 & 0 & 0 & 0 & 17 & 0\end{pmatrix}\text{C/m}^2,$$

$$[\varepsilon_{ij}]=\begin{pmatrix}1.302 & 0 & 0\\ 0 & 1.505 & 0\\ 0 & 0 & 1.505\end{pmatrix}\times 10^{-8}\,\text{C/Vm}.$$

When poling is along the x_2 axis,

$$[c_{pq}] = \begin{pmatrix} 12.6 & 8.41 & 7.95 & 0 & 0 & 0 \\ 8.41 & 11.7 & 8.41 & 0 & 0 & 0 \\ 7.95 & 8.41 & 12.6 & 0 & 0 & 0 \\ 0 & 0 & 0 & 2.3 & 0 & 0 \\ 0 & 0 & 0 & 0 & 2.325 & 0 \\ 0 & 0 & 0 & 0 & 0 & 2.3 \end{pmatrix} \times 10^{10}\ \mathrm{N/m^2},$$

$$[e_{ip}] = \begin{pmatrix} 0 & 0 & 0 & 0 & 0 & 17 \\ -6.5 & 23.3 & -6.5 & 0 & 0 & 0 \\ 0 & 0 & 0 & 17 & 0 & 0 \end{pmatrix} \ \mathrm{C/m^2},$$

$$[\varepsilon_{ij}] = \begin{pmatrix} 1.505 & 0 & 0 \\ 0 & 1.302 & 0 \\ 0 & 0 & 1.505 \end{pmatrix} \times 10^{-8}\ \mathrm{C/Vm}.$$

Material constants of a few other polarized ceramics are given in the following tables [101, 108]:

Material	c_{11}	c_{12}	c_{13}	c_{33}	c_{44}	c_{66}
PZT-4	13.9	7.78	7.40	11.5	2.56	3.06
PZT-5A	12.1	7.59	7.54	11.1	2.11	2.26
PZT-6B	16.8	8.47	8.42	16.3	3.55	4.17
PZT-5H	12.6	7.91	8.39	11.7	2.30	2.35
PZT-7A	14.8	7.61	8.13	13.1	2.53	3.60
PZT-8	13.7	6.99	7.11	12.3	3.13	3.36
$BaTiO_3$	15.0	6.53	6.62	14.6	4.39	4.24
	$\times 10^{10}\ \mathrm{N/m^2}$					

Material	e_{31}	e_{33}	e_{15}	ε_{11}	ε_{33}
PZT-4	-5.2	15.1	12.7	0.646	0.562
PZT-5A	-5.4	15.8	12.3	0.811	0.735
PZT-6B	-0.9	7.1	4.6	0.360	0.342
PZT-5H	-6.5	23.3	17.0	1.505	1.302
PZT-7A	-2.1	9.5	9.2	0.407	0.208
PZT-8	-4.0	13.2	10.4	0.797	0.514
$BaTiO_3$	-4.3	17.5	11.4	0.987	1.116
	C/m^2			$\times 10^{-8}$ C/Vm	

Density	PZT-5H	PZT-5A	PZT-6B	PZT-4
kg/m^3	7500	7750	7550	7500

Density	PZT-7A	PZT-8	$BaTiO_3$
kg/m^3	7600	7600	5700

Material constants for additional piezoceramics are [109]:

Material	Pz24	Pz26	Pz27	Pz28	Pz34
ρ (kg/m^3)	7.65	7.65	7.75	7.65	7.6

Material	Pz24	Pz26	Pz27	Pz28	Pz34
c_{11}^E (GPa)	177.3	171.3	142.8	142.2	188.4
c_{12}^E (GPa)	106.5	15.5	99.8	88.1	80.2
c_{13}^E (GPa)	98.2	107.4	92.2	82.1	82.3
c_{33}^E (GPa)	127.2	133.2	114.5	108.1	127.2
c_{44}^E (GPa)	33.5	33.3	22.8	29.8	58.9

Material	Pz24	Pz26	Pz27	Pz28	Pz34
e_{15} (C/m^2)	8.10	8.84	11.74	9.26	2.31
e_{31} (C/m^2)	−0.26	−1.16	−3.71	−2.80	3.81
e_{33} (C/m^2)	9.73	15.67	15.77	12.1	6.87

Material	Pz24	Pz26	Pz27	Pz28	Pz34
$\varepsilon_{11}^S/\varepsilon_0$	477	890	1120	910	181
$\varepsilon_{33}^S/\varepsilon_0$	239	790	880	520	154

Material constants for a few crystals of class 6mm are listed below from [110] which also has material constants of other crystals.

	Zinc Oxide	Aluminum Nitride	α - Silicon Carbide
	ZnO	AlN	α - Sic
ρ (10^3 kg/m^3)	5.665		3.211
c_{11} (GPa)	209	345	500
c_{12} (GPa)		125	92
c_{13} (GPa)	104.6	120	
c_{33} (GPa)	210.6	395	564
c_{44} (GPa)	42.3	118	168
c_{66} (GPa)	44.25	110	204
e_{15} (C/m^2)	−0.48	−0.48	0.08
e_{31} (C/m^2)	−0.57	−0.58	
e_{33} (C/m^2)	1.32	1.55	0.2
ε_{11} (ε_0)			6.7
ε_{33} (ε_0)			6.52

	Cadium Selenide SdSe	Cadium Selenide SdSe	Zinc Sulfide ZnS
$\rho\ (10^3\,\mathrm{kg/m^3})$	5.684	4.820	3.980
c_{11} (GPa)	74.1	90.7	120.4
c_{12} (GPa)	45.2	58.1	69.2
c_{13} (GPa)	39.3	51.0	62.0
c_{33} (GPa)	83.6	93.8	127.6
c_{44} (GPa)	13.17	15.04	22.8
c_{66} (GPa)	14.45	16.3	25.6
$e_{15}\ (\mathrm{C/m^2})$		-0.21	-0.0683
$e_{31}\ (\mathrm{C/m^2})$		-0.24	-0.0140
$e_{33}\ (\mathrm{C/m^2})$		0.44	0.272
$\varepsilon_{11}\ (\varepsilon_0)$		9.02	
$\varepsilon_{33}\ (\varepsilon_0)$		9.53	

Material constants for AlN are given in [111]:

$$\rho = 3512\,\mathrm{kg/m^3},$$

$$[c_{pq}] = \begin{pmatrix} 345 & 125 & 120 & 0 & 0 & 0 \\ 125 & 345 & 120 & 0 & 0 & 0 \\ 120 & 120 & 395 & 0 & 0 & 0 \\ 0 & 0 & 0 & 118 & 0 & 0 \\ 0 & 0 & 0 & 0 & 118 & 0 \\ 0 & 0 & 0 & 0 & 0 & 110 \end{pmatrix} \times 10^9\,\mathrm{N/m^2},$$

$$[e_{ip}] = \begin{pmatrix} 0 & 0 & 0 & 0 & -0.48 & 0 \\ 0 & 0 & 0 & -0.48 & 0 & 0 \\ -0.58 & -0.58 & 1.55 & 0 & 0 & 0 \end{pmatrix} \mathrm{C/m^2},$$

$$[\varepsilon_{ij}] = \begin{pmatrix} 8.0 & 0 & 0 \\ 0 & 8.0 & 0 \\ 0 & 0 & 9.5 \end{pmatrix} \times 10^{-11}\,\mathrm{F/m}.$$

This page intentionally left blank

References

[1] A. H. Meitzler, D. Berlincourt, F. S. Welsh, III, H. F. Tiersten, G. A. Coquin and A. W. Warner, *IEEE Standard on Piezoelectricity*, IEEE, New York, 1988.

[2] H. F. Tiersten, *Linear Piezoelectric Plate Vibrations*, Plenum, New York, 1969.

[3] J. S. Yang, *An Introduction to the Theory of Piezoelectricity*. Springer, New York, 2005.

[4] H. F. Tiersten, On the nonlinear equations of thermoelectroelasticity, *Int. J. Engng. Sci.*, **9**, 587-604, 1971.

[5] R. Holland, Representation of dielectric, elastic, and piezoelectric losses by complex coefficients, *IEEE Trans. on Sonics and Ultrasonics*, **14**, 18-20, 1967.

[6] H. F. Tiersten, On the influence of material objectivity on electroelastic dissipation in polarized ferroelectric ceramics, *Mathematics and Mechanics of Solids*, **1**, 45-55, 1996.

[7] J. S. Yang, Nonlinear equations of thermoviscoelectroelasticity, *Mathematics and Mechanics of Solids*, **3**, 113-124, 1998.

[8] J. S. Yang and R. C. Batra, Free vibrations of a piezoelectric body, *Journal of Elasticity*, **34**, 239-254, 1994.

[9] J. S. Yang, Frequency shifts in a piezoelectric body due to small amounts of additional mass on its surface, *IEEE Trans. Ultrason.*, *Ferroelect.*, *Freq. Contr.*, **51**, 1199-1202, 2004.

[10] J. S. Yang and S. H. Guo, Frequency shifts in a piezoelectric body due to a surface mass layer with consideration of the layer stiffness, *IEEE Trans. Ultrason.*, *Ferroelect.*, *Freq. Contr.*, **52**, 1200-1203, 2005.

[11] H. S. Zhou, *Piezoelectric Shells*, Kluwer, Dordrecht, the Netherlands, 1993.

[12] J. S. Yang, *The Mechanics of Piezoelectric Structures*, World Scientific, Singapore, 2006.

[13] J. S. Yang and S. H. Guo, Vibrations of a crystal body with a shear-deformable surface mass layer, *Acta Mechanica*, **190**, 223-232, 2007.

[14] J. S. Yang, Frequency shifts in a crystal resonator due to submersion in a fluid, *IEEE Trans. Ultrason., Ferroelect., Freq. Contr.*, **53**, 662-664, 2006.

[15] J. S. Yang, *Antiplane Motions of Piezoceramics and Acoustic Wave Devices*, World Scientific, Singapore, 2010.

[16] I. Koga, Thickness vibrations of piezoelectric oscillating crystals, *Physics*, **3**, 70-80, 1932.

[17] G. Sauerbrey, Verwendung von schwingquarzen zur wägung dünner schichten und zur mikrowägung, *Zeitschrift für Physik*, **155**, 206-222, 1959.

[18] J. G. Miller and D. J. Bolef, Acoustic wave analysis of the operation of quartz-crystal film-thickness monitors, *J. Appl. Phys.* **39**, 5815-5816, 1968.

[19] R. D. Mindlin, High frequency vibrations of plated, crystal plates, *Progress in Applied Mechanics* (the Prager Anniversary Volume), Macmillan, New York, 1963, pp. 73-84.

[20] K. K. Kanazawa and J. G. Gordon II, The oscillation frequency of a quartz resonator in contact with a fluid, *Analytica Chemica Acta*, **175**, 99-105, 1985.

[21] R. L. Panton, *Incompressible Flow*, John Wiley and Sons, New York, 1984.

[22] C. L. Zhang, N. Liu, J. S. Yang and W. Q. Chen, Thickness-shear vibration of AT-cut quartz plates carrying finite-size particles with rotational degree of freedom and rotatory inertia, *IEEE Trans. Ultrason., Ferroelect., Freq. Contr.*, **58**, 666-670, 2011.

[23] N. Liu, J. S. Yang and J. Wang, Thickness-stretch vibration of a crystal plate carrying a micro-rod array, *Science in China-G*, **55**, 2152-2157, 2012.

[24] J. M. Gere, *Mechanics of Materials*, 5th ed., Brooks/Cole, Pacific Grove, California, 2001.

[25] L. Meirovitch, *Analytical Methods in Vibrations*, Macmillan, New York, 1967.

[26] N. Liu, J. S. Yang and J. Wang, Shear vibration of a crystal plate carrying an array of microbeams, *Philosophical Magazine Letters*, **91**, 572-581, 2011.

[27] R. D. Mindlin and H. F. Tiersten, Effects of couple-stresses in linear elasticity, *Archive for Rational Mechanics and Analysis*, **11**, 415-448, 1962.

[28] R. Y. Zhang, J. M. Xie, Y. T. Hu, J. S. Yang and X. D. Chen, Thickness-shear vibration of an elastic plate carrying an array of rigid microbeams with consideration of couple stresses, *International Journal of Engineering Science*, **51**, 179-189, 2012.

[29] Y. Y. Chen, J. Wang, J. K. Du and J. S. Yang, Characterization of material property gradient in a functionally graded material using an AT-cut quartz thickness-shear mode resonator, *Philosophical Magazine Letters*, in press.

[30] H. F. Tiersten, Thickness vibrations of piezoelectric plates, *J. Acoust. Soc. Am.*, **35**, 53-58, 1963.

[31] H. F. Tiersten, A corrected modal representation of thickness vibrations in quartz plates and its influence on the transversely varying case, *IEEE Trans. Ultrason., Ferroelect., Freq. Contr.*, **50**, 1436-1443, 2003.

[32] S. J. Martin, V. E. Granstaff and G. C. Frye, Characterization of a quartz crystal microbalance with simultaneous mass and liquid loading, *Anal. Chem.*, **63**, 2272-2281, 1991.

[33] Y. Jing, J. Chen, X. Chen and X. Gong, Frequency shift of thickness-shear vibrations of AT-cut quartz resonators due to a liquid layer with the electrode stiffness considered, *IEEE Trans. on Ultrasonics, Ferroelectrics, and Frequency Control*, **54**, 1290-1292, 2007.

[34] C. E. Reed, K. K. Kanazawa and J. H. Kaufman, Physical description of a viscoelastically loaded AT-cut quartz resonator, *J. Acoust. Soc. Am.*, **68**, 1993-2001, 1990.

[35] W. C. Duncan-Hewitt and M. Thompson, Four-layer theory for the acoustic shear wave sensor in liquids incorporating interface slip and liquid structure, *Anal. Chem.*, **64**, 94-105, 1992.

[36] F. Ferrante, A. L. Kipling and M. Thompson, Molecular slip at the solid-liquid interface of an acoustic-wave sensor, *J. Appl. Phys.*, **76**, 3448-3462, 1994.

[37] B. Liu, Q. Jiang and J. S. Yang, Fluid-induced frequency shift in a piezoelectric plate driven by lateral electric fields, *Int. J. of Applied Electromagnetics and Mechanics*, **34**, 171-180**,** 2010.

[38] Z. T. Yang, S. H. Guo, Y. T. Hu and J. S. Yang, Thickness-shear vibration of rotated y-cut quartz plates with unattached electrodes

and asymmetric air gaps, *Philosophical Magazine Letters*, **89**, 313-321, 2009.

[39] J. A. Kosinski, Thickness vibration of flat piezoelectric plates with massy electrodes of unequal thickness, *Proc. IEEE Ultrasonics Symp.*, 2003, pp. 70-73.

[40] J. S. Yang, Y. T. Hu, Y. Zeng and H. Fan, Thickness-shear vibration of rotated Y-cut quartz plates with imperfectly bounded surface mass layers, *IEEE Trans. on Ultrasonics*, *Ferroelectrics*, *and Frequency Control*, **53**, 241-245, 2006.

[41] F. Boersma and E. C. van Ballegooyen, Rotated Y-cut quartz crystal with two different electrodes treated as a one-dimensional acoustic composite resonator, *J. Acoust. Soc. Am.*, **62**, 335-340, 1977.

[42] J. Wang and L. J. Shen, Exact thickness-shear resonance frequency of electroded piezoelectric crystal plates, *J. Zhejiang Univ. SCI*, **6A**, 980-985, 2005.

[43] J. S. Yang, H. G. Zhou and W. P. Zhang, Thickness-shear vibration of rotated Y-cut quartz plates with relatively thick electrodes of unequal thickness, *IEEE Trans. on Ultrasonics*, *Ferroelectrics*, *and Frequency Control*, **52**, 918-922, 2005.

[44] B. Liu, Q. Jiang and J. S. Yang, Frequency shifts in a quartz plate piezoelectric resonator in contact with a viscous fluid under a separated electrode, *Int. J. of Applied Electromagnetics and Mechanics*, **35**, 177-187, 2011.

[45] R. K. Hind, E. McLaughlin and A. R. Ubbelohde**,** Structure and viscosity of liquids. Camphor+pyrene mixtures, *Trans. Faraday Soc*., **56**, 328-330, 1960.

[46] W. H. Zhu, W. Z. Wei, Z. H. Mo, L. H. Nie and S. Z. Yao, Piezoelectric detection of water with a separated electrode, *Anal. Chem*., **65**, 2568-2571, 1993.

[47] V. M. Bazhenov and A. F. Ulitko, Investigation of the dynamic behavior of a piezoelectric ceramic layer during instantaneous electric loading, *International Applied Mechanics*, **11**, 16-20, 1975.

[48] N. A. Shulga and L. O. Grigoreva, Method of characteristics in analysis of the propagation of electroelastic thickness oscillators in a piezoelectric layer under electric excitation, *International Applied Mechanics*, **44**, 1093-1097, 2008.

[49] N. Liu, J. S. Yang and F. Jin, Transient thickness-shear vibration of a piezoelectric plate of monoclinic crystals, *Int. J. of Applied Electromagnetics and Mechanics*, **38**, 27-37, 2012.

[50] R. D. Mindlin, Face-shear waves in rotated Y-cut quartz plates, *Mechanics of the Solid State*, F. P. J. Rimrott and J. Schwaighofer, ed., University of Toronto Press, 1968, pp. 143-145.

[51] R. D. Mindlin, Thickness-twist vibrations of an infinite, monoclinic, crystal plate, *Int. J. Solids Structures*, **1**, 141-145, 1965.

[52] R. D. Mindlin, Bechmann's number for harmonic overtones of thickness/twist vibrations of rotated-Y-cut quartz plates, *J. Acoust. Soc. Am.*, **41**, 969-973, 1967.

[53] J. S. Yang and S. H. Guo, Propagation of thickness-twist waves in a quartz plate with asymmetric mass layers, *IEEE Trans. Ultrason., Ferroelect., Freq. Contr.*, **53**, 1560-1561, 2006.

[54] Y. Y. Chen, J. K. Du, J. Wang and J. S. Yang, Shear-horizontal waves in a rotated Y-cut quartz plate with an imperfectly bonded mass layer, *IEEE Trans. Ultrason., Ferroelect., Freq. Contr.*, **58**, 616-622, 2011.

[55] Z. T. Yang, Y. T. Hu and J. S. Yang, Effect of mass layer stiffness on propagation of thickness-twist waves in rotated Y-cut quartz crystal plates, *Ultrasonics*, **49**, 401-403, 2009.

[56] L. Yang, J. K. Du, J. Wang and J. S. Yang, Shear-horizontal waves in a rotated Y-cut quartz plate with an isotropic elastic layer of finite thickness, *Acta Mechanica Solida Sinica*, **25**, 82-89, 2012.

[57] Y. M. Chen, J. Wang, J. K. Du and J. S. Yang, Shear-horizontal waves in a rotated Y-cut quartz plate on an elastic half space, *Philosophical Magazine Letters*, **92**, 77-85, 2012.

[58] J. B. Sun, J. K. Du, J. S. Yang and J. Wang, Shear-horizontal waves in a rotated Y-cut quartz plate in contact with a viscous fluid, *Ultrasonics*, **52**, 133-137, 2012.

[59] J. Zhu and W. Q. Chen, Thickness-twist and face-shear waves in piezoelectric plates of monoclinic crystals, *IEEE Trans. Ultrason., Ferroelect., Freq. Contr.*, **58**, 2763-2767, 2011.

[60] W. Shockley, D. R. Curran and D. J. Koneval, Trapped-energy modes in quartz filter crystals, *J. Acoust. Soc. Am.*, **41**, 981-993, 1967.

[61] C. van der Steen, F. Boersma and E. C. van Ballegooyen, The influence of mass loading outside the electrode area on the

resonant frequencies of a quartz-crystal microbalance, *J. Appl. Phys*., **48**, 3201-3205, 1977.

[62] E. C. van Ballegooyen, F. Boersma and C. van der Steen, Influence of the thickness of tabs on the resonating properties of a quartz crystal, *J. Acoust. Soc. Am*., **62**, 1189-1195, 1977.

[63] R. D. Mindlin, Thickness-twist vibrations of a quartz strip, *Proc. 26th Annual Frequency Control Symp*., 1970, pp. 17-20.

[64] H. J. He, G. Q. Nie, J. X. Liu and J. S. Yang, Energy trapping of thickness-shear and thickness-twist modes in a partially electroded AT-cut quartz resonator, *Acta Mechanica Solida Sinica*, **25**, 579-585, 2012.

[65] Y. P. Kong, J. X. Liu and Jiashi Yang, Effects of mass layer dimension on a finite quartz crystal microbalance, *Acta Mechanica*, **222**, 103-113, 2011

[66] H. J. He, J. X. Liu and J. S. Yang, Effects of mismatched electrodes on an AT-cut quartz resonator, *IEEE Trans. Ultrason*., *Ferroelect*., *Freq. Contr*., **59**, 281-286, 2012.

[67] N. Liu, J. S. Yang, J. Wang and J. A. Kosinski, Thickness-shear and thickness-twist vibrations of a crystal plate with a nonperiodic array of mass layers, *Japanese Journal of Applied Physics*, submitted.

[68] H. J. He, J. X. Liu and J. S. Yang, Thickness-shear and thickness-twist vibrations of an AT-cut quartz mesa resonator, *IEEE Trans. Ultrason*., *Ferroelect*., *Freq. Contr*., **58**, 2050-2055, 2011.

[69] H. J. He, J. X. Liu and J. S. Yang, Analysis of a monolithic crystal plate acoustic wave filter, *Ultrasonics*, **51,** 991-996, 2011.

[70] H. J. He, J. S. Yang and J. A. Kosinski, Shear-horizontal vibration modes of an oblate elliptical cylinder and energy trapping in contoured acoustic wave resonators, *IEEE Trans. Ultrason*., *Ferroelect*., *Freq. Contr*., **59**, 1774-1780, 2012.

[71] Y. Wang, T. Xiao, Q. Jiang and J. S. Yang, Effects of asymmetric and nonuniform mass layers on quartz crystal microbalances, *Philosophical Magazine Letters*, **93**, 27-33, 2013.

[72] X. J. Li, Y. Wang, T. Xiao, Q. Jiang and J. S. Yang, Effects of mass layer stiffness and imperfect bonding on a quartz crystal microbalance, *IEEE Sensors Journal*, **13**, 574-580, 2013.

[73] J. Zhu, W. Q. Chen and J. S. Yang, Overtone frequency spectra for x_3-dependent modes in at-cut quartz resonators, *IEEE Trans. Ultrason*., *Ferroelect*., *Freq. Contr*., **60**, 858-863, 2013.

[74] H. Ekstein, High frequency vibrations of thin crystal plates, *Phys. Rev*., **68**, 11-23, 1945.

[75] E. G. Newman and R. D. Mindlin, Vibrations of a monoclinic crystal plate, *J. Acoust. Soc. Am*., **29**, 1206-1218, 1957.

[76] R. K. Kaul and R. D. Mindlin, Vibrations of an infinite, monoclinic crystal plate at high frequencies and long wavelengths, *J. Acoust. Soc. Am.*, **34**, 1895-1901, 1962.

[77] R. K. Kaul and R. D. Mindlin, Frequency spectrum of a monoclinic crystal plate, *J. Acoust. Soc. Am*., **34**, 1902-1910, 1962.

[78] J. Wang, L. J. Yang and J. K. Du, The dispersion relations and vibration modes of infinite quartz crystal plates at higher frequencies, *Proc. Joint Conference of the Symp. on Piezoelectricity*, *Acoustic Waves and Device Applications and the China Symp. on Frequency Control Technology*, Y. T. Hu, C. F. Gao and W. Q. Chen, ed., IEEE, 2009, pp. 494-499.

[79] D. W. Haines, Bechmann's number for harmonic overtones of thickness-shear vibrations of rotated-Y-cut quartz plates, *Int. J. Solids Structures*, **5**, 1-15, 1969.

[80] R. D. Mindlin, High frequency vibrations of quartz plates by expansion in series of Ekstein functions, *Int. J. Solids Structures*, **16**, 785-791, 1980.

[81] H. F. Tiersten, Wave propagation in an infinite piezoelectric plate, *J. Acoust. Soc. Am*., **35**, 234-239, 1963.

[82] H. F. Tiersten, Analysis of intermodulation in thickness-shear and trapped energy resonators, *J. Acoust. Soc. Am*., **57**, 667-681, 1975.

[83] H. F. Tiersten, Analysis of trapped-energy resonators operating in overtones of coupled thickness shear and thickness twist, *J. Acoust. Soc. Am*., **59**, 879-888, 1976.

[84] H. F. Tiersten, Analysis of overtone modes in monolithic crystal filters, *J. Acoust. Soc. Am*., **62**, 1424-1430, 1977.

[85] H. F. Tiersten and R. C. Smythe, An analysis of contoured crystal resonators operating in overtones of coupled thickness shear and thickness twist, *J. Acoust. Soc. Am*., **65**, 1455-1460, 1979.

[86] H. F. Tiersten and R. C. Smythe. Coupled thickness-shear and thickness-twist vibrations of unelectroded AT-cut quartz plates, *J. Acoust. Soc. Am*., **78**, 1684-1689, 1985.

[87] R. D. Mindlin, Vibrations of quartz plates with the HP-67 pocket calculator, *Computers and Structures*, **10**, 751-759, 1979.

[88] H. J. McSkimin, Theoretical analysis of modes of vibration of isotropic rectangular plates having all surfaces free, *Bell System Technical Journal*, **23**, 151-177, 1944.

[89] H. J. He, J. S. Yang, J. A. Kosinski and J. Wang, Thickness-shear vibration of a rectangular quartz plate, *Acta Mechanica Solida Sinica*, in press

[90] C. J. Wilson, Vibration modes of AT-cut convex quartz resonators, *J. Phys. D*: *Appl. Phys*., **7**, 2449-2455, 1974.

[91] H. J. He, J. S. Yang and Q. Jiang, Thickness-shear and thickness-twist vibrations of circular AT-cut quartz plates, *Acta Mechanica Solida Sinica*, accepted.

[92] P. Li, F. Jin and J. S. Yang, Thickness-shear vibration of an AT-cut quartz resonator with a hyperbolic contour, *IEEE Trans. Ultrason*., *Ferroelect*., *Freq. Contr*., **59**, 1006-1012, 2012.

[93] W. J. Wang, R. X. Wu, J. Wang, J, K. Du and J. S. Yang, Thickness-shear acoustic modes in an elliptical quartz plate with nonuniform thickness, *IEEE Trans. Ultrason*., *Ferroelect*., *Freq. Contr*., in press.

[94] D. S. Stevens and H. F. Tiersten, An analysis of doubly rotated quartz resonators utilizing essentially thickness modes with transverse variation, *J Acoust. Soc. Am*., **79**, 1811-1826, 1986.

[95] B. K. Sinha, Doubly rotated contoured quartz resonators, *IEEE Trans. Ultrason*., *Ferroelect*., *Freq. Contr.*, **48**, 1162-1180, 2001.

[96] E. P. EerNisse, Analysis of thickness modes of contoured, doubly rotated, quartz resonators, *IEEE Trans. Ultrason*., *Ferroelect*., *Freq. Contr.*, **48**, 1351-1361, 2001.

[97] R. D. Mindlin, Optimal sizes and shapes of electrodes for quartz resonators, *J. Acoust. Soc. Am*., **43**, 1329-1331, 1968.

[98] Z. T. Yang and J. S. Yang, Optimal electrode shape and size of a few singly rotated quartz and langasite resonators, *IEEE Trans. Ultrason*., *Ferroelect*., *Freq. Contr*., **56**, 237-238, 2009.

[99] Z. T. Yang, J. S. Yang and Y. T. Hu, Optimal electrode shape and size of doubly rotated quartz plate thickness mode piezoelectric resonators, *Appl. Phys. Lett*., **92**, 103516, 2008.

[100] R. Bechmann, Elastic and piezoelectric constants of alpha-quartz, *Phys. Rev*., **110**, 1060-1061, 1958.

[101] B. A. Auld, *Acoustic Fields and Waves in Solids*, vol. 1, John Wiley and Sons, New York, 1973.

[102] B. P. Sorokin, P. P. Turchin, S. I. Burkov, D. A. Glushkov and K. S. Alexandrov, Influence of static electric field, mechanical pressure and temperature on the propagation of acoustic waves in $La_3Ga_5SiO_{14}$ piezoelectric single crystals, *Proc. IEEE Int. Frequency Control Symp*., 1996, pp. 161-169.

[103] Yu. V. Pisarevsky, P. A. Senushencov, P. A. Popov and B. V. Mill, New strong piezoelectric $La_3Ga_{5.5}Nb_{0.5}O_{14}$ with temperature compensation cuts, *Proc. IEEE International Frequency Control Symp.*, 1995, pp. 653-656.

[104] B. T. Sturtevant, P. M. Davulis and M. P. da Cunha, A new set of LGT constants and temperature coefficients extracted through resonant and pulse echo technique, *Proc. of IEEE Frequency Control Symp.*, 2007, pp. 754-758.

[105] P. M. Davulis and M. P. da Cunha, High-temperature langatate elastic constants and experimental validation up to 900°C, *IEEE Trans. Ultrason*., *Ferroelect*., *Freq. Contr*., **57**, 59-65, 2010.

[106] A. W. Warner, M. Onoe and G. A. Couqin, Determination of elastic and piezoelectric constants for crystals in class (3m), *J. Acoust. Soc. Am*., **42**, 1223-1231, 1967.

[107] R. T. Smith and F. S. Welsh, Temperature dependence of the elastic, piezoelectric, and dielectric constants of lithium tantalate and lithium niobate, *J. Appl. Phys*., **42**, 2219-2230, 1971.

[108] H. Jaffe and D. A. Berlincourt, Piezoelectric transducer materials, *Proc. of IEEE*, **53**, 1372-1386, 1965.

[109] G. Feuillard, M. Lethiecq, Y. Janin, C. Alemany, B. Jimenez, C. Miller and W. Wolny, Experimental determination of SAW properties of 5 standard piezoceramics, *Proc. IEEE Ultrasonics Symp*., 1994, pp. 447-451.

[110] J. G. Gualtieri, J. A. Kosinski and A. Ballato, Piezoelectric materials for acoustic wave applications, *IEEE Trans. Ultrason.*, *Ferroelect*., *Freq. Contr*., **41**, 53-59, 1994.

[111] K. Tsubouchi, K. Sugai and N. Mikoshiba, AlN material constants evaluation and SAW properties on AlN/Al_2O_3 and AlN/Si, *Proc. IEEE Ultrasonics Symp*., 1981, pp. 375-380.

This page intentionally left blank

Index

admittance 143, 154
air gap 115
antiplane 31, 35
array 63, 72, 258
AT-cut 29, 347

beam 72, 80
Bechmann's number 183, 325, 392
bending 72
Bessel equation 379
boundary condition 3
BT-cut 29

capacitance 112
Cauchy 323
ceramics 33, 402
charge 1, 4
compact matrix notation 4
compliance 38
compound resonator 97
constitutive relation 1, 30, 32, 34, 37, 38, 40
contoured resonator 282, 341, 363, 368, 376
couple stress 80
crystallographic axes 27, 39
current 4
cutoff frequency 178, 183

digonal axis 27, 319
dispersion 176, 177, 181, 185, 190, 192, 195, 197, 200, 215, 221, 229, 322, 325, 328, 393
doubly-rotated cut 28

effective mass 58
eigenvalue problem 6
electric potential 2
electrode
  full 108, 120, 123, 131, 332
  imperfectly bonded 123
  inertia 120
  lateral 113, 147
  misaligned 254
  optimal 392
  partial 243, 334
  separated 114, 138
  shear stiffness 131
  thick 131
elliptical coordinates 356
energy trapping 183, 246, 270, 290, 337, 373, 374, 381
enthalpy 1
equivalent mass 66, 75
extension 63, 324

face shear 174, 323
FGM 96
filter 272
flexure 323
fluid 24, 51, 54, 138, 147, 215
four vector 7
Fourier series 267, 273
Frequency spectra 314
Frobenius method 379
functionally graded material 96
fundamental mode 42

Green's identity 8

half space 208
harmonic 42
Helmholtz equation 284
Hermite polynomial 364
Hexagonal 35
hyperbolic contour 368
hypergeometric
  equation 371
  function 372

impedance 156

Lamé coefficients 19
langanate 399
langasite 27, 231, 232, 398
langatate 399
lateral field excitation 113, 147
Legendre equation 371
lithium niobate 31, 399
lithium tantalate 31, 400
long wave approximation 203, 222, 323, 325
Love wave 212

m-monoclinic 32
mass layer 13, 18, 44, 45, 47
  array 258
  asymmetric 47, 185, 298
  imperfertly bonded 190, 303
  nonuniform 298
  partial 183, 250
  stiffness 18, 196
  symmetric 179
  thick 200
mass ratio 45, 122, 259, 333,135, 336
Mathieu equation 285, 287
matrix notation 4
membrane 19
mesa resonator 265
monoclinic 29, 39, 50

orthogonality 9
overtone mode 42

parabolic contour 363, 376
particle 55
perturbation 12, 13, 15, 18, 21, 26, 45, 54
piezoelectric stiffening 107
plane stress, 304
plane stress 198, 304
plate
  circular 354
  elliptical 352, 376
  fully electroded 108, 120, 123, 131, 158, 160, 231, 239, 332, 349, 390
  partially electroded 243, 325, 334
  rectangular 350
  unelectroded 105, 156, 230, 232, 237, 330, 348, 389
polarized ceramics 33, 402
positive definite 2, 38

quartz 27, 397
quasistatic 70, 79

radiation 71
Rayleigh quotient 11
reciprocal theorem 8
rigid-body mode 42
rod 63
rotated Y-cut 29, 39
rotatory inertia 55

Saint Venant's principle 316
Sauerbrey equation 44
SC-cut 28, 387
scalar equation
  AT-cut 347
  canonical form 391
self-adjointness 8

separation of variable 239, 254, 267, 273, 284, 305, 330, 343, 364
shear-horizontal 31, 35, 173, 233
shear-slip 123, 191, 303
shell 18
singly-rotated cut 29
stiffening 107
stiffness 38
straight crested 319, 325, 326
strain energy 37

thickness field excitation 108
thickness shear 41
thickness stretch 41
thickness-twist 175
thin film approximation 206
tilted edge 233
transient 159
trigonal axis 27, 31

variation 11, 12
viscoelasticity 160
viscosity 25, 52, 218

Weber's equation 344, 364